

NOVEL MAGNETIC NANOSTRUCTURES

Unique Properties and Applications

Edited by
Natalia Domracheva
Maria Caporali
Eva Rentschler

Micro & Nano Technologies Series

Novel Magnetic Nanostructures

This page intentionally left blank

Novel Magnetic Nanostructures

Unique Properties and Applications

Edited by

Natalia Domracheva

Maria Caporali

Eva Rentschler



Elsevier
Radarweg 29, PO Box 211, 1000 AE Amsterdam, Netherlands
The Boulevard, Langford Lane, Kidlington, Oxford OX5 1GB, United Kingdom
50 Hampshire Street, 5th Floor, Cambridge, MA 02139, United States

Copyright © 2018 Elsevier Inc. All rights reserved.

No part of this publication may be reproduced or transmitted in any form or by any means, electronic or mechanical, including photocopying, recording, or any information storage and retrieval system, without permission in writing from the publisher. Details on how to seek permission, further information about the Publisher's permissions policies and our arrangements with organizations such as the Copyright Clearance Center and the Copyright Licensing Agency, can be found at our website: www.elsevier.com/permissions.

This book and the individual contributions contained in it are protected under copyright by the Publisher (other than as may be noted herein).

Notices

Knowledge and best practice in this field are constantly changing. As new research and experience broaden our understanding, changes in research methods, professional practices, or medical treatment may become necessary.

Practitioners and researchers must always rely on their own experience and knowledge in evaluating and using any information, methods, compounds, or experiments described herein. In using such information or methods they should be mindful of their own safety and the safety of others, including parties for whom they have a professional responsibility.

To the fullest extent of the law, neither the Publisher nor the authors, contributors, or editors, assume any liability for any injury and/or damage to persons or property as a matter of products liability, negligence or otherwise, or from any use or operation of any methods, products, instructions, or ideas contained in the material herein.

Library of Congress Cataloging-in-Publication Data

A catalog record for this book is available from the Library of Congress

British Library Cataloguing-in-Publication Data

A catalogue record for this book is available from the British Library

ISBN: 978-0-12-813594-5

For information on all Elsevier publications
visit our website at <https://www.elsevier.com/books-and-journals>



Publisher: Matthew Deans

Acquisition Editor: Kayla Dos Santos

Editorial Project Manager: Natasha Welford

Production Project Manager: Joy Christel Neumarin Honest Thangiah

Cover Designer: Matthew Limbert

Typeset by SPi Global, India

Dedication

Dedicated to E.K. Zavoisky, who discovered the phenomenon of electron paramagnetic resonance in 1944.

This page intentionally left blank

Contents

Contributors	xiii
Preface	xv
1: Molecular Nanomagnets Based on <i>f</i>-Elements	1
Eufemio Moreno-Pineda, Lydia E. Nodaraki, Florian Tuna	
1.1 Introduction.....	1
1.2 General Aspects of <i>4f</i> and <i>5f</i> Ions.....	3
1.2.1 Electronic Structure of Lanthanides.....	3
1.2.2 Electronic Structure of Actinides.....	4
1.3 Slow Magnetic Relaxation in <i>f</i> -Element Nanomagnets.....	6
1.3.1 Effect of Single-Ion Anisotropy.....	6
1.3.2 Effect of Local Geometry.....	7
1.3.3 Symmetry Aspects.....	9
1.3.4 Magnetic Relaxation Mechanisms.....	11
1.4 Experimental Methods.....	13
1.4.1 DC Magnetometry.....	14
1.4.2 AC Magnetometry.....	15
1.4.3 μ -SQUID Arrays.....	17
1.5 Slow-Relaxing Systems.....	18
1.5.1 <i>f</i> -Elements Single-Ion Magnets (<i>f</i> -SIMs).....	18
1.5.2 <i>f</i> -Elements Single-Molecule Magnets (<i>f</i> -SMMs).....	31
1.5.3 <i>f</i> -Elements Single-Chain Magnets (<i>f</i> -SCM).....	39
1.6 Conclusions and Perspectives.....	44
References.....	45
2: Metallocrown Complexes Reaching the Nanosize Regime	51
Angeliki A. Athanasopoulou, Christoph Gamer, Lara Völker, Eva Rentschler	
2.1 Introduction.....	51
2.2 Metallocrown Complexes.....	52
2.2.1 Ligands.....	52
2.2.2 Metal Ion Variation— <i>3d</i> to <i>4f</i> Compounds.....	54
2.2.3 Luminescent Metallocrown Complexes.....	61
2.2.4 Metallocrown Complexes as Single-Molecule Magnets (SMMs).....	70
2.3 Moving from 0 to 3D Structures.....	80
2.3.1 Metallocrown Linkage.....	80

2.3.2 Multidimensionality of Extended Networks	85
2.4 Conclusion and Perspectives	91
References.....	92
Further Reading	96
3: Multifunctional Properties of γ-Fe₂O₃ Nanoparticles Encapsulated Into Liquid-Crystalline Poly(propylene imine) Dendrimer.....	97
Natalia Domracheva	
3.1 Introduction.....	97
3.2 Presentation of the Iron-Dendrimeric Nanocomposite and Identification of Its Liquid-Crystalline Properties.....	99
3.3 Characterization of γ -Fe ₂ O ₃ NPs by Electron Magnetic Resonance	101
3.4 Mössbauer Spectroscopy Study.....	106
3.5 Optical Properties and the Band Gap Width of γ -Fe ₂ O ₃ NPs.....	109
3.6 Photoinduced Superparamagnetic Effect in γ -Fe ₂ O ₃ NPs: EPR Detection	113
3.7 EMR Searching of Quantum Behavior of Superparamagnetic γ -Fe ₂ O ₃ Nanoparticles in Dendrimeric Nanocomposite	116
3.8 Conclusion	120
References.....	121
4: Magnetic Disorder in Nanostructured Materials.....	127
Giuseppe Muscas, Nader Yaacoub, Davide Peddis	
4.1 Introduction.....	127
4.2 Magnetism in Nanostructures: An Overview	128
4.2.1 Magnetic Anisotropy at the Nanoscale	129
4.2.2 Superparamagnetism.....	132
4.2.3 Magnetic Interactions at the Nanoscale: Supermagnetism.....	134
4.3 Magnetic Disorder at the Nanoscale	136
4.3.1 Noncollinear Spin Structure in Nanostructured Spinel Ferrites	137
4.3.2 Experimental Investigation of Magnetic Disorder: Mössbauer Spectrometry	139
4.4 Magnetic Properties of Spinel Ferrites Nanoparticles: Influence of the Magnetic Disorder	143
4.4.1 Magnetic Properties of CoFe ₂ O ₄ Nanoparticles: Effect of the Magnetic Structure.....	143
4.4.2 Magnetic Properties of Spinel Ferrite Nanoparticles: Effect of the Chemical Composition.....	149
4.4.3 Surface and Interface Magnetism: The Role of Molecular Coating.....	152
4.5 Conclusions and Perspectives	156
References.....	158
5: Self-Assembly of Magnetic Iron Oxide Nanoparticles Into Cuboidal Superstructures	165
Sabine Rosenfeldt, Stephan Förster, Thomas Friedrich, Ingo Rehberg, Birgit Weber	
5.1 Motivation.....	165

5.1.1 Properties of Magnetic Iron Oxide Nanoparticles	165
5.1.2 Applications of Magnetic Iron Oxide Nanoparticles.....	166
5.2 Synthesis and Properties of Nanoparticles.....	166
5.2.1 Synthesis of Spherical and Cubic Iron Oxide Nanoparticles	167
5.2.2 Magnetic Properties of the Nanoparticles.....	171
5.3 Self-Assembly Into Superstructures	173
5.3.1 Crystallization of Cuboids.....	174
5.3.2 Influence of the Magnetic Field.....	177
5.4 Conclusion	187
Acknowledgments	188
References.....	188
6: Nanomaterials for Magnetoplasmonics	191
Francesco Pineider, Claudio Sangregorio	
6.1 Introduction.....	191
6.2 Experimental Methods for the Study of Magnetoplasmonics and Related Effects.....	193
6.2.1 Polarization States of Light.....	193
6.2.2 Magneto-Optical Techniques	195
6.3 Plasmonics and Magnetoplasmonics.....	197
6.3.1 Plasmonics and Active Plasmonics.....	197
6.3.2 Magnetoplasmonics	201
6.4 Magnetoplasmonics in Single-Component Nanostructures	202
6.4.1 Nonmagnetic Metals.....	202
6.4.2 Ferromagnetic Metals	208
6.5 Hybrid Magnetoplasmonic Nanostructures	210
6.5.1 Plasmonic Metals/Magnetic Metals	210
6.5.2 Plasmonic Metals/Magnetic Oxides.....	214
6.5.3 Plasmonic Metals/Magnetic Molecules	215
6.6 Conclusion	217
Acknowledgment	217
References.....	217
7: Highly Responsive Magnetoactive Elastomers.....	221
Mikhail Shamonin, Elena Yu. Kramarenko	
7.1 Introduction.....	221
7.2 Constitutive Materials.....	222
7.2.1 Polymer Matrix.....	222
7.2.2 Filler Particles.....	223
7.2.3 Filler-Filler Interactions in Magnetic Fields.....	225
7.3 Mechanical Properties in Homogeneous Magnetic Fields	226
7.3.1 Magnetostriction	226
7.3.2 Magnetorheological Effect	228
7.3.3 Filler-Matrix Interactions in Magnetic Fields: Payne Effect.....	232
7.3.4 Hysteretic Behavior	234

7.3.5 Magnetodeformation in Inhomogeneous Fields.....	235
7.4 Electromagnetic and Acoustic Properties	237
7.5 Prospects of Research and Development	238
7.6 Conclusion	239
Acknowledgments	240
References.....	240
8: Neel Effect: Exploiting the Nonlinear Behavior of Superparamagnetic Nanoparticles for Applications in Life Sciences up to Electrical Engineering	247
Luc Lenglet, Laurence Motte	
8.1 Louis Néel, Superparamagnetism, and Neel Effect®	247
8.2 Neel Effect for Particle Sensing.....	249
8.2.1 Magnetic Immunoassays	249
8.2.2 Magnetic Particle Imaging	254
8.2.3 Real-Time Monitoring.....	255
8.2.4 Magnetic Colorization.....	257
8.3 Neel Effect for Magnetic Field Sensing	260
8.3.1 Current Sensors.....	260
8.3.2 Position Sensors.....	262
References.....	262
9: Ferrimagnetic Heterostructures for Applications in Magnetic Recording.....	267
Florin Radu, Jaime Sánchez-Barriga	
9.1 Magnetic Recording: Fundamentals and Perspectives	267
9.1.1 Perpendicular Magnetic Recording and Superparamagnetism.....	269
9.1.2 Future Areal Density Progress and Emergent Technologies.....	269
9.1.3 Heat-Assisted Magnetic Recording.....	270
9.1.4 Heat-Assisted Magnetic Recording on Bit-Patterned Media	271
9.1.5 Spin-Valve Systems for Magnetic Read Heads.....	273
9.1.6 Tunneling Magnetoresistance.....	276
9.1.7 Spin-Transfer Torque Effect	278
9.1.8 Spin Hall and Rashba-Edelstein Effects	280
9.1.9 All-Optical Switching and Topological Skyrmions.....	281
9.2 Ferrimagnetism	283
9.3 Selected Examples of Ferrimagnetic Thin Films	287
9.3.1 Ferrimagnetic Spin Valves	295
9.4 Ferrimagnetic Nanostructures for Magnetic Memory Bits.....	297
9.4.1 Magnetic Properties of FeTb Nanodots	303
9.4.2 DyCo ₅ Antidots for Heat-Assisted Magnetic Recording.....	306
9.4.3 Laser-Induced Switching of FeGdCo Nanostructures	311
9.5 Conclusion and Outlook.....	314
References.....	315

10: Nanomagnetic-Supported Catalysts	333
Vincent Terrasson, Erwann Guénin	
10.1 Introduction.....	333
10.2 Synthesis and Property of Magnetic Nanoparticles.....	334
10.3 Preparation of NanoMagnetic-Supported Catalysts.....	336
10.3.1 Uncoated Nanoparticles.....	336
10.3.2 Nanoparticle Coating.....	337
10.4 Different Types of Catalysts Immobilized Onto Nanomagnetic Support.....	341
10.4.1 Immobilization of Enzymes	341
10.4.2 Immobilization of Organocatalysts	343
10.4.3 Immobilization of Organometallic Catalysts or Metal Nanoparticles	344
10.5 Application of Magnetic Nanocatalysts.....	345
10.5.1 Reduction Reactions.....	345
10.5.2 Oxidation Reactions	347
10.5.3 C—C Bond Formation	349
10.5.4 C-Heteroatom Bond Formation.....	352
10.5.5 Cycloaddition Reactions.....	353
10.5.6 C—H Activation.....	355
10.5.7 Hydrolysis.....	355
10.5.8 Kinetic Resolution by Esterification.....	355
10.6 Limitations and Outlooks	356
Acknowledgments	357
References.....	358
11: Spin and Charge Tunneling Transport in Magnetic Tunnel Junctions With Embedded Nanoparticles	373
Artur Useinov, Chih-Huang Lai, Niazbeck Kh. Useinov, Lenar R. Tagirov	
11.1 Introduction.....	373
11.2 Giant Magnetoresistance in Ferromagnetic Heteronanocontacts	375
11.3 Tunnel Magnetoresistance in Single- and Double-Barrier MTJ	380
11.4 Spin-Transfer Torque, Size Distribution, and Temperature-Related Effects in MTJs With Embedded Nanoparticles	387
11.5 Conclusions.....	395
Acknowledgments	397
References.....	397
Further Reading	400
12: An Overview of Spin Crossover Nanoparticles.....	401
David J. Harding	
12.1 Introduction to Spin Crossover	401
12.2 Nanoparticles and Nanocrystals.....	403
12.2.1 Triazole Systems.....	403
12.2.2 Hofmann Systems.....	405
12.2.3 Molecular Systems	406

12.3 Spin Crossover Nanocomposites.....	409
12.3.1 Silica Systems.....	409
12.3.2 Au Systems.....	411
12.3.3 Polymer Systems.....	412
12.3.4 Cellulose Systems.....	412
12.3.5 Graphene Systems.....	414
12.4 Spin Crossover Thin Films.....	415
12.4.1 Au, Cu, and Silica.....	415
12.4.2 Polymers.....	417
12.5 SCO Devices.....	417
12.5.1 Single Molecule Devices.....	417
12.5.2 Nanoparticle Systems.....	419
12.6 Conclusions and Future Prospects.....	422
Acknowledgments.....	422
References.....	423

**13: Magnetic Metal-Nonstoichiometric Oxide Nanocomposites:
Structure, Transport, and Memristive Properties..... 427**

**Vladimir V. Rylkov, Vyacheslav A. Demin, Andrey V. Emelyanov,
Alexander V. Sitnikov, Yurii E. Kalinin, Victor V. Tugushev,
Alexander B. Granovsky**

13.1 Introduction.....	427
13.2 Samples and Investigation Methods.....	428
13.2.1 Samples Preparation.....	428
13.2.2 Methods of Investigation and Technique.....	432
13.3 Structural Characterization.....	432
13.4 Temperature Dependence of Conductivity.....	435
13.5 Anomalous Hall Effect and Magnetization.....	437
13.5.1 Background and Motivation.....	437
13.5.2 Scaling Behavior of AHE and Peculiarities of Magnetization.....	439
13.5.3 Nature of Paramagnetic Centers.....	447
13.5.4 Qualitative Model of the AHE Behavior.....	448
13.5.5 Manifestation of Superferromagnetic Ordering.....	452
13.6 Memristive Properties.....	453
13.6.1 Introduction to Memristive Properties of Oxides.....	453
13.6.2 Resistive Switching Effects in Nanocomposites.....	455
13.6.3 Qualitative Model of the Resistive Switching Mechanism.....	457
13.7 Concluding Remarks.....	460
Acknowledgments.....	462
References.....	462

Index..... 465

Contributors

Angeliki A. Athanasopoulou University of Mainz; Graduate School of Excellence Materials Science in Mainz, Mainz, Germany

Vyacheslav A. Demin National Research Centre “Kurchatov Institute”, Moscow, Russia

Natalia Domracheva Zavoisky Physical-Technical Institute, Federal Research Center “Kazan Scientific Center of RAS”, Kazan, Russia

Andrey V. Emelyanov National Research Centre “Kurchatov Institute”, Moscow, Russia

Stephan Förster University of Bayreuth, Bayreuth, Germany

Thomas Friedrich University of Bayreuth, Bayreuth, Germany

Christoph Gamer Graduate School of Excellence Materials Science in Mainz, Mainz, Germany

Alexander B. Granovsky Lomonosov Moscow State University, Moscow, Russia

Erwann Guénin Sorbonne Universités, Université de Technologie de Compiègne, Integrated Transformations of Renewable Matter Laboratory (EA TIMR 4297 UTC-ESCOM), Compiègne, France

David J. Harding Walailak University, Nakhon Si Thammarat, Thailand

Yurii E. Kalinin Voronezh State Technical University, Voronezh, Russia

Elena Yu. Kramarenko Faculty of Physics, Lomonosov Moscow State University; A.N. Nesmeyanov Institute for Organoelement Compounds RAS, Moscow, Russia

Chih-Huang Lai National Tsing Hua University, Hsinchu, Taiwan

Luc Lenglet Normafin, Levallois-Perret, France

Eufemio Moreno-Pineda Institute of Nanotechnology (INT), Karlsruhe Institute of Technology (KIT), Eggenstein-Leopoldshafen, Germany

Laurence Motte Inserm, U1148, Laboratory for Vascular Translational Science, UFR SMBH, Université Paris 13, Sorbonne Paris Cité, Bobigny, France

Giuseppe Muscas Department of Physics and Astronomy, Uppsala University, Uppsala, Sweden

Lydia E. Nodaraki University of Manchester, Manchester, United Kingdom

Davide Peddis Institute of Structure of Matter—CNR, Monterotondo Scalo, Rome, Italy

Francesco Pineider Department of Chemistry and Industrial Chemistry, University of Pisa and INSTM, Pisa, Italy

Florin Radu Helmholtz-Zentrum Berlin für Materialien und Energie, Berlin, Germany

Ingo Rehberg University of Bayreuth, Bayreuth, Germany

Eva Rentschler University of Mainz, Mainz, Germany

Sabine Rosenfeldt University of Bayreuth, Bayreuth, Germany

Vladimir V. Rylkov National Research Centre “Kurchatov Institute”, Moscow, Russia

Contributors

Jaime Sánchez-Barriga Helmholtz-Zentrum Berlin für Materialien und Energie, Berlin, Germany

Claudio Sangregorio ICCOM—CNR and INSTM, Sesto Fiorentino, Italy

Mikhail Shamonin Ostbayerische Technische Hochschule Regensburg, Regensburg, Germany

Alexander V. Sitnikov Voronezh State Technical University, Voronezh, Russia

Lenar R. Tagirov Kazan Federal University; E. K. Zavoisky Physical-Technical Institute of RAS; Institute for Advanced Studies of ASRT, Kazan, Russia

Vincent Terrasson Sorbonne Universités, Université de Technologie de Compiègne, Integrated Transformations of Renewable Matter Laboratory (EA TIMR 4297 UTC-ESCOM), Compiègne, France

Victor V. Tugushev National Research Centre “Kurchatov Institute”, Moscow, Russia

Floriana Tuna University of Manchester, Manchester, United Kingdom

Artur Useinov National Chiao Tung University, Hsinchu, Taiwan

Niazbeck Kh. Useinov Kazan Federal University, Kazan, Russia

Lara Völker University of Mainz, Mainz, Germany

Birgit Weber University of Bayreuth, Bayreuth, Germany

Nader Yaacoub Institute of Molecules and Materials of Le Mans CNRS UMR-6283, University of Le Mans, Le Mans, France

Preface

A sharp increase in research activity in the field of magnetic nanostructures prompted us to present new scientific results obtained in the last decade. Magnetic nanoscale materials are the key to the future of the storage industry.

The demand for higher density of information storage and the emergence of completely new technologies call for entirely new types of magnetic nanostructures. This book provides the latest research on novel magnetic nanostructures, including molecular nanomagnets, magnetic dendrimers, self-assembling magnetic nanoparticles, nanoparticles with spin-crossover properties, multifunctional nanostructures, and much more.

Nanomagnets based on *d*- and *f*-block coordination compounds as single-molecule magnets demonstrate properties that are suitable for quantum information processing. The book reviews the synthesis, design, characterization, and detection of unusual properties in new magnetic nanostructures. It discusses the physical properties and potential industry-oriented applications such as magnetic data storage, magnetic sensors, magnetic tunnel junctions, spintronics, and biomedical applications.

This book is primarily intended for graduate students, but will be of great interest also to all scientists and engineers working in field of magnetic nanoscale materials.

This page intentionally left blank

Molecular Nanomagnets Based on *f*-Elements

Eufemio Moreno-Pineda*, Lydia E. Nodaraki†, Floriana Tuna†

*Institute of Nanotechnology (INT), Karlsruhe Institute of Technology (KIT), Eggenstein-Leopoldshafen, Germany, †University of Manchester, Manchester, United Kingdom

1.1 Introduction

The first observation of slow magnetic relaxation in a single molecule in response to an energy barrier that opposes the reversal of the magnetization was reported in the beginning of 1990, for $[\text{Mn}_{12}\text{O}_{12}(\text{OAc})_{16}(\text{H}_2\text{O})_4]\cdot 4\text{H}_2\text{O}\cdot 2\text{AcOH}$ [1–3]. The complex featured a $\{\text{Mn}_{12}\}$ cage in which four Mn(IV) ($s = 3/2$) and eight Mn(III) ($s = 2$) ions couple magnetically to yield a well-isolated $S = 10$ ground state at low temperatures. Notably, this large spin ground state is characterized by a large negative zero field splitting (ZFS) term, D , resulted from the nearly collinear alignment of the Jahn-Teller axes of the Mn(III) ions. The resulting magnetic anisotropy causes significant energy level splitting, and thus a large energy barrier that opposes the reversal of the magnetization. This leads to slow magnetic relaxation that is when the molecule remains magnetized after removal of the applied magnetic field. Below a certain temperature, generally associated with the blocking temperature (T_B) of the magnetic moment, an open hysteresis can be observed whose origin is purely molecular. Molecules exhibiting such unusual properties are termed single-molecule magnets (SMMs) [4–7], although it is very common for researchers to name monometallic complexes exhibiting slow magnetic relaxation as single-ion magnets (SIMs) [8–10], in order to distinguish them from polymetallic cages where exchange-coupling interactions between metal centers can also occur. A plethora of magnetic and quantum phenomena have been observed in these systems, including quantum tunneling of the magnetization and Berry phase quantum interference, among others [11,12]. These properties make SMMs attractive candidates for a number of applications, including for innovative quantum information technologies, as molecular magnetic memories for high-density data storage, molecular quantum information processors, molecular transistors, or spintronic devices, to cite only few from their many applications [13–18].

In the early stage of the molecular magnetism field, most of the reported SMMs were based on transition metal ions, where exchange coupling between neighboring metal ions resulted in a

large spin ground state (S) with a large and negative ZFS term (D), and thus a high relaxation barrier $U_{\text{eff}} = DS^2$, and particularly on using Mn(III) ions as spin carriers due to the Jahn-Teller characteristics [19–21]. The same property was subsequently observed in polymetallic complexes of other metal ions [22–25].

Synthesizing exchange-coupled SMMs with large U_{eff} barriers is a real challenge, due to the difficulty to simultaneously achieve strong magnetic exchange within polymetallic cages of several metal centers (preferably of ferromagnetic nature, to produce a large spin, S), and collinear arrangement of the local Ising axes (requested to enhance the overall molecular anisotropy). To date, only few polymetallic clusters with SMM behavior were found to display energy barriers higher than those of $\{\text{Mn}_{12}\}$ -type systems [21,26–28].

A novel approach was introduced by Ishikawa and coworkers in 2003, who discovered the occurrence of slow magnetic relaxation in monometallic lanthanide phthalocyaninato double-decker complexes of formula $(\text{Bu}_4\text{N})[\text{LnPc}_2]$ ($\text{Ln} = \text{Tb(III)}$ or Dy(III) ; $\text{Pc} = \text{phthalocyanine}$) [29,30]. Notably, the energy barrier associated with the Tb derivative turned to be an order of magnitude higher than that of any transition metal polynuclear-SMM [29]. In these systems, termed single-ion magnets (SIMs), the magnet-like behavior (i.e., slow magnetic relaxation) is associated with the unquenched spin-orbit coupling of the $4f$ ion, and the ligand field surrounding that metal [8]. Such factors dictate the order and the gaps existent between various m_J (J is the angular momentum) states, and thus the height of the relaxation barrier. Nowadays, nanomagnets based on lanthanides and actinides are intensively researched. A significant number of f -block SIMs have already been reported [8,31]. Many lanthanide-based SIMs were found to display incredibly high energy barriers and improved blocking temperatures, compared to d -block SIMs or SMMs [32–45]. Moreover, some design criteria developed for f -SIMs were subsequently applied to transition metals, enabling access to transition metal single-ion magnets (d -SIMs) with energy barriers much larger than those of the exchange-coupled polymetallic SMMs [46–51]. Interestingly, the slow magnetization dynamics of polymetallic cages based on lanthanide were often found to be a summation of single-ion behaviors [52–54]. Nevertheless, both lanthanide-SIMs and lanthanide-SMMs attract a lot of interest in the magnetism community, being proposed for various types of applications, including for quantum information technologies [8,17,18,55–57]. Fascination around actinide-SMMs is fueled by the larger extent of the $5f$ orbitals compared to the $4f$ orbitals, allowing for stronger ligand-metal interactions, and thus a stronger magnetic exchange [8,31,58–61].

It is the scope of this chapter to present the reader with a succinct introduction to the f -element single-molecule magnets field. Following a brief description of the general characteristics of lanthanide and actinide ions, we will discuss key aspects regarding the slow magnetic relaxation property of f -element nanomagnets, the relaxation mechanisms involved, and the experimental methods commonly used in the investigation of SMMs. The magnetic characteristics of some single-ion magnets (SIMs), regarded as zero dimensional polymetallic

SMMs, and of one-dimensional SMMs, termed single-chain magnets (SCMs), will also be summarized. This section is far from complete, due to the high number of publications and impressive properties of *f*-based SMMs reported so far. A selection of examples will be used to bring insights into magneto-structural correlations, and key design principles underpinning the performance of *f*-block SMMs. The last section is dedicated to conclusions and perspectives.

1.2 General Aspects of 4*f* and 5*f* Ions

Many *f*-block metal complexes exhibit interesting electronic, magnetic, and optical properties, which make them attractive candidates for a wide range of applications [62–66]. In particular, 4*f* molecular nanomagnets are investigated as potential cryogenic magnetic coolers [67–69], high-density information storage devices [31], and quantum devices [17,18,55–57]. On the other hand, actinides have been largely used as nuclear power fuels, and ordinary smoke detectors. More recently, the more diffused nature of 5*f*-orbitals has led to their investigation in molecular magnetism, on the ground that a larger anisotropy is possible in these systems [8,31]. Here we discuss the electronic structure of *f*-block metal ions and analyze the most important factors that contribute to their unusual magnetic behavior.

1.2.1 Electronic Structure of Lanthanides

The electronic configuration of lanthanides (known also as rare earth elements) is [Xe] 4*f*^{*n*−1}5*d*¹6*s*², with the 4*f*-orbital being well shielded by the 5*s* and 5*p* orbitals (Fig. 1.1). The inner nature of the 4*f* orbitals renders a highly stable +3 oxidation state, and prevents the 4*f*-orbital to participate in extended covalent bonding to ligands. It is worth noting that

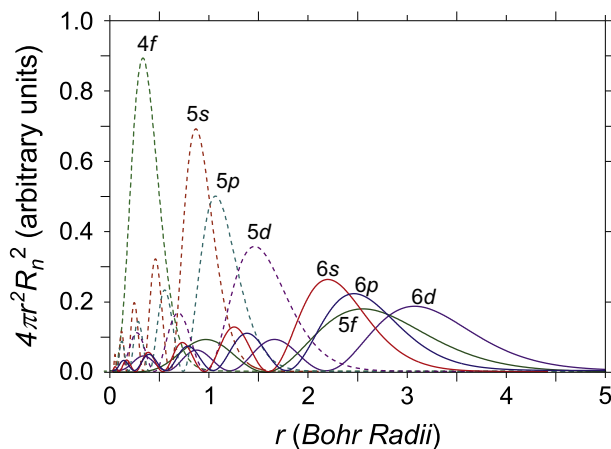


Fig. 1.1

Radial distribution functions for 4*f*, 5*s*, 5*p*, 5*d*, 5*f*, 6*s*, 6*p*, and 6*d* orbitals, showing that the 4*f* orbitals are less diffused compared to 5*f* orbitals.

scandium and yttrium are also regarded as rare earth elements, despite lacking electrons in the 4*f* shells. Taking advantage of their diamagnetic nature, Y(III) molecular analogues are commonly used as diamagnetic hosts for the magnetic dilution of other lanthanide complexes. This is particularly useful for the study of the magnetic properties of the molecules in a nearly isolated environment, where dipolar magnetic fields are strongly reduced by such magnetic dilution.

As the atomic number increases along the 4*f* series, the atomic radius decreases gradually from La to Lu. This effect has been termed as “lanthanide contraction” and is due to poor screening of 4*f* electrons. For example, an increase in electron repulsion cannot compensate for the increase in nuclear charge; thus, the effective nuclear charge (Z_{eff}) increases across the period, leading to pronounced orbital contraction.

Lanthanides exhibit several coordination numbers and geometries. Most commonly, they form compounds with a large coordination number ($n \geq 6$). In a limited number of cases, di-coordinate 4*f* complexes could be isolated through using very bulky organic ligands [70]. Such low-coordinate ligand environments are important for magnetism. Early reports by Ungur and Chibotaru [71] have predicted enormous axial anisotropy, and thus huge energy barriers, for one- and two-coordinated dysprosium(III) systems, which was recently probed experimentally [38,72].

The large anisotropy of the lanthanide ions is primarily due to their strong spin-orbit coupling (SOC), which exceeds that of transition metal ions, and is stronger than the ligand-field (LF) splitting. The Russell-Saunders (RS) coupling, applicable when the electron-electron repulsion (Coulomb interaction) is considerably stronger than SOC ($\hat{H}_{\text{res}} > \hat{H}_{\text{SO}}$), facilitates the coupling of the total spin (S) with the orbital angular momentum (L). This gives the total angular momentum (J), whose size varies in the range $|L - S| \leq J \leq L + S$. Thus, the single-ion electronic configurations of 4*f*-ions consist of $^{2S+1}L_J$ terms (Fig. 1.2). For a Dy(III) ion (4*f*⁹ configuration), for example, the spin-orbit coupling stabilizes a ${}^6H_{15/2}$ ground state, where $S = 5/2$, $L = 5$ and $J = 15/2$ (Table 1.1). In the absence of a crystal field, the $2J + 1$ states are equal in energy. However, an axial ligand field can remove the degeneracy of the ground state, placing the excited m_J multiplets at large energy separations with respect to the ground m_J multiplet. This situation gives rise to an energy barrier that opposes the relaxation of the magnetization, as it is discussed in Section 1.3. Bigger the energy separation to the lowest lying excited states, slower the relaxation of the magnetic moment.

1.2.2 Electronic Structure of Actinides

The electronic structure of 5*f* elements is far more complicated than that of 4*f* elements. For example, the oxidation states from Ac to Pu resemble more those of the transition metals, with a variety of stable oxidation states, while for Bk to Lr ions, a more lanthanide-like behavior

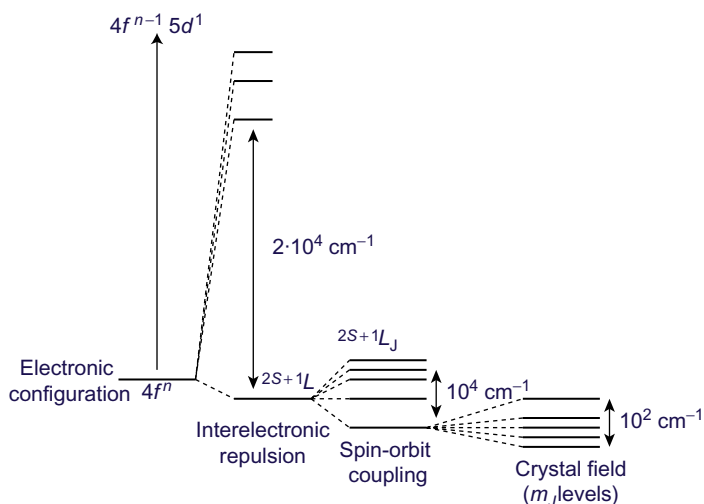


Fig. 1.2

Schematic energy diagram showing the relative magnitude of the interelectronic repulsion, the spin-orbit coupling, and ligand-field effects.

Table 1.1 Ground and first excited state terms of $4f$ ions, g_j -values, and energy gaps to the first excited states

Ln(III)	Configuration	Ground Term	First Excited State Term	g_j	Energy (cm^{-1})
La	$4f^0$	1S_0	1S_1	—	—
Ce	$4f^1$	$^2F_{5/2}$	$^2F_{7/2}$	6/7	2200
Pr	$4f^2$	3H_4	3H_5	4/5	2100
Nd	$4f^3$	$^4I_{9/2}$	$^4I_{11/2}$	8/11	1900
Pm	$4f^4$	5I_4	5I_5	3/5	1600
Sm	$4f^5$	$^6H_{5/2}$	$^6H_{7/2}$	2/7	1000
Eu	$4f^6$	7F_0	7F_1	—	300
Gd	$4f^7$	$^8S_{7/2}$	$^6P_{7/2}$	2	30,000
Tb	$4f^8$	7F_6	7F_5	3/2	2000
Dy	$4f^9$	$^6H_{15/2}$	$^6H_{13/2}$	4/3	—
Ho	$4f^{10}$	5I_8	5I_7	5/4	—
Er	$4f^{11}$	$^4I_{15/2}$	$^4I_{13/2}$	6/5	6500
Tm	$4f^{12}$	3H_6	3H_5	7/6	—
Yb	$4f^{13}$	$^2F_{7/2}$	$^2F_{5/2}$	8/7	10,000
Lu	$4f^{14}$	1S_0	—	—	—

is observed with the +3 oxidation state being the most stable. Moreover, actinides possess more diffused $5f$ -orbitals, compared to lanthanides (Fig. 1.1), and therefore are more involved in bonding to ligand orbitals. Lastly, actinides, similar to lanthanides, can exhibit a large variety of coordination numbers.

From the magnetic viewpoint, the properties of actinides are more complicated than those of lanthanides. The energies of the $5f$ orbitals are strongly affected by the ligand field, and thus are more susceptible to ligand variations. This is particularly true for early actinides. It is also common for actinide complexes to exhibit extended covalency. The RS coupling approximation, where the spin-orbit coupling is treated as a perturbation, is not applicable for actinides, due to SOC being much stronger than the Coulomb (electrostatic) interaction. Similarly, a j - j coupling scheme, where the electrostatic repulsion is weaker compared to the spin-orbit coupling, is not applicable. Consequently, an intermediate coupling scheme between the RS and j - j models is a more appropriate model for actinides.

1.3 Slow Magnetic Relaxation in f -Element Nanomagnets

Slow relaxation of the magnetization is a characteristic of some systems to stay magnetized along a quantization axis (easy axis) for a long period of time, after removal of the magnetic field. For f -block elements, the slow-relaxation property is very sensitive to changes in the ligand-field environment and its symmetry, and relates to the local ion magnetic anisotropy. Some key aspects regarding the slow magnetic relaxation of f elements will be discussed in the next section. We also succinctly explain the different relaxation mechanisms involved.

1.3.1 Effect of Single-Ion Anisotropy

As explained in Section 1.2.1, the increased single-ion anisotropy of $4f$ -elements is primarily due to their large unquenched orbital angular momentum. With exception of gadolinium and lutetium, the electronic and magnetic properties of $4f$ ions are best described by the spin-orbit coupled quantum number (J) (vide supra). In this picture, the barrier to relaxation is determined by the energetic spacing of the m_J microstates. Importantly, despite the magnetic anisotropy being related to SOC (spin-orbit coupling), the nature of the ground m_J multiplet, and the energetic distribution of the low-lying m_J microstates are strongly dependent on crystal field effects (see Section 1.3.2). For example, a spacing between the ground state $m_J = \pm 6$ and the first excited state $m_J = \pm 5$ of ca. 400 cm^{-1} led to the observation of slow magnetic relaxation to 40–50 K in $(\text{Bu}_4\text{N})[\text{TbPc}_2]$ [29,30]. A much weaker behavior was observed for the isostructural Dy(III) derivative, $(\text{Bu}_4\text{N})[\text{DyPc}_2]$, consistent with a smaller energy gap to the lowest lying excited m_J microstate [29].

Dysprosium(III) has a $4f^9$ electronic configuration; SOC stabilizes the $^6\text{H}_{15/2}$ ground multiplet, characterized by $S = 5/2$, $L = 5$ and $J = 15/2$. Crystal field interactions can break the 16-fold degeneracy of the ground multiplet into eight Kramers doublets, $m_J = \pm 15/2, \pm 13/2, \pm 11/2, \pm 9/2, \pm 7/2, \pm 5/2, \pm 3/2, \pm 1/2$, whose energies depend on both the symmetry and strength of the ligand field. Strongly axial ligand fields are expected to stabilize the $m_J = \pm 15/2$ microstate (Fig. 1.3), placing the other states at high separations above the ground state. Stronger the

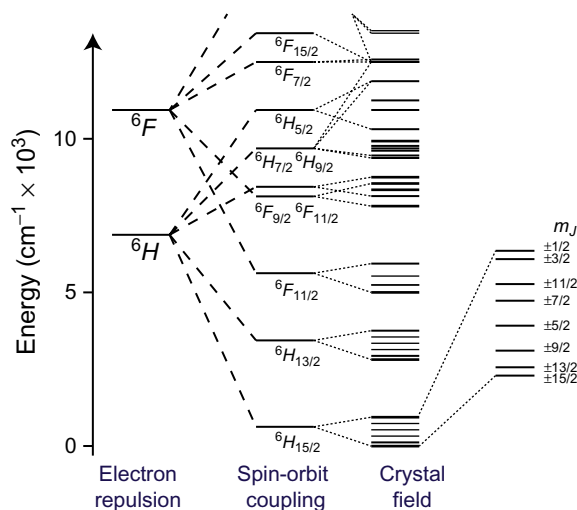


Fig. 1.3

Schematic energy diagram showing the relative magnitude of the interelectronic repulsion, spin-orbit coupling, and ligand-field effects. Low-energy electronic structure of the Dy(III) ion with sequential perturbations of electron-electron repulsions, spin-orbit coupling, and the crystal field.

axiality, bigger the Ising anisotropy is, and thus larger the energy separation between microstates is. This situation gives rise to slow magnetic relaxation, which often manifests as a hysteresis in the field dependence of the magnetization, because the magnetic moment is prevented to relax in time to its equilibrium value [8]. The loop width generally increases with increasing the field-sweeping rate, and upon lowering the temperature [35]. In some circumstances, relaxation of the magnetization via the lowest-lying excited states is blocked; thus, superior excited states would engage in spin relaxation. This leads to even longer magnetization relaxation times.

The ground terms and SOC constants associated with other lanthanide(III) ions are shown in Table 1.1.

1.3.2 Effect of Local Geometry

The large anisotropy of *f*-ions is due to their inherent strong SOC. Interestingly, the ligand field, although small compared to the spin-orbit coupling, is responsible for the splitting of the $2J + 1$ manifold, undoubtedly playing a key role in the determination of the SMM behavior. The key approach to high-performance SMMs is to systematically engineer a ligand field that provides a large splitting between $\pm m_J$ states. Rinehart and Long have proposed a simple electrostatic model allowing to predict which ligand environment is likely to favor SMM behaviors in *f*-element complexes [73].

The electron densities of lanthanide ions are determined by the quadrupolar moment of the electron cloud, resulting in three shapes: spherical (Gd^{III}), equatorially expanded or “*oblate*”

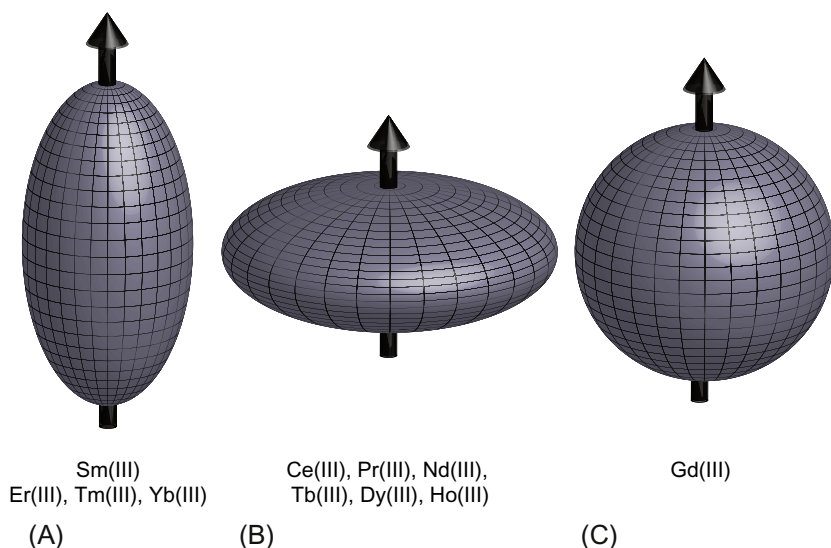


Fig. 1.4

Electron density distribution of trivalent lanthanide ions employing quadrupolar approximations:
 (A) prolate, (B) oblate, and (C) spherical electron densities.

(Ce^{III}, Pr^{III}, Nd^{III}, Tb^{III}, Dy^{III}, and Ho^{III}) and axially elongated or “prolate” (Pm^{III}, Sm^{III}, Er^{III}, Tm^{III}, and Yb^{III}) (Fig. 1.4). The isotropic nature of Gd^{III} makes this ion unsuitable for SMM purposes, while the high multiplicity of states associated with the series of late lanthanides makes these ions very appealing for the investigation of slow magnetization dynamics in single molecules. The axial electronic potential caused by the surrounding ligand field induces two energetically different orientations of the magnetic anisotropy, easy axis or easy plane, depending on the metal ion used. As a result, the ligand field maximizing highly anisotropic ground states can be inferred upon simple inspection of the lanthanide electron density and the ligand-field environment.

For example, highly axial ligand fields are best suited for oblate ions, such as Tb(III), Dy(III), and Ho(III), while axial ligand fields are more suited for prolate ions, such as Er(III) and Yb(III) (Fig. 1.5). Rinehart and Long rationalized the m_j ground and excited states of the archetypical TbPc₂, among other examples highlighting the application of their model [73]. A compressed ligand field acting on an oblate ion such as Dy(III) or Tb(III) favors an easy axis anisotropy due to a radial distribution of the electron densities. This is the case of the phthalocyanine MPC₂ system (M = Tb or Dy) [29,73]. The magnetic behaviors of several other f -based SMMs were associated with similar electrostatic effects. Conversely, the anisotropy axis of a prolate ion subjected to a compressed crystal field is not maximized. Similar conclusions have been drawn from ab initio calculations, which demonstrated that the oblate ions yield extremely large energy barriers in systems of highly axial ligand fields [71,74,75]. Additionally, an ab initio CASSCF model relying on calculations of the electrostatic field produced by charge on the

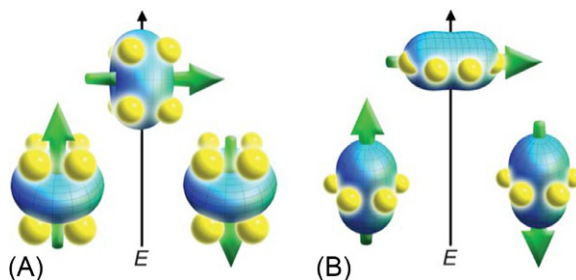


Fig. 1.5

Schematic representation of low- and high-energy configurations of *f*-orbital electron density of oblate (A) and prolate (B) electron density. The *thick arrow* represents the spin angular momentum coupled to the orbital moment. As observed, an axial-type crystals field minimizes the energy of m_j states with highest multiplicity, while prolate ions, an equatorial configuration, minimizes the m_j with highest multiplicity. *Reproduced with permission from J.D. Rinehart, J.R. Long, Exploiting single-ion anisotropy in the design of *f*-element single-molecule magnets, Chem. Sci. 2 (2011) 2078–2085. Royal Society of Chemistry.*

ligands within a valence bond model was shown to predict with ease the orientation of the anisotropy axis in Dy-SMMs, using crystallographic data alone [76].

Additionally, ligand modification provides an additional versatile route to controlling SMM behavior. Examples of ligand modifications include chemical modifications, such as oxidation or protonation; the substitution of coordinated donor atoms as a means to control the anisotropic properties of SMMs.

1.3.3 Symmetry Aspects

Another important aspect for the design of efficient SMMs concerns the symmetry of the ligand field surrounding the lanthanide ion, which removes the degeneracy of the $2J + 1$ microstates. The mathematical representation of the ligand field can be achieved employing the Stevens formalism [77], which leads to a Hamiltonian of the form:

$$H = \sum_{k=2,4,6} \beta_k \sum_{q=-k}^k B_k^q \hat{O}_k^q \quad (1.1)$$

where B_k^q and \hat{O}_k^q are crystal field parameters, β_k is the so-called Stevens constant that is contingent upon the f^n configuration and k accounts for the electrostatic potential. For *f*-elements, k runs from 0 to 7, while q depends on the local symmetry of the lanthanide ion. The ligand-field potential (Eq. 1.1) can be divided into two parts: (i) even part ($k = \text{even}$), responsible for the ligand-field splitting; and (ii) odd part ($k = \text{odd}$), responsible for the intensity of the induced electric dipole transitions. The nature of the B_k^q terms is related to the local symmetry of the lanthanide ion. Under no symmetry conditions, a total of 27 nonzero

Table 1.2 Symmetry and ligand-field parameters dependence

Symmetry	LF Parameters (Real)	LF Parameters (Complex)
C_1, C_i	$B_2^0, B_2^1, B_4^0, B_6^0$	$B_2^2, B_4^1, B_4^2, B_4^3, B_4^4, B_6^1, B_6^2, B_6^3, B_6^4, B_6^5,$ B_6^6
C_2, C_{2h}, C	$B_2^0, B_2^2, B_4^0, B_6^0$	$B_4^2, B_4^4, B_6^2, B_6^4, B_6^6$
D_2, D_{2h}, C_{2v}	$B_2^0, B_2^2, B_4^0, B_4^2, B_4^4, B_6^0, B_6^2, B_6^4, B_6^6$	
C_3, S_6	$B_2^0, B_4^0, B_4^3, B_6^0$	B_6^3, B_6^6
C_4, C_{4h}, S_4	$B_2^0, B_4^0, B_4^2, B_6^0$	B_6^4
C_5	$B_2^0, B_4^0, B_6^0, B_6^5$	
D_3, D_{3d}, C_{3v}	$B_2^0, B_4^0, B_4^3, B_6^0, B_6^2, B_6^3, B_6^6$	
$D_{4h}, D_{2d}, C_{4v}, D_2, D_{2h}, D_4$	$B_2^0, B_4^0, B_4^2, B_6^0, B_6^4$	
$D_{6h}, D_{3h}, C_{3h}, D_6, C_{6v}, C_{6h}, C_6$	$B_2^0, B_4^0, B_6^0, B_6^6$	
$O_h, T_d, O, D_2, T_h, T^a$	$B_4^0, B_4^4, B_6^0, B_6^4$	
I, I_h^a	B_6^0, B_6^5	
$D_{4d}, C_{5h}, D_{5h}, D_{6d}, C_n, C_{nv}, C_{nh}, D_{nh},$ $D_{nd} \forall n > 6$	B_2^0, B_4^0, B_6^0	

^aFor cubic and icosahedral groups, not all parameters are independent.

coefficients must be included, making the experimental determination of ligand-field parameters practically impossible. Table 1.2 shows the ligand-field parameter upon symmetry dependence.

Undoubtedly, the symmetry of the ligand field plays a key role in the dynamic magnetic properties of f -SMMs. For a square antiprismatic geometry (SAP) (D_{4d} point group), which characterizes the TbPc₂ family and a number of well-performing SMMs such as the LnPOMs (Fig. 1.6), there are four symmetry parameters that define their magnetic behavior: the distance between the squares (d_{pp}), the shorter L-L distance within the square (d_{in}), the skew angle (Φ), and the angle between the C_4 axis and the Ln-L direction (α) [78]. For an idealized SAP geometry, $d_{pp} = d_{in}$, $\Phi = 45$ degrees and $\alpha = 54.74$ degrees.

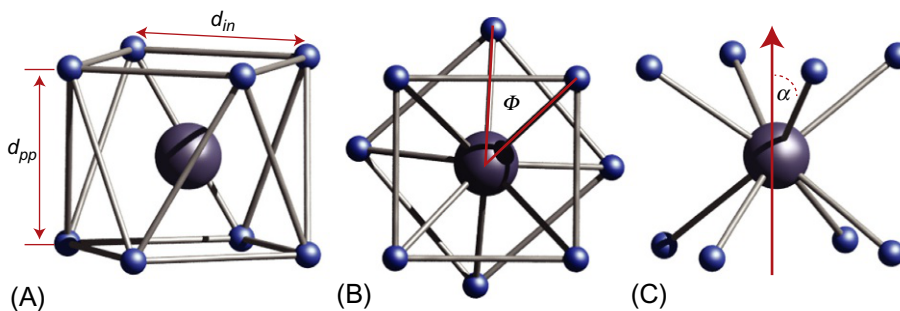


Fig. 1.6

Structural parameters in square antiprismatic geometry (SAP). (A) Schematic structures of SAP geometry. (B) Skew angle (Φ) and (C) angle between the C_4 axis and lanthanide-ligand direction in SAP geometry.

A lanthanide ion embedded in such a ligand-field environment experiences the effect of three terms ($B_2^0 + B_4^0 + B_6^0$), which preclude mixing of ground and excited states. Mixing of other terms into the ground state activates a temperature-independent relaxation pathway known as quantum tunneling of the magnetization (QTM). This effect is observed at discrete field positions and depends upon transverse, hyperfine fields and symmetry. For example, for a Dy(III)- or Tb(III) SMM with SAP geometry, the highly symmetric environment will dramatically reduce the QTM effect. Conversely, Gatteschi et al. [78] showed that upon variation of Φ , that is, if the symmetry of the same material is reduced from D_{4d} to C_4 , the $B_4^4 + B_6^4$ summation needs to be included. These terms are important, since they allow the mixing of states, i.e., $|J_z$ and $|J_z - 4$, and enhancement of QTM at low fields and low temperatures (vide infra) [79]. It is also important to mention that although QTM is not desirable for data storage applications, it is a property of utmost importance for quantum computation applications, where QTM at the avoided level crossings may be used to manipulate electronic states [17,80].

Besides the effect of Φ upon the B_4^4 and B_6^4 terms, compression or elongation along the C_4 axis, that is modification of α , have shown to change the sign of the B_2^0 term. As a result, an elongation of the SAP geometry is more favorable for a Dy(III) ion, where stabilization of the highest m_J ground doublet is preferred, while compression favors the highest m_J ground doublet for Er(III) ions.

1.3.4 Magnetic Relaxation Mechanisms

In *f*-element SMMs, a highly anisotropic ground doublet is responsible for the preferential alignment of the magnetic axis along a certain direction, i.e., magnetic anisotropy. As described in the earlier section, the anisotropic character of *f*-elements is highly influenced by the ligand field in which the ions are embedded, the symmetry, coordination number, neighboring centers among others. Below a certain temperature, known as the blocking temperature (T_B), the magnetic axis becomes frozen, while above T_B , spin reversal can occur through thermally activated processes. The temperature dependence of the experimentally measured relaxation time (τ) follows the Arrhenius law, $\tau = \tau_0 \exp(\Delta E/k_B T)$ (or $\tau = \tau_0 \exp(U_{\text{eff}}/k_B T)$), where τ_0 is the relaxation rate, U_{eff} is the effective energy barrier, and the other symbols have their usual meaning. Experimentally, relaxation times can commonly be obtained from fitting the alternating current magnetic susceptibility data, while the energy barrier can be easily calculated from the linear portion of the Arrhenius plot of $\ln \tau$ versus $1/T$, describing the thermally activated process. Interestingly, the relaxation of the magnetization involves different mechanisms. The *spin-lattice relaxation* processes occur through absorption and emission of one or two phonons. Their efficacy depends on the nature of the metal ion involved, i.e., the low-temperature processes depend on the Kramers or non-Kramers spin parity character of the ions involved. For a Kramers ion, a minimum degeneracy of two is

always attained due to time reversal considerations, while in the non-Kramers case the ground state can be totally nondegenerated. Three processes are primarily involved in the relaxation dynamics of f -SMMs: (i) direct, (ii) Raman, and (iii) Orbach process [81]. These are briefly described as follows:

Direct relaxation mechanism: In a direct relaxation process, a transition between one m_j state to a different m_j state is modulated by emission (absorption) of a photon to (from) the surrounding bath, with the same quanta of energy of the transitions (Fig. 1.7A). The required frequency ν for the transition follows $h\nu = \Delta$, where Δ is the energy of the two distinct levels. During this process, the frequency of the emitted (absorbed) photon is very short and is limited by the phonon density of states. This mechanism is efficient just at very low temperatures and is ion dependent. For example, the relaxation for Kramers ions follows the form $\tau^{-1} = R_d(\hbar\omega)^5 \coth\left(\frac{\hbar\omega}{2kT}\right)$, while for non-Kramers ions is $\tau^{-1} = R_d(\hbar\omega)^3 \coth\left(\frac{\hbar\omega}{2kT}\right)$.

Raman and Orbach relaxation mechanisms: The Raman relaxation process involves inelastic scattering of phonons, where the energies of the involved phonons decrease or increase, with the difference in energy ($h\nu_{i+1} - h\nu_i$) being absorbed or released by the system. When the scattered energy causes a direct transition, the respective relaxation process is termed first-order Raman (Fig. 1.7B). Spin relaxation occurring via virtual states is associated with a second-order Raman mechanism (Fig. 1.7C). These Raman processes require the presence of

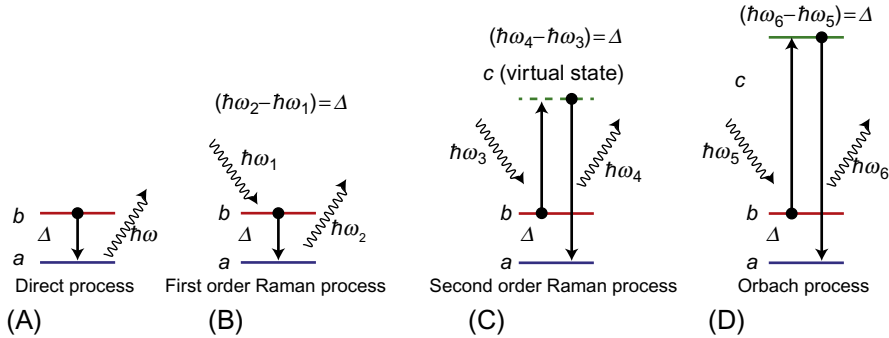


Fig. 1.7

Schematic representation of common spin-lattice relaxation processes in f -SMMs. (A) Direct relaxation process, where a phonon corresponding to the difference between states a and b is absorbed (emitted) causing a transition between states b and a . (B) First-order Raman process, where the difference in energy of the scattered phonon cause a de-excitation from state b to a . (C) Relaxation through a second-order Raman process. Similar to the first-order Raman process, the difference in energy of the scattered phonon is absorbed by the spin system. In contrast, however, the spin system is excited to a virtually excited state and followed by de-excitation to the ground state. (D) In the Orbach process, absorption of a phonon excites the spin system to a low-lying excited state, followed by de-excitation to state a and emission of a photon of energy corresponds to the difference in energy of the low-lying excited state and the ground state.

phonons and become important at finite temperatures. Similar to the direct relaxation process, the Raman relaxation mechanisms are contingent upon the lanthanide ion involved, i.e., for Kramers ions: $\tau^{-1} = T^9 + R'_R(\hbar\omega)^5 T^9$, and for non-Kramers ions: $\tau^{-1} = R_R T^7$.

In the Orbach process, on the other hand, the relaxation of the doubly degenerated ground state occurs via a low-lying excited state. Absorption of a phonon by the spin system causes an excitation to a low-lying excited state. This is accompanied by the emission of a photon with an energy corresponding to the difference between the ground and the low-lying excited state, providing a pathway for the relaxation between the low-lying states (Fig. 1.7D). From all the considered processes, only the Orbach process gives rise to an exponential temperature

dependence, i.e., $\tau^{-1} = R_{Or} \Delta^3 \left[\exp\left(\frac{\Delta}{kT}\right) - 1 \right]^{-1}$.

In addition to the mentioned spin-lattice relaxation processes, quantum tunneling of the magnetization (QTM) is an important path for spin relaxation. This relaxation mechanism allows the spin to tunnel through the energy barrier when the $\pm m_J$ substates are equal in energy. QTM is contingent upon distortion of the ligand fields, hyperfine interaction, and transverse fields. For Kramers ions, lowering of the ligand-field symmetry does not prompt QTM. On the other hand, Kramers and non-Kramers ions are extremely susceptible to small transverse fields. Such transverse fields cause symmetric and antisymmetric superposition of states, leading to an energy difference between the two states, commonly known as tunnel splitting (Δ_T). The tunnel splitting is a measure of the rate of tunneling between the two states involved and has the form

[4]: $\tau_{\text{tunnel}}^{-1} = \frac{2\omega^2 \tau_{nm'}}{1 + \tau_{nm'}^2 (E_m - E_{m'})^2 / \hbar^2}$. Simplification of the tunneling rate is expressed as $\tau_{\text{tunnel}}^{-1} = \frac{B_1}{1 + B_2 H^2}$, where B_1 and B_2 are fitting parameters [50].

When all the processes are gathered in a single form, they result in relaxation for Kramers and non-Kramers rates of the form:

$$\tau^{-1} = R_d(\hbar\omega)^5 \coth\left(\frac{\hbar\omega}{2kT}\right) + R_{Or} \Delta^3 \left[\exp\left(\frac{\Delta}{kT}\right) - 1 \right]^{-1} + R_R T^9 + R'_R(\hbar\omega)^5 T^9 + \frac{B_1}{1 + B_2 H^2} \text{ and}$$

$$\tau^{-1} = R_d(\hbar\omega)^3 \coth\left(\frac{\hbar\omega}{2kT}\right) + R_{Or} \Delta^3 \left[\exp\left(\frac{\Delta}{kT}\right) - 1 \right]^{-1} + R_R T^7 + \frac{B_1}{1 + B_2 H^2}, \text{ respectively.}$$

1.4 Experimental Methods

The performance of SMMs can be evaluated through three main parameters, the effective energy barrier, the blocking temperature, and the hysteresis of the system. The energy barrier defines the high-temperature dynamics of the SMMs, following the Arrhenius law, $\tau = \tau_0 \exp\left(\frac{U_{\text{eff}}}{k_B T}\right)$, where τ is the relaxation time at a given isotherm, τ_0 is a measure of the relaxation rate, and k_B is Boltzmann's constant. A plot of $\ln \tau$ vs $1/T$ yields a linear behavior where the slope is U_{eff}/k_B . The linear trend marks the temperature dependence of the relaxation

of the magnetization. At low temperatures, on the other hand, deviation from the linear behavior is often observed, due to dominance of alternative relaxation processes (vide supra).

Another measure of the anisotropy in SMMs is the maximum temperature at which the hysteresis loops are observed. These values are obtained through magnetization versus field studies at different temperatures. In the following section, we will discuss the most common magnetic techniques employed for the characterization of the magnetic properties of SMMs.

1.4.1 DC Magnetometry

The static magnetic properties of SMMs have been extensively studied employing superconducting quantum interference devices (SQUIDs). SQUID magnetometers operate based on inductive detection of the magnetic moment of the sample. When a paramagnetic material is placed in an external magnetic field (H), the spin of the substance tends to align with the H , lowering the energy of the system. The rate of change in magnetization upon application of a magnetic field defines the susceptibility of the substance, $\chi = dM/dH$. At weak fields, this relationship becomes independent of H .

Typically, the $\chi_M T$ (where χ_M stands for the molar magnetic susceptibility) versus temperature (T) plots yield information regarding interactions and/or crystal field effects in the studied material. For $4f$ materials, the room-temperature value is usually close to the free ion $\chi_M T$ value, i.e., $\chi_M T = \frac{Ng_J^2\beta^2}{3k} J(J+1) \approx \frac{g_J^2}{8} J(J+1)$. This is due to the inherent poor interaction of $4f$ -electrons with the surroundings due to shielding effects. However, at low temperatures, an upsurge or decrease in $\chi_M T$ can shed some light into the type of interactions or crystal field effects.

When kT/H is small, the magnetic moment tends to fully align with the external magnetic field leading to the saturation of the magnetization (M). These measurements hint information regarding the ground m_J state that is populated at the lowest temperature. Moreover, in SMMs with strong anisotropy and large separation between the ground and first excited states, $M(H)$ can be employed to probe the remnant magnetization through hysteresis curves in field-dependent-magnetization measurements at different temperatures (Fig. 1.8A) [27]. Commonly, hysteresis loops increase with sweeping rates and with lowering temperatures.

For slow-relaxing systems, DC magnetic susceptibility studies can also be employed for the determination of relaxation times. During these experiments, the time dependence of the magnetization at different isotherms is investigated, where the decay is fitted to an exponential law of the form, $M(t) = M_0 + M \exp\left(-\frac{t-t_0}{\tau}\right)$.

Moreover, magnetic susceptibility measurements of single crystals have proven powerful for the determination of the anisotropic axis of SMMs. Susceptibilities tensors of single crystals can be obtained through rotation through the three orthogonal directions of the single crystals and the relationships: $M(\theta) = \chi_{\alpha\alpha} H(\cos(\theta))^2 + \chi_{\beta\beta} H(\sin(\theta))^2 + 2\chi_{\alpha\beta} H \sin(\theta) \cos(\theta)$ (Fig. 1.8B) [82].

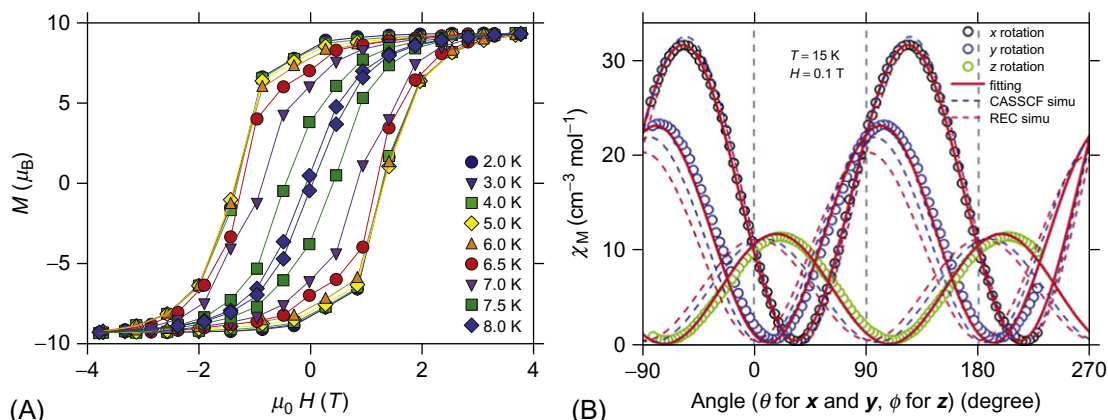


Fig. 1.8

(A) Magnetization (M) vs dc magnetic field (H) for $[\text{K}(\text{18-crown-6})]\{[(\text{Me}_3\text{Si})_2\text{N}]_2(\text{THF})\text{Dy}\}_2(\mu\text{-}\eta_2\text{:}\eta_2\text{-N}_2)$ at a field sweep rate of 0.08 T s^{-1} . (B) Angular dependence of the magnetic susceptibility of $\text{Dy}(\text{}^t\text{Bu-acac})_3\text{bpy}$ at $T = 2.5 \text{ K}$ for three orthogonal rotations. (A) Reproduced with permission from J.D. Rinehart, M. Fang, W.J. Evans, J.R. Long, A N23-radical-bridged terbium complex exhibiting magnetic hysteresis at 14 K, *J. Am. Chem. Soc.* 133 (2011) 14236–14239. Copyright 2011 American Chemical Society; (B) Reproduced with permission from K. Qian, J.J. Baldovi, S.-D. Jiang, A. Gaita-Arino, Y.-Q. Zhang, J. Overgaard, B.-W. Wang, E. Coronado, S. Gao, Does the thermal evolution of molecular structures critically affect the magnetic anisotropy? *Chem. Sci.* 6 (2015) 4587–4593. Royal Society of Chemistry.

1.4.2 AC Magnetometry

The most common method to analyze the slow-relaxation property of SMMs is through alternating current (*ac*) magnetic susceptibility measurements. In these measurements, the sample is placed between two coils, where current flows at different frequencies. The dynamic magnetic properties of SMMs are obtained by detecting the response of the sample after application of a small oscillating magnetic field that induces a small magnetization in the sample, detected by secondary coils. During the measurements, the frequency (ν) of the small oscillating magnetic field is varied (between 0.1 and 10,000 Hz in commercial SQUIDs), resulting in in-phase (χ') and out-of-phase (χ'') *ac* magnetic susceptibility signals. An out-of-phase *ac* susceptibility signal is observed when the rate of the operating frequency of the *ac* field is close to the flipping rate of the magnetic moment of the molecule. When an SMM is kept at a certain temperature and the frequency of the *ac* field is varied, a maximum is observed once the rate of the *ac* relaxation equals the rate at which the molecule interconverts between the halves of the potential-energy double well. This characterization is performed over a temperature range at zero field, or under the application of small DC fields.

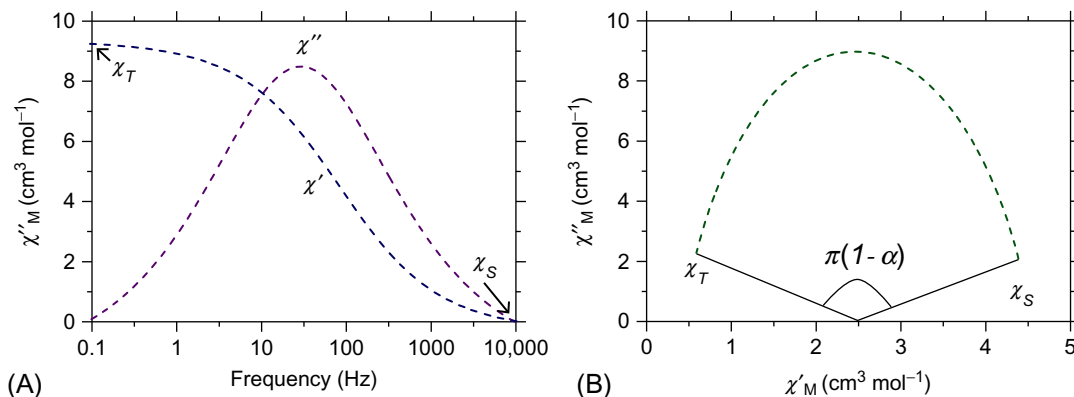


Fig. 1.9

(A) Frequency dependence of the real and imaginary component of the magnetic susceptibility. χ_T and χ_S are the isothermal and adiabatic susceptibility, respectively and (B) Argand plot (or Cole-Cole): χ'' vs χ' at a given temperature.

The energy barrier of the relaxation of the magnetization U_{eff} can be finally obtained through fitting of the in-phase (χ') and out-of-phase (χ'') susceptibility data (Fig. 1.9). χ' and χ'' for a single relaxation process are given by $\chi'(\omega) = \chi_S + \left(\frac{\chi_T - \chi_S}{1 + \omega^2 \tau^2}\right)$ and $\chi''(\omega) = \left(\frac{\chi_T - \chi_S}{1 + \omega^2 \tau^2}\right) \omega \tau$, respectively, where χ_S and χ_T are the adiabatic and isothermal susceptibilities, respectively, $\omega = 2\pi\nu$ is the angular frequency, and τ is the relaxation time. Experimentally, on the other hand, single relaxation processes are uncommon, due to small inequalities across the SMM molecules present in the crystal lattice; therefore, the in- and out-of-phase components are fitted to a distribution of processes. These are given by

$$\chi'(\omega) = \chi_S + \frac{(\chi_T - \chi_S)[1 + (\omega\tau)^{1-\alpha} \sin(\frac{\alpha\pi}{2})]}{1 + 2(\omega\tau)^{1-\alpha} \sin(\frac{\alpha\pi}{2}) + (\omega\tau)^{(2-2\alpha)}} \text{ and } \chi''(\omega) = \frac{(\chi_T - \chi_S)[1 + (\omega\tau)^{1-\alpha} \cos(\frac{\alpha\pi}{2})]}{1 + 2(\omega\tau)^{1-\alpha} \sin(\frac{\alpha\pi}{2}) + (\omega\tau)^{(2-2\alpha)}}$$

where α is a measure of the distribution of relaxation processes, with values ranging from 0 to 1. A narrow distribution of relaxation processes is associated with a small α value.

Application of dc fields is known to reduce QTM (quantum tunneling of the magnetization), which is a source of electron spin relaxation; thus, studies are often performed under the applied fields at which the relaxation process has the slowest rate. $\chi_M''(\nu)$ isotherms are conveniently employed for the determination of the energy barrier to the relaxation of the magnetization (U_{eff}), by plotting the relaxation times (τ) as a function of temperature, and using the Arrhenius equation $\tau = \tau_0 \exp(U_{\text{eff}}/k_B T)$. Analysis of the τ vs T^{-1} , where the slope of the graph represents the U_{eff} , offers some insight into the type of relaxation pathways to the magnetization, i.e., direct, Orbach, Raman, or quantum tunneling processes (vide infra).

1.4.3 μ -SQUID Arrays

Although commercial SQUID magnetometers offer a great deal of information on the dynamics of the magnetization, their sensitivity falls short when compared to μ -SQUIDs arrays (Fig. 1.10) [83]. These micro-SQUID magnetometers are very sensitive apparatuses, which besides enabling to measure with accuracy the magnetic properties of microcrystals, offer the advantage of exploring the dynamics of SMMs down to 30 mK, leading to the observation of quantum effects such as quantum tunneling of the magnetization. Moreover, direct quantum tunneling of the magnetization manifested between S_z states often originates from inter- and intramolecular interactions, level crossing between ground and excited states, and/or hyperfine-based tunneling, which are difficult to be monitored using traditional devices. Micro-SQUID instruments detect such events with a high degree of sensitivity. Due to working at the milli-Kelvin temperatures, such devices also permit to determine the U_{eff} values of weak SMMs far more accurately than traditionally measured with commercial SQUID devices.

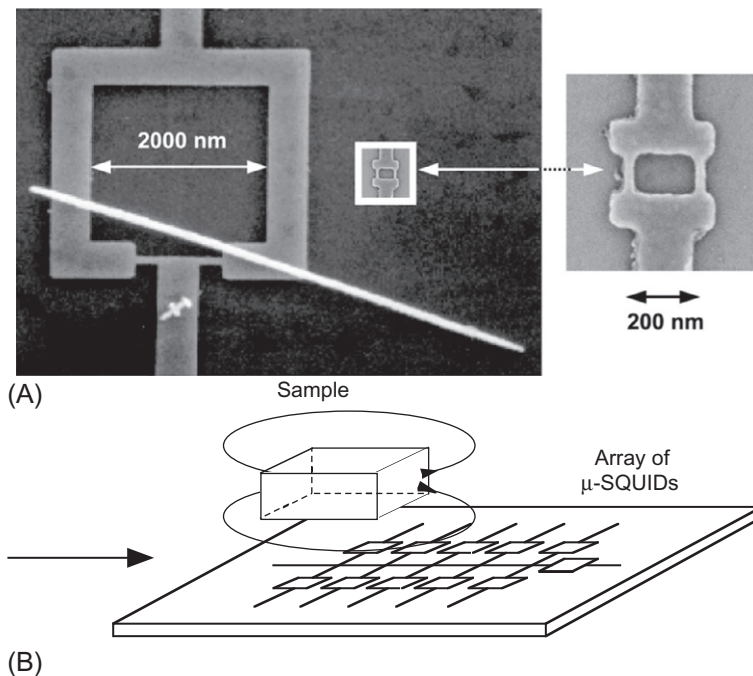


Fig. 1.10

(A) Micrographic image of a Nb μ -SQUID and a Ni wire of diameter of about 90 nm, deposited on the μ -SQUID and (B) an array of μ -SQUIDs used for macroscopic crystal studies. *Reproduced with permission from W. Wernsdorfer, From micro-to nano-SQUIDs: applications to nanomagnetism, Supercond. Sci. Technol. 22 (2009) 64013.*

1.5 Slow-Relaxing Systems

Since the discovery of slow relaxation in lanthanides, a plethora of *f*-based SMMs has been synthesized and characterized by a number of techniques. For simplicity, herein we classify them depending on the number of metal centers and their arrangements. When the anisotropic magnetic properties result from a single center, the term single-ion magnets (SIMs) is employed. When more than a single center is present, then depending on the arrangement, they can be either single-molecule magnets (SMMs) (for zero-dimensional systems), or single-chain magnets (for 1D systems). The following sections are far from being complete, but the selected examples allow drawing some general conclusions on factors that affect the magnetic dynamics of *f*-element nanomagnets.

1.5.1 *f*-Elements Single-Ion Magnets (*f*-SIMs)

The term single-ion magnet (SIM) has been extensively used to distinguish single-molecule magnets comprised by a single metal ion from those formed by more than one *f*-ion. Strictly speaking, the “magnet-like” behavior is not associated with the metal ion alone, but arises from the collective behavior of the *f*-ion and the ligand field exerted by the surrounding binding moieties. Despite this, in this section, we employed the acronym SIMs to describe slow-relaxing molecular magnets comprised by a single *f*-ion, to differentiate them from polynuclear-based SMMs.

The field of lanthanide single-ion magnets started in 2003 with the report by Ishikawa and coworkers of the first mononuclear lanthanide complexes showing SIM behavior, of general formula $[\text{LnPc}_2]$ [29]. Since then, many other *f*-element SIMs have been reported [8,35–39]. The origin of the slow-relaxation properties lies on the strong spin-orbit coupling inherent in *f*-elements and the strength of the surrounding ligand field. The discovery of such astonishing behavior prompted a great deal of investigations leading to a large number of SIMs with large energy barriers, blocking temperatures, and the observation of quantum effects. In the following sections, a brief description of the magnetic characteristics of selected SIMs will be described.

1.5.1.1 Lanthanide double deckers $[\text{LnPc}_2]$

The first and most investigated family of lanthanide complexes displaying slow relaxation of the magnetization at single-ion level was that of double deckers $[\text{LnPc}_2]^-$ ($\text{Ln} = \text{Tb}, \text{Dy}, \text{Ho}, \text{Er}, \text{Tm}, \text{Yb}$, and $\text{Pc}^{2-} = \text{phthalocyanine dianion}$), where the lanthanide ion is sandwiched between two phthalocyanato moieties [29]. The ligands are bound in a way that provides a square antiprismatic coordination environment to the metal ion of crystal field symmetry D_{4d} (Fig. 1.11A and B). Initial NMR and magnetic susceptibility studies by Ishikawa et al. indicated the existence of a large energy gap between the ground and the first low-lying excited state for

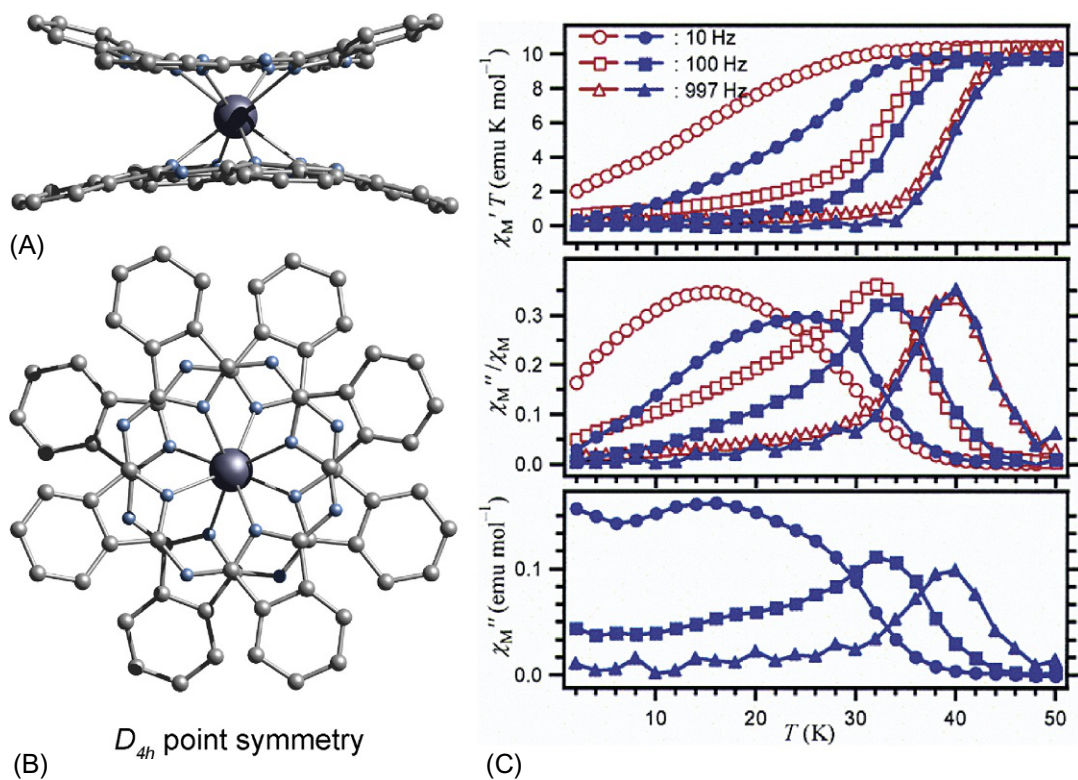


Fig. 1.11

(A) Side and (B) top view of molecular structure of $[\text{TbPc}_2]^-$ complex. (C) Slow relaxation magnetic susceptibility characteristics of $[\text{TbPc}_2]^-$ complex, at 100% concentration (*empty symbols*) and after magnetic dilution into the $[\text{YPC}_2]^-$ analogue (*filled symbols*). Modified from N. Ishikawa, M. Sugita, T. Ishikawa, S.-Y. Koshihara, Y. Kaizu, *Lanthanide double-decker complexes functioning as magnets at the single-molecular level*, *J. Am. Chem. Soc.* 125 (2003) 8694–8695. Copyright 2003 American Chemical Society.

some of the lanthanides ions of the $[\text{TBA}]^+[\text{TbPc}_2]^-$ family [84], with the largest gap being observed in the $[\text{TbPc}_2]^-$ complex, of ca. 400 cm^{-1} .

Additionally, Ishikawa and coworkers found that the ground state of Tb(III) was the multiplet with the highest m_J value, i.e., $|\pm 6\rangle$, while for the Dy(III) analogue the second highest possible m_J state was the ground doublet, i.e., $|\pm 13/2\rangle$. AC magnetic susceptibility data have confirmed the occurrence of slow magnetic relaxation in both Tb(III) and Dy(III) compounds, with $[\text{TBA}]^+[\text{TbPc}_2]^-$ showing a larger energy barrier than $[\text{TBA}][\text{DyPc}_2]$ ($U_{\text{eff}} = 230\text{ cm}^{-1}$ and $U_{\text{eff}} = 28\text{ cm}^{-1}$ respectively). As observed in Fig. 1.11C, a frequency- and temperature-dependent out-of-phase behavior was found for $[\text{LnPc}_2]^-$ ($\text{Ln} = \text{Tb(III)}$ or Dy(III)). In addition, ac measurements of diluted samples in diamagnetic $[\text{TBA}]^+[\text{YPC}_2]^-$ confirmed that the

observed SIM behavior is an intrinsic molecular property, typically associated with a temperature- and/or frequency-dependent shift of the out-of-phase maxima.

Extensive studies on such systems have allowed the observation of quantum effects, such as Quantum Tunneling of the magnetization (QTM) [79]. Under strict D_{4d} symmetry, no QTM is expected to operate in the $[\text{LnPc}_2]^{0,\pm 1}$ family. On the contrary, small deviation from the D_{4d} geometry makes quantum tunneling at the avoided level crossing possible. For a D_{4d} symmetry, the system is characterized by a ligand-field Hamiltonian of the form $\mathcal{H}_{lf} = \alpha B_2^0 O_2^0 + \beta (B_4^0 O_4^0 + B_4^4 O_4^4) + \gamma (B_6^0 O_6^0 + B_6^4 O_6^4)$, where B_q^k are the ligand-field parameters and α , β , and γ are the Stevens constants. Upon lowering the symmetry to C_4 , two additional terms become available, i.e. $(B_4^4 O_4^4 + B_6^4 O_6^4)$, causing mixing of the $|J_z = \pm 6$ states, and avoiding level crossing at zero field. It has been shown that the level crossing at zero field can be further split into four components due to the strong hyperfine interaction between the $|J_z = \pm 6$ and $I = 3/2$ of Tb^{3+} . The crossing corresponds to the tunneling at the level crossings, i.e., $m_I = \pm 3/2$ and $\pm 1/2$, where the electron spin flips, while the nuclear states are conserved. Similar behaviors have been observed for the holmium [85] and dysprosium [86] double-decker analogues. These observations clearly exemplify the role of symmetry and ligand field upon the magnetic properties of SMMs. It is worth mentioning that, although QTM is not often desirable, in the double-decker family of complexes, the QTM at the level crossings is supposed to be useful for initialization, manipulation, and read-out of qubit spin states [17,55].

1.5.1.2 Heteroleptic and homoleptic erbium COT SIMs

In contrast to the Dy(III) and Tb(III) lanthanide SMMs, where electronic state of maximum m_J is stabilized for axial geometries, Er-based systems require equatorial ligand fields to promote single-molecule magnetism and stabilization of high- m_J ground states. Rotational ligands derived from cyclopentadienide (Cp) or cyclooctatetraene (COT) were proven to be efficient in promoting equatorial ligand fields in f -element systems. Depending on the nature of the ligands surrounding the erbium ion, these SIMs can be classified into two categories: (i) heteroleptic (involving both Cp and COT ligands), and (ii) homoleptic (either COT or Cp ligands).

In 2011, Jiang and coworkers reported an erbium complex with formula $[(\text{Cp}^*)\text{Er}(\text{COT})]$ as the first organometallic Ln-SIM (Fig. 1.12A) [41]. Magnetic studies revealed two effective energy barriers of 224 and 137 cm^{-1} , attributed to the different thermally activated relaxation processes present in the molecule (Fig. 1.12B). In addition, magnetic hysteresis was observed up to 5 K in a diluted sample. In the $[(\text{Cp}^*)\text{Er}(\text{COT})]$, the two aromatic ligands are not parallel, which indicated a diversion from the ideal axial symmetry. The strong SIM behavior of the Er(III) complex originates from the strong equatorial ligand field provided by the sets of π -orbitals of the COT ligands, whose effect results in efficient stabilization of a $m_J = \pm 15/2$ ground state, with the lowest-lying excited state ($m_J = \pm 13/2$) placed at a separation of 190 cm^{-1} above the ground state.

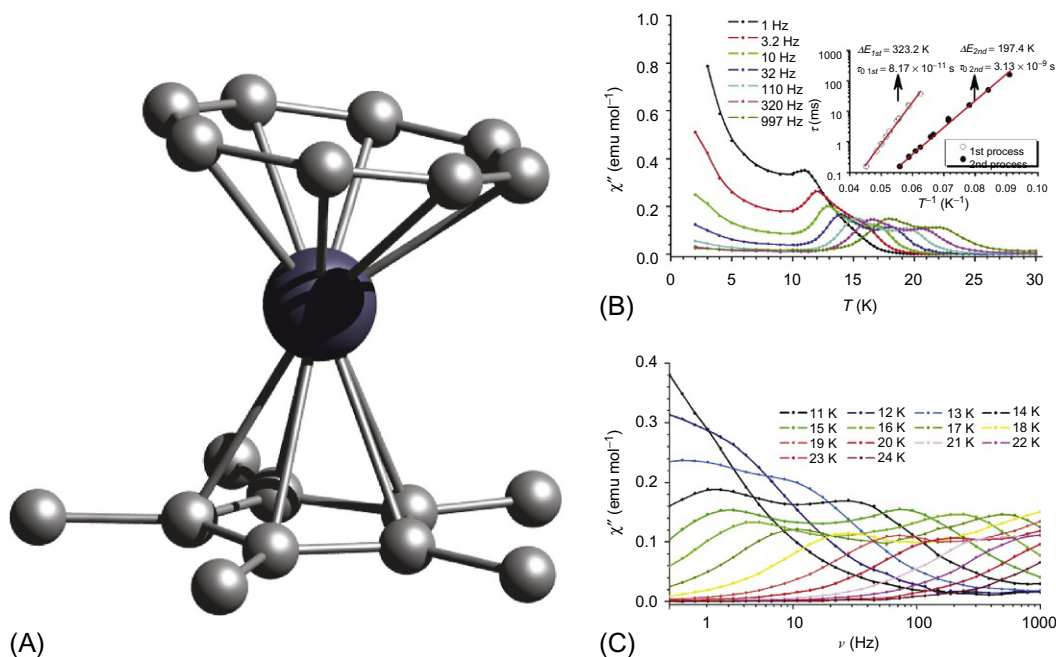


Fig. 1.12

(A) Molecular structure of complex [(Cp*)Er(COT)]. (B) Temperature dependent and (C) frequency dependent magnetic susceptibility data for [(Cp*)Er(COT)]. Modified with permission from S.-D. Jiang, B.-W. Wang, H.-L. Sun, Z.-M. Wang, S. Gao, *An organometallic single-ion magnet*, *J. Am. Chem. Soc.* 133 (2011) 4730–4733. Copyright 2011 American Chemical Society.

A second Er-based SIM system was reported by Meihaus and Long in 2013 [87]. The compound comprised an homoleptic complex anion of formula $[\text{Er}(\eta^8\text{-COT})_2]^-$ (Fig. 1.13A and B) charged balanced by either a $[\text{K}(18\text{-crown-6})]^+$ or a $[\text{K}(18\text{-crown-6})(\text{THF})_2]^+$ cation. In this case, the π electron density of the COT^{2-} rings is concentrated above and below the given rings, thus producing a strong equatorial crystal field. This field matches well the prolate electron density of the Er(III) ion. The two aromatic COT ligands are almost parallel to each other with a tilt angle of 2.8 degrees, which suggests a higher symmetry compared to the $[(\text{Cp}^*)\text{Er}(\text{COT})]$ complex. AC magnetic susceptibility studies revealed a frequency-dependent shift in the out-of-phase component of the magnetic susceptibility between 15 and 27 K, with $U_{\text{eff}} = 147 \text{ cm}^{-1}$ (Fig. 1.13C). Remarkably, the complex displays open hysteresis loops up to 10 K, which is notable for Er-SIMs. Ab initio calculations undertaken on $[\text{Er}(\eta^8\text{-COT})_2]^-$ have confirmed that the local high symmetry of $[\text{Er}(\text{COT})_2]^-$ determines the magnetic properties of the complex [33]. Similarly, the ground state was found to be well separated from the first excited states. Interestingly, the first excited state is highly pure and collinear with the ground state, making the relaxation mechanism via the first excited state less probable. This allowed the authors to conclude that the relaxation of the magnetization in this compound occurs through the second lowest excited state.

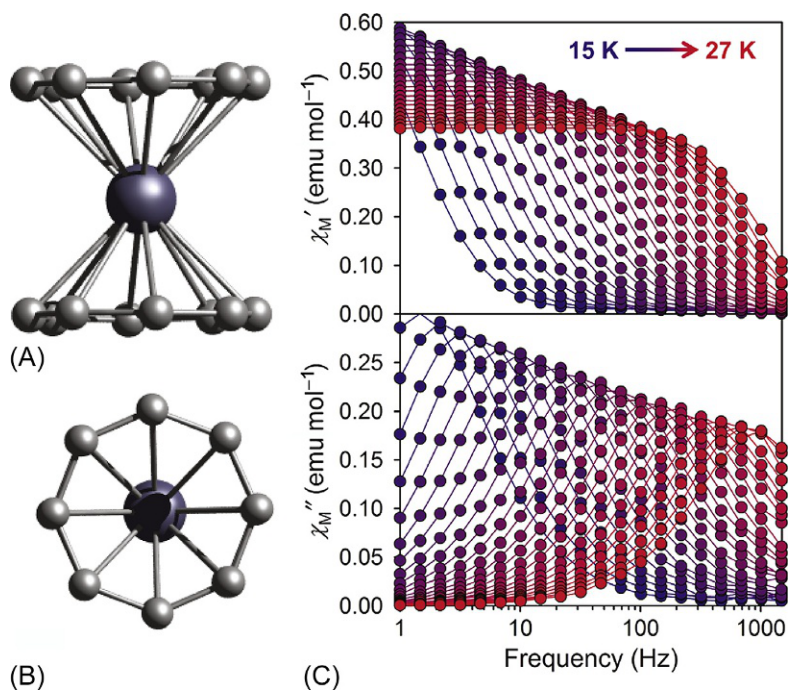


Fig. 1.13

(A) Side view and (B) top view of $[\text{Er}(\eta^8\text{-COT})_2]^+$ SIM, highlighting the high rotational symmetry.

(C) In-phase and (B) out-of-phase frequency-dependent magnetic susceptibility data. *Modified with permission from K.R. Meihaus, J.R. Long, Magnetic blocking at 10 K and a dipolar-mediated avalanche in salts of the bis(η^8 -cyclooctatetraenide) complex $[\text{Er}(\text{COT})_2]^-$, J. Am. Chem. Soc. 135 (2013) 17952–17957.*

Copyright 2013 American Chemical Society.

Employing a similar approach that allows enhancement of the equatorial ligand field at the Er(III) site, several other Er-SIMs with interesting properties were developed [8].

Comprehension of the structure-magnetic properties in the reported materials allows chemists to rationalize and better design well-performing SMMs.

1.5.1.3 Highly axial dysprosium SIMs

Dysprosium is the lanthanide ion that has provided the largest number of molecular systems with SIM behavior [8]. Their study has allowed to draw important conclusions on factors and structural characteristics that impact the slow-relaxation behavior of *f*-SIMs, and thus to gain a deep understanding of the magnetic properties and design criteria allowing optimization of these properties [71,75,76]. For example, it is largely accepted that a strictly linear motif provides a strongly axial ligand field that matches best the oblate electronic density of Dy(III). This was demonstrated for several pseudo linear Dy-SIMs [8].

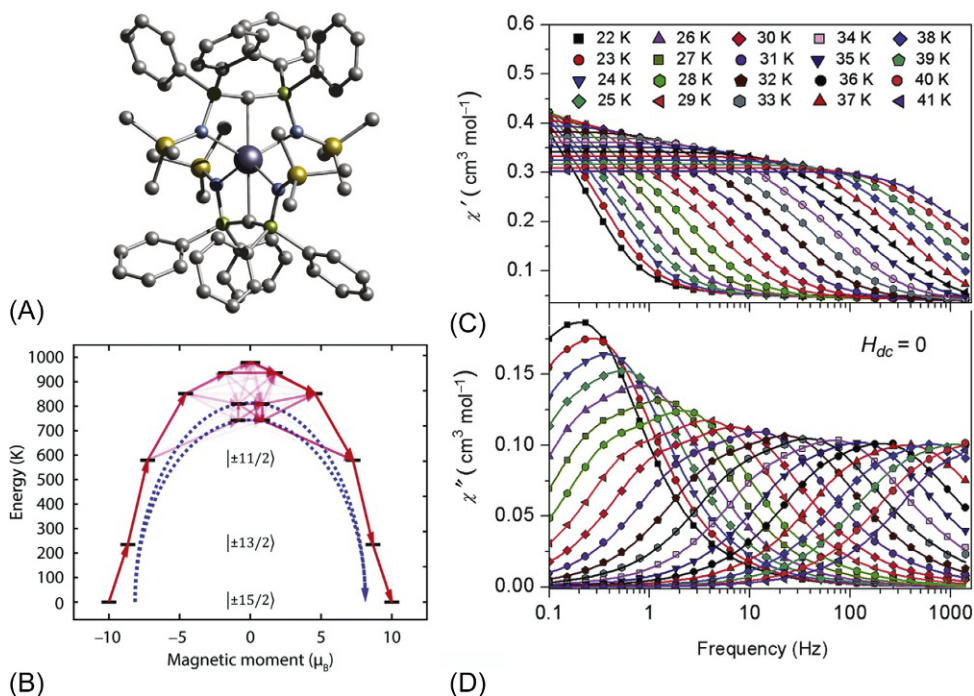


Fig. 1.14

(A) Crystal structure of $[\text{Dy}(\text{BIPM}^{\text{TMS}})_2][\text{K}(18\text{-crown-6})]$ ($\text{BIPM}^{\text{TMS}} = \{\text{C}(\text{PPh}_2\text{NSiMe}_3)_2\}^{2-}$); (B) calculated energy-level diagram for $[\text{Dy}(\text{BIPM}^{\text{TMS}})_2][\text{K}(18\text{-crown-6})]$. The high collinear and pure character of the first, second, and third excited states in the complex forces the relaxation through the fourth and fifth excited states; (C) χ' and (D) χ'' frequency-dependent data at zero field. *Modified from M. Gregson, N.F. Chilton, A.-M. Ariciu, F. Tuna, I.F. Crowe, W. Lewis, A.J. Blake, D. Collison, E.J.L. McInnes, R.E.P. Winpenny, S.T. Liddle, A monometallic lanthanide bis(methanediide) single molecule magnet with a large energy barrier and complex spin relaxation behaviour, Chem. Sci. 7 (2016) 155–165. Royal Society of Chemistry.*

An example of this is a mononuclear dysprosium complex with formula $[\text{Dy}(\text{BIPM}^{\text{TMS}})_2][\text{K}(18\text{-crown-6})]$ ($\text{BIPM}^{\text{TMS}} = \{\text{C}(\text{PPh}_2\text{NSiMe}_3)_2\}^{2-}$) (Fig. 1.14A) [35]. In the complex, the Dy(III) ion is hexa-coordinate with an approximately linear C=Dy=C arrangement. The Dy...C angle was found to be 176.2(2) degrees cf. 180 degrees for an idealized linear system. Ac magnetic susceptibility measurements of this complex at zero dc field show frequency- and temperature-dependent χ'' out-of-phase signals with maxima observable up to 42 K (Fig. 1.14C and D). Two thermally activated Orbach processes were identified with $U_{\text{eff}} = 500$ and 565 cm^{-1} , respectively, which dominate the relaxation process at high temperatures. A two-phonon Raman process prevails the relaxation mechanism as the temperature decreases, which is expected for Kramers ions. Furthermore, the lowest three excited states are found to be highly pure and with their anisotropy axes collinear to that of the ground state, i.e., oriented along the same C=Dy=C axis. These characteristics force the magnetization to relax via the fourth and fifth excited states, which explains the remarkably high-energy barriers

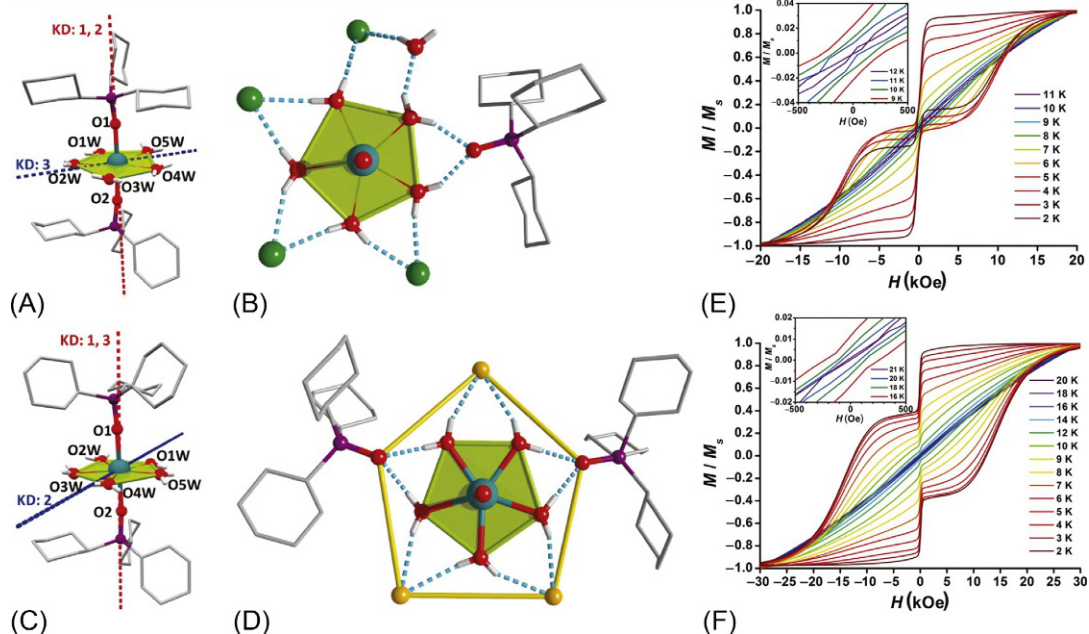


Fig. 1.15

Crystal structures of $[\text{Dy}(\text{Cy}_3\text{PO})_2(\text{H}_2\text{O})_5]\text{Cl}_3$ (A, C) and $[\text{Dy}(\text{Cy}_3\text{PO})_2(\text{H}_2\text{O})_5]\text{Br}_3$ (B, D) showing the D_{5h} geometry. The *dashed lines* show the main anisotropy axes in the excited Kramer's doublet (KD) through which the activated relaxation proceeds. (E) and (F) show the magnetic hystereses for 5% dilution of $[\text{Dy}(\text{Cy}_3\text{PO})_2(\text{H}_2\text{O})_5]\text{Cl}_3$ and $[\text{Dy}(\text{Cy}_3\text{PO})_2(\text{H}_2\text{O})_5]\text{Br}_3$ into the yttrium analogue, respectively. Reproduced with permission from Y.-C. Chen, J.-L. Lu, L. Ungur, J. Liu, Q.-W. Li, L.-F. Wang, Z.-P. Ni, L.F. Chibotaru, X.-M. Chen, M.-L. Tong, *Symmetry-supported magnetic blocking at 20 K in pentagonal bipyramidal Dy(III) single-ion magnets*, *J. Am. Chem. Soc.* 138 (2016) 2829–2837. Copyright 2016 American Chemical Society.

of $U_{\text{eff}} = 515$ and 563 cm^{-1} , respectively. In agreement with this, the field dependence of the magnetization shows open magnetic hysteresis loops that are observable up to the temperature of 16 K (Fig. 1.14B).

Another example of highly axial coordination SIMs is provided by $[\text{Dy}(\text{Cy}_3\text{PO})_2(\text{H}_2\text{O})_5]\text{Cl}_3$ and $[\text{Dy}(\text{Cy}_3\text{PO})_2(\text{H}_2\text{O})_5]\text{Br}_3$ (Cy_3PO = tricyclohexylphosphine oxide), which possess D_{5h} pentagonal bipyramidal geometry (Fig. 1.15A–D) [42]. In both complexes, the Dy(III) ion is seven-coordinated, with two phosphine ligands occupying the apical positions, and five water molecules coordinated in the equatorial plane. The compounds display slow magnetic relaxation with energy barriers of 328 cm^{-1} for the Cl^- analogue, and 377 cm^{-1} for the Br^- analogue, measured under zero applied dc field. Application of a small dc magnetic field has had no impact on magnetic relaxation dynamics, suggesting that QTM is unlikely to facilitate spin relaxation. Magnetic hysteresis studies revealed open loops up to 11 K for Cl^- , and to 20 K for Br^- derivative (Fig. 1.15E and F).

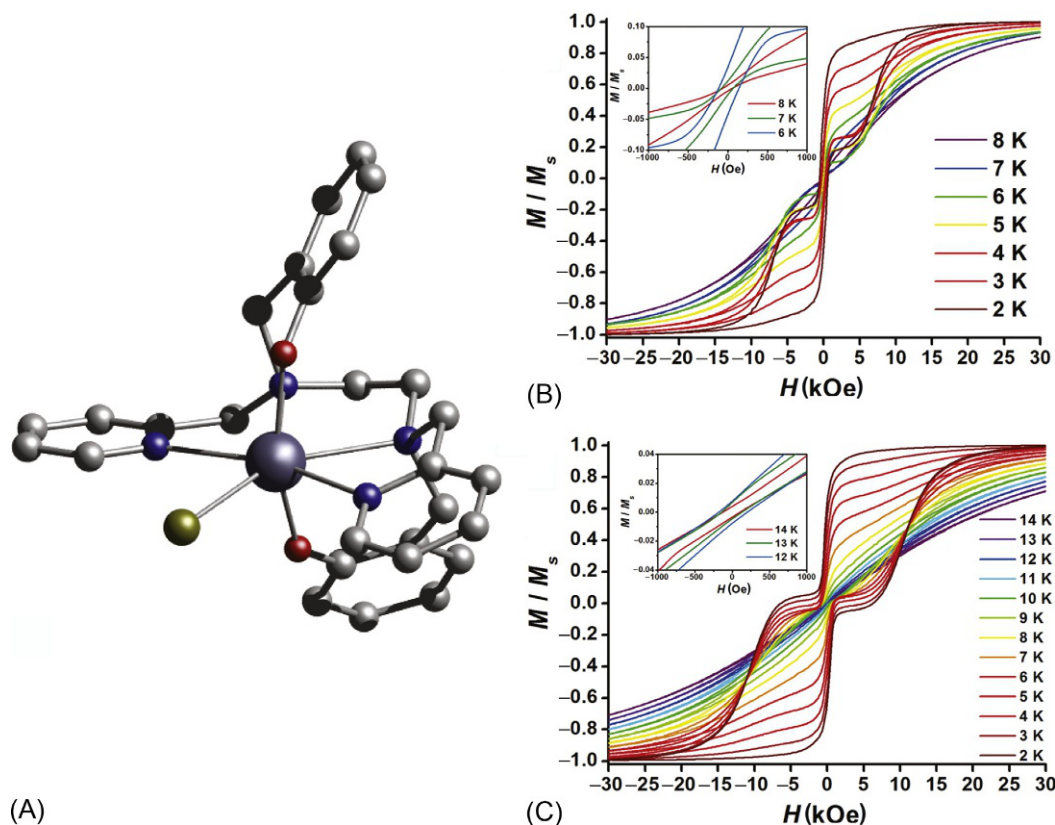


Fig. 1.16

(A) Molecular structure of $[\text{Dy}(\text{bbpen})\text{X}]$ ($\text{X} = \text{Cl}^-$, Br^-). (B) and (C) are hysteresis loops for $[\text{Dy}(\text{bbpen})\text{Cl}]$ and $[\text{Dy}(\text{bbpen})\text{Br}]$, respectively. Modified from J. Liu, Y.C. Chen, J.L. Liu, V. Vieru, L. Ungur, J.H. Jia, L.F. Chibotaru, Y. Lan, W. Wernsdorfer, S. Gao, X.-M. Chen, M.-L. Tong, *A stable pentagonal bipyramidal Dy(III) single-ion magnet with a record magnetization reversal barrier over 1000 K*, *J. Am. Chem. Soc.* 138 (2016) 5441–5450. Copyright 2016 American Chemical Society.

Similarly, a very large energy barrier has been observed in a complex with molecular formula $[\text{Dy}(\text{bbpen})\text{X}]$ ($\text{X} = \text{Cl}^-$, Br^- , and $\text{H}_2\text{bbpen} = N,N'$ -bis(2-hydroxybenzyl)- N,N' -bis(2-methylpyridyl)ethylenediamine) (Fig. 1.16A) [39]. As in the previous examples, the Dy(III) center adopts a distorted pentagonal bipyramidal coordination geometry. The U_{eff} were measured to be 492 and 712 cm^{-1} for $[\text{Dy}(\text{bbpen})\text{Cl}]$ and $[\text{Dy}(\text{bbpen})\text{Br}]$, respectively. This observation can be rationalized employing Long's procedure, that is the anisotropy of the oblate Dy(III) ions is enhanced by a strong axial crystal field [73]. In this case, a stronger axial ligand field is expected for $[\text{Dy}(\text{bbpen})\text{Br}]$ compared to $[\text{Dy}(\text{bbpen})\text{Cl}]$, and implicitly a larger energy barrier and hysteresis for the Br-containing analogue (Fig. 1.16B and C).

A high energy barrier has been reported for $[\text{Dy}(\text{O}^t\text{Bu})_2(\text{py})_5][\text{BPh}_4]$ (Fig. 1.17A) [37]. The remarkable magnetic characteristics are attributed to the combination of a strong axial ligand field with a weak equatorial field. The coordination geometry of the metal ion is pentagonal

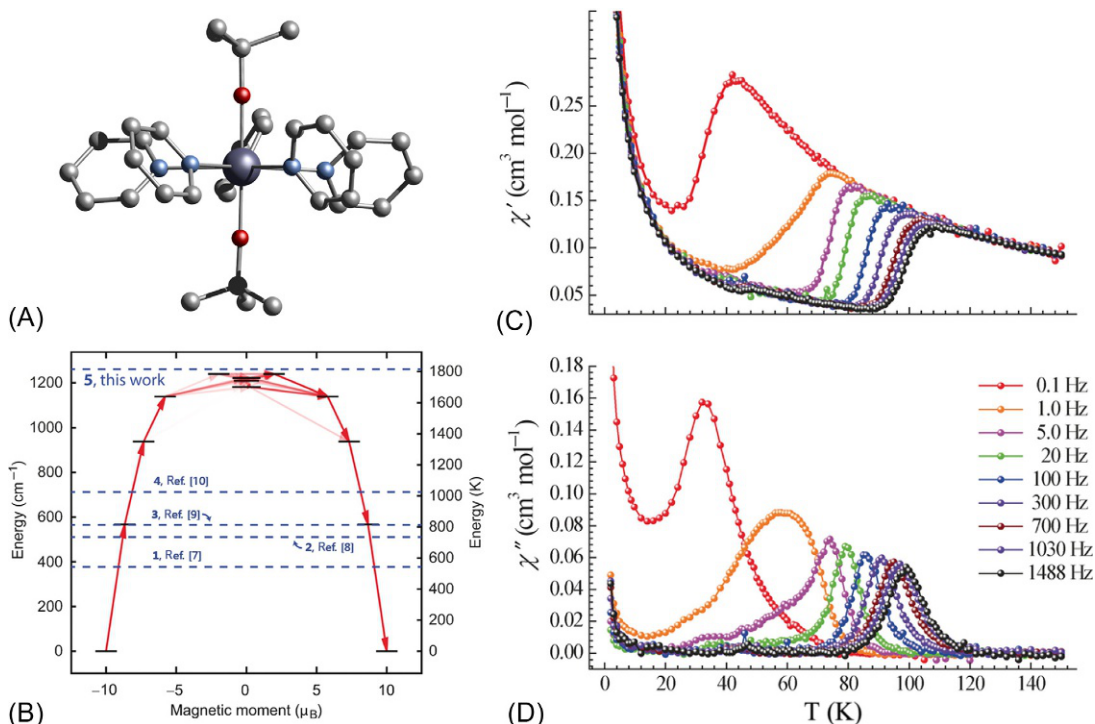


Fig. 1.17

(A) Crystal structure of $[\text{Dy}(\text{O}^t\text{Bu})_2(\text{py})_5][\text{BPh}_4]$. (B) Relaxation mechanism operating in the complex, determined through ab initio calculations. (C) χ' and (D) χ'' frequency-dependent data at zero field extending above 100 K. Modified from Y.-S. Ding, N.F. Chilton, R.E.P. Winpenny and Y.-Z. Zheng, *On approaching the limit of molecular magnetic anisotropy: a near-perfect pentagonal bipyramidal dysprosium(III) single-molecule magnet*, *Angew. Chem. Int. Ed.* 55 (2016) 16071–16074. Copyright 2017 Wiley-VCH.

bipyramidal with two negatively charged ligands on the axial sites and five neutral equatorial donors, which gives rise to a high magnetic relaxation barrier. Compared to other Dy-SIMs with D_{5h} local symmetry, in this complex, the Dy—O bonds are the shortest ever found in a seven-coordinate Dy-complex. Ac magnetic susceptibility studies show a frequency χ'' with the maxima ranging above 100 K (Fig. 1.17C and D). The system relaxes via two processes: in the high-temperature region, an Orbach relaxation process is dominant, while below 60 K, the Raman relaxation process becomes more important. Ab initio calculations demonstrated that the trans-disposed tert-butoxide ligands contribute to the enhancement of the Dy anisotropy. Surprisingly, the system seems to relax via superior excited states leading to $U_{\text{eff}} = 1260 \text{ cm}^{-1}$ (Fig. 1.17B). Remarkably, an even larger energy barrier ($U_{\text{eff}} = 1277 \text{ cm}^{-1}$) and open hysteresis loops up to 60 K have been observed very recently in a metallocenium dysprosium cation $[(\text{Cp}^{\text{tBu}})_2\text{Dy}]^+$ ($\text{Cp}^{\text{tBu}} = 1,2,4\text{-tri(tert-butyl)cyclopentadienide}$) [38]. The authors ascribed the large magnetic anisotropy due to relaxation via the seventh excited state; the inefficient relaxation through lower Kramers doublet states was assigned to the highly pure character of those states.

1.5.1.4 Actinide-based SIMs

Mononuclear complexes based on actinides elements are promising candidates for the field of single-ion magnets due to the large radial extension of $5f$ -orbitals, when compared to lanthanides. This feature allows an increased spin-orbit coupling and enhanced magnetic anisotropy. Moreover, the crystal field splitting is more significant in the case of actinides. For actinide complexes, a high axial symmetry is essential to display slow relaxation of the magnetization.

The first reported mononuclear actinide complex showing SIM behavior has been a complex with formula $[(U(\text{Ph}_2\text{BPz}_2)_3)]$ (Ph_2BPz^- = diphenylbis(pyrazolyl)borate) (Fig. 1.18A) [58]. The complex adopts a trigonal prismatic geometry with C_3 point symmetry. The trivalent uranium ion has a $5f^3$ configuration and exhibits an oblate-shaped electron density. Slow magnetic relaxation occurs in this complex, with an effective energy barrier $U_{\text{eff}} = 20 \text{ cm}^{-1}$ (Fig. 1.18B). A related complex with trigonal prismatic coordination geometry, $[(U(\text{H}_2\text{BPz}_2)_3)]$, has been published a few months later by the same group [59]. The modification of the ligand slightly elongates the prism along the main axis, causing a reduction of the energy gaps between m_J states. Ac susceptibility studies at zero dc field showed no SIM behavior for this complex. However, application of a small dc field of 50 Oe has minimized the QTM effect enabling to observe slow relaxation with an effective energy barrier of 8 cm^{-1} . Computational studies undertaken on both systems suggested an energy gap between the ground and the lowest-lying excited state of 190 and 230 cm^{-1} , respectively, which are far below those of lanthanide SIMs.

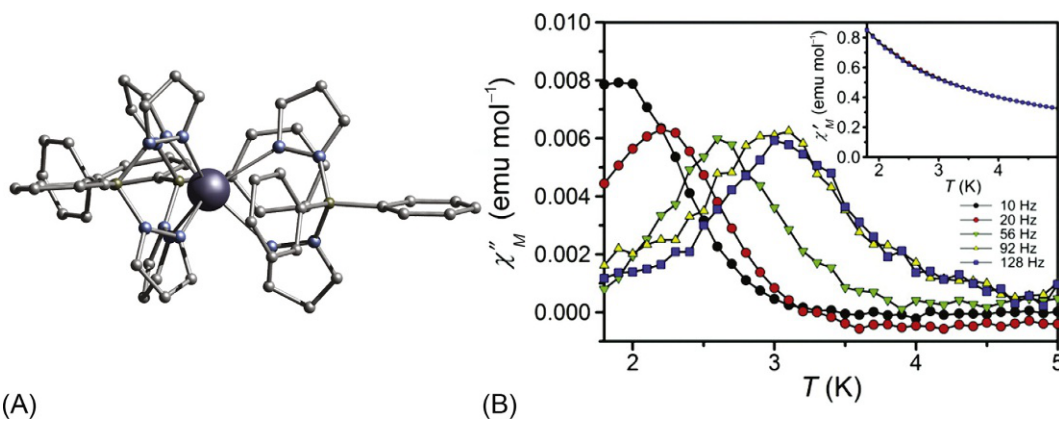


Fig. 1.18

(A) Molecular structure and (B) χ'' frequency-dependent data, for $[(U(\text{Ph}_2\text{BPz}_2)_3)]$. Modified from J.D. Rinehart, J.R. Long, *Slow magnetic relaxation in a trigonal prismatic uranium(III) complex*, *J. Am. Chem. Soc.* 131 (2009) 12558–12559. Copyright 2009 American Chemical Society.

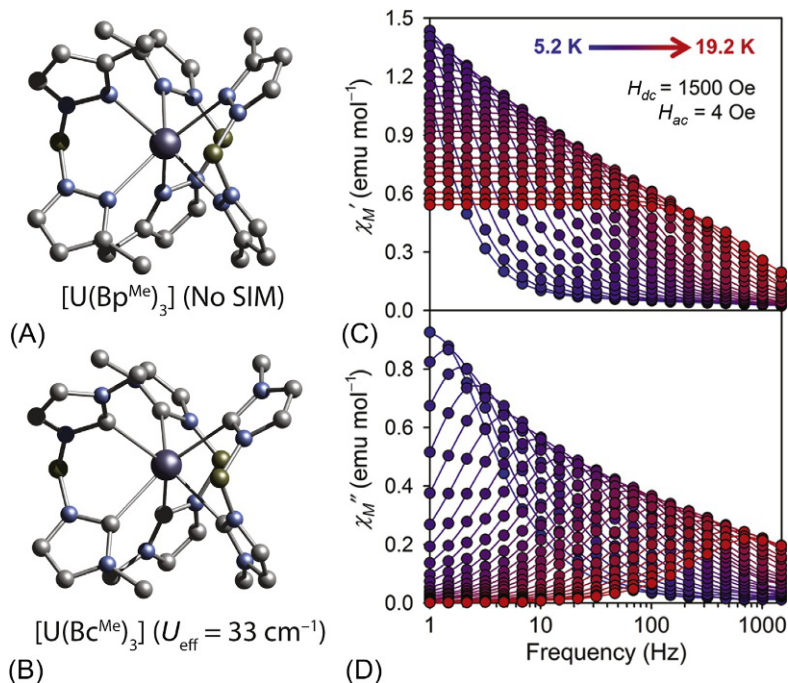


Fig. 1.19

(A) Crystals structure for $[\text{U}(\text{Bp}^{\text{Me}})_3]$ (where $\text{Bp}^{\text{Me-}}$ = dihydrobis(methylpyrazolyl)borate) and (B) $[\text{U}(\text{Bc}^{\text{Me}})_3]$ (with $\text{Bc}^{\text{Me-}}$ = dihydrobis(methylimidazolyl)borate) complexes. (C) χ'_M and (D) χ''_M frequency-dependent data at zero field for $[\text{U}(\text{Bc}^{\text{Me}})_3]$. Modified from K.R. Meihaus, S.G. Minasian, W.W. Lukens Jr., S.A. Kozimor, D.K. Shuh, T. Tyliczszaki, J.R. Long, *Influence of pyrazolate vs N-heterocyclic carbene ligands on the slow magnetic relaxation of homoleptic trischelate lanthanide(III) and uranium(III) complexes*, *J. Am. Chem. Soc.* 136 (2014) 6056–6068; Copyright 2014 American Chemical Society.

The effect of donor atoms was investigated in two isostructural trivalent uranium complexes, $[\text{U}(\text{Bp}^{\text{Me}})_3]$ and $[\text{U}(\text{Bc}^{\text{Me}})_3]$ (Bp^{Me} = dihydrobis(methylpyrazolyl)borate; Bc^{Me} = dihydrobis(methylimidazolyl)borate) (Fig. 1.19A and B) [60]. The Bp^{Me} ligand coordinates to the metal center via a pyrazolate carbon, while the Bc^{Me} counterpart involves an imidazolyl *N*-donor. AC susceptibility measurements revealed slow magnetic relaxation in the case of the *N*-heterocyclic carbene complex (Fig. 1.19C and D), while $[\text{U}(\text{Bp}^{\text{Me}})_3]$ showed no relaxation dynamics. This behavior is ascribed to the stronger axial ligand field of the former. Analysis of the data yielded a relaxation barrier $U_{\text{eff}} = 32 \text{ cm}^{-1}$, which is among the highest values for actinide-SIMs. At high temperatures, the magnetization of the system was found to relax via an Orbach process, while in the lower temperate region the Raman and Direct processes are dominant.

The first mononuclear $5f^1$ complex showing slow magnetic relaxation was reported in 2013 by Liddle and coworkers [43]. The complex, $[\text{U}(\text{O})(\text{Tren}^{\text{TIPS}})]$ ($\text{Tren}^{\text{TIPS}} = \{\text{N}(\text{CH}_2\text{CH}_2\text{NSi}^i\text{Pr}_3)_3\}$), has a C_{3v} symmetry and the U(V) ion adopts a distorted trigonal

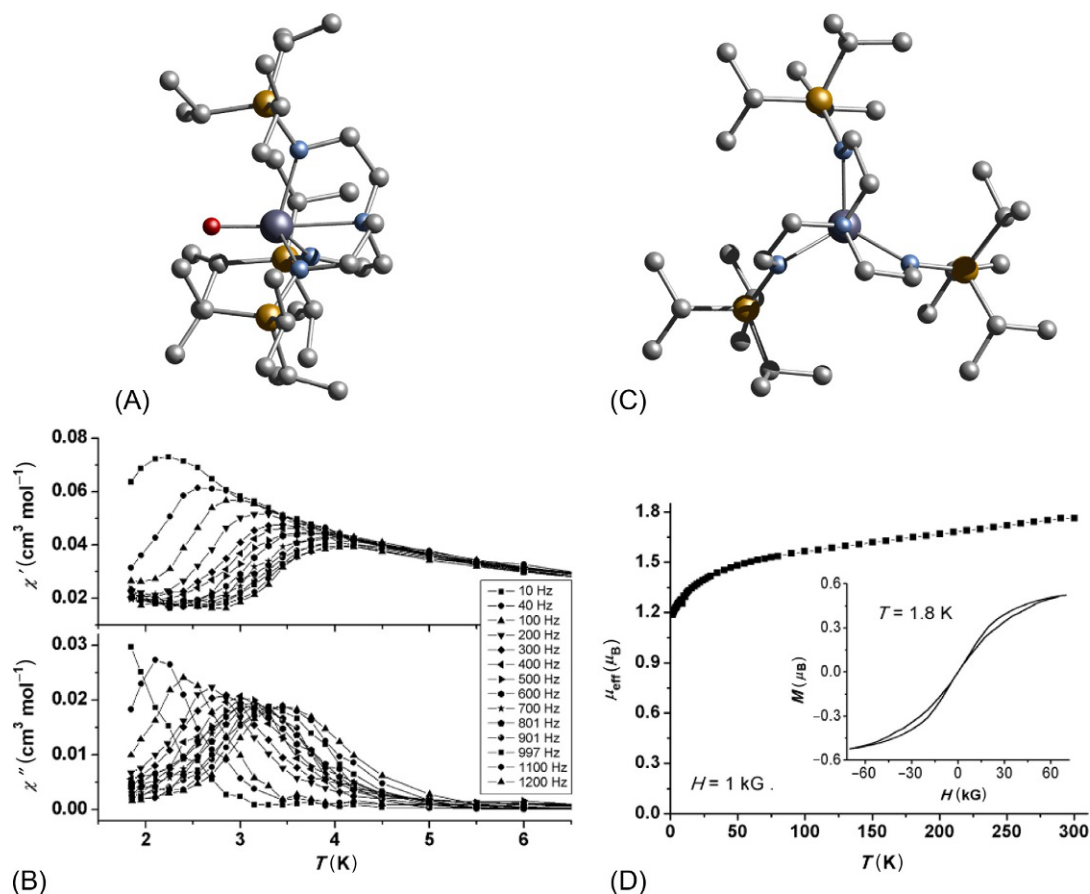


Fig. 1.20

(A) Side view and (C) top view of molecular structure of $[\text{U}(\text{O})(\text{Tren}^{\text{TIPS}})]$ ($\text{Tren}^{\text{TIPS}} = \{\text{N}(\text{CH}_2\text{CH}_2\text{NSi}^i\text{Pr}_3)_3\}$) exhibiting a C_{3v} symmetry. (B) χ' (top) and (D) χ'' (bottom) temperature-dependent magnetic data of $[\text{U}(\text{O})(\text{Tren}^{\text{TIPS}})]$. (D) Magnetic susceptibility and hysteresis loop (inset) showing the SIM behavior. Modified from D.M. King, F. Tuna, J. McMaster, W. Lewis, A.J. Blake, E.J.L. McInnes, S.T. Liddle, *Single-molecule magnetism in a single-ion triamidoamine uranium(V) terminal mono-oxo complex*, *Angew. Chem. Int. Ed.* 52 (2013) 4921–4924. Copyright 2013 Wiley-VCH.

bipyramidal geometry (Fig. 1.20A and C). The temperature-dependent χ'' shows a maximum at 3.5 K, while the frequency-dependent χ'' at varied temperatures reveals a $U_{\text{eff}} = 15 \text{ cm}^{-1}$, while open hysteresis loops are observed up to 3 K (Fig. 1.20B and D). Liddle et al. have also studied U(V) nitrides of general formula $[\text{U}(\text{Tren}^{\text{TIPS}})(\text{N})][\text{M}(\text{crown})_2]$ and $[\text{U}(\text{Tren}^{\text{TIPS}})(\mu\text{-N})][\text{M}(\text{crown})_2]$ ($\text{M} = \text{Li}, \text{Na}, \text{K}, \text{Rb}, \text{and Cs}$), respectively, which were found to display SIM characteristics [44]. In all these complexes, the U(V) center is coordinated by a nitride-nitrogen and other four nitrogen donors of a $\text{Tren}^{\text{TIPS}}$ ligand, in a way that provides a strongly axial ligand field of C_{3v} symmetry and distorted trigonal bipyramidal geometry. Analysis of the

frequency-dependent data yielded energy barriers $U_{\text{eff}} = 14\text{--}28\text{ cm}^{-1}$. Comparison across $[\text{U}^{\text{V}}(\text{Tren}^{\text{TIPS}})(\text{X})]$ ($\text{X} = \text{N}$ or O) complexes, both of axial (C_3) symmetry but with different axial ligands, enabled to study the effect of axial substitutions on magnetic anisotropy and magnetization dynamics. Ab initio calculations indicated that the ground state of $[\text{U}^{\text{V}}(\text{O})(\text{Tren}^{\text{TIPS}})]$ is a $jz = \pm 3/2$ term, while for the N^{3-} derivative, either a $jz = \pm 5/2$ or a nearly degenerate $\pm 5/2$ and $\pm 3/2$ are likely to be the lowest energetic states.

The first transuranic single-ion magnet $[\text{Np}(\text{COT})_2]$ ($\text{COT} = \text{cyclooctatetraene}$) was reported in 2011 [45], and is isostructural with the $[\text{Er}(\text{III})(\text{COT})_2]$ complex discussed in Section 1.5.1.2. The compound contains a $\text{Np}(\text{IV})$ ($5f^3$) ion sandwiched between two COT rings, thus forming a double-decker-type structure with D_{8h} symmetry (Fig. 1.21). The complex shows magnetic relaxation with $U_{\text{eff}} = 28\text{ cm}^{-1}$ under static magnetic fields larger than 0.1 T. However, the temperature dependence of the relaxation time (τ) measured under different external fields shows various combinations of relaxation pathways. Under low magnetic fields (0.5–2 T), both Orbach and QTM paths dominate the relaxation behavior. However, application of an intermediate field of 3 T successfully suppresses QTM. Moreover, at larger magnetic fields (above 5 T), the relaxation becomes frequency independent, suggesting a two-phonon process that involves excited ligand-field states. In addition, magnetization hysteresis loops are observed only at very high magnetic fields. By contrary, the corresponding $\text{U}(\text{III})$ ($4f^3$) analogue $[\text{U}(\text{COT})_2]^*$ does not show slow magnetic relaxation most likely due to its lower symmetry [45].

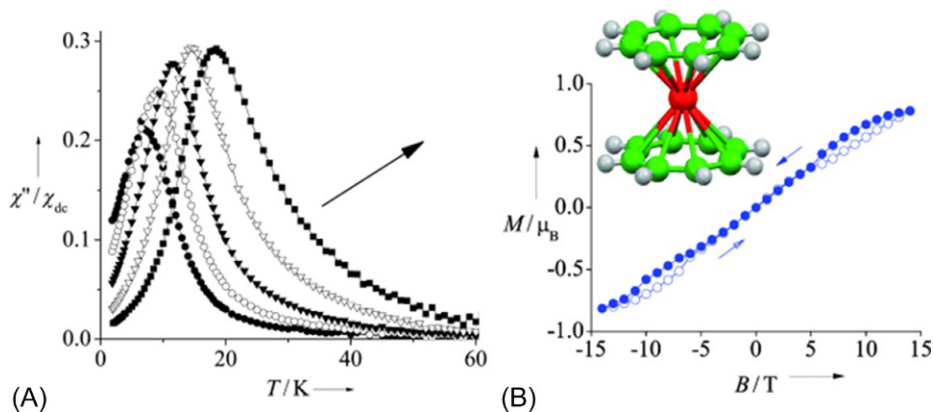


Fig. 1.21

(A) χ'' temperature-dependent magnetic susceptibility data and (B) hysteresis loop at 1.8 K for $[\text{Np}(\text{COT})_2]$. Reproduced with permission from N. Magnani, C. Apostolidis, A. Morgenstern, E. Colineau, J.-C. Griveau, H. Bolvin, O. Walter, R. Caciuffo, *Magnetic memory effect in a transuranic mononuclear complex*, *Angew. Chem. Int. Ed.* 50 (2011) 1696–1698. Copyright 2011 Wiley-VCH.

1.5.2 *f*-Elements Single-Molecule Magnets (*f*-SMMs)

As discussed in Section 1.5.3, the slow relaxation of the magnetization of *f*-block monometallic complexes primarily arises from the anisotropy of the ligand field surrounding the *f*-ion. However, when two or more lanthanide ions are brought together within a complex entity, the overall magnetic behavior can depart from the magnetic behavior of the single *f*-ion, particularly if the metals interact very strongly between them. This was demonstrated for several polymetallic cages, whose fascinating magnetic behaviors such as spin chirality [88–90] or blocking of magnetization at remarkable temperatures [26–28,54], are the resulting effect of magnetic exchange. However, most homometallic lanthanide complexes show very weak intermetal interactions due to lanthanide ion “contraction,” which results in narrow hysteresis loops, reduced U_{eff} barriers, and even quenching of the slow dynamics properties due to fast quantum tunneling rates. Dilution of the samples using isostructural diamagnetic hosts is a common technique used to slow down the magnetization relaxation rates. A few selected examples of polymetallic SMMs are presented in the next section. It is worth noting that weak intermetal interactions are sufficient to cause exchange bias quantum tunneling of the magnetization, which was demonstrated in a number of compounds [54,91–93].

1.5.2.1 Radical bridged $\{\text{Dy}_2\}$ and $\{\text{Tb}_2\}$ SMMs

The intrinsic inner nature of *f*-orbitals generally allows very small interactions between magnetic centers. In an attempt to enhance such Ln...Ln magnetic exchange, Rinehart and coworkers have proposed a radical-based strategy for the design of exchange-coupled SMMs. It consists in using paramagnetic radicals as bridging ligands between lanthanide ions, with the aim of mediating the magnetic exchange between the metals [27,28]. To this end, two interesting compounds were reported, $[\text{K}(\text{18-crown-6})]\{[\text{Me}_3\text{Si})_2\text{N}]_2(\text{THF})\text{Ln}\}_2(\mu\text{-}\eta\text{:}\eta\text{-N}_2)$, where Ln = Dy(III) or Tb(III) (Fig. 1.22A), which were obtained by reduction of the N_2^{2-} bridging ligand of $\{[\text{Me}_3\text{Si})_2\text{N}]_2(\text{THF})\text{Ln}\}_2(\mu\text{-}\eta\text{:}\eta\text{-N}_2)$ to $\text{N}_2^{\cdot-}$ in the presence of potassium graphite [27].

Both complexes are highly anisotropic, showing a frequency-dependent out-of-phase component of the magnetic susceptibility, characteristic of SMMs. Fitting the data to a single Debye process followed by an Arrhenius treatment of the relaxation times yields U_{eff} barriers of 123 and 227 cm^{-1} for the Dy(III) and Tb(III) derivatives, respectively (Fig. 1.22C and D). The energy barriers were significantly higher than those of the nonradical-bearing compounds, suggesting that the radical significantly strengthens the interaction between the lanthanide centers. The large anisotropy of the Tb and Dy ions precluded an accurate quantification of the magnetic exchange occurring between metal centers. To circumvent this problem, the authors have studied the isotropic version of the complexes, i.e., $[\text{K}(\text{18-crown-6})]\{[\text{Me}_3\text{Si})_2\text{N}]_2(\text{THF})\text{Gd}\}_2(\mu\text{-}\eta\text{:}\eta\text{-N}_2)$ and $\{[\text{Me}_3\text{Si})_2\text{N}]_2(\text{THF})\text{Gd}\}_2(\mu\text{-}\eta\text{:}\eta\text{-N}_2)$, respectively. The temperature-dependent dc magnetic susceptibility data revealed an exchange interaction >50 times stronger

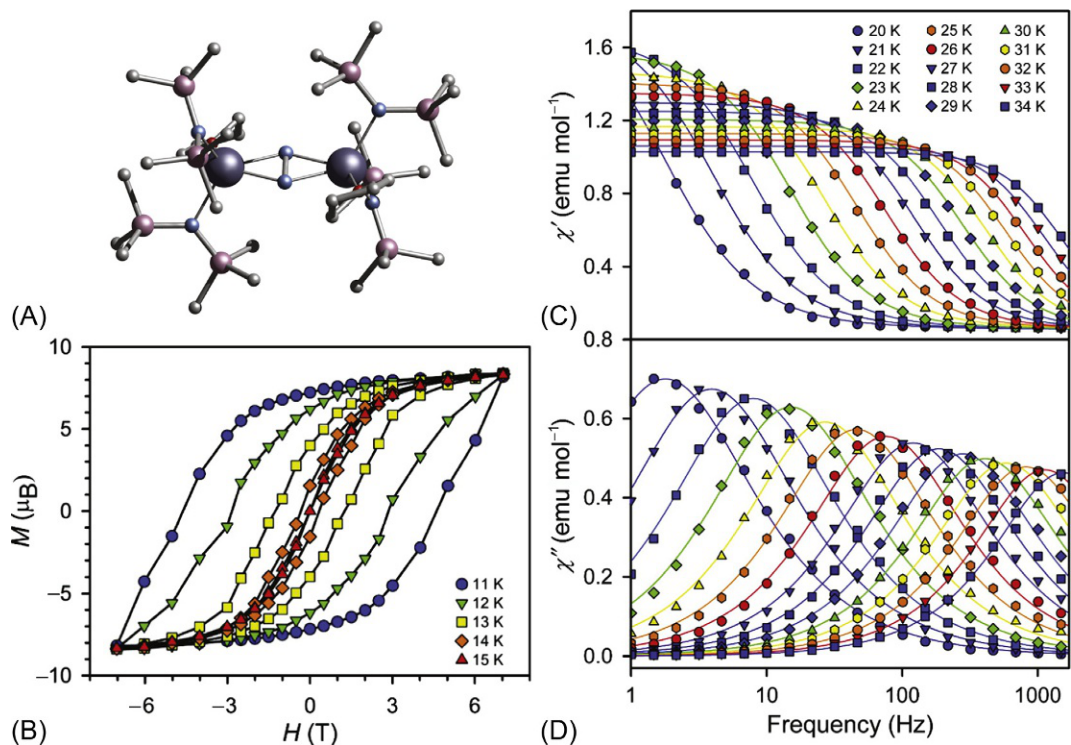


Fig. 1.22

(A) Crystal structure of $\{[\text{Me}_3\text{Si})_2\text{N}]_2(\text{THF})\text{Tb}\}_2(\mu\text{-}\eta\text{-}\eta\text{-N}_2)$; (B) open magnetic hysteresis loops at different temperatures between 11 and 15 K.; (C) χ' and (D) χ'' frequency-dependent data at zero field for same complex. Reproduced with permission from J.D. Rinehart, M. Fang, W.J. Evans, J.R. Long, *A N23-radical-bridged terbium complex exhibiting magnetic hysteresis at 14 K*, *J. Am. Chem. Soc.* 133 (2011) 14236–14239. Copyright 2011 American Chemical Society.

in the radical bridged dimers, compared to the nonradical analogues. The results clearly indicate that the occurrence of strong magnetic exchange positively impacts the magnetization dynamics of lanthanide SMMs (Fig. 1.22B). Indeed, field dependence of the magnetization at different temperatures shows hysteresis loops that are open up to 8 K for the radical-bridged Dy(III) dimer, and to 14 K for the radical-bridged Tb(III) dimer [27], while their nonradical versions do not show such magnetization blocking.

1.5.2.2 Asymmetric $\{\text{Dy}_2\}$ SMMs

The energy barrier of polymetallic f -based SMMs can be augmented by exchange interactions, as discussed in the previous section. However, many of the reported poly-lanthanide complexes show differences in the local environment at different metal sites, and rather weak magnetic interactions. Their spin dynamics are far of being improved through magnetic exchange. One example is the asymmetric lanthanide dimer with formula

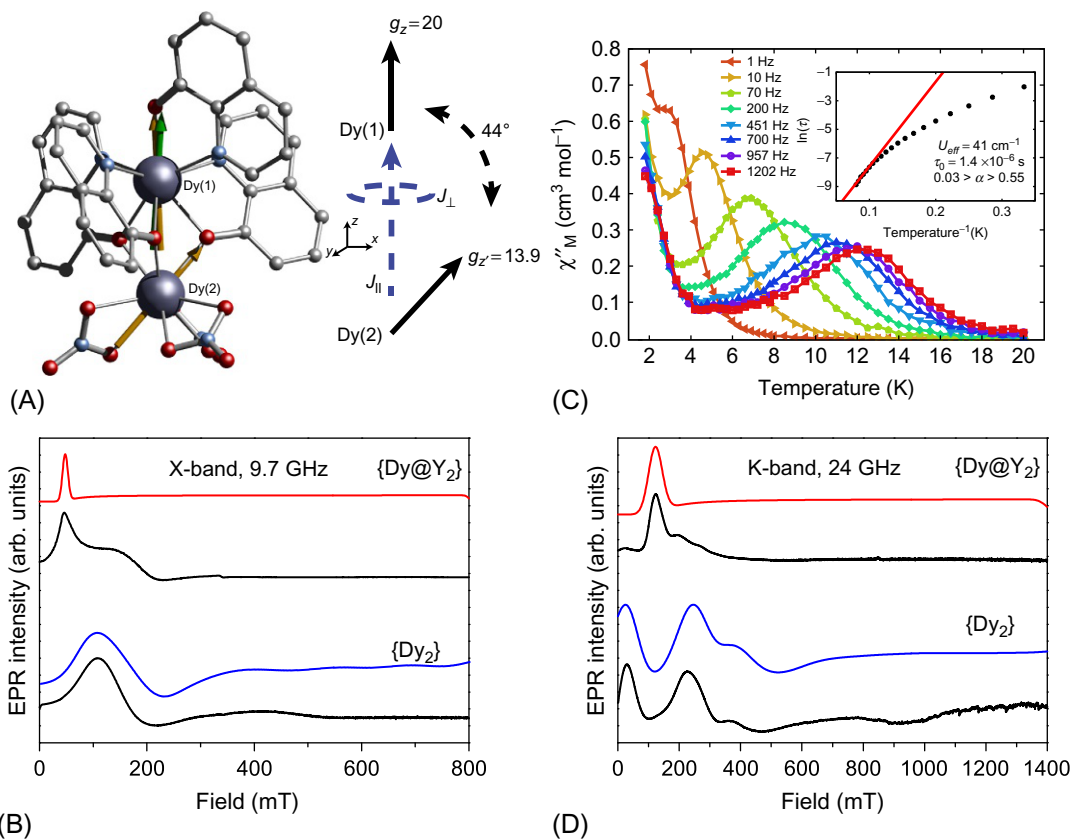


Fig. 1.23

(A) Crystal structure of $[\text{hdH}_2][\text{Dy}_2(\text{hq})_4(\text{NO}_3)_3]$ and orientation magnetic axes for Dy(1) and Dy(2) in the ground Kramers doublet from ab initio calculations (*tilted arrow*) and that for Dy(1) from electrostatic calculations (*vertical arrow*) and schematic of the magnetic model for the EPR simulation. (C) χ'' (T) and Arrhenius treatment (inset) for $\{\text{Dy@Y}_2\}$. X- (B) and K-band (D) experimental EPR spectra at 5 K (*second and fourth traces (from top to bottom)*) and simulated data for $\{\text{Dy@Y}_2\}$ (*first trace (from top to bottom)*) and $[\text{hdH}_2][\text{Dy}_2(\text{hq})_4(\text{NO}_3)_3]$ (*third trace (from top to bottom)*). Reproduced with permission from E. Moreno Pineda, N.F. Chilton, R. Marx, M. Dorfel, D.O. Sells, P. Neugebauer, S.-D. Jiang, D. Collison, J. van Slageren, E.J.L. McInnes, R.E.P. Winpenny, Direct measurement of dysprosium(III)···dysprosium(III) interactions in a single-molecule magnet, *Nat. Commun.* 5 (2014) 5243. Copyright 2014. Managed by Nature Publishing Group.

$[\text{hdH}_2][\text{Ln}_2(\text{hq})_4(\text{NO}_3)_3]$ (Ln = Y(III), Dy(III) or Lu(III)) (Fig. 1.23A) [94]. The two distinct coordination modes occurring in the complex, $[\text{Dy}(1)\text{N}_4\text{O}_4]$ and $[\text{Dy}(2)\text{O}_9]$, introduce a preferential distribution of the lanthanide ions contingent upon ionic radii. Thus, when a small amount of Dy(III) is doped into $[\text{hdH}_2][\text{Y}_2(\text{hq})_4(\text{NO}_3)_3]$, an almost 1:1 distribution in both pockets is obtained, due to a good match between the ionic radii of Y(III) and Dy(III) ions. In sharp contrast, when Dy(III) is doped into $[\text{hdH}_2][\text{Lu}_2(\text{hq})_4(\text{NO}_3)_3]$, the smaller ionic radius lanthanide prefers the N_4O_4 coordination environment.

AC magnetic susceptibilities studies show no maximum in the $\chi''(\nu)$ for the neat $\{\text{Dy}_2\}$ complex nor for the $5\%\text{Dy}@{\text{Lu}_2}$ sample. Conversely, a clear frequency-dependent maximum was obtained in the $5\%\text{Dy}@{\text{Y}_2}$ complex, demonstrating that at single-ion level, the Dy(III) ion residing in the N_4O_4 pocket is responsible for the observed SMM behavior, while the O_9 coordination environment does not propitiate the Ising characteristics of the Dy(III) ion (Fig. 1.23B). Ab initio calculation confirms these observations, where highly axial g -factors are obtained for the Dy(1), i.e., $g_x = g_y \approx 0$ and $g_z = 20$, characteristic of a pure $m_J = 15/2$, with an energy gap to the first excited state of $\sim 100\text{cm}^{-1}$, while for the Dy(2) the ground doublet the ground $m_J = 15/2$ state can mix with the excited state placed at ca. 24cm^{-1} above the ground state, via a nonzero transverse term. The three g -tensor values associated with the ground state were deducted to be: $g_x = 1.54$; $g_y = 0.05$, and $g_z = 15.42$, respectively. Ab initio calculations have shown that the angle between the principal axes for Dy(1) and Dy(2) lies at 44 degrees of each other (Fig. 1.23A). Field-dependent far-infrared (FIR) data associated with the Dy(2) pocket display two independent bands ascribed to the crystal field transitions at 39 and 59cm^{-1} , respectively, which compares well with the relevant transitions at 24 and 39cm^{-1} from ab initio calculations. Modeling the data using the Lines methodology, which assumes an isotropic exchange coupling between the Dy(III) ions, gave a weak ferromagnetic exchange constant of $J_{\text{Lines}} = +0.0047\text{cm}^{-1}$.

To achieve further understanding of the diminished SMM properties of the neat $\{\text{Dy}_2\}$ and $5\%\text{Dy}@{\text{Y}_2}$ systems, the compounds were further characterized by electron paramagnetic resonance (EPR). Multifrequency EPR spectra of the neat $\{\text{Dy}_2\}$ dimer provided clear evidence of magnetic exchange interactions within the dimeric units. The similitude between the EPR spectra of $5\%\text{Dy}@{\text{Y}_2}$ and $5\%\text{Dy}@{\text{Lu}_2}$ let the authors conclude that only one of the Dy pockets is responsible for the observed transitions. Due to the highly axial symmetry properties of the Dy(1) in the N_4O_4 pocket, it was assumed that no EPR signal would be observed in this case, while the mixed nature of the Dy(2) is more likely to yield EPR spectroscopic transitions. Indeed, the g -value measured by EPR spectroscopy, $g_z = 13.9$, is very close to the obtained value from ab initio calculations.

Modeling of the EPR data using the spin effective formalism ($S_{\text{eff}} = 1/2$) and taking into account the projection of the axial components of both Dy ions, of 44 degrees, as obtained from ab initio calculations, has provided excellent results, yielding an anisotropic exchange interaction characterized by $J_{\perp} = +0.525\text{cm}^{-1}$ and $J_{\parallel} = +1.52\text{cm}^{-1}$, respectively (Fig. 1.23B and D). Close inspection of the lowest-lying energy states of the coupled systems indicates that the responsible factor for the diminished SMM behavior on the neat $\{\text{Dy}_2\}$ dimer is most likely the noncollinear arrangement of the principal magnetic axes of the Dy(III) ions, which provides an additional channel for the relaxation of the magnetization. Obviously, limitation of the magnetic exchange by doping the dysprosium(III) system in the yttrium(III) analogue reveals the behavior of the single Dy(III) ion in the N_4O_4 pocket [94].

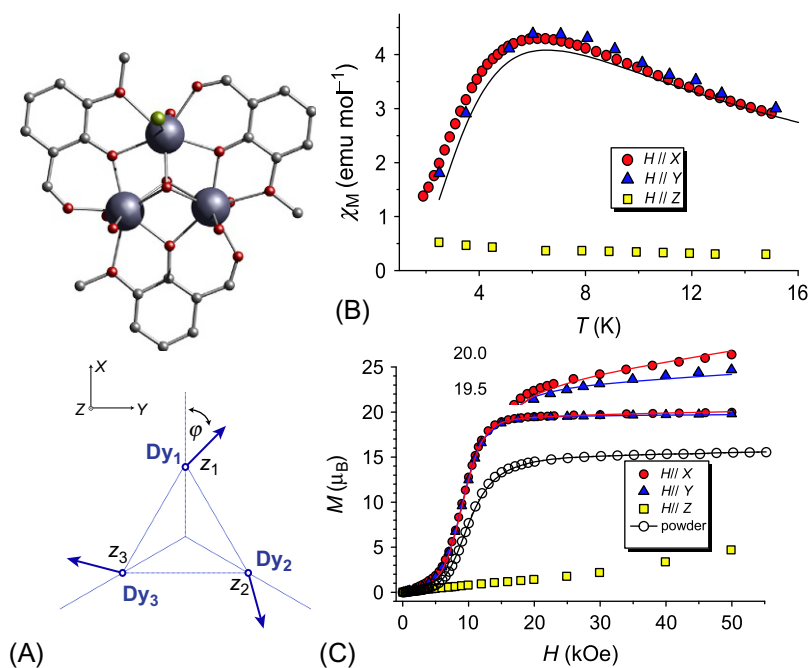


Fig. 1.24

(A) (top) Molecular structure of $[\text{Dy}_3(\mu_3\text{-OH})_2\text{L}_3\text{Cl}(\text{H}_2\text{O})_5]\text{Cl}_3$ (hydrogen atoms, the chloride counter ion and solvent molecules omitted for clarity), (bottom) scheme of the spin structure of the $\{\text{Dy}_3\}$ complex and the orientation of the local easy axes in respect of the laboratory XYZ reference frame. (B) Magnetic susceptibility and (C) magnetization data of a single crystal of $\{\text{Dy}_3\}$ at different crystallographic orientations. *Reproduced with permission from J. Luzon, K. Bernot, I.J. Bernot, C.E. Anson, A.K. Powell, R. Sessoli, Spin chirality in a molecular dysprosium triangle: the archetype of the noncollinear Ising model, Phys. Rev. Lett. 100 (2008) 247205. Copyright 2008 American Physical Society.*

1.5.2.3 Toroidal momentum in $\{\text{Dy}_3\}$ SMMs

An interesting magnetic behavior was reported in 2006 by Tang et al., who studied two related dysprosium(III) molecular triangles of formula $\text{Dy}_3(\mu_3\text{-OH})_2\text{L}_3\text{Cl}_2(\text{H}_2\text{O})_4$ $[\text{Dy}_3(\mu_3\text{-OH})_2\text{L}_3\text{Cl}(\text{H}_2\text{O})_5]\text{Cl}_5 \cdot 19\text{H}_2\text{O}$ and $[\text{Dy}_3(\mu_3\text{-OH})_2\text{L}_3\text{Cl}(\text{H}_2\text{O})_5]\text{Cl}_3 \cdot 4\text{H}_2\text{O} \cdot 2\text{MeOH} \cdot 0.7\text{MeCN}$ (where HL = *o*-vanillin), respectively (Fig. 1.24A) [88]. Static magnetic measurements on the $\{\text{Dy}_3\}$ triangles revealed a room temperature $\chi_M T$ value close to the expected one for the noninteracting Dy(III) ions. Upon cooling, however, $\chi_M T(T)$ goes roughly to zero, suggesting antiferromagnetic interactions between the metal centers. The low-temperature field-dependent study confirms this picture, with an $M(H)$ starting from zero at low fields, while for fields larger than 0.95 T the $M(H)$ curve increases up to the value of 15.3 μ_B , indicating that at high fields the ground state is purely $m_j = 15/2$. The intriguing $\chi_M T(T)$ and $M(H)$ behaviors of the $\{\text{Dy}_3\}$ triangles is a result of spin canting of the magnetic anisotropic axes, which are arranged in the XY plane, with a tilting angle of 120 degrees from each other. The arrangement of the axis of the

Dy(III) ions leads to a vortex spin-chiral singlet ground state (Fig. 1.24B and C) [89]. Upon application of fields larger than 0.95 T, a crossover between the ground singlet and an excited state is induced, which becomes the ground state at high fields.

The dynamics of the magnetization of $\{\text{Dy}_3\}$ were studied by ac magnetic susceptibility measurements, which revealed slow magnetic relaxation despite the compound possessing a diamagnetic ground state. An energy barrier of 25 cm^{-1} was deduced from data recorded at zero dc field, but this increased to 83 cm^{-1} by application of a small DC field of 3 kG.

1.5.2.4 High-nuclearity cages as SMMs: $\{\text{Dy}_4\text{K}_2\}$ and $\{\text{Dy}_5\}$ cages

Large energy barriers to the reversal of the magnetization have also been observed in two related alkoxide Dy(III) cages, one featuring a Dy(III) oxo-centered octahedron with a cis arrangement of potassium ions of formula $[\text{Dy}_4\text{K}_2\text{O}(\text{O}^t\text{Bu})_{12}]$ (Fig. 1.25B), while the second cage features a square-based pyramid with formula $[\text{Dy}_5\text{O}(\text{O}^i\text{Pr})_{13}]$ (Fig. 1.25C). Dynamic magnetic studies performed on the neat samples revealed a strong frequency-dependent behavior for both complexes, where a single relaxation process is observed for $\{\text{Dy}_5\}$ yielding an energy barrier of $U_{\text{eff}} = 528\text{ K}$. Interestingly, dynamic studies of the $\{\text{Dy}_4\text{K}_2\}$ compound revealed two relaxation processes, as noted in the Cole-Cole plots, with energy barriers of 480 and 220 cm^{-1} [54].

In order to determine whether exchange or dipolar interactions play a role in the magnitude on the energetic barrier to the reversal of the spin, dilution studies were conducted employing the diamagnetic analogues. The first set of molecules comprised a small amount of the preformed dysprosium cages, i.e., $\{\text{Dy}_4\text{K}_2\}$ and $\{\text{Dy}_5\}$ cocrystallized with the diamagnetic $\{\text{Y}_4\text{K}_2\}$ and

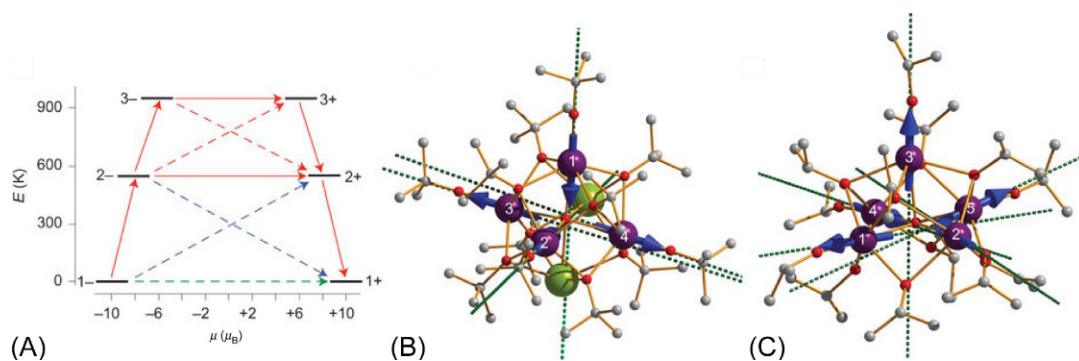


Fig. 1.25

(A) Relaxation mechanism diagram operating in complexes $[\text{Dy}_4\text{K}_2\text{O}(\text{O}^t\text{Bu})_{12}]$ and $[\text{Dy}_5\text{O}(\text{O}^i\text{Pr})_{13}]$; (B) and (C) crystal structures of $[\text{Dy}_4\text{K}_2\text{O}(\text{O}^t\text{Bu})_{12}]$ and $[\text{Dy}_5\text{O}(\text{O}^i\text{Pr})_{13}]$. Dotted lines show the orientation of local magnetic anisotropy axes, as obtained from ab initio calculations. Reproduced with permission from R.J. Blagg, L. Ungur, F. Tuna, J. Speak, P. Coman, D. Collison, W. Wernsdorfer, E.J.L. McInnes, L.F. Chibotaru, R.E.P. Winpenny, *Magnetic relaxation pathways in lanthanide single-molecule magnets*, *Nat. Chem.* 5 (2013) 673–678. Copyright 2013 Nature Publishing Group.

{Y₅} isostructural analogues, followed by dynamic magnetic susceptibility studies. The energy barrier thus obtained showed to be identical to those measured for nondiluted materials. A second study, consisting in adding a small amount of DyCl₃ (5%) in the crystallization solutions of the {Y₄K₂} or {Y₅} cages, lead to a partial occupancy of Dy(III) into the cages. In contrast to the neat {Dy₄K₂}, a single process was observed in the magnetic susceptibility studies of the Dy@{Y₄K₂} cage with a significantly improved energy barrier of 585 cm⁻¹. Similar results were obtained for the Dy@{Y₅} cage, where a $U_{\text{eff}} = 559 \text{ cm}^{-1}$ was obtained. These results indicate that intramolecular magnetic exchange is a contributor to relaxation.

Ab initio calculations have provided a better picture on the origin of such large energy barriers in both cages. First, the ligand field exerted by the OⁱPr⁻ with very short Dy...OⁱPr distances induces a very axial ligand field, yielding a highly pure $m_J = 15/2$ ground state for all Dy ions. Electronic calculation also shows a large separation between the ground doublet and the first excited state. In addition, rationalization of the relaxation to the magnetization observed for the neat compounds and the isolated Dy(III) ions doped in the cages shows that transverse fields from neighboring Dy ions strongly contribute to the relaxation of the magnetization. For the neat {Dy₄K₂} complex, the calculated energy barriers suggest that the relaxation paths involve the first and second excited states, while for {Dy₅} relaxation occurs through the first excited state only (Fig. 1.25A). For site-doped Dy cages, the measured energy barriers are much larger than the separations between relevant ground and first excited states, suggesting relaxation through the second excited state as a potential path. Interestingly, in both cages, the first excited state is very axial and practically collinear with the ground doublet; therefore, Orbach relaxation through this state is hindered.

1.5.2.5 Exchange bias quantum tunneling in a {Dy₄} SMM

Another example of the role of exchange interactions and spin canting onto the magnetic properties of SMMs was studied in a carbamate cage, obtained after CO₂ fixation [91]. The tetramer with formula [Dy₄(O₂CNⁱPr₂)₁₂] is composed of 12 carbamates and four dysprosium ions. Crystallographically, two molecules are present in the asymmetric unit, related by an inversion center, an important characteristic for subsequent single-crystals experiments (Fig. 1.26A). The tetramer is an SMM, as observed in the $\chi''(\nu, T)$ profiles. A single broad Debye process is observed with a moderate energy barrier of $U_{\text{eff}} = 22 \text{ cm}^{-1}$.

To further characterize the magnetic properties of the cage, single crystals μ -SQUID studies were conducted at different field sweep rates and temperatures, with the field applied parallel and perpendicular to the easy axis of the magnetization. Two different behaviors are observed depending on the direction of the applied magnetic field, suggesting spin canting.

Understanding of such behavior was achieved employing an electrostatic model, where the crystallographic coordinates of the ligands and the metal center involved and their charge distribution are considered. Electrostatic calculations show that the anisotropic axes on the complexes are canted, in good agreement with the μ -SQUID observations (Fig. 1.26B and C).

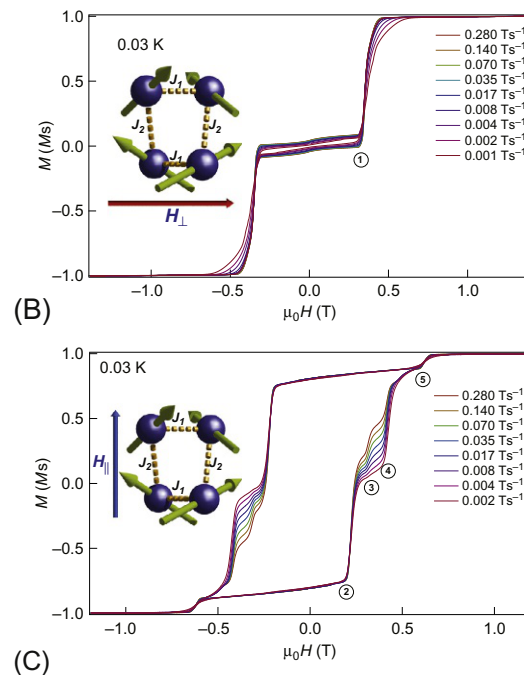
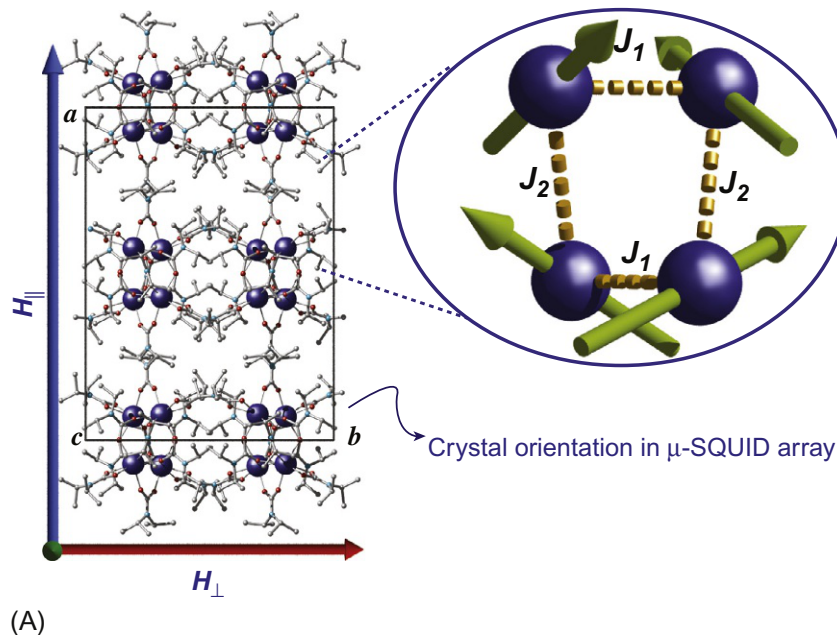


Fig. 1.26

(A) Crystal packing representation of $[\text{Dy}_4(\text{O}_2\text{CN}^i\text{Pr}_2)_{12}]$ molecules in the unit cell. The zoomed region shows the orientation of the principal magnetic axes of the Dy(III) ions obtained through electrostatic calculations (green arrow). Dashed lines connecting the Dy(III) represent the exchange pathways operating within the cluster. μ -SQUID loops obtained from single crystals study with the field applied parallel and perpendicular to the molecular easy axes. Panel (B) shows the antiferromagnetic behavior with a typical double S-shape while panels, while (C) shows the ferromagnetic behavior. Reproduced with permission from E. Moreno Pineda, Y. Lan, O. Fuhr, W. Wernsdorfer, M. Ruben, Exchange-bias quantum tunnelling in a CO₂-based Dy₄-single molecule magnet, *Chem. Sci.* 8 (2017) 1178–1185. Royal Society of Chemistry.

Rationalization of the μ -SQUID can be achieved employing the projection of the anisotropic axis and two exchange pathways occurring between the Dy(III) pairs. When the field is applied perpendicular to the easy axis, the ferromagnetic exchange between the Dy ions leads to a double S-shaped hysteresis with small QTM near zero field. Furthermore, a crossover with an excited state is observed at ± 0.35 T. Conversely, when the field is applied along the easy axis, the ferromagnetic interaction between the Dy ions along the edge results in open loops, with appreciable QTM at certain level crossings. Thus, both exchange pathways, i.e., ferromagnetic and antiferromagnetic, lead to two distinct behaviors depending on the direction of the applied magnetic field. Thus, in this example, exchange interactions not only improve the SMM properties, but also lead to other interesting magnetic phenomena.

1.5.2.6 Actinides-based SMMs

The variety of magnetic behaviors observed in polymetallic lanthanide complexes propitiated a significant effort in the synthesis, characterization, and understanding of the properties of the aggregates. Although polymetallic complexes with large U_{eff} were reported, their behavior, with only few exceptions, is primarily defined by the local symmetry of individual lanthanide ions. Strong exchange interactions in homometallic lanthanide complexes are very difficult to achieve, due to the “lanthanide contraction” effect. In this context, actinides are promising candidates for strongly exchanged SMMs. They have a larger spin-orbit coupling, which potentially yields larger anisotropies. The $5f$ orbitals of actinides are more diffuse than the $4f$ orbitals, promoting stronger interactions with the surrounding atoms, and potentially a stronger magnetic exchange.

Mill and coworkers have reported an arene-bridged dimeric uranium complex, $[(\text{U}(\text{BIPM}^{\text{TMS}}\text{H}(\text{I})_2(\mu\text{-}\eta^6\text{:}\eta^6\text{-C}_5\text{H}_5\text{CH}_3)_2)]$, which displayed slow magnetic relaxation at low temperatures and a hysteresis loop (Fig. 1.27A–C) [95]. Although DC magnetic susceptibility studies showed no significant magnetic exchange between the uranium centers, in agreement with the density functional theory (DFT) data, the compound showed that polymetallic SMMs can be assembled from actinide ions.

1.5.3 *f*-Elements Single-Chain Magnets (*f*-SCM)

The prediction of Roy J. Glauber in 1963 that one-dimensional ferromagnetic Ising chains would display slow relaxation of the magnetization at low temperature was experimentally demonstrated in 2001 in a Co(II)-nitronyl nitroxide single chain [96]. Such single-chain magnets (SCMs) are 1D molecular spin systems that relax slowly below a blocking temperature. They consist of magnetically isolated chains that can be magnetized and have the ability to preserve their magnetization in the absence of an external magnetic field. They are commonly formed by two components: a building block (metal ion), which provides the electron spin and the anisotropy of the chain, and the linker (organic ligand) connecting the

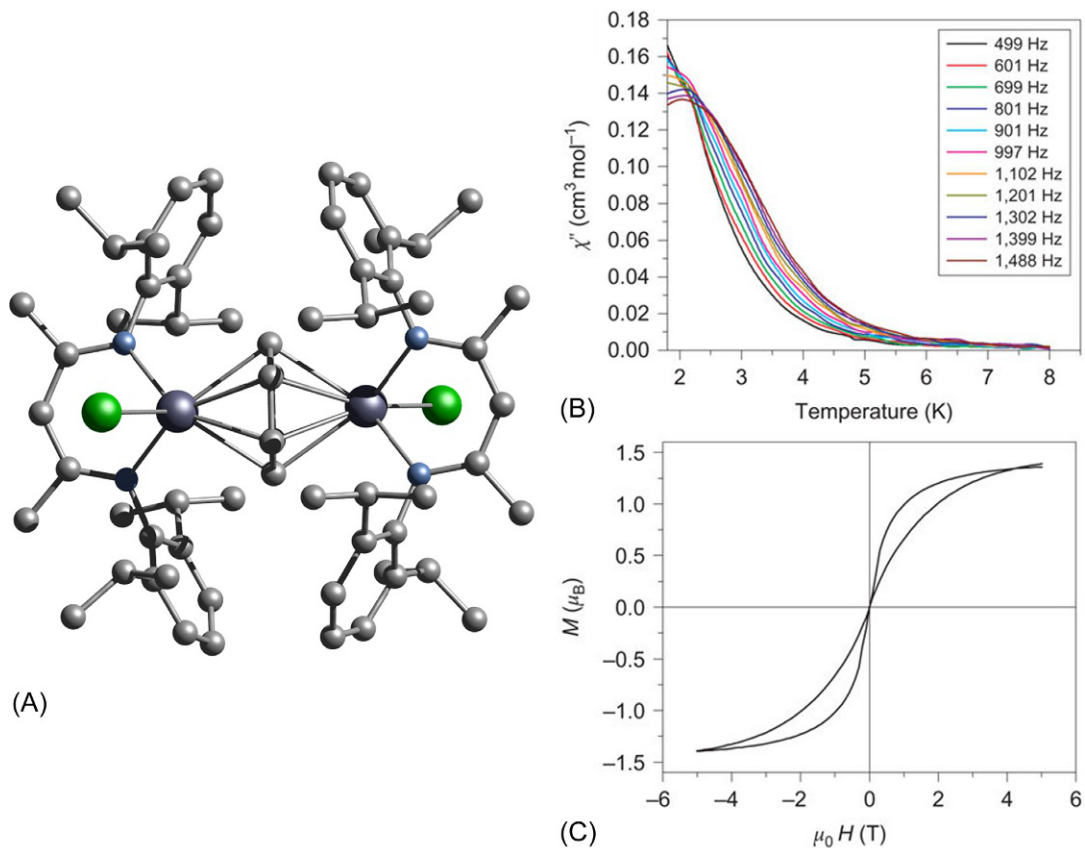


Fig. 1.27

(A) Crystal structure of $[(\text{U}(\text{BIPM}^{\text{TMS}}\text{H}(\text{l})_2(\mu-\eta^6-\eta^6-\text{C}_5\text{H}_5\text{CH}_3)_2)]$, (B) temperature-dependent χ'' , and (C) hysteresis loop at 1.8 K for the same complex. *Reproduced with permission from D.P. Mills, F. Moro, J. McMaster, J. van Slageren, W. Lewis, A.J. Blake, S.T. Liddle, A delocalized arene-bridged diuranium single-molecule magnet, Nat. Chem. 3 (2011) 454–460. Copyright 2011 Nature Publishing Group.*

building blocks in a one-dimensional fashion. The SCM property requires the presence of uniaxial anisotropy, along with significant exchange interactions along the chain. Additionally, any interchain interactions must be very weak. In these systems, slow relaxation of magnetization is a consequence of interchain magnetic exchange, and of uniaxial anisotropy enhanced by the orientation of the molecules parallel with the easy axis of magnetization.

Lanthanide ions are appealing building blocks because of their high-spin quantum numbers and large magnetic anisotropy. The first rare-earth SCM reported in 2005 by Gatteschi and coworkers was $[\text{Dy}(\text{hfac})_3\text{NIT}(\text{C}_6\text{H}_4p\text{-OPh})]$, where $\text{NIT}(\text{C}_6\text{H}_4p\text{-OPh})$ is a radical linker (Fig. 1.28A) [97]. The related $[\text{Dy}(\text{hfac})_3\{\text{NIT}(\text{Et})\}]$ complex showed a transition to 3D magnetic order at 4.3 K. Bulkier ligands such as biphenyl allowed isolation of the single chains

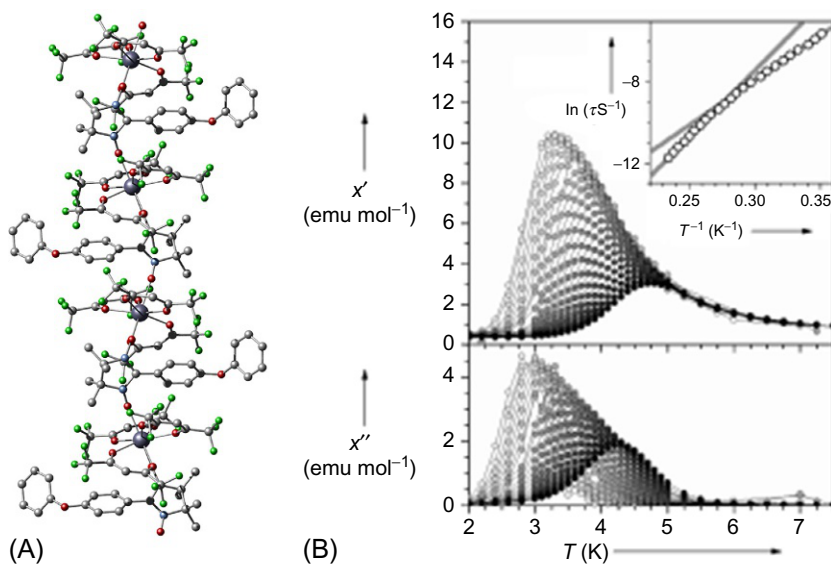


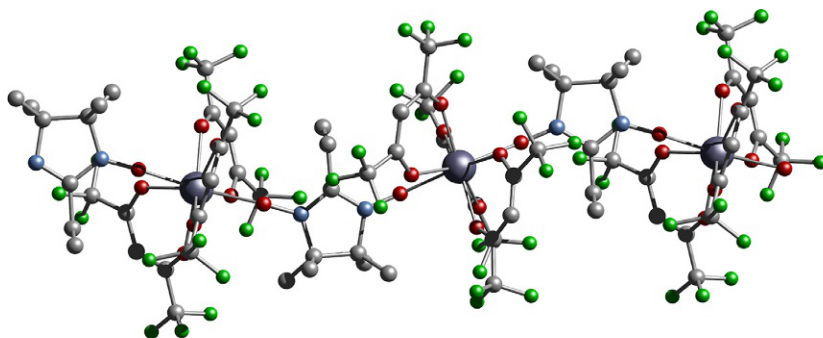
Fig. 1.28

(A) Crystal structure of $[\text{Dy}(\text{hfac})_3\text{NIT}(\text{C}_6\text{H}_4p\text{-OPh})]$; and (B) χ' (top) and (bottom) χ'' temperature-dependent magnetic susceptibility data. Modified from L. Bogani, C. Sangregorio, R. Sessoli, D. Gatteschi, *Molecular engineering for single-chain-magnet behavior in a one-dimensional dysprosium-nitronyl nitroxide compound*, *Angew. Chem. Int. Ed.* 44 (2005) 5817–5821. Copyright 2005 Wiley-VCH.

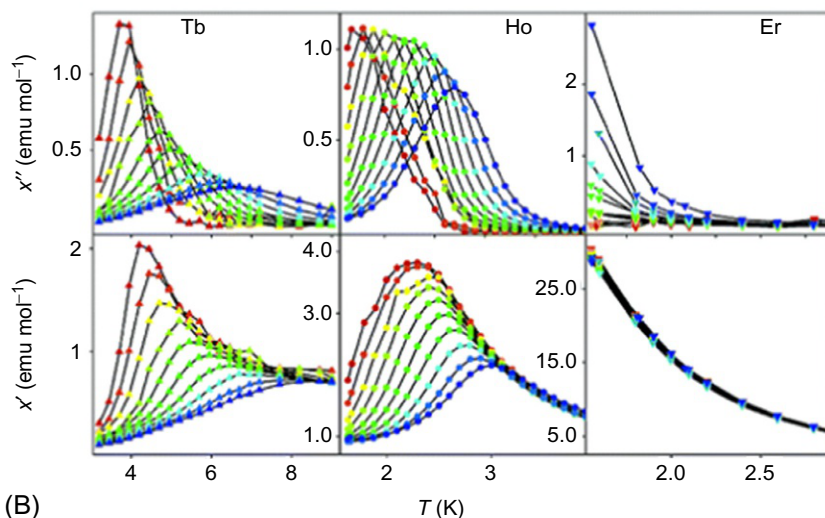
leading to SCM behavior. $[\text{Dy}(\text{hfac})_3\text{NIT}(\text{C}_6\text{H}_4p\text{-OPh})]$ is a chain in which octacoordinate $\text{Dy}(\text{hfac})_3$ units are interlinked by bis-monodentate radical NIT ligands. The chain displays typical SCM behavior, with $\chi''(T)$ showing a maximum at 4.5 K (Fig. 1.28B). Two different activated regimes were evidenced in the Arrhenius plot, from which anisotropy barriers of 29 and 48 cm^{-1} were deduced. Hysteretic behavior was also observed at 1.6 K, with two different field sweep independent steps.

In a subsequent study, the family of $[\text{Ln}(\text{hfac})_3\text{NIT}(\text{C}_6\text{H}_4p\text{-OPh})]$ ($\text{Ln} = \text{Eu}(\text{III}), \text{Gd}(\text{III}), \text{Tb}(\text{III}), \text{Dy}(\text{III}), \text{Ho}(\text{III}), \text{Er}(\text{III}), \text{Tm}(\text{III}),$ and $\text{Yb}(\text{III})$) was extended to include late lanthanide elements (Fig. 1.29A) [98]. The Tb, Ho, Er, and Tm derivatives show similar behavior with the preliminary Dy complex through steps in the magnetization hysteresis loops at different magnetic fields. The anisotropy barriers estimated from ac data of the Tb, Dy, and Ho derivatives measured 12–18 cm^{-1} (for both finite and infinite regimes), while those of the Er and Tm compounds could not be determined (Fig. 1.29B).

The $[\{\text{Dy}(\text{hfac})_3\text{NitPhIm}_2\}\text{Dy}(\text{hfac})_3]$ (NitPhIm = 2-[4-(1-imidazole)-phenyl]nitronyl nitride radical) complex (Fig. 1.30A) was shown to display slow relaxation of the magnetization with two different relaxation regimes, of an SMM at low temperatures, and an SCM at higher temperatures [99]. The chain consists of a $\{\text{Dy}(\text{Nit})_2\}$ unit linked via an NIT radical ligand to a $\{\text{Dy}(\text{hfac})_3\}$ moiety. The isostructural Gd(III) derivative displays ferromagnetic exchange



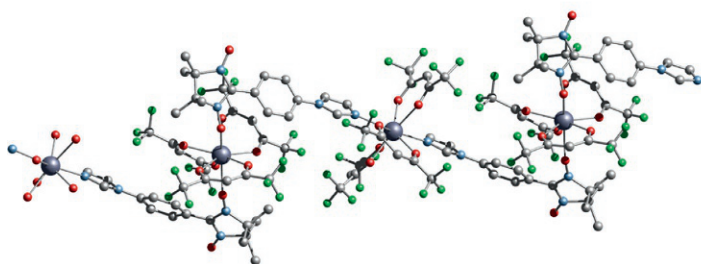
(A)



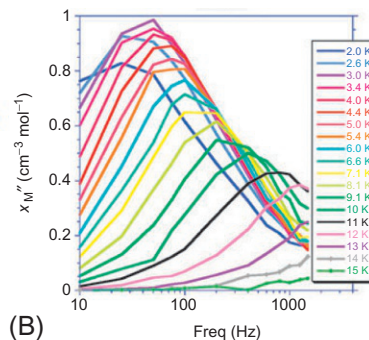
(B)

Fig. 1.29

(A) Molecular structure of $[\text{Tb}(\text{hfac})_3\text{NIT}(\text{C}_6\text{H}_4p\text{-OPh})]$ SCM. (B) Temperature dependence of χ' (top) and χ'' (bottom) magnetic susceptibilities at zero dc field for $[\text{Ln}(\text{hfac})_3\text{NIT}(\text{C}_6\text{H}_4p\text{-OPh})]$ ($\text{Ln} = \text{Tb}(\text{III}), \text{Ho}(\text{III})$) complexes. Reproduced with permission from K. Bernot, L. Bogani, A. Caneschi, D. Gatteschi, R. Sessoli, *A family of rare-earth-based single chain magnets: playing with anisotropy*, *J. Am. Chem. Soc.* 128 (2006) 7947–7956. Copyright 2006 American Chemical Society.



(A)



(B)

Fig. 1.30

(A) Molecular structure of $[\{\text{Dy}(\text{hfac})_3\text{NIT}(\text{PhIm})_2\}\text{Dy}(\text{hfac})_3]$ and (B) χ'' frequency-dependent magnetic susceptibility data. Reproduced with permission from R. Liu, X. Wang, P. Yang, C. Wang, D. Liao, J.-P. Sutter, *Smooth transition between SMM and SCM-type slow relaxing dynamics for a 1-D assemblage of $\{\text{Dy}(\text{nitronyl nitroxide})_2\}$ units*, *Chem. Commun.* 46 (2010) 2566–2568. Royal Society of Chemistry.

across the chain, with $J_1 = 3.53 \text{ cm}^{-1}$, $J_2 = -8.93 \text{ cm}^{-1}$, and $zJ' = 0.017 \text{ cm}^{-1}$, where J_1 represents the Ln-rad interaction, J_2 is the rad-rad coupling, and zJ' accounts for interchain interactions. The Arrhenius plot revealed two different relaxation regimes characterized by $U_{\text{eff}} = 12 \text{ cm}^{-1}$ and $U_{\text{eff}} = 57 \text{ cm}^{-1}$, respectively (Fig. 1.30B).

$[\text{Dy}_2(\text{hfac})_6(\text{NITThienPh})_2]_n$ was reported in 2003 (Fig. 1.31A) [100]. Its energy barrier was found to be $U_{\text{eff}} = 19 \text{ cm}^{-1}$ (Fig. 1.31B and C). The compound displays an uncommon

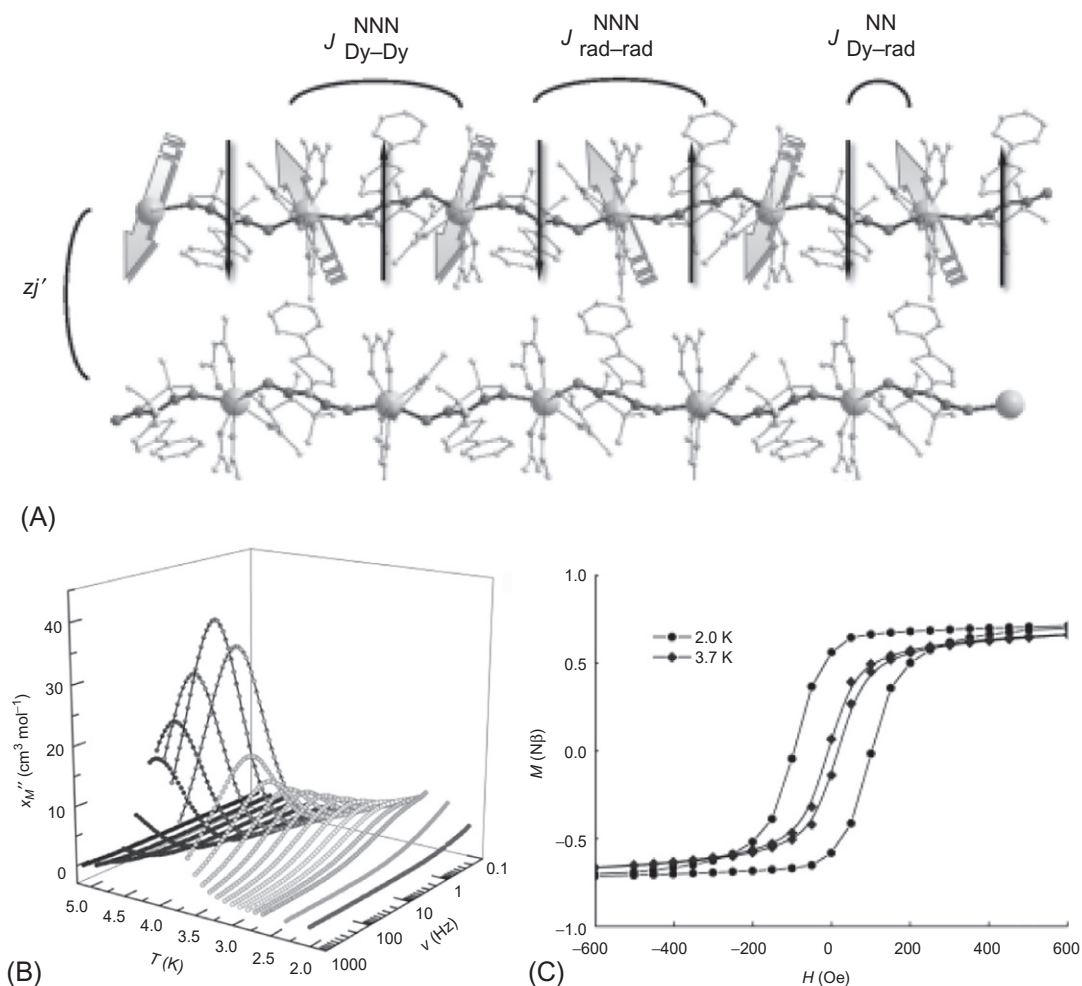


Fig. 1.31

(A) Molecular structure of the $[\text{Dy}_2(\text{hfac})_6(\text{NITThienPh})_2]_n$ SCM; arrows illustrate the orientation of the spins; (B) χ'' frequency-dependent magnetic susceptibility data; and (C) hysteresis loops at 2 and 3.7 K. Modified from T. Han, W. Shi, Z. Niu, B. Na, P. Cheng, *Magnetic blocking from exchange interactions: slow relaxation of the magnetization and hysteresis loop observed in a dysprosium–nitronyl nitroxide chain compound with an antiferromagnetic ground state*, *Chem. Eur. J.* 19 (2013) 994–1001. Copyright 2013 Wiley-VCH.

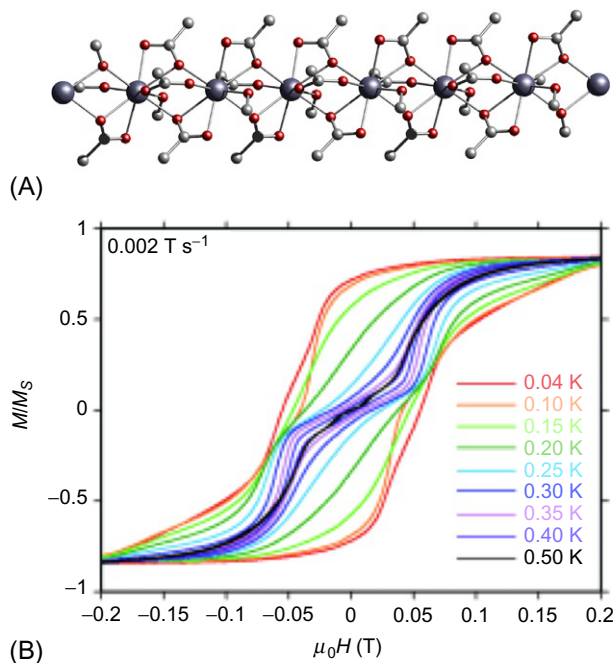


Fig. 1.32

(A) Crystal structure of $[\text{Dy}(\text{OAc})_3(\text{MeOH})]_n$ and (B) hysteresis loops along the easy axis of magnetization for $[\text{Dy}(\text{OAc})_3(\text{MeOH})]_n$ with an orientated single crystal at different temperatures. Data from Y.-Z. Zheng, Y. Lan, W. Wernsdorfer, C.E. Anson, A.K. Powell, *Polymerisation of the dysprosium acetate dimer switches on single-chain magnetism*, *Chem. Eur. J.* 15 (2009) 12566–12570. Copyright 2009 Wiley-VCH.

combination of an antiferromagnetic ground state with coexistence of superparamagnetic and metamagnetic behavior. Both in-phase and out-of-phase peaks display temperature and frequency dependence, with the Arrhenius law yielding two energy barrier values, $U_{\text{eff}} = 37 \text{ cm}^{-1}$ and $U_{\text{eff}} = 68 \text{ cm}^{-1}$, due to a crossover point at 3.5 K.

The Ising-type zig-zag polymer $[\text{Dy}(\text{OAc})_3(\text{MeOH})]_n$ was shown to exhibit SCM behavior (Fig. 1.32A) [101], and magnetic hysteresis loops observable at 0.5 K; the S-shaped loops indicated a weak interchain interaction (Fig. 1.32B).

1.6 Conclusions and Perspectives

Molecular nanomagnets are at the center of intensive research in the field of molecular magnetism, contributing over years to some of the most intriguing and interesting scientific discoveries. In particular, since the discovery of the $\{\text{Mn}_{12}\}$ cage that showed a magnet-like behavior at single-molecule level, huge scientific efforts were invested in the search for new

SMMs, primarily incorporating transition metal complexes. The field re-emerged upon the discovery of blockage of the magnetization at single-ion level. Undoubtedly, *f*-elements are better positioned as possible materials in futuristic applications, as their behavior relies on their own anisotropic characteristics and ability to engineer the ligand field in which they are placed, rather than cooperative effects. They can also provoke unusual physical phenomena.

To some extent, the magnetic properties of *f*-based SMMs can be rationalized, and design criteria for improving the performance of SMMs have been developed. The basic comprehension of the magnetic characteristic of *f*-SMMs, and the factor affecting this character is of utmost importance for the successful implementation of these systems in futuristic technological schemes. Additionally, these studies provide some insight into the type of possible effects influencing the SMM characteristics of the molecules upon their introduction in hybrid materials, where surface-SMM interactions are a need and can activate or quench other relaxation pathways.

Remarkably, the recent reports of some SIMs and SMMs with large energy barriers and hysteresis loops at high temperatures, position *f*-based molecules very close of employing these characteristics in data storage applications, where extremely dense data storage devices are foreseen. Moreover, it is also important to mention that although the majority of *f*-SMMs do not exhibit large blocking temperatures and hysteresis loops, their integration in other futuristic applications is yet plausible. An example is the implementation of *f*-SMMs as quantum bits, or *qubits*, taking advantage of the isolated ground doublet and the inner nature of *f*-orbitals, which cause low error rates.

References

- [1] A. Caneschi, D. Gatteschi, R. Sessoli, A.L. Barra, L.C. Brunel, M. Guillot, Alternating current susceptibility, high field magnetization, and millimeter band EPR evidence for a ground $S = 10$ state in $[\text{Mn}_{12}\text{O}_{12}(\text{CH}_3\text{COO})_{16}(\text{H}_2\text{O})_4] \cdot 2\text{CH}_3\text{COOH} \cdot 4\text{H}_2\text{O}$, *J. Am. Chem. Soc.* 113 (1991) 5873–5874.
- [2] R. Sessoli, H.L. Tsai, A.R. Schake, S.Y. Wang, J.B. Vincent, K. Folting, D. Gatteschi, G. Christou, D.N. Hendrickson, High-spin molecules: $[\text{Mn}_{12}\text{O}_{12}(\text{O}_2\text{CR})_{16}(\text{H}_2\text{O})_4]$, *J. Am. Chem. Soc.* 115 (1993) 1804–1816.
- [3] R. Sessoli, D. Gatteschi, A. Caneschi, M.A. Novak, Magnetic bistability in a metal-ion cluster, *Nature* 365 (1993) 141–143.
- [4] D. Gatteschi, R. Sessoli, J. Villain, *Molecular Nanomagnets: Mesoscopic Physics and Nanotechnology*, Oxford University Press, Oxford, 2006.
- [5] G. Aromi, E.K. Brechin, R. Winpenny (Ed.), *Single-Molecule Magnets and Related Phenomena*, Springer-Verlag, Berlin, Heidelberg, 2006, pp. 1–67 and references therein.
- [6] B. Barbara, J. Bartolomé, F. Luis, J.F. Fernández (Eds.), *Molecular Magnets: Physics and Applications*, Springer-Verlag, Berlin, Heidelberg, 2014, pp. 17–60 and references therein.
- [7] C. Benelli, D. Gatteschi, *Introduction to Molecular Magnetism. From Transition Metals to Lanthanides*, Wiley-VCH, Weinheim, 2015.
- [8] S.G. McAdams, A.-M. Ariciu, A.K. Kostopoulos, J.P.S. Walsh, F. Tuna, Molecular single-ion magnets based on lanthanides and actinides: design considerations and new advances in the context of quantum technologies, *Coord. Chem. Rev.* 346 (2017) 216–239.
- [9] G.A. Craig, M. Murrie, 3D single-ion magnets, *Chem. Soc. Rev.* 44 (2015) 2135–2147.

- [10] J.M. Frost, K.L.M. Harriman, M. Murugesu, The rise of 3-d single-ion magnets in molecular magnetism: towards materials from molecules? *Chem. Sci.* 7 (2016) 2470–2491.
- [11] W. Wernsdorfer, N. Aliaga-Alcalde, D.N. Hendrickson, G. Christou, Exchange-biased quantum tunnelling in a supramolecular dimer of single-molecule magnets, *Nature* 416 (2002) 406–409.
- [12] W. Wernsdorfer, R. Sessoli, Quantum phase interference and parity effects in magnetic molecular clusters, *Science* 284 (1999) 133–135.
- [13] M.N. Leuenberger, D. Loss, Quantum computing in molecular magnets, *Nature* 410 (2001) 789–793.
- [14] F. Luis, A. Repolles, M.J. Martínez-Pérez, D. Aguila, O. Roubeau, D. Zuego, P. J. Alonso, M. Evangelisti, A. Camon, J. Sese, L.A. Barrios, G. Aromi, Molecular prototypes for spin-based CNOT and SWAP quantum gates, *Phys. Rev. Lett.* 107 (2011) 117203.
- [15] M.J. Martínez-Pérez, S. Cardona-Serra, C. Schlegel, F. Moro, P.J. Alonso, H. Prima-García, J.M. Clemente-Juan, M. Evangelisti, A. Gaita-Ariño, J. Sesé, J. van Slageren, E. Coronado, F. Luis, Gd-based single-ion magnets with tunable magnetic anisotropy: molecular design of spin qubits, *Phys. Rev. Lett.* 108 (2012) 247213.
- [16] L. Bogani, W. Wernsdorfer, Molecular spintronics using single-molecule magnets, *Nat. Mater.* 7 (2008) 179–186.
- [17] R. Vincent, S. Klyatskaya, M. Ruben, W. Wernsdorfer, F. Balestro, Electronic read-out of a single nuclear spin using a molecular spin transistor, *Nature* 488 (2012) 357–360.
- [18] M. Urdampilleta, S. Klyatskaya, J.-P. Cleuziou, M. Ruben, W. Wernsdorfer, Supramolecular spin valves, *Nat. Mater.* 10 (2011) 502–506.
- [19] T. Glaser, Rational design of single-molecule magnets: a supramolecular approach, *Chem. Commun.* 47 (2010) 116–130.
- [20] R. Bagai, G. Christou, The Drosophila of single-molecule magnetism: $[\text{Mn}_{12}\text{O}_{12}(\text{O}_2\text{CR})_{16}(\text{H}_2\text{O})_4]$, *Chem. Soc. Rev.* 38 (2009) 1011–1026.
- [21] C.J. Milios, A. Vinslava, W. Wernsdorfer, S. Moggach, S. Parsons, S.P. Perlepes, G. Christou, E. K. Brechin, A record anisotropy barrier for a single-molecule magnet, *J. Am. Chem. Soc.* 129 (2007) 2754–2755.
- [22] I.-R. Jeon, R. Clérac, Controlled association of single-molecule magnets (SMMs) into coordination networks: towards a new generation of magnetic materials, *Dalton Trans.* 41 (2012) 9569–9586.
- [23] C. Sangregorio, T. Ohm, C. Paulsen, R. Sessoli, D. Gatteschi, Quantum tunneling of the magnetization in an iron cluster nanomagnet, *Phys. Rev. Lett.* 78 (1997) 4645–4648.
- [24] S.J. Langley, M. Helliwell, R. Sessoli, P. Rosa, W. Wernsdorfer, R.E.P. Winpenny, Slow relaxation of magnetisation in an octanuclear cobalt(II) phosphonate cage complex, *Chem. Commun. (Camb.)* (2005) 5029–5031.
- [25] E. Tancini, M.J. Rodriguez-Douton, L. Sorace, A.L. Barra, R. Sessoli, A. Cornia, Slow magnetic relaxation from hard-axis metal ions in tetranuclear single-molecule magnets, *Chem. Eur. J.* 16 (2010) 10482–10493.
- [26] S. Demir, J.M. Zadrozny, M. Nippe, J.R. Long, Exchange coupling and magnetic blocking in bipyrimidyl radical-bridged di-lanthanide complexes, *J. Am. Chem. Soc.* 134 (2012) 18546–18549.
- [27] J.D. Rinehart, M. Fang, W.J. Evans, J.R. Long, A N_2^{3-} radical-bridged terbium complex exhibiting magnetic hysteresis at 14 K, *J. Am. Chem. Soc.* 133 (2011) 14236–14239.
- [28] J.D. Rinehart, M. Fang, W.J. Evans, J.R. Long, Strong exchange and magnetic blocking in N_2^{3-} radical-bridged lanthanide complexes, *Nat. Chem.* 3 (2011) 538–542.
- [29] N. Ishikawa, M. Sugita, T. Ishikawa, S.-Y. Koshihara, Y. Kaizu, Lanthanide double-decker complexes functioning as magnets at the single-molecular level, *J. Am. Chem. Soc.* 125 (2003) 8694–8695.
- [30] N. Ishikawa, M. Sugita, T. Okubo, N. Tanaka, T. Iino, Y. Kaizu, Determination of ligand-field parameters and f-electronic structures of double-decker bis(phthalocyaninato) lanthanide complexes, *Inorg. Chem.* 42 (2003) 2440–2446.
- [31] S.T. Liddle, J.V. Slageren, Improving f-element single molecule magnets, *Chem. Soc. Rev.* 44 (2015) 6655–6669.
- [32] T. Pugh, F. Tuna, L. Ungur, D. Collison, E.J.L. McInnes, L.F. Chibotaru, R.A. Layfield, Influencing the properties of dysprosium single-molecule magnets with phosphorus donor ligands, *Nat. Commun.* 6 (2015) 7492.

- [33] T. Pugh, N.F. Chilton, R.A. Layfield, A low-symmetry dysprosium metallocene single-molecule magnet with a high anisotropy barrier, *Angew. Chem. Int. Ed.* 55 (2016) 11082–11085.
- [34] L. Ungur, J.J. Le Roy, I. Korobkov, M. Murugesu, L.F. Chibotaru, Fine-tuning the local symmetry to attain record blocking temperature and magnetic remanence in a single-ion magnet, *Angew. Chem. Int. Ed.* 53 (2014) 4413–4417.
- [35] M. Gregson, N.F. Chilton, A.-M. Ariciu, F. Tuna, I.F. Crowe, W. Lewis, A.J. Blake, D. Collison, E.J. L. McInnes, R.E.P. Winpenny, S.T. Liddle, A monometallic lanthanide bis(methanediide) single molecule magnet with a large energy barrier and complex spin relaxation behaviour, *Chem. Sci.* 7 (2016) 155–165.
- [36] D.N. Woodruff, R.E.P. Winpenny, R.A. Layfield, Lanthanide single-molecule magnets, *Chem. Rev.* 113 (2013) 5110–5148.
- [37] Y.-S. Ding, N.F. Chilton, R.E.P. Winpenny, Y.-Z. Zheng, On approaching the limit of molecular magnetic anisotropy: a near-perfect pentagonal bipyramidal dysprosium(III) single-molecule magnet, *Angew. Chem. Int. Ed.* 55 (2016) 16071–16074.
- [38] F.-S. Guo, B.M. Day, Y.-C. Chen, M.-L. Tong, A. Mansikkamaki, R.A. Layfield, A dysprosium metallocene single-molecule magnet functioning at the axial limit, *Angew. Chem. Int. Ed.* 56 (2017) 11445–11449.
- [39] J. Liu, Y.C. Chen, J.L. Liu, V. Vieru, L. Ungur, J.H. Jia, L.F. Chibotaru, Y. Lan, W. Wernsdorfer, S. Gao, X.-M. Chen, M.-L. Tong, A stable pentagonal bipyramidal Dy(III) single-ion magnet with a record magnetization reversal barrier over 1000 K, *J. Am. Chem. Soc.* 138 (2016) 5441–5450.
- [40] S.-D. Jiang, S.-S. Liu, L.-N. Zhou, B.-W. Wang, Z.-M. Wang, S. Gao, Series of lanthanide organometallic single-ion magnets, *Inorg. Chem.* 51 (2012) 3079–3087.
- [41] S.-D. Jiang, B.-W. Wang, H.-L. Sun, Z.-M. Wang, S. Gao, An organometallic single-ion magnet, *J. Am. Chem. Soc.* 133 (2011) 4730–4733.
- [42] Y.-C. Chen, J.-L. Lu, L. Ungur, J. Liu, Q.-W. Li, L.-F. Wang, Z.-P. Ni, L.F. Chibotaru, X.-M. Chen, M.-L. Tong, Symmetry-supported magnetic blocking at 20 K in pentagonal bipyramidal Dy(III) single-ion magnets, *J. Am. Chem. Soc.* 138 (2016) 2829–2837.
- [43] D.M. King, F. Tuna, J. McMaster, W. Lewis, A.J. Blake, E.J.L. McInnes, S.T. Liddle, Single-molecule magnetism in a single-ion triamidoamine uranium(V) terminal mono-oxo complex, *Angew. Chem. Int. Ed.* 52 (2013) 4921–4924.
- [44] D.M. King, P.A. Cleaves, A.J. Wooles, B.M. Gardner, N.F. Chilton, F. Tuna, W. Lewis, E.J.L. McInnes, S.T. Liddle, Molecular and electronic structure of terminal and alkali metal-capped uranium(V) nitride complexes, *Nat. Commun.* 7 (2016) 13773.
- [45] N. Magnani, C. Apostolidis, A. Morgenstern, E. Colineau, J.-C. Griveau, H. Bolvin, O. Walter, R. Caciuffo, Magnetic memory effect in a transuranic mononuclear complex, *Angew. Chem. Int. Ed.* 50 (2011) 1696–1698.
- [46] J.M. Zadrozny, D.J. Xiao, M. Atanase, G.J. Long, F. Grandjean, F. Neese, J.R. Long, Magnetic blocking in a linear iron(I) complex, *Nat. Chem.* 5 (2013) 577–581.
- [47] D. Yoshihara, S. Karasawa, N. Koga, Cyclic single-molecule magnet in heterospin system, *J. Am. Chem. Soc.* 130 (2008) 10460–10461.
- [48] Y. Rechkemmer, F.D. Breitgoff, M. van der Meer, M. Atanasov, M. Hakl, M. Orlita, P. Neugebauer, F. Neese, A four-coordinate cobalt(II) single-ion magnet with coercivity and a very high energy barrier, *Nat. Commun.* 7 (2016) 10467.
- [49] X.-N. Yao, J.-Z. Du, Y.-Q. Zhang, X.-B. Leng, M.-W. Yang, S.-D. Jiang, Z.-X. Wang, Z.-W. Ouyang, L. Deng, B.W. Wang, Two-coordinate co(II) imido complexes as outstanding single-molecule magnets, *J. Am. Chem. Soc.* 139 (2017) 373–380.
- [50] J.M. Zadrozny, M. Atanasov, A.M. Bryan, C.-Y. Lin, B.D. Rekker, P.P. Power, F. Neese, J.R. Long, Slow magnetization dynamics in a series of two-coordinate iron(II) complexes, *Chem. Sci.* 4 (2013) 125–138.
- [51] M. Dey, N. Gogoi, Geometry-mediated enhancement of single-ion anisotropy: a route to single-molecule magnets with a high blocking temperature, *Angew. Chem. Int. Ed.* 52 (2013) 12780–12782.
- [52] J.W. Sharples, Y.-Z. Zheng, F. Tuna, E.J.L. McInnes, D. Collison, Lanthanide disks chill well and relax slowly, *Chem. Commun.* 47 (2011) 7650–7652.

- [53] R.J. Blagg, C.A. Muryn, E.J.L. McInnes, F. Tuna, R.E.P. Winpenny, Single pyramid magnets: {Dy₃} pyramids with slow magnetic relaxation to 40 K, *Angew. Chem. Int. Ed.* 50 (2011) 6530–6533.
- [54] R.J. Blagg, L. Ungur, F. Tuna, J. Speak, P. Coman, D. Collison, W. Wernsdorfer, E.J.L. McInnes, L. F. Chibotaru, R.E.P. Winpenny, Magnetic relaxation pathways in lanthanide single-molecule magnets, *Nat. Chem.* 5 (2013) 673–678.
- [55] S. Thiele, F. Balestro, R. Ballou, S. Klyatskaya, M. Ruben, W. Wernsdorfer, Electrically driven nuclear spin resonance in single-molecule magnets, *Science* 344 (2014) 1135–1138.
- [56] M. Ganzhorn, S. Klyatskaya, M. Ruben, W. Wernsdorfer, Strong spin-phonon coupling between a single-molecule magnet and a carbon nanotube nanoelectromechanical system, *Nat. Nanotechnol.* 8 (2013) 165–169.
- [57] M. Shiddiq, D. Komijani, Y. Duan, A. Gaita-Arino, E. Coronando, S. Hill, Enhancing coherence in molecular spin qubits via atomic clock transitions, *Nature* 531 (2016) 348–351.
- [58] J.D. Rinehart, J.R. Long, Slow magnetic relaxation in a trigonal prismatic uranium(III) complex, *J. Am. Chem. Soc.* 131 (2009) 12558–12559.
- [59] J.D. Rinehart, K.R. Meihaus, J.R. Long, Observation of a secondary slow relaxation process for the field-induced single-molecule magnet U(H₂BPz₂)₃, *J. Am. Chem. Soc.* 132 (2010) 7572–7573.
- [60] K.R. Meihaus, S.G. Minasian, W.W. Lukens Jr, S.A. Kozimor, D.K. Shuh, T. Tylliszczaki, J. R. Long, Influence of pyrazolate vs N-heterocyclic carbene ligands on the slow magnetic relaxation of homoleptic trischelate lanthanide(III) and uranium(III) complexes, *J. Am. Chem. Soc.* 136 (2014) 6056–6068.
- [61] L. Chatelain, J.P.S. Walsh, J. Pécaut, F. Tuna, M. Mazzanti, Self-assembly of a 3d-5f trinuclear single-molecule magnet from a pentavalent uranyl complex, *Angew. Chem. Int. Ed.* 53 (2014) 13434–13438.
- [62] J. Rocha, L.D. Carlos, F.A.A. Paz, D. Ananias, Luminescent multifunctional lanthanides-based metal–organic frameworks, *Chem. Soc. Rev.* 40 (2011) 926–940.
- [63] J.F. Suyver, A. Aebischer, D. Biner, P. Gerner, J. Grimm, S. Heer, K.W. Kramer, C. Reinhard, H. U. Gudel, Novel materials doped with trivalent lanthanides and transition metal ions showing near-infrared to visible photon upconversion, *Opt. Mater.* 27 (2005) 1111–1130.
- [64] S. Han, R. Deng, X. Xie, X. Liu, Enhancing luminescence in lanthanide-doped upconversion nanoparticles, *Angew. Chem. Int. Ed.* 53 (2014) 11702–11715.
- [65] M.C. Heffern, L.M. Matosziuk, T.J. Meade, Lanthanide probes for bioresponsive imaging, *Chem. Rev.* 114 (2014) 4496–4539.
- [66] R. Sessoli, Record hard magnets: glauher dynamics are key, *Angew. Chem. Int. Ed.* 47 (2008) 5508–5510.
- [67] G. Lorusso, J.W. Sharples, E. Palacios, O. Roubeau, E.K. Brechin, R. Sessoli, A. Rossin, F. Tuna, E.J. L. McInnes, D. Collison, M. Evangelisti, A dense metal-organic framework for enhanced magnetic refrigeration, *Adv. Mater.* 25 (2013) 4653–4656.
- [68] R. Sessoli, Chilling with magnetic molecules, *Angew. Chem. Int. Ed.* 51 (2011) 43–45.
- [69] E. Moreno Pineda, G. Lorusso, K.H. Karzan, E. Palacios, J. Schnack, M. Evangelisti, R.E.P. Winpenny, E.J. L. McInnes, Observation of the influence of dipolar and spin frustration effects on the magnetocaloric properties of a trigonal prismatic {Gd₇} molecular nanomagnet, *Chem. Sci.* 7 (2016) 4891–4895.
- [70] C.A.P. Goodwin, N.F. Chilton, G.F. Vettese, E.M. Pineda, I.F. Crowe, J.W. Ziller, R.E.P. Winpenny, W. J. Evans, D.P. Mills, Physicochemical properties of near-linear lanthanide(II) bis(silylamide) complexes (Ln = Sm, Eu, Tm, Yb), *Inorg. Chem.* 55 (2016) 10057–10067.
- [71] L. Ungur, L.F. Chibotaru, Magnetic anisotropy in the excited states of low symmetry lanthanide complexes, *Phys. Chem. Chem. Phys.* 13 (2011) 20086–20090.
- [72] C.A.P. Goodwin, F. Ortu, D. Reta, N.F. Chilton, D.P. Mills, Molecular magnetic hysteresis at 60 K in dysprosocenium, *Nature* 548 (2017) 439–442.
- [73] J.D. Rinehart, J.R. Long, Exploiting single-ion anisotropy in the design of f-element single-molecule magnets, *Chem. Sci.* 2 (2011) 2078–2085.
- [74] L. Ungur, L.F. Chibotaru, Ab initio crystal field for lanthanides, *Chem. Eur. J.* 23 (2017) 3708–3718.
- [75] N.F. Chilton, Design criteria for high-temperature single-molecule magnets, *Inorg. Chem.* 54 (2015) 2097–2099.

- [76] N.F. Chilton, D. Collison, E.J.L. McInnes, R.E.P. Winpenny, A. Soncini, An electrostatic model for the determination of magnetic anisotropy in dysprosium complexes, *Nat. Commun.* 4 (2013) 2551.
- [77] K.W.H. Stevens, Matrix elements and operator equivalents connected with the magnetic properties of rare earth ions, *Proc. Phys. Soc. London, Sect A* 65 (1952) 209–215.
- [78] L. Sorace, C. Benelli, D. Gatteschi, Lanthanides in molecular magnetism: old tools in a new field, *Chem. Soc. Rev.* 40 (2011) 3092–3104.
- [79] D. Gatteschi, R. Sessoli, Quantum tunneling of magnetization and related phenomena in molecular materials, *Angew. Chem. Int. Ed.* 42 (2003) 268–297.
- [80] S. Thiele, R. Vincent, M. Holzmann, S. Klyatskaya, M. Ruben, F. Balestro, W. Wernsdorfer, Electrical readout of individual nuclear spin trajectories in a single-molecule magnet spin transistor, *Phys. Rev. Lett.* 111 (2013) 037203.
- [81] A. Abragam, B. Bleaney, *Electron Paramagnetic Resonance of Transition Ions*, Clarendon Press, Oxford, 2012.
- [82] K. Qian, J.J. Baldovi, S.-D. Jiang, A. Gaita-Arino, Y.-Q. Zhang, J. Overgaard, B.-W. Wang, E. Coronado, S. Gao, Does the thermal evolution of molecular structures critically affect the magnetic anisotropy? *Chem. Sci.* 6 (2015) 4587–4593.
- [83] W. Wernsdorfer, From micro-to nano-SQUIDS: applications to nanomagnetism, *Supercond. Sci. Technol.* 22 (2009) 64013.
- [84] N. Ishikawa, T. Iino, Y. Kaizu, Determination of ligand-field parameters and f-electronic structures of heterodinuclear phthalocyanine complexes with a diamagnetic yttrium(III) and a paramagnetic trivalent lanthanide ion, *J. Phys. Chem. A* 106 (2002) 9543–9550.
- [85] N. Ishikawa, M. Sugita, W. Wernsdorfer, Nuclear spin driven quantum tunneling of magnetisation in a new lanthanide single-molecule magnet: bis(phthalocyaninato)-holmium anion, *J. Am. Chem. Soc.* 127 (2005) 3650–3651.
- [86] E. Moreno Pineda, M. Damjanovic, O. Fuhr, W. Wernsdorfer, M. Ruben, Nuclear spin isomers: engineering a $\text{Et}_4\text{N}[\text{DyPc}_2]$ spin qubit, *Angew. Chem. Int. Ed.* 56 (2017) 9915–9919.
- [87] K.R. Meihaus, J.R. Long, Magnetic blocking at 10 K and a dipolar-mediated avalanche in salts of the bis(η^8 -cyclooctatetraenide) complex $[\text{Er}(\text{COT})_2]^-$, *J. Am. Chem. Soc.* 135 (2013) 17952–17957.
- [88] K. Tang, I. Hewitt, N.T. Mahdu, G. Chastanet, W. Wernsdorfer, C.E. Anson, C. Benelli, R. Sessoli, A. K. Powell, Dysprosium triangles showing single-molecule magnet behavior of thermally excited spin states, *Angew. Chem. Int. Ed.* 45 (2006) 1729–1733.
- [89] J. Luzon, K. Bernot, I.J. Bernot, C.E. Anson, A.K. Powell, R. Sessoli, Spin chirality in a molecular dysprosium triangle: the archetype of the noncollinear Ising model, *Phys. Rev. Lett.* 100 (2008) 247205.
- [90] L. Ungur, S.-Y. Lin, J. Tang, L.F. Chibotaru, Single-molecule toroids in Ising-type lanthanide molecular clusters, *Chem. Soc. Rev.* 43 (2014) 6894–6905.
- [91] E. Moreno Pineda, Y. Lan, O. Fuhr, W. Wernsdorfer, M. Ruben, Exchange-bias quantum tunnelling in a CO_2 -based Dy_4 -single molecule magnet, *Chem. Sci.* 8 (2017) 1178–1185.
- [92] J. Long, F. Habib, P.-H. Lin, I. Korobkov, G. Enright, L. Ungur, W. Wernsdorfer, L. F. Chibotaru, M. Murugesu, Single-molecule magnet behavior for an antiferromagnetically superexchange-coupled dinuclear dysprosium(III) complex, *J. Am. Chem. Soc.* 133 (2011) 5319–5328.
- [93] F. Habib, P.-H. Lin, J. Long, I. Korobkov, W. Wernsdorfer, M. Murugesu, The use of magnetic dilution to elucidate the slow magnetic relaxation effects of a Dy_2 single-molecule magnet, *J. Am. Chem. Soc.* 133 (2011) 8830–8833.
- [94] E. Moreno Pineda, N.F. Chilton, R. Marx, M. Dorfel, D.O. Sells, P. Neugebauer, S.-D. Jiang, D. Collison, J. van Slageren, E.J.L. McInnes, R.E.P. Winpenny, Direct measurement of dysprosium(III)–dysprosium(III) interactions in a single-molecule magnet, *Nat. Commun.* 5 (2014) 5243.
- [95] D.P. Mills, F. Moro, J. McMaster, J. van Slageren, W. Lewis, A.J. Blake, S.T. Liddle, A delocalized arene-bridged diuranium single-molecule magnet, *Nat. Chem.* 3 (2011) 454–460.
- [96] R.J. Glauber, Time-dependent statistics of the Ising model, *J. Math. Phys.* 4 (1963) 294–307.
- [97] L. Bogani, C. Sangregorio, R. Sessoli, D. Gatteschi, Molecular engineering for single-chain-magnet behavior in a one-dimensional dysprosium-nitronyl nitroxide compound, *Angew. Chem. Int. Ed.* 44 (2005) 5817–5821.

- [98] K. Bernot, L. Bogani, A. Caneschi, D. Gatteschi, R. Sessoli, A family of rare-earth-based single chain magnets: playing with anisotropy, *J. Am. Chem. Soc.* 128 (2006) 7947–7956.
- [99] R. Liu, X. Wang, P. Yang, C. Wang, D. Liao, J.-P. Sutter, Smooth transition between SMM and SCM-type slow relaxing dynamics for a 1-D assemblage of {Dy(nitronyl nitroxide)₂} units, *Chem. Commun.* 46 (2010) 2566–2568.
- [100] T. Han, W. Shi, Z. Niu, B. Na, P. Cheng, Magnetic blocking from exchange interactions: slow relaxation of the magnetization and hysteresis loop observed in a dysprosium–nitronyl nitroxide chain compound with an antiferromagnetic ground state, *Chem. Eur. J.* 19 (2013) 994–1001.
- [101] Y.-Z. Zheng, Y. Lan, W. Wernsdorfer, C.E. Anson, A.K. Powell, Polymerisation of the dysprosium acetate dimer switches on single-chain magnetism, *Chem. Eur. J.* 15 (2009) 12566–12570.

Metallacrown Complexes Reaching the Nanosize Regime

Angeliki A. Athanasopoulou^{*,†}, Christoph Gamer[†], Lara Völker^{*}, Eva Rentschler^{*}

^{*}University of Mainz, Mainz, Germany, [†]Graduate School of Excellence Materials Science in Mainz, Mainz, Germany

2.1 Introduction

Since the first description of metallacrown complexes (MCs) in 1989 by Pecoraro [1], these molecules have been established as an exceptional class of coordination compounds [2]. The combination of structural predictability and the variability in their synthetic routes offers great opportunities for metallacrown complexes in different fields such as host-guest chemistry, molecular magnetism, extended networks, or the ability of MCs to act as recognition agents [3]. While there are several excellent reviews available in literature that extensively describe the structural and functional properties of metallacrown complexes [2–7], the present chapter focuses on extended networks formed from MCs.

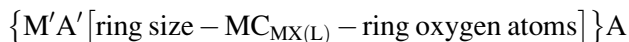
In supramolecular chemistry, coordination polymers or metal-organic frameworks are usually formed from organic molecules bridging either single metal ions or at most small coordination clusters. This constraint to monomeric or dimeric metal centers is mostly owed to the fact that larger coordination clusters themselves—although thermodynamically stable—are often kinetically not inert and as such they are not stable in solution. In contrast, it was recognized very early that MCs—formed in self-assembly reactions from metal ions and appropriate chelating ligands—show remarkable strong stability in solution. This makes them very good candidates for building up nanosized materials while maintaining their interesting molecular properties.

The present chapter reviews the basic design strategies for the discrete oligonuclear MC complexes. Thereafter, it focuses on just two of the outstanding molecular properties, namely, the magnetic and luminescence characteristics. Finally, possible strategies to move from 0D to 3D structures, thus from molecular to nanosized compounds, are discussed.

2.2 Metallacrown Complexes

Structurally, MCs are related to organic crown ethers, for which the repeating unit is $—[C—C—O]—_n$, and host-guest properties are tuned by varying the ring sizes. The repeating unit of the typical metallacrown complex is $—[M—N—O]—_n$, which can be described as a metal-heteroatom coordination unit [6]. Well-established ring sizes are 9-MC-3, 12-MC-4, 15-MC-5, and 18-MC-6 (Fig. 2.1).

The commonly accepted general nomenclature for MCs by Pecoraro is as follows:



with M' = core metal, A' = bound anion, M = ring metal ion, X = heteroatom coordinating the ring metal ions, L = ligand, and A = noncoordinated anions [6] (Fig. 2.2).

Beside the $[M—N—O]—_n$ metallacrown complexes azametallacrown-analogous are known, which comprise $—[M—N—N—]_n$ repeating units [8]. Typically tetrazole, pyrazole, or triazole ligands build up such aza-MCs (Fig. 2.3) [9]. Another prominent structural motif for MCs is the so-called inverse MC with a repetition unit of $[M—O—N—M—N—O]$. Here the ring metal ions face the cavity and often they bind anions in their inner cavity [10]. If no guest ion is present in the central cavity, the supplement “vacant” is used [2].

2.2.1 Ligands

A successful design strategy for a specific chelate ring size built by the ligands is based on the consideration of the bite angle of the donor atoms of the latter. In Fig. 2.2, the two most prominent examples of 12-MC-4 and 15-MC-5, based on salicylhydroxamic acid and picoline hydroxamic acid ligands, are sketched showing how the ligand configuration influences the MC ring size [5]. For the mechanism of MC formation, many more factors have to be considered.

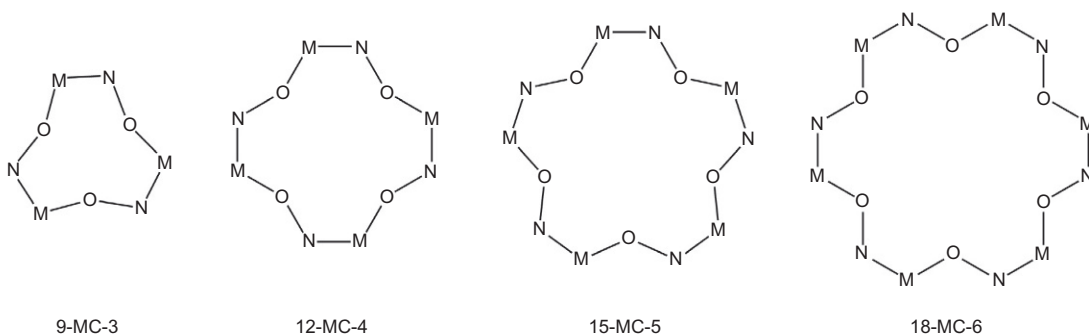
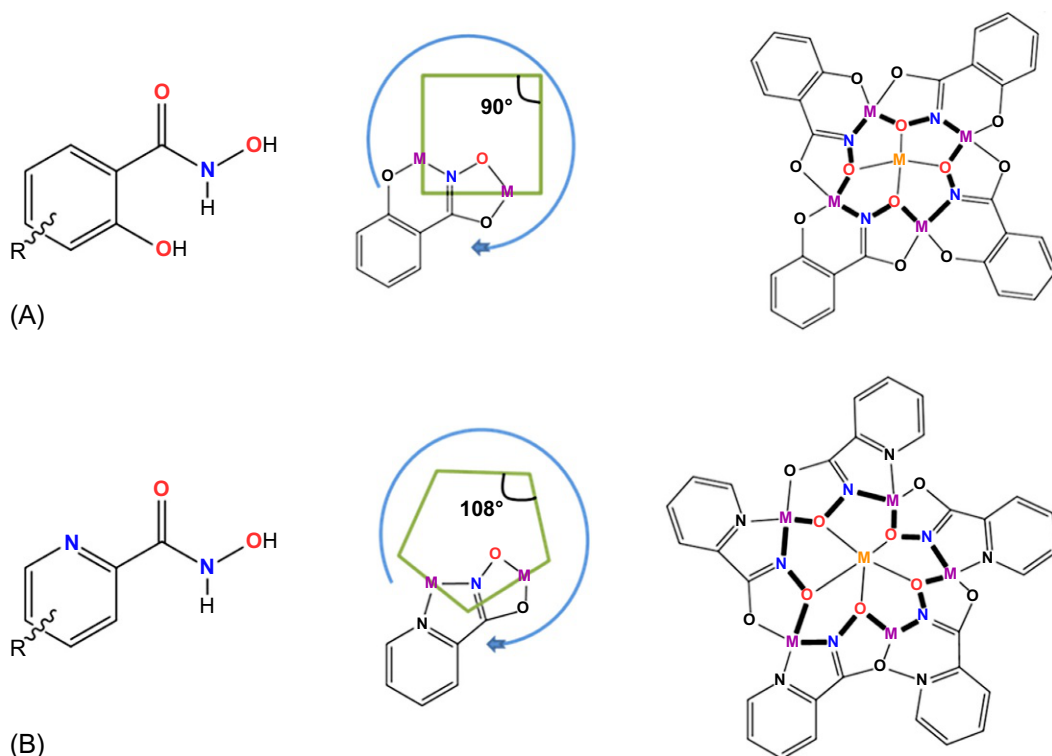
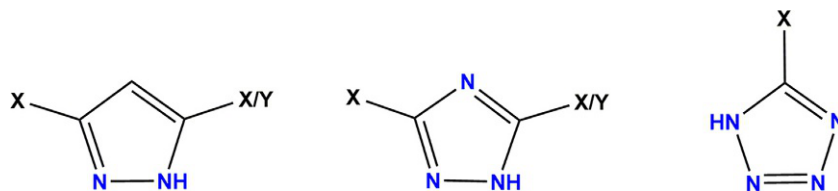


Fig. 2.1

Schematic representation of selected MCs with ring sizes of 9-MC-3, 12-MC-4, 15-MC-5, and 18-MC-6.


Fig. 2.2

MC design strategy based on the chelate ring geometry: (A) square-shaped 12-MC-4 is generated from ligands, which form a 90 degree internal angle (such as salicyl hydroxamic acid or their derivatives); (B) pentagonal 15-MC-5 is generated from ligands, which form a 108 degree internal angle (such as picoline hydroxamic acid or their derivatives). Adapted from C.Y. Chow, E.R. Trivedi, V. Pecoraro, C.M. Zaleski, *Comments Inorg. Chem.* 35 (2015) 214–253.


Fig. 2.3

Sketch of pyrazole (left), triazole (middle), and tetrazole (right) rings providing N—N-units to assemble azaMC complexes.

Besides the choice of ligands, also metal ions, the stoichiometry, solvents, and counterions influence the synthesis of MCs. However, respecting these aspects, the synthesis of MCs allows for a high degree of predictability [5].

The N—N donor ligands show more flexibility in the coordination than the hydroxamate-based ligands. Upon variation of the residue R, a huge variety of different azaMC ring sizes is

possible. Examples for aza9-MC-3 up to aza60-MC-20 are reported [4]. Most described azaMCs are homometallic species using copper(II), manganese(III), iron(III), gallium(III), cobalt(II), and zinc(II) as ring ions [9].

2.2.2 Metal Ion Variation—3d to 4f Compounds

For the synthesis of MC complexes with interesting physical properties not only the ligands decide, but it is equally important to choose the proper metal ions. Many interesting metal ion-based systems are known from the literature. The majority of MCs are homometallic complexes with 3d metal ions being coordinated both in the periphery and in the center. Complexes with manganese [1,11–14], cobalt [2,15], nickel [16–18], and copper [2,19–21] ions are reported. As a purely 3d heterometallic MC complex, only one example is known today [2,19,22]. In combination with 4f metal ions 3d-4f-MCs are established, where the lanthanide ion sits in the cavity of the 3d metal-ion MC complexes [9,23–31]. The broad variability of the metal ions will be described.

Homometallic 3d metallacrown complexes

Manganese(II/III)-MCs

The first homometallic 12-MC-4 based on manganese(II/III) ions was isolated and characterized in 1989 by Lah and Pecoraro [1]. This MC, with the formula $\{\text{Mn}^{\text{II}} [[\text{Mn}^{\text{III}}(\text{salicylhydroximate})_4](\text{acetate})_2(\text{DMF})_6] \cdot 2\text{DMF}$, was also the first complex that was given the name $\text{M}^{\text{II}}(12\text{-crown-4})$ in analogy to an organic crownether. The ring metal ions are manganese(III), the ligand salicylhydroxamic acid is triply deprotonated; thus, the central guest ion is a manganese(II) ion [32]. Following this first mixed-valent manganese(II/III) MC complex, many other homometallic manganese-containing MCs were published [31]. Beside 12-MC-4 complexes, it was also possible to synthesize 15-MC-5 complexes [11–13]. Today a huge variety of manganese-containing MCs is described in literature.

Cobalt(II/III)-MCs

In 2005 Stamatatos et al. [15] published a mixed-valent cobalt(II/III) 12-MC-4 complex as an *inverse* MC. This structural motif is rare, and with cobalt ions in two different oxidation states it was the first example, only a few others followed [2,33]. Only in 2015, about a dozen new cobalt complexes with the ligand salicylhydroxamic acid were published by Happ et al. [2]. Starting from a vacant MC like $[12\text{-MC}_{\text{Co}^{\text{III}}_{\text{N}(\text{Shi})} - 4](\text{Py})_8$ [2], it was possible to synthesize and characterize different complexes with the general structural motif $\text{Co}^{\text{II}}[12\text{-MC}_{\text{Co}^{\text{III}}_{\text{N}(\text{Shi})} - 4]$, see for example Fig. 2.4 [2]. The cobalt(II) ion in the core of the MC complex is coordinated via additional coligands that bridge the ring metal cobalt(III) and the central guest ion. In dependence on the geometrical constraint imposed on the central Co^{II} ion via the bridging ligand, its geometry changes from an almost ideal octahedral to an

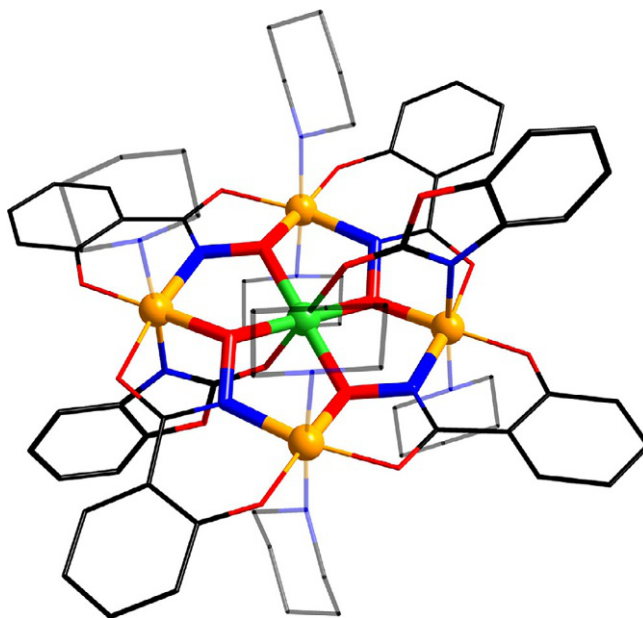


Fig. 2.4

Molecular structure of $\text{Co}^{\text{II}}(\text{Boa})_2[12\text{-MC}_{\text{Co}^{\text{III}}_{\text{N}(\text{Shi})} - 4](\text{Pip})_6$; central metal ion: $\text{Co}(\text{II})$, peripheral ions: $\text{Co}(\text{III})$, highlighted bridging atoms: O and N. From P. Happ, C. Plenk, E. Rentschler, *Coord. Chem. Rev.* 289–290 (2015) 238–260.

almost trigonal prismatic coordination environment. This leads to changes of the electronic structure for the cobalt(II) ion and thus varies the magnetic properties of the compound (for further reading see [Section 2.2.3](#)).

Nickel(II)-MCs

An important $3d$ metal ion for the synthesis of MC structures is nickel(II). The first example of a fused dimeric MC is $\text{Ni}^{\text{II}}_2(\text{mcpa})_2(\text{CH}_3\text{OH})_3(\text{H}_2\text{O})[12\text{-MC}_{\text{Ni}^{\text{II}}_{\text{N}(\text{Shi})2(\text{pko})2} - 4][12\text{-MC}_{\text{Ni}^{\text{II}}_{\text{N}(\text{Shi})3(\text{pko})} - 4]$ shown in [Fig. 2.5](#) [16]. The MC is built up from a mixture of the two different chelating ligands salicylhydroxamic acid (H_3Shi) and di-(2-pyridyl)ketone oxime (Hpko).

The herbicide ligand 2-methyl-4-chlorphenoxyacetate (mcpa) coordinates the nickel(II) ions as coligand in the MC scaffold in a syn-syn-confirmation bridging mode to the ring nickel(II) ions [16]. An MC structure with the same chelate ligands H_3Shi and Hpko was published in 2003 by Alexiou et al. [17]. This nickel(II) 12-MC-4 differs due to the additional coordination of thiocyanate anions [17]. Although there are more nickel(II) MCs known, the number is low compared to the pioneering manganese MCs. Some of the nickel complexes have been tested in biochemistry applications, such as affecting the DNA or an antibacterial activity [17]. This nicely illustrates the multidisciplinary nature of the research on MCs.

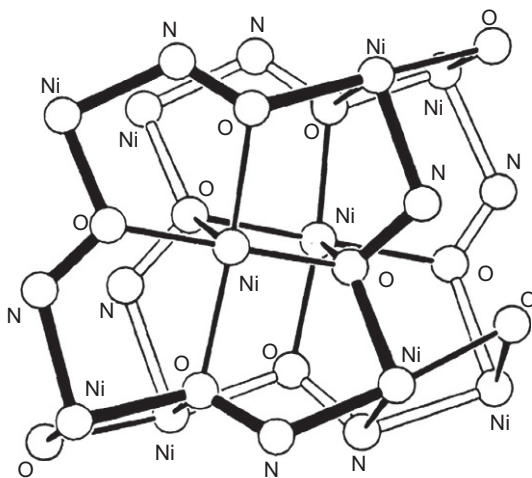


Fig. 2.5

ORTEP diagram of

$\text{Ni}^{\text{II}}_2(\text{mcpa})_2(\text{CH}_3\text{OH})_3(\text{H}_2\text{O})\left[12\text{-MC}_{\text{Ni}^{\text{II}}\text{N}(\text{Shi})_2(\text{pko})_2}-4\right]\left[12\text{-MC}_{\text{Ni}^{\text{II}}\text{N}(\text{Shi})_3(\text{pko})}-4\right]$ showing only the two MC cores. From G. Psomas, C. Dendrinou-Samara, M. Alexiou, A. Tsohos, C.P. Raptopoulou, A. Terzis, D.P. Kessissoglou, *Inorg. Chem.* 37 (1998) 6556–6557.

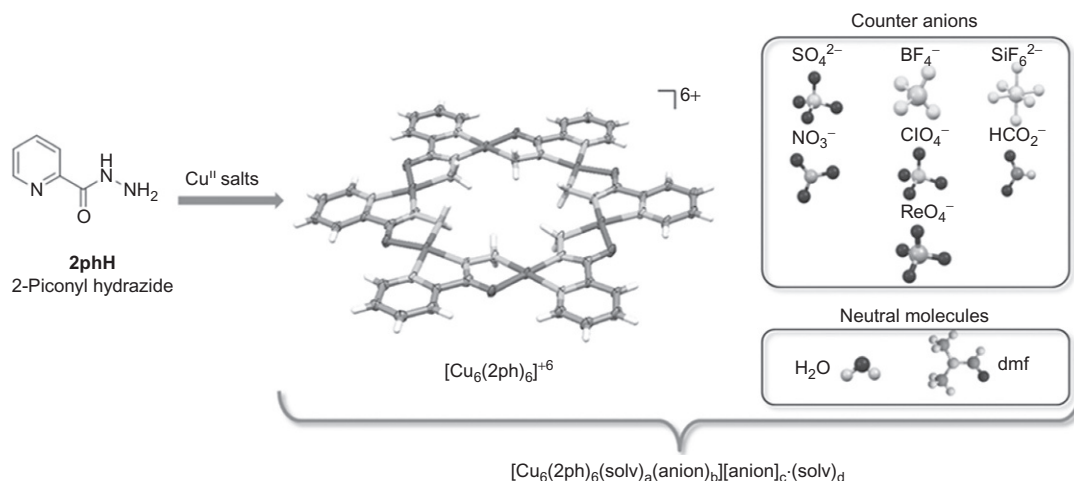
Copper(II)-MCs

Homometallic MCs with copper(II) ions are known from the literature since the early 1990s. In 1994, copper(II) 12-MC-4 complexes were synthesized by Gibney et al. [21] using various derivatives of hydroxamic acids. Based on salicylhydroxamic acid, phenyl ring functionalized derivatives were used to affect the electronic and physical properties of the resulting MCs [21]. In 2014 XMCD-measurements on a copper(II)-containing 12-MC-4 have been published by Happ et al. [22], confirming spectroscopically the $S = 1/2$ ground state estimated before from magnetic data [19]. Very interesting examples for sizeable copper(II) MCs are the molecules synthesized by Rodríguez-Hermida et al., which act as pertechnetate and perrhenate scavenger [20]. These hexanuclear 18-membered aza-MCs with the general structural formula $\left[18\text{-MC}_{\text{Cu}^{\text{II}}\text{N}(2\text{ph})}-6\right]^{6+}$ (2phH = 2-piconyl hydrazide, Fig. 2.6, [20]) can accommodate different anions in their cavity due to the positive total charge of the complexes.

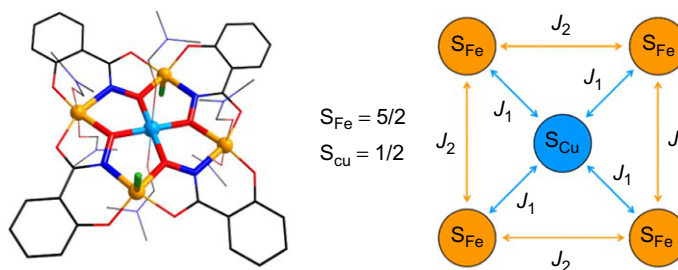
Heterometallic 3d metallacrown complexes

Iron(III)-copper(II)-MC

The only example so far of a 12-MC-4 was formed with different 3d-metal ions was published in 2014 by Happ et al. [22]. The MC is built from one copper(II) ion in the central position and four iron(III) ions in the periphery and is described by the molecular formula of $\text{Cu}^{\text{II}}(\text{DMF})_2\text{Cl}_2\left[12\text{-MC}_{\text{Fe}^{\text{III}}\text{N}(\text{Shi})}-4\right](\text{DMF})_4 \cdot 2\text{DMF}$ (Fig. 2.7).


Fig. 2.6

Representation showing the structure of the hexanuclear copper(II)-containing 18-membered MC $[18 - MC_{Cu^{II}N(2ph)} - 6]^{6+}$ (additional ligands such as solvent molecules and anions are omitted for clarity). From S. Rodríguez-Hermida, A.B. Lago, A. Pino-Cuevas, A. Hagenbach, L. Cañadillas-Delgado, R. Carballo, U. Abram, E.M. Vázquez-López, *Chem. Eur. J.* (2015) 1847–1853.


Fig. 2.7

Molecular structure of the $CuFe_4$ 12-MC-4 complex with salicylhydroxamic acid (H_3Shi) as ligand (left); central metal ion: $Cu(II)$, peripheral metal ion: $Fe(III)$. Square magnetic model of the $CuFe_4$ 12-MC-4 with a radial (J_1) and tangential (J_2) coupling constant (right). From P. Happ, A. Sapozhnik, J. Klanke, P. Czaja, A. Chernenkaya, K. Medjanik, S. Schuppler, P. Nagel, M. Merz, E. Rentschler, H.J. Elmers, *Phys. Rev. B* 93 (2016).

The electronic structure of the $\{CuFe_4\}$ complex (Fig. 2.7) and the analogue homometallic copper(II) $\{CuCu_4\}$ MC, was examined by XMCD-spectroscopy [19]. To achieve a high-spin state for the $\{CuFe_4\}$ -MC complex, the so-called magnetic director approach was applied. By a purposeful combination of the central and the peripheral metal ions, a high-spin ground state is enforced [19]. It is the ratio of the radial (J_1) and tangential (J_2) coupling constants (J_1/J_2) that determines the electronic structure of the complex. The higher the ratio, the lower the energy of high spin states. While for the homometallic $\{CuCu_4\}$ system, a ratio $J_1/J_2 < 2$ is found leading to a low-lying low-spin state, for the heterometallic $\{CuFe_4\}$ complex the ratio is high, thus

favoring a high-spin state being lowest in energy. Another very interesting mixed-metal MC was also reported by Cao et al. in 2016 as a mixed $3d-4f-5d$ hexanuclear complex based on the ligand salicylhydroxamic acid [24]. Four Mn^{III} ions build the ring while one Y^{III} and an W^{V} ion are coordinated in the axial coordination sphere [24].

Heterometallic 3d-4f metallacrown complexes

Lanthanide(III)-manganese(III)-MCs

Today a limited number of MC complexes built up from lanthanide(III) and manganese(III) ions are known. In 2015 Yang et al. published a family of 12-azaMC-4 complexes with an heterometallic $\text{Mn}^{\text{III}}-\text{Ln}^{\text{III}}-\text{Mn}^{\text{III}}-\text{Ln}^{\text{III}}$ ($\text{Ln} = \text{Dy}, \text{Er}, \text{Yb}, \text{Tb}, \text{Y}$) arrangement [9]. These mixed-metal complexes with the formula $[\text{Mn}_2\text{Ln}_2(\text{OH})_2(\text{hppt})_4(\text{OAc})_2(\text{DMF})_2] \cdot 2\text{DMF} \cdot \text{H}_2\text{O}$ were synthesized by using the 1,2,4-triazole ligand system 3-(2-hydroxyphenyl)-5-(pyrazin-2-yl)-1,2,4-triazole (H_2hppt) [9]. The complexes of the whole series of azaMC are isostructural and consist of alternating arrangements of two manganese(III) and two lanthanide(III) ions in the MC scaffold (Fig. 2.8).

Coordination leads to an incorporation of the lanthanide(III) ions as a result of the flexible organic linking ability of those triazole ligand derivatives. The combination of manganese(III) and lanthanide(III) ions leads to clusters showing slow relaxation of the magnetization. Single-molecule magnet behavior is reported for the complexes with Dy^{III} , Er^{III} , Yb^{III} , and Tb^{III} [9]. Another class of heterometallic $3d-4f$ MCs is based on the encapsulation of lanthanide(III) ions into the cavity of the $3d$ -MC structures. The salicylhydroxamic acid leads to a 12-MC-4

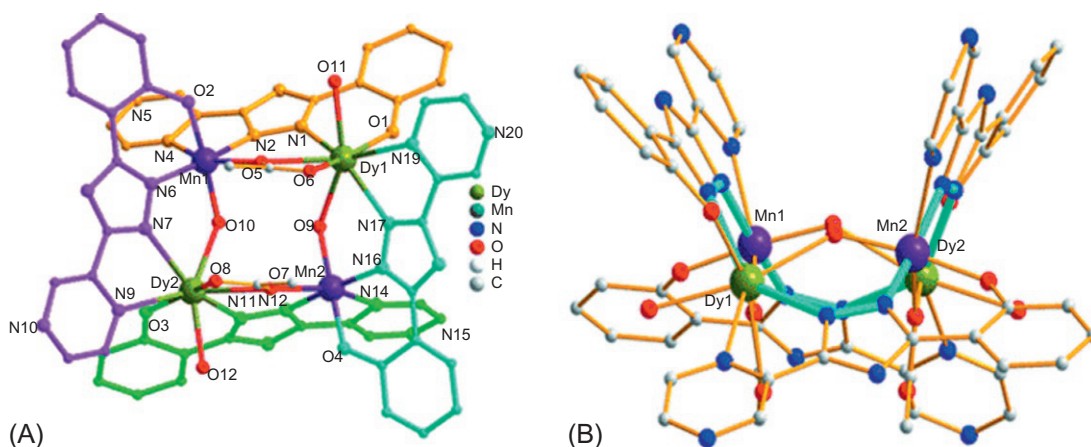


Fig. 2.8

(A) Top view and (B) side view of the overall molecular structure of $[\text{Mn}_2\text{Ln}_2(\text{OH})_2(\text{hppt})_4(\text{OAc})_2(\text{DMF})_2]$ with numbering of selected atoms. Hydrogen atoms and solvent molecules have been omitted for clarity. The axial oxygen atoms O11 and O12 represent metal-bound DMF molecules. From H. Yang, F. Cao, D. Li, S. Zeng, Y. Song, J. Dou, *Chem. Eur. J.* 21 (2015) 14478–14485.

ring size with a resulting out-of-plane coordination mode of the lanthanide(III) ion by four oxygen atoms. About 10 compounds with a $[12 - \text{MC}_{\text{Mn}}^{\text{III}} \text{N}_{(\text{shi})} - 4]$ framework and incorporated lanthanide(III) ions were investigated [23,31]. By changing the lanthanide(III) ions, it is possible to influence the physical properties such as SMM behavior or luminescence properties. Lanthanide(III)-manganese(III) MCs show potentially interesting magnetic behavior or other remarkable molecular properties. Sections 2.2.3 and 2.2.4 are devoted to this subject.

Lanthanide(III)-copper(II)-MCs

For heterometallic lanthanide(III)-copper(II) MCs, mainly 15-MC-5 structures are known. In 2015 and 2016, interesting results were published that show good solubility of lanthanide(III)-containing $15 - \text{MC}_{\text{Cu}}^{\text{II}}(\text{L}) - 5$ complexes in water [27,30,34]. The ligands are based on aminohydroxamic acids or substituted aminohydroxamate derivatives [27]. Typically for these 15-MC-5 complexes, an approximately in-plane encapsulation of the lanthanide(III) ion in the MC-cavity is observed. The water solubility is important for bioinspired applications (e.g., potential MRI contrast agents for ultra-high magnetic fields [30]) as well as certain metabolism activities (e.g., DNA binding via an intercalative mode [29]). The cerium(III)-copper(II) MC, $\text{Ce}(\text{H}_2\text{O})_4[12 - \text{MC}_{\text{Cu}}^{\text{II}} \text{Glyha} - 5]\text{Cl}_3$, has been synthesized in a one-pot synthesis by Kremlev et al. and was tested as a new precursor for heterobimetallic composite materials (Cu_2O and CeO_2) on carbon nanotubes [34]. Wang et al. published in 2015 three novel copper(II)-lanthanide(III) 15-MC-5 complexes based on pyrazinohydroxamic acid [28]. These heterometal-organic cavities bear a central encapsulated lanthanide(III) ion ($\text{Ln}^{\text{III}} = \text{Sm}, \text{Nd}, \text{Eu}$). The crystal structure of the MC complex $[\text{Sm}^{\text{III}}(\text{H}_2\text{O})_3\{\text{Cu}(\text{pyzha})\}_5(\text{H}_2\text{O})_2(\text{MeOH})(\text{HSO}_4)_2] \cdot (\text{H}_2\text{O})_2 \cdot (\text{HSO}_4)$ is shown in Fig. 2.9 [28].

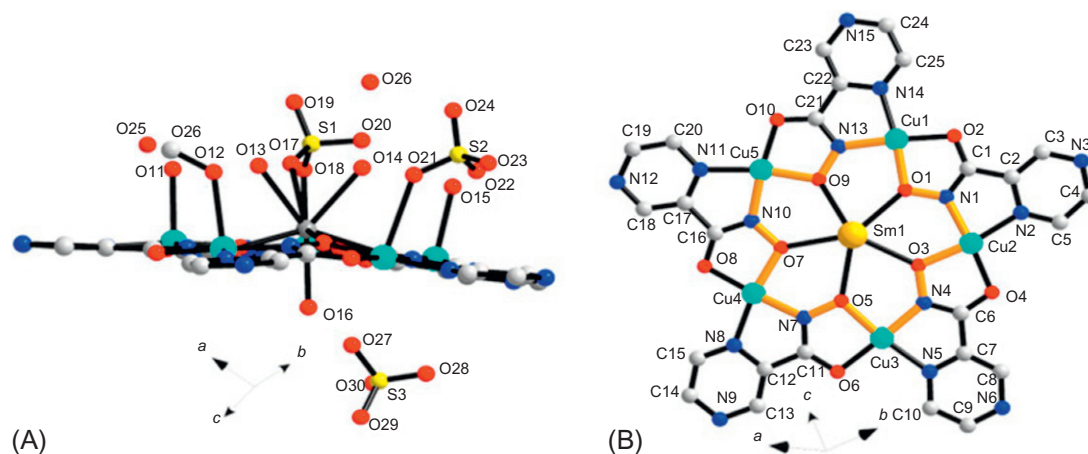


Fig. 2.9

The molecular structure of Sm^{III} encapsulated 15-MC-5 complexes has been presented: (A) side view of the complex; (B) top view of $[\text{Sm}^{\text{III}}(\text{H}_2\text{O})_3\{\text{Cu}(\text{pyzha})\}_5(\text{H}_2\text{O})_2(\text{MeOH})(\text{HSO}_4)_2] \cdot (\text{H}_2\text{O})_2 \cdot (\text{HSO}_4)$ (a ring based on the $-\text{Cu}-\text{N}-\text{O}-$ unit is outlined in a bold bright line). From Y. Wang, W.-S. Wu, M.-L. Huang, *Chin. Chem. Lett.* 27 (2016) 423–427.

For all three recently published MC complexes, luminescence properties are reported. While the luminescence of the samarium(III) compound results from the lanthanide ion itself, for the other two compounds ($\text{Ln}^{\text{III}} = \text{Nd}$ and Eu) luminescence arises from the π -electronic system of the investigated ligand. The luminescence features of MCs will be described in more detail in a following chapter. To summarize, for a targeted synthesis of MC complexes, the choice of the ligand system and the transition metal and lanthanide ions is of outmost importance. With a variation of the ring metal ions, the guest ions, and the ligands, it is possible to achieve various MC structures with different physical properties.

Lanthanide(III)-zinc(II)-MCs

Beneficial for investigations on the luminescence of MCs is the use of diamagnetic ring ions such as the $3d^{10}$ zinc(II) in combination with lanthanide(III) ions. A few examples with a 12-MC-4 motif are published [25,26]. In 2015 the first “half-sandwich” metallacrown complex has been reported by Li et al. that consist of an out-of-plane coordinated Yb^{III} ion in an $[12 - \text{MC}_{\text{Zn}^{\text{II}}} - 4]$ scaffold [26]. Very important to note is that the local symmetry of the lanthanide(III) ion is of great importance when considering electronic structure and related electronic or magnetic properties [35]. The 12-MC-4 motif is an excellent candidate to build an appropriate D_{4d} symmetry around the central lanthanide(III) ion. Both reported complexes contain the ligand quinaldichydroxamic acid (Hquina, Fig. 2.10), but they have different additionally coordinated molecules (py = pyridine and iqn = isoquinoline, Fig. 2.10 [26]).

A few examples with a full “sandwich”-like structure motif are known. One complex, which was published in 2011 by Jankolovits et al., has an $\text{Tb}^{\text{III}} [12 - \text{MC}_{\text{Zn}^{\text{II}}} - 4]_2$ pattern [25]. This MC complex shows interesting luminescent properties and will be discussed in more detail hereafter.

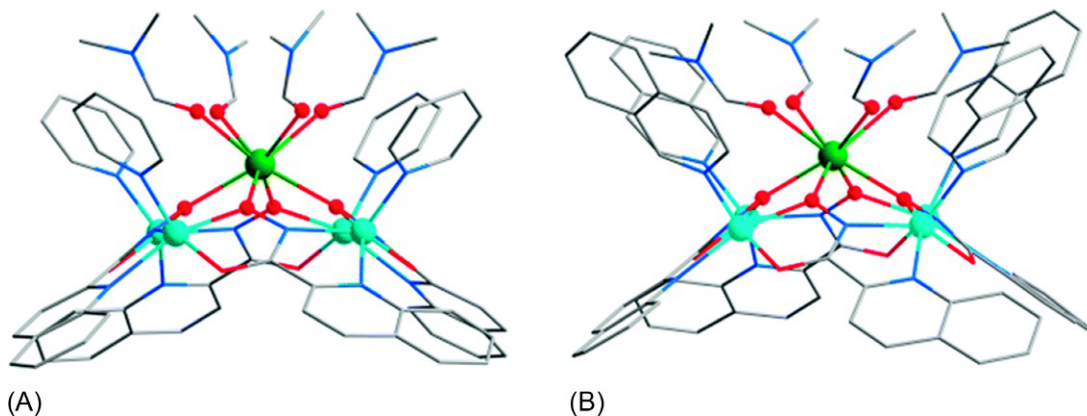


Fig. 2.10

Side view of the $\text{Yb}^{\text{III}}[12 - \text{MC}_{\text{Zn}^{\text{II}}} - 4]$ cation; $[\text{Yb}^{\text{III}}\text{Zn}^{\text{II}}_4(\text{quina})_4(\text{py})_4(\text{DMF})_4]$ (A) and $[\text{Yb}^{\text{III}}\text{Zn}^{\text{II}}_4(\text{quina})_4(\text{iqn})_4(\text{DMF})_4]$ (B); central metal ion $\text{Yb}(\text{III})$, peripheral metal ions: $\text{Zn}(\text{II})$, oxygen atoms coordinated to $\text{Yb}(\text{III})$ are highlighted as balls. H atoms are omitted for clarity. From Q.-W. Li, J.-L. Liu, J.-H. Jia, Y.-C. Chen, J. Liu, L.-F. Wang, M.-L. Tong, *Chem. Commun.* 51 (2015) 10291–10294.

2.2.3 Luminescent Metallacrown Complexes

A large number of novel technologies and applications are based on lanthanide ions due to the specificity of their $f-f$ emission signals and long luminescent lifetimes [36–40]. The unusual spectroscopic properties of the Ln^{III} ions result from the shielding of the $4f$ orbitals by the filled $5s^2$ and $5p^6$ subshells and that's why the $4f$ orbitals do not participate significantly in the formation of coordination bonds. As a consequence, the luminescence of the various lanthanides can be shown as atom-like sharp emission bands that are available across the visible and near-infrared (NIR) spectral regions, while their wavelengths most of the times are not affected by the coordination environment of the Ln^{III} (Fig. 2.11) [41]. Most of these $f-f$ transitions are Laporte forbidden and so the direct excitation of luminescence Ln^{III} is not efficient [42].

This limitation can be surpassed with the assistance of a highly absorbing “antenna” placed in a sufficiently close proximity to the lanthanide [43]. This “antenna” comprises an organic chromophore (group in close proximity to the luminescent lanthanide ion). The chromophore absorbs incident light and then transfers this excitation to the metal ion, which, in turn, then can be deactivated by undergoing the so-called luminescent emission (Fig. 2.12).

Upon relaxation of the system back to the ground state, the subsequent Ln^{III} emission goes on with long luminescence lifetimes. This “antenna” sensitization tactic has led to the evolution of a wide variety of Ln^{III} -based luminescent complexes and nanomaterials composed with organic chromophores or ligands. The choice of the lanthanide ions plays an important role to the acquisition of the specific wavelengths of emission bands in the visible and NIR regions [41,44]. A light-absorbing species (termed the antenna), upon irradiation with an appropriate wavelength, will convert to its singlet electronically excited state (S1) and then radiative decay

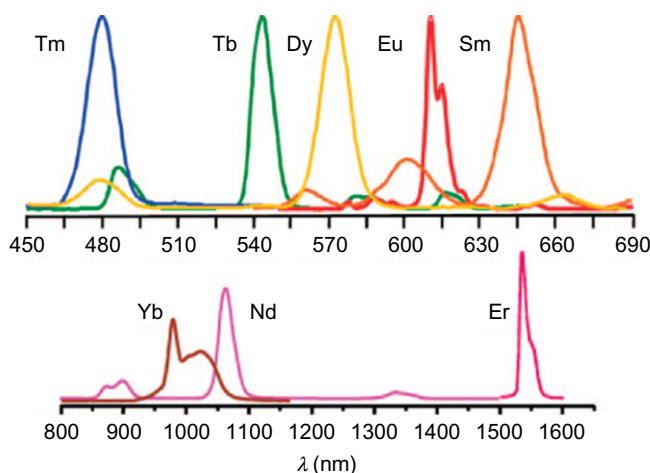


Fig. 2.11

Luminescence spectra of some lanthanide tris(β -diketonates). From J.-C.G. Bünzli, *Chem. Rev.* 110 (2010) 2729–2755.

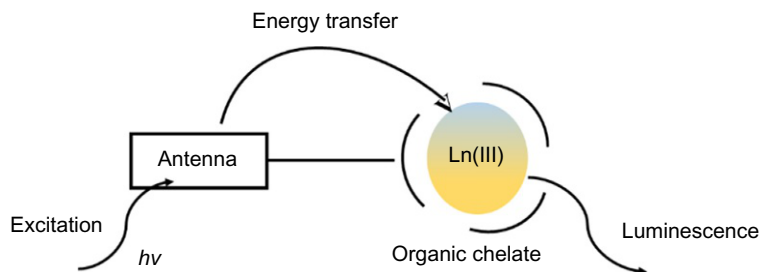


Fig. 2.12

A schematic representation of the “antenna” effect, where incident excitation is absorbed by an organic chelating shell and then it is transferred to the lanthanide.

from this state can occur via fluorescence (i.e., the molecule is a fluorophore) and is typically short-lived (commonly smaller than 50ns) (Fig. 2.13). Alternatively, the lower-lying triplet excited state (T_1) can be generated by intersystem crossing (ISC). This is a spin-forbidden process since $\Delta S \neq 0$ and radiative decay from the triplet state to the ground state is slow, occurring via phosphorescence. The T_1 state can be very long-lived and susceptible to other nonradiative processes, comprising quenching by molecular oxygen and that’s due to the spin-forbidden nature of the radiative relaxation [45]. Light will be emitted without any change in spin-state (i.e., $S_1 \rightarrow S_0$ fluorescence) by most luminescent organic moieties, and thus generally relatively small Stokes’ shifts (e.g., $<3000\text{ cm}^{-1}$) will be observed.

However, since the $4f-4f$ transitions are responsible for the luminescence of the Ln^{III} ions and these transitions are often sharp and characteristic of the specific ion, emission can occur in the UV, visible or NIR regions as mentioned earlier (Table 1). However, the sensitivity of $4f$ -centered excited states to O—H, N—H, and C—H vibrational oscillators (especially for the lanthanides that emit at the NIR region) are highly affecting the overall quantum yields of the emissive lanthanide complexes, providing efficient nonradiative deactivation pathways (k_{nr}) and should be suppressed to enhance the emission.

The luminescent properties of MC’s have attracted the scientific interest—especially the last years—due to the fact that they can bind lanthanide ions as central metal ion. As such, this complexes can function as organometallic antenna, which absorbs and transfers energy through the lanthanide. Moreover, MCs represent a class of compounds that exclude effectively the vibrational oscillators mentioned, due to their unique structural form allowing a higher distance between the lanthanide and the organic scaffold, thus protecting it from interactions with the high energy N—H, O—H, and C—H oscillators. It results in an enhancement of the luminescent signal and nonradiative deactivation is prevented. The most common ions used in all the reported luminescent MCs are Zn^{II} and Ga^{III} since they are diamagnetic and when they are used as ring metal ions the quenching through the $d-d$ transitions can be avoided [25,26,44,46].

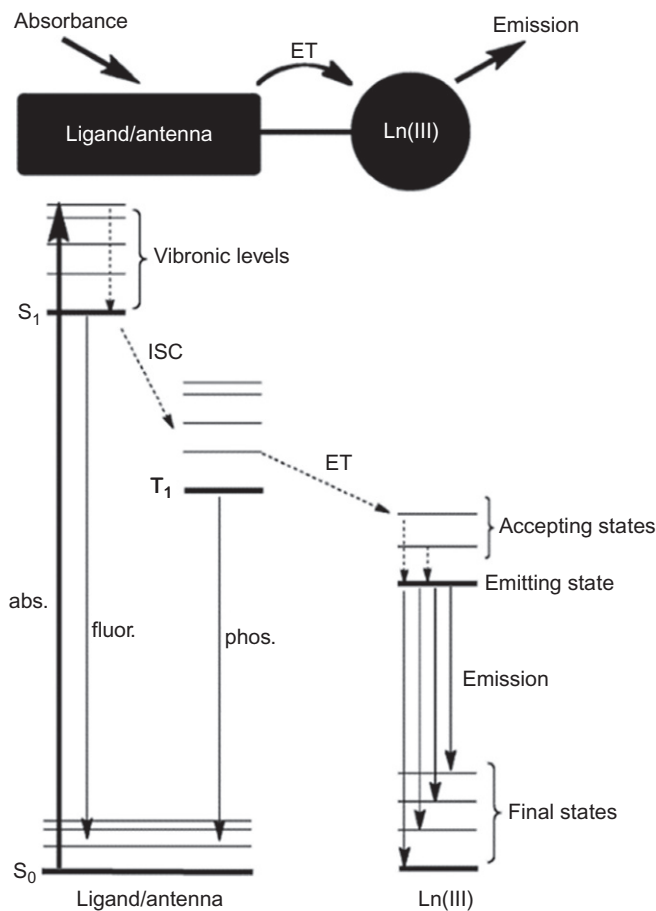


Fig. 2.13

Typical energy level diagram for an emissive chromophore-appended lanthanide complex sensitized via a ligand-centered triplet excited state (*abs.*, absorbance; *fluor.*, fluorescence; *phos.*, phosphorescence; *ISC*, intersystem crossing; *ET*, energy transfer). From A.J. Amoroso, S.J.A. Pope, *Chem. Soc. Rev.* 44 (2015) 4723–4742.

The first luminescent Ln^{III} MCs were reported in the literature by Pecoraro et al., who synthesized a series of hydroxamate MCs based on the picHA ligand with the formula $\text{Ln}^{\text{III}}[12 - \text{MC}_{\text{Zn}}^{\text{II}}\text{N}(\text{picHA}) - 4]_2[24 - \text{MC}_{\text{Zn}}^{\text{II}}\text{N}(\text{picHA}) - 8]^{3+}$, where $\text{Ln}^{\text{III}} = \text{Yb}^{\text{III}}$ and Nd^{III} (Fig. 2.14) [25]. The absorption bands of the picHA ligand appear between 200 and 400 nm with the maxima being at 284 and 325 nm. Both NIR-emitting complexes are readily sensitized in methanol and acetonitrile, after the excitation of the picHA absorption bands. A characteristic ${}^5\text{F}_{5/2} \rightarrow {}^5\text{F}_{7/2}$ transition is observed for Yb^{III} (Fig. 2.15), while for Nb^{III} the ${}^4\text{F}_{3/2} \rightarrow {}^4\text{F}_{11/2}$ and ${}^4\text{F}_{3/2} \rightarrow {}^5\text{F}_{13/2}$ transitions are observed as well [6,25].

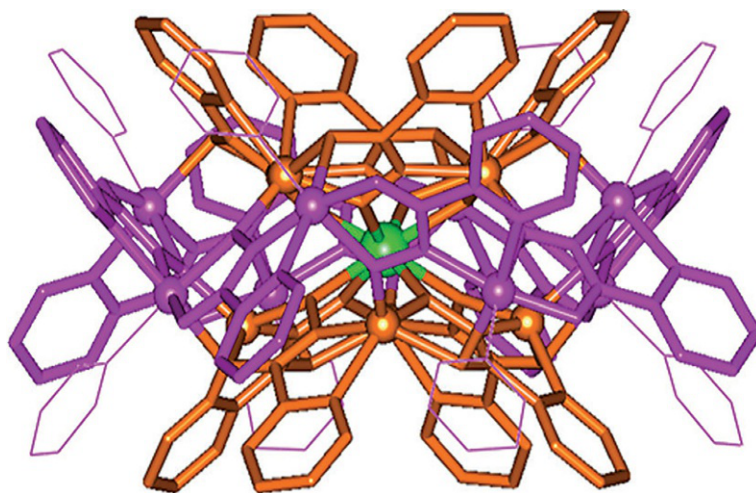


Fig. 2.14

Crystal structure of $\text{Tb}^{\text{III}} [12 - \text{MC}_{\text{Zn}}^{\text{II}} \text{N}(\text{picHA}) - 4]_2 [24 - \text{MC}_{\text{Zn}}^{\text{II}} \text{N}(\text{picHA}) - 8]^{3+}$. Redrawn from J. Jankolovits, C.M. Andolina, J.W. Kampf, K.N. Raymond, V.L. Pecoraro, *Angew. Chem. Int. Ed.* 50 (2011) 9660–9664.

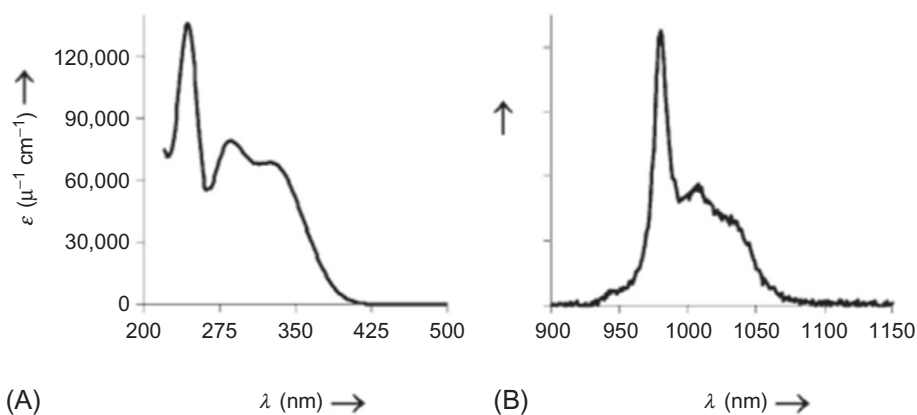


Fig. 2.15

(A) Absorption and (B) emission spectra for Yb-complex in methanol at 25.0°C. From J. Jankolovits, C.M. Andolina, J.W. Kampf, K.N. Raymond, V.L. Pecoraro, *Angew. Chem. Int. Ed.* 50 (2011) 9660–9664.

The complexes mentioned here exhibit strong luminescence and are the first examples reported, supporting the idea that these compounds can be effective tools for the production of bright NIR-emitting chromophores.

A very important feature that needs highlighting is that the nearest C—H bond in this complex is located over 6.7 Å from the Ln^{III} ion justifying further that the topology of the MCs effectively can exclude the high-energy X-H oscillators from the proximity of the lanthanide.

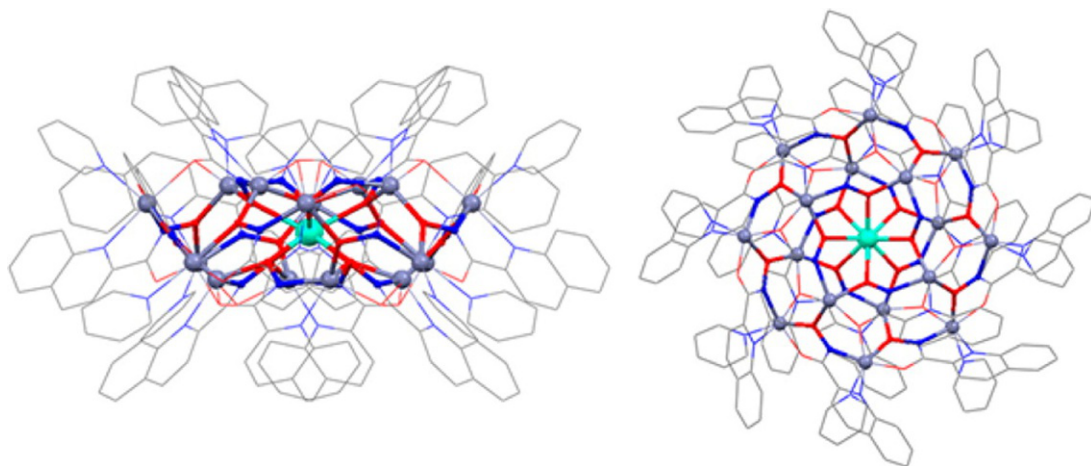


Fig. 2.16

Crystal structure of $\text{Dy}^{\text{III}}[\text{Zn}^{\text{II}}\text{MC}_{\text{quinHA}}]$. From E.R. Trivedi, S.V. Eliseeva, J. Jankolovits, M.M. Olmstead, S. Petoud, V.L. Pecoraro, *J. Am. Chem. Soc.* 136 (2014) 1526–1534.

In order to shift the absorption to lower energy, there is a new family of analogous MCs that were synthesized by the same group, this time using quinaldichydroxamic acid (quinHA) as a ligand with the formula $\text{Ln}^{\text{III}}[12 - \text{MC}_{\text{Zn}^{\text{II}}\text{N}(\text{quinHA})} - 4]_2[24 - \text{MC}_{\text{Zn}^{\text{II}}\text{N}(\text{quinHA})} - 8]^{3+}$ ($\text{Ln}^{\text{III}} = \text{Y}^{\text{III}}, \text{Nd}^{\text{III}}, \text{Eu}^{\text{III}}, \text{Gd}^{\text{III}}, \text{Tb}^{\text{III}}, \text{Dy}^{\text{III}}, \text{Er}^{\text{III}}, \text{Yb}^{\text{III}}$) (Fig. 2.16) [46]. The quinHA ligand is similar to picHA and so it has several absorption bands in the UV region that can be attributed to $\pi-\pi^*$ transitions. The luminescent properties of Nd^{III} , Yb^{III} , and Er^{III} were studied with quinHA as a ligand and it was observed that in the presence of the lanthanide, a new broad band with a maximum at 380nm is observed. This near-visible band can be attributed most likely to interligand charge transfer across one single quinHA ligand and that feature is unique for the quinHA ligand. The energy that comes from this absorption is still not enough in order to sensitize the Ln^{III} , which emit in the visible region but not the ones that emit in the NIR. The Nd^{III} , Yb^{III} , and Er^{III} MCs exhibit strong emission due to the ${}^2\text{F}_{5/2} \rightarrow {}^2\text{F}_{7/2}$, ${}^4\text{F}_{5/2} \rightarrow {}^4\text{I}_J$ ($J=9/2, 11/2, 13/2$), and ${}^4\text{I}_{13/2} \rightarrow {}^4\text{I}_{15/2}$, respectively.

As a result, the replacement of picoline with quinoline hydroxamic acid led to a shift in the absorption wavelength to a lower energy, which undoubtedly improves the photophysical properties of MCs. It is also important to point out that in this case the Dy-CH distance was found to be 7.0 Å, significantly larger than the one of 6.7 Å reported for the picoline analogues. That led to an improvement of the quantum yields of Nd^{III} and Er^{III} MCs, which, in fact, are among the highest NIR-emitting complexes containing C—H bonds. Extended details can be provided at Ref. [46].

Two other examples that have been reported in literature belonging to the 12-MC-4 category of complexes are two $\text{Zn}^{\text{II}}\text{-Yb}^{\text{II}}$ compounds with the formulas $[\text{YbZn}_4(\text{quinha})_4(\text{py})_4(\text{DMF})_4]$

$(\text{CF}_3\text{SO}_3)_3 \cdot 5\text{DMF} \cdot 7\text{H}_2\text{O}$ and $[\text{YbZn}_4(\text{quinha})_4(\text{iqn})_4(\text{DMF})_4](\text{CF}_3\text{SO}_3)_3 \cdot 6\text{DMF} \cdot 4\text{H}_2\text{O}$ [26]. Both complexes exhibit NIR emission bands in the range of 960–1080 nm, and it is possible to observe the ${}^2\text{F}_{5/2} \rightarrow {}^2\text{F}_{7/2}$ transitions for both Yb^{III} compounds. It was also possible to estimate the energy gap values between the ground state and first excited state of ${}^2\text{F}_{7/2}$ multiplet, which were found to be 112 cm^{-1} for $[\text{ZbZn}_4(\text{quinha})_4(\text{py})_4(\text{DMF})_4](\text{CF}_3\text{SO}_3)_3 \cdot 5\text{DMF} \cdot 7\text{H}_2\text{O}$ and 169 cm^{-1} for $[\text{YbZn}_4(\text{quinha})_4(\text{iqn})_4(\text{DMF})_4](\text{CF}_3\text{SO}_3)_3 \cdot 6\text{DMF} \cdot 4\text{H}_2\text{O}$. Note that the emission spectra were recorded at 15 K and the values reported correspond to the numbers measured at this temperature [6].

Very recently, there was a paper presenting a new family of visible and NIR-emitting MCs with the general formula $[\text{LnGa}_4(\text{shi})_4(\text{C}_6\text{H}_5\text{CO}_2)(\text{C}_5\text{H}_5\text{N})(\text{CH}_3\text{OH})]$ ($\text{Ln}^{\text{III}} = \text{Sm}^{\text{III}}, \text{Eu}^{\text{III}}, \text{Gd}^{\text{III}}, \text{Tb}^{\text{III}}, \text{Dy}^{\text{III}}, \text{Ho}^{\text{III}}, \text{Er}^{\text{III}}, \text{Tm}^{\text{III}}, \text{Yb}^{\text{III}}$) (Fig. 2.17). The absorption bands of salicylhydroxamic acid are between 200 and 340 nm and it was observed that the formation of the MCs led to a red shift of the absorption bands as well as an increase of the molar absorption coefficients.

Characteristic bands are observed in the NIR ($\text{Ln}^{\text{III}} = \text{Ho}^{\text{III}}, \text{Er}^{\text{III}}, \text{Yb}^{\text{III}}$) and in the visible ($\text{Ln}^{\text{III}} = \text{Eu}^{\text{III}}, \text{Tb}^{\text{III}}$) regions upon excitation in the range of 320–350 nm. Nevertheless, Dy^{III} and Sm^{III} complexes can emit in both regions (Fig. 2.18).

The gallium ions were shown to affect the luminescence properties, in comparison with the previously reported [12-MC-4]₂[24-MC-8] complexes. The authors state that, in the case of the Yb^{III} MC, there was a reduction of the radiative lifetime and an improvement in the sensitization efficiency. When the MCs were in solution, quenching induced by the solvate molecules was apparent and obvious. The radiative lifetimes, sensitization efficiencies, and the intrinsic quantum yields of the complexes are thoroughly presented and discussed at Ref. [44].

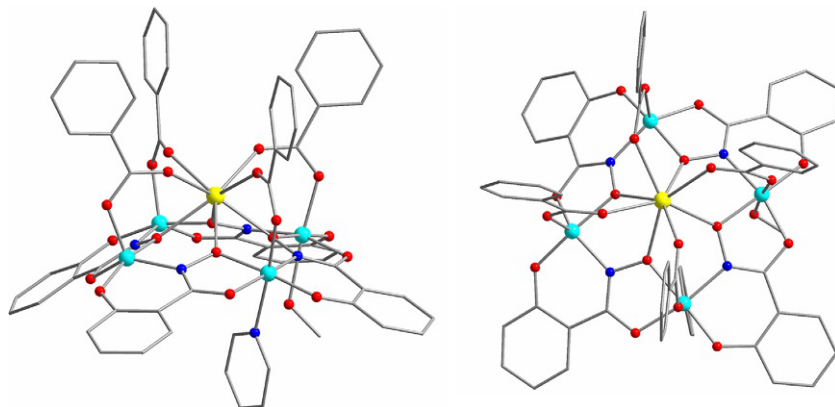


Fig. 2.17

Schematic representation of $[\text{DyGa}_4(\text{shi})_4(\text{C}_6\text{H}_5\text{CO}_2)(\text{C}_5\text{H}_5\text{N})(\text{CH}_3\text{OH})]$. Central metal ion: $\text{Dy}(\text{III})$
 peripheral metal ions: $\text{Ga}(\text{III})$, N and O atoms represented as smaller balls. Redrawn from
 C.Y. Chow, S.V. Eliseeva, E.R. Trivedi, T.N. Nguyen, J.W. Kampf, S. Petoud, V.L. Pecoraro, *J. Am. Chem. Soc.* 138
 (2016) 5100–5109.

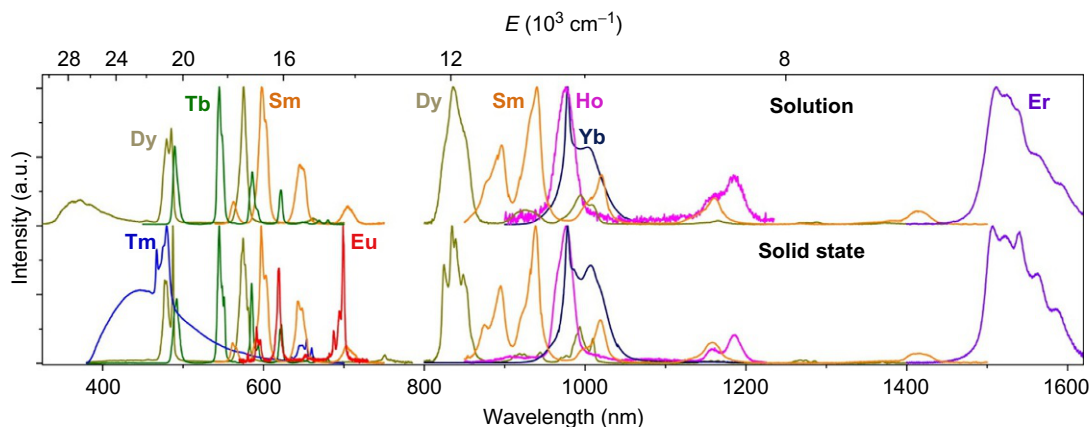
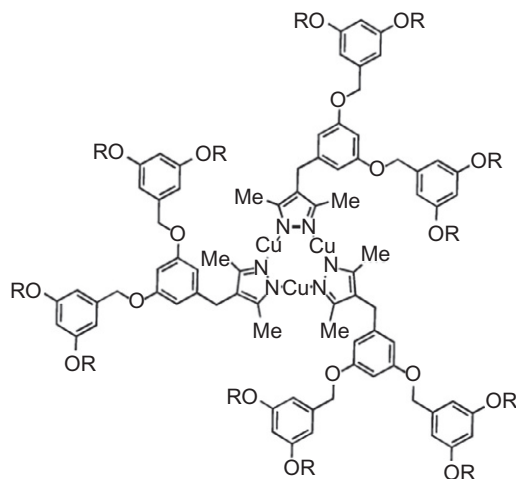


Fig. 2.18

Corrected and normalized emission spectra of the $[\text{DyGa}_4(\text{shi})_4(\text{C}_6\text{H}_5\text{CO}_2)(\text{C}_5\text{H}_5\text{N})(\text{CH}_3\text{OH})]$ MCs in the solid state and in CD_3OD solution (1 mg/mL) under ligand excitation at 320–350 nm at room temperature. From C.Y. Chow, S.V. Eliseeva, E.R. Trivedi, T.N. Nguyen, J.W. Kampf, S. Petoud, V.L. Pecoraro, *J. Am. Chem. Soc.* 138 (2016) 5100–5109.

At this point, briefly some examples of 9-azaMC-3 complexes are referred that have been found to exhibit photophysical properties. More specifically, multiple trimeric Cu^{I} , Ag^{I} , and Au^{I} pyrazolate complexes have been synthesized and thoroughly examined with an identical 9-azaMC-3 core (with various substituents), showing luminescent properties [47–50]. Aida et al. first reported the luminescent properties of these trinuclear metallacycles of Cu^{I} , Ag^{I} , and Au^{I} , and a series of 4-benzyl-3,5-dimethylpyrazolate pyrazolate dendrimeric ligands [48]. Highly symmetric cyclic structures can be formed by these metal pyrazolate complexes that actually can be expressed as highly luminescent superhelical fibers upon heating at 200°C and cooling to room temperature. The Cu^{I} trinuclear complexes that form these superhelical fibers, upon excitation at 280 nm, can emit an intense orange light at 605 nm, without strong fluorescence resulting from the dendritic moiety at 305 nm. What is of utmost importance is the fact that after the dissociation of the fibers, the fluorescence band at 305 nm increases while the characteristic emission band at 605 nm disappears [6,48].

Kashimura et al. reported some dendrimeric Cu^{I} pyrazolate complexes with long alkyl chains that can also create a columnar assembly through intermolecular $\text{Cu}^{\text{I}} \cdots \text{Cu}^{\text{I}}$ interactions (Fig. 2.19) [49]. $[\text{Cu}([\text{C}18]\text{L}2\text{PZ})_3]$ is one of the synthesized complexes that possess dichroic luminescence at room temperature. More specifically, a red luminescence band of a hot melt of the sample appears at 650 nm, upon excitation at 280 nm. This red emission is also preserved after cooling and only a very small blue shift is observed. However, a yellow luminescence emission at 615 nm is observed when this hot melt is cooled down slowly. The authors of the paper attributed these red and yellow emissions to a triple metal-centered excited state reshaped by intramolecular metal-metal interactions [6,49].



Trinuclear metallacycle
of Cu[C18]L2pz

Fig. 2.19

A schematic representation of the self-assembly of a trinuclear metallacycle of Cu[C18]L2pz [49].

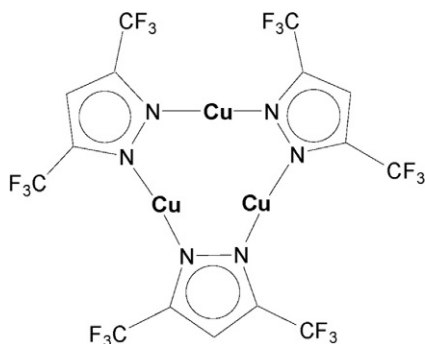


Fig. 2.20

Molecular Structure of {[3,5-(CF₃)₂Pz]Cu}₃. From H.V.R. Dias, H.V.K. Diyabalanage, M.A. Rawashdeh-Omary, M.A. Franzman, M.A. Omary, *J. Am. Chem. Soc.* 125 (2003) 12072–12073.

Dias and Omary in 2003 reported the photophysical properties of a Cu^I complex with the formula {[3,5-(CF₃)₂Pz]Cu}₃ (Fig. 2.20) [50]. Temperature, solvent, concentration, and excitation wavelength are factors that were found to highly affect the luminescence properties of that metallacrown complex.

In the solid state at room temperature, a bright orange emission is observed while after cooling down, the color of the emission changes to red between room temperature and 77 K. What is interesting is the fact that the orange band reappears at 77 K and that's most likely due to the combination of a red emission peak at 665 nm and a yellow shoulder at 590 nm (Fig. 2.21).

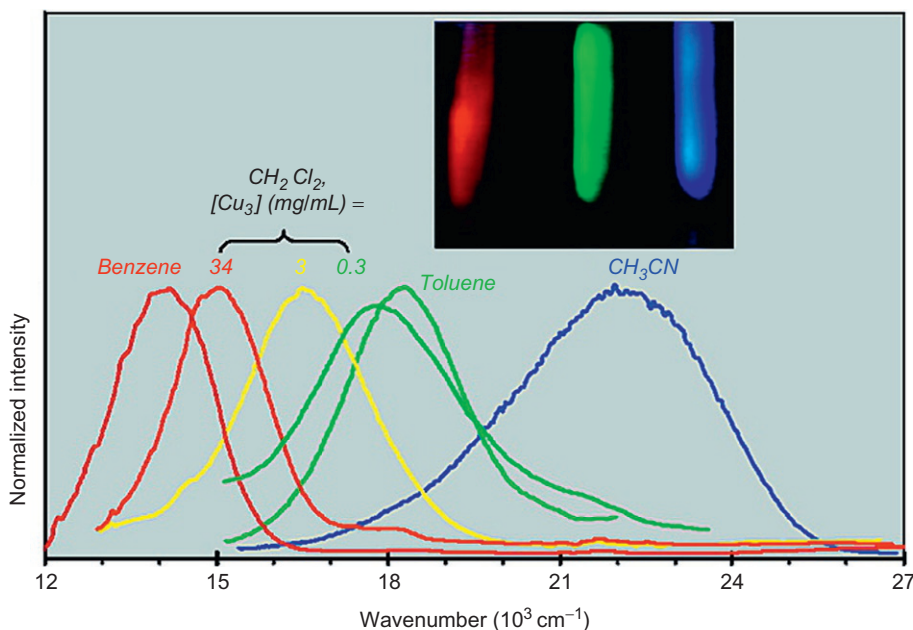


Fig. 2.21

Representative emission spectra of rigid frozen solutions (77 K) of Cu_3 versus solvent and concentration. From H.V.R. Dias, H.V.K. Diyabalanage, M.A. Rawashdeh-Omary, M.A. Franzman, M.A. Omary, *J. Am. Chem. Soc.* 125 (2003) 12072–12073.

The authors also point out that this yellow shoulder disappears at high temperatures while it appears again when the temperature is driven to more ambient ones. Furthermore, a solution of the Cu^{I} compound exhibits luminescence thermochromism, which is attributed to a contraction of the intramolecular Cu^{I} distances in the excited state as well as solvatochromism luminescence, which is due to the different electronic structures of the trinuclear complexes in different solvents. More detailed information can be found at Ref. [50].

Photoluminescence studies of multiple other related trinuclear Cu^{I} complexes have been reported, but the explanation and rationalization of all of them is beyond the scope of this chapter. For further knowledge on the topic, detailed information is provided through the references cited [51–54].

To conclude, what is profoundly shown is that there is much work that can be done in this field in order to improve the photophysical properties of near-infrared-emitting MC and not only complexes in such a way the applicability of these compounds can be broadened and extended. It is also definitely apparent that the versatility of the MC strategy is the key for shifting the excitation wavelength toward lower energy. It was also demonstrated in this chapter that when appropriate and rational design of the chromophore is done (based on the considerations set earlier), an enhancement of the luminescent parameters without affecting

the MC topology is possible. Thus, the MC strategy—when carefully and sensibly implemented—opens up, a new way toward the improvement of luminescent properties and sets the base for possible use of these compounds for numerous luminescence applications.

2.2.4 Metallocrown Complexes as Single-Molecule Magnets (SMMs)

In the early 1990s, the field of molecular magnetism was established after the discovery that a single molecule can retain its magnetization, even in the absence of an external magnetic field, at low temperatures (at liquid-helium temperatures) [55,56]. The first molecule that was found to retain its magnetization was the famous $[\text{Mn}^{\text{III}}_8\text{Mn}^{\text{IV}}_4\text{O}_{12}(\text{O}_2\text{CMe})_{16}(\text{H}_2\text{O})_4]$ or Mn_{12}Ac cluster, which led to the initiation of a new research area, known as single-molecule magnets (SMMs) [57]. These molecules can find applications in various fields of interest such as in high-density data storage, as quantum bits for quantum computing or as components of spintronic devices, and others [58–64].

However, an SMM is capable of retaining its magnetization for an extensive amount of time only as long as it is kept below a characteristic blocking temperature, T_B , which corresponds to the highest temperature in which an SMM can display hysteresis loops in plots of magnetization (M) versus magnetic field (H) [57]. For 3d-SMMs, the blocking temperature is dependent on the magnitude of the energy barrier (or anisotropy barrier), U_{eff} , for the magnetization reversal. The magnitude of the energy barrier is $S^2|D|$ for integer spin systems and $(S^2 - 1/4)|D|$ for half-integer spin systems. Thus, the two properties that block the magnetization reversal are the Ising-type magnetic anisotropy, which can be expressed as the axial zero-field splitting parameter (ZFS), D , and the total spin of the molecule, S . The projection of the total spin gives rise to $[2S + 1] m_s$ microstates, which are split at zero field, and the $m_s = \pm S$ lie lowest in energy when $D < 0$. For the magnetization to relax, it is required to flip the spin from the $m_s = +S$ to the $m_s = -S$, and that can be done when the magnetization relaxes over the barrier (thermally assisted process) with increments of 1 ($m_s = \pm 1$ steps) till a thermal equilibrium is reached. Apart from the thermal relaxation process, relaxation can also occur via resonant quantum tunneling of magnetization (QTM) between degenerate m_s states, a phenomenon that can be observed experimentally as the characteristic steps in the M vs H hysteresis loops measurements. For many years, research was focused on the synthesis of SMMs with large U_{eff} values focusing mostly on maximizing the spin, a strategy that was proven to be quite debatable later on [65].

The Mn_{12}Ac was found to possess a $U_{\text{eff}} = 51 \text{ cm}^{-1}$, which resulted from an $S = 10$ and $D = -0.51 \text{ cm}^{-1}$ [55] (Fig. 2.22). The hexametallc Mn^{III} cage, $[\text{Mn}_6\text{O}_2(\text{sao})_6(\text{O}_2\text{CPh})_2(\text{EtOH})_4] (\{\text{Mn}_6\})$ ($\text{saoH}_2 = 2$ -hydroxybenzaldehyde oxime), has one of the largest anisotropy barriers among multinuclear 3d-SMMs, where a combination of $S = 12$ and $D = -0.43 \text{ cm}^{-1}$ results in a $U_{\text{eff}} = 62 \text{ cm}^{-1}$ [66].

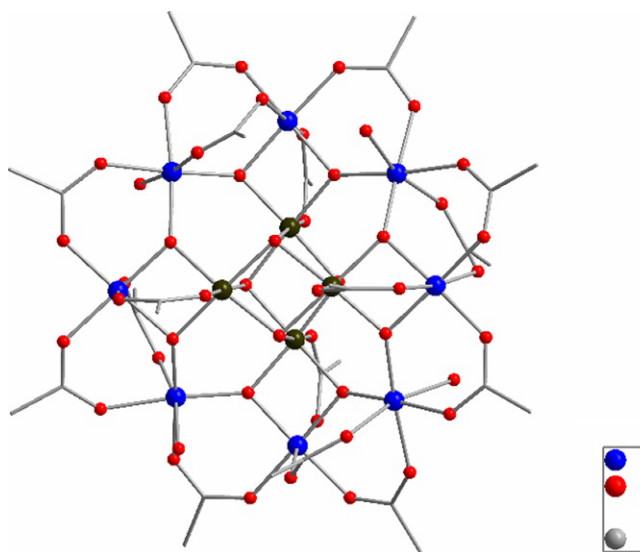


Fig. 2.22
Structure of the Mn_{12}Ac SMM.

Rinehart and Long in 2011 provided the scientific community with an interesting review that highlighted the importance of the use of f -elements in the development of new SMMs [67]. In lanthanides, the orbital contribution to the magnetic moment is large and unquenched, apart from the ones with electronic ground terms $^1\text{S}_0$ and $^8\text{S}_{7/2}$. Thus, the ligand field can cause a small but still significant perturbation [68,69]. On the other hand, for transition metals, the spin-orbit coupling is subjected to ligand field effects; thus, lanthanides differ from $3d$ -metal SMMs in the nature of their bistable ground state. In transition metal SMMs, the total spin S and the $[2S+1] m_s$ sublevels lead to the ground state bistability, while in lanthanides the bistability arises from the $[2J+1] m_J$ microstates within the spin-orbit coupled ground term $^{2S+1}\text{L}_J$ [57]. So, generally the bigger the m_J value, the bigger the magnetic moment of the Ln-SMM (always depending on the lanthanide used). Most of the Ln-SMMs reported to date are complexes with Dy^{III} or Tb^{III} . These two lanthanides provide some of the largest U_{eff} values and that can be rationalized in terms of electronic structure. Dysprosium SMMs show high U_{eff} values because Dy^{III} ions have high magnetic anisotropy and the energy gap of the ground state and the first excited m_J state is most of the times quite large. Moreover, dysprosium is a Kramer's ion (odd number of $4f$ electrons) and that means that the ground state is always bistable independent of the ligand field symmetry. Some terbium SMMs, now, have also large U_{eff} values because terbium can have greater magnetic anisotropy and bigger m_J gaps than Dy^{III} . Terbium though it is not a Kramer's ion (even number of $4f$ electrons); thus, the ground state is not always bistable (here the ligand field symmetry plays an important role). As a consequence, scientists soon realized that manipulating and controlling the ligand field symmetry is extremely important for the enhancement of single-ion anisotropy [67,70].

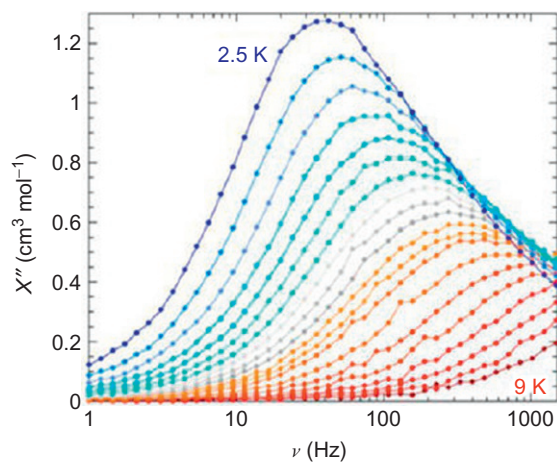


Fig. 2.23

Out-of-phase signals at various temperatures in the range of 2.5–9 K in an applied field of 600 Oe. From R.A. Layfield, *Organometallics* 33 (2014) 1084–1099.

The indications for a molecule to exhibit SMM behavior is the appearance of an out-of-phase signal (alternating current or ac measurements) in a χ_M'' vs T plot and the observation of hysteresis loops, which is the diagnostic property of a magnet. During the ac measurements, the in-phase (χ_M') and the out-of-phase susceptibilities (χ_M'') are measured as a function of the temperature and as the function of the ac frequency (ν). The magnetization cannot keep up with the oscillating field and the $\chi_M''(\nu)$ data allow relaxation times, τ , to be calculated from $\tau = 1/(2\pi\nu)$, where ν corresponds to the peak maxima (Fig. 2.23).

The relaxation time τ is related to the anisotropy barrier U_{eff} based on the equation $\tau = \tau_0 \exp(U_{\text{eff}}/k_B T)$. U_{eff} then is extracted from the linear regression of the Arrhenius plot of $\ln \tau$ vs $1/T$, which describes the area in which the relaxation is thermally activated.

The second, and most important, measurement for the establishment of the SMM behavior is the M vs H measurement. If a molecule is indeed a magnet, after being subjected to a reverse field and then returned to zero-field conditions, it has to display nonzero magnetization (M). The phenomenon is temperature dependent and, apart from that, other factors such as field sweep rate can affect the maximum temperature at which hysteresis is observed.

MC complexes can exhibit very interesting magnetic properties and that makes them quite famous among other polynuclear compounds, in the magnetism research. Although there are numerous studies that discuss the structural features, the formation, and the stability of MCs, there are not many articles commenting and trying to rationalize in depth the magnetic behavior of MCs [5]. Multiple 9-MC-3 or inverse 9-MC-3 complexes have been synthesized, using various 3d-metal ions, and for some of them, magnetic measurements were also performed [8,18,71–77]. Cu^{II} oxime-based 9-MC-3 complexes have been the main focus on the magnetic

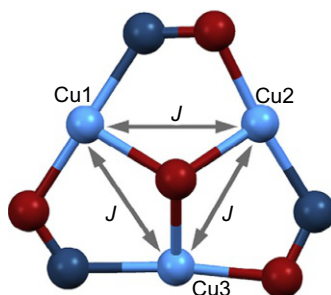


Fig. 2.24

Exchange pathway scheme in trinuclear Cu^{II} inverse 9-MC-3. From M. Ostrowska, I.O. Fritsky, E. Gumienna-Kontecka, A.V. Pavlishchuk, *Coord. Chem. Rev.* 327 (2016) 304–332.

investigation due to the fact that this type of topology, which Cu^{II} possesses, can be also obtained with diamagnetic metal ions (Pd^{II} , Zn^{II} , and Ni^{II} in a square planar coordination environment, or low-spin Co^{III}) [18,73–77].

Most of the oximate-based trinuclear Cu^{II} MCs have a central cavity, which is captured by bridging hydroxy or methoxy groups, and they can thus be considered as 9-MC-3 complexes [78–85]. The N—O bridge, though in these complexes, is not responsible for the exchange interaction between the Cu^{II} ions, which is actually propagated via the oxygen atom from an anion in the cavity (Fig. 2.24).

The magnetic properties of Fe^{III} complexes containing inverse 9-MC-3 parts, $\text{Na}_3[\text{Fe}_6\text{O}_2\text{H}(\text{CH}_3\text{O})_3(\text{OH})_3]$, and $\text{Na}_9[\text{Fe}_6\text{O}_2\text{H}(\text{sao})_6(\text{CH}_3)_3(\text{OH})_3]_2[\text{Fe}_3(\text{sao})_6]$ were reported and magnetically investigated. The $\chi_{\text{M}}T$ product decreases with decreasing temperature indicating that within the Fe^{III} ions antiferromagnetic (AF) exchange interactions prevail [86].

The pure 12-MC-4 as well as inverse 12-MC-4 complexes is a category of MC compounds that have been (and still is) extensively investigated. Various metal ions have been used for the synthesis of these complexes such as $\text{Co}^{\text{II/III}}$, Ni^{II} , Fe^{III} , Zn^{II} , $\text{Mn}^{\text{II/III}}$, Ga^{III} , Cu^{II} , and some lanthanide ions [2,16,18,21,22,26,44,72,74,87–98]. The structure motif of 12-MC-4 compounds includes four peripheral metal ions and one additional metal ion that is located in the center of the cavity.

The pentacopper(II) 12-MC-4 complexes have been synthesized and extensively investigated, but it has been found that within the metals of that compound, antiferromagnetic interactions prevail and no out-of-phase signals could be observed, meaning that the compound is not an SMM. Apart from the classical 12-MC-4 complexes, examples of collapsed or inverse tetranuclear Cu^{II} and Zn^{II} compounds have been also reported [99–103]. The tetranuclear $[\text{Cu}_4(\text{dmv})_4(\text{H}_2\text{O})_8](\text{ClO}_4)_4 \cdot 2\text{H}_2\text{O}$ possesses a vacant space in the metallamacrocycle ring, something that is not really common for 12-MC-4 complexes (Fig. 2.25) [102]. In this example, the peripheral Cu^{II} ions contribute to the magnetic behavior of the complex and the exchange

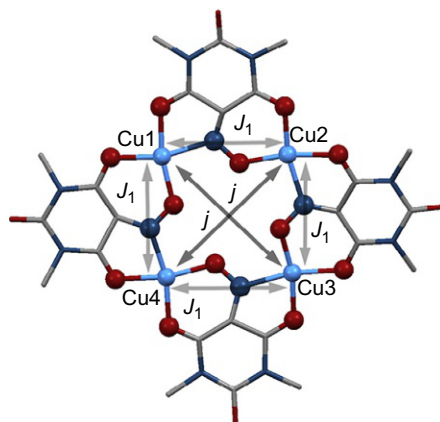


Fig. 2.25

Schematic representation of $[\text{Cu}_4(\text{dmv})_4(\text{H}_2\text{O})_8](\text{ClO}_4)_4 \cdot 2\text{H}_2\text{O}$ and exchange pathways within the complex. From M. Ostrowska, I.O. Fritsky, E. Gumienna-Kontecka, A.V. Pavlishchuk, *Coord. Chem. Rev.* 327 (2016) 304–332.

interactions are mediated only via the N—O group. Within the copper(II) ions, strong antiferromagnetic exchange interactions are present and no out-of-phase signals were observed.

Cobalt^{II/III} 12-MC-4 metallacrown complexes have been synthesized and extensively analyzed as well. Some exhibit the SMM behavior. The magnetic properties of $(\text{Hpip})(\text{Piv})[\text{Li}[\text{Co}^{\text{II}}(\mu_2 - \text{Piv})_2(\text{Piv})[12 - \text{MC}_{\text{Co}^{\text{III}}\text{N}(\text{Shi}) - 4}](\text{Pip})_5]]_2$ (**1**), $\text{Co}^{\text{II}}(\text{Boa})(\text{Piv})[12 - \text{MC}_{\text{Co}^{\text{III}}\text{N}(\text{Shi}) - 4}](\text{Morph})_5(\text{MeOH})$ (**2**), and $\text{Co}^{\text{II}}(\text{NO}_2)(\text{Piv})[12 - \text{MC}_{\text{Co}^{\text{III}}\text{N}(\text{Shi}) - 4}](\text{Pic})_6$ (**3**) have been investigated and reported (Fig. 2.26) [2].

The room-temperature $\chi_{\text{M}}T$ values for these cobalt(II/III) compounds are 3.15 (**1**), 3.03 (**2**), and $3.23 \text{ cm}^3 \text{ mol}^{-1} \text{ K}$ for complex number (**3**), much higher than the expected spin-only value of $1.876 \text{ cm}^3 \text{ mol}^{-1} \text{ K}$ for a spin of $S = 3/2$ with a g -factor of $g = 2$ (Fig. 2.27A). Note that the periphery Co^{III} ions are diamagnetic, so they do not contribute to the overall magnetic response. The $\chi_{\text{M}}T$ product decreases with decreasing temperature and at 2 K reaches a value of 2.18, 2.26 and $2.79 \text{ cm}^3 \text{ mol}^{-1} \text{ K}$, respectively. The shape of the curve indicates the presence of a pronounced anisotropy of the cobalt(II) magnetic moment.

The recorded magnetization data of all three complexes at low temperatures further support the presence of high magnetic anisotropy (Fig. 2.27B). The corresponding $M/N_{\text{A}}\mu_{\text{B}}$ values of 2.28, 2.23, and 2.17 for (**1**), (**2**), and (**3**) at 2 K and with an applied field of 7 T are significantly below the saturation magnetization of an isolated $S = 3/2$ state with a $g = 2$. Finally, alternating current measurements revealed out-of-phase signals for all of three complexes exhibit and the U_{eff} values calculated were 14, 35, and 79 K for (**1**), (**2**), and (**3**), respectively (Fig. 2.28). That big difference in the U_{eff} values can be rationalized by taking into account the coordination

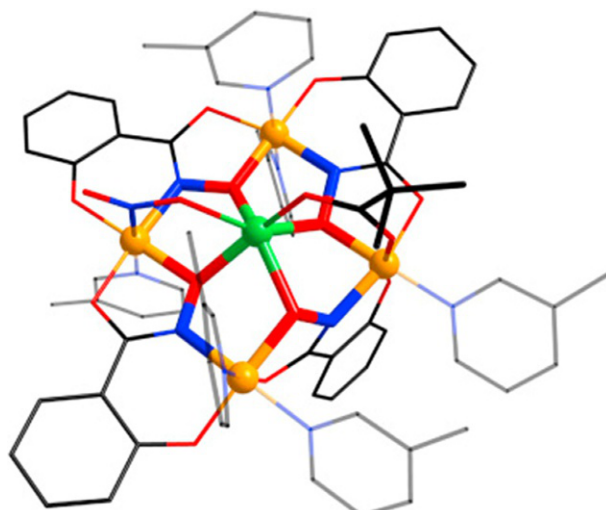


Fig. 2.26

Schematic representation of $\text{Co}^{\text{II}}(\text{NO}_2)(\text{Piv})[12 - \text{MCo}^{\text{III}}_{\text{N}(\text{Shi})} - 4](\text{Pic})_6$. Central metal ion: $\text{Co}(\text{II})$, peripheral metal ions: $\text{Co}(\text{III})$, bridging metal atoms N & O bold highlighted bold. From P. Happ, C. Plenck, E. Rentschler, *Coord. Chem. Rev.* 289–290 (2015) 238–260.

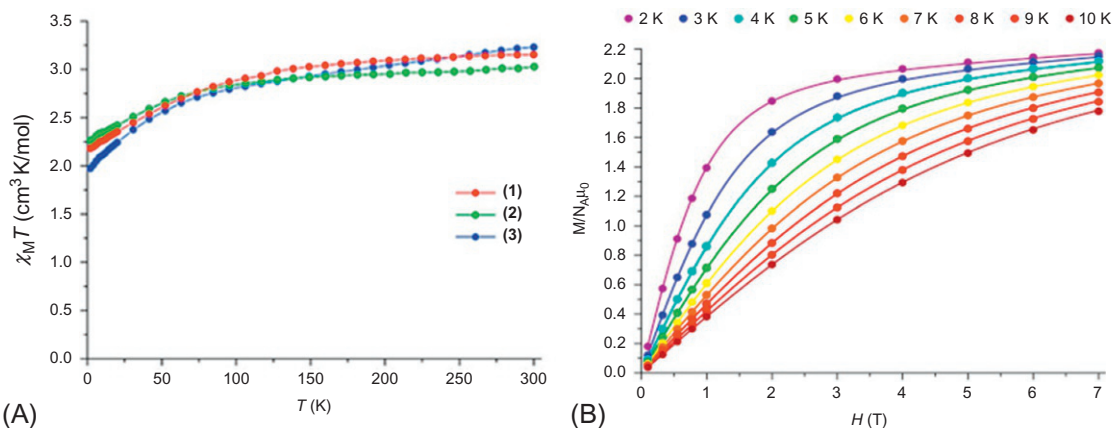


Fig. 2.27

(A) Temperature dependence of the $\chi_M T$ product for (1), (2), and (3), solid lines represent guidelines for the eyes. (B) Field dependence of the reduced magnetization for (3) at different temperatures from 2 to 10 K; solid lines represent the best fit parameters according to an effective spin Hamiltonian with isotropic g -factor and ZFS parameter. From P. Happ, C. Plenck, E. Rentschler, *Coord. Chem. Rev.* 289–290 (2015) 238–260.

environment of the central Co^{II} ion in each case. It was strongly observed that further distortion of the central Co^{II} ion from the octahedral coordination sphere toward the trigonal prismatic led to deviations (going from O_h symmetry to D_{3h}) and that had a strong impact on the anisotropy of the complexes thus leading to larger U_{eff} values.

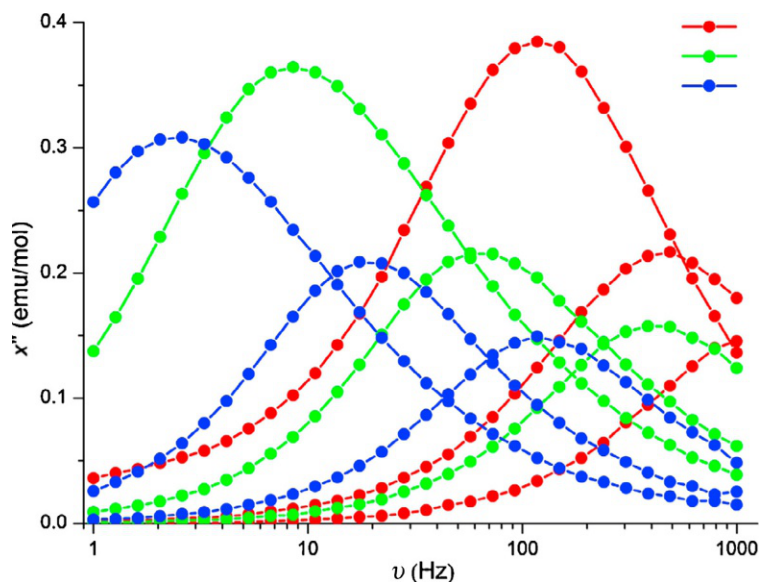


Fig. 2.28

Frequency dependence of the out-of-phase signals of the ac susceptibility for **(1)**, **(2)**, and **(3)** at 2, 4, and 6 K; solid lines represent guidelines for the eye. From P. Happ, C. Plenck, E. Rentschler, *Coord. Chem. Rev.* 289–290 (2015) 238–260.

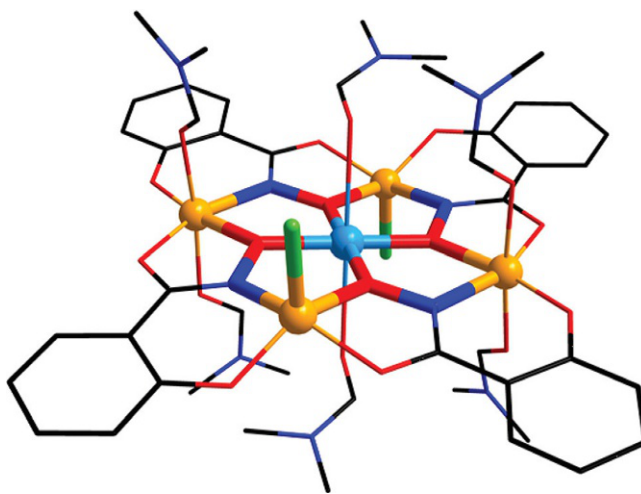


Fig. 2.29

Structure of $\text{Cu}^{\text{II}}(\text{DMF})_2\text{Cl}_2[12 - \text{MC}_{\text{Fe}^{\text{III}}\text{N}(\text{shi})} - 4](\text{DMF})_4$. Central metal ion: $\text{Co}(\text{II})$, peripheral metal ions: $\text{Co}(\text{III})$, bridging metal atoms N & O bold highlighted bold. From P. Happ, E. Rentschler, *Dalton Trans.* 43 (2014) 15308–15312.

In 2014, Happ et al. reported a heterometallic 12-MC-4 complex with the formula $[\text{CuFe}_4(\text{shi})_4\text{Cl}_2\text{DMF}_6] \cdot 2\text{DMF}$. The complex consists of four peripheral Fe^{III} ions connected through the triply deprotonated (shi^{-3}) salicylhydroxamate anions while a Cu^{II} ion is occupying the central cavity of the 12-MC-4 compound (Fig. 2.29) [22].

The $\chi_M T$ value of $17.12 \text{ cm}^3 \text{ mol}^{-1} \text{ K}$ at room temperature agrees with the theoretical spin-only value of $17.88 \text{ cm}^3 \text{ mol}^{-1} \text{ K}$, of four noninteracting Fe^{III} ions with $S = 5/2$ and one Cu^{II} ion with $S = 1/2$. The $\chi_M T$ product increases with decreasing temperature from 300 to 40 K and reaches a maximum value of $22.45 \text{ cm}^3 \text{ mol}^{-1} \text{ K}$, while after that the $\chi_M T$ value decreases with decreasing temperature up to 2 K to a value of $10.1 \text{ cm}^3 \text{ mol}^{-1} \text{ K}$. The best-fit parameters of the $\chi_M T$ vs T plot gave the following parameters: $J_1 = -49.2 \text{ cm}^{-1}$, $J_2 = -3.8 \text{ cm}^{-1}$, and $g_{\text{av}} = 2.03$. The ratio of J_1/J_2 of the $[\text{CuFe}_4(\text{shi})_4\text{Cl}_2\text{DMF}_6] \cdot 2\text{DMF}$ complex, based on the energy diagram, is 13, which corresponds to a spin ground state of $S_T = 11/2$, while the energy separation between the first and second excited states, $S_T = 13/2$ and $S_T = 9/2$ are 3.3 and 4.2 cm^{-1} , respectively [22]. What is important here to mention is that forcing a higher spin ground state for our system was not a result of plain luck, but it was the outcome of the concept named “the magnetic director approach.” Cu^{II} ion was assigned as the guest ion and played the role of the central magnetic director, as its natural magnetic orbital $d_{x^2-y^2}$ points directly toward basal donor atoms and can induce strong AF interactions. On the other hand, Fe^{III} ions were chosen to build up the cyclic host providing high single-ion contributions as well as suitable magnetic orbitals [22]. In such a way, it was possible to direct the magnetic behavior of our metallacrown setting the grounds for new approaches when wanting to maximize the spin ground state of a molecular system.

One last example that belongs to the 12-MC-4 family and needs highlighting is the two Zn^{II} - Yb^{III} complexes with the formula $[\text{YbZn}_4(\text{quinha})_4(\text{py})_4(\text{DMF})_4](\text{CF}_3\text{SO}_3)_3 \cdot 5\text{DMF} \cdot 7\text{H}_2\text{O}$ and $[\text{YbZn}_4(\text{quinha})_4(\text{iqn})_4(\text{DMF})_4](\text{CF}_3\text{SO}_3)_3 \cdot 6\text{DMF} \cdot 4\text{H}_2\text{O}$ [26]. The $\chi_M T$ vs T plots obtained were attributed to the thermal depopulation of the Stark sublevels of the ground state multiplet ${}^2F_{7/2}$. The authors state that the ac data obtained show no signal above 1.8 K, and they attribute that to fast quantum tunneling of magnetization. After the application of a small 600 Oe field, the authors could determine the frequency out-of-phase signal (Fig. 2.30). After analysis of the relaxation time, it was shown that in both complexes a direct and a Raman relaxation process take place, but the Orbach process is excluded. The data obtained from analyzing the Arrhenius plot yield $U_{\text{eff}}/k_B = 12.6(7) \text{ K}$ (9 cm^{-1}), $\tau_0 = 9.32 \times 10^{-7} \text{ s}$ and $U_{\text{eff}}/k_B = 22.76(6) \text{ K}$ (16 cm^{-1}), $\tau_0 = 3.90 \times 10^{-7} \text{ s}$, respectively [26].

Moving onward to the family of 15-MC-5 complexes, the magnetic properties of $[\text{Mn}^{\text{II}}(2,4\text{-D})_2][\text{Mn}_5^{\text{III}}(\text{shi})_5(\text{py})_6]$ in a dc field suggested the presence of AF exchange interactions within the metal centers. The fitting model as well as the data that were extracted by this model can be found and extensively analyzed in Ref. [96]. In 1999, Pecoraro et al. reported a series of $\text{Cu}^{\text{II}}\text{-Ln}^{\text{III}}$ ($\text{Ln}^{\text{III}} = \text{La}, \text{Nd}, \text{Sm}, \text{Eu}, \text{Gd}, \text{Dy}, \text{Ho}, \text{Er}, \text{and Yb}$) 15-MC-5 complexes using picoline hydroxamic acid, or different α -aminohydroxamic acids as ligands. The dc magnetic studies revealed the presence of dominating AF magnetic exchange interactions in all these complexes. Between the neighboring Cu^{II} ions in the metallamacrocycle, there are antiferromagnetic interactions predicted, while the interaction between the Cu^{II} and Gd^{III} was predicted to be small and ferromagnetic [104]. Pavlishchuk et al. in 2014 studied the $\{[\text{GdCu}_5(\text{Glyha})_5(\text{H}_2\text{O})_2](\text{GdCu}_5(\text{Glyha})_5(\text{H}_2\text{O})_3)(1,3\text{-bdc})_3\} \cdot 16\text{H}_2\text{O}\}_n$ compound and fitted

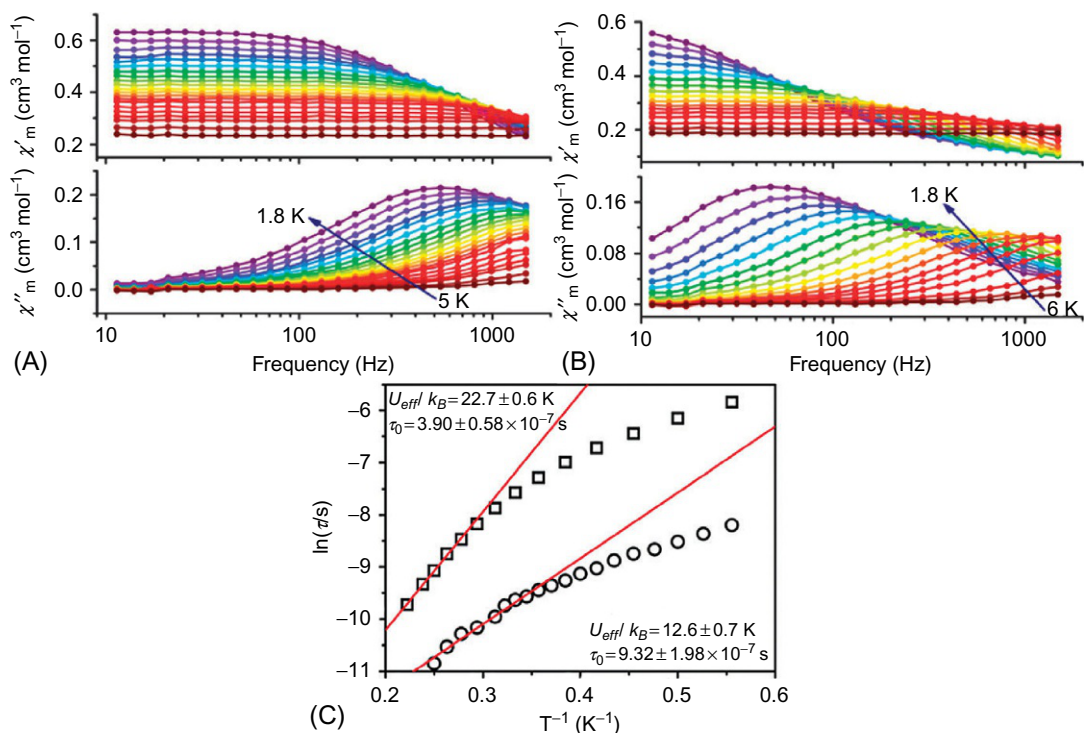


Fig. 2.30

Frequency dependencies of the in-phase and out-of-phase signals for [YbZn₄(quinha)₄(py)₄(DMF)₄·(CF₃SO₃)₃·5DMF·7H₂O (A) and [YbZn₄(quinha)₄(iqn)₄(DMF)₄·(CF₃SO₃)·6DMF·4H₂O (B) ($H_{dc} = 600$ Oe and $T = 1.8$ K), and the temperature dependence of the relaxation time (Arrhenius plot). From Q.-W. Li, J.-L. Liu, J.-H. Jia, Y.-C. Chen, J. Liu, L.-F. Wang, M.-L. Tong, *Chem. Commun.* 51 (2015) 10291–10294.

the complex with two fitting models [105]. Pecoraro et al. also demonstrated that it is possible to get SMMs based on the Cu^{II}-Ln^{III} 15-MC-5 blocks [106]. Based on the solvent used, for the [LnCu₅(LpheHA)₅](NO₃)₃, (Ln^{III} = Dy, Ho), dimers of 15-MC-5 complexes or helical chains are formed within the crystal. The ac measurements performed, suggest that the complexes belong to the SMM family since in solid state the compounds shows a glassy or magnetic ordering. The Ho^{III} complexes didn't show any out-of-phase signal in frozen solution, suggesting the presence of glassy or magnetic ordering only in solid samples. On the other hand, the Dy-analogue displayed SMM and single-chain magnet (SCM) properties. More details are provided in the paper published by Pecoraro [106].

Apart from the famous 9-MC-3, 12-MC-4, and 15-MC-5 structural topologies, there are also some complexes reported with rare MC topologies. The $\{[\text{Mn}^{\text{III}}_4\text{Ln}^{\text{III}}_2(\text{salicylHA})_4(\text{OAc})(\text{NO}_3)_2(\mu - \text{O})(\mu - \text{OH})(\text{DMF})_2(\text{py})_6] \cdot 2\text{DMF} \cdot \text{py}\}$ (Ln^{III} = Y, Gd, Tb, Dy, Ho) and $\{[\text{Mn}^{\text{III}}_4\text{Ln}^{\text{III}}_2(\text{ClSalicylHA})_4(\text{OAc})_3(\mu_3 - \text{OCH}_3)(\mu_3 - \text{O})(\text{CH}_3\text{OH})_6(\text{H}_2\text{O})] \cdot 2\text{CH}_3\text{OH} \cdot n\text{H}_2\text{O}\}_2$ (Ln^{III} = Eu,

Gd, Tb, Dy) complexes belong to a family of 14-MC-5 compounds. The dc magnetic studies showed that predominant AF magnetic exchange interactions dominate within the complexes, but the $\chi_M T$ value at low temperatures suggests a high-spin ground state [107,108]. Ac measurements confirmed that $\{[\text{Mn}^{\text{III}}_4\text{Ln}^{\text{III}}_2(\text{salicylHA})_4(\text{OAc})(\text{NO}_3)_2(\mu-\text{O})(\mu-\text{OH})(\text{DMF})_2(\text{py})_6] \cdot 2\text{DMF} \cdot \text{py}\}$ ($\text{Ln}^{\text{III}} = \text{Tb}, \text{Dy}, \text{Ho}$) and $\{[\text{Mn}^{\text{III}}_4\text{Dy}^{\text{III}}_2(\text{ClSalicylHA})_4(\text{OAc})_3(\mu_3-\text{OCH}_3)(\mu_3-\text{O})(\text{CH}_3\text{OH})_6(\text{H}_2\text{O})] \cdot 2\text{CH}_3\text{OH} \cdot n\text{H}_2\text{O}\}_2$ belong to the SMM family. The relaxation time and the energy barrier was calculated for the 14-MC-5 $\{[\text{Mn}^{\text{III}}_4\text{Dy}^{\text{III}}_2(\text{ClSalicylHA})_4(\text{OAc})_3(\mu_3-\text{OCH}_3)(\mu_3-\text{O})(\text{CH}_3\text{OH})_6(\text{H}_2\text{O})] \cdot 2\text{CH}_3\text{OH} \cdot n\text{H}_2\text{O}\}_2$ complex, and the values found were $\tau_0 = 4.9 \times 10^{-8}$ s and $U_{\text{eff}} = 16.7$ K, respectively. Note that the U_{eff} value is among the highest values reported for these kinds of systems (Fig. 2.31).

There was also another MC complex of manganese reported $[\text{Mn}_9\text{O}_4(\text{Mesao})_6(\text{MeO})_3(\text{OAc})_3(\text{OH})(\text{MeOH})_2] \cdot 2.5\text{DMF}$ with an interesting topology. The compound consists of

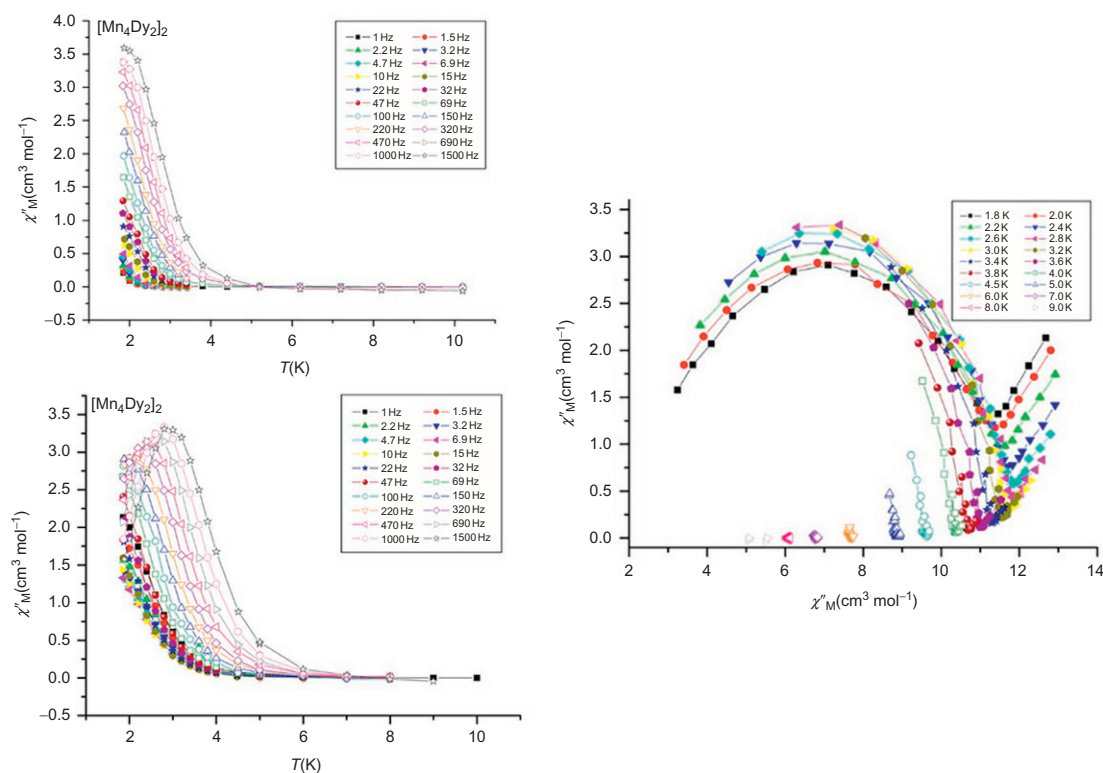


Fig. 2.31

Out-of-phase signals for complex

$\{[\text{Mn}^{\text{III}}_4\text{Dy}^{\text{III}}_2(\text{ClSalicylHA})_4(\text{OAc})_3(\mu_3-\text{OCH}_3)(\mu_3-\text{O})(\text{CH}_3\text{OH})_6(\text{H}_2\text{O})] \cdot 2\text{CH}_3\text{OH} \cdot n\text{H}_2\text{O}\}_2$ in a χ_M'' vs T plot in a 5.0 Oe oscillating field with a zero dc field in the top left picture and with an applied dc of 2 kOe at the bottom left pic. The Cole-Cole plot is also shown. The solid lines are guidelines for the eyes. From F. Cao, S. Wang, D. Li, S. Zeng, M. Niu, Y. Song, J. Dou, *Inorg. Chem.* 52 (2013) 10747–10755.

two fragments: a 15-MC-6 $[\text{Mn}^{\text{III}}_6(\mu_4 - \text{O})_3(\mu_3 - \text{ON})_3(\mu - \text{O})_3]^{3+}$ and a 9-MC-3 $[\text{Mn}^{\text{III}}_3(\mu_3 - \text{O})(\mu_4 - \text{ON})_3]^+$ that are connected via apical Mn—O bonds. Magnetic studies were also performed and are thoroughly discussed in the corresponding paper [109]. Finally, another interesting example of MC rare nuclearities with exciting magnetic properties is one more Mn^{III}/Ln^{III} complex $[\text{Dy}^{\text{III}}_4\text{Mn}^{\text{III}}_6(\text{H}_2\text{salicylHA})_2(\text{salicylHA})_6(\text{sal})_2(\text{OAc})_4(\text{OH})_2(\text{CH}_3\text{OH})_8] \cdot 4\text{CH}_3\text{OH}$ (Ln^{III} = Ho and Dy), which can be considered as a 22-MC-8 compound. The Dy-analogue belongs to the SMM family and the magnetic properties are extensively analyzed and discussed at Ref. [110].

To summarize, for sure, the area of single-molecule magnets (SMMs), even though it is already known since the early 1990s, has yet not reached its limit. There are still many discoveries to be made, many more exciting structures to be synthesized and analyzed, and apparently the metallacrown scaffold is an excellent base for securing the boundaries of SMM progress. Chemists have already done huge leaps toward the successful development of this field and surely much more is yet to be done. Hopefully, 1 day molecules that function as permanent magnets at room temperature will be discussed, something which is the ultimate goal of all scientists that are working in this field.

2.3 Moving from 0 to 3D Structures

Of major interest in coordination chemistry are hybrid materials offering huge cavities and large reactive surfaces. These coordination polymers or metal-organic frameworks are built up by a network of nodes and linkers. Linkers are often organic molecules connecting metal ions or small coordination clusters representing the nodes. In such frameworks, it is possible to combine the reactivity and properties of the molecular building blocks such as luminescence, slow magnetic relaxation, catalysis, and molecular recognition with a variety of porous structures leading to effective, applicable materials [2,6,22,25,26,46,87,93,102,103].

The previously mentioned characteristics of MCs allow to use them as molecular units in a rational approach to construct macromolecular structures [111]. In particular, the broad ligand variety, their stability under different conditions, and the availability of out-of-plane coordination sites make MCs highly effective building blocks to create new frameworks with desired features [6]. An additional benefit from using MCs as nodes lies in the more predictable properties of the resulting extended network as this approach is started from the supramolecular and not the less predictable molecular level [112].

2.3.1 Metallacrown Linkage

The variety of linkers for the construction of porous coordination polymers is very broad. Using MCs as nodes, several possibilities to connect these metal clusters exist. The following chapter should give an overview on published bridging species of extended metallacrown systems.

As mentioned previously, the ring-building metal ions in MCs exhibit unoccupied out-of-plane coordination sites, well suited to connect additional coligands. These ligands are directly influencing the extended network, as they imply a certain geometry for the MC linkage. They have to be chosen in accordance with the respective metal ions. Another possibility to connect metallamacrocycles is the use of bridging counter ions, that is, in the easiest way simply, alkali ions could link MCs. Finally, a very sophisticated way of interconnection is given via optimized main ligand design. Here, the ligands backbone has to be extended with additional coordinating side arms, leading to polydentate organic molecules.

Mezei et al. showed that for the Gd^{III} -centered Cu^{II} 15-MC-5 [113], the isonicotinate ligand (see Fig. 2.32), is a well-fitting coligand. The pyridine nitrogen is able to coordinate in the axial position to the copper ions while the carboxylate group is bridging the central guest ion and one copper ion. Hereby, a compartment of two nearly coplanar MCs forms. The exchange of the linking molecule to the symmetrical terephthalate clearly demonstrates the possibility to adjust the compartment size, which increases to 11.6 Å compared to 9.7 Å for the isonicotinate bridged 15-MC-5.

Carboxylate ligands are appropriate to coordinate lanthanide ions. Thus, aromatic and aliphatic dicarboxylates of different chain length represent ideal linker for lanthanide-centered 15-MC-5 complexes. As the MC itself often is charged, counterions represent another possibility to build the favored intermolecular connections. In $[\text{Cu}(\text{en})_2(\text{H}_2\text{O})(m\text{-H}_2\text{O})\{\text{Cu}_5(\text{L}_4\text{H}_4)(\text{H}_2\text{O})_3\}_2]_n$, synthesized in 2007 [114], the copper 12-MC-4 nodes with malonomonohydroxamic acid as main ligand are bridged by a $[\text{Cu}(\text{en})_2(\text{H}_2\text{O})_2]^{2+}$ cation. Water molecules coordinate to the mononuclear Cu^{II} complex and the double-decker MC building blocks. In combination with

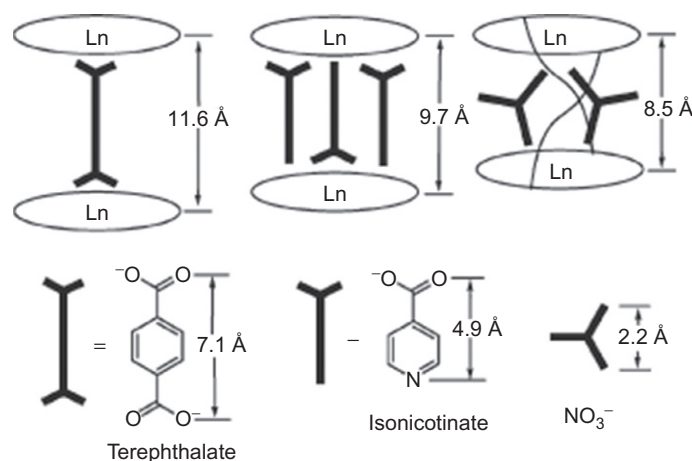


Fig. 2.32

Schematic overview of 15-MC-5 linked via different coligands. From G. Mezei, J.W. Kampf, S. Pan, K.R. Poepfelmeier, B. Watkins, V.L. Pecoraro, *Chem. Commun.* (2007) 1148–1150.

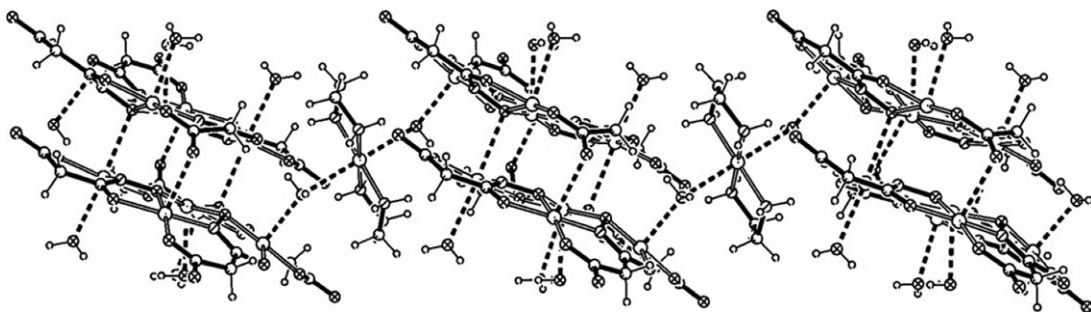


Fig. 2.33

Extract of the crystal structure of the polymeric chain $[\text{Cu}(\text{en})_2(\text{H}_2\text{O})(m\text{-H}_2\text{O})\{\text{Cu}_5(\text{L}_4\text{H}_4)(\text{H}_2\text{O})_3\}_2]_n$. From E. Gumienna-Kontecka, I.A. Golenya, N.M. Dudarenko, A. Dobosz, M. Haukka, I.O. Fritsky, J. Swiatek-Kozłowska, *New J. Chem.* 31 (2007) 1798–1805.

two 1,2-diaminoethane (en) molecules, they fill up the octahedral coordination environment of the bridging metal ion (Fig. 2.33).

A completely different network could be constructed using alkali metal ions as linkers. Even though the same main ligand (malonomonohydroxamic acid) is used, Lago et al. [92] varied the framework using potassium ions to build a three-dimensional network with Cu^{II} 12-MC-4 units. This connection mode is solely possible having free donor atoms in the main ligands backbone. Here, the carboxylato group is the coordinating functional group.

One of the first extended networks with MC building units was published by Percoraro et al. In the compound $\{\text{Cu}(\text{NO}_3)_2[12\text{-MC}_{\text{Cu}^{\text{II}}}\text{N}(\text{S-}\beta\text{-pheHA})-4]\} - \{\text{Cu}_2(\text{benzoate})_4\}$ in between the Cu^{II} 12-MC-4 molecules, a neutral, dinuclear paddle-wheel copper(II) benzoate is implemented in the framework (see Fig. 2.34) [115].

Varying the ligands backbone is probably the most elegant way to create extended networks. In this case, the supramolecular structure does not depend on any additional connector.

Polydentate ligands that provide a hydrazide or hydroxamic acid function and auxiliary coordinating groups can build up multidimensional MC structures. For the smallest type of the metallamacrocycles, an aza-9-MC-3, Ding et al. [116] showed that 1,2,4-triazoles are able to construct 3D coordination polymers with Cu^{II} ions. The MCs are directly linked to each other as the third nitrogen atom of the triazole ligand pointing away from the ring center coordinates a Cu^{II} ion from the neighboring MC (see Fig. 2.35).

Another example for an effective ligand variation in order to interconnect MCs directly is illustrated in Fig. 2.36 [111]. The salicylhydroxamic acid related ligand, (3-hydroxyisonicotinic hydroxamic acid), builds up a 2D network coordinating to bridging $\{\text{Cu}^{\text{II}}(\text{AcO})\text{Py}\}^+$ cations. This connection is possible, as the ligand provides an additional coordinating nitrogen atom in its aromatic backbone.

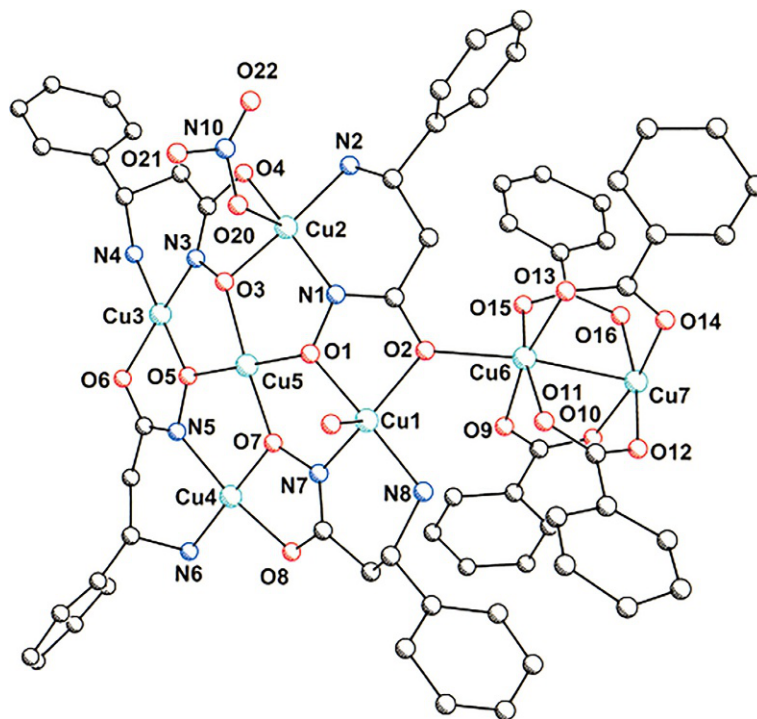


Fig. 2.34

Molecular structure of $\{\text{Cu}(\text{NO}_3)_2[12\text{-MC}_{\text{Cu}^{\text{II}}\text{N}(\text{S}-\beta\text{-pheHA})-4}]\} - \{\text{Cu}_2(\text{benzoate})_4\}$. From J.J. Bodwin, V.L. Pecoraro, *Inorg. Chem.* 39 (2000) 3434–3435.

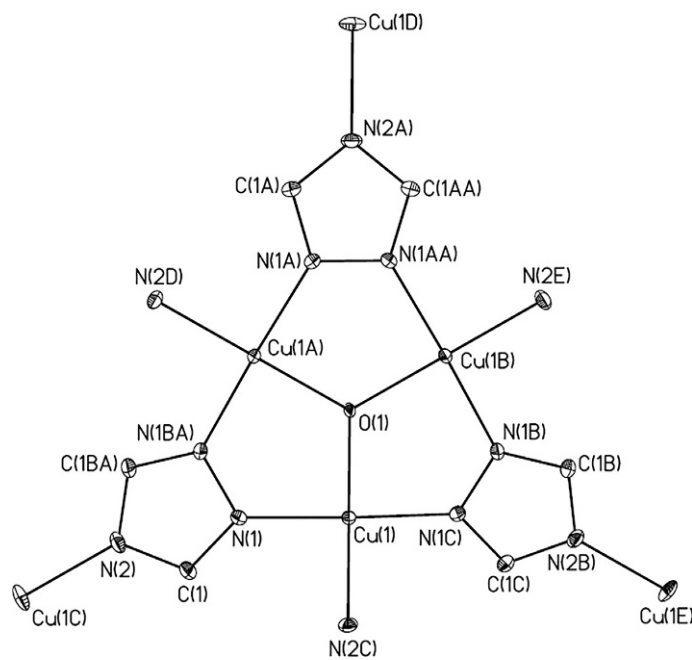


Fig. 2.35

ORTEP view of the aza-9-MC-3 building unit for a 3D coordination polymer. From B. Ding, L. Yi, P. Cheng, D.-Z. Liao, S.-P. Yan, *Inorg. Chem.* 45 (2006) 5799–5803.

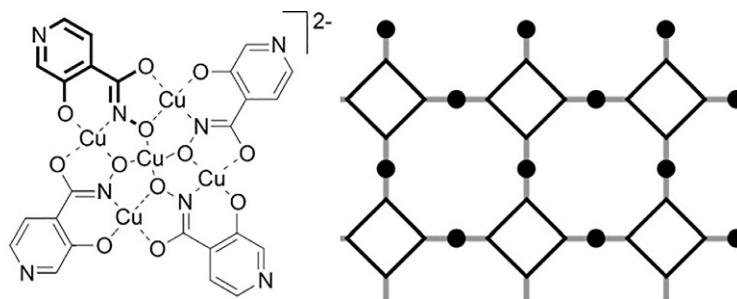


Fig. 2.36

Left: Scheme of a Cu^{II} 12-MC-4 with 3-hydroxyisonicotinic acid as the main ligand. Right: Connection scheme for the 12-MC-4 motif. From C. Atzeri, L. Marchiò, C.Y. Chow, J.W. Kampf, V.L. Pecoraro, M. Tegoni, *Chem. Eur. J.* 22 (2016) 6482–6486.

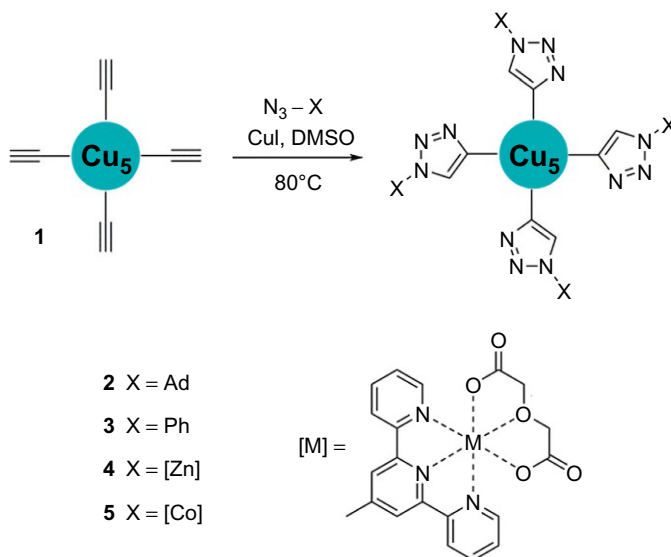


Fig. 2.37

Synthesis strategy for Cu^{II} 12-MC-4 units which could be connected using click chemistry. From C. Plenk, J. Krause, M. Beck, E. Rentschler, *Chem. Commun.* 51 (2015) 6524–6527.

In order to adjust the cavity size of the desired porous network, the ligand has to be rationally adapted. A very recent and promising approach to reach this ambitious goal could lie in the field of click chemistry. It has already been demonstrated that a copper 12-MC-4 formed by alkyne-functionalized salicylhydroxamic acid can be used as paramagnetic building block [117]. The click reaction resulted in the 12-MC-4 triazole bridged with adamantyl, phenyl, Zn and Co complex moieties as shown in Fig. 2.37.

2.3.2 Multidimensionality of Extended Networks

The broad variety of ligands, bridging counter ions, and intermolecular connectors available for MC building units offers a unique opportunity to set up rationally designed coordination polymers. Starting from double-decker complexes, bigger compartments, 1D chains, even 2D layer structures, and 3D networks with different cavity sizes are achievable. An overview of such extended systems and their properties is presented in this section.

As MC molecules describe nearly planar structures, the simplest way to combine them is a face-to-face dimerization. The first fused MC structure is a double-decker Ni^{II} 12-MC-4 [16]. Within this dimer, shown in Fig. 2.38, 8 of 10 Ni^{II} ions are embedded in an octahedral environment leading to 8 paramagnetic centers in this molecule. The $\chi_M T$ vs. T diagram shows a significant difference compared to a single Ni^{II} 12-MC-4 compound. The measurement indicates strong antiferromagnetic interaction, whereas for the single one, small ferromagnetic exchange interaction was proposed.

As shown for the nickel dimer, the face-to-face assembling leads to strong antiferromagnetic exchange interaction resulting in a diamagnetic ground state for the dimer regardless of the ground state for each single Ni^{II} MC. In order to obtain a higher spin multiplicity, an increase of the stack size is one possibility. An odd number of assembled MCs should lead to an overall paramagnetic compound. The $\chi_M T$ data of a triple-decker structure formed by a Cu^{II} 12-MC-4 trimer capped with Cr(C₂O₄)₃³⁻ anions on both ends revealed that these expectations could be satisfied (see Fig. 2.39) [118]. The magnetic data were in good agreement with

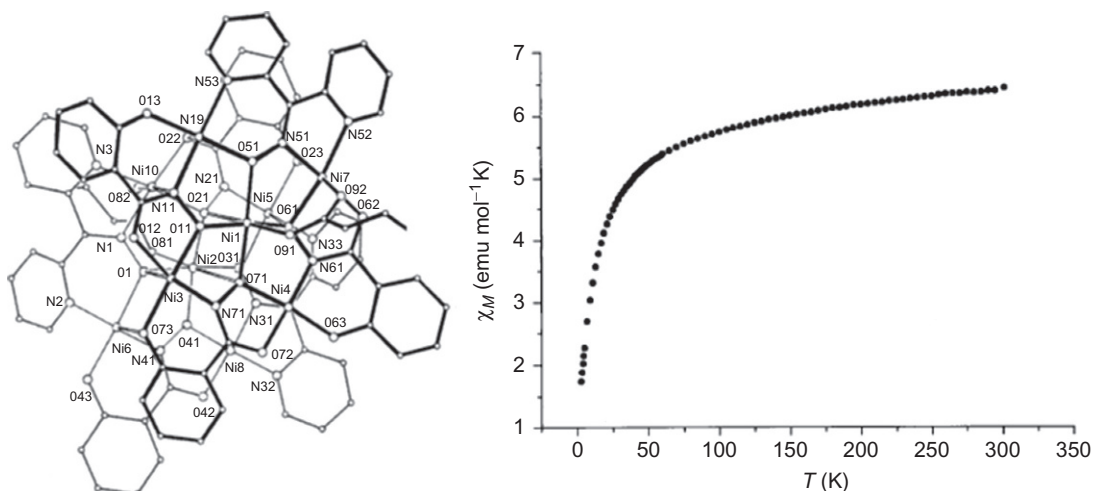


Fig. 2.38

Left: Double-decker MC structure of a Ni^{II} 12-MC-4. Right: $\chi_m T$ vs. T plot of the Ni^{II} MC dimer. From G. Psomas, C. Dendrinou-Samara, M. Alexiou, A. Tsohos, C.P. Raptopoulou, A. Terzis, D.P. Kessissoglou, *Inorg. Chem.* 37 (1998) 6556–6557.

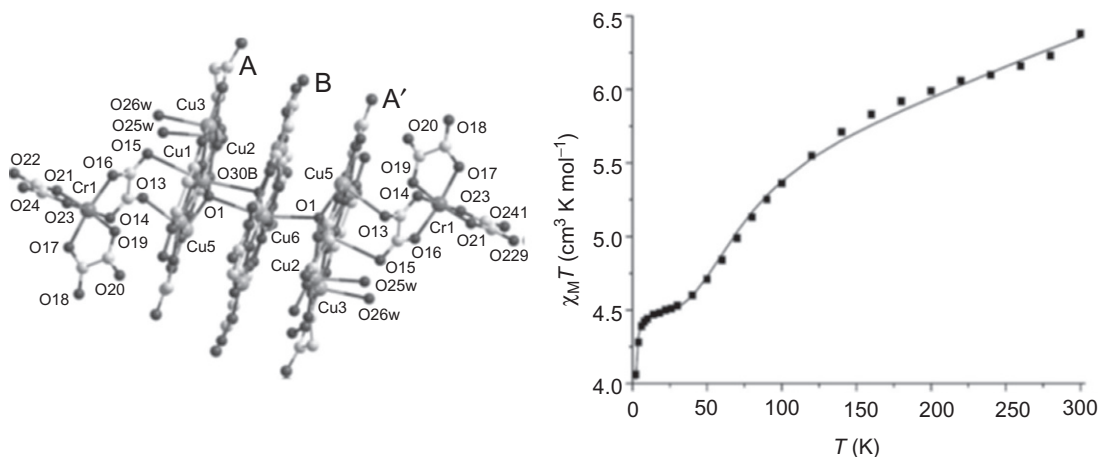


Fig. 2.39

Left: Molecular structure of a Cu^{II} 12-MC-4 triple decker. Right: $\chi_m T$ vs. T plot of the Cu^{II} MC trimer. Adapted from A.V. Pavlishchuk, S.V. Kolotilov, M. Zeller, L.K. Thompson, I.O. Fritsky, A.W. Addison, A.D. Hunter, *Eur. J. Inorg. Chem.* 2010 (2010) 4851–4858.

the expected values for each building unit. Therefore, the authors suggested that the magnetic properties of related coordination polymers could be determined from the individual MC building element [118].

Compared to 12-MC-4 based structures, the resulting extended networks for 15-MC-5 complexes show dense packing; therefore, they often do not provide any voids [6,119]. Even though, a direct face-to-face connection with 15-MC-5 complexes is not possible as the central guest ion needs further coordination in axial position, addition of linking molecules was shown to lead to the formation of bigger 15-MC-5 compartments, Mezei et al. [113]. The coplanar pentacopper(II) 15-MC-5 coordinating each one Gd^{III} ion in the center are linked via coligands like isonicotinate or terephthalate and counterions like nitrates (see Fig. 2.40). As mentioned in Section 2.3.1, the compartment size is directly influenced by the linking molecule.

Bigger supramolecular compartments are available with the appropriate choice of lanthanide ion and MC linker [88,120]. La^{III} [15-MC_{Cu^{II}}_{L-pheHA}-5](NO₃)₃ (Fig. 2.41, left) shows the huge difference between the resulting dimer for Ln = Dy and the tetramer for Ln = La, when pimelate or suberate linkers are used, respectively. The Lewis acid Dy^{III} ion is coordinated by the carboxylate linkers whereas for the La^{III} compound the linkers are coordinating Cu^{II} ions from adjacent MCs. The La^{III} tetramer is additionally connected by two water molecules yielding in a bowl-shaped formation. Within the crystal lattice, two bowls combine and open up a hydrophilic cavity of ca. 2300 Å³. The hexagonal packing of these octameric units provokes nanochannels with a diameter of 2.4 nm (see Fig. 2.41, right). Therefore, >40% of the compounds volume can be used for solvent or guest ion uptake.

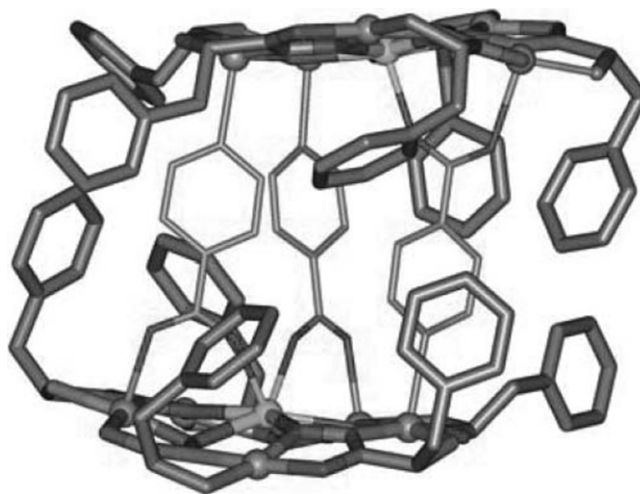


Fig. 2.40

Cu^{II} 15-MC-5 compartment encapsulating three isonicotinate coligands. From G. Mezei, J.W. Kampf, S. Pan, K.R. Poeppelmeier, B. Watkins, V.L. Pecoraro, *Chem. Commun.* (2007) 1148–1150.

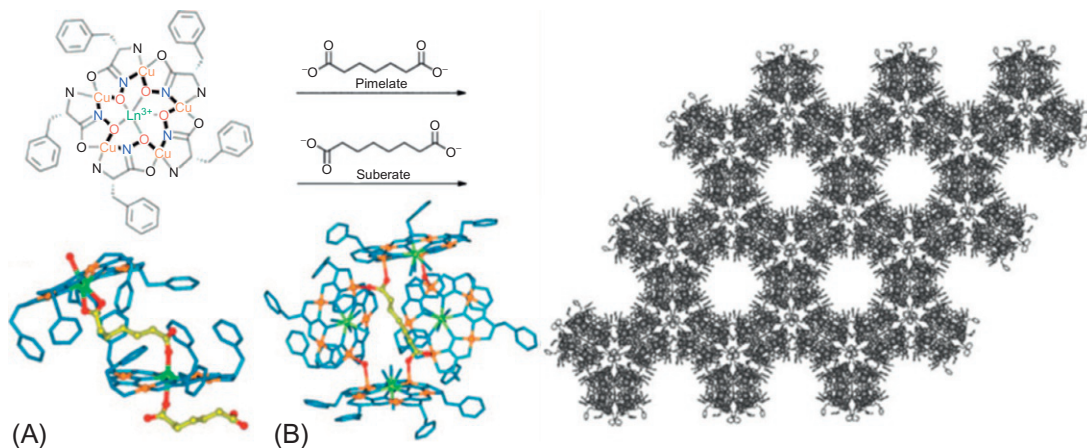


Fig. 2.41

Left: Schematic view of the Ln^{III} centered 15-MC-5 and resulting molecular structures with Dy^{III} (A) and La^{III} (B). Right: Part of the crystal structure for the La^{III}-centered compound. From C.-S. Lim, J. Jankolovits, J.W. Kampf, V.L. Pecoraro, *Chem. Asian J.* 5 (2010) 46–49.

For 12-MC-4 units, 1D chains have successfully been synthesized by Gumienna-Kontecka et al. [114]. The pentacopper 12-MC-4 dimers are bridged by [Cu(en)₂(H₂O)₂]²⁺ cations. The chain structure and especially the interconnection have already been clearly described in the previous section. The magnetic properties of this coordination polymer are difficult to describe (see Fig. 2.42, right). Additional to the interchain antiferromagnetic interactions, the authors suggest weak ferromagnetic interactions within the MC dimer and between the double decker and the connecting copper monomers.

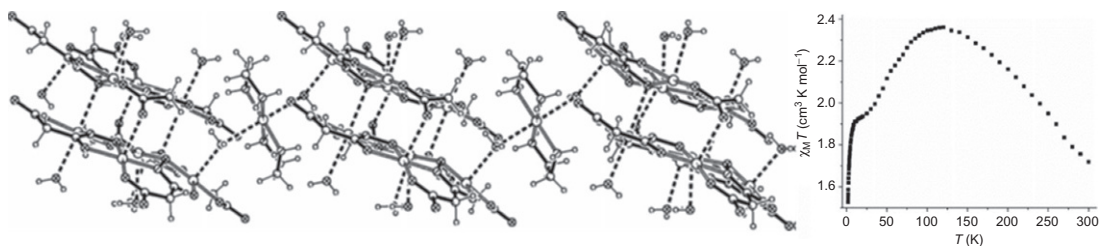


Fig. 2.42

Left: Part of the crystal structure of $[\text{Cu}(\text{en})_2(\text{H}_2\text{O})_2]_n[\text{Cu}(\text{en})_2(\text{H}_2\text{O})(\mu\text{-H}_2\text{O})\{\text{Cu}_5(\text{L}_4\text{H}_4)(\text{H}_2\text{O})_3\}_2]_n \cdot 20n\text{H}_2\text{O}$ ($\text{L} =$ malonomonohydroxamic acid; $\text{en} =$ 1,2-diaminoethane) building one-dimensional chains. Right: $\chi_m T$ vs. T data for this compound. From E. Gumienka-Kontecka, I.A. Golenya, N.M. Dudarenko, A. Dobosz, M. Haukka, I.O. Fritsky, J. Swiatek-Kozłowska, *New J. Chem.* 31 (2007) 1798–1805.

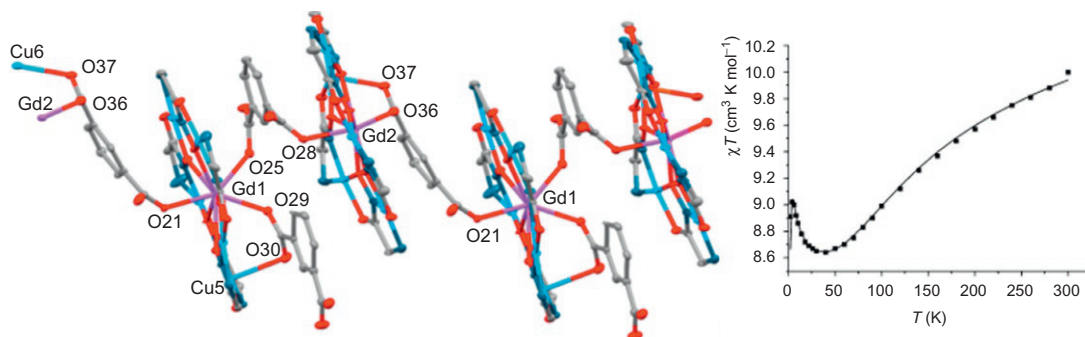


Fig. 2.43

Left: Extract of the crystal structure of a Gd^{III} centered 15-MC-5 forming a 1D chain. Right: $\chi_m T$ data for the 1D chain. From A.V. Pavlishchuk, S.V. Kolotilov, M. Zeller, L.K. Thompson, A.W. Addison, *Inorg. Chem.* 53 (2014) 1320–1330.

An analogue structure to this 1D chain is not accessible when using 15-MC-5 building units. Nonetheless, with 1,3-phthalates as linking molecules a polymeric 1D strand can be obtained. As shown in Fig. 2.43, left, the MC monomers consist of hexanuclear GdCu_5 complexes formed from five doubly deprotonated glycinehydroxamic acid molecules. Additionally, these nearly planar crowns are coordinated by three 1,3-phthalate linkers. Both carboxyl groups of one phthalate ligand bind in a monodentate mode. Another one acts as a tridentate ligand and one is bridging a Gd^{III} and a Cu^{II} ion within the same crown, whereas the other carboxylate group remains noncoordinated. Fitting of the $\chi_m T$ data for this compound yielded exchange interaction values of $J_{\text{Gd-Cu}} = +0.60(2) \text{ cm}^{-1}$, $J_{\text{Cu-Cu}} = -61.0(5) \text{ cm}^{-1}$, and $zJ' = -0.035(4) \text{ cm}^{-1}$. The small values for Cu-Gd exchange interaction and especially for the intermolecular exchange zJ' demonstrate that the dominating interaction is of antiferromagnetic nature between copper ions within one crown. Therefore, the overall magnetic properties of this polymeric chain could be explained with the exchange interaction within one building unit [105].

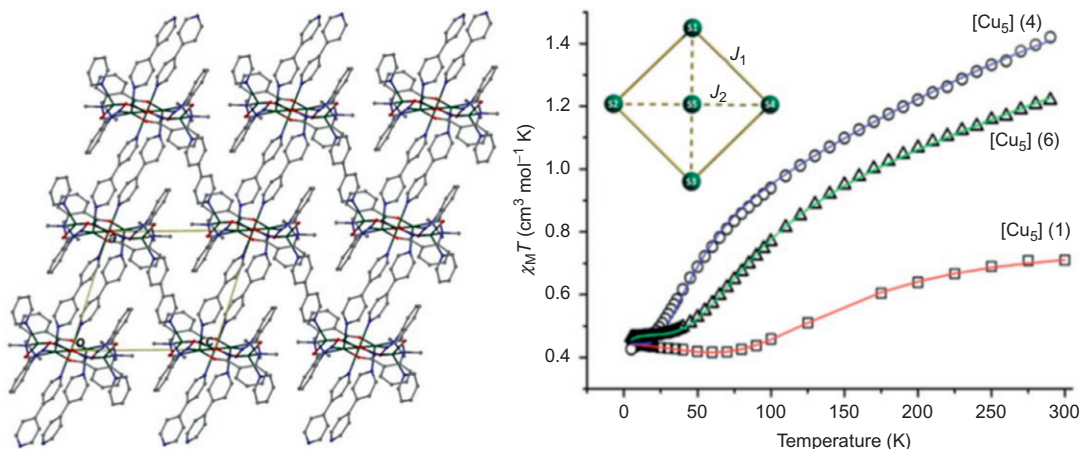


Fig. 2.44

Left: Extract of the crystal structure of $\{[\text{Cu}_5(\text{L}_1)_4(4,4'\text{-bipy})_3](\text{ClO}_4)_2 \cdot \text{H}_2\text{O}\}_n$ ($\text{L}_1 = 2\text{-(dimethylamino)phenylhydroxamic acid}$; bipy = bipyridine) showing the 2D network. *Right:* $\chi_m T$ vs. T plot for the $\text{Cu}_5\text{-MC}$ framework connected via bipy ligands and the star-shaped 12-MC-4 coupling scheme. From C. McDonald, T. Whyte, S.M. Taylor, S. Sanz, E.K. Brechin, D. Gaynor, L.F. Jones, *CrystEngComm* 15 (2013) 6672–6681.

Increasing the dimensionality, 2D networks have been obtained with $\text{Cu}_5\text{-12-MC-4}$ molecular units [94,111,115]. The extended architecture, shown in Fig. 2.44, left, was achieved via an incorporation of three additional ditopic 4,4'-bipyridine linkers, using 2-(dimethylamino) phenylhydroxamic acid as crown building ligand. Two of the bridging molecules coordinate in axial position to Cu^{II} ions, while the third accomplishes the interconnection between 1D chains coordinating apical to a Cu^{II} ion from the MC periphery. The 2D layers are stacked on top of each other via H-bonding to ClO_4^- counter anions. From the $\chi_m T$ measurement (Fig. 2.44 right), it is clearly seen that strong intramolecular antiferromagnetic interactions and a spin ground state of $S = 1/2$ is present in the structure. Fitting of the data with two exchange parameters according to the coupling scheme in Fig. 2.44, right resulted in $J_1 = -48.81 \text{ cm}^{-1}$ and $J_2 = -85.68 \text{ cm}^{-1}$. The magnetic behavior of the extended structure again is reasonably explained considering only the single MCs properties.

Even though there are not too many examples yet, the 12-MC-4 building block has successfully been used to construct a three-dimensional network described by the formula $\{[\text{K}(\text{H}_2\text{O})_2][\text{Cu}_5(\text{mmh})_4]\}_n$. The MC unit, shown in Fig. 2.45, left, consists of five Cu^{II} ions coordinated by four malonomonohydroxamic acid (mmh) molecules. As mentioned in the previous section, this ligand provides the ability of additional metal coordination using the attached carboxylate group. The interconnecting potassium ions are nine-coordinated by four mmh ligands and additional water molecules. The potassium ion channel contains dimers sharing one face of their polyhedron, which are connected to the next dimer via a shared edge (see Fig. 2.45 middle). Regarding the $\chi_m T$ vs. T plot in Fig. 2.45, right, the best-fit parameters

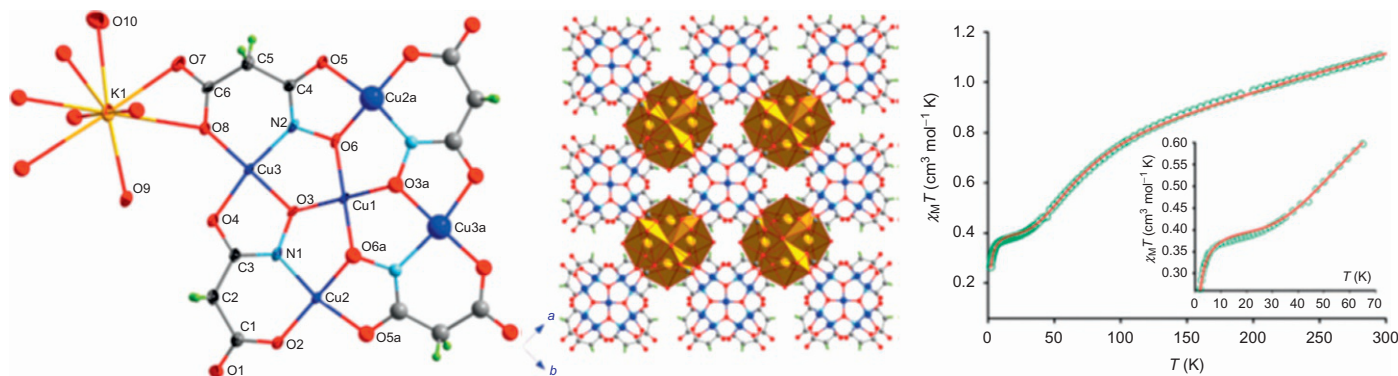


Fig. 2.45

Left: Molecular structure of a Cu_5 -12-MC-4 with mmh as main ligand coordinating an additional potassium cation. *Middle:* Crystal structure of the potassium bridged Cu_5 MC three-dimensional network. *Right:* Fitted $\chi_m T$ data for the 3D MC framework. From A.B. Lago, J. Pasán, L. Cañadillas-Delgado, O. Fabelo, F.J.M. Casado, M. Julve, F. Lloret, C. Ruiz-Pérez, *New J. Chem.* 35 (2011) 1817–1822.

were calculated as $J_1 = -124(1) \text{ cm}^{-1}$, $J_2 = -266(2) \text{ cm}^{-1}$, $zJ' = -3.30(8) \text{ cm}^{-1}$, $g_{\text{Cu}} = 2.107(4)$, corresponding to the previous introduced coupling scheme for 12-MC-4 structures and an intermolecular mean field parameter zJ' to take into account the intermolecular interaction. In comparison with the values of aforementioned Cu^{II} 12-MC-4 networks, they are of similar magnitude although this compound has overcome the barrier to the third dimension.

The magnetic behavior of several distinct extended networks with MCs as building units has been compared with respect to their architecture. In summary, the observed magnetic data for multidimensional compounds are governed by the molecular building unit, the single metallacrown motif. Independent from the dimensionality or the present linking method, the frameworks $\chi_m T$ data are reasonably explained with exchange interactions within one building unit. This observation holds true for a plain stacking of Cu_5 MCs, one-, two-, and three-dimensional networks of the 12-MC-4 motif and even for chain structures of the 15-MC-5 class.

2.4 Conclusion and Perspectives

Summing up, metallacrown complexes (MCs) represent a family of complexes with great potential for future applications. With the appropriate choice of ligand and by selecting the suitable—for every case—metal ion, one can design complexes with a specific structural scaffold. What makes MCs important is that this structural motif is the outcome of careful design, which allows us to tune the properties of the resulting molecule, giving us at the same time a high degree of control, something that is very important and not easy to achieve in inorganic synthesis.

What is apparent and clear already is that the nature of the metal ion used as well as the choice of the organic chelate (ligand) play an important role in the final properties of the molecular complexes. Molecular systems that combine more than one property are of great importance and rather paramount for the next steps of this area of research. These materials are called “Multifunctional” molecular materials and are somehow forming the next scientific steps of research within the field of molecular systems. The great benefit from these materials is the fact that properties such as magnetism and luminescence can be combined in one single molecule; thus, these properties can cofunction and coexist always depending on the external stimuli used. In our case, MCs could definitely function as multifunctional molecular compounds, when carefully designed and that sets the stepping stone to be overcome for the next years to come. Still what makes metallacrown complexes special is the fact that the unique scaffold that they possess is of utmost importance for luminescent properties, as it was already mentioned in the main text. Therefore, if 1 day it will be possible to synthesize such complexes that also contain interesting magnetic properties, it will be important not to forget that the origin of all these, is just a single molecule.

Regarding not only the molecular level, it has been clearly demonstrated that MCs are suitable building blocks to construct multidimensional coordination polymers. The presented possibilities to connect MCs range from direct dimerization of these molecules over bigger compartments and triple-decker structures up to molecular chains, layers, and 3D frameworks. This broad diversity can be achieved via different kinds of MC linkage. Versatile tools for the interconnection of these metallamacrocycles are bridging coligands or counterions. Additional linking ligands have to be chosen with regard to the metal cluster-building block. Hence, a rational design of multidimensional architecture is possible with the right MC-coligand combination. Due to the charged crown structure motif, counterions, from the very simplest alkali ion to transition metal ion complexes, also represent a good compound class of MC connectors. An elaborate manner of MC linkage is the main ligand optimization. Therefore, the crown building organic molecule needs an extended backbone able to build coordinative bonds pointing to the crowns exterior. In addition, there are successful approaches connecting MCs using ligands, which are prepared for click chemistry.

Magnetic studies of coordination polymers with different dimensionality have been evaluated. The $\chi_m T$ vs. T data revealed that the overall magnetic properties of the compounds are mostly governed by the single MC building blocks. Therefore, by understanding and predicting the molecular MC properties, extended networks with rational designed magnetic behavior could be reached.

Some of the introduced frameworks provide huge voids and channels suitable for gas absorption or guest ion uptake, which is why MC networks are in focus for a very exciting development of multifunctional devices. The fine-tuning of their molecular properties by accommodation of various guest ions in the cavities between MCs could be the next milestone in the research field of hybrid materials.

References

- [1] M.S. Lah, V.L. Pecoraro, *J. Am. Chem. Soc.* 111 (1989) 7258–7259.
- [2] P. Happ, C. Plenk, E. Rentschler, *Coord. Chem. Rev.* 289–290 (2015) 238–260.
- [3] J.J. Bodwin, A.D. Cutland, R.G. Malkani, V.L. Pecoraro, *Coord. Chem. Rev.* 216–217 (2001) 489–512.
- [4] G. Mezei, C.M. Zaleski, V.L. Pecoraro, *Chem. Rev.* 107 (2007) 4933–5003.
- [5] C.Y. Chow, E.R. Trivedi, V. Pecoraro, C.M. Zaleski, *Comments Inorg. Chem.* 35 (2015) 214–253.
- [6] M. Ostrowska, I.O. Fritsky, E. Gumienna-Kontecka, A.V. Pavlishchuk, *Coord. Chem. Rev.* 327 (2016) 304–332.
- [7] M. Tegoni, M. Remelli, *Coord. Chem. Rev.* 256 (2012) 289–315.
- [8] V.L. Pecoraro, *Inorg. Chim. Acta* 155 (1989) 171–173.
- [9] H. Yang, F. Cao, D. Li, S. Zeng, Y. Song, J. Dou, *Chem. Eur. J.* 21 (2015) 14478–14485.
- [10] A.J. Stemmler, J.W. Kampf, V.L. Pecoraro, *Inorg. Chem.* 34 (1995) 2271–2272.
- [11] D.P. Kessissoglou, J. Kampf, V.L. Pecoraro, *Polyhedron* 13 (1994) 1379–1391.
- [12] C. Dendrinou-Samara, A.N. Papadopoulos, D.A. Malamataris, A. Tarushi, C. P. Raptopoulou, A. Terzis, E. Samaras, D.P. Kessissoglou, *J. Inorg. Biochem.* 99 (2005) 864–875.
- [13] B. Emerich, M. Smith, M. Zeller, C.M. Zaleski, *J. Chem. Crystallogr.* 40 (2010) 769–777.

- [14] C.M. Zaleski, J.C. Lutter, M. Zeller, *J. Chem. Crystallogr.* 45 (2015) 142–150.
- [15] T.C. Stamatatos, S. Dionyssopoulou, G. Efthymiou, P. Kyritsis, C. P. Raptopoulou, A. Terzis, R. Vicente, A. Escuer, S.P. Perlepes, *Inorg. Chem.* 44 (2005) 3374–3376.
- [16] G. Psomas, C. Dendrinou-Samara, M. Alexiou, A. Tsohos, C.P. Raptopoulou, A. Terzis, D. P. Kessissoglou, *Inorg. Chem.* 37 (1998) 6556–6557.
- [17] M. Alexiou, I. Tsivikas, C. Dendrinou-Samara, A.A. Pantazaki, P. Trikalitis, N. Lalioti, D.A. Kyriakidis, D. P. Kessissoglou, *J. Inorg. Biochem.* 93 (2003) 256–264.
- [18] A. Audhya, M. Maity, K. Bhattacharya, R. Clérac, M. Chaudhury, *Inorg. Chem.* 49 (2010) 9026–9035.
- [19] P. Happ, A. Sapozhnik, J. Klanke, P. Czaja, A. Chernenkaya, K. Medjanik, S. Schuppler, P. Nagel, M. Merz, E. Rentschler, H.J. Elmers, *Phys. Rev. B* 93 (2016) 1744041–1744047.
- [20] S. Rodríguez-Hermida, A.B. Lago, A. Pino-Cuevas, A. Hagenbach, L. Cañadillas-Delgado, R. Carballo, U. Abram, E.M. Vázquez-López, *Chem. Eur. J.* 22 (2015) 1847–1853.
- [21] B.R. Gibney, D.P. Kessissoglou, J.W. Kampf, V.L. Pecoraro, *Inorg. Chem.* 33 (1994) 4840–4849.
- [22] P. Happ, E. Rentschler, *Dalton Trans.* 43 (2014) 15308–15312.
- [23] T.T. Boron, J.C. Lutter, C.I. Daly, C.Y. Chow, A.H. Davis, A. Nimthong-Roldán, M. Zeller, J.W. Kampf, C. M. Zaleski, V.L. Pecoraro, *Inorg. Chem.* 55 (2016) 10597–10607.
- [24] F. Cao, R.-M. Wei, J. Li, L. Yang, Y. Han, Y. Song, J.-M. Dou, *Inorg. Chem.* 55 (2016) 5914–5923.
- [25] J. Jankolovits, C.M. Andolina, J.W. Kampf, K.N. Raymond, V.L. Pecoraro, *Angew. Chem. Int. Ed.* 50 (2011) 9660–9664.
- [26] Q.-W. Li, J.-L. Liu, J.-H. Jia, Y.-C. Chen, J. Liu, L.-F. Wang, M.-L. Tong, *Chem. Commun.* 51 (2015) 10291–10294.
- [27] M.A. Katkova, G.S. Zabrodina, M.S. Muravyeva, A.S. Shavyrin, E.V. Baranov, A.A. Khrapichev, S. Y. Ketkov, *Eur. J. Inorg. Chem.* 2015 (2015) 5202–5208.
- [28] Y. Wang, W.-S. Wu, M.-L. Huang, *Chin. Chem. Lett.* 27 (2016) 423–427.
- [29] Y. Meng, H. Yang, D. Li, S. Zeng, G. Chen, S. Li, J. Dou, *RSC Adv.* 6 (2016) 47196–47202.
- [30] M.S. Muravyeva, G.S. Zabrodina, M.A. Samsonov, E.A. Kluev, A.A. Khrapichev, M.A. Katkova, I. V. Mukhina, *Polyhedron* 114 (2016) 165–171.
- [31] M.R. Azar, T.T. Boron, J.C. Lutter, C.I. Daly, K.A. Zegalia, R. Nimthong, G.M. Ferrence, M. Zeller, J. W. Kampf, V.L. Pecoraro, C.M. Zaleski, *Inorg. Chem.* 53 (2014) 1729–1742.
- [32] C.J. Pedersen, *J. Am. Chem. Soc.* 89 (1967) 7017–7036.
- [33] J.I. van der Vlugt, S. Demeshko, S. Dechert, F. Meyer, *Inorg. Chem.* 47 (2008) 1576–1585.
- [34] K.V. Kremlev, M.A. Samsonov, G.S. Zabrodina, A.V. Arapova, P.A. Yunin, D.A. Tatarsky, P.E. Plyusnin, M. A. Katkova, S.Y. Ketkov, *Polyhedron* 114 (2016) 96–100.
- [35] J.J. Baldoví, J.J. Borrás-Almenar, J.M. Clemente-Juan, E. Coronado, A. Gaita-Ariño, *Dalton Trans.* 41 (2012) 13705–13710.
- [36] M.H.V. Werts, *Sci. Prog.* 88 (2005) 101–131.
- [37] M.L. Cable, J.P. Kirby, H.B. Gray, A. Ponce, *Acc. Chem. Res.* 46 (2013) 2576–2584.
- [38] A.K. Hagan, T. Zuchner, *Anal. Bioanal. Chem.* 400 (2011) 2847–2864.
- [39] S.V. Eliseeva, J.-C.G. Bünzli, *New J. Chem.* 35 (2011) 1165–1176.
- [40] S.J. Butler, D. Parker, *Chem. Soc. Rev.* 42 (2013) 1652–1666.
- [41] J.-C.G. Bünzli, *Chem. Rev.* 110 (2010) 2729–2755.
- [42] P. Hänninen, H. Härmä, *Lanthanide Luminescent—Photophysical, Analytical and Biological Aspects*, Springer Series on Fluorescence, Springer-Verlag Berlin, Heidelberg, 2011.
- [43] H. Uh, S. Petoud, *C.R. Chim.* 13 (2010) 668–680.
- [44] C.Y. Chow, S.V. Eliseeva, E.R. Trivedi, T.N. Nguyen, J.W. Kampf, S. Petoud, V.L. Pecoraro, *J. Am. Chem. Soc.* 138 (2016) 5100–5109.
- [45] A.J. Amoroso, S.J.A. Pope, *Chem. Soc. Rev.* 44 (2015) 4723–4742.
- [46] E.R. Trivedi, S.V. Eliseeva, J. Jankolovits, M.M. Olmstead, S. Petoud, V.L. Pecoraro, *J. Am. Chem. Soc.* 136 (2014) 1526–1534.
- [47] H.V.R. Dias, H.V.K. Diyalanage, M.G. Eldabaja, O. Elbjeirami, M.A. Rawashdeh-Omary, M. A. Omary, *J. Am. Chem. Soc.* 127 (2005) 7489–7501.

- [48] M. Enomoto, A. Kishimura, T. Aida, *J. Am. Chem. Soc.* 123 (2001) 5608–5609.
- [49] A. Kishimura, T. Yamashita, K. Yamaguchi, T. Aida, *Nat. Mater.* 4 (2005) 546–549.
- [50] H.V.R. Dias, H.V.K. Diyabalanage, M.A. Rawashdeh-Omary, M.A. Franzman, M.A. Omary, *J. Am. Chem. Soc.* 125 (2003) 12072–12073.
- [51] G. Yang, R.G. Raptis, *Inorg. Chem.* 42 (2003) 261–263.
- [52] M.A. Omary, M.A. Rawashdeh-Omary, M.W.A. Gonser, O. Elbjeirami, T. Grimes, T.R. Cundari, H.V. K. Diyabalanage, C.S.P. Gamage, H.V.R. Dias, *Inorg. Chem.* 44 (2005) 8200–8210.
- [53] F. Gong, Q. Wang, J. Chen, Z. Yang, M. Liu, S. Li, G. Yang, L. Bai, J. Liu, Y. Dong, *Inorg. Chem.* 49 (2010) 1658–1666.
- [54] M. Veronelli, N. Kindermann, S. Dechert, S. Meyer, F. Meyer, *Inorg. Chem.* 53 (2014) 2333–2341.
- [55] R. Sessoli, H.L. Tsai, A.R. Schake, S. Wang, J.B. Vincent, K. Folting, D. Gatteschi, G. Christou, D. N. Hendrickson, *J. Am. Chem. Soc.* 115 (1993) 1804–1816.
- [56] R. Sessoli, D. Gatteschi, A. Caneschi, M.A. Novak, *Nature* 365 (1993) 141–143.
- [57] D. Gatteschi, R. Sessoli, J. Villain, *Molecular Nanomagnets*, Oxford Scholarship, 2006.
- [58] M.N. Leuenberger, D. Loss, *Nature* 410 (2001) 789–793.
- [59] B. Zhou, R. Tao, S.-Q. Shen, J.-Q. Liang, *Phys. Rev. A* 66 (2002). 010301.
- [60] M. Affronte, F. Troiani, A. Ghirri, A. Candini, M. Evangelisti, V. Corradini, S. Carretta, P. Santini, G. Amoretti, F. Tuna, G. Timco, R.E.P. Winpenny, *J. Phys. Appl. Phys.* 40 (2007) 2999.
- [61] R. Vincent, S. Klyatskaya, M. Ruben, W. Wernsdorfer, F. Balestro, *Nature* 488 (2012) 357–360.
- [62] L. Bogani, W. Wernsdorfer, *Nat. Mater.* 7 (2008) 179–186.
- [63] K. Katoh, H. Isshiki, T. Komeda, M. Yamashita, *Chem. Asian J.* 7 (2012) 1154–1169.
- [64] K. Katoh, H. Isshiki, T. Komeda, M. Yamashita, *Coord. Chem. Rev.* 255 (2011) 2124–2148.
- [65] F. Neese, D.A. Pantazis, *Faraday Discuss.* 148 (2010) 229–238.
- [66] C.J. Milios, A. Vinslava, W. Wernsdorfer, S. Moggach, S. Parsons, S.P. Perlepes, G. Christou, E. K. Brechin, *J. Am. Chem. Soc.* 129 (2007) 2754–2755.
- [67] J.D. Rinehart, J.R. Long, *Chem. Sci.* 2 (2011) 2078–2085.
- [68] B.G. Wybourne, *Spectroscopic Properties of Rare Earths*, Interscience Publishers, New York, London, Sydney, 1965.
- [69] A. Abragam, B. Bleaney, *Electron Paramagnetic Resonance of Transition Ions*, Oxford University Press, Oxford, NY, 2012.
- [70] J. Sievers, Z. Für, *Phys. B Condens. Matter* 45 (1982) 289–296.
- [71] B.R. Gibney, A.J. Stemmler, S. Pilotek, J.W. Kampf, V.L. Pecoraro, *Inorg. Chem.* 32 (1993) 6008–6015.
- [72] M.S. Lah, M.L. Kirk, W. Hatfield, V.L. Pecoraro, *J. Chem. Soc. Chem. Commun.* 21 (1989) 1606–1608.
- [73] A. Audhya, K. Bhattacharya, M. Maity, M. Chaudhury, *Inorg. Chem.* 49 (2010) 5009–5015.
- [74] L.K. Das, A. Biswas, J.S. Kinyon, N.S. Dalal, H. Zhou, A. Ghosh, *Inorg. Chem.* 52 (2013) 11744–11757.
- [75] G. Vlahopoulou, A. Escuer, M. Font-Bardia, T. Calvet, *Inorg. Chem. Commun.* 16 (2012) 78–80.
- [76] M. Alexiou, E. Katsoulakou, C. Dendrinou-Samara, C.P. Raptopoulou, V. Psycharis, E. Manessi-Zoupa, S. P. Perlepes, D.P. Kessissoglou, *Eur. J. Inorg. Chem.* 2005 (2005) 1964–1978.
- [77] C.P. Raptopoulou, V. Psycharis, *Inorg. Chem. Commun.* 11 (2008) 1194–1197.
- [78] G.-X. Liu, W. Guo, S. Nishihara, X.-M. Ren, *Inorg. Chim. Acta* 368 (2011) 165–169.
- [79] A. Chakraborty, K.L. Gurunatha, A. Muthulakshmi, S. Dutta, S.K. Pati, T.K. Maji, *Dalton Trans.* 41 (2012) 5879–5888.
- [80] A. Escuer, G. Vlahopoulou, S.P. Perlepes, F.A. Mautner, *Inorg. Chem.* 50 (2011) 2468–2478.
- [81] S. Speed, M. Font-Bardía, M.S.E. Fallah, R. Vicente, *Dalton Trans.* 43 (2014) 16919–16927.
- [82] T. Afrati, C. Dendrinou-Samara, C. Raptopoulou, A. Terzis, V. Tangoulis, A. Tsipis, D. P. Kessissoglou, *Inorg. Chem.* 47 (2008) 7545–7555.
- [83] L.K. Das, M.G.B. Drew, C. Diaz, A. Ghosh, *Dalton Trans.* 43 (2014) 7589–7598.
- [84] S. Karmakar, O. Das, S. Ghosh, E. Zangrando, M. Johann, E. Rentschler, T. Weyhermüller, S. Khanra, T. K. Paine, *Dalton Trans.* 39 (2010) 10920–10927.
- [85] L. Croitor, E.B. Coropceanu, O. Petuhov, K.W. Krämer, S.G. Baca, S.-X. Liu, S. Decurtins, M. S. Fonari, *Dalton Trans.* 44 (2015) 7896–7902.

- [86] M. Hołyńska, R. Clérac, T. Langer, R. Pöttgen, S. Dehnen, *Polyhedron* 52 (2013) 1425–1430.
- [87] C.M. Zaleski, S. Tricard, E.C. Depperman, W. Wernsdorfer, T. Mallah, M.L. Kirk, V.L. Pecoraro, *Inorg. Chem.* 50 (2011) 11348–11352.
- [88] J. Jankolovits, J.W. Kampf, V.L. Pecoraro, *Inorg. Chem.* 53 (2014) 7534–7546.
- [89] B.R. Gibney, H. Wang, J.W. Kampf, V.L. Pecoraro, *Inorg. Chem.* 35 (1996) 6184–6193.
- [90] C. Dendrinou-Samara, G. Psomas, L. Iordanidis, V. Tangoulis, D.P. Kessissoglou, *Chem. Eur. J.* 7 (2001) 5041–5051.
- [91] M.S. Lah, B.R. Gibney, D.L. Tierney, J.E. Penner-Hahn, V.L. Pecoraro, *J. Am. Chem. Soc.* 115 (1993) 5857–5858.
- [92] A.B. Lago, J. Pasán, L. Cañadillas-Delgado, O. Fabelo, F.J.M. Casado, M. Julve, F. Lloret, C. Ruiz-Pérez, *New J. Chem.* 35 (2011) 1817–1822.
- [93] A.V. Pavlishchuk, S.V. Kolotilov, M. Zeller, O.V. Shvets, I.O. Fritsky, S.E. Lofland, A.W. Addison, A. D. Hunter, *Eur. J. Inorg. Chem.* 2011 (2011) 4826–4836.
- [94] C. McDonald, T. Whyte, S.M. Taylor, S. Sanz, E.K. Brechin, D. Gaynor, L.F. Jones, *CrystEngComm* 15 (2013) 6672–6681.
- [95] Y. Song, J.-C. Liu, Y.-J. Liu, D.-R. Zhu, J.-Z. Zhuang, X.-Z. You, *Inorg. Chim. Acta* 305 (2000) 135–142.
- [96] G. Psomas, A.J. Stemmler, C. Dendrinou-Samara, J.J. Bodwin, M. Schneider, M. Alexiou, J.W. Kampf, D. P. Kessissoglou, V.L. Pecoraro, *Inorg. Chem.* 40 (2001) 1562–1570.
- [97] C. McDonald, S. Sanz, E.K. Brechin, M.K. Singh, G. Rajaraman, D. Gaynor, L.F. Jones, *RSC Adv.* 4 (2014) 38182–38191.
- [98] D. Mandal, V. Bertolasi, G. Aromí, D. Ray, *Dalton Trans.* 20 (2007) 1989–1992.
- [99] I.A. Golenya, E. Gumienna-Kontecka, A.N. Boyko, M. Haukka, I.O. Fritsky, *Inorg. Chem.* 51 (2012) 6221–6227.
- [100] J. Jankolovits, J.W. Kampf, V.L. Pecoraro, *Inorg. Chem.* 52 (2013) 5063–5076.
- [101] B. Gole, R. Chakrabarty, S. Mukherjee, Y. Song, P.S. Mukherjee, *Dalton Trans.* 39 (2010) 9766–9778.
- [102] E. Colacio, C. López-Magaña, V. McKee, A. Romerosa, *J. Chem. Soc. Dalton Trans.* 17 (1999) 2923–2926.
- [103] S. Giri, D. Maity, J.F. Godsell, S. Roy, M.G.B. Drew, A. Ghosh, G. Mukhopadhyay, S.K. Saha, *Inorg. Chim. Acta* 377 (2011) 99–104.
- [104] A.J. Stemmler, J.W. Kampf, M.L. Kirk, B.H. Atasi, V.L. Pecoraro, *Inorg. Chem.* 38 (1999) 2807–2817.
- [105] A.V. Pavlishchuk, S.V. Kolotilov, M. Zeller, L.K. Thompson, A.W. Addison, *Inorg. Chem.* 53 (2014) 1320–1330.
- [106] C.M. Zaleski, E.C. Depperman, J.W. Kampf, M.L. Kirk, V.L. Pecoraro, *Inorg. Chem.* 45 (2006) 10022–10024.
- [107] T.T. Boron, J.W. Kampf, V.L. Pecoraro, *Inorg. Chem.* 49 (2010) 9104–9106.
- [108] F. Cao, S. Wang, D. Li, S. Zeng, M. Niu, Y. Song, J. Dou, *Inorg. Chem.* 52 (2013) 10747–10755.
- [109] S. Wang, L. Kong, H. Yang, Z. He, Z. Jiang, D. Li, S. Zeng, M. Niu, Y. Song, J. Dou, *Inorg. Chem.* 50 (2011) 2705–2707.
- [110] C.M. Zaleski, J.W. Kampf, T. Mallah, M.L. Kirk, V.L. Pecoraro, *Inorg. Chem.* 46 (2007) 1954–1956.
- [111] C. Atzeri, L. Marchiò, C.Y. Chow, J.W. Kampf, V.L. Pecoraro, M. Tegoni, *Chem. Eur. J.* 22 (2016) 6482–6486.
- [112] D. Moon, J. Song, M.S. Lah, *CrystEngComm* 11 (2009) 770–776.
- [113] G. Mezei, J.W. Kampf, S. Pan, K.R. Poepelmeier, B. Watkins, V.L. Pecoraro, *Chem. Commun.* 11 (2007) 1148–1150.
- [114] E. Gumienna-Kontecka, I.A. Golenya, N.M. Dudarenko, A. Dobosz, M. Haukka, I.O. Fritsky, J. Swiatek-Kozłowska, *New J. Chem.* 31 (2007) 1798–1805.
- [115] J.J. Bodwin, V.L. Pecoraro, *Inorg. Chem.* 39 (2000) 3434–3435.
- [116] B. Ding, L. Yi, P. Cheng, D.-Z. Liao, S.-P. Yan, *Inorg. Chem.* 45 (2006) 5799–5803.
- [117] C. Plenk, J. Krause, M. Beck, E. Rentschler, *Chem. Commun.* 51 (2015) 6524–6527.
- [118] A.V. Pavlishchuk, S.V. Kolotilov, M. Zeller, L.K. Thompson, I.O. Fritsky, A.W. Addison, A.D. Hunter, *Eur. J. Inorg. Chem.* 2010 (2010) 4851–4858.

- [119] A.V. Pavlishchuk, Y.A. Satska, S.V. Kolotilov, I.O. Fritsky, *Curr. Inorg. Chem.* (2015) 5–25.
[120] C.-S. Lim, J. Jankolovits, J.W. Kampf, V.L. Pecoraro, *Chem. Asian. J.* 5 (2010) 46–49.

Further Reading

- [1] Z. Chen, M. Jia, Z. Zhang, F. Liang, *Cryst. Growth Des.* 10 (2010) 4806–4814.
[2] R.A. Layfield, *Organometallics* 33 (2014) 1084–1099.

Multifunctional Properties of γ -Fe₂O₃ Nanoparticles Encapsulated Into Liquid-Crystalline Poly(propylene imine) Dendrimer

Natalia Domracheva

Zavoisky Physical-Technical Institute, Federal Research Center “Kazan Scientific Center of RAS”, Kazan, Russia

3.1 Introduction

Multifunctional nanoparticles (NPs) are among the most interesting nanomaterials with promising applications. Inorganic core nanoparticles coated with organic monolayers are a fundamental building block in nanotechnology [1]. The nanoscopic size of the inorganic core provides optical, magnetic, conductive, and semiconductor properties unique to quantum-confined materials. Uses for such systems include fluorescent biomacromolecule tags for activity assays [2], magnetic resonance imaging (MRI) contrast agents [3], and components for nanoscale electronic devices [4] or data storage elements [5].

As an ideal organic macromolecule, dendrimers have attracted considerable attention because of their remarkable properties, including their three 3D architecture, monodispersity, highly branched macromolecular characteristics, and tunable terminal functionalities [6,7].

Dendrimers have been successfully used in the field of biomedicine [8], in particular for use as a drug and gene delivery [9], cancer diagnosis [10], and sensors [11]. The incorporation of inorganic nanoparticles into dendrimers has received much attention due to the combination of the properties of inorganic nanoparticles and dendrimers [12–15].

Magnetic nanometer-sized inorganic particles, as known, are key components in modern technology, with applications ranging from high-density information storage [16] to MRI contrast agents [17]. For this reason, iron oxide nanoparticles are the subject of intense scientific and technological research, resulting in their application as high-density magnetic storage [18,19], ferrofluids [20,21], and for biomedical purposes [22]. Magnetic NPs display

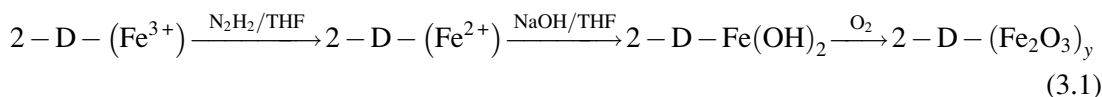
unique size-dependent properties [23], which include superparamagnetism [24]; a state in which the net magnetic moment of a single-domain particle is based on ambient thermal activation [25]. Out of six known crystalline phases of iron oxides, maghemite (γ -Fe₂O₃) NPs have been extensively studied. Maghemite shows ferrimagnetic ordering and its crystalline structure comprises two different magnetic high-spin Fe³⁺ ions occupying two kinds of lattice sites: tetra- and octahedral. Fabrication of γ -Fe₂O₃ nanoscale material with magnetic single-domain particles ranging from 1 to 10 nm in diameter is of particular importance [26]. The size of magnetic NPs can be controlled by means of a dendrimer template, by variations of the generations of dendrimers [27,28]. Dendrimers successfully stabilize nanoparticles, playing the role of nanoreactors, and the NPs can be formed inside or outside of the dendrimer network [29,30]. At present, only the fabrication of ferrimagnetic γ -Fe₂O₃ nanoparticles outside the dendrimer network has been studied [31,32]. Cationic superparamagnetic iron oxide NPs were formed by using anionic polyamidoamine dendrimers; however, in this case, the size of fabricated NPs was large and the diameter was in the range from 20 to 30 nm [31,32].

For nanoscale devices, not only NP size control, but NP self-organization is also important. Liquid crystals are a beautiful example of self-organizing nano-objects. Therefore, it is very tempting to use liquid-crystalline (LC) properties to cause NP self-organization. Substituted poly(propylene imine) (PPI) dendrimers exhibit mesomorphic properties and display the formation of columnar mesophases [33]. The aim of our work was to use liquid-crystalline PPI dendrimers attached to iron oxide NPs as promoters to organize the positional order of NPs on the nanometer scale and to generate mesomorphism in such a combined system. Only a few examples of the combination of NPs (generally gold NPs) with liquid-crystalline dendrimers have been reported in the literature to date [34–36]. The recent discovery that gold NPs can show ferromagnetism at room temperature [37] could open new perspectives in the domain of magnetic information storage, provided one becomes able to rationally control the organization of these tiny magnetic bits. The first example of dendrimer-functionalized gold NPs able to self-assemble was reported by Donnio et al. [34]. Using such an approach, they could control the positional order of NPs. These materials were formed during the self-assembly of 2.1-nm gold NPs, in which dodecanethiol ligands in the shell were replaced with the second-generation dendrons. Although the dendrons themselves were not mesogenous, the obtained materials, both on the surface and in the volume, formed 2D or 3D thermotropic cubic phases. These materials are ferromagnetic within the temperature range of 1.8–400 K, although they do not contain magnetic components. It is clear that material ordering provides spin ordering and collective magnetic properties.

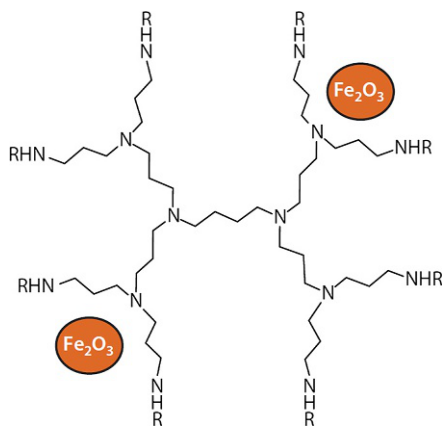
Along this line of thought, our strategy has been based on integrating a whole number of properties (magnetic/semiconductor NPs, dendrimeric, and mesogenic) in a single material. In this chapter, we report about the magnetic, optical, semiconductor, and photoinduced superparamagnetic properties of ultra-thin γ -Fe₂O₃ NPs incorporated into LC, second-generation PPI dendrimer and about the possibility to consider NPs as a quantum objects.

3.2 Presentation of the Iron-Dendrimeric Nanocomposite and Identification of Its Liquid-Crystalline Properties

The iron-dendrimer nanocomposite was obtained from the second-generation PPI dendrimer-iron(III) complex that was characterized in Ref. [38]. The structure of the liquid crystalline, second-generation PPI dendrimer is presented in Scheme 3.1. The preparation of the sample is described as follows. The iron-dendrimer nanocomposite $[2\text{-D-(Fe}_2\text{O}_3)_y]$ was synthesized in three stages. Eq. (3.1) gives the synthetic scheme for the nanocomposite based on the dendrimer complex derived from second-generation 3,4-bis-(decyloxybenzoyl) PPI and iron (III) chloride $[2\text{-D-(FeCl}_3)_{4,7}]$: [38–40].



The general procedure is set forth as follows: in a vacuum line, a solution of the second-generation dendrimer-iron complex in THF was quickly degassed and put under argon (Ar). Afterwards, degassed 1 M N_2H_4 in THF was added and the mixture was stirred for 1.5 h. The color of the solution changed from brown to yellowish-green, which was indicative of the reduction of Fe^{3+} to Fe^{2+} . Addition of NaOH (in THF) to the solution resulted in a color change from yellowish-green to olive-green, indicating the formation of Fe(OH)_2 . The mixture was stirred under Ar for 2 h and O_2 bubbling for 2.5 h. The color instantly changed to reddish brown. The mixture was filtered through a glass filter with a porosity of four. The solid residue on the filter was washed with cold ethanol until neutral pH and was redissolved in THF and filtered through a 450-mesh polytetrafluoroethylene (PTFE) filter. The clear solution was evaporated to dryness. The solid residue was dissolved in benzene, filtered through a 200-nm mesh PTFE



Scheme 3.1

Liquid crystalline, second-generation PPI dendrimer used to prepare the dendrimeric $\gamma\text{-Fe}_2\text{O}_3$ NPs and a possible model for locating the NPs in the dendrimer.

filter, frozen with liquid N_2 , and lyophilized by evaporating benzene from the still cold, solid sample under fine vacuum (2×10^{-2} mbar). The product was a soft, amorphous, light-yellow compound soluble in THF, benzene, chloroform, and dichloromethane. The average yield was 55.9%.

A complete characterization (UV spectroscopy, mass spectroscopy, gel chromatography) of the synthesized iron oxide dendrimeric nanocomposite is given in Refs. [40,41]. Investigations by polarizing optical microscopy, differential scanning calorimetry (DSC), and X-ray scattering established that the iron oxide dendrimeric nanocomposite was mesomorphic and demonstrated a hexagonal columnar (Col_h) packing of the molecules in the mesophase. The nongeometrical texture of the mesomorphic compound is shown in Fig. 3.1, and the temperatures of phase transitions are presented in Table 3.1.

The size of the γ - Fe_2O_3 NPs was estimated by examining the transmission electron microscopy (TEM) and X-ray diffraction data. Since the differences in electron density between the atoms of different parts of the dendrimer (polyamine core, benzyl groups, alkyl shell of the PPI derivatives) are minor, no contrast in the image of pure dendrimer is observed by TEM.

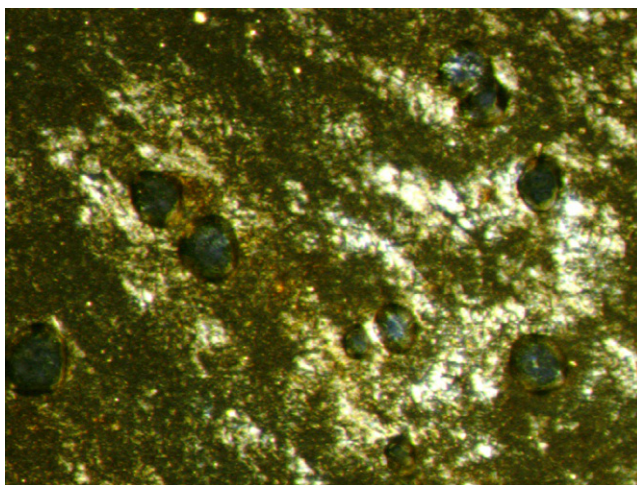


Fig. 3.1
Nongeometrical texture of 2-D- $(Fe_2O_3)_y$ at heating, $T = 90.5^\circ C$.

Table 3.1 Transition temperatures for the dendritic nanocomposite

Compound	T_g [$^\circ C$]	T_m [$^\circ C$]	I [$^\circ C$]	Phase	T_{dec} [$^\circ C$]
2-D- $(Fe_2O_3)_2$	26.0	72.5	96.5	Col_h	144.0

Note: T_g is the temperature of vitrification; T_m is the temperature of the mesophase; I is the temperature of transition mesophase-isotrope; T_{dec} is the temperature of decomposition from thermogravimetric data; Col_h is the columnar hexagonal phase.

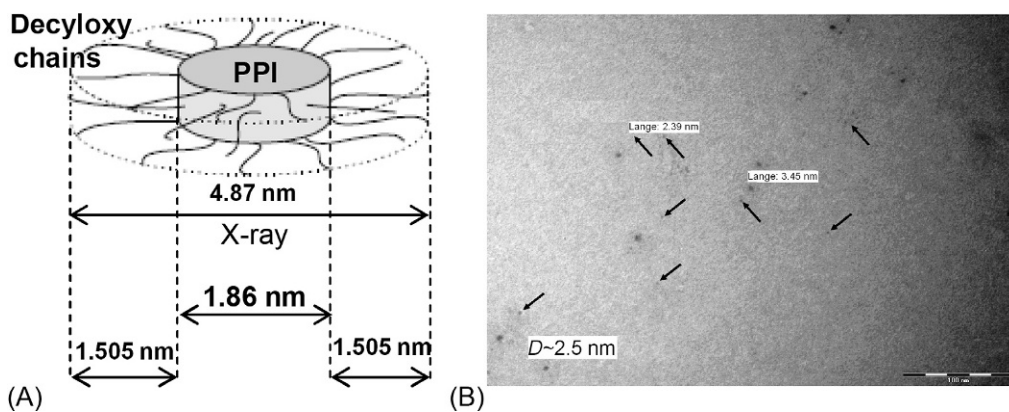


Fig. 3.2

(A) Schematic representation of the second-generation dendrimeric $\gamma\text{-Fe}_2\text{O}_3$ NPs, dimensions of the PPI core, and decyloxy chains segments estimated from X-ray diffractometry. (B) TEM image of the dendrimeric $\gamma\text{-Fe}_2\text{O}_3$ NPs. Scale bar = 100 nm.

After obtaining the nanocomposite, dark spots appeared in the TEM image. Due to the high electron density of magnetic NPs, their location relative to the selected parts of the dendrimer can be determined. The average diameter, \bar{D} , of iron oxide NPs (see Fig. 3.2B) estimated from the TEM image is about 2.5 nm. The hexagonal lattice constant, a_h (intercolumnar distance), of the second-generation dendrimeric $\gamma\text{-Fe}_2\text{O}_3$ composite was calculated from X-ray diffractometry measurements to be about 4.87 nm (see Fig. 3.2A). The diameter of the PPI core, including the benzamide units, was estimated from Refs. [42,43] to be 1.86 nm. Therefore, the value of the length of the decyloxy chain segment surrounding the PPI core of 1.505 nm was obtained by subtracting the diameter of the core (1.86 nm) from the value of a_h (4.87 nm). According to our results [30,38] and those published by other groups [28,29,44], we may conclude that maghemite NPs are electrostatically coupled with reactive (amido and amino) nitrogen periphery atoms and incorporated among the branches of PPI dendrimer. It has also been shown that iron oxide NPs have a narrow size distribution (0.5 nm) [44]. Iron oxide NPs are relatively well separated inside the dendrimer and the suggested model for the location of the NPs is presented in Scheme 3.1.

3.3 Characterization of $\gamma\text{-Fe}_2\text{O}_3$ NPs by Electron Magnetic Resonance

Electron magnetic resonance (EMR) is a very effective method of studying magnetic NPs. The theory of magnetic resonance in superparamagnetic systems was developed in Refs. [45–47]. One of the first contributions for understanding the temperature variation of the EMR spectra of NPs came from the work of de Biasi and Devezas [45]. Then, Raikher and Stepanov (RS) [46] developed a more elaborate theoretical approach to consider superparamagnetic resonances in the limit of large Zeeman interactions as compared to the anisotropy energy.

This approach is based on a rotary diffusion equation of magnetic moment motion in the presence of thermal fluctuations. In this approach, the effective field acting on NPs is the linear addition of the applied field, H , and anisotropy fields. RS results indicated that, in the superparamagnetic regime, the effective anisotropy decreased as the temperature increased, and the rate of decrease was determined by the ratio of Zeeman to thermal energies. This theory allows one to obtain the physical parameters of magnetic NPs: anisotropy, magnetic moment.

Fig. 3.3 shows the EMR spectra of a polycrystalline sample recorded at different temperatures from 290 to 4.2 K. The spectra are composed of a single line and the behavior is typical for that of superparamagnetic materials. One can see that upon cooling the resonance line is monotonically broadened and shifts to the lower magnetic fields. Such behavior is found in various magnetic NP systems [48–53].

As a second step, we additionally studied the effect of NP alignment in the columnar phase under field-freezing (FF) conditions. NP alignment in the mesophase was achieved by slow cooling of the sample from isotropic (375 K) to columnar (350 K) phases at an external magnetic field of $H_{fr} = 7$ kG. The detected alignment, which was due to the freezing field, H_{fr} , was maintained when the sample was cooled to the glassy state upon lowering the temperature. Thus, by rotating a frozen sample through the vertical axis, one can investigate the EMR line

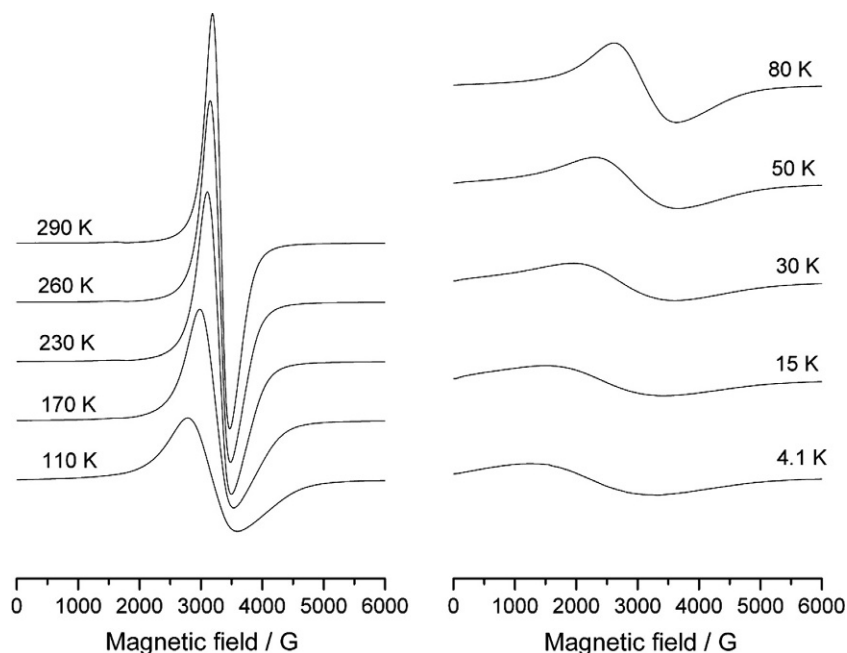


Fig. 3.3

Temperature dependences of EMR spectra for γ - Fe_2O_3 NPs encapsulated into dendrimer. All spectra are recorded at the same conditions.

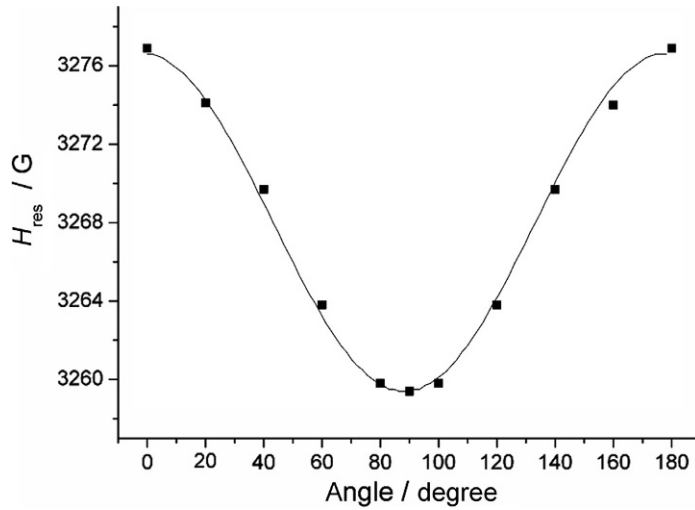


Fig. 3.4

The EMR line position dependence on the angle β at $T = 100$ K. Filled squares are experimental points and the solid line corresponds to $\cos^2\beta$.

position dependence on the angle, β , between the measuring field, H_{res} , and the direction of the alignment related to H_{fr} . The observed angular dependence of the line position is shown in Fig. 3.4.

As the temperature decreases, the blocking effect is expected to occur for the magnetic NPs. The blocking effect has been observed and discussed for many superparamagnetic systems, but detection by EMR spectroscopy has only been reported for a few examples (see, for example, Ref. [50]). The EMR line intensity obtained by numerical double integration of the experimental spectrum was measured under zero-field cooling (ZFC) condition. The sample was cooled to 4.2 K at $H = 0$ and then the EMR spectra were recorded at the heating sample up to 300 K. Fig. 3.5 shows the temperature dependence of the EMR line integrated intensity for the ZFC procedure; the maximum occurs around 60 K. This dependence is similar to that observed for the ZFC susceptibility behavior in superparamagnetic systems [52,54]. The existence of a maximum is clear evidence that the low-temperature blocking of the NPs magnetic moments takes place. The blocking temperature (T_b) represents the point at which the thermal energy ($k_B T_b$) is comparable to the effective magnetocrystalline energy barrier (KV).

It should be noted, however, that T_b depends on the time scale, τ_m , of the experiment. In defining the superparamagnetic behavior of single-domain NPs, it is important to compare the characteristic time window of measurement, τ_m , associated with a particular experimental technique, with the relaxation time, τ , associated with overcoming the energy barrier (KV). For a given measurement time, typical for the experimental technique, the blocking temperature is defined as [55]:

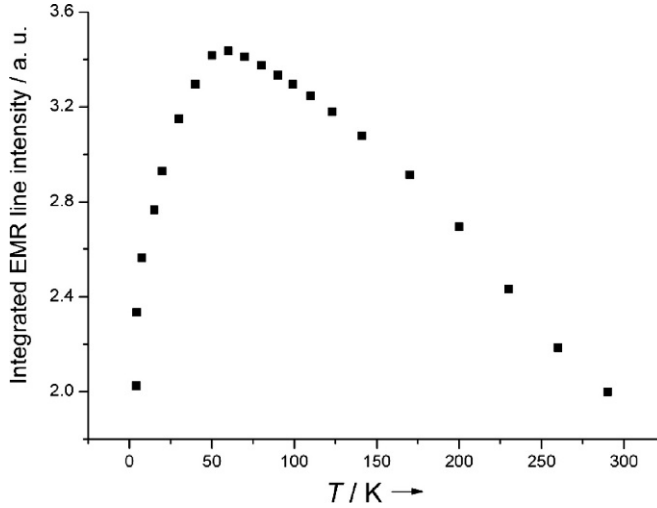


Fig. 3.5

Temperature variation of the EMR line integrated intensity of $\gamma\text{-Fe}_2\text{O}_3$ NPs.

$$T_b = \frac{KV}{k_B \ln(\tau_m/\tau_0)}, \quad (3.2)$$

where the value of τ_0 typically ranges from 10^{-11} to 10^{-9} s. For *dc* susceptibility measurements with a typical measurement time on the order of 100 s, the blocking temperature of magnetic NPs is $T_b \cong KV/25k_B$. For *ac* susceptibility measurements, τ_m is given by the inverse of the excitation field frequency; for Mossbauer spectroscopy, $\tau_m \sim 10^{-7}$ – 10^{-9} s; for ferromagnetic resonance measurement, $\tau_m \sim 10^{-9}$ s, and for neutron scattering, $\tau_m \sim 10^{-7}$ – 10^{-12} s.

To understand the origin of the EMR line in the powdered sample, we refer to Raikher and Stepanov (RS) theory [46] for the effect of thermal fluctuation and anisotropy on the EMR in single-domain NPs of dispersed ferrimagnets when the anisotropy field, H_a , is smaller than the external field, H . Note that the Curie temperature of bulk maghemite, $(T_c)_{\text{bulk}} = 860$ K [50], is higher than the measurement temperatures (4.2–380 K), and the NPs are formally in the ferrimagnetic single-domain state. When studying the magnetodynamics of single-domain particles below the Curie point, RS theory assumes that the value of the NP magnetic moment $\mu = MV$ is constant (in which V is the volume and M is the magnetization of the particle). According to the RS model, the EMR spectrum in the superparamagnetic regime strongly depends on temperature. At low temperature, the anisotropy energy barrier is larger than the thermal fluctuations ($k_B T < KV$), and so the absorption is smeared along the random distribution of the effective anisotropy fields H_a ($H_a = 2|K|/M$, here k_B is the Boltzmann constant, T is the absolute temperature, K is the effective anisotropy energy constant). On increasing the temperature, thermal fluctuations lead to a decrease of the effective anisotropy field, the temperature dependence of which is given by $H_a(T) = h_a(1/L(\xi)) - 3/\xi$, where h_a

is the “true” anisotropic field, $\xi = MVH/k_B T$, and $L(\xi)$ is the Langevin function. Because we are dealing with real systems, in which the distribution of both volumes and easy axes occurs, the absorption will be distributed along the random direction of the anisotropy axes, thus providing an asymmetric line shape at low temperature. At high temperatures, when the relaxation of magnetization through the anisotropy energy barrier is much faster than the Larmor precession, thermal fluctuations will smear out the influence of anisotropy: the resonance spectrum will be just like a normal paramagnetic spectrum with a symmetric Lorentzian line at $h\nu = g\mu_B H$.

The observed EMR spectra provide an opportunity to estimate the anisotropic field (h_a), the magnetic moment of the individual nanoparticle (μ), the mean diameter of NP, and the value of the anisotropy constant from the temperature dependence of the effective anisotropy field, $H_a(T)$, which was determined to be $H_{\text{res}} - H_0$ (in which $H_0 = 3342$ G represents the asymptotic value of H_{res} at high temperature or the value inherent to the isotropic superparamagnet). As seen from the equation, the character of the temperature dependence of the resonance field is connected in a simple way with the nature and sign of NP magnetic anisotropy: as the temperature decreases, H_{res} increases for systems with $K > 0$ and decreases for systems with $K < 0$. The best fit of the experimental dependence (Fig. 3.6) is obtained at $h_a = -1375$ G and $(MVH/k_B) = 77$ K. Thus, the magnetic moment of the individual nanoparticle is about $\mu = 343$ Bohr magnetons. Assuming a spherical form of the particle and taking the magnetization $M = 389$ emu/cm³ [56] for the bulk $\gamma\text{-Fe}_2\text{O}_3$, we obtained values for mean volume, $V = 8.18$ nm³, and mean diameter, $d = 2.5$ nm, for the particles. The diameter estimated coincides with the value of \bar{D} found from TEM studies. From h_a , the value and the negative sign of the average anisotropy constant, $K = -2.64 \times 10^5$ erg/cm³, was obtained.

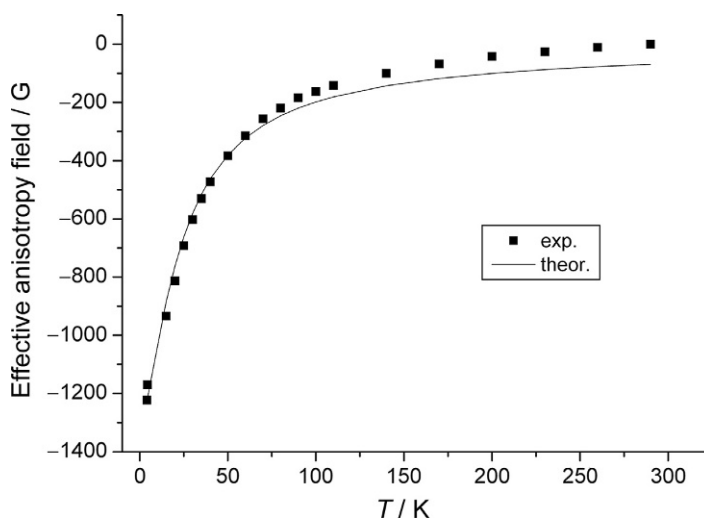


Fig. 3.6

Temperature variation of $H_a(T)$ of $\gamma\text{-Fe}_2\text{O}_3$ NPs incorporated into dendrimer. The *solid line* shows the theoretical dependence simulated by RS theory (see text).

It is known that the bulk anisotropy of $\gamma\text{-Fe}_2\text{O}_3$ is cubic with $K_V = -4.64 \times 10^4 \text{ erg/cm}^3$ [57]. The evaluated constant, K , is an order of magnitude higher than the magnetocrystalline anisotropy (K_V). However, for noninteracting, uniformly magnetized particles, the effective anisotropy constant, K , results from the combined action of magnetocrystalline anisotropy, K_V , shape anisotropy, K_{sh} , and surface anisotropy, K_S : $K = K_V + K_{\text{sh}} + K_S$. Thus, the growth of the magnetic anisotropy constant may be caused by contributions from surface and shape effects. This conclusion in favor of surface and shape contributions to anisotropy constant was obtained earlier by magnetic susceptibility measurements [58,59], as well as Mössbauer [58,59] and EMR spectroscopy [50] for small $\gamma\text{-Fe}_2\text{O}_3$ NPs embedded into other diamagnetic matrices, but not dendrimers.

Let us now consider the effect of NP alignment in the columnar phase under field-freezing (FF) conditions (Fig. 3.4). The specific angular dependence of the resonance field after the FF procedure is observed. As seen from Fig. 3.4, this dependence has only one minimum in the range of 0–180 degrees, and it fits equation $H_{\text{res}} = \frac{a}{\gamma} - H_a P_2(\cos \beta)$, in which P_2 is the second Legendre polynomial. The obtained behavior of H_{res} is inherent to a particle with uniaxial anisotropy [45,46], but not to a particle with cubic magnetocrystalline anisotropy [45,46], for which H_{res} exhibits two minima. Thus, the angular analysis allows us to conclude that NPs encapsulated into the dendrimeric matrix possess negative uniaxial anisotropy. The anisotropy sign found coincides now with the sign of magnetocrystalline anisotropy in bulk $\gamma\text{-Fe}_2\text{O}_3$ and with the sign of the “true” anisotropic field, h_a , determined from the temperature dependence of the line shift ($H_{\text{res}} - H_0$), for the powdered sample, but in contrast to cubic anisotropy typical for bulk $\gamma\text{-Fe}_2\text{O}_3$, we observe the appearance of uniaxial anisotropy. This result leads to the conclusion that the uniaxial anisotropy of NPs is caused by surface and shape effects.

Thus, we can conclude that a temperature-driven transition from superparamagnetic to ferrimagnetic resonance was observed by EMR for the $\gamma\text{-Fe}_2\text{O}_3$ NPs. The low-temperature blocking of the NP magnetic moments was clearly shown in the behavior of the integrated EMR line intensity. The physical parameters of magnetic NPs (magnetic moment, effective magnetic anisotropy) were determined from the analyses of the EMR data. The effective magnetic anisotropy constant is enhanced relative to bulk $\gamma\text{-Fe}_2\text{O}_3$ and this enhanced value is associated with the influence of the surface and shape effects. The angular dependence of the EMR signal position for field-freezing sample from liquid-crystalline phase showed that NPs possessed uniaxial anisotropy, in contrast to bulk material maghemite.

3.4 Mössbauer Spectroscopy Study

The Mössbauer spectroscopy on ^{57}Fe was used to determine the structure heterogeneity and composition of the iron oxide NPs. The Mössbauer spectrum observed at 298 K is a superposition of a singlet and quadrupole doublet. The parameters of a single line with $\delta = 0 \text{ mm/s}^*$ (* indicates with respect to $\alpha\text{-Fe}$ at 298 K) correspond to an $\alpha\text{-Fe}$ metallic core in a paramagnetic state with an area under the curve $S \sim 15\%$ (Fig. 3.7a).

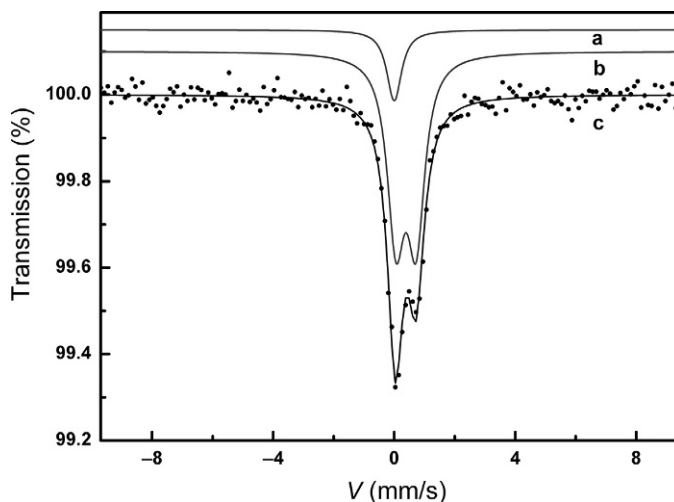


Fig. 3.7

Mössbauer spectrum of core-shell iron oxide NPs at 298 K (c). The *solid curves*, which are located above the experimental spectrum, show the $\alpha\text{-Fe}$ metallic core (a) and $\gamma\text{-Fe}_2\text{O}_3$ shell (b).

The doublet with parameters ($\delta = 0.39 \text{ mm/s}^*$, $\Delta E_Q = 0.668 \text{ mm/s}$, and $S \sim 85\%$) corresponds to the shell of $\gamma\text{-Fe}_2\text{O}_3$ on the surface of the NP (Fig. 3.7b). The parameters of this doublet are in good agreement with the parameters for magnetic single-domain $\gamma\text{-Fe}_2\text{O}_3$ NPs encapsulated within sol-gel derived silica (SiO_2) [59].

At $T = 80 \text{ K}$, the second doublet (Fig. 3.8c) with parameters $\delta = 0.33 \text{ mm/s}^*$, $\Delta E_Q = 3.08 \text{ mm/s}$, $S \sim 12\%$ is clearly resolved. An additional detailed study [60] of this doublet showed that this signal corresponds to the Fe^{3+} atoms of the surface monoatomic layer of NP, which is in contact with the dendrimer molecule, and the quadrupole splitting value of this signal indicates the low-spin state of Fe^{3+} atoms of the surface monoatomic layer on the high-spin shell. The mechanism of the appearance of low-spin centers has the “surface,” not the “bulk” character as for the traditional spin-crossover systems. The fraction of atoms in the low-spin state depends weakly on the temperature and is due to the relative number of surface atoms, which have other properties of the phonon spectrum, only.

At $T = 5 \text{ K}$, the spectrum exhibited a magnetic hyperfine structure consisting of two superpositioned sextets. The first one (Fig. 3.9a), with an isomer shift of $\delta = 0.08 \text{ mm/s}^*$ and an observed hyperfine field of 329.1 kOe, corresponds to the $\alpha\text{-Fe}$ core of the NPs. The observed parameters differ from the parameters of bulk $\alpha\text{-Fe}$ due to the defective structure of the core. The second sextet (Fig. 3.9b), with parameters $\delta = 0.45 \text{ mm/s}^*$, $\Delta E_Q = -0.16 \text{ mm/s}$, and a hyperfine field of 511.9 kOe, we think is responsible for the $\gamma\text{-Fe}_2\text{O}_3$ shell of the NPs [61]. A significant fraction ($\sim 78\%$) of the superparamagnetic part relative to the total spectral absorption area (Fig. 3.9d) conforms to fast dynamics in

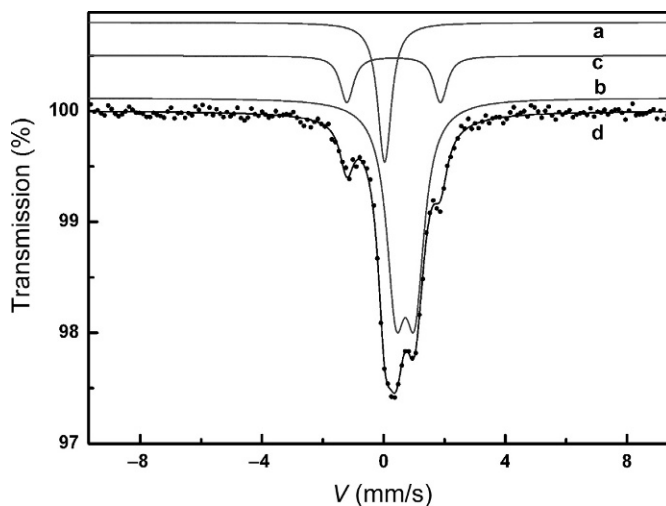


Fig. 3.8

Spectrum of core-shell iron oxide NPs at 80 K (d). The *solid curves*, which are located above the experimental spectrum, show the α -Fe metallic core (a), γ - Fe_2O_3 shell (b) and Fe^{3+} ions of NP_s bound to the dendrimer (c).

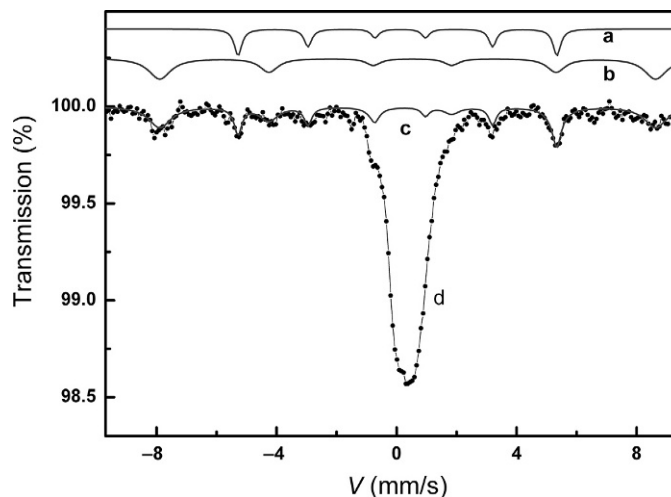


Fig. 3.9

Spectrum of core-shell iron oxide NPs at 5 K (d). The *solid curves*, which are located above the experimental spectrum, show the α -Fe metallic core (a), γ - Fe_2O_3 shell (b), and (c) is a superposition of curves (a) and (b).

magnetic subsystems at 5 K. Such dynamics lead to transformation of the absorption lines shapes and an indefiniteness of the mathematical description of this spectrum.

A considerable part of the paramagnetic (superparamagnetic) ferric ion (Fe^{3+}) state also confirms a weak influence of interparticle interactions on the properties of core-shell iron oxide NPs encapsulated into dendrimers.

3.5 Optical Properties and the Band Gap Width of $\gamma\text{-Fe}_2\text{O}_3$ NPs

Besides the magnetic properties, maghemite ($\gamma\text{-Fe}_2\text{O}_3$) also has semiconductor properties [62]. Bulk material is an n-type semiconductor with a band gap width of 2.2 eV, where the conduction band (CB) is composed of empty d -orbitals of Fe^{3+} and the valence band (VB) consists of occupied $3d$ crystal field orbitals of Fe^{3+} with some admixture from the oxygen antibonding $2p$ orbitals (Fig. 3.10).

The stability and semiconductor properties of maghemite allow it to be used in solar energy conversion, photocatalysis, and water splitting [63,64]. Despite numerous investigations, the semiconductor and optical properties of $\gamma\text{-Fe}_2\text{O}_3$ at the nanolevel have not been well characterized. A better understanding of their optical and magnetic properties will be invaluable in developing applications of iron oxide NPs in photocatalysis and magneto-optical devices. Nanoscale maghemite exhibits new physical properties as compared with bulk material: NPs can demonstrate quantum size effects [65,66]. Quantum size effects include improved magnetic properties such as superparamagnetism [24,67] (as shown in Section 3.2), quantum tunneling of magnetization [68,69], and shift of the optical absorption. As known, below a certain critical size, magnetic particles become a single domain as opposed to multidomain in the bulk. $\gamma\text{-Fe}_2\text{O}_3$ NPs become superparamagnetic when their critical size is smaller than $\sim 10\text{nm}$ [70]. A decrease in the size of semiconductor particles should lead to a significant increase in the band gap width and in the total energy of optical transitions (“blue” shift in optical absorption) [71].

In this section, we will focus our attention on the influence of the size of semiconductor $\gamma\text{-Fe}_2\text{O}_3$ NPs on the optical properties.

Fig. 3.11A shows room-temperature UV-Vis absorption spectrum of $\gamma\text{-Fe}_2\text{O}_3$ /dendrimeric nanocomposite in dichloromethane solution in coordinates (α) versus wavelength (λ). Spectrum is characterized by the presence of two well-resolved absorption bands near 254 and 287 nm and the extended tail to 500 nm. After subtracting the extended tail, the spectrum

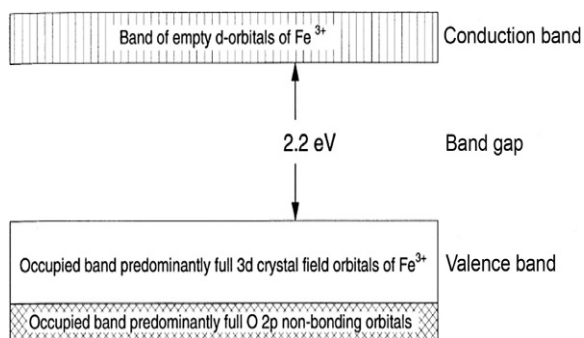


Fig. 3.10

Band structure of maghemite.

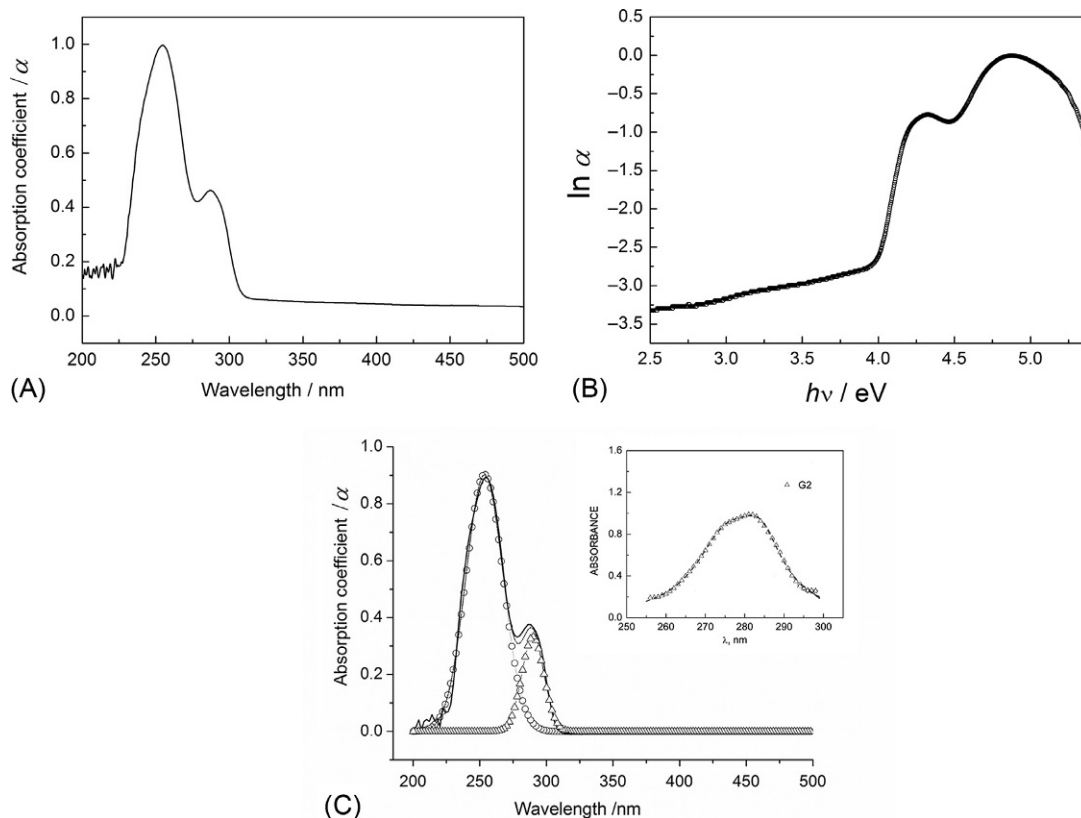


Fig. 3.11

UV-Vis absorption spectra shown in the coordinates of α versus λ (A) and $\ln \alpha$ versus $h\nu$ (B) for $\gamma\text{-Fe}_2\text{O}_3$ /dendrimeric nanocomposite. (C) Experimental (solid line) and simulated (dashed line) absorption spectra. The contributions from two components at 254 and 287 nm are indicated by symbols (\circ) and (Δ), respectively. The absorbance spectrum of the pure PPI dendrimer of the second generation (G2) is shown in the inset for comparison.

was analyzed in the model of Gaussian-type lines. Two Gaussian-type components of 27.7 and 16.5 nm width observed at 254 and 287 nm, respectively, relatively well described the experimental spectrum (Fig. 3.11C).

In the general case, the relationship between the band gap width of a semiconductor (E_g), the absorption coefficient (α), and the radiation frequency (ν) can be expressed as [72–74]:

$$\alpha = \sum_i \alpha_i = \sum_i \frac{A_i (h\nu - E_{gi})^{m_i}}{h\nu}, \quad (3.3)$$

where h is the Planck constant and the values of A_i , E_{gi} , and m_i correspond to the transmission coefficient, the energy, and the nature of the particular optical transition with absorption coefficient α_i , respectively. For allowed direct, allowed indirect, forbidden direct, and forbidden indirect transitions, the value of m_i corresponds to 1/2, 2, 3/2, and 3, respectively [73,74]. For a semiconductor material having one kind of transition, we can write

$$\alpha = \frac{A_1}{h\nu} (h\nu - E_{g1})^{m_1}, \quad (3.4)$$

Eq. (3.4) can be written as

$$\ln \alpha = \ln A_1 - \ln h\nu + m_1 \ln (h\nu - E_{g1}), \quad (3.5)$$

and

$$\frac{d(\ln \alpha)}{d(h\nu)} = -1/h\nu + m_1/(h\nu - E_{g1}). \quad (3.6)$$

Eq. (3.6) suggests that a plot of $\ln \alpha$ versus $h\nu$ will indicate a divergence at $h\nu = E_{g1}$ from which it should be distinctly possible to obtain the value of E_{g1} . Once E_{g1} is found, the value of m_1 can easily be obtained from the slope of the straight line plot of $\ln(\alpha \cdot h\nu)$ versus $\ln(h\nu - E_{g1})$. Likewise, one can expect divergence in a $\ln \alpha$ versus $h\nu$ plot at other probable transitions occurring at E_{g2} , E_{g3} , and E_{g4} , and the corresponding m_i values can be determined as before.

Fig. 3.11B presents the absorption spectrum rearranged in the $\ln \alpha$ versus $h\nu$ coordinates. This plot shows two sharp jumps at $E_{g1} = 4.0$ eV and $E_{g2} = 4.5$ eV that indicates the presence of two transitions in the energy spectrum of the system. The values of exponents m_i for each transition were determined from the slope of the straight line plotted in the coordinates of $\ln(\alpha_i \cdot h\nu)$ versus $\ln(h\nu - E_{gi})$ as depicted in Fig. 3.12A and B, respectively. The value of m_1 for the first transition (E_{g1}) was 1.16, while the m_2 value for the second transition (E_{g2}) was found to be 0.53. Thus, the first transition registered in the spectrum of dendrimeric $\gamma\text{-Fe}_2\text{O}_3$ NPs is not associated with transfer of electron to the conduction band, while the second transition (with the energy of $E_{g2} = 4.5$ eV) corresponds to allowed direct transition from valence band to the conduction band.

This conclusion is also confirmed by UV optical data obtained on pure PPI dendrimer of the second generation, which displays only the absorption band at 270–290 nm [75] (see inset in Fig. 3.12C). The band gap width for the second transition ($E_{g2} = 4.5$ eV) changes toward greater value relative to that of the bulk ($E_g(\gamma\text{-Fe}_2\text{O}_3) = 2.2$ eV) material, that corresponds to the so-called blue shift. The fact of increasing band gap width has been previously registered for larger $\gamma\text{-Fe}_2\text{O}_3$ NPs. Thus, for NPs with average diameter of 7.8 nm, the band gap width was evaluated as $E_{g2} = 3.22$ eV [76], and for NPs with diameter of 4.2 nm, it was equal to $E_{g2} = 3.51$ eV [77].

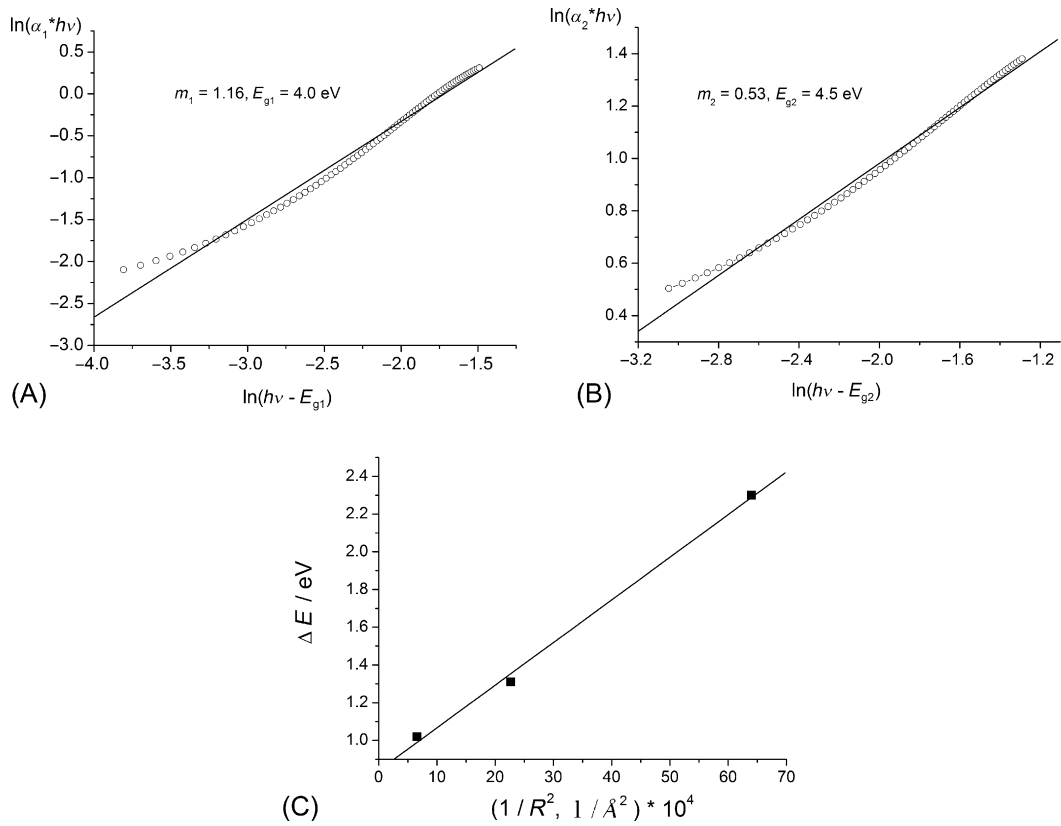


Fig. 3.12

The linear fit of $\ln(\alpha_i \cdot h\nu)$ versus $\ln(h\nu - E_{gi})$, where $E = E_{g1}$ (A) and $E = E_{g2}$ (B) for $\gamma\text{-Fe}_2\text{O}_3/\text{dendrimeric}$ nanocomposite. (C) The dependence of the shift of the optical absorption from the average radius of $\gamma\text{-Fe}_2\text{O}_3$ NPs.

The “blue” shift with respect to the bulk material ($E_g(\gamma\text{-Fe}_2\text{O}_3) = 2.2 \text{ eV}$) can be described by the following expression [76–78]:

$$\Delta E_g = \frac{\hbar^2 \pi^2}{2m_{\text{eff}} R^2}, \quad (3.7)$$

where m_{eff} is the effective mass of the excitons, R is the average radius of NPs, and ΔE_g is the difference between the band gap widths for ferric oxide NPs and for bulk material. To check this relationship, the dependence of the blue shifts on the average radius of $\gamma\text{-Fe}_2\text{O}_3$ NPs was plotted (Fig. 3.12C). The experimental data were taken from Refs. [76,77] and the present work. As can be seen, a linear dependence from $1/R^2$ is really observed.

Thus, we can conclude that the “blue” shift caused by size effect is really detected in our sample. In addition, we know now that in order to observe the influence of light radiation on the superparamagnetic properties of semiconductor $\gamma\text{-Fe}_2\text{O}_3$ NPs, we must use the wavelength of $\sim 254 \text{ nm}$.

3.6 Photoinduced Superparamagnetic Effect in γ -Fe₂O₃ NPs: EPR Detection

Let us consider the influence of light on superparamagnetic properties of single-domain γ -Fe₂O₃ NPs. EPR spectroscopy is a powerful technique for studying superparamagnetic properties of NPs and for observing trapped electrons and trapped holes formed following band gap irradiation.

Crystalline γ -Fe₂O₃ is ferrimagnetic and consists of an alternation of two opposed and unequal magnetic sublattices [79]. The atomic Fe³⁺ moments within each sublattice are coupled parallel, whereas those of the A (tetrahedral) and B (octahedral) sublattices are coupled antiparallel through an intervening O²⁻ anion. The unit cell of γ -Fe₂O₃ is cubic, with both octahedrally and tetrahedrally coordinated Fe³⁺ sites (defect spinel structure). The formula of maghemite is represented as (Fe³⁺)₈^t(Fe_{5/6}³⁺ □_{1/6})₁₆^o O₃₂, where the brackets () and t designate 8 tetrahedral coordinated sites and the brackets () and o designate 16 octahedral coordinated sites. Note that all Fe³⁺ ions are in the high-spin ($S = 5/2$) states. The charge neutrality of the cell is guaranteed by the presence of vacancies (□) in Fe position, and these vacancies are known to be located in the octahedral sites [80].

As shown in Section 3.3, the EPR spectrum in the superparamagnetic regime strongly depends on the temperature. At low temperature, the magnetic anisotropy energy dominates over the thermal fluctuations, and the resonance line will be smeared along the random distribution of the effective anisotropy fields. An extremely broad resonance signal is observed in this case. At high temperature, thermal fluctuations suppress the influence of anisotropy and narrow EPR signal is detected. Superparamagnetic behavior of single-domain magnetic NPs is characterized by a Langevin-type temperature dependence of the resonance field and manifests itself as a gradual shift of the resonance line to a lower field upon cooling (in the case of a negative sign of the effective anisotropy constant, K). The blocking temperature is the temperature below which the fluctuation of the NPs magnetic moments is blocked.

Zero-field-cooled (ZFC) and field-cooled (FC) magnetization measurements were performed to determine the blocking temperature. The ZFC and FC temperature dependences of the product χT shown in Fig. 3.13 give rise to the blocking temperature value $T_B = 18$ K. The temperature T_B was determined as divergence point of ZFC and FC curves. Below this point, the magnetic relaxation in the superparamagnetic ensemble of NPs moments is frozen, which is known as blocked regime ($KV \gg k_B T$, KV – anisotropy energy).

Irradiation of the sample was carried out by a laser with the wavelength of $\lambda = 266$ nm. The influence of light was studied as for sample in vacuo (outgassing to 3×10^{-5} mmHg), as well for out of vacuo sample. The behavior of the out of vacuo sample is presented in Fig. 3.14A. It shows that pulsed laser irradiation results in a decrease of the intensity of EPR signal, which is not restored after switching off the laser. The “impurity signal” coming from the material (Mo^{III} in the sapphire ring) of the dielectric resonator was used

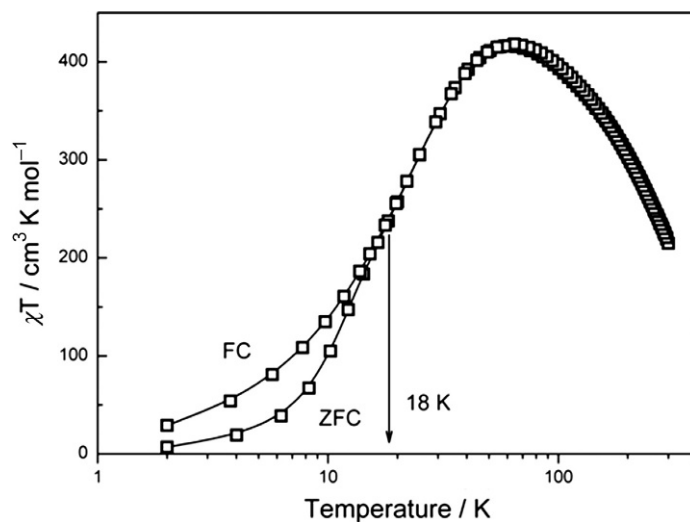


Fig. 3.13

The ZFC and FC (external magnetic field of 100 Oe) temperature dependences of the product χT for γ - Fe_2O_3 NPs formed in dendrimer.

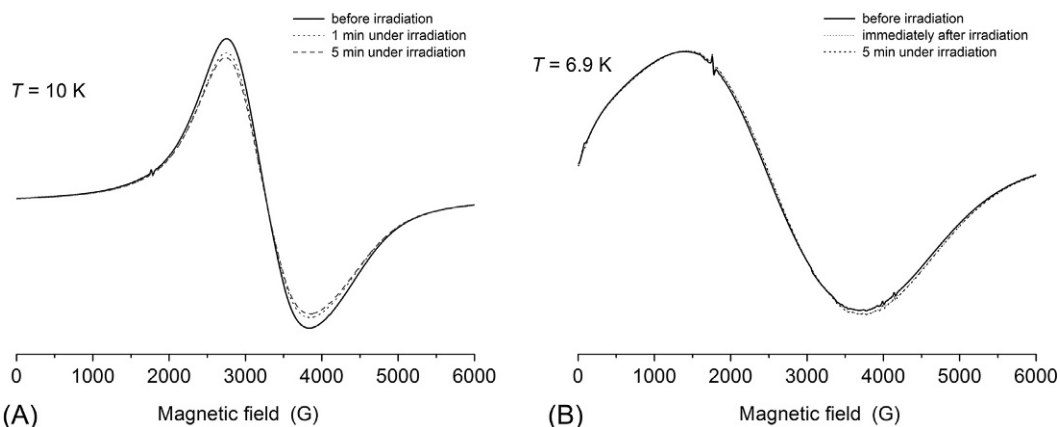


Fig. 3.14

(A) Changes in the EPR signal upon laser irradiation for out of vacuo sample at $T = 10$ K. (B) Changes in the EPR signal during and after laser irradiation with a wavelength 266 nm at 6.9 K for FC sample held in vacuum.

as a calibration signal to monitor the identical conditions of measurements. The sample in vacuum was studied by two types cooled in the presence (FC) and the absence (ZFC) of the external magnetic field. As seen in Figs. 3.14B and 3.15, samples demonstrate a different behavior under irradiation. The irradiation of FC sample cooled down to 6.9 K does not change the EPR signal (Fig. 3.14B), whereas ZFC sample exhibits very interesting features in EPR

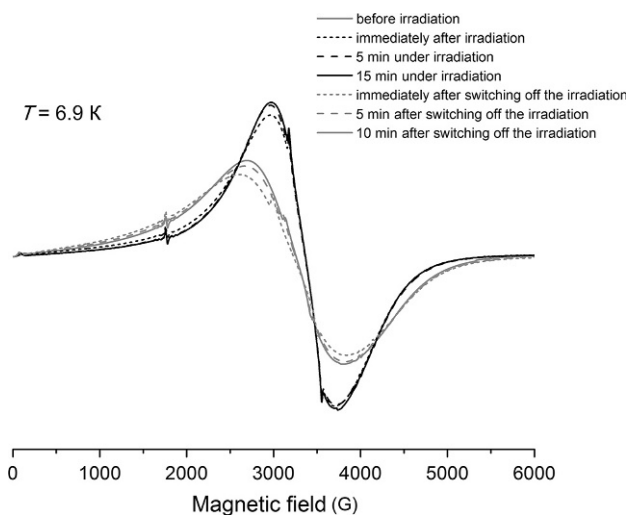


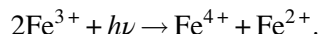
Fig. 3.15

Changes in the EPR signal during laser irradiation with a wavelength of 266 nm at 6.9 K for ZFC sample held in vacuum.

spectrum under irradiation (Fig. 3.15). The irradiation of ZFC sample held in vacuo at 6.9 K causes the appearance of an intense new EPR signal at $g_n = 2.06$ with line width of 740 G, the position of which is significantly shifted relative to the original EPR signal ($g = 2.12$). The signal decays immediately when the irradiation is stopped and after 10 min, the original EPR signal is fully restored. The appearance and disappearance of this new signal can be repeated many times at 6.9 K when we turn on/turn off the laser.

Let us discuss the possible explanation of the observed effects. The possibility of direct heating from the light source inducing superparamagnetism in the maghemite NPs can be rejected, since the behavior of all three samples is radically different upon irradiation. Moreover, the comparison of the shifts and widths of the resonance lines obtained upon irradiation at 6.9 K at ZFC procedure with those measured in the dark shows that the apparent sample temperature should raise by 50 K less than 1 s. It is not realistic. In the experiment, the sample is held in a flow of liquid helium and its temperature is controlled with an accuracy of 0.5 K.

We believe the observed effects are a consequence of electronic excitation of γ -Fe₂O₃ semiconductor. Bulk maghemite is a semiconductor with a band gap of 2.2 eV [66]. The valence band comprises $2p$ orbitals of O²⁻ and occupies Fe $3d$ orbitals, and the conduction band corresponds to vacant Fe $3d$ orbitals. Promotion of electrons into the conduction band upon absorption of light will populate previously vacant Fe $3d$ orbitals, effectively reducing Fe³⁺ to Fe²⁺. If the promoted electrons originate from the top of the valence band, the resulting positive holes may be written as Fe⁴⁺ cations. The overall process may thus be represented as



So, we can suggest that under irradiation, the redistribution of iron cations and vacancies and hence the change of the coupling between A and B magnetic sublattices take place in maghemite NPs. As a result, the magnetic anisotropy and superparamagnetic properties of NPs are also changing.

The behavior of the sample containing oxygen confirms our explanation. Oxygen is known to be a scavenger of conduction band electrons in oxide semiconductors. Therefore, under irradiation of out of vacuo sample, the oxygen captures the electrons passing into the conduction band, so that a part of the Fe^{3+} ions passes from paramagnetic to diamagnetic state and EPR signal is reduced in the intensity. The charge neutrality of this new system is achieved due to the redistribution of the charges between iron cations and vacancies, and that is why the initial EPR signal is not restored after irradiation is stopped.

The photoinduced superparamagnetic effect was registered by EPR for the first time in nanostructured $\alpha\text{-Fe}_2\text{O}_3$ [81]. The authors of this work, studying $\alpha\text{-Fe}_2\text{O}_3$ NPs of the average size 5–7 nm, believed that the appearance of a new EPR signal upon irradiation is due to the electronic excitation of the $\alpha\text{-Fe}_2\text{O}_3$ semiconductor. However, they explained the effect by change of the coupling between the magnetic domains in NPs. In this work, comparison of the behavior of $\alpha\text{-Fe}_2\text{O}_3$ NPs cooled in the presence and absence of the external magnetic field was not carried out.

3.7 EMR Searching of Quantum Behavior of Superparamagnetic $\gamma\text{-Fe}_2\text{O}_3$ Nanoparticles in Dendrimeric Nanocomposite

In the world of nanoscale magnetic systems, two classes of nano-objects can be distinguished: magnetic NP_S and molecular nanomagnets (MNM). The behavior of MNMs is known to be described by quantum mechanics, where calculations begin by considering the behavior of a single ion, while NPs behavior is described in terms of classical physics on the basis of parameters obtained for bulk materials. It seems interesting to develop a common approach for the consideration of nanoscale magnetic systems, which could provide a better understanding of their properties. Electron magnetic resonance (EMR) is an excellent tool to demonstrate the similarities in the behavior of NPs and MNMs, and its use can provide experimental evidences of quantum behavior of single-domain NPs. Some evidences in favor of the discrete nature of spin levels of NPs are already known in the literature. For example, a small signal is observed in the half-field of EMR spectra [82–85], which, according to some authors, is attributed to forbidden transitions between states with $\Delta m = \pm 2$. Its appearance is interpreted as a proof of the quantum nature of the system, and in such approach a nanoparticle is considered to be a giant exchange-coupled cluster with a total spin S .

In this section, we try to find the quantum nature of ultrafine $\gamma\text{-Fe}_2\text{O}_3$ NPs encapsulated into dendrimeric matrix, and for this purpose we offer to use the approach proposed in Ref. [86]—to

record EMR spectra of NPs in both (parallel and perpendicular) configurations, that is, when the H_1 field of the microwave radiation is parallel or perpendicular to the external magnetic H_0 field. These alternative configurations have different selection rules for the allowed transitions between the total spin projections, and therefore, provide the opportunity to “feel” the quantum nature of the system.

In Section 3.3, the behavior of superparamagnetic single-domain $\gamma\text{-Fe}_2\text{O}_3$ NPs was investigated by EMR spectroscopy, using the classical theoretical approach [87]. The typical EMR spectra (for the configuration $H_1 \perp H_0$) are shown in Fig. 3.3, and the estimate of the anisotropic field of NPs gives the value $h_a = -1375$ G.

The magnetic measurements carried out for this system [88] (Fig. 3.16) in two cooling regimes—in the presence (FC) and in the absence of an external magnetic field (ZFC)—have shown that there is a temperature-driven transition from the superparamagnetic to the ferrimagnetic state, and the value of the effective magnetic moment of NPs is $\mu_{\text{eff}} \approx 60 \mu_B$.

Besides the basic signal ($g \sim 2$), EMR spectra demonstrate the presence of a small signal in the half-field around 1500 G (Fig. 3.17), which has been attributed in the literature to “partially” forbidden transitions between states with $\Delta m = \pm 2$, where m is the expectation value of S_z and S the total spin of the NP. If this interpretation is correct, then the intensity of this small signal should increase when the EMR spectra are recorded in a parallel configuration ($H_1 \parallel H_0$). EMR experiments carried out by us for this configuration confirmed that it is indeed the case (Fig. 3.18) and the intensity of the transitions in the half-field really increases. X-band EMR measurements were performed on a CW-EPR EMXplus Bruker spectrometer equipped with helium ER 4112HV cryostat, ER 4131VT temperature control system, and

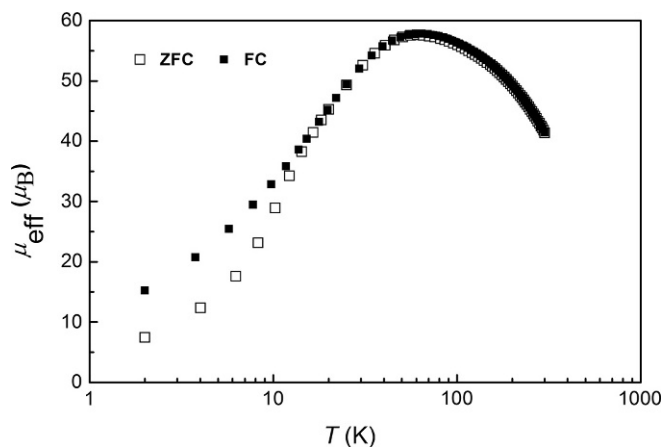
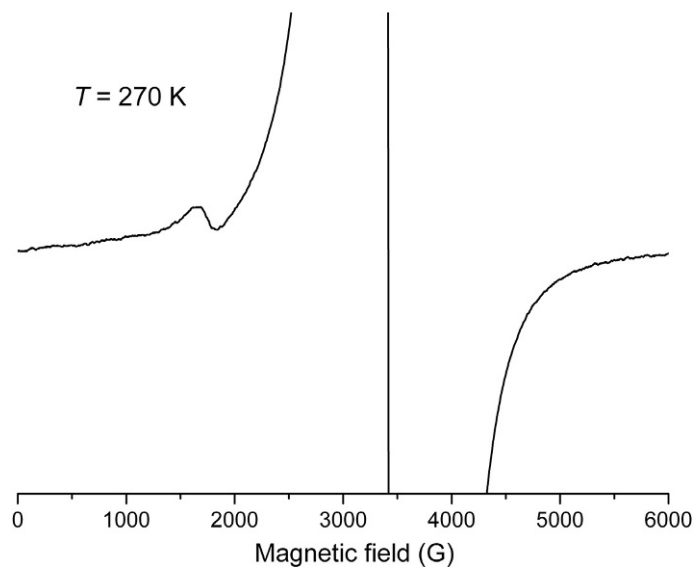
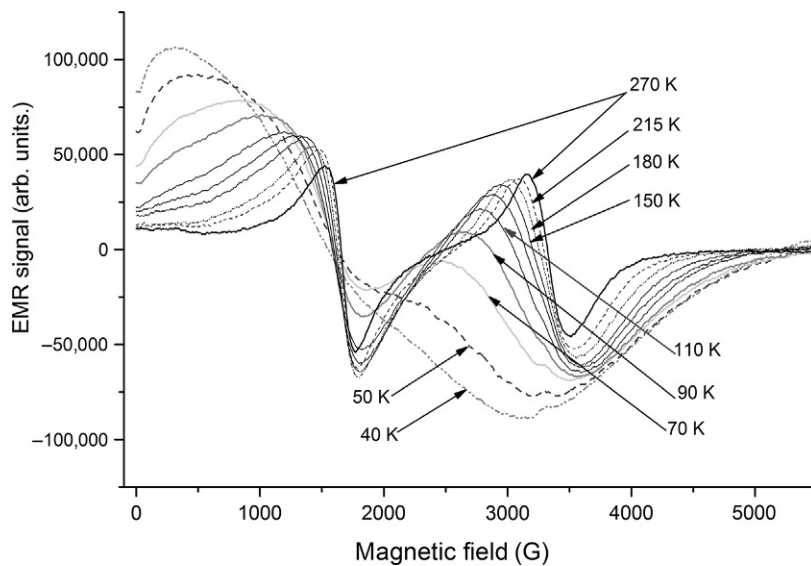


Fig. 3.16

Temperature dependences of the effective magnetic moment of $\gamma\text{-Fe}_2\text{O}_3$ NP measured at 10 kOe in FC and ZFC regimes.

**Fig. 3.17**

EMR spectrum of maghemite NPs in dendrimer at 270 K with a small signal at the half-field (~ 1500 G).

**Fig. 3.18**

Temperature dependence of EMR spectra recorded at X-band in parallel configuration ($\nu = 9.39$ GHz) for γ -Fe₂O₃ NPs encapsulated in dendrimer.

the ER 4116DM EPR resonator (Bruker, Germany) was used. The spectra were recorded using the modulation frequency of 100kHz and a microwave power for the perpendicular configuration was 25 μW and 20mW for the parallel configuration. So, one can see that the proposed approach opens additional possibilities for the analysis of the properties of magnetic nanoparticles with using a model where each NP is treated as a quantum object with a large spin, similar to the approach that was successfully used to MNMs.

Thus, the following spin Hamiltonian can be used to calculate the EMR spectra:

$$H = \mu_B \hat{S} \cdot g \cdot \hat{H} + \hat{S} \cdot D \cdot \hat{S}, \quad (3.8)$$

where the first term gives the splitting of energy levels in the external magnetic field H , and the second term determines the fine structure of the levels of NP with spin S .

The value of spin S for NPs was estimated from magnetic SQUID measurements according to the expression $S = \mu/g\mu_B$ [86], and in our case $S \approx 30$.

Using the relation $D = -\gamma h_a/2S$ [86] together with the known values of the anisotropic field (h_a), and spin S value, we can obtain the estimated value of the fine structure parameter D for the NP, which is equal to $D \sim 64$ MHz. Simulation of the EMR spectra for both magnetic field configurations was performed using the Easyspin program (version 5.1.5 [89]) with the matrix diagonalization method. The experimental and the simulated spectra at $T = 180$ K are shown in Fig. 3.19. The best agreement between the experimental and theoretical spectra was obtained for the following parameters: $S = 30$, $D = 40$ MHz with individual Lorentzian line shape and

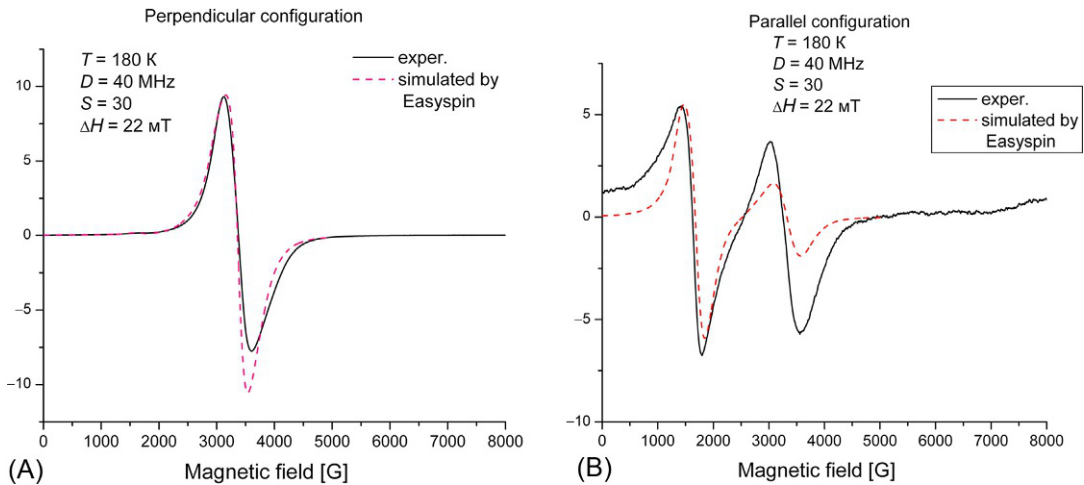


Fig. 3.19

Experimental EMR spectra (*continuous lines*) acquired in the perpendicular (A) and parallel (B) configurations at 180 K, and simulated (*dashed lines*) spectra.

line width $\Delta H = 220\text{G}$. It can be seen that a fairly well qualitative agreement between the spectra is observed.

Thus, we can conclude that the obtained results demonstrate the possibility to analyze the magnetic properties of NP using the large spin value $S = 30$; hence, NP can be considered as a quantum object.

3.8 Conclusion

A liquid-crystalline, second-generation PPI dendrimer was used as a nanoreactor for the formation of single-domain ferrimagnetic/semiconductor $\gamma\text{-Fe}_2\text{O}_3$ NPs in the dendrimeric matrix. The average diameter of NPs fabricated into dendrimer was 2.5 nm. The iron oxide dendrimeric nanocomposite exhibited mesomorphic properties and demonstrated columnar (Col_h) packing of the molecules in the mesophase. Electron magnetic resonance (EMR), Mössbauer spectroscopy and SQUID magnetometry were used to study the magnetic properties of NPs. A temperature-driven transition from superparamagnetic to ferrimagnetic resonance was observed for the iron-dendrimeric nanocomposite. Upon cooling, the EMR resonance line monotonically broadened and shifted to lower magnetic fields. Such behavior is typical for the superparamagnetic materials and was described by the theoretical approach of Raikher-Stepanov. A quantitative analysis of the temperature dependence of the effective anisotropy field of $\gamma\text{-Fe}_2\text{O}_3$ NPs found an enhanced value of the magnetic anisotropy constant of NPs relative to bulk material, which is associated with the influence of surface and shape effects. The analysis of the angular dependence performed on the field-freezing (FF) sample from the liquid-crystalline state allowed the determination of the anisotropy of the NPs, which turned out to be uniaxial and negative. This result led to the conclusion that this anisotropy is induced by the particle surface and shape effects. Mössbauer spectroscopy found that the NPs consist of the $\alpha\text{-Fe}$ core (15%) and the $\gamma\text{-Fe}_2\text{O}_3$ shell (85%) formed by high-spin Fe^{3+} ions. But in the surface monoatomic layer, which is in contact with the dendrimer, Fe^{3+} ions demonstrate the low-spin state.

Optical and photoinduced superparamagnetic properties of $\gamma\text{-Fe}_2\text{O}_3$ NPs were also investigated. The study of the optical absorption of semiconductor NPs found a direct allowed transition with a band gap width of 4.5 eV, the value of which is significantly increased in comparison with the bulk material (2.2 eV). This increased value has been explained by quantum size effects. The low-temperature blocking of the NPs magnetic moments was determined by SQUID measurements, and the blocking temperature turned out to be 18 K.

The influence of pulsed laser irradiation on the superparamagnetic properties of $\gamma\text{-Fe}_2\text{O}_3$ NPs was studied by EPR spectroscopy. It has been shown that irradiation of the sample held in vacuo and cooled in zero magnetic field to 6.9 K leads to the appearance of a new EPR signal, which decays immediately after the irradiation is stopped. The appearance and

disappearance of this new signal can be repeated many times at 6.9 K when we turn on/turn off the laser. We suppose that the generation of conduction band electrons by irradiation into the band gap of the γ -Fe₂O₃ changes the superparamagnetic properties and the magnetic anisotropy of NPs. This effect is suppressed in the sample containing oxygen, since oxygen captures the conduction band electrons.

At the end, the possibility to describe the behavior of γ -Fe₂O₃ NPs by quantum mechanics is considered. It has been shown that the model based on the spin value $S = 30$, corresponding to the total magnetic moment of the nanoparticle, can be used for interpreting the experimental EPR results and the proof of the quantum behavior of γ -Fe₂O₃ nanoparticles.

References

- [1] A.N. Shipway, E. Katz, I. Willner, Nanoparticle arrays on surfaces for electronic, optical, and sensor applications, *ChemPhysChem* 1 (1) (2000) 18–52.
- [2] (a) M. Bruchez Jr., M. Moronne, P. Gin, S. Weiss, A.P. Alivisatos, Semiconductor nanocrystals as fluorescent biological labels, *Science* 281 (5385) (1998) 2013–2016. (b) W.C.W. Chan, S. Nie, Quantum dot bioconjugates for ultrasensitive nonisotopic detection, *Science* 281 (5385) (1998) 2016–2018.
- [3] (a) T.T. Shen, A. Bogdanov Jr., A. Bogdanove, K. Poss, T.J. Brady, R. Weissleder, Magnetically labeled secretin retains receptor affinity to pancreas acinar cells, *Bioconjug. Chem.* 7 (3) (1996) 311–316. (b) D. Högemann, L. Josephson, R. Weissleder, J.P. Babilion, Improvement of MRI probes to allow efficient detection of gene expression, *Bioconjug. Chem.* 11 (6) (2000) 941–946. (c) L. Josephson, J.M. Perez, R. Weissleder, Magnetic nanosensors for the detection of oligonucleotide sequences, *Angew. Chem. Int. Ed. Eng.* 40(17) (2001) 3204–3206.
- [4] C.B. Murray, C.R. Kagan, M.G. Bawendi, Self-organization of CdSe nanocrystallites into three-dimensional quantum dot superlattices, *Science* 270 (5240) (1995) 1335–1338.
- [5] (a) C.T. Black, C.B. Murray, R.L. Sandstrom, S.H. Sun, Spin-dependent tunneling in self-assembled cobalt-nanocrystal superlattices, *Science* 290 (5494) (2000) 1131–1134. (b) M.P. Pileni, Nanocrystal self-assemblies: fabrication and collective properties, *J. Phys. Chem. B* 105 (17) (2001) 3358–3371.
- [6] F. Aulenta, W. Hayes, S. Rannard, Dendrimers: a new class of nanoscopic containers and delivery devices, *Eur. Polym. J.* 39 (9) (2003) 1741–1771.
- [7] U. Boas, P.M.H. Heegaard, Dendrimers in drug research, *Chem. Soc. Rev.* 33 (1) (2004) 43–63.
- [8] C.M. Paleos, D. Tsiourvas, Z. Sideratou, Molecular engineering of dendritic polymers and their application as drug and gene delivery systems, *Mol. Pharmacol.* 4 (2) (2007) 169–188.
- [9] T. Kim, H.J. Seo, J.S. Choi, H.S. Jang, J.U. Baek, K. Kim, J.S. Park, PAMAM-PEG-PAMAM: novel triblock copolymer as a biocompatible and efficient gene delivery carrier, *Biomacromolecules* 5 (6) (2004) 2487–2492.
- [10] I.J. Majoros, A. Myc, T. Thomas, C.B. Mehta, J.R. Baker, PAMAM dendrimer-based multifunctional conjugate for cancer therapy: synthesis, characterization, and functionality, *Biomacromolecules* 7 (2) (2006) 572–579.
- [11] A. Myc, I.J. Majoros, T.P. Thomas, J.R. Baker, Dendrimer-based targeted delivery of an apoptotic sensor in cancer cells, *Biomacromolecules* 8 (1) (2007) 13–18.
- [12] X. Shi, S. Wang, S. Meshinchi, M.E. Van Antwerp, X. Bi, I. Lee, J.R. Baker, Dendrimer-entrapped gold nanoparticles as a platform for cancer cell targeting and imaging, *Small* 3 (7) (2007) 1245–1252.
- [13] R.W.J. Scott, A.K. Datye, R.M. Crooks, Bimetallic palladium-platinum dendrimer-encapsulated catalysts, *J. Am. Chem. Soc.* 125 (13) (2003) 3708–3709.
- [14] Y. Jiang, J. Jiang, Q. Gao, M. Ruan, H. Yu, L. Qi, A novel nanoscale catalyst system composed of nanosized Pd catalysts immobilized on Fe₃O₄@SiO₂-PAMAM, *Nanotechnology* 19 (7) (2008). 075714.
- [15] D. Mandal, A. Maran, M.J. Yaszemski, M.E. Bolander, G. Sarkar, Cellular uptake of gold nanoparticles directly cross-linked with carrier peptides by osteosarcoma cells, *J. Mater. Sci. Mater. Med.* 20 (1) (2009) 347–350.

- [16] G.C. Hadjipanayis, G.A. Prinz (Eds.), *Science and Technology of Nanostructured Materials*, In: NATO ASI Series, Series B, Physics, vol. 259, Plenum Press, New York, 1991, p. 719.
- [17] Q.A. Pankhurst, J. Connolly, S.K. Jones, J. Dobson, *Applications of magnetic nanoparticles in biomedicine*, *J. Phys. D. Appl. Phys.* 36 (13) (2003) R167–R181.
- [18] J.L. Dormann, D. Fiorani, E. Tronc, I. Prigogine, S.A. Rice, *Magnetic relaxation in fine-particle systems*, in: I. Prigogine, S.A. Rice (Eds.), *Advances in Chemical Physics*, vol. 98, Wiley, New York, 1997, pp. 283–494 (Chapter 4).
- [19] D.E. Speliotis, *Magnetic recording beyond the first 100 years*, *J. Magn. Magn. Mater.* 193 (1–3) (1999) 29–35.
- [20] S. García-Jimenoa, J. Estelrich, *Ferrofluid based on polyethylene glycol-coated iron oxide nanoparticles: characterization and properties*, *Colloids Surf. A Physicochem. Eng. Asp.* 420 (2013) 74–81.
- [21] Y.L. Raikher, V.I. Stepanov, J.-C. Bacri, R. Perzynski, *Orientational dynamics of ferrofluids with finite magnetic anisotropy of the particles: relaxation of magneto-birefringence in crossed fields*, *Phys. Rev. E* 66 (2) (2002) 021203.
- [22] C.C. Berry, A.S.G. Curtis, *Functionalisation of magnetic nanoparticles for applications in biomedicine*, *J. Phys. D. Appl. Phys.* 36 (3) (2003) R 198.
- [23] X. Batlle, A. Labarta, *Finite-size effects in fine particles: magnetic and transport properties*, *J. Phys. D. Appl. Phys.* 35 (6) (2002) R15.
- [24] C.P. Bean, J.D. Livingston, *Superparamagnetism*, *J. Appl. Phys.* 30 (4) (1959) S120–S129.
- [25] H. Pfeiffer, *Influence of thermal fluctuations on the magnetic properties of particle assemblies*, *Phys. Status Solidi A* 122 (1) (1990) 377–389.
- [26] J.L. Dormann, D. Fiorani (Eds.), *Magnetic Properties of Fine Particles*, North-Holland, Amsterdam, 1992.
- [27] K. Esumi, *Dendrimers for nanoparticle synthesis and dispersion stabilization*, in: M. Antonietti (Ed.), *Colloid Chemistry II*, Top. Curr. Chem. Series, , vol. 227, Springer, Berlin, Heidelberg, 2003, pp. 31–52 (Chapter 2).
- [28] R.M. Crooks, M. Zhao, L. Sum, V. Chechik, L.K. Yeung, *Dendrimer-encapsulated metal nanoparticles: synthesis, characterization, and applications to catalysis*, *Acc. Chem. Res.* 34 (3) (2001) 181–190.
- [29] P.N. Floriano, C.O. Noble, J.M. Schoonmaker, E.D. Poliakoff, R.L. McCarley, *Cu(0) nanoclusters derived from poly(propylene imine) dendrimer complexes of Cu(II)*, *J. Am. Chem. Soc.* 123 (43) (2001) 10545–10553.
- [30] N.E. Domracheva, A. Mirea, M. Schwoerer, L. Torre-Lorente, G. Lattermann, *Liquid-crystalline dendrimer Cu(II) complexes and Cu(0) nanoclusters based on the Cu(II) complexes: an electron paramagnetic resonance investigation*, *Phys. Solid State* 49 (7) (2007) 1392.
- [31] E. Strable, J.W.M. Bulte, B. Moskowitz, K. Vivekanandan, M. Allen, T. Douglas, *Synthesis and characterization of soluble iron oxide-dendrimer composites*, *Chem. Mater.* 13 (6) (2001) 2201–2209.
- [32] B.L. Frankamp, A.K. Boal, M.T. Tuominen, V.M. Rotello, *Direct control of the magnetic interaction between iron oxide nanoparticles through dendrimer-mediated self-assembly*, *J. Am. Chem. Soc.* 127 (27) (2005) 9731–9735.
- [33] J.H. Cameron, A. Facher, G. Lattermann, S. Diele, *Poly(propyleneimine) dendromesogens with hexagonal columnar mesophase*, *Adv. Mater.* 9 (5) (1997) 398–403.
- [34] B. Donnio, P. Garcia-Vazquez, J.-L. Gallani, D. Guillon, E. Terazzi, *Dendronized ferromagnetic gold nanoparticles self-organized in a thermotropic cubic phase*, *Adv. Mater.* 19 (21) (2007) 3534–3539.
- [35] S. Frein, J. Boudon, M. Vonlanthen, T. Scharf, J. Barbera, G. Süss-Fink, T. Bürgi, R. Deschenaux, *Liquid-crystalline thiol- and disulfide-based dendrimers for the functionalization of gold nanoparticles*, *Helv. Chim. Acta* 91 (12) (2008) 2321–2337.
- [36] J. Boudon, Ph.D. thesis, Université de Neuchâtel, 2009.
- [37] A. Hernando, P. Crespo, M.A. Garcia, *Origin of orbital ferromagnetism and giant magnetic anisotropy at the nanoscale*, *Phys. Rev. Lett.* 96 (5) (2006). 057206.
- [38] N.E. Domracheva, V.I. Morozov, M.S. Gruzdev, R.A. Manapov, A.V. Pyataev, G. Lattermann, *Iron-containing poly(propylene imine) dendromesogens with photoactive properties*, *Macromol. Chem. Phys.* 211 (7) (2010) 791–800.
- [39] M. Gruzdev, N. Usol'seva, L. Torre-Lorente, G. Lattermann, N. Domracheva, *Liquid crystals and their application*, *Russ. J. 4* (2006) 89–94.

- [40] M.S. Gruzdev, Ph.D. thesis, Ivanovo State University (Russia) 2006.
- [41] N.E. Domracheva, A.V. Pyataev, R.A. Manapov, M.S. Gruzdev, Magnetic resonance and mössbauer studies of superparamagnetic γ -Fe₂O₃ nanoparticles encapsulated into liquid-crystalline poly(propylene imine) dendrimers, *ChemPhysChem* 12 (16) (2011) 3009–3019.
- [42] A. Facher, Ph.D. thesis, University of Bayreuth (Germany), 2000.
- [43] L. Torre-Lorente, Ph.D. thesis, University of Bayreuth (Germany), 2007.
- [44] H.C. Choi, W. Kim, D. Wang, H. Dai, Delivery of catalytic metal species onto surfaces with dendrimer carriers for the synthesis of carbon nanotubes with narrow diameter distribution, *J. Phys. Chem. B* 106 (48) (2002). 1236112365.
- [45] R.S. de Biasi, T.C. Devezas, Anisotropy field of small magnetic particles as measured by resonance, *J. Appl. Phys.* 49 (4) (1978) 2466–2469.
- [46] Y.L. Raikher, V.I. Stepanov, Ferromagnetic resonance in a suspension of single-domain particles, *Phys. Rev. B* 50 (9) (1994) 6250–6259.
- [47] R. Berger, J. Kliava, J.-C. Bissey, V. Baietto, Superparamagnetic resonance of annealed iron-containing borate glass, *J. Phys. Condens. Matter* 10 (38) (1998) 8559–8572.
- [48] K. Nagata, A. Ishihara, ESR of ultrafine magnetic particles, *J. Magn. Magn. Mater.* 104–107 (3) (1992) 1571–1573.
- [49] F. Gazeau, V. Shilov, J.C. Bacri, E. Dubois, F. Gendron, R. Perzynski, Y.L. Raikher, V.I. Stepanov, Magnetic resonance of nanoparticles in a ferrofluid: evidence of thermofluctuational effects, *J. Magn. Magn. Mater.* 202 (2–3) (1999) 535–546.
- [50] F. Gazeau, J.C. Bacri, F. Gendron, R. Perzynski, Y.L. Raikher, V.I. Stepanov, E. Dubois, Magnetic resonance of ferrite nanoparticles: evidence of surface effects, *J. Magn. Magn. Mater.* 186 (1–2) (1998) 175–187.
- [51] R. Berger, J. Kliava, J.-C. Bissey, V. Baietto, Magnetic resonance of superparamagnetic iron-containing nanoparticles in annealed glass, *J. Appl. Phys.* 87 (10) (2000) 7389–7396.
- [52] Y.A. Koksharov, S.P. Gubin, I.D. Kosobudsky, M. Beltran, Y. Khodorkovsky, A.M. Tishin, Low temperature electron paramagnetic resonance anomalies in Fe-based nanoparticles, *J. Appl. Phys.* 88 (3) (2000) 1587–1592.
- [53] N. Noginova, F. Chen, T. Weaver, E.P. Giannelis, A.B. Bourlinos, V.A. Atsarkin, Magnetic resonance in nanoparticles: between ferro- and paramagnetism, *J. Phys. Condens. Matter* 19 (24) (2007) 246208 (pp. 1–15).
- [54] G. Ennas, A. Musini, G. Piccaluga, D. Zedda, D. Gatteschi, C. Sangregorio, J. L. Stanger, G. Concas, G. Spano, Characterization of iron oxide nanoparticles in an Fe₂O₃-SiO₂ composite prepared by a sol-gel method, *Chem. Mater.* 10 (2) (1998) 495–502.
- [55] J.L. Gittleman, B. Abeles, S. Bozowski, Superparamagnetism and relaxation effects in granular Ni-SiO₂ and Ni-Al₂O₃ films, *Phys. Rev. B* 9 (9) (1974) 3891–3897.
- [56] P. Dutta, A. Manivannan, M.S. Seehra, N. Shah, G.P. Huffman, Magnetic properties of nearly defect-free maghemite nanocrystals, *Phys. Rev. B* 70 (17) (2004) 174428 (pp. 1–7).
- [57] E. Schmidbauer, R.J. Keller, Magnetic properties and rotational hysteresis of Fe₃O₄ and γ -Fe₂O₃ particles ~250 nm in diameter, *J. Magn. Magn. Mater.* 152 (1–2) (1996) 99–108.
- [58] J.L. Dormann, F.L. D’Orazio, E. Tronc, P. Prene, J.P. Jolivet, D. Fiorani, R. Cherkaoui, M. Nogues, Thermal variation of the relaxation time of the magnetic moment of γ -Fe₂O₃ nanoparticles with interparticle interactions of various strengths, *Phys. Rev. B* 53 (21) (1996) 14291–14297.
- [59] L. Zhang, G.C. Papaefthymiou, J.Y. Ying, Size quantization and interfacial effects on a novel γ -Fe₂O₃/SiO₂ magnetic nanocomposite via sol-gel matrix-mediated synthesis, *J. Appl. Phys.* 81 (10) (1997) 6892–6900.
- [60] A.F. Abdullin, A.V. Pyataev, N.E. Domracheva, M.S. Gruzdev, Mössbauer study of the surface of core-shell type nanoparticles, *J. Surf. Invest.: X-Ray, Synchrotron Neutron Tech.* 10 (1) (2016) 35–38.
- [61] L.T. Kuhn, A. Bojesen, L. Timmermann, K. Fauth, E. Goering, E. Johnson, M.M. Nielsen, S. Mørup, Core-shell iron-iron oxide nanoparticles: magnetic properties and interactions, *J. Magn. Magn. Mater.* 272–276 (2) (2004) 1485–1486.
- [62] R.M. Cornell, U. Schwertmann (Eds.), *The Iron Oxides: Structure, Properties, Reactions, Occurrences and Uses*, Wiley-VCH Verlag GmbH, Weinheim, 2003, p. 703.

- [63] A. Kudo, Y. Miseki, Heterogeneous photocatalyst materials for water splitting, *Chem. Soc. Rev.* 38 (2009) 253–278.
- [64] K.G.U. Wijayantha, D.H. Auty, *Encyclopaedia of Materials: Science and Technology Updates*, Elsevier, Oxford, 2005, 15.
- [65] R.F. Ziolo, E.P. Giannelis, B.A. Weinstein, M.P. O'Horo, B.N. Ganguly, V. Mehrotra, M.W. Russell, D. R. Huffman, Matrix-mediated synthesis of nanocrystalline γ -Fe₂O₃: a new optically transparent magnetic material, *Science* 257 (5067) (1992) 219–223.
- [66] M. Chirita, I. Grozescu, Fe₂O₃-nanoparticles, physical properties and their photochemical and photoelectrochemical applications, *Chem. Bull. "Politehnica" Univ. (Timisoara)* 54 (68) (2009) 1–8.
- [67] I.S. Jacobs, C.P. Bean, Fine particles, thin film and exchange anisotropy, in: G.T. Rado, H. Suhl (Eds.), *Magnetism*, vol. III, Academic Press, New York, 1963, pp. 271–350.
- [68] E.M. Chudnovsky, L. Gunther, Quantum tunneling of magnetization in small ferromagnetic particles, *Phys. Rev. Lett.* 60 (8) (1988) 661–664.
- [69] A.J. Leggett, S. Chakravarty, A.T. Dorsey, M.P.A. Fisher, A. Garg, W. Zuerger, Dynamics of the dissipative two-state system, *Rev. Mod. Phys.* 59 (1) (1987) 1–85.
- [70] F.T. Parker, M.W. Foster, D.T. Margulies, A.E. Berkowitz, Spin canting, surface magnetization, and finite-size effects in γ -Fe₂O₃ particles, *Phys. Rev. B* 47 (13) (1993) 7885–7891.
- [71] A.L. Efros, M. Rosen, The electronic structure of semiconductor nanocrystals, *Annu. Rev. Mater. Sci.* 30 (2000) 475–521.
- [72] J.I. Pankove, *Optical Processes in Semiconductors*, Prentice-Hall, New Jersey, 1971, 422.
- [73] S. Chakrabarti, D. Ganguli, S. Chaudhuri, Optical properties of γ -Fe₂O₃ nanoparticles dispersed on sol-gel silica spheres, *Phys. E* 24 (2004) 333–342.
- [74] D. Bhattacharyya, S. Chaudhuri, A.K. Pal, Bandgap and optical transitions in thin films from reflectance measurements, *Vacuum* 43 (4) (1992) 313–316.
- [75] M. Franckevičius, J. Tamulienė, J. Babonas, I. Šimkienė, L. Rasteniene, A. Kulbickas, A. Iržikevičius, R. Vaišnoras, UV spectral features of poly(propylene imine) dendrimers, *Lith. J. Phys.* 51 (3) (2011) 207–211.
- [76] M.V. Kharlamova, N.A. Sapoletova, A.A. Eliseev, I.P. Suzdalev, Y.V. Maksimov, A.V. Lukashin, Y. D. Tret'yakov, Optical properties of nanostructured γ -iron oxide, *Dokl. Chem.* 415 (1) (2007) 176–179.
- [77] M.V. Kharlamova, N.A. Sapoletova, A.A. Eliseev, A.V. Lukashin, Optical properties of γ -ferric oxide nanoparticles in a mesoporous silica matrix, *Tech. Phys. Lett.* 34 (4) (2008) 288–291.
- [78] A.I. Ekimov, A.A. Onushchenko, Quantum size effect in semiconductor three-dimensional microcrystals, *Pis'ma Zh. Eksp. Teor. Fiz.* 34 (1981) 363–366.
- [79] M.L. Neel, Proprietes magnetiques des ferrites; ferrimagnetisme et antiferromagnetisme, *Ann. Phys.* 12 (3) (1948) 137–198.
- [80] G.A. Waychunas, Crystal chemistry of oxides and oxyhydroxides, *Rev. Mineral. Geochem.* 25 (1) (1991) 11–68.
- [81] I.R. Macdonald, R.F. Howe, S. Saremi-Yarahmadi, K.G.U. Wijayantha, Photoinduced superparamagnetism in nanostructured α -Fe₂O₃, *J. Phys. Chem. Lett.* 1 (2010) 2488–2492.
- [82] N. Noginova, T. Weaver, E.P. Giannelis, A.B. Bourlinos, V.A. Atsarkin, V.V. Demidov, Observation of multiple quantum transitions in magnetic nanoparticles, *Phys. Rev. B* 77 (1) (2008) 014403 (pp. 1–5).
- [83] M.M. Noginov, N. Noginova, O. Amponsah, R. Bah, R. Rakhimov, V.A. Atsarkin, Magnetic resonance in iron oxide nanoparticles: quantum features and effect of size, *J. Magn. Magn. Mater.* 320 (18) (2008) 2228–2232.
- [84] N. Noginova, Y. Barnakov, A. Radocea, V.A. Atsarkin, Role of dipole-dipole interactions in half-field quantum transitions in magnetic nanoparticles, *J. Magn. Magn. Mater.* 323 (17) (2011) 2264–2270.
- [85] M. Fittipaldi, C. Innocenti, P. Ceci, C. Sangregorio, L. Castelli, L. Sorace, D. Gatteschi, Looking for quantum effects in magnetic nanoparticles using the molecular nanomagnet approach, *Phys. Rev. B* 83 (10) (2011) 104409 (pp. 1–10).
- [86] M. Fittipaldi, R. Mercatelli, S. Sottini, P. Ceci, E. Falvo, D. Gatteschi, Sensing the quantum behaviour of magnetic nanoparticles by electron magnetic resonance, *Phys. Chem. Chem. Phys.* 18 (2016) 3591–3597.

- [87] Y.L. Raikher, V.I. Stepanov, Magnetization dynamics of single-domain particles by superparamagnetic theory, *J. Magn. Magn. Mater.* 316 (2) (2007) 417–421.
- [88] N. Domracheva, V. Vorobeva, M. Gruzdev, A. Pyataev, Blue shift in optical absorption, magnetism and light-induced superparamagnetism in γ -Fe₂O₃ nanoparticles formed in dendrimer, *J. Nanopart. Res.* 17 (2) (2015)83 (pp. 1–8).
- [89] Stefan Stoll, <http://easyspin.org/easyspin/documentation/references.html> (accessed 17.05.17).

This page intentionally left blank

Magnetic Disorder in Nanostructured Materials

Giuseppe Muscas*, Nader Yaacoub†, Davide Peddis‡

*Department of Physics and Astronomy, Uppsala University, Uppsala, Sweden, †Institute of Molecules and Materials of Le Mans CNRS UMR-6283, University of Le Mans, Le Mans, France, ‡Institute of Structure of Matter—CNR, Monterotondo Scalo, Rome, Italy

4.1 Introduction

A physical property depends on the size of an object, if its size is comparable to a dimension relevant to that property. In magnetism, typical sizes—as for example the dimensions of magnetic domains or lengths of exchange coupling interactions affecting the polarization of neighboring ferromagnetic particles—are in the nanometer range. For this reason, starting a few decades ago, great attention has been directed toward nanostructured magnetic materials, where the term nanostructured describes materials with constituent phase or grain structures modulated on a length scale from 1 to 100 nm [1].

Among nanostructured materials, magnetic nanoparticles (MNPs) are unique complex physical objects whose physical properties differ greatly from their parent massive materials. The magnetic properties are particularly sensitive to the particle size, being determined by finite size effects on the core properties, related to the reduced number of spins cooperatively linked within the particle, and by surface effects, becoming more important as the particle's size decreases [2,3]. The modification of the structural and electronic properties near and at the particle surface results in breaking of lattice symmetry and broken bonds, which give rise to site-specific surface anisotropy, weakened exchange coupling, magnetic frustration, and spin disorder. Such disorder may propagate from the surface to the particle core, such that the picture of the particle as a perfectly ordered single domain, whose spins rotate in a synchronous way as a large single spin, is no longer valid [4–8]. Among nanoscaled magnetic materials, nanoparticles of iron oxide with a spinel structure (MeFe_2O_4 , $\text{Me} = \text{Fe}^{2+}$, Co^{2+} , Ni^{2+} , Mg^{2+} , Mn^{2+} , Zn^{2+} , etc.) have generated great interest not only because of their technological applications but also from the point of view of fundamental science. In fact, the structural properties and the rich crystal chemistry of spinels offer excellent opportunities for understanding and finetuning the magnetic properties. In addition, they are good model

systems for studies on the relationship between magnetic behavior and magnetic structure at the atomic level [9,10].

The aim of this chapter is to gain a better insight into the effect of magnetic disorder and, more in general of the spin structure, on magnetic properties of nanoparticles. Due to their rich crystal chemistry, nanoparticles of spinel ferrites will be taken as a model system.

After a short overview on magnetism at the nanoscale (Section 4.2), in Section 4.3 a physical description of magnetic disorder (i.e., spin canting) and experimental investigation of spin structure, mainly by Mössbauer spectrometry under intense magnetic field, will be given. Section 4.4 will be devoted to show the effect of magnetic disorder on macroscopic magnetic properties of nanoparticle systems, highlighting the complex relationship between cationic distribution and spin canting in nanoscaled spinel ferrites. In addition, particular attention will be given on the possibility to have a “molecular control” of magnetic disorder, discussing the role of molecules bonded on particles surface [11–19]. In fact, the role of surfactant is not limited to the synthesis process of nanoparticles, and it can affect also the magnetic properties of the material, allowing to modify the whole particle anisotropy [20], with visible effects on the coercive field [21], and the saturation magnetization [22,23]. Finally (Section 4.5), new perspectives in the investigation of magnetic disorder at the nanoscale will be discussed.

4.2 Magnetism in Nanostructures: An Overview

Broadly speaking, the physical properties of a material are size dependent, being the results of phenomena that occur only at a specific size scale [1,9]. On entering the nanometer-scale regime, the magnetic properties of condensed matter show substantial differences with respect to the bulk state, leading to new physics [2,26,27] and applications [1,28].

One of the breakthrough points for magnetic materials occurs when their constituents undergo a critical radius below which a single domain configuration, with all atomic moments aligned in the same direction, becomes energetically more convenient than a multidomain one. Such critical radius r_c is characteristic for each material and, for systems with uniaxial anisotropy, it can be written as:

$$r_c \approx 9 \frac{(AK)^{\frac{1}{2}}}{\mu_0 M_S^2} \quad (4.1)$$

where A is the exchange constant, K is the anisotropy constant, and μ_0 is the vacuum magnetic permeability. Typical values of r_c are ~ 15 nm for Fe, ~ 35 nm for Co, ~ 30 nm for γ -Fe₂O₃, ~ 55 nm for Ni, and ~ 750 nm per SmCo₅ [29]. Such entities act as single magnetic domains with a compressive magnetic moment of $\sim 10^3$ – $10^5 \mu_B$. They are similar to atomic moments in paramagnetic materials, but with a much larger magnetization magnitude and a specific time scale for the magnetization reversal; for this reason, they are often defined as *superspins* [29].

4.2.1 Magnetic Anisotropy at the Nanoscale

The internal energy of a superspin varies for different orientation of the magnetization, describing a specific anisotropy symmetry with easy and hard directions of alignment separated by a magnetic anisotropy energy (MAE) barrier that is affected by different components. Fig. 4.1 shows a sketch of the field dependence of the magnetization recorded with the magnetic field applied parallel to an easy and a hard axis.

In a certain materials, the crystalline structure and its symmetry induce the so-called magnetocrystalline anisotropy [30]. In the simplest case of a spherical particle with uniaxial magnetocrystalline anisotropy (i.e., a single easy axis in which the alignment of the magnetization is favored), the magnetization can switch between the two antiparallel easy directions overcoming the energy barrier defined as:

$$E_a^{uni} = K_1 V \sin^2 \theta + K_2 V \sin^4 \theta + \dots \approx KV \sin^2 \theta \quad (4.2)$$

where the magnetocrystalline anisotropy energy constant K can be approximated to K_1 , being $K_1 \gg K_2, K_3, \dots$, V is the particle volume, and ϑ represents the angle between the easy axis and the magnetization.

The first source of magnetocrystalline anisotropy is the single ion contribution. For a specific atomic site, the crystal field tends to stabilize a particular orbital and, due to the spin-orbit coupling, this effect stabilizes a specific orientation of spins along a given crystallographic orientation [31]. A second contribution arises from the dipolar coupling among moments,

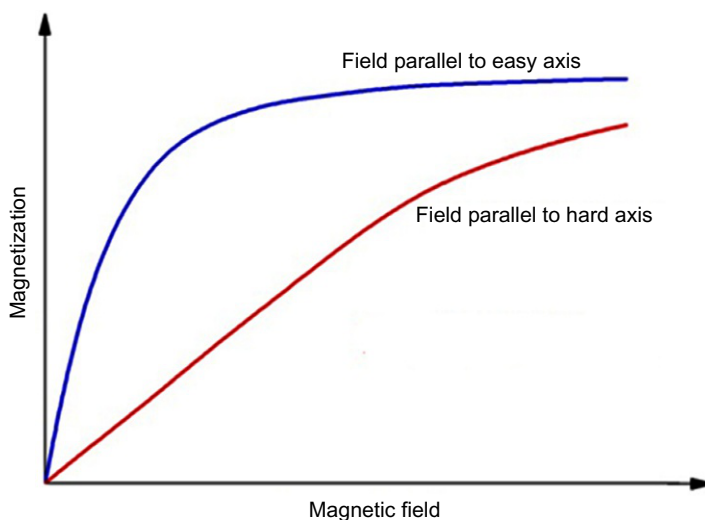


Fig. 4.1

Examples of magnetization curves recorded with the magnetic field applied parallel to an easy axis and a hard axis.

which tend to align head to tail, owing such configuration the minimal energy. The dipole sum has to be extended to the whole lattice, and for certain lattices (e.g., all cubic ones) it can vanish [30,32].

The shape of the monodomain entity plays an additional role. For a sample with magnetization M_i along a specific axis i , a corresponding internal magnetization field H_i^d can be defined:

$$H_i^d = -N_i M_i \quad (4.3)$$

where N_i is the demagnetizing factor along that axis. For a sphere, the N factors are equal to $1/3$ in all x - y - z axis, resulting in an isotropic demagnetization field, then no shape anisotropy appears. For particles with elongated shape, a smaller demagnetizing field emerges for the long axis, due to the larger distance of the two magnetic poles. Thus, for a general uniform magnetized ellipsoid of revolution around the z axis, the difference in energy when the ellipsoid is magnetized along its hard and easy directions represents the shape anisotropy E_a^{shape} :

$$E_a^{shape} = \frac{1}{2} \mu_0 V M_S^2 (N_z \cos^2 \vartheta + N_x \sin^2 \vartheta) \quad (4.4)$$

where the $N_x = N_y$, and N_z represent the demagnetization factors and M_S the saturation magnetization.

A further anisotropy energy can come from a stress applied to a material that can modify its magnetic structure. Similarly, an external applied field can induce a distortion in the crystalline structure, modifying the shape of the crystal. Such anisotropy energy can be defined as:

$$E_a^{strain} = -\frac{3}{2} \lambda_S \sigma S \cos^2 \vartheta' \quad (4.5)$$

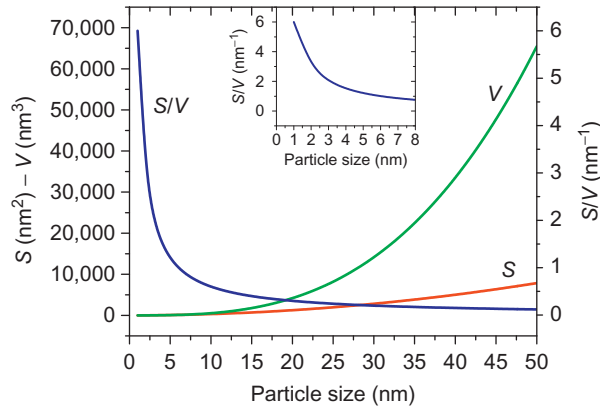
where λ_S is the saturation magnetostriction, σ is the strain value by surface unit, S is the particle surface, and ϑ' is the angle between the magnetization and the strain tensor axis.

A further contribution to the anisotropy energy comes from the broken symmetry at particles surface. This reduces the nearest-neighbors' coordination leading to a different local magneto-crystalline anisotropy. Reducing particles size, the surface-to-volume ratio increases; thus, smaller particles manifest larger effect of surface anisotropy (Fig. 4.2). For the simple case of small spherical particles with diameter d , the effective anisotropy constant can be defined as:

$$K_{eff} = K + \frac{6}{d} K_S \quad (4.6)$$

where K and K_S represent the magnetocrystalline and surface component of anisotropy, respectively [33].

The magnetic interaction between two different phases at nanoscale represents an additional source of the anisotropy, which can be exploited to modify and improve the magnetic

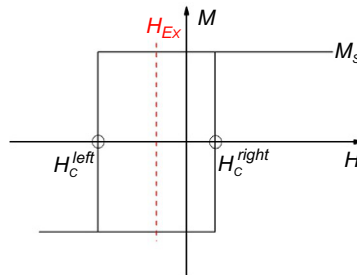

Fig. 4.2

Assuming nanoparticles with spherical shape, their surface (S) and volume (V) are calculated and plotted as function of the particle diameter. Inset: detail of S/V vs particles' diameter.

properties, designing new composite materials. In 1956, Meiklejohn and Bean reported a new source of anisotropy arising from the interface exchange coupling between an AFM and a FM material [34]. They studied an FM/AFM core/shell structure of Co/CoO. When such system was cooled from $T_N < T < T_C$ to a temperature $T < T_N$ under an applied magnetic field, the AFM spins were aligned parallel to the FM spins at interface. Measuring the $M(H)$ loop at that temperature, the exchange coupling makes easier for the FM component to align parallel to the surface spins of the AFM phase, requiring a higher opposite field to reverse the magnetization, and producing a loop shifted toward negative fields (Fig. 4.3).

The field corresponding to the shifting of the loop is defined as exchange bias field (E_{ex}), which is evaluated with the relation:

$$E_{ex} = \frac{\mu_0 H_C^{left} + \mu_0 H_C^{right}}{2} \quad (4.7)$$


Fig. 4.3

Sketch of an $M(H)$ curve showing exchange bias after field cooling.

where $\mu_0 H_C^{left}$ and $\mu_0 H_C^{right}$ are the coercive field measured in the negative and positive part of the field axis, respectively (Fig. 4.3). This effect has been reported to increase the anisotropy energy of a Co/CoO system embedded in a CoO matrix, up to 2 orders of magnitude [35]. Exchange coupled bimagnetic hard/soft and soft/hard magnetic core/shell nanoparticles represent a strong field of interest since they allow to combine and improve the magnetic properties of the original materials creating new multiphase compounds, which find applications in several fields, from permanent magnets, to magnetorecording, microwave adsorption, or biomedical applications [36].

4.2.2 Superparamagnetism

As discussed before, in case of uniaxial anisotropy, the effective anisotropy energy of a monodomain nanoparticles can be defined as:

$$E_d^{eff} \approx K_{eff} V \sin^2 \theta \quad (4.8)$$

Its value reaches a minimum for the two antiparallel easy axis orientations and the maximum when it is perpendicular to those. Such energy is proportional to the effective anisotropy constant of the material and to the particles' volume (Fig. 4.4).

For a system of single domain particles with uniaxial anisotropy, at a temperature high enough such as the thermal energy $k_B T \gg K_{eff} V$, the superspins can freely rotate and the magnetization process can be treated with the Langevin model for atomic paramagnetism. Under the influence of an applied magnetic field $\mu_0 H$, a particle with total dipolar moment m owns an average effective dipole moment in the field direction z that is $m_z = mL(x)$, where $L(x) = \coth(x) - 1/x$ is the Langevin function, and $x = \mu_0 mH/k_B T$.

Due to the enhanced time and magnetization scale with respect to atomic systems, the suffix super has been used, and this paramagnetic-like behavior is called *superparamagnetism*.

When the thermal energy is larger but comparable to the anisotropy energy, the magnetization process significantly differs from the Langevin model [37], due to the measurable effect of the anisotropy energy barrier. The magnetostatic energy of a particle with superspin moment m_p can be defined as:

$$E_m = -(K_{eff} V) \cos^2 \theta - \mu_0 \vec{\mu}_p \cdot \vec{H} \quad (4.9)$$

The switching between the two energy minima happens with a given frequency (f), which corresponds to a relaxation time $\tau = 1/(2 \pi f)$ described by the Néel-Brown relation [38,39]:

$$\tau = \tau_0 \exp \left[\frac{K_{eff} V}{k_B T} \right] \quad (4.10)$$

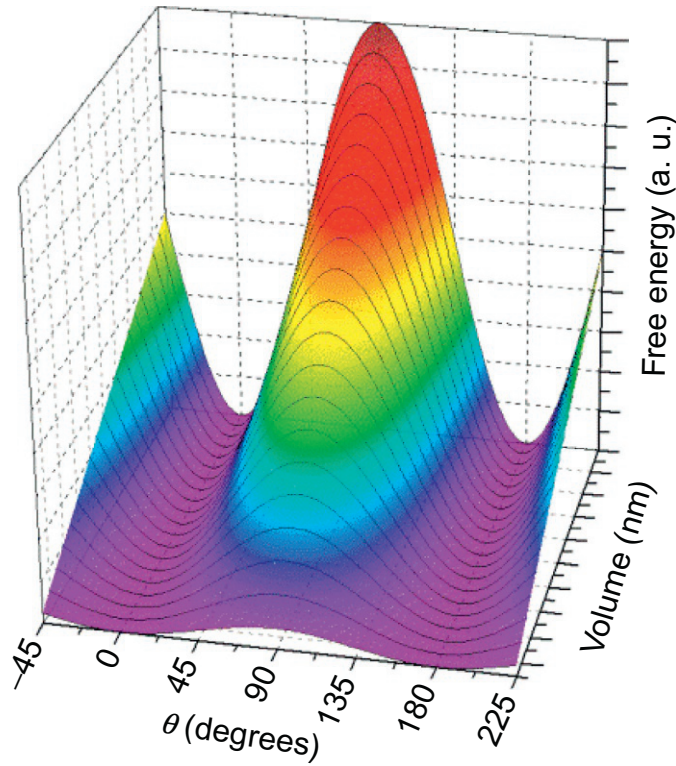


Fig. 4.4

Dependence of the magnetic anisotropy energy from the angle between the particle magnetization and the anisotropy easy axis. Furthermore, the dependence from particles volume is considered.

where k_B is the Boltzmann constant and τ_0 represents the inverse attempt frequency. The system appears static when the superparamagnetic (SPM) relaxation time τ becomes much longer than the experimental measuring time τ_m . For a given experimental technique, these two quantities become comparable only at a specific temperature, at which the system appears as “blocked.” Hence, the corresponding blocking temperature can be defined as:

$$T_B = \frac{K_{eff}V}{k_B \ln(\tau_m/\tau_0)} \quad (4.11)$$

At a temperature low enough such as $k_B T < K_{eff}V$, the magnetization reversal of a single domain particle is described by the Wohlfarth and Stoner model (WS) [40]. According to that, the free energy of the particles is related to the applied field $\mu_0 H$ and to the angles φ and ϑ , which the field and the particle moment μ_p form with respect to the easy axis (Fig. 4.5):

$$E = K_{eff}V \sin^2\theta - m\mu_0 H \cos(\varphi - \theta) \quad (4.12)$$

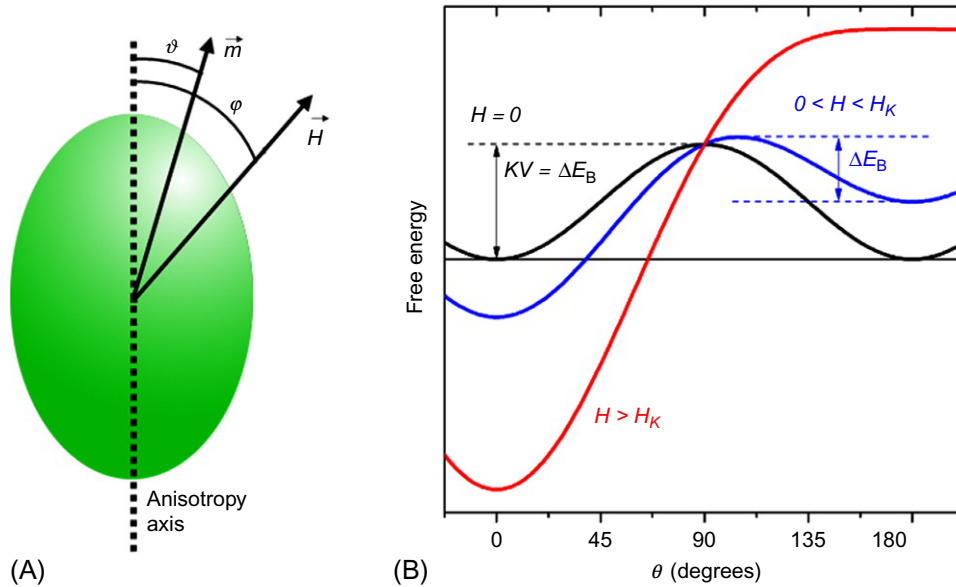


Fig. 4.5

(A) Sketch of the magnetization reversal for a monodomain particle with uniaxial anisotropy with an applied field H . (B) The dependence of the free energy from the angle between the easy axis and the magnetization is reported for different applied fields.

The application of an external field reduces the anisotropy energy barrier according to the relation $\Delta E_B = KV(1 - \mu_0 H / \mu_0 H_K)$ [41], up to force the alignment of the particle along its direction.

According to the WS model, the $M(H)$ curve can show hysteresis and the reversal of the magnetization at a coercive field $\mu_0 H_C$. No hysteresis occurs for $\varphi = 90$ degrees, while the curve shows squared shape for a field applied parallel ($\varphi = 0$ degree) or antiparallel ($\varphi = 180$ degrees) to the easy axis. In this condition, the coercive field reaches its maximum value defined as the anisotropy field $\mu_0 H_K = 2K/M_S$. For an ensemble of particles with randomly distributed orientation of easy anisotropy axis, the $M(H)$ curve shows hysteresis with a ratio between the remnant magnetization M_R (at $H=0$) and the saturation magnetization M_S equal to $M_{red} = M_R/M_S = 0.5$. Furthermore, it is possible to identify a coercive field $H_C = 0.48 \mu_0 H_K$ as the field necessary to reduce to zero the magnetization [26].

4.2.3 Magnetic Interactions at the Nanoscale: Supermagnetism

Interparticle interactions show a deep influence on the magnetic behavior of an ensemble of superspins. Depending on the type (e.g., dipolar interaction, exchange interaction) and the strength of the interactions, the magnetic behavior of an assembly of superspins can evolve

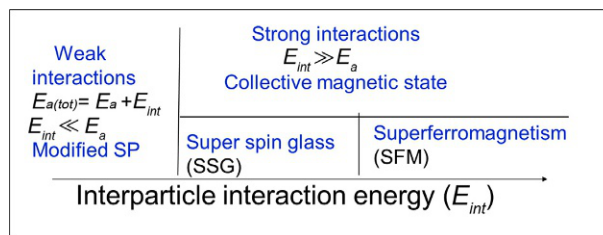


Fig. 4.6
Supermagnetism.

from ferromagnetic (FM)-like behavior to paramagnetic-like behavior, through spinglass-like behavior. In analogy to what discussed previously, due to the enhanced time and magnetization scale of superspins with respect to atomic systems, these interacting magnetic states are called superferromagnetism (SFM), and superspinglass (SSG) [26,42,43]. Thus the magnetism of nanoparticle assemblies, including SPM, SFM, and SSG, has been often called *supermagnetism* [26,29,44,45] (Fig. 4.6).

For an ensemble of monodomain particles of average moment μ_p and average distance d , the energy of dipolar interactions can be evaluated as:

$$E_{dip} \approx \frac{\mu_0 \mu_p^2}{4\pi d^3} \quad (4.13)$$

In case of atoms, such energy owns almost negligible values of $10^{-23} J \approx 1 \text{ K}$, due to the low magnitude of the atomic moments (few μ_B), and their distance (0.1–1 nm) in the crystalline lattice. Replacing atoms with the moments of superspins (10^3 – $10^5 \mu_B$), and considering interparticle distances of few nm, the energy involved rises up to tens of K [45]. The influence of dipolar interaction can produce an increment in the effective anisotropy, increasing the blocking temperature and inducing a modified SPM behavior [29,46]. In case of concentrated particles' systems, dipolar interactions can be strong enough to produce a collective behavior, which, due to the intrinsically anisotropic character of the dipolar interactions, leads to frustrated magnetic order, in a spin-glass like or superspin glass (SSG) behavior [45,47].

In case of particles in close contact, *exchange coupling* can occur for surface atomic spins through the overlapping of magnetic orbitals (direct exchange). Interparticle exchange interactions can be described by using the Heisenberg spin Hamiltonian [30,31]:

$$H_{exc} = 2 \sum_{i,j} J_{i,j} \vec{S}_i \cdot \vec{S}_j \quad (4.14)$$

where $J_{i,j}$ is the exchange integral describing the magnitude of coupling between the spins \vec{S}_i and \vec{S}_j . Such interactions are responsible for long-range magnetic order and

superferromagnetic (SFM) behavior can be expected for an assembly of strong exchange coupled superspins [29,43].

In case of particles embedded in an insulating matrix, intermediate atoms or ions (e.g., oxygen) can act like bridge for indirect superexchange interactions among magnetic atoms [30].

On the other hand, for metallic particles in a metallic matrix, RKKY (Ruderman-Kittel-Kasuya-Yosida) interactions can occur among electrons of inner *d* or *f* shells through conduction electrons [48–50]. Indirect exchange interactions can manifest also by tunnel effect, but only across a barrier of few tenths of nm among particles' surface [51,52].

4.3 Magnetic Disorder at the Nanoscale

Generally speaking, certain magnetic materials exhibit a noncollinear spin structure where the spins are not perfectly magnetically ordered, exhibiting a certain degree of disorder. This magnetic disorder can be due to the competition between ferromagnetic and antiferromagnetic exchange interactions [53–55], allowing frustrated interactions as in topological glasses, spin glasses, and substitutional alloys [55a,55b]. Geometric frustration of antiferromagnetic interactions allows also to natural noncollinear spin structure: Triangular, Kagomé, and tetrahedral lattices are some examples of crystal lattices where nearest-neighbor interactions are naturally frustrated [55c,55d]. The competition between exchange interactions and magnetic anisotropy also contributes to noncollinear magnetism.

In this general framework, a key point is to understand the nature of the magnetic ground state in disordered materials. In amorphous oxide, when exchange is antiferromagnetic, topological disorder leads to frustration of the individual superexchange bonds, the atomic spins are frozen in essentially random orientations with an isotropic probability distribution. Site-averaged spin correlations rapidly average to zero at longer distances. This random spin freezing is known as *speromagnetism* [56]. This type of magnetic order was originally established in 1973 from consideration of the magnetic properties and Mössbauer spectra of a finely divided, amorphous natural ferric gel [57,58]. Other types of highly frustrated magnetism are the so-called *Asperomagnetism* and *Sperimagnetism*. *Asperomagnetism* is an intermediate situation when random spin freezing arises. This behavior is observed when the exchange distribution is broad, but biased toward a net positive value, allowing local net magnetization. A *Sperimagnetic* structures could be observed in the case of two topological amorphous sublattices, as for example binary amorphous alloys made of two elements A and B, if A-A and B-B ferromagnetic interactions, and A-B antiferromagnetic interactions are present. They couple two asperomagnetic “sublattices,” or an asperomagnet and a ferromagnet [58,59].

This quite complex framework becomes even more complex and more fascinating at the nanoscale. In fact, in magnetic nanostructures, and especially in small (<5 nm) nanoparticles,

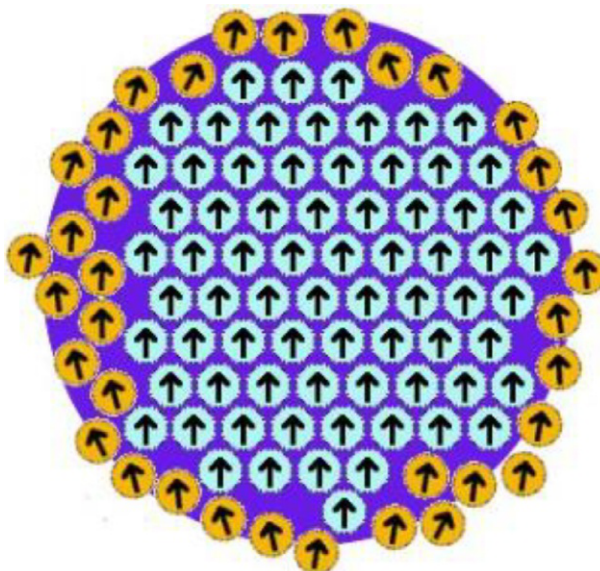


Fig. 4.7

Graphical sketch of surface disorder of magnetic moments.

magnetic properties differ in many aspects from those of the corresponding bulk materials [4,10,60] due to finite-size effects and surface effects. Surface effects result from the symmetry breaking of the crystal structure at the surface or the boundary of the particle, dangling bonds, oxidation, surface strain. Surface atoms experience different environments than those in the core of the particle due to changes in the coordination, the presence of certain vacancies, and lattice disorder (Fig. 4.7). Several magnetic effects could result from the finite size and surface effects of nanoparticles, including the existence of randomly oriented uncompensated spins, canted spins, a spin-like glass behavior of surface spins, magnetically dead surface layer, in addition to the enhancement of magnetic anisotropy, which results from surface anisotropy [6,33,61,62]. The symmetry breaking at the surface induces changes in exchange integrals, related to the variation of superexchange angles and/or distances among moments, giving rise to topological magnetic frustration. Consequently, a noncollinear structure (spin canting) at the particle surface may occur.

4.3.1 Noncollinear Spin Structure in Nanostructured Spinel Ferrites

Among the magnetic nanomaterials, spinel structure ferrite nanoparticles (MeFe_2O_4 , $\text{Me} = \text{Fe}^{2+}$, Co^{2+} , Ni^{2+} , Mg^{2+} , Mn^{2+} , Zn^{2+} , etc.) have attracted a lot of attention. This is both because of the variety of their rich crystal chemistry, allowing a fine tuning of the physical properties (magnetic, electronic, transport, etc.), and for their application in several fields (biomedicine, catalysis, electronics) [1,63–65]. The spinel oxides have a general chemical

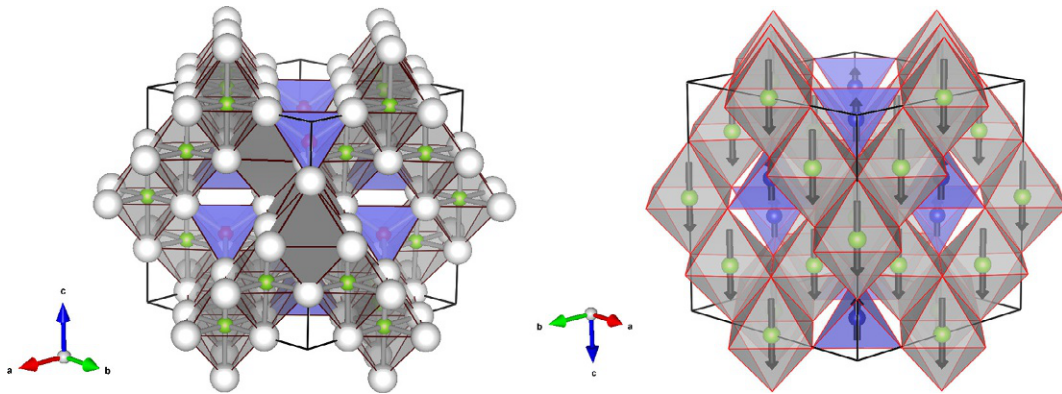


Fig. 4.8

(left-side) Graphical sketch of the crystalline normal spinel structure highlighting the two interstitial site with octahedral [B, gray] and tetrahedral (A, blue (*light gray in print*)) oxygen coordination. Blue (*light gray in print*) and red (*dark gray in print*) spheres represent Y^{3+} and a X^{2+} cations, respectively; (right-side) schematic representation of the magnetic structure in normal spinel: the dominant intralattice J_{AA} interactions induce a noncompensated antiferromagnetic (ferrimagnetism) order between A and B sublattices. Black arrows represent magnetic moments, with module proportional to the length, associated to magnetic cations.

formula $X^{2+}Y_2^{3+}O_4$ where X and Y are cations of a transition material. The associated space group is $Fd\bar{3}m$. Oxygen anions O^{2-} crystallize in a centered cubic stack, defining tetrahedral and octahedral sites into which the metal cations will be inserted. The tetrahedral sites are designated by (A) and the octahedral sites by [B]. The unit cell consists of 8 formulas; we have 32 oxygen atoms generating 64 A sites where usually the eighth is occupied; and 32 sites B, half of which is occupied. If the divalent cations occupy the site A and the trivalent cations occupy the site B, this leads to a direct spinel structure $(X^{2+})[Y^{3+}]_2O_4$. In the case where the divalent cations occupy the site A and the trivalent cations are distributed equally between the sites A and B, one speaks of an inverse spinel structure $(Y^{3+})[X^{2+}Y^{3+}]_2O_4$ (Fig. 4.8 left-side). Generally, the cationic distribution in the tetrahedral and octahedral sites is defined by the degree of inversion γ , which is defined as the fraction of divalent ions in the octahedral sites.

The spinel structure of ferrites (i.e., compounds where $Y^{3+} = Fe^{3+}$) are ferrimagnetic materials (Néel theory) below a critical temperature (Curie temperature, T_c) [27]. The magnetic order in these structures results from exchange interactions between A sites (denoted J_{AA}), between sites B (denoted J_{BB}) and between sites A and B (denoted J_{AB}). The exchange mechanisms are mainly the superexchange and the double exchange via oxygen. It should be noted that the interaction between the (A) and [B] site ions is antiferromagnetic, and this interaction is ~ 10 times greater than the J_{AA} and J_{BB} interactions. Therefore, J_{AB} is dominant and consequently imposes an uncompensated antiferromagnetic order called ferrimagnetism

(Fig. 4.8-right side) [1,9]. Therefore, the net magnetization can be considered proportional to the difference between A and B sublattices magnetization [66]. Also the magnetic anisotropy is related to the cationic distribution because single-ion anisotropy of divalent ions depends on its interstitial site. As an example, (Co^{2+}) located in tetrahedral sites (${}^4\text{A}_2$ crystal field ground energy term, -79×10^{-24} J/ion) shows a lower single anisotropy compared to Co^{2+} in octahedral sites ($+850 \times 10^{-24}$ J/ion,). The larger magnetocrystalline anisotropy of [Co^{2+}] is related to the orbital contribution in the ${}^4\text{T}_1$ ground energy term [10].

Of course, the superexchange coupling is related to the chemical compositions and the crystallographic structure of the materials. In fact, the J_{AA} , J_{BB} , and J_{AB} couplings depend on the metal nature of the X^{2+} , its position in the interstitial sites, and the superexchange angle. For example, in CoFe_2O_4 the [Fe^{3+}] $-\text{O}^{2-}$ $-(\text{Co}^{2+})$ superexchange interactions are weaker than those of [Fe^{3+}] $-\text{O}^{2-}$ $-(\text{Fe}^{3+})$, and in the case of MnFe_2O_4 [Mn^{2+}] $-\text{O}^{2-}$ $[\text{Mn}^{2+}]$ are negligible with respect to (Mn^{2+}) $-\text{O}^{2-}$ $-(\text{Mn}^{2+})$ [67,68]. Therefore, the choice of the chemical nature of X^{2+} and the control of the cationic distribution will allow to master the spin structure and consequently to obtain different magnetic behaviors of the spinel ferrites [69–72]. Generally speaking, the spin canting in spinel ferrites nanostructures may be explained in terms of the Yafet-Kittel triangular arrangement due to the magnetic frustration resulting from the competition between A-B and B-B exchange interactions [73–75]. More recently, several studies on CoFe_2O_4 noninteracting nanoparticles [4,9,10,76] show a direct correlation between cationic distribution and superexchange interactions giving rise to magnetic topological frustration and, consequently, spin canting occurs. Finally, when the assembly consists of interacting particles, the role of dipolar interactions does also contribute to the noncollinear magnetic structure [76a,b], although this effect will not be discussed in this chapter. From this simple description, it is clear that the magnetic properties of the spinel structure can be explained by the magnetic couplings. At the nanoscale, the presence of spin canting makes physical properties more difficult to control and predict. Thus, the magnetic properties of nanoparticles of spinel structure ferrites are due to a complex competition between different effects, among which the cationic distribution and the spin “canting” play a fundamental role.

4.3.2 Experimental Investigation of Magnetic Disorder: Mössbauer Spectrometry

Investigation of the spin structure (spin disorder, spin canting, etc.) and the correlation with magnetic and structural properties are key points to understand the behavior of magnetic nanostructures. Neutron Diffraction represents a powerful tool to investigate spin structure, this technique being sensitive to the reduction of local magnetic moment [77]. Spin disorder was investigated in maghemite nanoparticles by a combination of polarized small-angle neutron scattering and nuclear forward-scattering techniques. Both methods are sensitive to magnetization on the nanoscale and they allow investigating of the particle

morphology and spatial magnetization distribution and the orientation of the hyperfine field experienced by the iron nuclei [78–80]. X-ray magnetic circular Dichroism (XMCD) can be also used to investigate spin structure by studying the contribution of each local moment. In general, the correlation between these techniques and the macroscopic ones, such as SQUID magnetometry leads to a detailed description of the complex spin structure in the magnetic nanostructures [81,82]. Among these techniques, especially when measurements are performed under intense magnetic field, Mössbauer spectrometry plays a relevant role to have a quantitative description of the spin structure.

^{57}Fe Mössbauer spectrometry (MS) is a selective nuclear technique, which appears as an excellent tool to provide local information (local electron density, effective magnetic moment, etc.) of Fe-containing nanostructured materials, particularly about their magnetic spin structure, through the hyperfine parameters. Indeed, it is able to distinguish the different iron species, including their spin and valence states, according to their atomic arrangement (i.e., crystalline grains and disordered grain boundaries) and to estimate the Fe content of both components. It is based on recoil-free emission and absorption of γ -ray, emitted from a radioactive nucleus (source) and absorbed by similar nucleus located in the absorbing system (sample). The Lorentzian natural line shape for resonance is characterized by extremely narrow width related to the average finite lifetime of the excited nuclear state that allows the hyperfine interactions between the nuclear and electronic charges to be observed and determined. Their description and analysis give rise to hyperfine parameters: the electric monopole interaction resulting in the isomer shift (δ), the electric quadrupole interaction causing the quadrupole splitting or the quadrupole shift ($2e$) and the magnetic dipole interaction giving rise to the hyperfine field (B_{hyp}). These parameters can be useful in determining ligand bonding states, electron shielding, oxidation state, electrons density, magnetic structure and magnetic moments [83,84]. In the case of magnetic materials, additional information can be obtained from the shape and intensities of the six lines of the spectra. These lines are correlated to the Fe moment configuration with respect to the γ -ray direction. Indeed, the relative area ratios are given by 3:p:1:1:p:3, where $p = 4(\sin\theta)^2 / (2 - (\sin\theta)^2)$ where θ is the angle between the hyperfine field and the propagation direction of the γ -ray. In the case of powders, or when the Fe moments are randomly oriented, we expect the relative ratio 3:2:1:1:2:3. Other configurations occur when the material is submitted to an external magnetic field (B_{app}). Indeed, when the magnetic moments are oriented parallel or perpendicular to the γ -beam, we obtain 3:0:1:1:0:3 (perfect ferromagnetic or ferrimagnetic material submitted to intense magnetic field) or 3:4:1:1:4:3 (antiferromagnetic system, this configuration due to the dominant antiferromagnetic interaction, the moments are oriented perpendicular to the external field), respectively (Fig. 4.9-left side). In addition, the values of the effective field ($\vec{B}_{eff} = \vec{B}_{app} + \vec{B}_{hyp}$) do allow to determine whether the hyperfine field is parallel or antiparallel to the magnetic moments, i.e., if the contribution of the Fermi (contact term) is positive or negative. The analysis of the relative intensities of the lines 2 and 5 allows us to measure the angle θ , which is often different from 0 or 90 degrees (the relative intensity of the lines

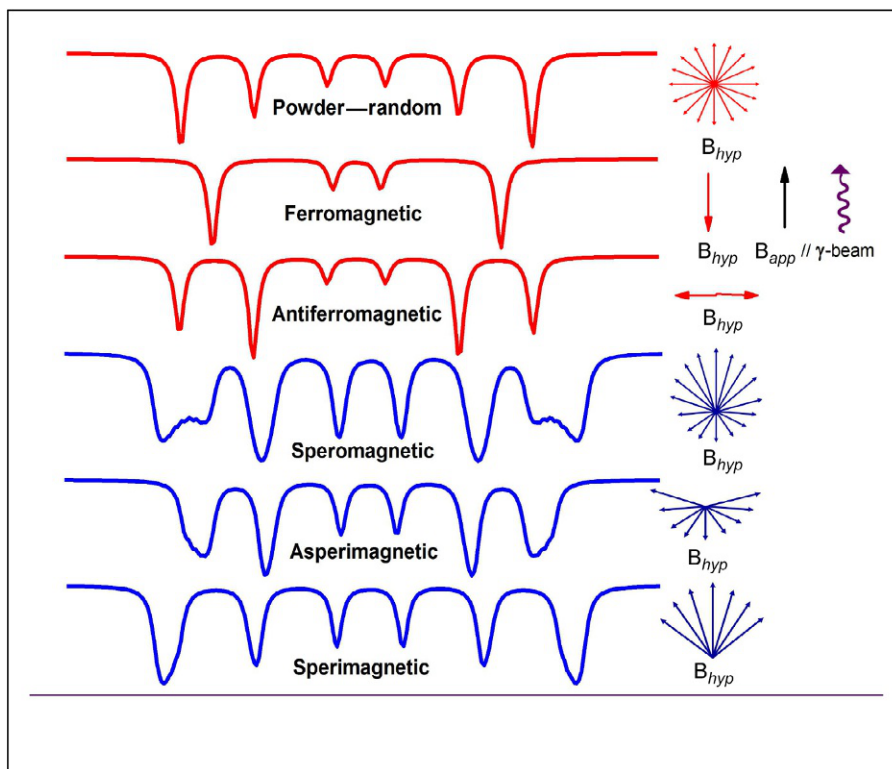


Fig. 4.9

Theoretical Mössbauer spectra on linear and noncollinear magnetic structures in presence of external field applied parallel to γ -beam: random powder in zero-field, ferromagnetic with magnetic moments antiparallel to the hyperfine field, antiferromagnetic structures and noncollinear magnetic structures.

(From J.M. Greneche, Chapter 4, pp. 187–241; Y. Yoshida, G. Langouche (Ed.), *Mössbauer Spectroscopy*, Springer, 2012.)

2 and 5 is intermediate between 0 and 4), in the case of magnetic nanoparticles. This allows us to estimate the mean spin canting (noncollinear magnetic structure) [5,6,85,86], the spin disorder (random orientation of spins), and consequently the hyperfine field using the following relation: $B_{hf}^2 = B_{eff}^2 + B_{app}^2 - 2B_{eff}B_{app} \cos\theta$. This methodology allows us to study the spin structure and to access to particular cases of noncollinear spin structure such as: asperomagnetic (ASP), speromagnetic (SP), or sperimagnetic (SPi) structure (Fig. 4.9-right side). In these cases, the magnetic materials are characterized by a direction of local anisotropy that varies randomly from site to site. Fig. 4.9 left-side shows the theoretical Mössbauer spectra of different magnetic structures through the intensities of intermediate lines when the external field is oriented parallel to the γ -beam.

The lattice effects, structural distortions, topology, vacancies, chemical disorder, size distribution, instrumental deviations, all can lead to some broadening in the Mössbauer line profile. In addition, at the nanoscale, Fe moment undergoes relaxation effects, inducing

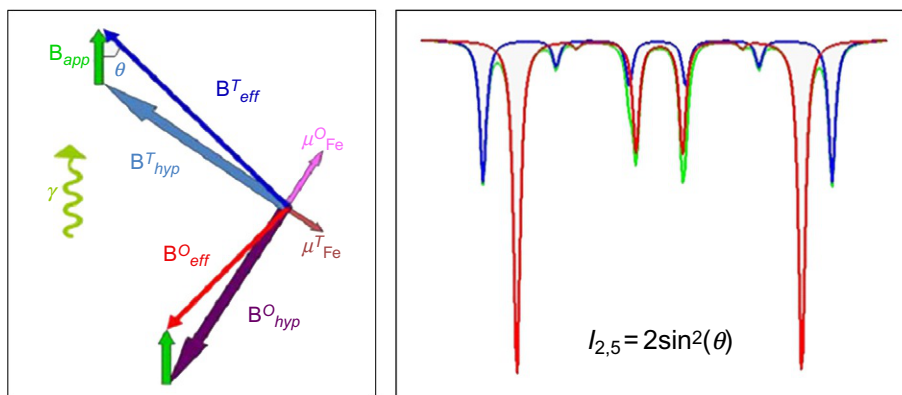


Fig. 4.10

Sketch representing the splitting between both tetrahedral and octahedral sites under the effect of applied magnetic field (left), theoretical spectrum of ferrite splitted under high field with the contribution of intensities of the intermediate lines (right).

modification on the shape and the hyperfine structure of the Mössbauer spectrum. Consequently, the modeling of the hyperfine structure of an assembly of magnetic nanoparticles, in order to investigate both structural and magnetic properties of nanostructures, is quite complex and becomes a delicate task.

In the case of ferrites with spinel structure, the best procedure to have an optimized quantitative analysis consists on applying a high external magnetic field at low T . This procedure allows a more reliable distinction between A- and B-site components than the zero field spectra (Fig. 4.10-left side). Indeed, the applied field is usually added to the A site hyperfine field and subtracted from the B site hyperfine field (as hyperfine fields are opposite to magnetic moments). Therefore, there is less overlap between the two components, and the zero-field unresolved magnetic sextet splits into two well-resolved sextets with respect to the ferrimagnetic structure (Fig. 4.10-right side). Furthermore, in the presence of an external magnetic field parallel to the gamma ray direction, the relative areas of the six lines give information about the degree of alignment of the magnetization with the applied field. Generally, in the case of a chemically ordered magnetic material, the lines of the spectrum are not broadened, allowing thus the values of B_{eff} and that of θ to be estimated and then to obtain the value of B_{hyp} . On the contrary, asymmetrical broadening of lines occurs when the structure is chemically disordered or influenced by surface or grain boundaries originating from finite size effects of nanostructured systems. In this case, the fitting model becomes quite complex, and it is necessary to take into account a discrete distribution of the effective field $P(B_{eff})$ and an average angle $\langle \theta \rangle$ (one assumes that the moments of iron are oriented in the same direction with respect to the applied magnetic field). This hypothesis will lead us to estimate the B_{hyp} and then to build the experimental zero-field spectrum and to compare it with the experimental one. If there is a disagreement between the model and

the experimental zero-field spectrum, i.e., the distribution of the effective field with an average angle does not succeed to reproduce the spectrum under field, it is necessary to take a discrete distribution of the effective field $P(B_{eff})$ correlated with the canting angle $P(\theta)$ distribution. It is thus necessary to carefully establish first such a joint distribution taking into account the physical origin and then to check whether the estimated $P(B_{hyp})$ is able to well describe the zero-field spectrum. In case of ferrites with spinel structure, we applied this procedure on A- and B-site components.

4.4 Magnetic Properties of Spinel Ferrites Nanoparticles: Influence of the Magnetic Disorder

Starting from this framework, is evident that magnetic disorder and more generally magnetic structure strongly affect macroscopic magnetic properties of spinel ferrite nanoparticles. In the following section, a short overview of some results obtained on cobalt ferrite CoFe_2O_4 nanoparticles obtained by sol-gel self-combustion technique (SC) and by polyol method (PL) will be provided. Using CoFe_2O_4 as a model system, an example of the effect on magnetic structure on macroscopic magnetic properties will be given, highlighting the size effect and the influence of synthesis method (Section 4.4.1). In Section 4.4.2, nanostructured spinel ferrites with complex stoichiometry will be discussed. In particular, ferrite nanoparticles with general formula $\text{Co}_x\text{Ni}_{1-x}\text{Fe}_2\text{O}_4$ ($0 \leq x \leq 1$) prepared by PL will be discussed, highlighting the complex relationship between cationic distribution, spin canting, and macroscopic magnetic properties.

4.4.1 Magnetic Properties of CoFe_2O_4 Nanoparticles: Effect of the Magnetic Structure

CoFe_2O_4 nanoparticles have been prepared by sol-gel self-combustion technique [7,76,87,88]. In a typical synthesis, aqueous solutions of $\text{Fe}(\text{NO}_3)_3 \cdot 9\text{H}_2\text{O}$ (Aldrich, 98%), $\text{Co}(\text{NO}_3)_2 \cdot 6\text{H}_2\text{O}$ (Aldrich, 98%), and citric acid (Aldrich, 99.9%) were mixed together in a Pyrex beaker with 1:1 M ratio of metals to citric acid; the pH of the sol thus obtained was < 1 . The sol was allowed to gel on a hot plate, maintaining the solution temperature at 80–90°C. A sudden increase of the temperature ($T > 200^\circ\text{C}$) induced a slow reaction that leads, after about 10 min, to a gray powder [89].

Crystalline and magnetic structures of the samples were investigated by Neutron powder diffraction (NPD) at 300 K. Rietveld Refinement of NPD pattern indicates the presence of only the CoFe_2O_4 phase crystallized in the $\text{Fd}\bar{3}\text{m}$ space group with mean particle size around 6 nm. The cation distribution is given by $(\text{Fe}_{0.73}\text{Co}_{0.27})[\text{Fe}_{0.63}\text{Co}_{0.37}]_2\text{O}_4$ with an inversion degree of $\gamma = 0.74$. Structural values obtained by Rietveld refinement are in very good agreement with the expected values for nanoscale CoFe_2O_4 [70,90]. The refined magnetic moments at the A and B sublattices are lower with respect to the values reported in literature

for CoFe_2O_4 nanoparticles with similar particle size and cationic distribution, inducing to believe that some noncollinear spin components coexist with the ordered spins. DC magnetization measurements were performed by a commercial Quantum Design SQUID magnetometer (hysteresis loops and magnetizations measured by Zero Field Cooled (ZFC) and Field Cooled (FC) protocols). Despite the small particle size, the values of saturation magnetization at 300 K ($M_s \cong 70 \text{ A m}^2 \text{ kg}^{-1}$) and at 5 K ($M_s \cong 100 \text{ A m}^2 \text{ kg}^{-1}$) are rather close to the bulk values (at 5 K $80\text{--}93 \text{ A m}^2 \text{ kg}^{-1}$) [10].

The Mössbauer spectrum recorded at 77 K without external field (not reported here) consists of a pure magnetic sextet composed of asymmetrical lines: it is concluded at 77 K and below that the nanoparticles are in the blocked magnetic state, thus excluding superparamagnetic relaxation phenomena. Mössbauer spectra of ferrites in large applied fields do allow a more reliable distinction between A- and B-site components than the zero field spectra as discussed later. Fig. 4.11 shows the spectrum obtained at 10 K under a magnetic field of 8 T applied parallel to the γ -beam. The spectrum is unambiguously consistent with a ferrimagnetic structure; the refinement allows to attribute clearly the two sextets to the Fe^{3+} in tetrahedral and octahedral sites, according to the values of the isomer shift. Then, accurate value of the atomic

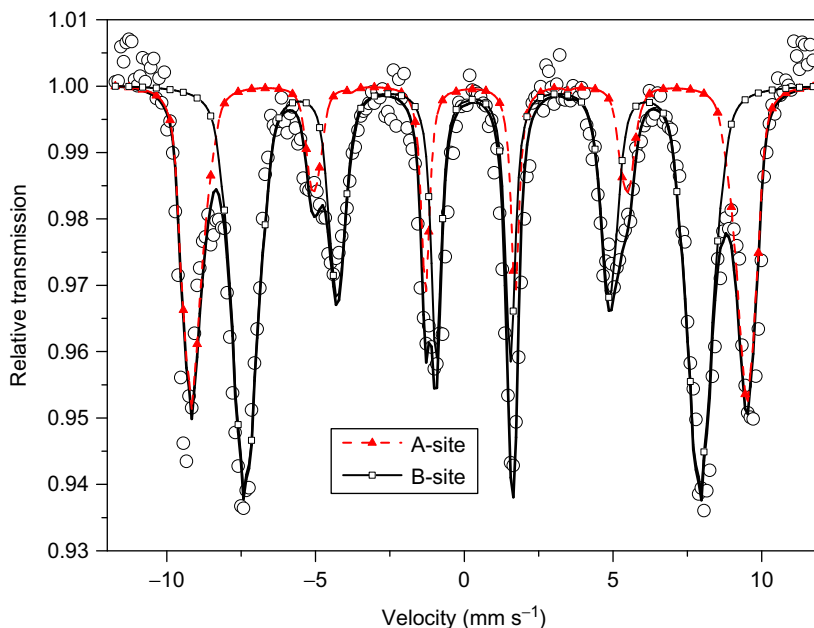


Fig. 4.11

^{57}Fe Mössbauer spectrum obtained at 10 K in 8 T magnetic field applied parallel to the γ -beam. Note that the second and fifth lines have nonzero intensity, showing that the magnetic structure is not collinear. (Modified from D. Peddis, N. Yaacoub, M. Ferretti, A. Martinelli, G. Piccaluga, A. Musinu, C. Cannas, G. Navarra, J.M. Greneche, D. Fiorani, *Cationic distribution and spin canting in CoFe_2O_4 nanoparticles*, *J. Phys. Condens. Matter* 23(42) (2011) 426004.)

Table 4.1 In-field Mossbauer fitted parameters of the CoFe_2O_4 : isomer shift (δ), quadruple shift (2ϵ), canting angle (θ), and the relative fraction of the Fe^{3+} located in A and B sites ($\text{Fe}_{\text{A,B}}^{3+}/\text{Fe}_{\text{total}}^{3+}$)

Mössbauer Hyperfine Parameters of the Co-Ferrite				
	$\langle \delta \rangle$ (mm s^{-1})	$\langle 2\epsilon \rangle$ (mm s^{-1})	$\langle \theta \rangle$ (degrees)	$\text{Fe}_{\text{A,B}}^{3+}/\text{Fe}_{\text{total}}^{3+}$
	± 0.01	± 0.01	± 10	± 0.01
$\text{Fe}_{\text{A}}^{3+}$	0.36	-0.04	41	0.38
$\text{Fe}_{\text{B}}^{3+}$	0.47	-0.03	36	0.62

$\text{Fe}_{\text{A}}^{3+}/\text{Fe}_{\text{B}}^{3+}$ population ratio has been obtained (Table 4.1). In addition, one can note that the hyperfine structure does not evidence at all the presence of Fe^{2+} ions. The cation distribution for stoichiometric CoFe_2O_4 can be given as $(\text{Fe}_{0.76}\text{Co}_{0.24})[\text{Fe}_{0.62}\text{Co}_{0.38}]_2\text{O}_4$, with $\gamma_{\text{Moss}} = 0.76$. It should be emphasized that the inversion degree obtained by in-field Mössbauer investigation is in good agreement with that estimated from NPD analysis ($\gamma_{\text{NPD}} = 0.74$), within the experimental error of the two techniques. Note that in-field spectrum shows that the second and fifth lines have a nonzero intensity. Usually, when these peaks are distinctly observed, they evidence a canted structure for Fe^{3+} magnetic moments with respect to the applied field (noncollinear magnetic structure).

The magnetic effective field distributions ($P(B_{\text{eff}})$) correlated to the canting angle distribution ($P(\theta)$) and the distribution of the hyperfine field ($P(B_{\text{hf}})$) corresponding to CoFe_2O_4 nanoparticles are illustrated in Fig. 4.12 for both Fe in A and B sites. We have already seen that the cationic inversion showed that both Co^{2+} and Fe^{3+} cations occupy simultaneously the A and B sites. The number of different B (A)-sites fields and their relative intensity could be correlated with the probability of having a certain number of Co^{2+} A(B)-sites surrounding a given Fe^{3+} B (A)-sites ions. The correlation between B_{hf} and canting angle allows us to relate $P(B_{\text{hf}})$ and $P(\theta)$ to the cation distribution (inversion degree, Fe^{3+} ions in B (A)-sites with nearest-neighbors Co^{2+} A (B)-site ions) and to surface effects. The mean values of hyperfine parameters are given in Table 4.1. The broadening of Mössbauer lines, due to angle and hyperfine field distributions, suggests unambiguously different atomic neighboring of Fe sites. As illustrated in Fig. 4.12, the corresponding hyperfine field distribution is ranged from 55.5 and 49.5 T, in agreement with Fe with 6 A-Fe up to 6 A-Co first neighbors. Indeed, it has been established that the hyperfine field at octahedral Fe site decreases by about 0.6–1.0 T per Co nearest neighbor located in tetrahedral site [67,89].

By correlation to the effective field distribution, one easily concludes that the smallest effective field values have to be associated to Fe moments, which are aligned to the external field to give rise to the lowest hyperfine field value (similarly, the increasing effective field values have to be associated to canted Fe^{3+} magnetic moments, giving rise to highest hyperfine field values). This description is rather confirmed by comparing hyperfine and effective field

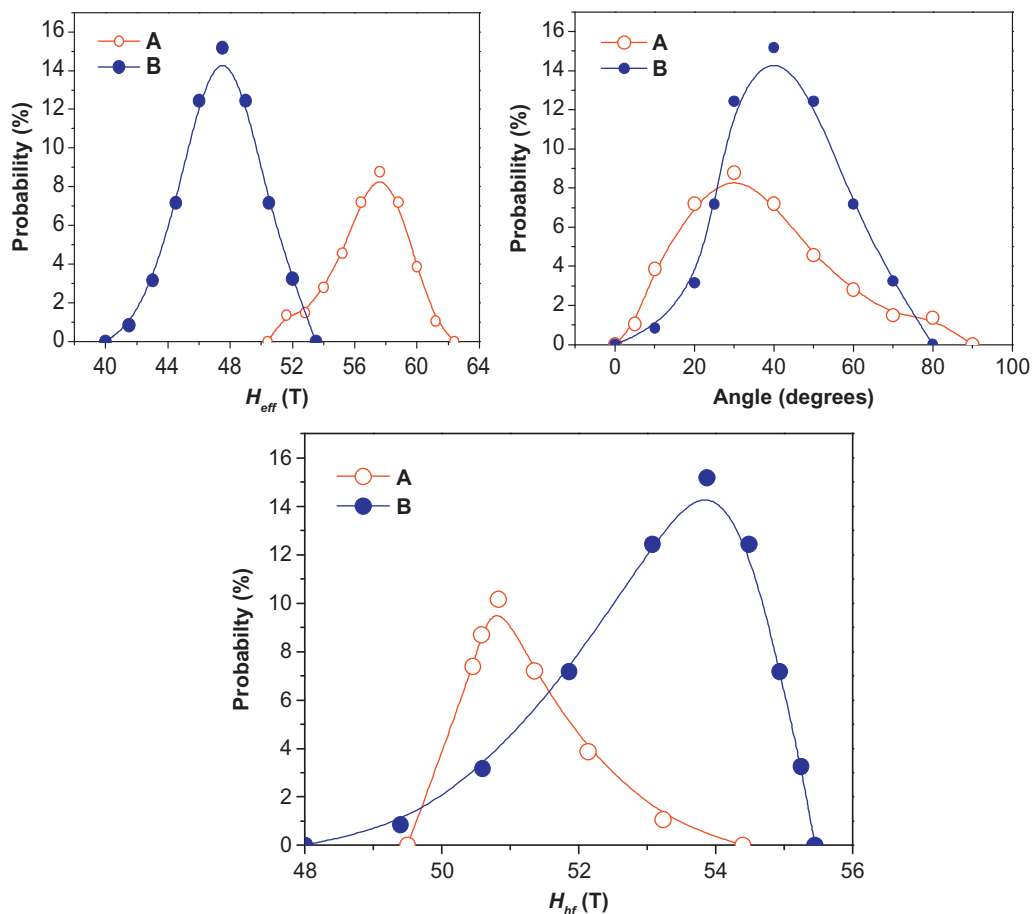


Fig. 4.12

Top-left part, the distribution of the effective magnetic field $P(H_{eff})$ correlated with the distribution of canting angle $P(\theta)$, top-right part, obtained by fitting procedure. Bottom part, the distribution of the hyperfine magnetic field $P(H_{hf})$ observed for both A and B sites. (Modified from D. Peddis, N. Yaacoub, M. Ferretti, A. Martinelli, G. Piccaluga, A. Musinu, C. Cannas, G. Navarra, J.M. Greneche, D. Fiorani, *Cationic distribution and spin canting in CoFe_2O_4 nanoparticles*, *J. Phys. Condens. Matter* 23(42) (2011) 426004.)

distributions characteristic of tetrahedral Fe^{3+} ions, but the effects are less important than in the case of octahedral Fe sites. Consequently, such features are consistent with a saturated Co-rich core and a canted Fe-rich shell, suggesting nonchemical homogeneous Co-ferrite nanoparticles originating from a cationic gradient.

In spinel ferrite structure, each tetrahedral Fe^{3+} ion is surrounded by twelve octahedral ions, while an octahedral Fe^{3+} ion has only six tetrahedral nearest neighbors. Starting from the cationic distribution obtained by in-field Mössbauer spectrum and NPD pattern, we can assume

that in our nanoparticles each B-Fe³⁺ has on average two A-Co²⁺ and four A-Fe³⁺ neighbors. On the other hand, a A-Fe³⁺ atom is surrounded on average by seven B-Fe³⁺ and five B-Co²⁺. These arguments qualitatively explain why the canting in this sample extends to both A and B sites. One of the most controversial issues in the physical chemistry of the ferrimagnetic nanoparticles is the reduction of the saturation magnetization with the particle size. In many studies on ferrimagnetic nanoparticles, a reduction has been observed and attributed to spin canting that yields magnetic disorder at the particle surface [91]. On the other hand, a steep rise in saturation magnetization at low temperature has been established in ferrimagnetic nanoparticles and was explained by the freezing of surface spins [92–94]. Generally, the effect on magnetic disorder on saturation magnetization can be explained by the interplay between spin canting and inversion degree. In these magnetic nanoparticles, the mean spin canting in each site A and B contributes to the decrease of the moments (measured by neutron powder diffraction). The high value of saturation magnetization is attributed to the decreasing of inversion degree (in the bulk $\gamma_{bulk} = 0.82$). For more details, please see the article [89].

The CoFe₂O₄ PL nanoparticles have been synthesized by forced hydrolysis in polyol. Precursor salts, anhydrous iron(III) chloride (Prolabo), anhydrous or trihydrated sodium acetate (Prolabo), tetrahydrated cobalt(II) acetate (Prolabo), and an appropriate volume of deionized water were added to 250 mL of 1,2-propanediol. The iron concentration was fixed to 0.2 M. The nominal molar ratio Fe/Co was varied from 2 to 1 according to the adopted hydrolysis ratio value to obtain stoichiometric CoFe₂O₄ size-controlled nanoparticles. The mixture was then refluxed at a rate of 6 K min⁻¹ up to the boiling temperature (398–447 K) under mechanical stirring for about 12 h. A dark brown magnetic powder was then separated from the supernatant by centrifugation and then washed. Finally, the product was dried overnight in air at 328 K leading to fine magnetic powder. By comparison of CoFe₂O₄ SC and CoFe₂O₄ PL with same average diameter (6 nm), the effect of synthesis method will be discussed. Then, CoFe₂O₄ PL nanoparticles of ~2.4 nm will be introduced in order to highlight the size effect [95].

The characterization by X-ray diffraction (XRD) and transmission electron microscopy (TEM) indicates the formation of spherical-like particles with high crystallinity. The saturation magnetization at 5 K for the CoFe₂O₄ (6 nm) is about 85 Am² kg⁻¹, which is close to that of the bulk (80–93 Am² kg⁻¹), while the saturation magnetization drops down to about 48 Am² kg⁻¹ for the smallest sample (2.4 nm).

The Mössbauer spectra recorded at 10 K under an intense magnetic field of 8 T for CoFe₂O₄ PM (6 and 2.4 nm) are illustrated in Fig. 4.13. They are unambiguously consistent with a ferrimagnetic structure. They clearly exhibit two well-resolved sextets corresponding to Fe³⁺ sites A and B according to the values of the isomer shift. The cationic distributions estimated from our spectra correspond to (Fe_{0.74}Co_{0.26})[Fe_{0.63}Co_{0.37}]₂O₄ corresponding to

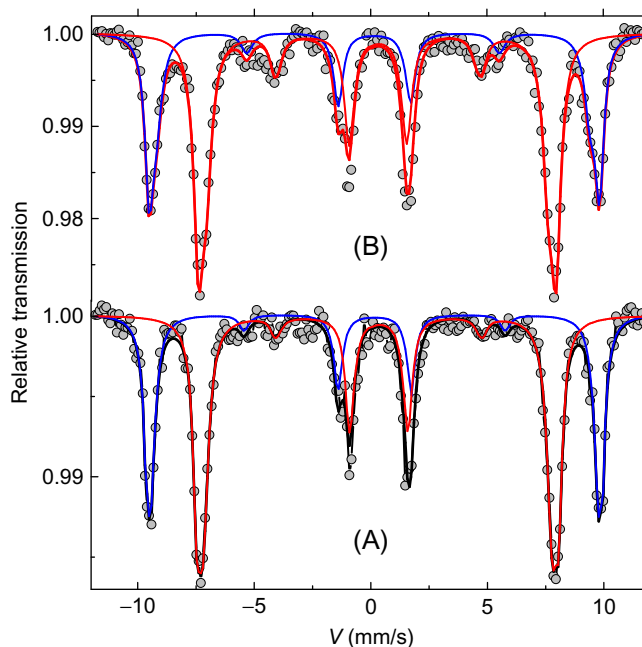


Fig. 4.13

^{57}Fe Mössbauer spectra obtained at 10 K in an 8-T field: (A) for CoFe_2O_4 B (6 nm) and (B) for CoFe_2O_4 B (2.4 nm). (Reproduced with permission from M. Artus, L.B. Tahar, F. Herbst, L. Smiri, F. Villain, N. Yaacoub, J.-M. Grenèche, S. Ammar, F. Fiévet, Size-dependent magnetic properties of CoFe_2O_4 nanoparticles prepared in polyol, *J. Phys. Condens. Matter* 23(50) (2011) 506001.)

a degree of structure inversion $\gamma_{\text{Moss}} = 0.74$. The isomer shifts in tetrahedral and octahedral sites are 0.38 and 0.53 mm s^{-1} , respectively, and those of hyperfine field are 52 and 54 T , respectively. The hyperfine structure, the shape, and the width of lines clearly suggest a homogeneous Co and Fe ion distribution within nanoparticles, contrary to that discussed in CoFe_2O_4 nanoparticles prepared by the thermal decomposition route where cationic inhomogeneity was in evidence.

The in-field spectrum of the 2.4 nm particles shows that the second and fifth lines have a nonzero intensity. Usually, when these peaks are distinctly observed, they evidence a canted structure for Fe magnetic moments with respect to the applied field in both A and B sites. In the present case, assuming a magnetic core-shell model, the canting angle provides a canted magnetic layer whose thickness is estimated at $< 0.2 \text{ nm}$ [5,96]. The surface spin canting (noncollinear spin structure) contributes in lowering the magnetization in this sample and improving the surface anisotropy when the particle size decreases. The high value of the saturation magnetization of the sample CoFe_2O_4 B (a) can be considered as a consequence of the high crystallographic quality of the NPs [95].

4.4.2 Magnetic Properties of Spinel Ferrite Nanoparticles: Effect of the Chemical Composition

Small crystalline ferrite nanoparticles of the formula $\text{Co}_x\text{Ni}_{1-x}\text{Fe}_2\text{O}_4$ ($x = 1$ MF1; $x = 0.6$, MF2; $x = 1$ MF3) having equal size ($\cong 4.5$ nm, Table 4.2) were investigated in order to gain better insight into the effect on the magnetic structure (noncollinear spin structure) on magnetic properties. All samples were prepared by polyol method. The XRD patterns and TEM images show high crystalline spherical-like particles with the same average size within the experimental error (Table 4.2). Therefore, any difference in magnetic properties can be ascribed to the effect of the chemical composition.

At 5 K, we observe a significant decrease of the magnetic anisotropy with the decrease of cobalt content, as is shown by the monotonic reduction of the coercive field (H_C , Table 4.2). Co^{2+} ions produce a marked magnetocrystalline anisotropy far above those of Ni^{2+} and Fe^{3+} ions; indeed, its orbital magnetic moment is not quenched by the crystal field, and spin-orbit coupling occurs, particularly strong for Co^{2+} ions located in octahedral sites [97,98]. For a cubic crystalline structure with magnetic easy axis along [99] direction, we can empirically evaluate the effective anisotropy constant according to: $K_{\text{eff}} = \frac{H_K M_S}{2}$. We observe the same downward tendency with increasing Ni content (Table 4.2) and all of the estimated values are higher than those reported for bulk and nanostructured cobalt ($\sim 1\text{--}4 \times 10^5 \text{ J m}^{-3}$) [99–101] and nickel ferrites ($\sim 1 \times 10^4 \text{ J m}^{-3}$) [102,103]. Assuming the atomic magnetic moment of $5 \mu_B$ for Fe^{3+} , $3 \mu_B$ for Co^{2+} , and $2 \mu_B$ for Ni^{2+} resulting from their electronic configuration [88,104], and considering the antiparallel arrangement of moments between tetrahedral and octahedral sites for the inverse spinel structure, the magnetization is expected to decrease when reducing the Co content at the expense of Ni one. As listed in Table 4.2, the experimental values of saturation magnetization confirm this hypothesis. We have to note that MF1 possesses a relative high value of magnetic saturation, compared to that of the bulk values ($83\text{--}90 \text{ A m}^2 \text{ kg}^{-1}$), and also to those reported for highly crystalline cobalt ferrite nanoparticles [105]. On the other hand, a relatively low value is estimated in the case of MF5 (bulk around $55 \text{ A m}^2 \text{ kg}^{-1}$). In this framework, the interplay between inversion degree and magnetic disorder (i.e., noncollinear spin structure) should play a key role.

Table 4.2 Chemical formula by ICP analysis; mean diameter ($\langle D_{\text{TEM}} \rangle$) evaluated using TEM images, saturation magnetization (M_S); coercive field ($\mu_0 H_C$); effective anisotropy constant (K_{eff})

Sample	Chemical Formula	$\langle D_{\text{TEM}} \rangle$ nm	M_S ($\text{A m}^2 \text{ kg}^{-1}$)	$\mu_0 H_C$ (T)	K_{eff} (J m^{-3})
MF1	$\text{Co}_{1.0}\text{Fe}_2\text{O}_4$	4.5(1)	130(10)	0.88(7)	$10.7(1) \times 10^{-5}$
MF2	$\text{Co}_{0.4}\text{Ni}_{0.6}\text{Fe}_2\text{O}_4$	4.6(1)	77(4)	0.50(4)	$4.9(1) \times 10^{-5}$
MF3	$\text{Ni}_{1.0}\text{Fe}_2\text{O}_4$	4.3(1)	37(4)	0.028(1)	$0.3(1) \times 10^{-5}$

Uncertainties on the last digit are given in parentheses.

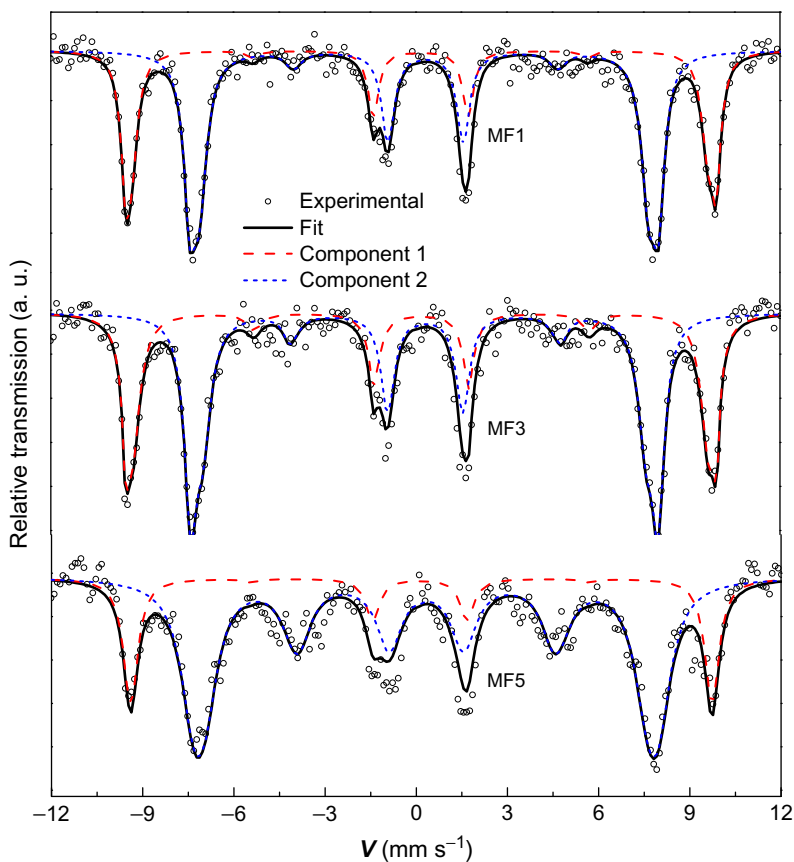


Fig. 4.14

In-field Mössbauer spectra recorded at 10 K under an applied magnetic field of 8 T, for MF1, MF3, and MF5 samples. The experimental data are represented as *open circles*, the fit as a *bold black line*, while the individual components for Fe in tetrahedral and octahedral sites are reported as a *red dashed line* (*dark gray dashed line in print*) and a *blue dotted line* (*light gray dotted line in print*), respectively. (Reproduced with permission from G. Muscas, N. Yaacoub, G. Concas, F. Sayed, R. Sayed Hassan, J.M. Greneche, C. Cannas, A. Musinu, V. Foglietti, S. Casciardi, C. Sangregorio, D. Peddis, *Evolution of the magnetic structure with chemical composition in spinel iron oxide nanoparticles*. *Nanoscale* 7(32) (2015) 13576–13585.)

Fig. 4.14 illustrates the ^{57}Fe Mössbauer spectra recorded at 10 K under a magnetic field of 8 T on the MF1, MF3, and MF5 samples. The hyperfine parameters do not evidence at all the presence of Fe^{2+} ions, and the isomer shift values allow to attribute clearly the two sextets to the Fe^{3+} in tetrahedral and octahedral sites, and to estimate their respective proportions from the relative absorptions areas. The estimated values of hyperfine field B_{hyp} and spin-canting angle (noncollinear magnetic structure) are presented in [Table 4.3](#). It is important to mention that an asymmetrical broadening of the lines in site B for sample MF5 was observed, probably due to the chemical disordered occupation of these sites, producing a wide range of possible chemical environments of Fe ions.

Table 4.3 The isomer shift (δ), the hyperfine field (B_{hyf}), the average canting angle (θ), and the ratio of each component evaluated from in-field Mössbauer fitted spectra are reported for samples MF1, MF3, and MF5

Sample	Site	δ (mm s ⁻¹)	B_{hyf} (T)	θ (degree) \pm		$Fe_{A,B}^{3+}/Fe_{total}^{3+}$
				10 degrees		
MF1	Fe _A ³⁺	0.34(1)	51(2)	10		0.37(1)
	Fe _B ³⁺	0.48(1)	54(2)	18		0.63(1)
MF3	Fe _A ³⁺	0.35(1)	51(2)	18		0.39(1)
	Fe _B ³⁺	0.48(1)	54(2)	22		0.61(1)
MF5	Fe _A ³⁺	0.35(1)	51(2)	12		0.22(1)
	Fe _B ³⁺	0.48(1)	53(2)	38		0.78(1)

Uncertainties on the last digit are given in parentheses.

ICP analysis has confirmed the 2:1 ratio between Fe³⁺ and divalent cations (i.e., Co²⁺ and Ni²⁺); thus, considering the hypothesis of absence of vacancies, the inversion degree γ can be simply estimated as the amount of divalent ions in octahedral sites. γ was estimated at 0.74(1) and 0.78(1) for MF1 and MF3, respectively, in agreement with values usually reported for cobalt ferrite ($\gamma \approx 0.7-0.8$) [95,106,107]. For sample MF5, γ was estimated at 0.44(1), significantly different from that expected for pure nickel ferrite ($\gamma \approx 0.9-1$) [107]. From these results, the cationic distribution was calculated. Giving the magnetic moment values of $5 \mu_B$ for Fe³⁺, $3 \mu_B$ for Co²⁺, $2 \mu_B$ for Ni²⁺, and considering the effect of the canting angle, the corresponding theoretical M_S values have been calculated as 90(1), 80(1) and 89(1) A m² kg⁻¹, for MF1, MF3, and MF5, respectively. Only for MF3 this value is comparable with the experimental one, inducing to hypothesize a nonhomogeneous cationic distribution for MF1 and MF5 samples. The calculation of the effective magnetic moments and the effective inversion degree γ_{sat} for the sample MF1 allow us to find the cationic distribution as ((Fe_{0.74-0.26})[Co_{1.00}Fe_{1.26}])O₄, so the presence of vacancies in A sites and an overpopulation of B sites) that can justify such elevated value of $M_S \approx 130$ A m² kg⁻¹. The result for sample MF5 leads to cationic distribution (Ni_{1.00}Fe_{0.44})[Fe_{1.56-0.44}]O₄, explaining at the same time the low saturation and the unusual iron distribution from Mössbauer spectrometry. The cationic distributions allow to estimate the environment surrounding the Fe³⁺ ions and to explain the measured canting angles. These spin-canted structures were evidenced and explained in terms of superexchange interactions energy produced by the average cationic distribution and vacancies in the spinel structure. Finally, the effect of the surface spin canting has been analyzed in terms of increased surface anisotropy, showing how the missing coordination of surface cations can induce an increase of the local anisotropy of more than one order of magnitude [72].

The examples cited here show that the magnetic properties of the magnetic nanoparticles of spinel structure are strongly correlated with the chemical compositions, and the competition between the cationic distribution and the presence of a noncollinear spin structure.

This study represents an example of further development in the understatement of the link between the structure and magnetic behavior of ferrite nanoparticles, which is of fundamental importance for the development of the engineering of magnetic ferrite nanomaterials for technological applications.

4.4.3 Surface and Interface Magnetism: The Role of Molecular Coating

For the simplest case of spherical particles with uniaxial anisotropy, the MAE can be defined by the Eq. (4.8). Several authors have shown the dependence of the anisotropy energy by the average particles size [108]; anyway, a careful analysis is necessary when particles size are reduced to few nanometers (diameter <10 nm) and the surface-to-volume ratio has a great increment (Fig. 4.2). In particular, below ~ 5 nm, the surface contribution can overcome the bulk magnetocrystalline one resulting the main agent in characterizing the particles anisotropy, which is related to the noncollinear surface spins [75]. Nanoparticles on such scale are usually prepared through colloidal synthesis, which makes use of surfactants in order to obtain narrow size and shape distribution [109], to protect particles from oxidation, disperse them in specific solvents [110], or to functionalize them for specific applications, in particular for biomedical ones (e.g., MRI, drug delivery, hyperthermia) [111,112]. It is usually reported that for small nanoparticles, a thin external shell with higher magnetic disorder is responsible of larger magnetic anisotropy and reduced saturation magnetization. Several authors have shown that the action of the surfactant plays a strong role on the magnetic properties of NPs surface, e.g., almost restoring the bulk saturation magnetization and influencing the local effective magnetic anisotropy, and thus the coercive field of small particles [13,21]. It is worth noting that the selection of the organic coating is not limited to just the synthesis process. While a specific ligand can be selected to control size, shape, and the crystalline structure produced during the synthesis, the original ligand can be exchanged in a subsequent process in favor of a different one, which can be used to finely tune specific magnetic properties of the nanoparticles [112].

The study of Salafranca et al. [22] has elucidated the action of organic acid coating on spinel ferrite nanoparticles surface. Even in fully crystalline nanoparticles, without disordered crystalline external shell, a lower local surface magnetic moment is evident due to the local breaking of the lattice symmetry. This induces a different electronic band structure, responsible for the lower magnetic moment. The authors of the study have experimentally investigated oleic-acid-coated particles by electron energy loss spectroscopy (EELS), evidencing that the local surface moment is almost the same of the particles' core. Such results have been reproduced by density functional theory (DFT) calculations, confirming that two oxygen atoms of the carboxylic group bond to two different Fe ions at the surface. This translates to surface Fe ions surrounded by six oxygens at an average distance of 2.05 \AA , very close to the six neighbors at 2.10 \AA in the bulk. As a result, their density of states and occupancies are

similar to those of Fe in bulk ferrite, resulting in a similar moment. Not all the Fe atoms at the surface are bonded to the oleic acid, for those the Fe-O distance corresponds to 1.92 Å, only 0.04 Å smaller than that found at the surface of bare particles, thus resulting in a d orbital occupancy that leads to a smaller moment. Anyway, the net result of the capping on the particle surface is a larger magnetization density per surface unit cell, 1 extra Bohr magneton, with respect to a corresponding bare surface, thus an intermediate value between the surface and the bulk moment.

On the other hand, studies on FePd particles have shown an opposite effect of oleic acid. It has been observed that the molecular coating binds primarily on the surface Fe sites, which are responsible for great part of the magnetic moment in FePd. Oleylamine and oleic acid bind with an electron donation process, which results in a strong reduction of the Fe site magnetic moment. Such phenomena have been confirmed by Wu et al. [113] observing that removing the oleic acid coating, responsible for what they consider a “dead-layer,” is enough to restore the full magnetic moment at the particles’ surface. In a further investigation, Tanaka et al. [23] have compared the effect of different molecular coatings on the saturation magnetization of FePd nanoparticles. The particles were synthesized using oleic acid and then treated to exchange the ligand with a different one, i.e., caprylic acid (C8Ac), lauric acid (C12Ac), 1-octanethiol (C8T), 1-dodecanethiol (C12T), 1-octylamine (C8Am), or 1-dodecylamine (C12Am) using the ligand exchange technique. The first effect observed confirmed that, keeping the same head group, ligands with longer chain, owning higher donor ability, produce smaller saturation magnetization. On the other hand, keeping constant the chain length, they observed a smaller reduction effect in the order of alkylamine, fatty acid, and alkanethiol. This is linked to the basicity of each individual group, where the larger the basicity, the stronger the electro donor ability, the smaller is the final saturation value. Apparently, thiols did not follow such trend; indeed, the actual picture is more complex. Each ligand is characterized by a different coupling mechanism, in case of thiols, they have a preference for binding with Pd. Additionally, they found that C8T induced the smallest magnetization reduction power among all investigated ligands, although the smallest estimated “dead-layer” was for the C12T-coated FePt particles. This is due to the much larger surface coverage of C8T (almost twice) with respect to C12T.

Vestal et al. [21] have shown that the nature of the organic molecule used for coating NPs has different effects on their magnetic anisotropy too. By using benzoic acid ligands substituted with different groups, they have underlined the effect of surfactants acidity on the surface anisotropy of the particles. Ligands with larger pKa, i.e., larger π -acidity, own a π -acceptor nature. It is well established by the ligand field theory that π -acceptor ligands are responsible for a coordination that induces a large crystal field splitting energy (CFSE) [114]. For transition metals, a large CFSE means a large d orbital splitting of energy levels and hence a small spin-orbit coupling. Such coupling represents a source for the magnetocrystalline anisotropy, which is thus reduced by π -acceptor ligands at particles surface. The work of Vestal

et al. investigated the same selection of ligands on ~ 4 , 12, and 25 nm MnFe_2O_4 particles. The results were similar for 4- and 12-nm particles, showing the same trend with the selected ligands, but with smaller effect on 12 vs 4 nm ones. The effect was visible but much weaker on the 25-nm particles. These results reflect the relative effect of the surface anisotropy on the overall magnetic anisotropy of the particles. While such effect is dominant on the anisotropy of 4-nm particles, it becomes smaller on the 12-nm ones and much more limited on the largest 25-nm particles. Interestingly, the authors observed an increment of saturation magnetization for all ligands used compared to bare particles. They proposed that each ligand used improve the local coordination at the particles' surface, thus "unlocking" the surface canted spins, which, due to the previous frozen misalignment, did not contribute to the saturation magnetization with their entire moment.

A more recent investigation by Mohapatra et al. [115] shows once more the effect of the donor-acceptor ability on the saturation magnetization of MnFe_2O_4 nanoparticles. Comparing oleylamine (OAm), oleic acid (OAc), and trioctylphosphine oxide (TOPO), the particles coated by OAm showed the larger saturation, which was reduced by 10% and 19% by OAc and TOPO. The π -donor nature of OAm, compared to the π -acceptor of OAc and TOPO, is then connected to a larger spin-orbit coupling and a more ordered, i.e., collinear surface spin structure, which translates into a larger saturation moment. The donor-acceptor behavior of ligands has been recently studied also by Rakshit et al. [116] analyzing the effect of tetradecyltrimethyl ammonium bromide (TTAB) ($\text{C}_{17}\text{H}_{38}\text{NBr}$), cetyltrimethyl ammonium bromide (CTAB) ($\text{C}_{19}\text{H}_{42}\text{NBr}$), sodium dodecyl sulfate (SDS) ($\text{C}_{12}\text{H}_{25}\text{NaSO}_4$), and dioctyl sodium sulfosuccinate (AOT) ($\text{C}_{20}\text{H}_{37}\text{NaO}_7\text{S}$) coatings on CoFe_2O_4 nanoparticles (average size ~ 65 nm).

All coatings induced an increment of coercivity, higher for the π -donor SDS and AOT compared to the π -acceptors TTAB and CTAB. In addition, within each group, those with longer chain (CTAB and AOT), due to the larger donor ability, induce a larger increment in coercivity compared to the bare particles. Furthermore, the authors observed that the higher the π -acceptors ability, and thus the CFSE, was not only able to reduce the coercivity more, but also to lead to the lowest magnetic moment, due to the quenching of the unpaired d -electrons on the bonded metallic ion (Co^{2+}), which results in a larger reduction of the saturation magnetization.

All the investigation is the effect of the CFSE on the relative change in coercivity (Fig. 4.15), due to the quenching of the spin-orbit coupling, larger for larger CFSE, which in turns produces a smaller effective surface anisotropy. The effect on the ligand on the saturation magnetization, on the other hand, seems to be a more debated argument, where different authors have found higher or smaller magnetic moment on bare or coated particles, and have found a variation related to the different d -band structure and occupancy related to the specific ligand-surface metallic ion interaction, thus requiring the specific analysis of the ligand-material combination to really describe the obtained results.

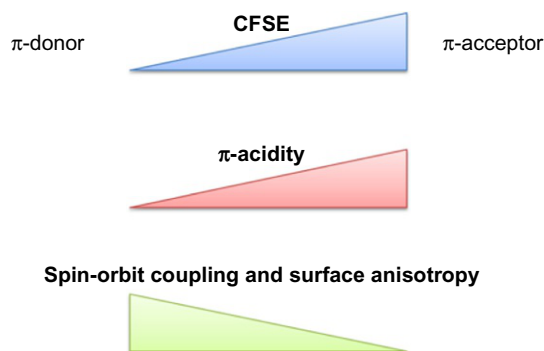


Fig. 4.15

Graphical sketch of the correlation between the crystal field splitting energy and the donor-acceptor nature of surfactants, and how it affects the spin-orbit coupling and local surface magnetic anisotropy.

In addition, the surface can be also strongly correlated to particle's shape too, with an additional effect on magnetic properties. For instance, despite cubic and spherical particles own isotropic demagnetizing factors in the three dimensions, i.e., there is no source of shape anisotropy, the breaking of the crystalline symmetry induces surface defects in the magnetic structure at a different degree for the two shapes, leading to a greater magnitude of surface anisotropy for spherical particles [117–119] (Fig. 4.16). As result, a larger effective anisotropy is exhibited by spherical particles compared to cubic ones, considering particles with the same volume [118].

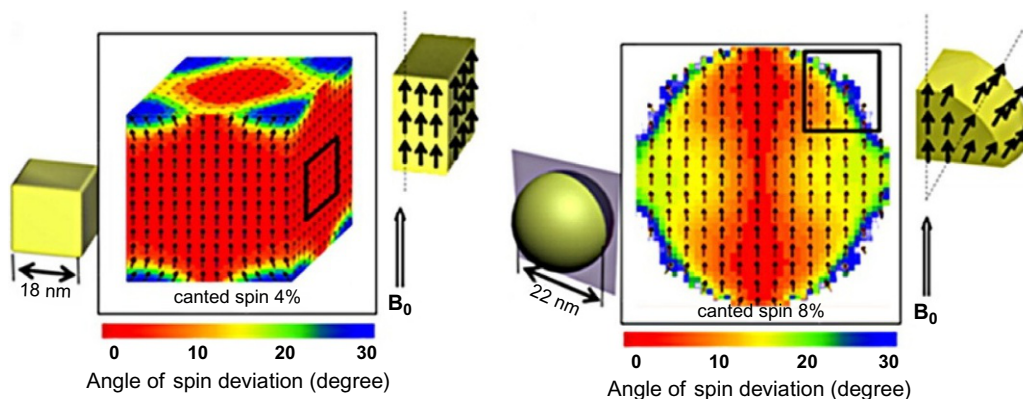


Fig. 4.16

Simulated magnetic spin states of a cubic (left) and spherical particle (right) by using OOMMF program. The *color map* indicates the degree of spin canting with respect to the external magnetic field B_0 . *Cube and sphere* exhibit a canted spin rate of 4% and 8%, respectively. (Reproduced with permission from S.-H. Noh, W. Na, J.-T. Jang, J.-H. Lee, E.J. Lee, S.H. Moon, et al., *Nanoscale magnetism control via surface and exchange anisotropy for optimized ferrimagnetic hysteresis*, *Nano Lett.* 12 (2012) 3716–21. <https://doi.org/10.1021/nl301499u>. Copyright © 2012 American Chemical Society.)

4.5 Conclusions and Perspectives

Magnetic disorder and, more generally, magnetic structure strongly affect magnetic properties of nanostructured materials. Even in the case of very well-studied and investigated materials such as spinel ferrites, a full understanding of the correlation between spin structure and magnetic properties is still lacking. In addition, the magnetic disorder can be a tool to modify magnetic properties by a “molecular control” of the spin structure at the surface of nanoparticles.

Nowadays, advanced synthesis approaches allow to achieve a strict control of the structural, morphological, and chemical properties of nanomaterials. Due to the strong size and morphology dependence of the magnetic properties, progress on the ability to manipulate the matter at the nanoscale has created new opportunities to develop magnetic materials with novel characteristics and applications also allowing to better understand the physics of nanostructured systems. In particular, to obtain systems with huge surface-to-volume ratio opens new perspective both to explore “the no-man’s land between molecular nanomagnets and magnetic nanoparticles” [120] and to investigate the effect of magnetic disorder in the physics of magnetic nanoparticles is needed. In this framework, hollow magnetic nanoparticles (HMNPs) exhibit extremely high surface effects that are related to symmetry breaking of the crystal structure and loss of coordination number at the surface of the particle (Fig. 4.17).

This enhanced role of surface results from the presence of extra surface layers (inner and outer) for the hollow morphology. So, these nanoparticles are good candidates to study both the surface effects and the complex mechanism of surface anisotropy and spin disorder. As a preliminary investigation, we studied the nanoparticles by numerical simulation based on Monte Carlo algorithm. In this aim, the effect of surface anisotropy (K_S) was investigated [121]. Thus, different simulations on the small HMNP (8 nm of diameter and 2 nm of thickness) were done by gradually increasing the value of surface anisotropy K_S . Three different spin structures (collinear, throttled, and spike) were obtained when varying K_S . For small K_S , the structure of spins is collinear. Increasing the surface anisotropy, fluctuations in spin directions start to favor a radial orientation for surface spins resulting in a “throttled” configuration. For larger values of K_S (typically 100 K), all spins are radially oriented, either inward or outward the center of the hollow nanosphere, giving rise to a “hedgehog” or “spike”-type spin structures. In order to find the effect of size on the spin structure of HMNPs, the same simulation was done for the HMNPs with different sizes (12, 14, and 18 nm) and approximately same thickness where for each size the critical value of K_S^* differs. As the size of the HMNP increases, smaller K_S^* is needed to obtain the spike structure (Fig. 4.18 left side). The effect of thickness on spin structure was also studied by considering a certain size of HMNP (12 nm) and varying the shell thickness (between 1 and 3.8 nm in our case). The results show that when the thickness of the shell increases, the value of K_S^* increases

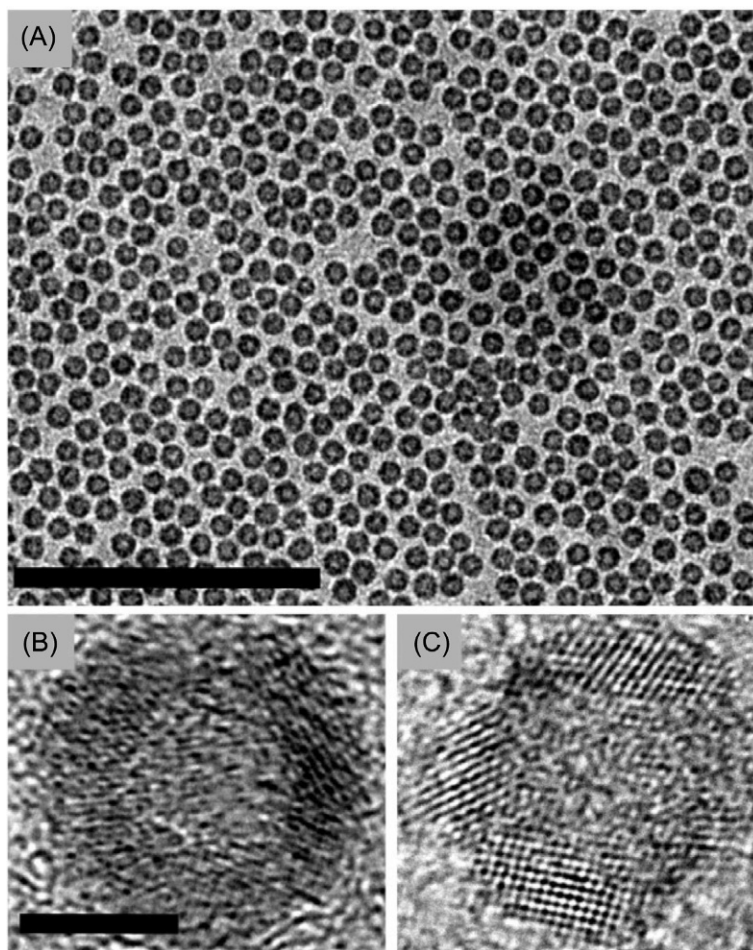


Fig. 4.17

Transmission electron microscopy micrographs of the hollow maghemite nanoparticles at different magnifications (A–C). Scale bars correspond to 100 nm for (A) and 4 nm for (B) and (C). *Reproduced with permission from A. Cabot, A.P. Alivisatos, V.F. Puntès, L. Balcells, Ò. Iglesias, A. Labarta, Magnetic domains and surface effects in hollow maghemite nanoparticles, Phys. Rev. B. 79 (2009) 94419. <http://link.aps.org/doi/10.1103/PhysRevB.79.094419>.*

(Fig. 4.18-right side). The slope at the beginning changes slowly, then increases clearly as the thickness becomes larger. This large slope could be related to the fact that the number of spins inside the shell of the hollow nanoparticle becomes significantly important in comparison to those spins lying at the inner or outer surfaces. This study thus shows the important competition between surface anisotropy and exchange energy in HMNPs and sheds light on the size and thickness effects on spin configuration of such system.

Davide will add few sentence to conclude.

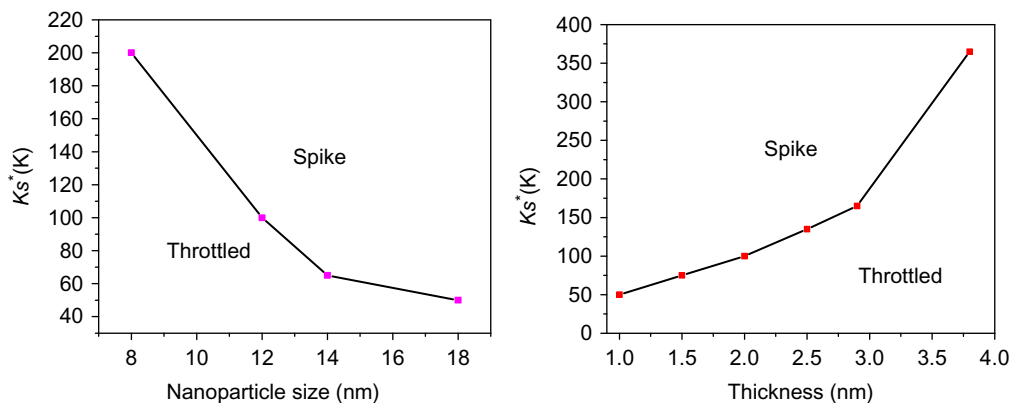


Fig. 4.18

Variation of the critical value of K_s as a function of the size and shell thickness of hollow nanoparticle, respectively. (Reproduced with permission from F. Sayed, Y. Labaye, R. Sayed Hassan, F. El Haj Hassan, N. Yaacoub, J.-M. Grenèche, *Size and thickness effect on magnetic structures of maghemite hollow magnetic nanoparticles*, *J. Nanoparticle Res.* 18(9) (2016) 279.)

References

- [1] L. Suber, D. Peddis, Approaches to synthesis and characterization of spherical and anisometric metal oxide magnetic nanomaterials, in: C.S.S.R. Kumar (Ed.), *Nanomaterials for Life Science*, vol. 4, Wiley, Weinheim, 2010, p. 431475.
- [2] J.L. Dormann, D. Fiorani, E. Tronc, Magnetic relaxation in fine-particle systems, *Adv. Chem. Phys.* XCVIII (1997) 283–494.
- [3] J.L. Dormann, D. Fiorani, in: *Magnetic properties of fine particles*, Proceedings of the International Workshop on Studies of Magnetic Properties of Fine Particles and Their Relevance to Materials Science, Rome, Italy, November 4–8, 1991, North-Holland, Ed., Amsterdam, 1992.
- [4] D. Peddis, M.V. Mansilla, S. Mørup, C. Cannas, A. Musinu, G. Piccaluga, F.D. Orazio, F. Lucari, D. Fiorani, Spin-canting and magnetic anisotropy in ultrasmall CoFe_2O_4 nanoparticles, *J. Phys. Chem. B* 112 (2008) 8507–8513.
- [5] J.M.D. Coey, Non-collinear spin arrangement in ultrafine ferrimagnetic crystallites, *Phys. Rev. Lett.* 27 (17) (1971) 1140.
- [6] M.P. Morales, C.J. Serna, F. Bodker, S. Morup, Spin canting due to structural disorder in maghemite, *J. Phys. Condens. Matter* 9 (25) (1997) 5461.
- [7] C. Cannas, A. Falqui, A. Musinu, D. Peddis, G. Piccaluga, G. Piccaluga, CoFe_2O_4 nanocrystalline powders prepared by citrate-gel methods: synthesis, structure and magnetic properties, *J. Nanopart. Res.* 8 (2) (2006) 255–267.
- [8] D. Peddis, C. Cannas, A. Musinu, G. Piccaluga, Coexistence of superparamagnetism and spin-glass like magnetic ordering phenomena in a $\text{CoFe}_2\text{O}_4\text{-SiO}_2$ nanocomposite, *J. Phys. Chem. C* 112 (2008) 5141–5147.
- [9] D. Peddis, Magnetic properties of spinel ferrite nanoparticles: influence of the magnetic structure, in: K.N. Trohidou (Ed.), *Magnetic Nanoparticle Assemblies*, vol. 7, Pan Stanford Publishing, Singapore, 2014, pp. 978–981.
- [10] C. Cannas, A. Musinu, G. Piccaluga, D. Fiorani, D. Peddis, H.K. Rasmussen, S. Mørup, Magnetic properties of cobalt ferrite-silica nanocomposites prepared by a sol-gel autocombustion technique, *J. Chem. Phys.* 125 (16) (2006) 164714.

- [11] A.G. Roca, D. Carmona, N. Miguel-Sancho, O. Bomatí-Miguel, F. Balas, C. Piquer, J. Santamaría, Surface functionalization for tailoring the aggregation and magnetic behaviour of silica-coated iron oxide nanostructures, *Nanotechnology* 23 (15) (2012) 155603.
- [12] A.G. Roca, D. Niznansky, J. Poltiero-Vejpravova, B. Bittova, M.A. Gonzalez-Fernandez, C.J. Serna, M.P. Morales, Magnetite nanoparticles with no surface spin canting, *J. Appl. Phys.* 105 (11) (2009) 114307–114309.
- [13] D. Peddis, F. Orrù, A. Ardu, C. Cannas, A. Musinu, G. Piccaluga, Interparticle interactions and magnetic anisotropy in cobalt ferrite nanoparticles: influence of molecular coating, *Chem. Mater.* 24 (6) (2012) 1062–1071.
- [14] S. Sun, H. Zeng, D.B. Robinson, S. Raoux, P.M. Rice, S.X. Wang, G. Li, Monodisperse MFe₂O₄ (M = Fe, Co, Mn) nanoparticles, *J. Am. Chem. Soc.* 126 (1) (2004) 273–279.
- [15] C. Cannas, A. Ardu, D. Peddis, C. Sangregorio, G. Piccaluga, A. Musinu, Surfactant-assisted route to fabricate CoFe₂O₄ individual nanoparticles and spherical assemblies, *J. Colloid Interface Sci.* 343 (2) (2010) 415–422.
- [16] F. Fiévet, R. Brayner, The polyol process, in: R. Brayner, F. Fiévet, T. Coradin (Eds.), *Nanomaterials: A Danger or a Promise? SE-1*, Springer, London, 2013, pp. 1–25.
- [17] W. Cai, J. Wan, Facile synthesis of superparamagnetic magnetite nanoparticles in liquid polyols, *J. Colloid Interface Sci.* 305 (2) (2007) 366–370.
- [18] G. Baldi, D. Bonacchi, C. Innocenti, G. Lorenzi, C. Sangregorio, Cobalt ferrite nanoparticles: the control of the particle size and surface state and their effects on magnetic properties, *J. Magn. Magn. Mater.* 311 (1) (2007) 10–16.
- [19] C. Cannas, A. Musinu, A. Ardu, F. Orrù, D. Peddis, M. Casu, R. Sanna, F. Angius, G. Diaz, G. Piccaluga, CoFe₂O₄ and CoFe₂O₄/SiO₂ core/shell nanoparticles: magnetic and spectroscopic study, *Chem. Mater.* 22 (11) (2010) 3353–3361.
- [20] R. Rakshit, M. Mandal, M. Pal, K. Mandal, Tuning of magnetic properties of CoFe₂O₄ nanoparticles through charge transfer effect, *Appl. Phys. Lett.* 104 (9) (2014) 092412.
- [21] C.R. Vestal, Z.J. Zhang, Effects of surface coordination chemistry on the magnetic properties of MnFe₂O₄ spinel ferrite nanoparticles, *J. Am. Chem. Soc.* 125 (32) (2003) 9828–9833.
- [22] J. Salafranca, J. Gazquez, N. Pérez, A. Labarta, S.T. Pantelides, S.J. Pennycook, X. Batlle, M. Varela, Surfactant organic molecules restore magnetism in metal-oxide nanoparticle surfaces, *Nano Lett.* 12 (5) (2012) 2499–2503.
- [23] Y. Tanaka, S. Saita, S. Maenosono, Influence of surface ligands on saturation magnetization of FePt nanoparticles, *Appl. Phys. Lett.* 92 (9) (2008) 93117.
- [24] Deleted in Review.
- [25] Deleted in Review.
- [26] S. Morup, M.F. Hansen, C. Frandsen, Magnetic nanoparticle, in: D.L. Andrews, G.D. Scholes, G. P. Wiederrecht (Eds.), *Comprehensive Nanoscience and Technology*, Elsevier, New York, 2011, pp. 437–491.
- [27] L. Néel, Théorie Du Trainage Magnétique Des Ferromagnétiques En Grains Fins Avec Applications Aux Terres Cuites, *Ann. Geophys.* 5 (2) (1949) 99–136.
- [28] C. Binns (Ed.), *Nanomagnetism: Fundamentals and Applications*, Elsevier, Oxford, 2014.
- [29] S. Bedanta, W. Kleemann, Supermagnetism, *J. Phys. D. Appl. Phys.* 42 (1) (2009) 13001.
- [30] J.M.D. Coey, *Magnetism and Magnetic Materials*, Cambridge University Press, New York, 2010.
- [31] S. Blundell, *Magnetism in Condensed Matter*, Oxford University Press, Oxford, 2001.
- [32] A.H. Morrish, *The Physical Principles of Magnetism*, Wiley, New York, 1965.
- [33] F. Bødker, S. Mørup, S. Linderoth, Surface effects in metallic iron nanoparticles, *Phys. Rev. Lett.* 72 (2) (1994) 282–285.
- [34] W.H. Meiklejohn, C.P. Bean, New magnetic anisotropy, *Phys. Rev.* 102 (5) (1956) 1413–1414.
- [35] T. Ic, S.T. Ic, Beating the superparamagnetic limit with exchange bias, *Nature* 423 (June) (2003) 19–22.
- [36] A. López-Ortega, M. Estrader, G. Salazar-Alvarez, A.G. Roca, J. Nogués, Applications of exchange coupled bi-magnetic hard/soft and soft/hard magnetic core/shell nanoparticles. *Phys. Rep.* 553 (2014) 1–32, <https://doi.org/10.1016/j.physrep.2014.09.007>.

- [37] F. Wiekhorst, E. Shevchenko, H. Weller, J. Kötzler, Anisotropic superparamagnetism of monodisperse cobalt-platinum nanocrystals, *Phys. Rev. B* 67 (22) (2003) 224416.
- [38] L. Néel, *Ann. Geophys.* 5 (1949) 99–109.
- [39] W.F.J. Brown, Thermal fluctuations of single-domain particle, *Phys. Rev.* 130 (1963) 1677–1686.
- [40] E.C. Stoner, E.P. Wohlfarth, A mechanism of magnetic hysteresis in heterogeneous alloys, *Philos. Trans. R. Soc. Lond. A Math. Phys. Eng. Sci.* 240 (826) (1948) 599–642.
- [41] M. Knobel, W. Nunes, Superparamagnetism and other magnetic features in granular materials: a review on ideal and real systems, *J. Nanosci. Nanotechnol.* 8 (4) (2008) 1880–1885.
- [42] S. Morup, M.B. Madsen, J. Franck, C.J.W. Koch, A new interpretation of mossbauer spectra of microcrystalline gehäite: super-ferromagnetism or superspin-glass behaviour? *J. Magn. Magn. Mater.* 40 (1983) 163–174.
- [43] D. Peddis, P. Jönsson, G. Varvaro, S. Laureti, Magnetic interactions: a tool to modify the magnetic properties of materials based on nanoparticles, in: C. Binns (Ed.), *Nanomagnetism Fundament and Application*, Elsevier B.V, Oxford, UK, 2014, pp. 129–189.
- [44] S. Bedanta, O. Petracic, W. Kleemann, Supermagnetism, in: K.F.H. Buschow (Ed.), *Handbook of Magnetic Materials*, Elsevier, Amsterdam, 2014, pp. 1–83.
- [45] S. Mørup, M.F. Hansen, C. Frandsen, Magnetic interactions between nanoparticles, *Beilstein J. Nanotechnol.* 1 (2010) 182–190.
- [46] C. Vestal, Q. Song, Z. Zhang, Effects of interparticle interactions upon the magnetic properties of CoFe_2O_4 and MnFe_2O_4 nanocrystals, *J. Phys. Chem.* 108 (2004) 18222–18227.
- [47] J.A. De Toro, S.S. Lee, D. Salazar, J.L. Cheong, P.S. Normile, P. Muñoz, J. M. Riveiro, M. Hillenkamp, F. Tournus, A. Tamion, P. Nordblad, A nanoparticle replica of the spin-glass state, *Appl. Phys. Lett.* 102 (18) (2013) 183104.
- [48] M.A. Ruderman, C. Kittel, Indirect exchange coupling of nuclear magnetic moments by conduction electrons, *Phys. Rev.* 96 (1) (1954) 99–102.
- [49] T. Kasuya, A theory of metallic ferro- and antiferromagnetism on Zener’s model, *Prog. Theor. Phys.* 16 (1) (1956) 45–57.
- [50] K. Yosida, Magnetic properties of Cu-Mn alloys, *Phys. Rev.* 106 (5) (1957) 893–898.
- [51] V.N. Kondratyev, H.O. Lutz, Shell effect in exchange coupling of transition metal dots and their arrays, *Phys. Rev. Lett.* 81 (20) (1998) 4508.
- [52] M. Scheinfein, K. Schmidt, K. Heim, G. Hembree, Magnetic order in two-dimensional arrays of nanometer-sized superparamagnets, *Phys. Rev. Lett.* 76 (9) (1996) 1541–1544.
- [53] J. La Villain, Structure des substance magentiques, *J. Phys. Chem. Solids* 11 (1) (1959) 303–309.
- [54] A. Yoshimori, A new type of antiferromagnetic structure in the rutile type crystal, *J. Phys. Soc. Jpn.* 14 (6) (1959) 807–821.
- [55] T.A. Kaplan, Classical spin-configuration stability in the presence of competing exchange forces, *Phys. Rev.* 116 (4) (1959) 888–889.
- [55a] H. Dvey-Aharon, M. Fibich, Magnetic properties of a disordered substitutional alloy—Heisenberg model, *Phys. Rev. B* 18 (1979) 3491.
- [55b] J. Stankiewicz, J. Bartolomé, D. Fruchart, Spin disorder scattering in magnetic metallic alloys, *Phys. Rev. Lett.* 89 (2002) 106602.
- [55c] S. Nishimoto, V.M. Katukuri, V. Yushankhai, H. Stoll, U.K. Röbler, L. Hozoi, I. Rousochatzakis, J. van den Brink, Strongly frustrated triangular spin lattice emerging from triplet dimer formation in honeycomb Li_2IrO_3 , *Nat Commun.* 18 (7) (2016) 10273, <https://doi.org/10.1038/ncomms10273>.
- [55d] B. Martinez, A. Alberta, R. Rodriguez-Sola, X. Obradors, Magnetic transition in highly frustrated $\text{SrCr}_8\text{Ga}_4\text{O}_{19}$: the archetypal Kagoné system, *Phys. Rev. B* 50 (21) (1994).
- [56] C.M. Hurd, Varieties of magnetic order in solids, *J. Contemp. Phys.* 23 (5) (1982) 469–493.
- [57] J.M.D. Coey, P.W. Readman, Characterisation and magnetic properties of natural ferric gel, *Earth Planet. Sci. Lett.* 21 (1) (1973) 45–51.
- [58] J.M.D. Coey, P.W. Readman, New spin structure in an amorphous ferric gel, *Nature* 246 (5434) (1973) 476–478.

- [59] J.M.D. Coey, Interpretation of the mossbauer spectra of speromagnetic materials, *J. Phys. Condens. Matter* (1993) 7297–7300.
- [60] S. Mørup, E. Brok, C. Frandsen, Spin structures in magnetic nanoparticles, *J. Nanomater.* 2013 (111) (2013) 1–8.
- [61] F. Bodker, S. Morup, Size dependence of the properties of hematite nanoparticles, *Europhys. Lett.* 52 (2) (2000) 217–223.
- [62] S. Linderoth, P.V. Hendriksen, F. Bodker, S. Wells, K. Davies, S.W. Charles, S. Morup, On spin-canting in maghemite particles, *J. Appl. Phys.* 75 (1994) 6583–6585.
- [63] R.H. Kodama, Magnetic nanoparticles, *J. Magn. Magn. Mater.* 200 (January) (1999) 359–372.
- [64] J.S. Choi, Y.W. Jun, S.I. Yeon, H.C. Kim, J.S. Shin, J. Cheon, Biocompatible heterostructured nanoparticles for multimodal biological detection, *J. Am. Chem. Soc.* 128 (50) (2006) 15982–15983.
- [65] Q.A. Pankhurst, J. Connelly, S.K. Jones, J. Dobson, Applications of magnetic nanoparticles in biomedicine, *J. Phys. D. Appl. Phys.* 36 (2003) R167–R181.
- [66] A.R. West, *Solid State Chemistry and Its Applications*, Wiley, New York, 1984.
- [67] G.A. Sawatzky, F. Van Der Woude, A.H. Morrish, Mossbauer study of several ferrimagnetic spinels, *Phys. Rev.* 187 (2) (1969) 747–757.
- [68] G.A. Sawatzky, F. Van Der Woude, A.H. Morrish, Cation distributions in octahedral and tetrahedral sites of the ferrimagnetic spinel CoFe_2O_4 , *J. Appl. Phys.* 39 (2) (1968) 1204–1205.
- [69] C. Liu, A.J. Rondinone, Z.J. Zhang, Synthesis of magnetic spinel ferrite CoFe_2O_4 nanoparticles from ferric salt and characterization of the size-dependent superparamagnetic properties, *Pure Appl. Chem.* 72 (1–2) (2000) 37–45.
- [70] C. Liu, B. Zou, A.J. Rondinone, Z.J. Zhang, Chemical control of superparamagnetic properties of magnesium and cobalt spinel ferrite nanoparticles through atomic level magnetic couplings, *J. Am. Chem. Soc.* 122 (26) (2000) 6263–6267.
- [71] V. Mameli, A. Musinu, A. Ardu, G. Ennas, D. Peddis, D. Niznansky, C. Sangregorio, C. Innocenti, N.T. K. Thanh, C. Cannas, Studying the effect of Zn-substitution on the magnetic and hyperthermic properties of cobalt ferrite nanoparticles, *Nanoscale* 8 (2016) 10124–10137.
- [72] G. Muscas, N. Yaacoub, G. Concas, F. Sayed, R. Sayed Hassan, J. M. Greneche, C. Cannas, A. Musinu, V. Foglietti, S. Casciardi, C. Sangregorio, D. Peddis, Evolution of the magnetic structure with chemical composition in spinel iron oxide nanoparticles, *Nanoscale* 7 (32) (2015) 13576–13585.
- [73] R.H. Kodama, S.A. Makhlof, A.E. Berkowitz, Finite size effects in antiferromagnetic NiO nanoparticles, *Phys. Rev. Lett.* 79 (7) (1997) 1393.
- [74] R.H. Kodama, A.E. Berkowitz, E. McNiff, S. Foner, J.E.J. McNiff, Surface spin disorder in NiFe_2O_4 nanoparticles, *Phys. Rev. Lett.* 77 (2) (1996) 394–397.
- [75] R.H. Kodama, A.E. Berkowitz, E.J. McNiff, S. Foner, Surface spin disorder in ferrite nanoparticles (invited), *J. Appl. Phys.* 81 (8) (1997) 5552–5557.
- [76] C. Cannas, A. Musinu, D. Peddis, G. Piccaluga, Synthesis and characterization of CoFe_2O_4 nanoparticles dispersed in a silica matrix by a sol-gel autocombustion method, *Chem. Mater.* 18 (16) (2006) 3835–3842.
- [76a] J. Rodríguez-Carvajal, Recent advances in magnetic structure determination by neutron powder diffraction, *Phys. B: Condensed Matter* 192 (1–2) (1993) 55–69.
- [76b] E.O. Wollan, W.C. Koehler, Neutron diffraction study of the magnetic properties of the series of Perovskite-type compounds $[(1-x)\text{La}, x\text{Ca}]\text{MnO}_3$, *Phys. Rev.* 100 (1955) 545.
- [77] D. Peddis, N. Yaacoub, M. Ferretti, A. Martinelli, G. Piccaluga, A. Musinu, C. Cannas, G. Navarra, J. M. Greneche, D. Fiorani, Cationic distribution and spin canting in CoFe_2O_4 nanoparticles, *J. Phys. Condens. Matter* 23 (42) (2011) 426004.
- [78] D. Lin, A.C. Nunes, C.F. Majkrzak, A.E. Berkowitz, Polarized neutron study of the magnetization density distribution within a CoFe_2O_4 colloidal particle II, *J. Magn. Magn. Mater.* 145 (1995) 343–348.
- [79] D. Peddis, C. Cannas, G. Piccaluga, E. Agostinelli, D. Fiorani, Spin-glass-like freezing and enhanced magnetization in ultra-small CoFe_2O_4 nanoparticles, *Nanotechnology* 21 (12) (2010) 125705.

- [80] L.G. Vivas, R. Yanes, A. Michels, Small-angle neutron scattering modeling of spin disorder in nanoparticles, *Sci. Rep.* 7 (2017) 1–11.
- [81] S. Yang, C. Feng, D. Spence, A.M.A.A. Al Hindawi, E. Latimer, A.M. Ellis, C. Binns, D. Peddis, S.S. Dhési, L. Zhang, Y. Zhang, K.N. Trohidou, M. Vasilakaki, N. Ntallis, I. Maclaren, F.M.F. De Groot, Robust ferromagnetism of chromium nanoparticles formed in superfluid helium, *Adv. Mater.* 29 (1) (2017) 1–6.
- [82] C. Binns, M.T. Qureshi, D. Peddis, S.H. Baker, P.B. Howes, A. Boatwright, S.A. Cavill, S.S. Dhési, L. Lari, R. Kroger, S. Langridge, Exchange bias in Fe@Cr core-shell nanoparticles, *Nanoletters* 13 (2013) 3334–3339.
- [83] Y. Yoshida, G. Langouche, *Mössbauer Spectroscopy*, Springer, London, 2012.
- [84] N.N. Greenwood, T.C. Gibb, *Mossbauer Spectroscopy*, Chapman and Hall Ltd., London, 1971.
- [85] J.L. Dormann, D. Fiorani, E. Tronc, Magnetic relaxation in fine particle systems, in: *Advances in Chemical Physics*, vol. XCVIII, Wiley, New York, 1997, pp. 283–494.
- [86] E. Tronc, J.P. Jolivet, F. Orazio, F. Lucari, D. Fiorani, Magnetic behaviour of gamma-Fe₂O₃ nanoparticles by Mössbauer spectroscopy and magnetic measurements, *Hyperfine Interact.* 95 (1995) 129–148.
- [87] C. Cannas, A. Musinu, D. Peddis, G. Piccaluga, New synthesis of ferrite–silica nanocomposites by a sol–gel auto-combustion, *J. Nanopart. Res.* 6 (2004) 223–232.
- [88] G. Concas, G. Spano, C. Cannas, A. Musinu, D. Peddis, G. Piccaluga, Inversion degree and saturation magnetization of different nanocrystalline cobalt ferrites, *J. Magn. Magn. Mater.* 321 (12) (2009) 1893–1897.
- [89] D. Peddis, N. Yaacoub, M. Ferretti, A. Martinelli, G. Piccaluga, A. Musinu, C. Cannas, G. Navarra, J. M. Grenèche, D. Fiorani, Cationic distribution and spin canting in CoFe₂O₄ nanoparticles, *J. Phys. Condens. Matter* 23 (42) (2011) 426004 1–8.
- [90] A.J. Rondinone, C. Liu, Z.J. Zhang, Determination of magnetic anisotropy distribution and anisotropy constant of manganese spinel ferrite nanoparticles, *J. Phys. Chem. B* 105 (2001) 7967–7971.
- [91] B. Martínez, X. Obradors, L. Balcells, A. Rouanet, C. Monty, Low temperature surface spin-glass transition in gamma G-Fe₂O₃ nanoparticles, *Phys. Rev. Lett.* 80 (1) (1998) 181–184.
- [92] D. Peddis, C. Cannas, G. Piccaluga, E. Agostinelli, D. Fiorani, Spin-glass-like freezing and enhanced magnetization in ultra-small CoFe₂O₄ nanoparticles, *Nanotechnology* 21 (12) (2010) 125705 1–10.
- [93] E. De Biasi, R.D. Zysler, C.A. Ramos, H. Romero, E. De Biasi, Magnetization enhancement at low temperature due to surface ordering in Fe–Ni–B amorphous nanoparticles, *Phys. B Condens. Matter* 320 (1–4) (2002) 203–205.
- [94] R. Aquino, J. Depeyrot, M.H. Sousa, F.A. Tourinho, E. Dubois, R. Perzynski, Magnetization temperature dependence and freezing of surface spins in magnetic fluids based on ferrite nanoparticles, *Phys. Rev. B* 72 (18) (2005) 184410–184435.
- [95] M. Artus, L.B. Tahar, F. Herbst, L. Smiri, F. Villain, N. Yaacoub, J.-M. Grenèche, S. Ammar, F. Fiévet, Size-dependent magnetic properties of CoFe₂O₄ nanoparticles prepared in polyol, *J. Phys. Condens. Matter* 23 (50) (2011) 506001.
- [96] E. Tronc, P. Prené, J.P. Jolivet, J.L. Dormann, J.M. Grenèche, Spin canting in γ -Fe₂O₃ nanoparticles, in: *Hyperfine Interactions*, Springer, Dordrecht, 1998, pp. 97–100.
- [97] E. Fantechi, C. Innocenti, M. Albino, E. Lottini, C. Sangregorio, Influence of cobalt doping on the hyperthermic efficiency of magnetite nanoparticles, *J. Magn. Magn. Mater.* 380 (2015) 365–371.
- [98] Q. Song, Z.J. Zhang, Correlation between spin-orbital coupling and the superparamagnetic properties in magnetite and cobalt ferrite spinel nanocrystals, *J. Phys. Chem. B* 110 (23) (2006) 11205–11209.
- [99] A.J. Rondinone, A.C.S. Samia, Z.J. Zhang, Characterizing the magnetic anisotropy constant of spinel cobalt ferrite nanoparticles, *Appl. Phys. Lett.* 76 (24) (2000) 3624–3626.
- [100] S. Laureti, G. Varvaro, A. M. Testa, D. Fiorani, E. Agostinelli, G. Piccaluga, A. Musinu, A. Ardu, D. Peddis, Magnetic interactions in silica coated nanoporous assemblies of CoFe₂O₄ nanoparticles with cubic magnetic anisotropy, *Nanotechnology* 21 (31) (2010) 315701.
- [101] A. Virden, S. Wells, K. O’Grady, Physical and magnetic properties of highly anisotropic cobalt ferrite particles, *J. Magn. Magn. Mater.* 316 (2) (2007) e768–e771.

- [102] E.C. Sousa, M.H. Sousa, G.F. Goya, H.R. Rechenberg, M.C.F.L. Lara, F.A. Tourinho, J. Depeyrot, Enhanced surface anisotropy evidenced by mössbauer spectroscopy in nickel ferrite nanoparticles, *J. Magn. Magn. Mater.* 272–276 (2004) E1215–E1217.
- [103] H. Nathani, S. Gubbala, R.D.K. Misra, Magnetic behavior of nanocrystalline nickel ferrite, *Mater. Sci. Eng. B* 121 (1–2) (2005) 126–136.
- [104] B. Pacakova, S. Kubickova, A. Reznickova, D. Niznansky, A. Reznickova, D. Niznansky, Spinel ferrite nanoparticles: correlation of structure and magnetism, in: M.S. Seehra (Ed.), *Magnetic Spinel-Synthesis, Properties and Applications*, InTech, 2017.
- [105] B. Cruz-franco, T. Gaudisson, S. Ammar, A.M. Bolarín-Miró, F.S. De Jesus, F. Mazaleyrat, S. Nowak, G. Vázquez-Victorio, R. Ortega-Zempoalteca, R. Valenzuela, U. Autónoma, M. de Reforma, Magnetic properties of nanostructured spinel ferrites, *IEEE Trans. Magn.* 50 (4) (2014) 2–7.
- [106] D. Carta, G. Mountjoy, G. Navarra, M.F. Casula, D. Loche, S. Marras, A. Corrias, X-ray absorption investigation of the formation of cobalt ferrite nanoparticles in an aerogel silica matrix, *J. Phys. Chem. C* 111 (17) (2007) 6308–6317.
- [107] D. Carta, M.F. Casula, A. Falqui, D. Loche, G. Mountjoy, C. Sangregorio, A. Corrias, A structural and magnetic investigation of the inversion degree in ferrite nanocrystals MFe_2O_4 ($M = Mn, Co, Ni$), *J. Phys. Chem. C* 113 (20) (2009) 8606–8615.
- [108] A. Demortière, P. Panissod, B.P. Pichon, G. Pourroy, D. Guillon, B. Donnio, S. Bégin-Colin, Size-dependent properties of magnetic Iron oxide nanocrystals, *Nanoscale* 3 (1) (2011) 225–232.
- [109] Y. Yin, A.P. Alivisatos, Colloidal nanocrystal synthesis and the organic-inorganic interface, *Nature* 437 (7059) (2005) 664–670.
- [110] W. Wu, Q. He, C. Jiang, Magnetic iron oxide nanoparticles: synthesis and surface functionalization strategies, *Nanoscale Res. Lett.* 3 (11) (2009) 397–415.
- [111] C. Berry, A. Curtis, Functionalisation of magnetic nanoparticles for applications in biomedicine, *J. Phys. D: Appl. Phys.* 36 (2003) 198.
- [112] D. Ling, M.J. Hackett, T. Hyeon, Surface ligands in synthesis, modification, assembly and biomedical applications of nanoparticles, *Nano Today* 9 (4) (2014) 457–477.
- [113] X.W. Wu, C. Liu, L. Li, P. Jones, R.W. Chantrell, D. Weller, Nonmagnetic shell in surfactant-coated FePt nanoparticles, *J. Appl. Phys.* 95 (11) (2004) 6810–6812.
- [114] B.N. Figgis, M.A. Hitchman, *Ligand Field Theory and Its Applications*, Wiley-VCH, Weinheim, 2000.
- [115] J. Mohapatra, A. Mitra, D. Bahadur, M. Aslam, Surface controlled synthesis of MFe_2O_4 ($M = Mn, Fe, Co, Ni$ and Zn) nanoparticles and their magnetic characteristics, *CrystEngComm* 15 (3) (2013) 524.
- [116] R. Rakshit, M. Mandal, M. Pal, K. Mandal, R. Rakshit, M. Mandal, M. Pal, K. Mandal, Tuning of magnetic properties of $CoFe_2O_4$ nanoparticles through charge transfer effect, *Appl. Phys. Lett.* 92412 (104) (2014) 92412.
- [117] S.-H. Noh, W. Na, J.-T. Jang, J.-H. Lee, E.J. Lee, S.H. Moon, Y. Lim, J.-S. Shin, J. Cheon, Nanoscale magnetism control via surface and exchange anisotropy for optimized ferrimagnetic hysteresis, *Nano Lett.* 12 (7) (2012) 3716–3721.
- [118] G. Salazar-Alvarez, J. Qin, V. Sepelak, Cubic versus spherical magnetic nanoparticles: the role of surface anisotropy, *J. Am. Chem. Soc.* (18) (2008) 13234–13239.
- [119] Q. Song, Z.J. Zhang, Shape control and associated magnetic properties of spinel cobalt ferrite nanocrystals, *J. Am. Chem. Soc.* 126 (19) (2004) 6164–6168.
- [120] D. Gatteschi, M. Fittipaldi, C. Sangregorio, L. Sorace, Exploring the no-man’s land between molecular nanomagnets and magnetic nanoparticles, *Angew. Chem. Int. Ed.* 51 (2012) 2–11.
- [121] F. Sayed, Y. Labaye, R. Sayed Hassan, F. El Haj Hassan, N. Yaacoub, J.-M. Greneche, Size and thickness effect on magnetic structures of maghemite hollow magnetic nanoparticles, *J. Nanopart. Res.* 18 (9) (2016) 279.

This page intentionally left blank

Self-Assembly of Magnetic Iron Oxide Nanoparticles Into Cuboidal Superstructures

Sabine Rosenfeldt, Stephan Förster, Thomas Friedrich, Ingo Rehberg,
Birgit Weber

University of Bayreuth, Bayreuth, Germany

5.1 Motivation

5.1.1 Properties of Magnetic Iron Oxide Nanoparticles

Nanoparticles possess at least in one dimension a size in the nanometer range. Their properties can differ from the ones of the corresponding bulk material. Spherical particles with a radius of 10 nm consist of about 8000 atoms, in which 6% are surface atoms. By contrast, a sphere with a radius of 1 mm exhibits only $6 \times 10^{-5}\%$ surface atoms. As consequence of the energetically unfavorable ratio of surface to volume, nanoparticles tend to aggregate. Colloidal stability of nanoparticles can be achieved by a protective cover. In case of short-range attractive interaction, the protecting layer screens attractive interaction such that the nanoparticles form stable dispersions. Hence, the resulting nanoparticles are by default surface-functionalized and often show a core-shell structure.

Nanoparticles exhibit physical properties that depend strongly on their size and shape. Magnetic nanoparticles may possess one or more than one Weiss-domain. Depending on their size and the temperature they show ferromagnetic or superparamagnetic behavior. If the nanoparticles are small enough they contain only one magnetic domain. At room temperature most sub-10 nm iron oxide magnetic nanoparticles show superparamagnetic behavior because the thermal energy is sufficient to flip the magnetization direction. The temperature dependence of the fluctuation time τ_N of the magnetization has been described by Néel as $\tau_N = \tau_0 \exp\left(\frac{\Delta E_{\text{mag}}}{k_B T}\right)$, where the ΔE_{mag} is the energetic barrier between the two magnetization states, k_B the Boltzmann constant, and T the temperature. τ_0 is a characteristic time in the order of nanoseconds. Below the so-called blocking temperature, the flipping of the magnetization is extremely rare and hysteresis is observed, that is, the material is ferromagnetic. As ΔE_{mag} depends strongly on size, anisotropy, and surface properties of the nanoparticles, so does the blocking temperature.

5.1.2 Applications of Magnetic Iron Oxide Nanoparticles

Nanostructured magnetic materials are omnipresent. They are used in medical, environmental, and technical applications [1]. Iron oxide nanoparticles consist mostly of maghemite ($\gamma\text{-Fe}_2\text{O}_3$) or magnetite (Fe_3O_4) and exhibit single domains of about 5–20 nm in diameter [2]. Magnetite is a cubic inverse spinel. The oxygen anions form a face centered cubic packing and the iron cations occupy interstitial tetrahedral (tetr) and octahedral (octa) sites. The formula can be written as $(\text{Fe}^{3+})^{\text{tetr}}(\text{Fe}^{3+}, \text{Fe}^{2+})^{\text{octa}}\text{O}_4$. The electrons can hop between Fe^{2+} and Fe^{3+} ions in the octahedral sites at room temperature. Maghemite can be considered as an Fe^{2+} -free magnetite. It results the formula $(\text{Fe}_8^{3+})^{\text{tetr}}(\text{Fe}_{40/3}^{3+}\text{O}_{8/3})^{\text{octa}}\text{O}_{32}$ (vacancies o) [3].

For medical and bioengineering in vivo applications superparamagnetic iron oxide nanoparticles (SPIONs) with high magnetization and sizes smaller than 100 nm are commonly used, because these nanoparticles are nontoxic and biocompatible [4]. For medical applications the magnetic moment of the particles is used in three different ways: (i) For hyperthermal applications parts of the in vivo material are heated locally by external time-dependent magnetic field. (ii) For magnetic particle imaging the nonlinear response of the magnetization is locally detected and interpreted as an indication for the particle concentration [5]. (iii) Surface functionalized magnetic nanoparticles are used for targeted drug delivery, where SPIONs are addressed by external magnetic fields and located in a specific area of the body [4].

Iron oxide nanoparticles are also used in environmental application [6]. Suitably coated with catalysts or enzymes, these nanoparticles can be used as cleaning agent, which can be extracted by external magnetic fields. In addition, these particles can be easily detected. Such strategies are used in oil-field rocks and contaminated geological systems [7].

Many technical applications are based on ferrofluids, which consist of magnetic nanoparticles in a nonmagnetic solvent. Examples are damping devices or magnetic seals for rotating shafts [8]. The field and temperature-dependent variation in the refractive index of these fluids is interesting for optical filters, optical gratings, or defect sensors [9, 10].

5.2 Synthesis and Properties of Nanoparticles

Synthesis of well-defined biocompatible, monodisperse iron oxide nanoparticles in aqueous media are demanding for three reasons: (i) generally, the synthesis is done in organic media and a solvent transfer is performed later on. (ii) Surface functionalization of the nanoparticles is crucial to circumvent aggregation and surface-oxidation. (iii) For monodispersity the reaction parameters and time must be controlled precisely.

Common methods to synthesize iron oxide nanoparticles are (i) coprecipitation, (ii) thermal decomposition, and (iii) hydrothermal or solvothermal synthesis. Moreover, the trend to

green-chemistry leads to the development of (iv) biological synthesis routes [11]. (i) During coprecipitation ferric (Fe^{3+}) and ferrous (Fe^{2+}) ions are mixed in basic solution. This is a classical way to obtain large amounts of iron oxide nanoparticles with a high saturation magnetization, but with the disadvantage of a broad particle size distribution. (ii) Monodisperse and highly crystalline particles are obtained via high-temperature thermal decomposition. The size of the nanoparticles is adjustable by parameters like the ageing temperature and the salt concentration. (iii) Hydrothermal and solvothermal syntheses are wet-chemical techniques of crystallization under high pressure. The synthesis routes allow a good control over the chemical composition and the shape of the iron oxide nanoparticles. This way, even capsules, nanotubes, or hollow iron oxide nanoparticles, can be produced. Such an architectural control requires a tremendous synthetic effort. (iv) Biological approaches use enzymes or bacteria for the reduction of salts and the conversion into the respective iron oxide nanoparticles. For example, *Actinobacter* spp. reacts with ferric chloride precursors to maghemite under aerobic conditions. Biosynthesis is ecofriendly, but the morphological control of the final nanoparticles is still in its infancy.

5.2.1 Synthesis of Spherical and Cubic Iron Oxide Nanoparticles

The iron oxide particles, which are discussed in the following, are synthesized by the thermal decomposition method originally invented by Park et al. [12]. Following this approach, small dispersed iron oxide nanoparticles are produced in a large-scale synthesis. Typically, iron oxide nanoparticles with dimensions between 5–30 nm are obtained. They are monodisperse due to a separation of nucleation and growth. The synthetic procedure bases on the thermal decomposition of iron oleate precursors in a high boiling solvent, like 1-hexadecene (b.p. 274°C) or 1-octadecene (b.p. 317°C). The reactivity of the iron oleate complex and thereby, the size of the nanoparticle, increases with increasing boiling point of the solvent. The metal-oleate precursor is prepared by reacting an iron salt and sodium oleate. The morphology of the iron oxide nanocrystals can be finer adjusted by the oleic acid concentration. Spherical nanoparticles are obtained with small excess of sodium-oleate, whereas cubic particles result for larger excess of stabilizing ligand. The transition from spherical to cubic occurs around a sodium oleate excess of approximately 5% in the precursor complex. The specific synthesis of iron oxide nanoparticles, discussed in this chapter, is summarized in Table 5.1.

The composition of the nanocrystals is $(\gamma\text{-Fe}_2\text{O}_3)_{1-x}(\text{Fe}_3\text{O}_4)_x$ ($x \in [0, 1]$) [12]. The oxidation of magnetite to maghemite leads to a lower magnetization of the nanoparticle. Park et al. report that magnetite dominates in small 5-nm sized spherical nanocrystals ($x = 0.8$), while the amount of maghemite increases with the particle size ($x = 1$ for a size of about 20 nm). The ratio of the two iron oxides in the nanocrystals can be determined by ^{57}Fe -Mössbauer spectroscopy. This technique is based on a recoilless absorption of high energy γ -quanta, which leads to

Table 5.1 Synthesis of iron oxide nanoparticles (cf. Fig. 5.2) and the basic precursors

Iron(III)-Oleate Precursor
21.6 g FeCl ₃ ·6H ₂ O, 73.0–80.3 g sodium oleate (240–263 mmol, corresponding to 0–10% excess), 160 mL ethanol, 120 mL distilled water, and 180 mL hexane are suspended and heated to 70°C for 4 h. After cooling to room temperature, the iron oleate complex containing organic phase is washed with water several times. After purification the solution is concentrated under vacuum conditions at 110°C until the red-brownish iron-oleate complex shows up in a waxy form.
Iron Oxide Nanoparticles
Typically, 36 g (40 mmol) of the iron oleate complex were dissolved in a mixture of 200 g 1-octadecene and 2.8–5.7 g oleic acid. The spherical particle shown in Fig. 5.2 is prepared with 5.7 g oleic acid and 0% sodium oleate excess during the synthesis of the precursor, and the cubic one with 2.85 g oleic acid and 10% sodium oleate excess in the iron oleate complex synthesis. The reaction mixture was heated up under stirring to 110°C with a heating rate of approximately 2 K/min. After insertion of nitrogen cover gas, the mixture is heated further to 318°C and kept at this temperature for about 15 min. Thereby the color of the solution turns to black. It indicates the formation of the iron oxide nanocrystals. At room temperature the volume is doubled with tetrahydrofuran. Precipitation of the nanoparticles is performed by adding acetone. The nanocrystals were separated by centrifugation (24 h with 4800 rpm, approximately 2500 g). After decantation of the upper phase, the iron oxide nanoparticles can be redissolved in organic solvents like toluene.

Note: The ratio of iron chloride to sodium oleate determines the shape of the iron oxide nanoparticles later on.

small changes in the energy levels of the atomic nuclei. For iron species the electron transitions from nuclei with orbital quantum moment of $l = 3/2$ to $l = 1/2$ are detected. Two examples of such ⁵⁷Fe-Mössbauer spectra are shown in Fig. 5.1. The characteristic sextets of Fe^{3+/2+}-ions in tetrahedral and octahedral sites are visible. A quantitative analysis of the spectrum shown on the top reveals 60% maghemite and 40% magnetite. The spectrum at the bottom is of nanocrystals with a core size of 5 nm. The line width increases with decreasing particle size, preventing a determination of the exact composition in this case [12].

The shape and size of the nanoparticles are further analyzed by electron microscopy. Fig. 5.2 shows high-resolution transmission microscopy images (STEM) of cubic (right) and spherical (left) nanoparticles, which are synthesized using a precursor wax with 10% and 0% sodium oleate excess. Due to the high electron contrast of iron species only the crystalline iron oxide core (the nanocrystal) is visible in STEM, whereas the oleic acid shell is invisible. The images show the nearly perfect geometry of the iron oxide nanocrystals. The spherical shape is nearly perfect, and even the cubic nanocrystal is only slightly truncated. A 2D-Fourier analysis of such images, followed by radial averaging (not shown here), reveals that the crystal structure is compatible with an inverse spinel type.

Complementary information about the shape and size of the particles can be obtained by small-angle X-ray scattering (SAXS), where the particles are dispersed in a fluid. Two examples are given in the insets of Fig. 5.3. The X-ray scattering is mainly determined by the metal oxide core of the particles, whereas the stabilizing shell is barely detectable. Quantitatively speaking, the excess electron density for the core is about 1200 nm⁻³, which is about 20 times larger than the excess electron density of the oleic acid shell.

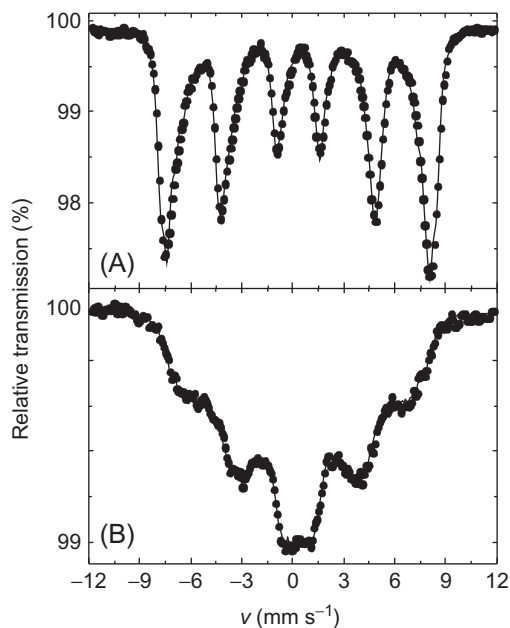


Fig. 5.1

Mössbauer spectra of iron oxide nanoparticles at 77 K. Both particles are stabilized by oleic acid. (A) Iron oxide cubes with a diameter of 9 nm. The composition is 60% maghemite and 40% magnetite. (B) Iron oxide spheres of 5 nm size.

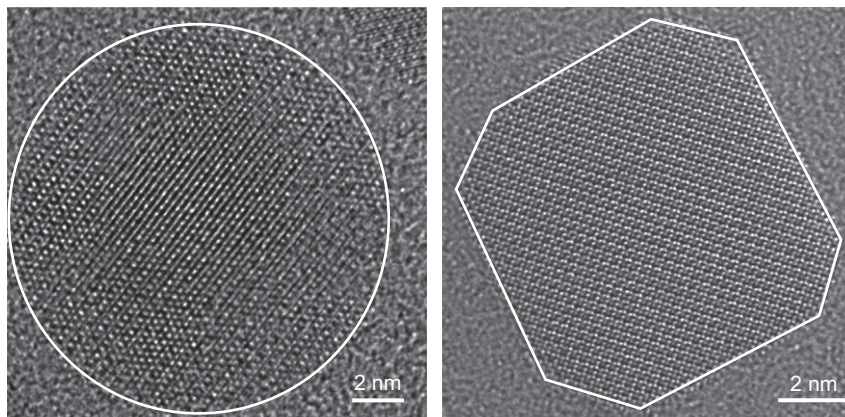


Fig. 5.2

STEM images of spherical (*left*) and cubic (*right*) nanoparticles, which consist of a crystalline iron oxide core (nanocrystal) and an oleic acid shell. The brightness of the images is determined by the electron density, thus the method is sensitive to the iron oxide core of the nanoparticles. The size of the nanocrystals is 13 nm (*left*) and 9 nm (*right*). The oleic acid shell contrast is too low to be detectable.

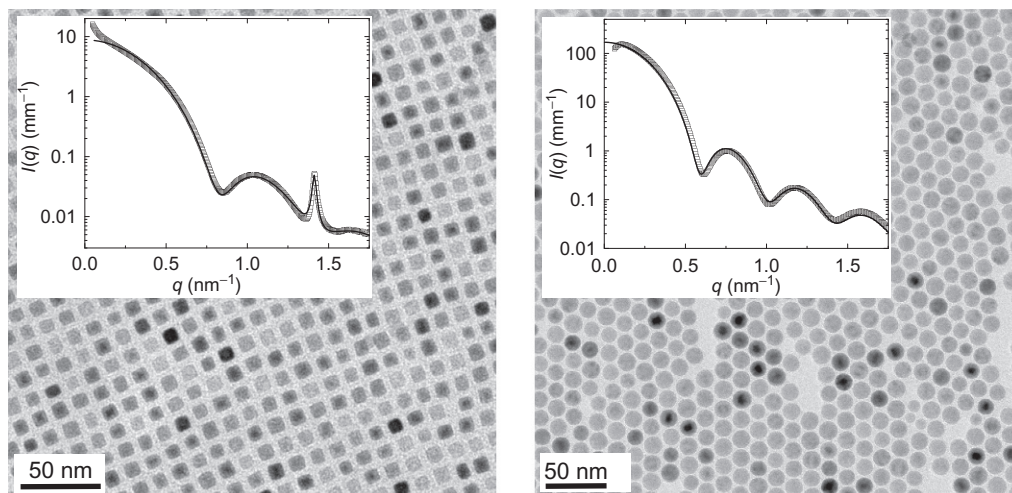


Fig. 5.3

Cyro-TEM (0.1 wt%) and SAXS data (2 wt%, insets) of iron oxide nanoparticles, which are stabilized by an oleic acid layer. Due to the low contrast (excess electron density) of the stabilizing oleic acid layer their X-ray scattering behavior is mainly determined by the metal-oxide core of the particles (1470 nm⁻³ for iron oxide, 300 nm⁻³ for oleic acid, and 238 nm⁻³ for toluene). The fits (*lines in insets*) reveal single cubes (9 nm) and spheres (13 nm). The Bragg reflex at $q = 1.41 \text{ nm}^{-1}$ seen in the SAXS pattern on the left side is attributed to crystalline oleic acid. The conditions under which this sharp peak develops are still unclear.

The SAXS intensity $I(q)$ is proportional to the product of the form factor $P(q)$ and the structure factor $S(q)$. $P(q)$ is determined by the shape, and $S(q)$ refers to the arrangement of the particles. At low concentrations the scattering is determined by the particle shape, for example, mainly by the form factor scattering of the iron oxide nanoparticles. The form factor of a homogeneous cube differs marginally from the one of a homogeneous sphere—the wavelength of the oscillations is broader and the deepness of the minima is smaller for cubes compared with the ones of volume identical spheres. The intensity decays in both cases with q^{-4} . The experimental data (open squares) can be well described by the corresponding form factor $P(q)$ indicated by the solid lines, when allowing for a small polydispersity. The fit of $P(q)$ leads to cubes of 9 nm and spheres of 13 nm. The standard deviation yields in both cases to 1 nm, when assuming a Gaussian particle distribution in diameter.

The measured intensity of the cubic nanoparticles has an additional feature, namely a sharp peak at $q = 1.41 \text{ nm}^{-1}$. This scattering vector corresponds to a crystalline structure with a characteristic length of 4.5 nm in real space. This reflex is attributed to oleic acid, as shown in Fig. 5.7 and discussed in detail later. Deviations between the fit and the data at scattering vectors smaller than $q < 0.15 \text{ nm}^{-1}$ are an indication for a minor fraction of aggregates, as described by Klokkenburg et al. [13] for magnetite ferrofluids.

The size of the iron oxide core obtained by SAXS is significantly smaller than the hydrodynamic radius obtained by dynamic light scattering (DLS). In DLS the overall size of the nanoparticle is seen, which includes the stabilizing oleic acid layer. The corresponding hydrodynamic diameters of the particles are 19.5 nm for the spherical and 16.7 nm for the cubic nanoparticles. The monodispersity is expressed by a polydispersity index of $PDI = 0.04$ for the spheres and $PDI = 0.08$ for the cubes [14]. The hydrodynamic radius obtained by DLS measurements leads to an oleic acid layer thickness of about 7 nm for one nanocube.

The core-shell morphology of oleic acid stabilized iron oxide nanoparticles is also clearly visible in the cryo-TEM images. The cubes show an almost perfectly ordered lattice. The oleic acid layer thickness can be estimated from the lattice plane distance to be about 5 nm. The peak seen at $q = 1.41 \text{ nm}^{-1}$ in the SAXS pattern corresponds to this distance. The smaller value of the oleic acid shell obtained from cryo-TEM analysis is explained by the fact that the particles overlap within their hydrodynamic radii in the packed state, which indicates a denser packing of oleic acid in the latter one.

5.2.2 Magnetic Properties of the Nanoparticles

Sufficiently small single domain ferromagnetic or ferrimagnetic nanoparticles become superparamagnetic. For superparamagnetic nanoparticles, in the absence of an external magnetic field, the time necessary to measure the magnetization of the nanoparticles is significantly longer than the Néel relaxation time τ_N and therefore the magnetization appears to be zero. In the presence of an external magnetic field, the nanoparticles are magnetized, however, the magnetic susceptibility is much larger compared with a paramagnet. The measurement time strongly depends on the method used. If the magnetic measurement time τ_m is much larger than τ_N , the magnetization flips many times during the measurement and the measured magnetization averages to zero. If τ_m is much smaller than τ_N , the nanoparticle shows a magnetic moment. The crossover from the ferromagnetic to the superparamagnetic state is observed when τ_m and τ_N have the same order of magnitude. Operationally, this transition is detected as a maximum in the temperature-dependent susceptibility. The corresponding temperature is called blocking temperature.

In Fig. 5.4, the temperature-dependent-specific magnetic moment σ of cube shaped and spherical nanoparticles is given. In Fig. 5.4A, both, zero field cooled measurement (ZFCM) and field cooled measurement (FCM) data of dried cube-shaped nanoparticles with an average size of 9 nm are displayed. The ZFCM data are shown as open squares and the FCM data as filled circles. For the FCM, the sample is cooled down while measuring the magnetization using a small external magnetizing field (0.005 T). The specific magnetic moment is detected using a vibrating sample. It decreases monotonically with increasing temperature. In preparation for the ZFCM, the external magnetizing field was set to zero at room temperature and the sample was cooled down to 2 K. Then a magnetizing field of 0.005 T was turned

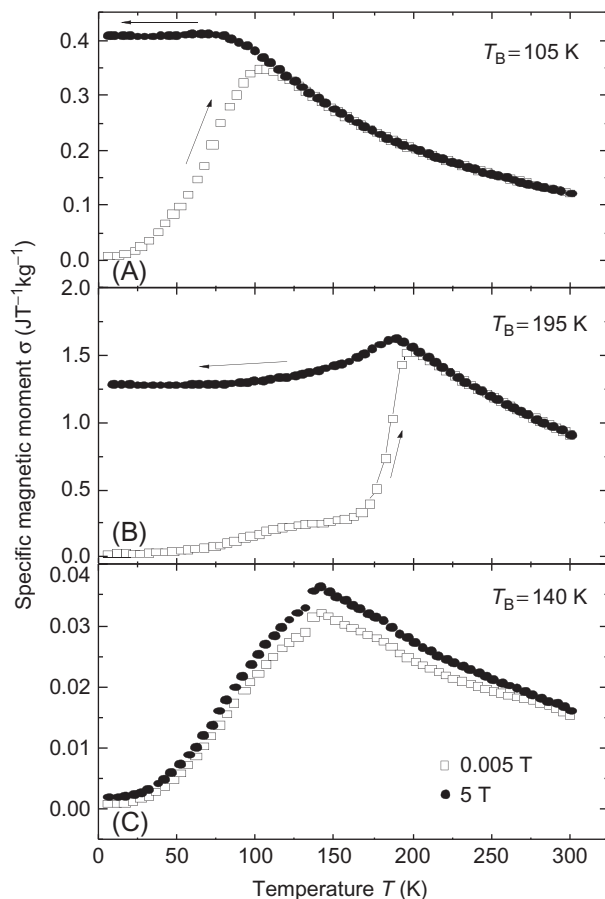


Fig. 5.4

FCM and ZFCM of (A) dried cube-shaped nanoparticles (9 nm), (B) dried spherical nanoparticles (13 nm), and (C) a suspension of cube-shaped nanoparticles (9 nm) in toluene/THF.

on and the magnetization is measured for increasing temperature. The specific magnetic moment increases up to 105 K and then decreases upon further heating. This maximum corresponds to the blocking temperature.

In Fig. 5.4B, the same measurement is performed for dried spherical nanoparticles with an average size of 13 nm. The FCM do not show a monotonic behavior in this case, a fact that we cannot explain. The blocking temperature derived from the ZFCM is located at 195 K. This is about a factor of 2 larger and reflects the larger volume of this particles.

In Fig. 5.4C, the ZFCM of cubic nanoparticles in suspension is presented. In preparation of the ZFCM, the nanoparticles in a toluene and tetrahydrofurane (THF) solvent mixture were exposed to an external magnetic field at room temperature for 30 min. The motivation behind this protocol was to trigger field-induced self-assembly of the nanoparticles. Please note the

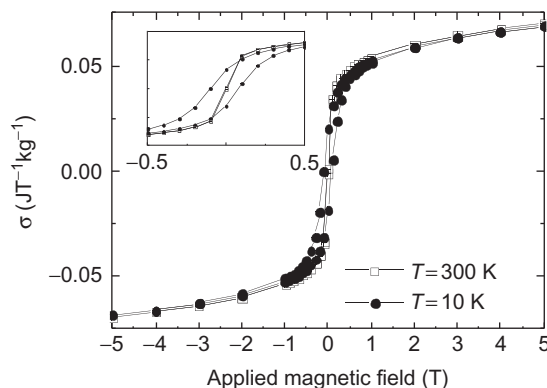


Fig. 5.5

Field dependence of σ of dried cube-shaped nanoparticles (9 nm) at 300 and 10 K. The *inset* shows a magnification of the hysteresis range.

melting points of the solvents toluene (178 K) and THF (165 K) are in the neighborhood of the maximum seen at 140 K. Thus this maximum might partly be caused by a liquid- to solid-phase transition, so that an interpretation of this curve seems to be difficult at this time. With increasing external magnetic field, a slight increase of σ is observed. This could be an indication for an increase in particle size through self-assembly.

In Fig. 5.5 the field dependence of σ at 300 and 10 K is shown. At 300 K (open squares) in the superparamagnetic state, the magnetization curve is a reversible S-shaped increasing function. The increasing applied field leads to an increasing alignment of the magnetic moments of the superparamagnetic nanoparticles along the applied field. At 10 K (filled circles) the nanoparticles are in the blocked state and a hysteresis of the magnetization is observed as expected for a ferro- or ferrimagnetic material.

5.3 Self-Assembly Into Superstructures

One of the most fascinating processes in nature is self-assembly. In the context of this chapter the term self-assembly is used in the following way: A transition from isolated nanoparticles dispersed in a fluid to a stable crystal-like assembly. This can lead to a large amount of structures, including chains, helices, sheets, cylinders, well-defined 3D superlattices, gyroids, or disordered clusters.

For magnetic nanoparticles, Van der Waals attraction and effective dipole-dipole interaction of magnetic nanoparticles can lead to well-ordered assembly structures [15–17]. The assembly of monodisperse magnetic nanoparticles into superstructures is considered as an important step toward fabrication of functional devices, like catalysts, targeting, or storage media. With on-going miniaturization of these applications, a lower size limit for the magnetic nanoparticles may be reached. In this limit the contributions of magnetic interaction energy,

thermal energy, and other interaction energies, such as Van der Waals and interfacial interaction energy, may be comparable.

In this section, the self-assembly of iron oxide nanoparticles is addressed. Faceted and, in particular, cubic nanoparticles forming lattice matched superstructures are of intriguing interest for materials with high magnetic anisotropy constant because of the possibility to align the easy magnetization axis of individual nanoparticles, leading to a new kind of artificial magnetic solid. Two- and three-dimensional self-assembled structures with controlled micro- and meso-scaled ordering consisting of iron oxide nanocubes can be produced by solvent-evaporation within a magnetic field [18–20]. Thereby the mesocrystal habit can be tuned from cubic, hexagonal to star-like, or pillar shapes depending on the particle size, shape, and magnetic field strength. Further, Wetterskog et al. [20] proposed a phase diagram for the formation of mesocrystals composed of oleic-capped iron oxide nanocubes in a magnetic field. Depending on the strength of the magnetic field and the size, single-domain or multidomain crystals and even Rosensweig instabilities are found. In contrast to cubes, evaporation-induced assemblies of Fe_2O_3 -nanospheres displayed rhombohedral structures [21]. These superstructures rearranged into an fcc-packing later on. This was explained by the capillary pressure at the interface between the saturated and partially saturated regions, which determine the internal order of the superlattices.

Magnetic field induced ordering of nanoparticles is crucial for many applications, where the magnetic particles are dispersed in a liquid. Self-assembled flower-like iron oxide nanoparticles are potential candidates as adsorbent in waste-water-treatment [22]. In medical applications, the coating of the iron oxide nanoparticles might trigger self-assembled structures. Their size plays a significant role for the biocompatibility in human bodies [4]. A prominent example in technical applications are ferrofluids [9, 23]. Depending on the external magnetic field and the nanoparticle concentration, ferrofluids undergo structural transitions into linear chains along the field direction or more complex structures such as columns [23].

5.3.1 Crystallization of Cuboids

We describe an in-deep investigation of the self-assembly behavior of small iron oxides nanocubes in dispersion (0.2–20 wt% in toluene), which was performed on the oleic acid stabilized 9 nm sized cubes, depicted in Fig. 5.3. The scattering intensities $I(q)$ presented in Fig. 5.6 demonstrate that the nanocubes are mainly isolated at low concentration (the 2 wt% data already shown in Fig. 5.3) and self-assemble at higher concentration (circles). The data at 18 wt% show the appearance of additional peaks. Analysis of these Bragg reflections reveals a simple cubic crystal lattice with an unit cell of 14 nm. This agrees well with face-to-face attachment of 9-nm sized iron oxide nanocubes, which are covered on all sides by an oleic acid layer, in agreement with the cryo-TEM image of Fig. 5.3. In Fig. 5.6 on the right-hand side an

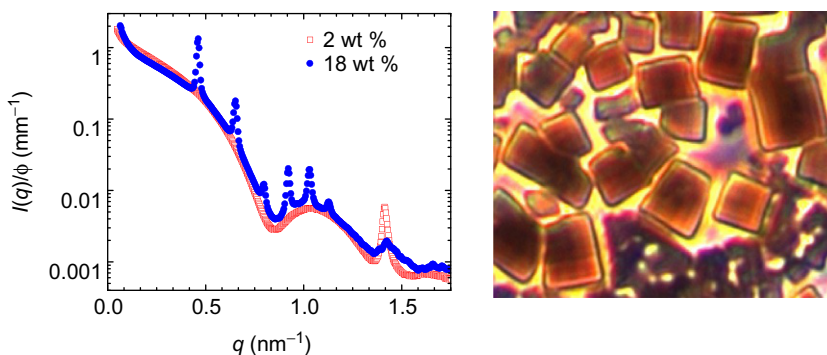


Fig. 5.6

Iron oxide nanocubes in dispersion (SAXS, *left*) and in dried (optical microscopy, *right*) state. For 2 wt % (*open squares*) the scattering intensity can be described by isolated cubes, whereas at 18 wt% (*filled circles*) the Bragg reflections clearly indicate a crystal lattice. The solid sample exhibits large cuboids (micrometer dimensions).

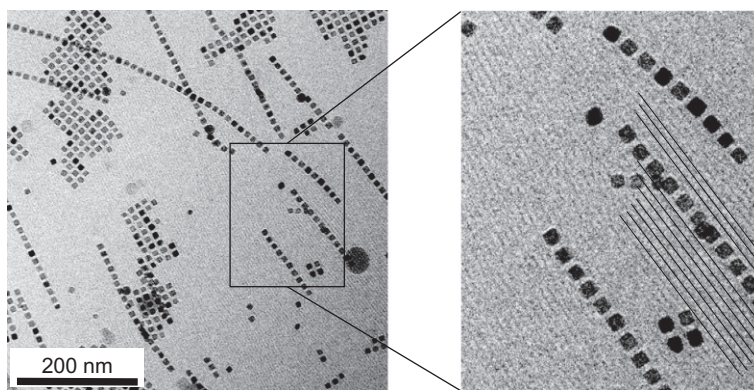


Fig. 5.7

Cryo-TEM image of the cubic nanoparticles (14 nm, 0.8 wt%) after preparing the sample in a magnetic field (200 mT). The assemblies clearly reveal oleic acid layers on the surface of the nanoparticles and free crystalline oleic acid bilayers. The *lines* in the zoom-in indicate a coplanar orientation of crystalline oleic acid chains.

optical microscopic image of the dried sample is presented. It shows 3D superstructures in the micrometer range, which we name cuboids in the following.

In order to understand the assembly of the cubes into cuboids, cryo-TEM studies are performed at lower concentrations of the cubes. A representative example is presented in [Fig. 5.7](#), and more cryo-TEM data are published elsewhere [24]. They reveal 1D lines and 2D sheets. The lines exhibit a remarkable internal order, namely a face-to-face attachment of the cubes. The sheets show a simple cubic 2D lattice. The zoom-in at the right-hand side shows these facts

even more clearly. In addition, a lamellar structure within the solvent (oleic acid and toluene) becomes apparent, as indicated by the thin lines added as a guide to the eye. We believe that this structure is formed by the oleic acid chains. The methyl terminals of the oleic acid enable a periodical contrast of the electron density along the lamellar stacking direction. The low-density region is attributed to the methyl terminals and the high-density region to the dimerizing carboxyl terminals. Similar structures are reported for the crystal structure of the α -, β - and γ -phase of oleic acid [25–28]. The lamellar structure of the oleic acid is oriented in the same direction as the 1D structures, which we referred to as lines. Thus, we believe that the crystalline oleic acid bilayers play a crucial role in the stabilization of those lines. In particular, it explains the coplanar arrangement of the cube surfaces. This explanation is substantiated by the fact that the self-assembly was observed only in samples which showed a significant Bragg reflex caused by crystalline oleic acid (cf. Fig. 5.3). This is underlined further by a similar explanation given by Schliehe et al. [27] to explain the formation of 2D sheets of PbS nanocrystals.

It seems plausible that the crystalline oleic acid bilayers stabilize coplanar structures, when the particles possess plane surfaces. Thus they mediate an oriented attachment of perfect cubes. This agrees with the observation that strongly truncated cubes do not crystallize in simple cubic packing [20].

With this assumption (oriented coattachment) a solution-mediated self-assembly of the iron oxide cubes into 2D sheets and even 3D cuboids is plausible. Fig. 5.8 left-hand side shows an example where the nanocubes have self-assembled into a very regular 3D cuboid. This scanning electron microscopic (SEM) image is obtained after drying a 3 wt% dispersion in a magnetic field

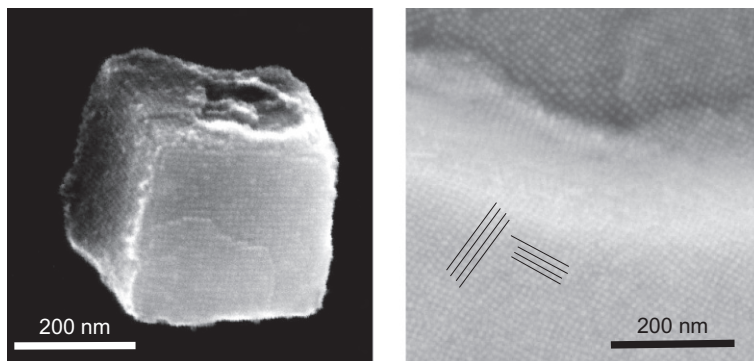


Fig. 5.8

Self-assembly of iron oxide nanocubes to cuboids. (Left) SEM image of the self-assembled structure of nanocubes (edge length of 9 nm, 60% maghemite, 40% magnetite, oleic acid stabilization). (Right) SEM image of a zoom into a mesocrystal with micrometer-dimension, consisting of self-assembled iron oxide nanocubes. The *black lines* are guides for the eyes to visualize the internal order, even near the mesocrystal edge.

of 130 mT. Fig. 5.8 right-hand side presents a zoom into a much larger cuboid (micrometer range), which was formed in a 0.3 wt% dispersion without additional field by evaporation of the solvent toluene at standard conditions. This figure demonstrates the astonishing internal order within a cuboidal mesocrystal. The crystal lattice of the nanocubes within both cuboids is best described as simple cubic with defects. It seems that an additional external magnetic field of 130 mT is no precondition for the internal sc-ordering of the nanocubes.

Further SEM images on the dried sample (Fig. 5.9) demonstrate that the formation of perfect cuboids is not an isolated phenomenon. Cubes and cuboids with micrometer sizes are found all over the sample. The nearly perfect shapes of the cuboids are clearly seen by the sharp contrasts of the cuboid edges. Looking at the figure one gets the impression that the cuboids may be preferentially oriented with a longer dimension into the direction of the external magnetic field. We will address this point in Section 5.3.2.

Additionally performed cryo-SEM experiments (Fig. 5.10) demonstrate that such large cuboids are already present in dispersion, thereby demonstrating that the formation of the 3D structures is not induced by the evaporation of the solvent.

5.3.2 Influence of the Magnetic Field

The influence of the magnetic field on the self-assembly of iron oxide nanoparticles can be studied indirectly by magnetogranulometry, an experimental method which makes use of the fact that a suspension of magnetic nanoparticles forms a polarizable fluid. Such a fluid behaves

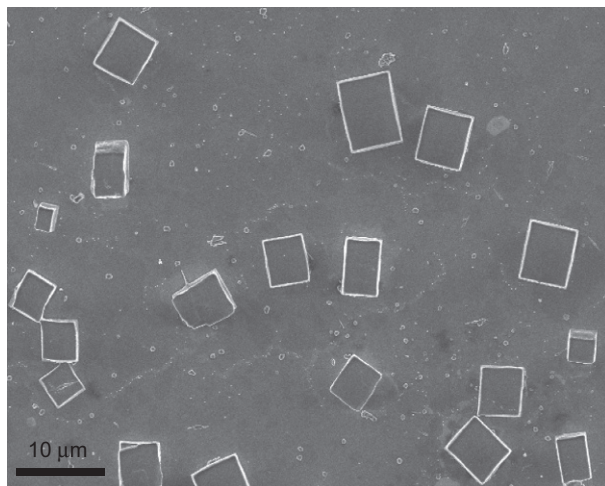


Fig. 5.9

SEM image of mesocrystals, consisting of self-assembled iron oxide nanocubes (edge length of 9 nm, 60% maghemite, 40% magnetite, oleic acid cover). The samples were prepared by evaporation drying in standard conditions of a 0.3 wt% dispersion, in presence of a magnetic field of 300 mT.

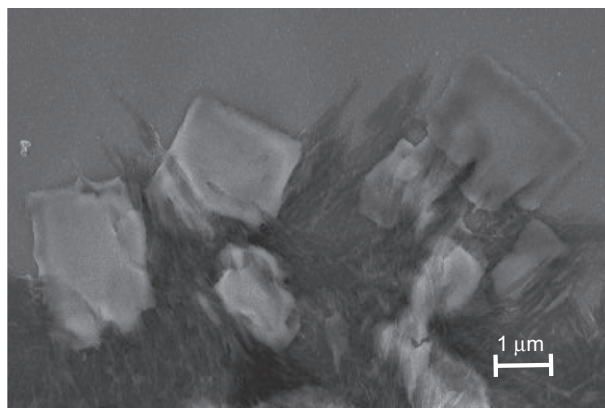


Fig. 5.10

Cryo-SEM image of self-assembled cubic nanoparticles (9 nm iron oxide core, stabilized by oleic acid in toluene). The nanocubes form mesoscaled cuboids, which appear scraggy due to a big amount of overlaying oleic acid. The *needle-like dark* structures are crystalline oleic acid, which is free in solution.

macroscopically like a paramagnetic substance, that is, it shows no spontaneous magnetization and no hysteresis in its magnetization curve. Its susceptibility $\chi_m = \frac{\partial M}{\partial H}$ is concentration and field dependent, and can be orders of magnitude higher compared with normal paramagnets. The magnetization curve $M(H)$ contains information about the size of the nanoparticles dispersed in the fluid—more precisely, it yields their magnetic moments (μ_{part}). The most elementary theoretical description considers a diluted suspension of monodisperse particles with a uniform magnetic moment in an external magnetizing field H . The magnetization M should then be given by the Langevin equation: $\frac{M}{M_s} = \coth(\alpha) - \frac{1}{\alpha}$ with $\alpha = \frac{\mu_{\text{part}} H}{k_B T}$, the saturation magnetization M_s , the Boltzmann constant k_B , the magnetizing field H , and the temperature T . If the diluted suspension is polydisperse, a superposition of such Langevin functions can be expected. For higher concentrations of the magnetic particles, both polydispersity and dipole-dipole interaction have to be taken into account, as described by Ivanov et al. [29, 30].

Fig. 5.11 shows seven examples of such magnetization curves for a 18 wt% iron oxide nanocube dispersion obtained with a vibrating sample magnetometer, which measures the magnetic dipole moment by vibrating the sample between a system of pickup coils. A more detailed description of the experimental setup and procedure can be found in Friedrich et al. [31]. The first dataset was obtained for a fresh sample (crosses, curve at the bottom for $H_i > 0$). The sample was subsequently exposed to a magnetizing field of about 800 kA/m for 4 h, and the measurement was repeated (\times symbols). The remaining five curves were then obtained after waiting between 18 to 157 h from the first measurement.

All curves demonstrate paramagnetic behavior in the sense that no magnetization is observed without a magnetizing field, as expected for a dispersion of particles in a fluid. Having in mind that the initial slope of the Langevin function is determined by the magnetic moment of the

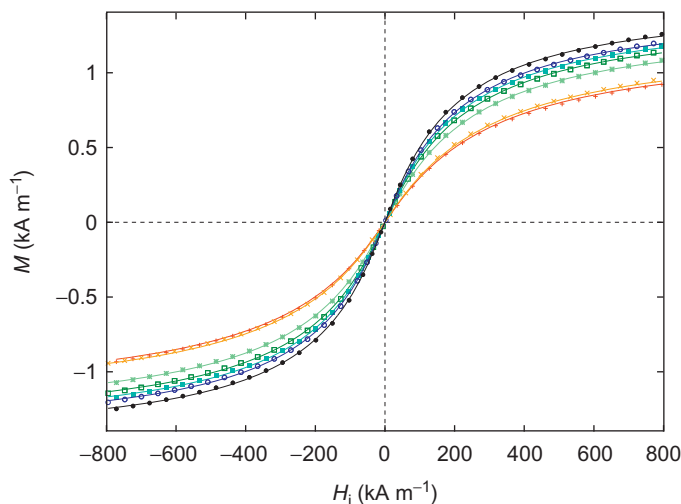


Fig. 5.11

The aging of cubic nanoparticles (18 wt%, iron oxide, edge length 9 nm) in solution (toluene and oleic acid) triggered by a magnetic field (800 kA/m for 4 h) as detected by a vibrating sample magnetometer. The first two datasets are magnetization curves measured before and immediately after that triggering event. The other five sets were obtained after waiting times of 18, 40, 65, 89, and 157 h. During the measurements the magnetizing field strength went from 800 to -800 kA/m and back to 800 kA/m (about ± 1 T), which takes about 108 min for one curve.

particles the ongoing increase in the initial slope of the magnetization curves with time can be qualitatively interpreted: There is an increasing fraction of particles with larger magnetic moment, which is likely to be a direct consequence of the aggregation of the nanoparticles. Indeed, cryo-SEM pictures of the aged sample show larger—micrometer sized—cuboidal objects (Fig. 5.10). The cuboids appear scraggy due to a big amount of overlaying oleic acid and consist of self-assembled nanocubes.

Moreover, the saturation magnetization can be obtained from the measurements, namely by extrapolating the data to very large magnetizing fields. In lowest approximation, a fitted Langevin equation could be used for that. For the data shown in Fig. 5.11 this model showed a systematic deviation from the magnetization curves of the nanocube dispersion. Thus, the refined model from Ivanov et al. [29, 30] was fitted to the data (solid line). With its additional fit parameter it describes the data perfectly well. Thus we consider it more reliable to extrapolate the data to the saturation magnetization. It turns out that this saturation magnetization increases monotonically with time. In case of iron oxide nanocubes this change continues over days. The saturation magnetization for the 9 nm iron oxide cubes in toluene turned out to be $M_s = 1.6$ kA/m after 1 week (Fig. 5.11). This value is significantly lower than 100 kA/m, the theoretically expected value for an iron oxide dispersion of 18 wt% [8].

The interpretation of the increase of the saturation magnetization M_s is less obvious than the interpretation of the initial slope of the curves. In lowest approximation, one would assume that the sum of all magnetic moments of the nanoparticles remains the same, that is, M_s should be independent from the amount of clustering. The measurement indicates that this is an oversimplified picture. It seems that particles embedded in an assembly show a stronger magnetic moment than isolated particles. This might be caused by the fact that free surfaces are effectively reduced in an assembly of nanoparticles.

Fig. 5.12 contains a detailed analysis of the data set from Fig. 5.11 obtained after 157 h. The measurement exhibits a systematic deviation from the fitted Langevin function (dashed line) expected for a diluted monodisperse solution. This deviation is interpreted as a consequence of the polydispersity of the dispersion, containing a mixture of nanoparticles and cuboidal clusters. When neglecting the dipole-dipole interaction in a dilute solution, the magnetization curve is expected to be a superposition of Langevin curves, according to the distribution function of the magnetic moments in the polydisperse mixture. In principle, the distribution function of the magnetic moments could be extracted from the curve by the Ivanov fit shown earlier, but it has to be kept in mind that this method is based on solving a mathematically ill-posed problem. It means that many different distribution functions will lead to almost the same magnetization curves.

To circumvent this difficulty and to bring out the essence of cluster formation more clearly, the magnetization data were modeled by assuming that the dispersion would be built from only two

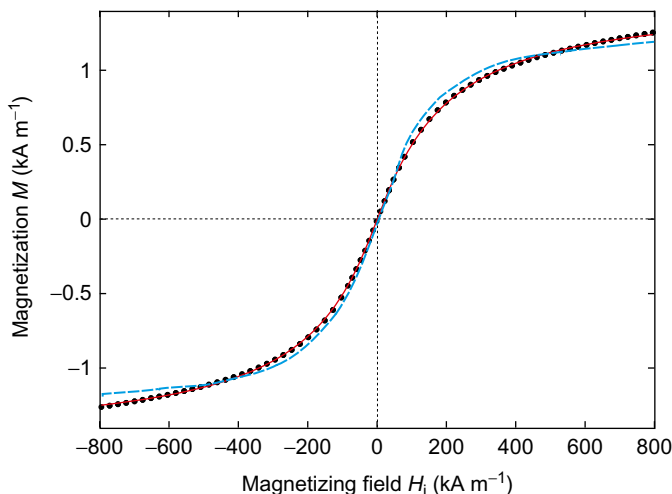


Fig. 5.12

Magnetization of cubic nanoparticles solution as function of the magnetic field strength. The *filled circles* are the experimental data already shown in Fig. 5.11. The *dashed line* is a fit of a Langevin function for a monodisperse solution, whereas the *solid line* represents a fit for a bidisperse solution.

different particle sizes, for example, nanoparticles with a small magnetic moment μ_1 and assemblies with a big magnetic moment μ_2 . The moments of the nanoparticles μ_1 and μ_2 as well as the concentration of corresponding particles were used as fit parameters, yielding $\mu_1 = 1269 \mu_B$ and $\mu_2 = 7225 \mu_B$ (cf. solid line).

This simplified ansatz describes the experimental data perfectly within the experimental resolution. Note that this does not mean that the suspension is really bidisperse. It rather shows that the magnetogranulometry reaches its limits at this point—it cannot convincingly be taken further to obtain a real distribution of the magnetic moments. However, the results of the fitting are still worth to be considered. The solution in this stage should contain 40% particles with a magnetic moment of about 1300 Bohr magnetons and 60% of particles with a magnetic moment six times larger.

To gain insight into the geometrical size of the bigger particles, a connection between magnetic moments and cluster size must be established. In a first attempt to model the magnetization of the clusters, the dipole-dipole interaction of identical magnetic dipoles (the nanocubes) in the arrangement of a simple cubic lattice is considered theoretically. An exact analysis yielding all the stationary solutions for the freely adjustable dipoles has only been given for the simplest cuboid, containing only $2 \times 2 \times 2 = 8$ nanoparticles. For this geometry the most important dipole arrangement, the ground state carries no magnetic moment at all [32]. For bigger clusters, a relaxation code described by Rehberg et al. [33] was used to relax dipoles located at fixed positions in simple cubic lattices into some minimum—not necessarily the ground state—of the interaction potential. The results are presented in Fig. 5.13.

Fig. 5.13A shows the numerically obtained magnetic part of the binding energy per particle within the cluster as a function of the size of the cluster, starting from a $2 \times 2 \times 2$ cuboid and going up to $13 \times 13 \times 13 = 2197$ particles. The dimensionless-specific binding energy plotted here is scaled by the specific energy that would be needed to disassemble a pair of two dipoles, located at a distance of the lattice parameter a . To give an example: The value of $2 - \sqrt{2}/16 - \sqrt{3}/18 \approx 1.815$ obtained for the smallest cuboid [32] means that the energy needed to disassemble this cuboid completely is $8 \times 1.815/2 \approx 7$ times the energy that would be needed to pull two magnetic dipoles of distance a apart. It turns out that this energy is a monotonically increasing function of the cluster size. It is expected to approach the asymptotic value of about 2.677 indicated by the dashed line, which is the value expected for an infinite simple cubic lattice [34]. The solid line indicates the energy in the corresponding 2D arrangement, and the dotted line gives the energy of a 1D chain of dipoles with its asymptotic limit 2.404. The insets show macroscopic realizations for the 1D, 2D, and 3D configuration build from 5 mm magnetic spheres for a better illustration of these geometries. So within the family of simple cubic arrangements the rule of thumb would be that for dipole numbers below 30 one-dimensional arrangements are energetically favored, for intermediate numbers between 30 and 300, a 2D checker-board arrangement maximizes the binding energy. For more particles a cuboid is the most stable arrangement within this sc-family.

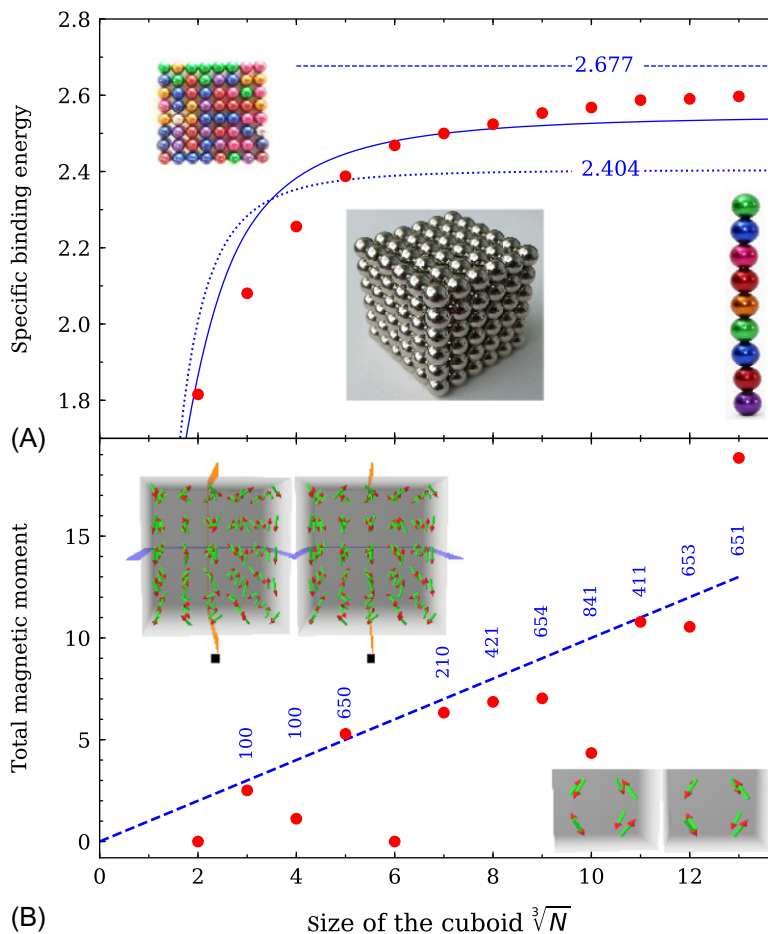


Fig. 5.13

Computationally obtained magnetic moment and specific binding energy of an equilibrium state of freely adjustable dipoles in a cuboidal cluster. The size of the cuboid is given by $\sqrt[3]{N}$, where N is the number of dipoles forming the cluster. (A) The specific binding energy of the cuboid is indicated by the *filled circles*. The *inset* in the middle shows a photo of a $6 \times 6 \times 6$ cuboid build from 5 mm spherical magnets. For comparison, the corresponding energy for dipoles arranged in a 1D line (*dotted curve*, with the corresponding inset at the right-hand side) or a 2D sheet (*solid curve*, with the corresponding inset at the left-hand side) is also indicated. The *dashed horizontal line* indicates the binding energy in an infinite simple cubic lattice. (B) The *filled circles* indicate the magnitude of the total magnetic moment. The *insets* show stereographic images of the equilibrium configuration of dipoles for a $5 \times 5 \times 5$ (left-hand side) and a $2 \times 2 \times 2$ (right-hand side) cuboid. The *dashed line* illustrates the rule of thumb for the magnetic moment. The *numbers* represent the direction of the magnetization, that is, $\langle 1\ 0\ 0 \rangle$ is along the x -axis of the cuboid and $\langle 6\ 5\ 4 \rangle$ is close to the volume diagonal. No direction is given when the total magnetic moment is 0.

The magnetic moment of the equilibrium arrangement of the dipoles in a cuboid is plotted in Fig. 5.13B. The inset provides stereographic images of the equilibrium configuration of dipoles in a $5 \times 5 \times 5$ and a $2 \times 2 \times 2$ cuboids. The total moment presented here is scaled with the moment of a single dipole. While the $2 \times 2 \times 2$ and the $6 \times 6 \times 6$ cuboids have no magnetic dipole moment at all, the $3 \times 3 \times 3$ cuboid has a moment of about 3, and the $5 \times 5 \times 5$ cuboid a moment of 5. It turns out that in particular the odd-numbered cuboids contain a magnetic moment. This moment increases with the cluster size, and as a rule of thumb one could conclude from this figure that the moment grows approximately as $\sqrt[3]{N}$, which is indicated by the dashed line. When applying this rule to the interpretation of the fitting result of Fig. 5.12, the cuboids should be formed from about 200 nanoparticles.

The orientation of the magnetization shown in the numerical results presented in Fig. 5.13 does not show a clear tendency for a preferred orientation. This triggers the question about the orientation of the magnetization in real cuboids like the ones shown in Fig. 5.9. To address this question experimentally, we exposed the cuboids to an external field and recorded the orientation with SAXS. The external field was applied either perpendicular or parallel to the incident X-rays. The corresponding scattering patterns $I(q_x, q_y)$ of a 18 wt% dispersion in a perpendicular applied magnetic field of 0.1 mT and 0.98 T are given in Fig. 5.14, and one for a parallel field of 0.79 T.

At earth field (0.1 mT) the scattering pattern $I(q_x, q_y)$ is rotational symmetric due to randomly oriented mesocrystals (Debye-Scherrer rings). From the analysis of the measured intensity, the crystal lattice, the lattice constant, and the mean displacement of the nanoparticles from the ideal lattice points can be obtained, provided that the domain size is given [35]. When using a domain size of 2000 nm, the analysis reveals a simple cubic lattice with a lattice constant of $a = 14$ nm. The lattice constant is in line with cubic iron oxide nanocrystals of 9 nm coated by an oleic acid layer (cf. Fig. 5.3). The displacement of the nanocubes is 1 nm.

In case of Fig. 5.14B, a magnetic field in the y -direction perpendicular to the beam direction (z -axis) was applied. At 0.03 T the Debye-Scherrer rings become anisotropic, indicating that the orientation of the cuboids—and accordingly the one of the nanocubes—are influenced by the external magnetic field. This anisotropy increases with increasing magnetic field and results in an arc-like pattern, as seen in Fig. 5.14B.

The peak seen at $\mathbf{q}_x = 0 \text{ nm}^{-1}$ and $\mathbf{q}_y = 0.44 \text{ nm}^{-1}$, that is, (0, 0.44), indicates that the cuboids orient their $\langle 100 \rangle$ direction along the field. In this case the scattering pattern is expected to be basically a superposition of the two calculated patterns shown in Fig. 5.14D and E, because the cuboids are free to rotate around the axis parallel to the field. The peak seen at (0.44, 0.44) on the $\langle 110 \rangle$ -ring is then in accordance with this interpretation, as well as the one at $(\sqrt{2} \cdot 0.44, 0.44)$ on the $\langle 111 \rangle$ -ring.

Alternatively, one could have assumed that the cuboids would orient their $\langle 110 \rangle$ -direction or $\langle 111 \rangle$ -direction along the field. The vanishing intensity at $(0, \sqrt{2} \cdot 0.44)$ makes it clear

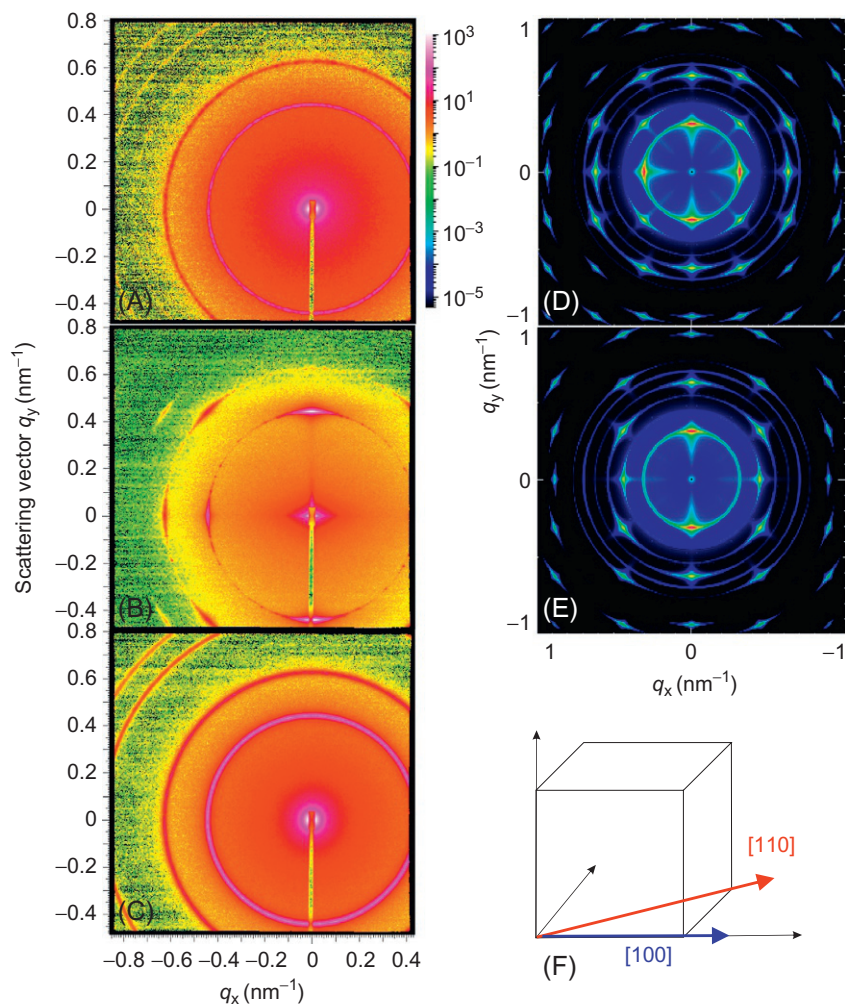


Fig. 5.14

SAXS patterns of nanocubes. (*Left*) Synchrotron SAXS patterns for 18 wt% iron oxide nanocubes of 9 nm size in toluene. The data are recorded at earth field (A), within a magnetic field of 0.98 T oriented perpendicular (B) or of 0.79 T (C) oriented parallel to the beam. (*Right*) Numerically obtained scattering patterns. The calculation is based on 9-nm sized cubes on a simple cubic lattice with a lattice constant of 14 nm. For one image the X-ray beam was assumed along the [100] direction (D), for the other one along the [110] direction (E). In addition, the spatial orientation of the cubes is visualized in (F).

that the $\langle 110 \rangle$ -direction is not the preferred one, while the decreasing intensity at $(0, \sqrt{3} \cdot 0.44)$ rules the $\langle 111 \rangle$ -direction out.

The azimuthal width of a Bragg spot gives a measure for the orientation fluctuations of the polar angle ψ . They decrease with increasing strength of the applied field. At 0.98 T we obtain $\psi = 4^\circ$ for the width of the Gauss distribution assumed in the analyzing program [35].

When the beam passes parallel to the direction of the magnetic field, Debye-Scherrer rings are observed. In this case the $\langle 111 \rangle$ reflection—which is present at earth field—is missing. This ring-pattern can be obtained as the radial distribution of the scattering image of Fig. 5.14D, where indeed the $\langle 111 \rangle$ -ring is very weak. Thus, this observation also supports the interpretation given earlier: The cuboids orient their $\langle 100 \rangle$ direction along the field.

In addition, an increase in the forward scattering with increasing magnetic field is observed. There are two explanations for this effect: (i) The cuboids grow by attaching further material, mediated by increasing magnetic field strength. (ii) The cuboids orient more and more along the field lines, hence the beam probes more matter, which is reflected by the increase of the forward scattering. Both effects may take place simultaneously.

After switching off the external magnetic field no marked difference in the Bragg reflections of the dispersed cuboids was obtained for at least 30 min. This comes as a surprise when considering the Brownian relation time for micrometer-sized particles, which should rather be on the order of seconds. To explain these extremely long relaxation times we propose that the cuboids might form even larger clusters, presumably chain-like ones, along the direction of the field.

When the concentration of the 9-nm sized iron oxide cubes is below 5 wt%, the scattering at room temperature shows no pronounced Bragg reflections. Hence, the concentration plays also a significant role for the formation of cuboids.

To investigate the influence of a magnetic field at lower concentrations, a 1 wt% dispersion of 9 nm iron oxide nanocubes was synthesized by carefully avoiding external magnetic fields, in particular magnetic stirrers, or magnets during precipitation of the nanocubes. The sample was split in four parts, two of them were stored at room temperature, and two at -20°C . At both temperatures one part was exposed to a magnetic field (130 mT) and the other not. The time-dependent self-assembly of those diluted iron oxide nanoparticles was subsequently followed by dynamic light scattering (DLS). Fig. 5.15 shows the resulting intensity correlation functions.

At room temperature (25°C), no change in the intensity correlation function is observed within weeks, neither within a magnetic field of 130 mT nor without one. The correlation function stays compatible with that expected for monodisperse particles, namely a simple exponential decay with a decay time of 9.8 μs . This yields a hydrodynamic diameter of 13 nm, which is larger than the 9 nm iron oxide core due to the oleic acid layer.

In Fig. 5.15C, the dispersion kept at -20°C in the absence of a magnetic field reveals changes of the correlation function with increasing storage time. While the fresh sample shows a purely exponential decay, deviations become prominent after about a week. The reduced slope for larger delay times indicates that the sample is not monodisperse any more. It now contains a fraction of larger particles, most likely aggregates of the nanocubes.

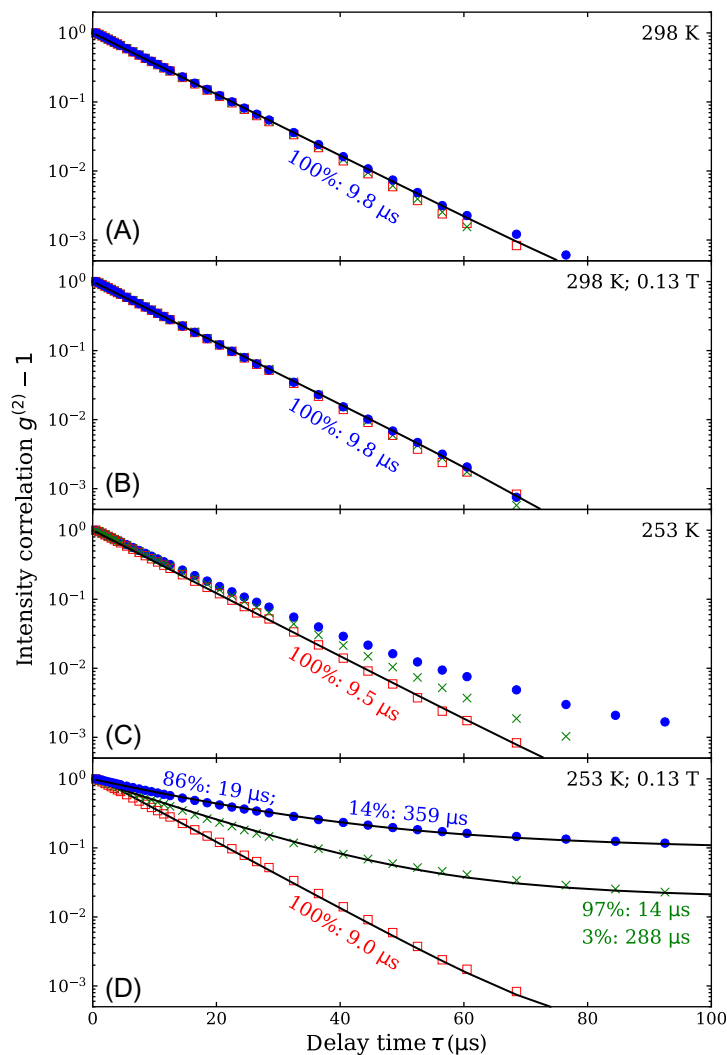


Fig. 5.15

DLS intensity correlation functions $g^2 - 1$ of a 1 wt% dispersions of 9 nm iron oxide cubes, which are stored under different conditions. (A) Data of the sample stored at 25°C without an additional external magnetic field. The data are taken after 0, 10, and 28 days of storage. (B) Dataset taken at 25°C after 0, 8, and 28 days of storage within a magnetic field of 130 mT. (C) Intensity correlation functions after 0, 6, and 8 days storage of the sample at -20°C without field. (D) DLS data obtained for the dispersion, which was stored 0, 6, and 7 days at -20°C within a field of 130 mT. The *solid lines* indicate fits to bidisperse samples. The relative signal strength and the corresponding decay times of the two components are given by the numbers at the fitted lines.

Fig. 5.15D shows that this effect becomes orders of magnitude stronger when the sample is exposed to a magnetic field of 130 mT at this temperature. Now the correlation function changes significantly within a week. Within the experimental resolution the curve can be fitted by assuming a bidisperse mixture, where the hydrodynamic radius of the larger component is about two orders of magnitude larger than that of the smaller one, as indicated by the ratio of the two decay times extracted by the fit. For the interpretation of these fitting results the same care must be taken as for the interpretation of the bidisperse fit in the magnetogranulometry: The fact that a bidisperse distribution of particle sizes fits the measured curve does not prove that this distribution is correct, but it indicates that the analysis cannot be taken further due to the ill-posed nature of this mathematical problem.

Visual inspection of the sample stored at -20°C and in presence of an external magnetic field showed a small amount of sedimented particles after about 1 week. After longer times, the amount of sedimented particles increased only slightly. After 3 weeks, the long-time tail of the correlation still revealed assemblies of about 200–400 nm. All these observations make it clear that two different species are present in the dispersion: (i) small particles, most probably single dispersed cubes, and (ii) larger particles, mainly the crystallized cuboids, which sediment with time.

In summary, magnetic fields are helpful for the formation of cuboids, especially at low temperatures and low concentrations. Once created, the cuboids are stable even without a field. Increasing the concentration facilitates nanoparticle assembly such that cuboids may also form at room temperature without the help of a magnetic field.

5.4 Conclusion

The understanding of the self-assembly of monodisperse magnetic nanoparticles into larger structures like cuboids is a relevant step toward their application, where these superstructures either are desired (e.g., for the fabrication of functional devices) or are to be avoided (e.g., in biological systems). The formation of self-assembled structures strongly depends on the particle shape and size. The self-assembly can be followed using (cryo-)TEM, (cryo-)SEM, SAXS, magnetogranulometry, and DLS measurements. These methods reveal that for the cuboids their concentration, the kind of solvent, the temperature, and the external magnetic field are additional important parameters.

The results indicate that the oleic acid used for the stabilization of the nanoparticles has a significant influence on the coplanar orientation of the nanoparticles. The oriented coattachment of the acid layers simplifies the cuboid formation.

An external magnetic field helps to form superlattices, but it is not a precondition—at high-concentration cuboids are formed even without the external field. Once formed, they are stable with and without an external field, and can be aligned by such a field.

The stability of cuboids can be explained by considering the surface free energy. When the nanocubes come in close contact up to a distance dictated by the oleic acid layer, they eliminate a pair of high-energy surfaces. This energy is larger than the magnetic interaction energy of the nanocubes. This interpretation is substantiated by the fact that no significant indication of self-assembly was found for spherical nanoparticles, even at large magnetic fields of 1 T.

Considering these facts, the kinematics of the self-assembly triggered by the magnetic field is an unresolved puzzle. While it is plausible that the field triggers the formation of chains along the field lines, the subsequent growth in 2D or 3D lattices cannot be understood on the basis of magnetic interaction. This force rather seems counterproductive because parallel magnetic chains repel each other. One can speculate that a short magnetic trigger leading to chains, and a subsequent surface energy-driven ordering in the absence of an external field might be the most efficient way to build cuboids, a hypothesis that should be tested in forthcoming experiments.

Acknowledgements

The authors thank Peter Bösecke, Markus Drechsler, Beate Förster, Andreas Kornowsk, Sara Mehdizadeh Taheri, Theyencheri Narayanan, and Florian M. Römer for fruitful cooperation and clarifying discussions. We thank the German Science Foundation for financial support (DFG-SFB 840). The Bavarian Polymer Institute and the European Synchrotron Radiation Facility (beamline ID2) are gratefully acknowledged for providing measurement times and technical support.

References

- [1] S. Singamaneni, V.N. Bliznyuk, et al., Magnetic nanoparticles: recent advances in synthesis, self-assembly and applications, *J. Mater. Chem.* 21 (2011) 16819–16845.
- [2] A.K. Gupta, M. Gupta, Synthesis and surface engineering of iron oxide nanoparticles for biomedical applications, *Biomaterials* 26 (18) (2005) 3995–4021.
- [3] R.M. Cornell, U. Schwertmann, *The Iron Oxides: Structure, Properties, Reactions, Occurrences and Uses*, Wiley-VCH, London, ISBN: 3527302743, 2013.
- [4] S. Laurent, D. Forge, et al., Magnetic iron oxide nanoparticles: synthesis, stabilization, vectorization, physicochemical characterizations, and biological applications, *Chem. Rev.* 108 (6) (2008) 2064–2110.
- [5] T.M. Buzug, J. Borgert, *Magnetic Particle Imaging*, Springer Proceedings in Physics 140, ISBN: 978-3-642-24132-1, 2012. Heidelberg, New York, Dordrecht, London.
- [6] K.S. Siddiqi, A. Ur Rahman, et al., Biogenic fabrication of iron/iron oxide nanoparticles and their application, *Nanoscale Res. Lett.* 11 (2016) 498.
- [7] W. Li, D. Liu, et al., Aqueous aggregation and surface deposition processes of engineered superparamagnetic iron oxide nanoparticles for environmental applications, *Environ. Sci. Technol.* 48 (20) (2014) 11892–11900.
- [8] R.E. Rosensweig, *Ferrohydro-Dynamics*, Dover Publication Inc, Mineola, NY, ISBN: 0-486-67834-2, 1997.
- [9] J. Philip, J.M. Laskar, Optical properties and applications of ferrofluids—a review, *J. Nanofluids* 1 (1) (2012) 3–20.
- [10] L.J. Felicia, S. Vinod, J. Philip, Recent advances in magnetorheology of ferrofluids (magnetic nanofluids)—a critical review, *J. Nanofluids* 5 (1) (2016) 1–22.
- [11] W. Wu, Z. Wu, et al., Recent progress on magnetic iron oxide nanoparticles: synthesis, surface functional strategies and biomedical applications, *Sci. Technol. Adv. Mater.* 16 (2) (2015) 023501.

- [12] J. Park, K. An, et al., Ultra-large-scale syntheses of monodisperse nanocrystals, *Nat. Mater.* 3 (12) (2004) 891–895.
- [13] M. Klokkenburg, B.H. Ern , et al., Dipolar structures in magnetite ferrofluids studied with small-angle neutron scattering with and without applied magnetic field, *Phys. Rev. E* 75 (2007) 051408.
- [14] B.J. Berne, R. Pecora, *Dynamic Light Scattering*, Courier Dover Publications, Mineola, NY, ISBN: 0-486-41155-9, 2000.
- [15] S. Bedanta, A. Barman, et al., Magnetic nanoparticles: a subject for both fundamental research and applications, *J. Nanomater.* 2013 (2013) 1–22.
- [16] H.W. Zhang, Y. Liu, S. Sun, Synthesis and assembly of magnetic nanoparticles for information and energy storage applications, *Front. Phys. China* 5 (4) (2010) 347–356.
- [17] E. Wetterskog, M. Agthe, et al., Precise control over shape and size of iron oxide nanocrystals suitable for assembly into ordered particle arrays, *Sci. Technol. Adv. Mater.* 15 (5) (2014) 055010.
- [18] D. Sabrina, E. Wetterskog, et al., Shape induced symmetry in self-assembled mesocrystals of iron oxide nanocubes, *Nano Lett.* 11 (4) (2011) 1651–1656.
- [19] A. Ahniyaz, Y. Sakamoto, L. Bergstr m, Magnetic field-induced assembly of oriented superlattices from maghemite nanocubes, *PNAS* 104 (45) (2007) 17570–17574.
- [20] E. Wetterskog, A. Klapper, et al., Tuning the structure and habit of iron oxide mesocrystals, *Nanoscale* 8 (2016) 15571–15580.
- [21] E. Josten, E. Wetterskog, et al., Superlattice growth and rearrangement during evaporation-induced nanoparticle self-assembly, *Sci. Rep.* 7 (2802) (2017) 1–4.
- [22] L.S. Zhong, J.S. Hu, et al., Self-assembled 3D flowerlike iron oxide nanostructures and their application in water treatment, *Adv. Mater.* 18 (2006) 2426–2431.
- [23] C. Huang, J. Yao, et al., Damping applications of ferrofluids: a review, *J. Magn.* 22 (1) (2017) 109–121.
- [24] S. Mehdizadeh Taheri, M. Michaelis, et al., Self-assembly of smallest magnetic particles, *PNAS* 112 (47) (2015) 14484–14489.
- [25] J.B. Rossell, B. King, M.J. Downes, Composition of oil, *JAOCs* 62 (2) (1985) 221–230.
- [26] F. Kaneko, K. Yamazaki, et al., Structure and crystallization behavior of the β phase of oleic acid, *J. Phys. Chem. B* 101 (10) (1997) 1803–1809.
- [27] C. Schliehe, B.H. Juarez, et al., Ultrathin PbS sheets by two-dimensional oriented attachment, *Science* 329 (5991) (2010) 550–553.
- [28] S. Kiyotaka, N. Sato, et al., Structure and transformation in polymorphism of petroselinic acid (*cis- ω -12-octadecenoic acid*), *J. Phys. Chem.* 94 (7) (1990) 3180–3185.
- [29] A.O. Ivanov, O.B. Kuznetsova, Magnetic properties of dense ferrofluids: an influence of interparticle correlations, *Phys. Rev. E* 64 (2001) 041405.
- [30] A. Ivanov, S. Kantorovich, et al., Magnetic properties of polydisperse ferrofluids: a critical comparison between experiment, theory, and computer simulation, *Phys. Rev. E* 75 (2007) 061405.
- [31] T. Friedrich, T. Lang, et al., Spherical sample holders to improve the susceptibility measurement of superparamagnetic materials, *Rev. Sci. Instr.* 83 (4) (2012) 045106.
- [32] J. Sch nke, T.M. Schneider, I. Rehberg, Infinite geometric frustration in a cubic dipole cluster, *Phys. Rev. B* 91 (020410(R)) (2015) 1–5.
- [33] T. Friedrich, I. Rehberg, R. Richter, Self-assembly of magnetic balls: from chains to tubes, *Phys. Rev. E* 91 (2015) 057201.
- [34] P.J. Belobrov, R.S. Gekht, V.A. Ignatchenko, Ground state in systems with dipole interaction, *Sov. Phys. JETP* 57 (1983) 636–642.
- [35] S. F rster, S. Fischer, et al., Calculation of scattering-patterns of ordered nano- and mesoscale materials, *Adv. Coll. Inter. Sci.* 163 (2011) 53–83.

This page intentionally left blank

Nanomaterials for Magnetoplasmonics

Francesco Pineider*, Claudio Sangregorio[†]

**Department of Chemistry and Industrial Chemistry, University of Pisa and INSTM, Pisa, Italy,*

[†]*ICCOM—CNR and INSTM, Sesto Fiorentino, Italy*

6.1 Introduction

In the last two decades plasmonics, which is the investigation of the physical behavior arising from electromagnetic wave-induced collective oscillation of charge carriers confined at an interface, has emerged as a promising field for science and technology. The strong localization and the dependence on the dielectric function of the surrounding environment, indeed, make plasmonics a promising candidate for application in fields such as nanophotonics and optical sensing [1–4]. What is indeed even more fascinating is the possibility to actively control the plasmonic functionalities with an external agent, in order to effectively stir the electronic and optical properties of the plasmonic system in a controlled and reversible manner, thus largely expanding their applicability in several technological areas [4–7]. Among the strategies proposed so far to realize active plasmonics, magnetoplasmonics, which is the use of an external magnetic field to modulate the resonance conditions of a plasmonic system, seems a very promising one; the realization of such a possibility, indeed, can pave the way to dramatic innovations in refractometric sensing, as well as in light guiding and optoelectronics [8]. The amplitude of the modulation is rather small in purely plasmonic resonators, but it can increase significantly if a magnetic metal able to sustain plasmon resonance is used, or by designing appropriate hybrid magnetic-plasmonic structures. Fast modulation of the plasmonic response can be used to dramatically increase the figure of merit in refractometric sensing [9,10]: this is particularly appealing in view of localized plasmon resonance-based sensing [11].

The successful design and production of efficient magnetoplasmonic materials must abide by three intertwined criteria, which form the magnetoplasmonic trilemma:

- (1) The magnetic component must be sufficiently strong and magnetically coupled.
- (2) The plasmonic component must give rise to sharp and well-defined plasmon resonances.
- (3) The two components must be coupled.

☆ Dedicated to Mildred.

Satisfying each of the three conditions tends to have a negative effect on the other two: for instance, noble metal materials, such as gold and silver, that perform well as plasmonic substrates, have a weak magnetic response, while strong ferromagnets such as iron, cobalt, and nickel are poor plasmonic metals, due to the strong interband absorption in the optical range where their plasmonic resonance occurs. On the other hand, the requirement that the magnetic and plasmonic functions interact has generally a negative influence on both magnetic and plasmonic functions.

The research of a suitable magnetoplasmonic material is thus a rather complex task, which requires on one hand the capability to accurately manipulate matter at the nanoscale so as to organize it in controlled structures, and on the other hand, a deep understanding of the complex phenomena underlying the interaction between magnetic and plasmonic properties. In the recent past, however, several strategies have been devised to overcome the limitations imposed by the trilemma, by finding the best balance between sharp plasmon resonance and strong response to the magnetic field. Here, we review some of the most interesting nanostructures discussed so far. Among the variety of magnetoplasmonic nanostructures, we will focus our attention only on those supporting localized surface plasmon resonance (LSPR), such as nanoparticles and nanodisks.

This chapter is organized as follows: since magneto-optics, MO, is the best suited experimental technique to observe magnetoplasmonics effect, we start by describing the basic principles underlying magneto-optical techniques ([Section 6.2](#)). In [Section 6.3](#), we briefly describe the basic principles of plasmonics and then we introduce the concept of active plasmonics and magnetoplasmonics. The remaining part of the chapter contains a review of the key research findings in the field of magnetoplasmonics. At first, in [Section 6.4](#), we discuss the magnetoplasmonic properties of single component metal nanostructures either of a pure noble metal or of a ferromagnetic metal. In fact, despite the difficulties discussed here, both classes of materials exhibit intriguing magnetoplasmonic behaviors: Magnetic field modulation of LSPR can be obtained in pure plasmonic nanostructures as a result of the modification of free charges oscillations induced by a magnetic field; on the other hand, nanostructures of some ferromagnetic metals (chiefly Ni) are known to support surface plasmon resonances, which are strongly affected by magnetic field, but are very broad. However, the best strategy to obtain an efficient material for plasmonic modulation, i.e., a material endowed with both a sharp optical resonances and a strong response to magnetic field, relies on the direct combination at the nanoscale of a magnetic and a plasmonic component. [Section 6.5](#) is dedicated to these hybrid magnetoplasmonic nanostructures. For the sake of clarity, they are grouped into three categories according to the nature of the magnetic component, i.e., noble metal/magnetic metal, noble metal/magnetic oxide, and noble metal/magnetic molecules. Finally, [Section 6.6](#) contains a brief conclusion and some projections of the future trends in magnetoplasmonics.

6.2 Experimental Methods for the Study of Magnetoplasmonics and Related Effects

When investigating magnetoplasmonic effects, several instrumental techniques are important to gain insight of the morphology, structure, and composition of the systems, and to correlate them to their physical properties. The ultimate technique to actually observe magnetoplasmonic effects, however, is magneto-optics. For this reason, and because this class of instrumental methods are in general slightly obscure to the nanoscientist, we begin our treatment with an introduction to the basic principles underlying the most commonly used magneto-optical techniques.

Magneto-optical (MO) techniques are based on the analysis of the polarization state of light transmitted or reflected by magnetized materials. The effect of a magnetic field, indeed, is that of inducing an optical anisotropy, i.e., introducing nondiagonal terms in the dielectric tensor of a given material. The off-diagonal terms represent the MO constant of the material, and are proportional to the applied field, in the case of diamagnetic or paramagnetic substances or to the total magnetization when magnetically ordered materials are considered. Therefore, the application of a magnetic field affects both the intensity and the polarization state of light, depending on the relative orientation of the magnetic field and propagation of light.

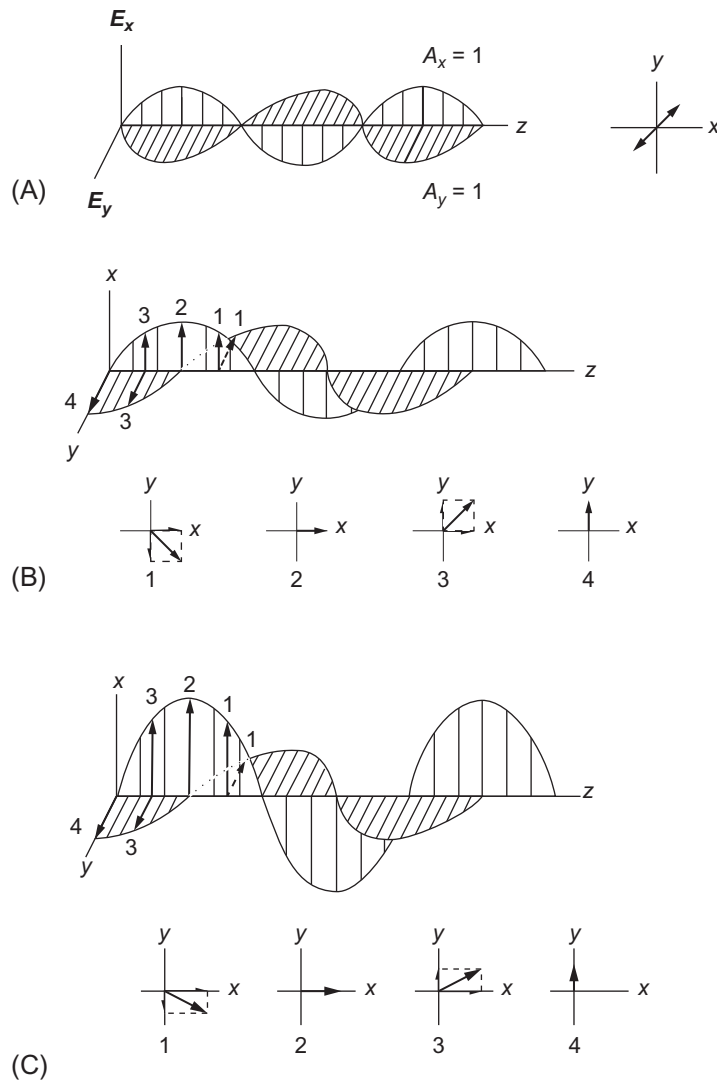
6.2.1 Polarization States of Light

Light consists of a coupled electric and magnetic field oscillating perpendicular to one another and to the propagation direction at the same frequency and amplitude. Since at optical frequencies magnetic field does not appreciably interact with matter, we can consider the electric component only. The direction of the electric field, thus, defines the polarization state of the electromagnetic wave.

The simplest case is represented by linearly polarized (LP) light, i.e., when the electric field oscillates in one plane (Fig. 6.1A). The time- and space-oscillation of the electric field amplitude of a light wave propagating along the z direction oriented in any direction of a generic xy plane, is described by the superposition of two in phase perpendicular components, E_x and E_y , linearly polarized along the x and y axes, respectively:

$$\mathbf{E} = E_x + E_y = \left[E_x^0 \mathbf{i} + E_y^0 \mathbf{j} \right] \sin [\omega t - kz + \phi_0] \quad (6.1)$$

where E_x^0 and E_y^0 are the maximum amplitude, ϕ_0 represents the absolute phase, ω is the angular frequency, k is the wavenumber, and \mathbf{i} and \mathbf{j} are the unit vectors along the x and y axes, respectively.

**Fig. 6.1**

(A) Linearly polarized light at 45 degrees between the x and y axes; (B) left circularly polarized light; and (C) left elliptically polarized light expressed as superposition of two perpendicular linear components along the x and y axes. Modified from D.S. Kliner, J.W. Lewis, *Polarized light in optics and spectroscopy*, Cora Einterz Randall. Copyright 1990 by Academic Press, Inc.

When the two components are of equal magnitude E^0 and the phase is shifted by 90 degrees (or -90 degrees), the polarization state corresponds to right, (left) circularly polarized light, RCP, (LCP), i.e., the electric field has a constant magnitude but rotates clockwise (counterclockwise) in the plane perpendicular to the propagation axis z (Fig. 6.1B):

$$\begin{aligned} \mathbf{E} &= E^0 \left\{ \sin[\omega t - kz + \phi_0] \mathbf{i} + \sin \left[\omega t - kz + \phi_0 \pm \frac{\pi}{2} \right] \mathbf{j} \right\} \\ &= E^0 \{ \sin[\omega t - kz + \phi_0] \mathbf{i} \pm \cos[\omega t - kz + \phi_0] \mathbf{j} \} \end{aligned} \quad (6.2)$$

Both linear and circularly polarized waves are special cases of the more general condition of elliptically polarized light (Fig. 6.1C):

$$\mathbf{E} = E_x^0 \sin[\omega t - kz + \phi_0] \mathbf{i} + E_y^0 \sin[\omega t - kz + \phi_0 + \Delta] \mathbf{j} \quad (6.3)$$

where Δ is the phase difference between components. If $0 < \Delta < 180$ degrees the elliptical polarization is right-handed, while when $-180 < \Delta < 0$ degrees it is left-handed. Two geometrical parameters characterize elliptically polarized light: ellipticity, defined as the ratio of the ellipse's major to minor axis, and the azimuth angle α , which is the angle between the major and the x axes.

The three states of polarization, schematized in Fig. 6.1, can be each expressed in terms of the others. For example, circularly polarized light can be divided into two orthogonal LP components, while LP light results from the sum of two CP waves of equal amplitude, and the phase shift defines the polarization plane. If the CP waves have different amplitudes, elliptical polarization state results.

6.2.2 Magneto-Optical Techniques

The first observation of the modification of the optical properties of a material induced by the application of a magnetic field dates back to 1845: Faraday discovered that a rotation of the polarization plane of LP light propagating through a glass occurs when a magnetic field is applied. The angle of rotation, θ , is proportional to the applied field H and to the sample thickness, the proportionality constant, V , called Verdet constant, being dependent on the light frequency and on the characteristic of the material:

$$\theta = VHL \quad (6.4)$$

Few decades later, Kerr observed a polarization change also in the light reflected from a magnetized surface (see discussion later).

The Faraday effect can be better described by expressing LP light as the combination of two CP waves with the same amplitude and electric field rotating in opposite directions. The two CP waves propagate through the material with different velocity, i.e., $c/n_+ \neq c/n_-$, n_{\pm} being the real parts of the refractive indexes for RCP and LCP light, respectively, and c the velocity of light. This effect originates a phase shift between the transmitted RCP and LCP modes resulting in elliptically polarized light, e.g., a rotation of the polarization plane. The Faraday rotation angle is then given by

$$\theta = \frac{\omega}{2c} (n_+ - n_-) L \quad (6.5)$$

The direct optical measurement of Faraday rotation in transmission geometry is often problematic since the very large contribution of the matrix, substrate, or solvent can mask the signal of the component of interest. In these cases, measuring the differential absorption of RCP and LCP waves is, in practice, much more convenient when working in transmission geometry. Indeed, when RCP and LCP modes propagate through a given medium, they are absorbed to a different extent, i.e., the imaginary part of the refractive index of the two modes is different, $k_+ \neq k_-$. This technique, which is the most common MO technique in transmission geometry, is called magnetic circular dichroism (MCD). LCP and RCP are shined one at each time on the sample and the absorption, A_- and A_+ , respectively, is separately measured. The MCD signal is then given by

$$\Delta A = A_- - A_+ = \Delta \epsilon_M c_M L H \quad (6.6)$$

$\Delta \epsilon_M$ being the difference in molar absorptivity per unit of magnetic field and c_M the molar concentration of the sample. MCD spectra are commonly interpreted as a sum of three terms, A, B, and C, each one characteristic for a given substance and for the considered transition [12]: A terms, called diamagnetic, due to the fact that they are temperature-independent, are related to the Zeeman splitting of the degenerate states; B terms arise from the field-induced mixing of the electronic states with other zero-field states of the system; C terms are observed in optical transition involving orbitally degenerate ground states, and since are temperature dependent are also called paramagnetic.

Magnetic-linear birefringence, also called Voigt or Cotton-Mouton effect, is a different kind of MO phenomenon. When a magnetic field is applied perpendicular to the light, birefringence occurs due to the different propagation velocity of LPs oriented parallel and perpendicular to the field. Unlike Faraday rotation and MCD, which depend linearly on the applied field, this effect is proportional to the square amplitude of the field. Therefore, magnetic-linear birefringence is often stronger than the Faraday effect.

The same MO phenomena as the Faraday effect can be observed also for reflected light. The change in the polarization state of the light reflected from a magnetized surface is called MO Kerr effect (MOKE). MO Kerr effect can be classified into three different types, depending on the relative orientation of the light incidence plane and the applied magnetic field (or the magnetization of the sample): polar, longitudinal, and transverse (Fig. 6.2). The polar configuration corresponds to the magnetization vector oriented perpendicular to the reflecting surface and parallel to the plane of incidence of light. In the longitudinal geometry, the magnetization is parallel to both the reflecting surface and the plane of incidence of light. In the same way as for the Faraday effect, in these two configurations, the reflected wave becomes elliptically polarized, and the change in polarization is proportional to the in-plane magnetization.

In the transverse configuration, the magnetization is parallel to the reflecting surface and perpendicular to the plane of incidence. Although the relative orientation of field and light is the

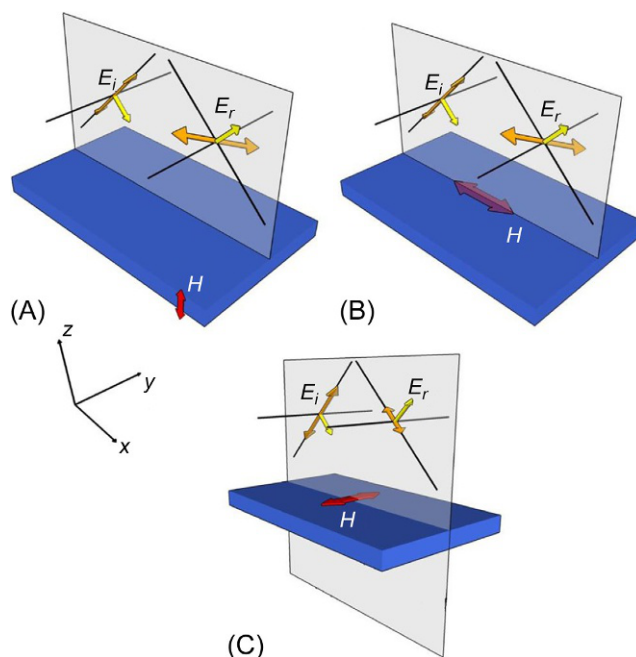


Fig. 6.2

Kerr effect in polar (A), longitudinal (B), and transverse (C) geometries. E_i and E_r indicate the electric field vectors of incoming and reflected light, respectively, H the static magnetic field.

same as the Voigt effect, the field dependence of the phase and intensity changes are not the same.

Transmission and reflection geometries are employed to investigate different kinds of materials: MCD is particularly suited to study molecular systems and colloidal suspension of nanoparticles dispersed in a liquid or solid transparent matrix, or nanostructures deposited on transparent support, while MO is suited for metal films.

6.3 Plasmonics and Magnetoplasmonics

In this section, we review the basic principles underlying plasmon resonances and present some of the potential applications of plasmonics. We then introduce the potential advantage of plasmon modulation through external stimuli (active plasmonics) and describe the principles of magnetic field modulation of LSPR, i.e., magnetoplasmonics.

6.3.1 Plasmonics and Active Plasmonics

Surface plasmons are surface confined electromagnetic waves coupled to collective oscillation of free charges, typically free electrons in metals. They are supported at the interface of the metal with a dielectric medium, provided that the real parts of dielectric constants of the two

media (e.g., a metal and a dielectric) have opposite sign. Most metallic materials, especially noble metals, can support plasmons since they are often characterized by optical constant with a strongly negative real part at optical frequencies. However, in many cases, large optical losses from interband transitions occur and strongly damp the plasmon resonance. Thus, only few metals exhibiting lower optical losses, such as Au and Ag, display well-defined sharp and intense plasmon resonance peaks, useful for plasmonic applications.

Fundamental characteristic of surface plasmons is their strong dimensional localization at the surface interface, with fields that decay exponentially moving away from the interface both in the metal and in the dielectric (Fig. 6.3). In the metal, the field decay depends on the skin depth, which is on the order of ca. 10 nm. Surface plasmons can be supported by a large variety of metallic nanostructures such as thin films, single surfaces, nanoparticles, nanopillars, and nanowires. They are normally classified into two categories, depending on the dimensionality

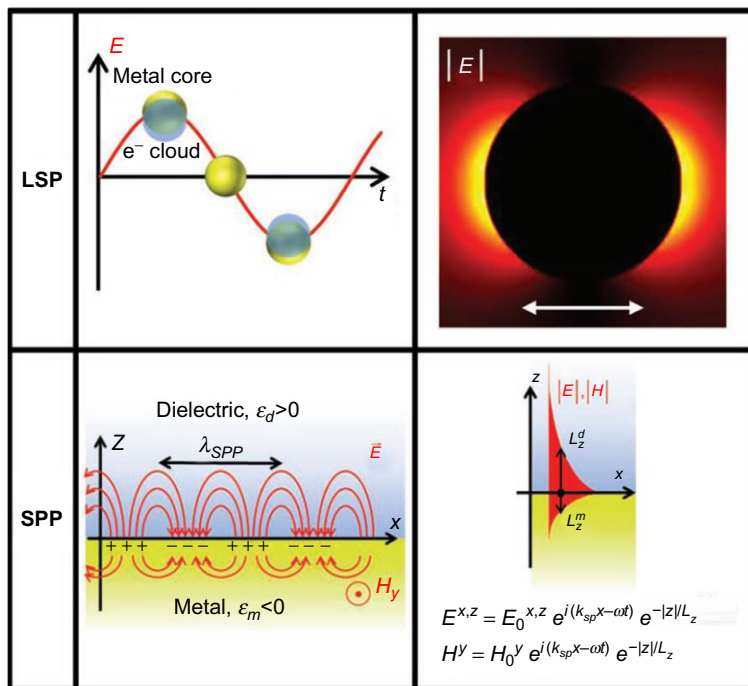


Fig. 6.3

Upper: Sketch of charges oscillation for an LSP in a noble metal nanoparticle (left) and field distribution for an Au nanodisk under LSP excitation (right); Bottom: charges oscillation and fields for an SPP at a metal/dielectric interface; (left) and evanescent SPP field distribution (right). Modified from G. Armelles, A. Cebollada, A. García-Martín, M. U. González, *Magnetoplasmonics: combining magnetic and plasmonic functionalities*, *Adv. Opt. Mater.* 1 (2013) 10–35. Copyright 2013 Wiley-VCH Verlag GmbH & Co. KGaA, Weinheim.

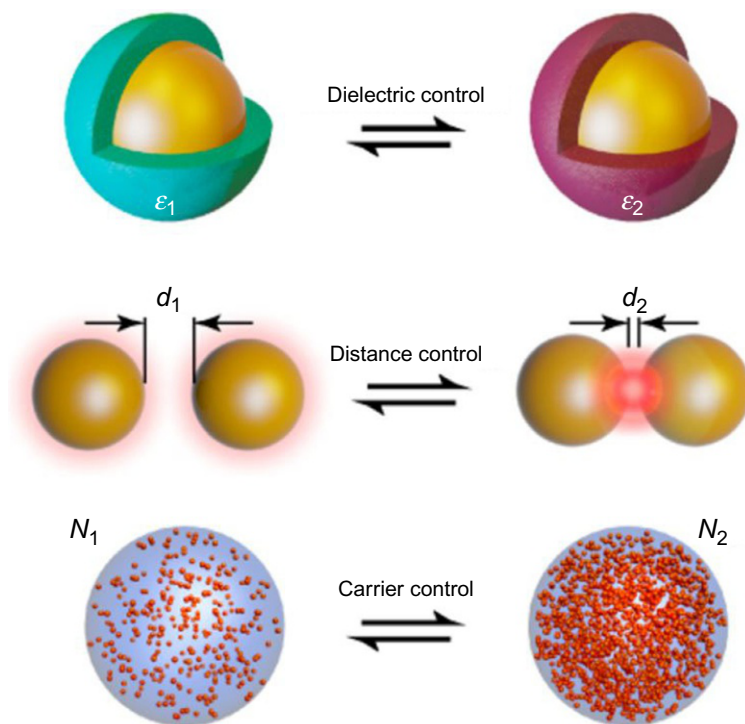
of the supporting structure (Fig. 6.3): when they are coupled to two-dimensional charge oscillations, such is the case of noble metal thin films and gratings, they are called surface propagating plasmons (SPP). For zero-dimensional confinement, plasmon resonances are called localized surface plasmons, (LSP). This is the case of nanoparticles and nanowires (at least in the perpendicular direction) of size of the order of or smaller than the wavelength of the exciting light.

Regardless of the dimensionality of the nanostructure, the main feature is the ability of surface plasmons to confine strong electromagnetic field within nanoscale regions, well below the diffraction limit. The result of the field localization is a strongly increased light-matter interaction, which in turn produces two main effects: on one side, a strong interaction with molecules placed in the field hot-spots, and on the other, a sizable sensitivity of the far-field optical properties of the plasmonic system to small local perturbations of the surrounding refractive index. These properties make plasmonic nanostructures ideal platforms for sensing applications [11,13,14].

In the case of SPPs on thin metallic films, plasmons can be excited optically in particular momentum-matching configurations, using a glass prism or with a grating coupler. Thanks to the strong SPP wavevector dependence on the surrounding dielectric medium, small changes in the local environment produce large momentum variations, visible as shift of the resonance in the reflection spectrum.

In the case of LSPs, coupling with electromagnetic radiation in free space is readily achieved, resulting in a narrow extinction resonance due to intense absorption and scattering of light. The optical properties of LSP depend on several parameters such as chemical composition, size and shape, spatial arrangement, coating, and surrounding environment. The ratio between absorption and scattering, indeed, critically depends on the size of the plasmonic nanostructure. In addition, large shift of the LSP resonance energy results from local change of the refractive index of the surrounding medium. Amplitude and width of LSPR are strictly related to the optical losses described by the imaginary part of the dielectric function. The possibility of tuning all these properties by control of the chemical, morphological, and structural parameters makes nanoparticles supporting LSP a versatile platform for the design of innovative high-performing devices such as switches or modulators, as well as more efficient refractometric sensors [4,11].

Despite the great progress made in the last few decades in terms of design of novel plasmonic nanostructures, the potential of these nano-optical components is still far from being fully exploited. A significant step forward in this sense can be realized by an active control of the plasmonic functionalities with an external stimulus, which would offer further advantage of largely expanding their applicability [7]. The past decade has witnessed a growing interest in these emerging research fields, which are now referred to as active plasmonics, a term originally introduced to describe the control of SPP in a metal-on-dielectric waveguide by

**Fig. 6.4**

Schematic representation of the active plasmonic nanostructures, consisting of plasmonic nanostructures in tunable dielectric surroundings (upper), plasmonic structures with tunable gap distances, (middle), and self-tunable plasmonic structures (bottom). *Reproduced with permission from N. Jiang, X. Zhuo, J. Wang, Active plasmonics: principles, structures, and applications, Chem. Rev. Copyright 2018 American Chemical Society.*

temperature or by external optical excitation [5]. Active plasmonic nanostructures can be classified according to the modulation mechanism involved into plasmonic structures embedded in tunable dielectric surroundings, plasmonic structures with tunable gap distances, and self-tunable plasmonic structures (Fig. 6.4).

In the last case, the active control is realized by inducing changes in the carrier density and dielectric function of the plasmonic materials. Examples of active plasmonics include chemical [15,16], temperature [17], and voltage control [18,19]. However, different approaches must be developed to obtain high switching and modulation speed. In this sense, purely photonic control of the optical properties is considered a strong candidate.

On the other hand, the use of magnetic fields to modulate the plasmonic activity is another promising approach, which has attracted considerable interest in recent times.

6.3.2 Magnetoplasmonics

Among several possibilities to externally control LSPR, magnetic field seems a very convenient option: its effect is fast and fully reversible, since it involves a modification of the oscillation of the free electrons of a conductor mediated by a magnetic field, and can act over a wide range of distances [2,20]. In addition, a very wide range of material combinations can be devised, especially for what concerns the choice of the magnetic material. Since a few years, the study of the interplay between magnetic and plasmonic materials has evolved into a well-defined research topic, referred to as magnetoplasmonics. In effect, this term is currently used for two different aspects: (i) the phenomena related to plasmon-mediated enhancement of the magneto-optical response of magnetic materials, and (ii) the modification of the resonance conditions of plasmonic architectures caused by a magnetic field arising from the proximity of a magnetic material. In fact, the distinction between these two fields of study is probably less well defined than what is currently considered, and a unifying model of these phenomena might be developed in the near future. In this contribution, we will restrict our analysis to systems supporting LSPR, while leaving out the conspicuous body of literature dedicated to magnetoplasmonic effects in systems supporting propagating plasmon resonances and in plasmonic gratings.

Magnetic field modulation of LSPR in its simplest form can be achieved in all plasmonic materials, even nonmagnetic ones, since an external magnetic field is able to modify the way free charges oscillate. The downside of this universal behavior, discussed in [Section 6.4.1](#), is that the magnitude of this effect is small. On the other hand, nanostructures made from ferromagnetic metals, such as iron, cobalt, or nickel, respond strongly to magnetic field thanks to their high magnetic moment. However, their high optical losses compromise their plasmonic properties, to the point that they cannot be considered plasmonic metals at all, with the partial exception of nickel ([Section 6.4.2](#)). Merging the properties of plasmonic materials and magnetic materials has indeed been an early and widely studied strategy to strike a balance between the two key requirements for efficient plasmonic modulation, i.e., sharp optical resonances and strong response to magnetic field. Some of these attempts are described in [Sections 6.5.1 and 6.5.2](#).

In order to observe magnetic-plasmonic hybridization, the magnetic material should be a conductor (metal or semimetal); in addition, the conjugation of this material to the plasmonic moiety should not damp significantly the LSPR. In view of these guidelines, heterostructures made up of Au or Ag on one side, and Fe, Co, or Ni on the other, represent strong candidates. Among bottom-up chemical methods, colloidal chemistry synthesis of core@shell heterodimeric nanoparticles appears a strong candidate, while the top-down approach is suited to prepare multilayer nanodisk structures.

A different possible configuration is the combination of the two materials into alloys, so that the nanostructure and its electronic properties are homogenous. While this class of materials has

been prepared in the form of nanoparticles (see for instance the work of Amendola, who successfully prepared magnetic-plasmonic AuFe alloy nanoparticles [21]), no report on their magnetoplasmonic properties has appeared yet.

Coupling a magnetic material to a plasmonic one is expected to influence the magneto-optical response of the hybrid architecture in two ways: (i) through electronic hybridization between the two components and (ii) through localization of the magnetic field in proximity of the plasmonic structure.

In the first case, plasmon resonance of the system at least partially involves the magnetic material, whose spin-polarized conduction electrons directly influence the free electrons of the plasmonic part. For this mechanism to take place, the magnetic material must have metallic character, to allow efficient hybridization. In the second case, a strongly magnetic material is required to significantly alter magnetic field distribution. Since this interaction propagates through space, the magnetic material does not need to be a conductor, and in principle direct contact between the two moieties is not required. On the other hand, since hybridization does not occur, the magnetic material does not participate in LSPR; for this reason, the MO response of the magnetic material must not have spectral overlap with LSPR; otherwise, the magnetoplasmonic response of the system, spectrally located at LSPR energy, would be drowned by the MO signal of the magnetic material. No direct observation of this effect has been reported to date.

6.4 Magnetoplasmonics in Single-Component Nanostructures

We begin our survey of magnetoplasmonic materials with two complementary classes of single-component nanostructures: nonmagnetic classical plasmonic metals and strongly magnetic, weakly plasmonic ferromagnetic metals. The former family of materials exhibits sharp optical LSP resonances and a weak magnetoplasmonic response, originating from Lorentz force components acting on conduction electrons. These simple systems are ideal for studying the fundamental principles of magnetic field modulation of LSPR. The latter family of materials exhibits strong sensitivity of their optical properties to magnetic field, but very broad LSPR. However, the correct choice of material and geometry allowed some very interesting findings on magnetoplasmonic effects.

6.4.1 Nonmagnetic Metals

Our survey on magnetoplasmonic nanostructured systems begins with the simplest plasmonic entity that is known: a gold nanoparticle. Nonmagnetic gold nanoparticles have been shown to exhibit a sizeable modulation of their plasmonic response in a magnetic field as early as 2001 by Mason's group [22], with theoretical predictions dating even earlier. In this account, the authors measured MCD spectra on colloidal gold nanoparticles

and found an asymmetric derivative signal, crossing zero at the maximum of the optical LSPR of the particle. They found the signal magnitude to scale linearly with the applied magnetic field with no saturation and no temperature dependence. They found this behavior to be reminiscent of a classical MCD A term [23], but gave no further insight on its origin. A more recent report by Artemyev et al. presented an extensive set of MCD measurements on silver and gold nanospheres, as well as on gold nanorods [24]. Also in this case, the presentation was only phenomenological.

A complete rationalization of the phenomenon was given by Pineider et al., who performed MCD experiments on gold nanoparticle dispersions and developed an analytical model based on the effect of Lorentz forces acting on the free charge carriers of the metal [9].

With this approach, the authors were able to explain the magneto-optical behavior of gold nanoparticles both qualitatively and quantitatively.

The model was developed for systems for which the quasi-static approach is valid (i.e., particle diameter is much smaller than the wavelength of light). In this case, only the dipolar term of the plasmonic response of the particle can be taken into account, and scattering can be considered negligible. In this case, particle polarizability $\alpha(\omega)$ can be expressed as:

$$\alpha(\omega) = -\frac{\pi D^3}{2} \frac{(\varepsilon(\omega) - \varepsilon_m)}{(\varepsilon(\omega) + 2\varepsilon_m)} \quad (6.7)$$

with ω angular frequency of the incoming radiation, D particle diameter, $\varepsilon(\omega)$ dielectric function of the metal, and ε_m the dielectric constant of the surrounding medium. With circularly polarized light, circularly polarized plasmon modes are excited [25], resulting in a circular collective oscillation of the free electrons in the particle. If a static magnetic field is applied perpendicular to the plane of charge carrier oscillation, an additional component of the Lorentz force acts on the moving charges:

$$m^* \frac{dv}{dt} + \gamma m^* v = -eE - ev \times B \quad (6.8)$$

with e , m^* charge and effective mass of the charge carrier, v its velocity, γ the damping constant, E the electric field of the incident light, and B the external magnetic induction. The magnetic induction-dependent term in Eq. (6.8) is small compared to electric field term and can be treated as a perturbation [26]. When we solve the Laplace equation inside and outside the particle volume and we apply the boundary conditions for circularly polarized incoming electric field of the form $E = E_0 e^{\pm i\omega t} = E_0 \cos(\omega t) \pm iE_0 \sin(\omega t) = E_x \pm iE_y$, we obtain a generalized expression for the field- and helicity-dependent polarizability:

$$\alpha_B(\omega) = -\frac{\pi D^3}{2} \frac{(\varepsilon(\omega) - \varepsilon_m) + (f(\omega) - f_m)B}{(\varepsilon(\omega) + 2\varepsilon_m) + (f(\omega) - f_m)B} \quad (6.9)$$

In this equation, we introduce $f(\omega)$ and f_m as coupling functions, which take into account perturbatively the interaction of the particle with the magnetic field B of the metal and the surrounding medium, respectively [9,26]. From Eq. (6.9), it follows that a static magnetic field causes a shift in energy of the LSPR. From symmetry considerations, we observe that a change in helicity is topologically equivalent to an inversion of the applied field direction, i.e., to a change in the algebraic sign of B in Eq. (6.9). We can then conclude that plasmon modulation can be achieved both with an inversion of the applied magnetic film and with a change in light helicity. This observation is critical for the rationalization of the MCD experiment, which is carried out at a fixed value of applied field, and light is modulated between the two circular helicities, LCP and RCP. As can be seen in Fig. 6.5, the derivative-like MCD spectrum of gold nanoparticles originates from the difference of two energy-shifted plasmon resonances, excited by LCP and RCP light.

The fact that field direction and light polarization can be interchanged to modulate LSPR is a key concept for magnetoplasmonics: as a consequence, in fact, a strong static magnetic field can be applied, while light polarization can be modulated at high speed thanks to advanced polarization optics, such as photoelastic modulators; these devices can reach modulation frequencies of the order of 10 kHz. This is a unique capability compared to other approaches to active plasmonics. High modulation frequency can be used to boost sensitivity of LSPR-based experimental setups for refractometric sensing, where a precise determination of the LSPR wavelength is required. LSPR in fact is in general a broad peak, and small shifts can be difficult to detect. The MCD signal, on the other hand, with its derivative-like shape due to field/polarization modulation, exhibits a steep slope at the plasmon resonance condition, thus making

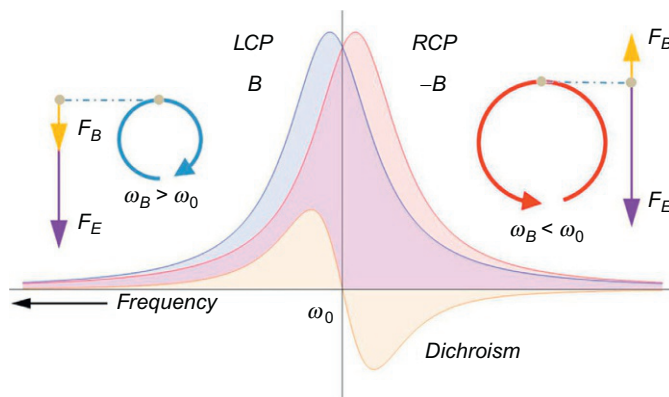


Fig. 6.5

Energy-splitting circular plasmonic modes under a static magnetic field. *Reproduced with permission from F. Pineider, G. Campo, V. Bonanni, J. Fernandez Cde, G. Mattei, A. Caneschi, D. Gatteschi, C. Sangregorio, Circular magnetoplasmonic modes in gold nanoparticles, Nano Lett. 13 (2013) 4785–4789. Copyright 2013 American Chemical Society.*

it easier to measure very small resonance shifts. Proofs of principle of magnetoplasmonic refractometric sensing were given by Pineider et al. [9] and Vavassori's group [10].

The main problem hampering actual exploitability of magnetoplasmonic modulation is the fact that the effect is small. Several strategies can be devised to overcome this problem. The simplest approach is to design LSPR systems with sharp optical resonances: in this respect, silver is a more convenient material than gold. From simple geometrical arguments, it can be observed that the difference of two equal peaks shifted in energy has the same absolute area, regardless of the width of the peaks, and only depends on the distance between the shifted peaks. On the other hand, peak-to-peak distance between the positive and the negative lobes is inversely proportional to the width of the peak: as a consequence, nanostructures with sharper LSPR will give a stronger MCD signal (Fig. 6.6).

Another important study of the magneto-optical response of nonmagnetic plasmonic nanostructures is the one by Sepúlveda et al. [27]: in this case, the authors used glass-supported gold nanodisks prepared by hole-mask colloidal lithography [28] and MOKE spectroscopy. Their qualitative model is based on linear plasmonic modes, as opposed to circular plasmonic modes; however, the explanation is also based on the onset of a field-induced Lorentz force component acting on the moving charge carriers.

A limitation of the simple model used by Pineider et al. to describe the magneto-optical response of plasmonic systems is that a symmetry between two orthogonal plasmonic modes is required. This is due to the fact that purely circular plasmonic modes are the result of a coupling of two degenerate resonances. Such condition is always fulfilled for spherical nanoparticles [9] and for nanodisks at normal light incidence [27]. The model will hold as an approximation also for systems in which energy separation of different resonances is small compared to their widths. In a general case, however, a plasmonic nanostructure can exhibit resonances at different energies, as in the case of nanorods, where longitudinal and transversal modes can be fully resolved as distinct peaks in the extinction spectrum. In this situation, the derivative-like

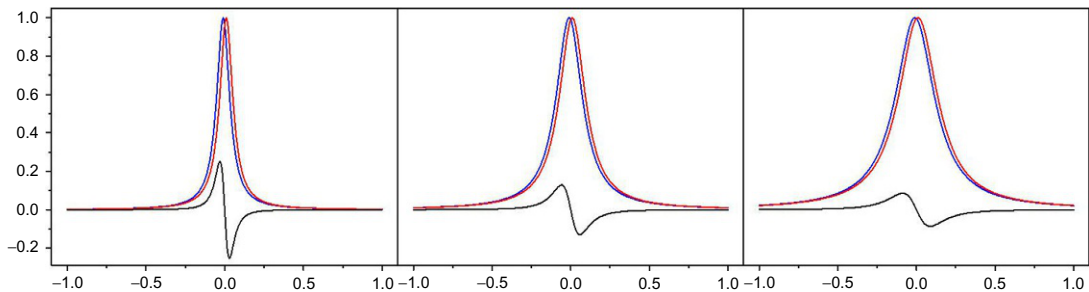


Fig. 6.6

Three cases of differential signals originating from shifted identical peaks. Every couple of peaks is shifted by the same energy. Peak height is kept constant. Sharper peaks give differential signals with bigger amplitude.

MCD signal is not observed, as previously noted by Artemyev et al. [24]. The rationalization of the MCD behavior of gold nanorods was recently hinted by Melnikau et al. [29], and fully developed by Han et al. [30] as the plasmonic equivalent of a classical MCD B term [23]. A plasmonic nanorod has three resonance modes: two degenerate transverse modes and a longitudinal one (Fig. 6.7A). When circularly polarized light impinges parallel to the long axis of the rod, the two degenerate transverse modes are excited into two circular plasmonic mode. Magnetic field splitting results in a derivative-like line shape, as in spherical nanoparticles (*blue trace (light gray in print) in Fig. 6.7B*). On the other hand, circularly polarized light perpendicular to the long axis of the rod is not able to excite purely circular plasmonic modes, since these would involve one transverse and one longitudinal mode, which are nondegenerate. In this case, magnetic field mixes the two modes, thus creating two new modes, which are excited each by light of opposite helicity. The MCD spectrum will then exhibit two peaks of opposite sign at the two resonances of the nanorod (*red trace (black in print) in Fig. 6.7B*), which add up to the derivative signal of the transverse modes. The magnitude of the mixing depends on the energy separation between modes, so an increase in the aspect ratio of the rod results in an intensity decrease of the MCD response.

Metals are not the only class of materials able to efficiently support plasmon resonances. Recently, several reports highlighted the potential of doped semiconductor nanoparticles for infrared plasmonics [31,32]. Doped semiconductors typically contain a lower free electron density N compared to metals ($N = 10^{19} - 10^{21} \text{ e cm}^{-3}$ against 10^{23} of metals). Since the energy of localized plasmon resonance is proportional to $N^{1/2}$ [33], it follows that LSPR in these

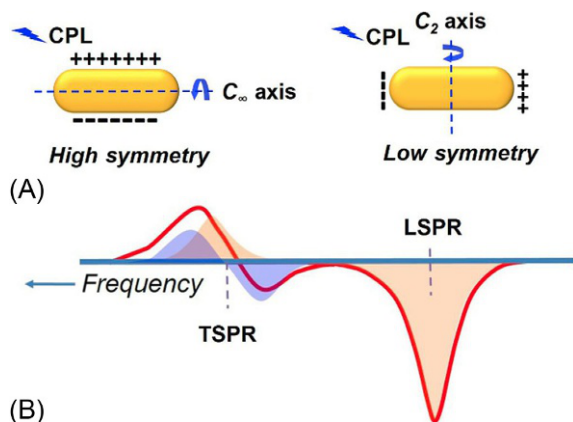


Fig. 6.7

(A) Sketch of the plasmon resonance modes in nanorod geometry. (B) Breakdown of the contributions from different plasmonic components in the MCD spectrum of a gold nanorod. Reproduced with permission from B. Han, X. Gao, L. Shi, Lin Y. Zheng, K. Hou, J. Lv, J. Guo, W. Zhang, Z. Tang, *Geometry-modulated magnetoplasmonic optical activity of Au nanorod-based nanostructures Nano Lett.* 17 (2017) 6083–6089. Copyright 2017 American Chemical Society.

materials falls at lower energy compared to their metallic counterparts, i.e., in the near IR instead of the visible wavelength interval. In addition, the amount of free carrier doping in these materials can be varied over a wide range of values, thus making their LSPR easily tunable. Moreover, depending on the class of material, also the character of free carrier can be very different: doped semiconductors of the covellite family exhibit hole conductivity; thus, LSPR is supported by holes instead of electrons and the value of the unit charge e is positive instead of negative. Effective mass m^* can also vary significantly (to $<10\%$) from the free electron value; in plasmonic metals, on the other hand, effective mass is always close to unity. In nonmagnetic plasmonic nanostructures, magnetic modulation is in first approximation proportional to the cyclotron frequency [9,27,34], $e \cdot B / 2m^*$, where B is magnetic induction. It follows that the magnetoplasmonic behavior of nonmagnetic, plasmonic nanostructures depends critically on the free carrier Drude parameters mentioned here. A key report by the Gamelin group elegantly showed this dependence experimentally, by studying with MCD a set of heavily doped semiconductors comprising p -Cu_{2-x}Se, n -ZnO, and tin-doped In₂O₃ (n -ITO) [35]. Each of these model systems shows a distinct MCD response at the plasmon resonance that sets it apart from standard gold and silver plasmonic systems (see Fig. 6.8). In the case of p -Cu_{2-x}Se, the derivative-like line shape is inverted in sign with respect to the case of Gold and Silver; this is

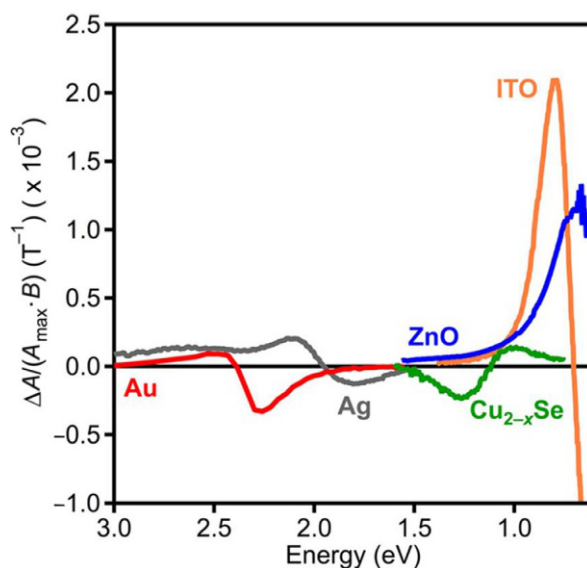


Fig. 6.8

A collection of MCD spectra of different plasmonic systems. Classic materials, such as Au and Ag, are compared to representative plasmonic doped semiconductors. Modified from K.H. Hartstein, A.M.

Schimpf, M. Salvador, D.R. Gamelin, Cyclotron splittings in the plasmon resonances of electronically doped semiconductor nanocrystals probed by magnetic circular dichroism spectroscopy, *J. Phys. Chem. Lett.* 8 (2017) 1831–1836. Copyright 2017 American Chemical Society.

coherent with the fact that LSPR is supported by positively charged holes; thus, their field response is opposite to electrons. For n -ZnO and n -ITO, the sign is the same of metals, since charge carriers are electrons. Effective mass for these charge carriers, however, is smaller than that of Gold and Silver ($m^* \sim 0.4$ for both n -ZnO and n -ITO); as a consequence, magnetic field modulation, thus the MCD signal is stronger with respect to metals. This is an extremely interesting observation, because it hints at the fact that doped semiconductors with very small effective charge carrier mass can be very efficient magnetoplasmonic modulators.

6.4.2 Ferromagnetic Metals

An alternative approach is represented by the use of pure ferromagnetic metal nanostructures, which combine in a single element magneto-optical activity and plasmonic properties. This class of materials has been scarcely investigated for a long time, mostly because of the large optical losses and broad plasmon resonances. Nevertheless, in the recent years, several reports appeared in the literature demonstrating the influence of plasmon resonance excitation on the magneto-optical properties in ferromagnetic metal nanostructures, most of them being focused on nickel [36,37].

Bonanni et al. investigated nickel nanodisks of different diameters (from 60 to 170 nm) fabricated by hole-mask colloidal lithography, and demonstrated the strong correlation between LSP and magneto-optical activity [38]: a wavelength-dependent reversal of Kerr rotation was indeed observed when the energy was changed from below to above the optical resonance, a behavior, which was related to the change in sign of the polarizability at the LSP resonance (Fig. 6.9).

A further contribution to the understanding of the coupling between the MO activity and the plasmonic resonance in nanoferromagnets was provided by the work of Maccaferri et al., which laid a more solid theoretical background both for what concerns the magnetoplasmonic response of spherical and elliptical Ni nanostructures [39], and the role played by a nonabsorbing substrates [40]. The possibility of a plasmon-controlled modulation of the light phase that modifies the polarization of the reflected light by engineering of the size and shape of the ferromagnetic metal nanostructures was demonstrated and a computational model, which reproduces the experimental polarization states (rotation and ellipticity), was developed [41]. In particular, the coupling between plasmon resonance and MO was described in terms of a simple model, based on two orthogonal damped harmonic oscillators coupled by the Spin-Orbit interaction; the LSP excitation transverse to the electric field of the incident light was found to determine the MO response observed in the nanometric ferromagnets. A generalized model, extended to three-dimensional nickel nanoantennas, was later presented by Lodewijks et al. [42]. This work provides the fundamental rules to design magnetoplasmonic nanostructures allowing for phase modulation of reflected light over a broad spectral range.

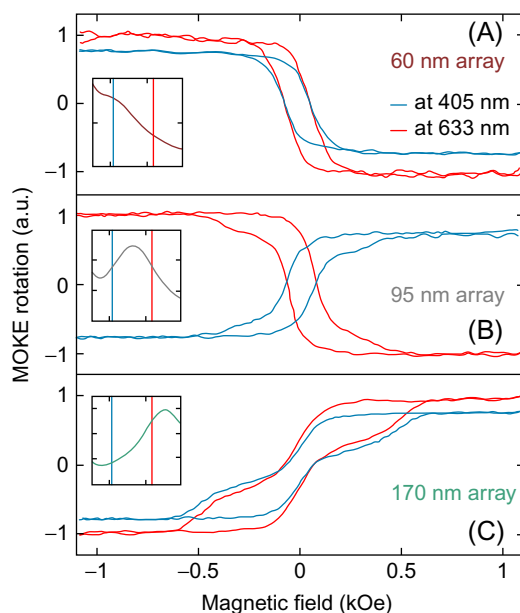


Fig. 6.9

Normalized longitudinal MO Kerr rotation for Ni nanodisks of 60- (A), 95- (B), and 170-nm diameter (C), using two different excitation wavelengths: 405 nm (blue (dotted line in print)) and 633 nm (red (dashed line in print)). The insets show the far-field extinction spectra for the corresponding nanodisks. The sign of the MO Kerr loops reverses when they are recorded at higher or lower energy with respect to the optical resonance. *Reproduced with permission from V. Bonanni, S. Bonetti, T. Pakizeh, Z. Pirzadeh, J. Chen, J. Nogués, P. Vavassori, R. Hillenbrand, J. Åkerman, A. Dmitriev, Designer magnetoplasmonics with nickel nanoferromagnets, Nano Lett. 11 (2011) 5333–5338. Copyright 2011, American Chemical Society.*

Large plasmon-dependent enhancement of the magneto-optic Kerr rotation was also reported for nickel [43] and iron [44] antidot arrays with hexagonal symmetry fabricated by patterning subwavelength holes into optically thin films of the corresponding metals. The tuning of the spectral position of the Kerr maxima could be obtained by modification of the antidot size and distance.

Much larger effects of the LSP-enhanced electric field were observed by Valev et al. [45] on the nonlinear MO response of a periodic array of G-shaped nickel nanostructures. When the G-shaped structures were rotated, an asymmetric MO second harmonic generation signal was reported inverting the magnetic field direction. The extreme sensitivity of the nonlinear MOKE effect to weak plasmonic modes can actually represent the breakthrough for effective applications in MO.

All these results point out that despite the broad LSP, nickel nanostructures exhibit a stronger MO activity compared to pure noble metal plasmonic nanosystems, which makes them

extremely appealing not only for fundamental investigation of magnetoplasmonic effects but also for application in ultrasensitive optical sensing. A proof of concept of the ultrasensitive sensing capabilities of ferromagnetic nanodisks was recently provided by Maccaferri et al. [10]. Short-range ordered nickel cylinders (103 ± 5 nm diameter and 30 ± 0.5 nm thickness) were organized on a transparent substrate so as to induce a null condition of the reflected light polarization ellipticity. The extremely precise phase-sensitive detection of LSP near null conditions allowed for revealing the spectral shift produced by local refractive index variations with unprecedented precision (Fig. 6.10). A large improvement of sensitivity compared to nanoplasmonic sensors (more than two order of magnitude in raw surface sensitivity) was obtained when the approach was tested versus extremely thin layers of polyamide-6.6, which was selected as representative for a large variety of polymers, peptides, and proteins. The sensitivity corresponded to ca. 0.8 ag of polyamide per nanodisk. The sensing capabilities of metal nanomagnets can be used in principle for a large number of applications, including chemical sensing of toxic materials, explosives, and ultra-precise thickness-monitoring applications.

Finally, it should be noted that the large breadth of LSP of small nickel nanoparticles chemically synthesized, prevented so far to observe magnetoplasmonic effects in this kind of nanostructures.

6.5 Hybrid Magnetoplasmonic Nanostructures

The most intriguing approach to magnetoplasmonics is represented by the assembling of hybrid nanostructures combining plasmonic and ferromagnetic materials. The combination of the two allows in principle to overcome the limitation arising from the too low MO activity of pure noble metals and the broad resonance of ferromagnetic nanostructures alone. Hybrid magnetic-plasmonic systems are currently extensively investigated for application in several research areas ranging from biomedicine, where the double functionality can be exploited to realize multifold theranostic agents, or for ultrasensitive sensing and heat-mediated magnetic recording [46–49]. In a perspective more specific to magnetoplasmonics, they are in principle ideal platforms to observe both the effect of the magnetic component on the field-dependent behavior of LSPR, and the effect of plasmon confinement of the electromagnetic field on the MO response of the magnetic material (plasmon-enhanced spectroscopies).

6.5.1 Plasmonic Metals/Magnetic Metals

A strong plasmon-related enhancement of the MO activity was first observed in nanosandwiches composed of stacked Au/Co/Au disks prepared by colloidal lithography. The single hybrid plasmonic mode arising from both the Au and Co layers, which can be tuned by modifying the aspect ratio of the nanosandwiches, is influenced by the magnetic field, resulting

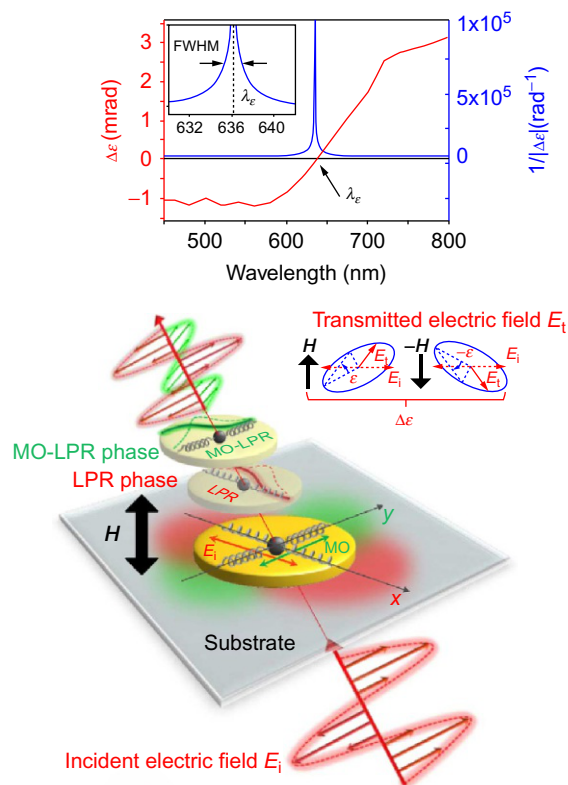


Fig. 6.10

The simultaneous excitation of LPR and MO-LPR in a ferromagnetic nanodisk induces an elliptical polarization of the transmitted field. By properly tuning the size of the nanodisk, it is possible to reach the null condition of ellipticity at a desired wavelength. This zero measurement provides a precise phase-sensitive detection of the LPR position. On the upper panel, the typical ellipticity (red (dotted line in print)) and the inverse ellipticity (blue (dashed line in print)) spectra are shown. The extremely precise phase-sensitive detection of LSP near null conditions allows for measuring the spectral shift produced by local refractive index variations with unprecedented precision. *Reproduced with permission from N. Maccaferri, K.E. Gregorczyk, T.V. de Oliveira, M. Kataja, S. van Dijken, Z. Pirzadeh, A. Dmitriev, J. Åkerman, M. Knez, P. Vavassori, Ultrasensitive and label-free molecular-level detection enabled by light phase control in magnetoplasmonic nanoantennas, Nat. Commun. 6 (2015) 6150. Copyright 2015, A Macmillan Publishers Limited.*

in strong MO at the plasmon resonance peak. The experimental results were confirmed by theoretical calculation, which related the observed phenomenon to the electromagnetic field enhancement in the nanodisk upon LSPR excitation [50].

A direct correlation between the strong enhancement of the Faraday rotation and the electromagnetic fields induced under LSPR excitation was also demonstrated by Wang and coworkers for Fe@Ag [51] and Co@Ag [52] core-shell nanoparticles prepared by controlled

chemical reduction in aqueous solution. In particular, for the latter system, the authors reproduced quantitatively the observed dependence of the MO activity on the electromagnetic field in the magnetic core, tuned by changing the Co/Ag relative ratio within the nanoparticle while keeping the total size constant (Fig. 6.11). A more rigorous description of the MO response of core-shell hybrid nanoparticles has been developed recently by Vartys et al. [53].

The correlation between MO activity and electromagnetic field can be exploited to probe the internal distribution of the electromagnetic field within the hybrid nanostructure. This possibility was theoretically demonstrated and experimentally verified by Meneses-Rodríguez and coworkers [54] by using a trilayer Au/Co/Au nanodisk geometry: the intensity of the MO signal was recorded for various positions of a Co layer with respect to the top and bottom Au layers and through accurate numerical modeling was found to be related to the local electromagnetic field intensity concentrated by the Au structures.

Interestingly, Armelles group demonstrated that the plasmonic and magnetoplasmonic components do not need to be in close contact to generate an enhancement in MO activity. They indeed investigated by polar MOKE spectroscopy a nanostructured system where Au/Co/Au stacked nanodisks were coupled to gold nanodisk separated by a SiO₂

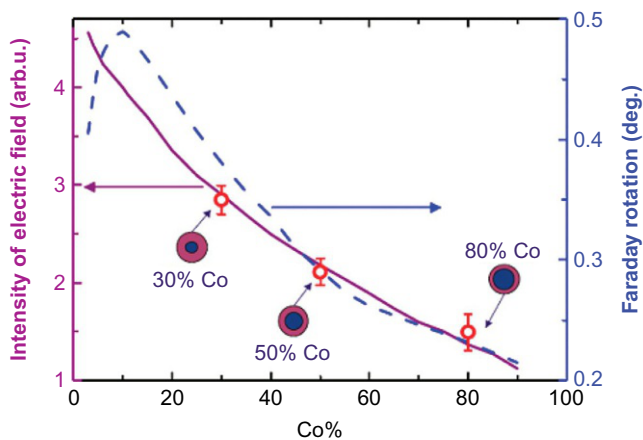


Fig. 6.11

Maximum Faraday rotation for Co-Ag core-shell nanoparticles with fixed diameter and variable Co:Ag ratio embedded in oil ($n = 1.5018$) and calculated intensity of the electric field at resonance within the Co core (dashed line). A clear correlation between the Faraday rotation and electromagnetic fields in the Co core is observed. Reproduced with permission from L. Wang, C. Clavero, Z. Huba, K.J. Carroll, E.E. Carpenter, D. Gu, R.A. Lukaszew, *Plasmonics and enhanced magneto-optics in Core-Shell Co-Ag nanoparticles*, *Nano Lett.* 11 (2011) 1237–1240. Copyright 2011, American Chemical Society.

layer. This system can be described as made up by two optical coupled resonators: by tuning the thickness of the dielectric spacer, the degree of coupling between the two moieties could be varied and for small enough thickness the electromagnetic field associated to the LSPR penetrates the magnetoplasmonic region modifying its MO response [55]. Furthermore, the study of similar magnetoplasmonic resonators (Au nanodisk/SiO₂/2 nm Co – 4 nm Au multilayer nanodisk) allowed the authors to demonstrate that when a magnetic field is applied perpendicular to the disks, MO activity can be produced in the purely plasmonic components due to the field-induced electric dipole perpendicular to the electric field of light [56]. In addition, they observed MO transparency in a narrow spectral range as a result of the interference between the contributions of the coupled magnetoplasmonic and plasmonic components. This interference leads to a Fano-like resonance of the MO response, which can find application for sensing and telecommunications [56].

A more detailed study of the dipole-dipole interaction in these hybrid nanostructures was later presented by the same group. The experimental and theoretical investigation of nanopillars formed by two coupled nanodisks separated by a dielectric spacer with different geometries (i.e., magnetoplasmonic at the bottom and plasmonic at the top, plasmonic at the bottom and magnetoplasmonic at the top and two magnetoplasmonic components) allowed for enlightening the dependence of the overall MO response on the nature of the components and on their relative arrangement [57]. In particular, it was found that for selected configurations the MO activity induced in the plasmonic component can be even larger than that of the magnetoplasmonic one.

A large enhancement of MO activity was observed also in array of gold-cobalt core@shell nanowires fabricated by electrochemical deposition into an anodized alumina template [58]. Most importantly, the authors reported a significant alteration by the magnetic field of the phases of plasmon-related optical features, which, thanks to the remnant magnetization of the cobalt shell, is preserved even in the absence of the magnetic field.

A more exotic example of hybrid magnetoplasmonic nanostructures is represented by chiral magnetoplasmonic Au/Co gammadion-shaped multilayers, which have been recently fabricated by Armelles et al. [59]. These systems exhibit the simultaneous presence of MO and optical activities, although no cooperative behavior such as magnetochirality between the magnetic and the chiral aspects of their samples was found.

Another fascinating example of the richness of physical behavior of hybrid magnetoplasmonic nanostructures is provided by a recent paper by the Armelles group [60]. Using polar MOKE spectroscopy, they compared the MO response of multilayered Au/Co nanodisks with that of an array of nanoholes with the same composition, hole diameter, and separation of the nanodisks (Fig. 6.12) and found that complementary magnetoplasmonic systems produce mirror imaged spectral MO responses at the plasmon resonances. With the help of numerical

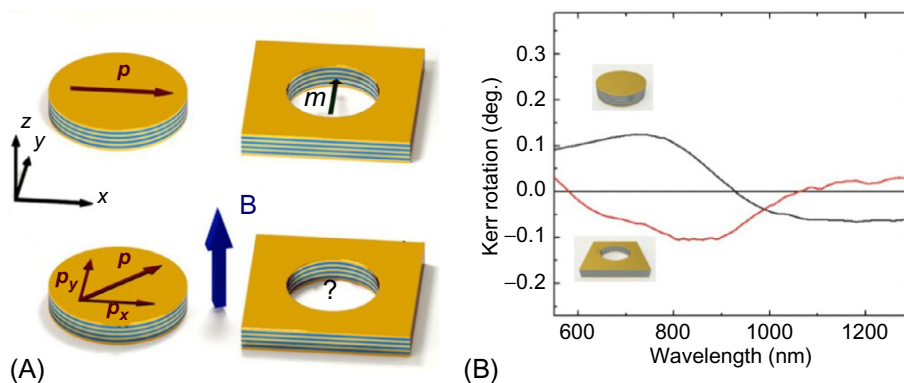


Fig. 6.12

(A) Electric dipole excited by light in a Au/Co multilayer nanodisk and magnetic dipole excited in the complementary nanohole structure (top) and effect of a static magnetic field on the dipoles (bottom). (B) A mirror behavior is observed in the MO Kerr rotation of the nanodisks (up) and nanoholes (bottom). *Modified from G. Armelles, B. Caballero, A. Cebollada, A. Garcia-Martin, D. Meneses-Rodríguez, Magnetic field modification of optical magnetic dipoles, Nano Lett. 15 (2015) 2045–2049. Copyright 2015 American Chemical Society.*

simulations, they recognized the common physical origin of this effect for both systems, demonstrating that MO dipoles can be influenced by a static magnetic field.

According to the authors, the observed behavior represents the magnetoplasmonic analogue of the Babinet principle, i.e., structurally complementary plasmonic systems produce complementary optical responses [61].

An alternative approach to the hybrid magnetoplasmonic nanostructures is the fabrication of systems where noble metal plasmonic nanoparticles are embedded in ferromagnetic dielectric matrices. As an example, sizeable enhancement effects have been found by Tomita et al. [62], in Au nanoparticles embedded in dielectric garnet matrices obtained by cosputtering together with thermal annealing.

6.5.2 Plasmonic Metals/Magnetic Oxides

Bifunctional magnetic plasmonic heteronanostructures based on gold/silver and magnetic oxides, mainly magnetite and derivative ferrites, have been widely studied due to their interesting capability of featuring two different functions on the same object. Core@shell nanoparticles and heterodimers, as well as more complex geometries, have been synthesized and proposed for a wealth of applications, especially in nanomedicine [46,47,63]. From the point of view of magnetoplasmonics, nanostructures based on magnetic oxides have been

mainly proposed as platforms for plasmon-enhanced magneto-optical spectroscopies. An early report by the Markovich group documented an increase in the MCD signal of magnetite nanoparticles in the vicinity of a gold surface [64]. While this is not strictly the case of an all-nanometric hybrid structure, it is an interesting case because it suggests the possibility of increasing the magneto-optical signal in the presence of a metallic surface. Later, a paper by Jain et al. [65] showed a weak enhancement of Faraday rotation in gold@magnetite core-shell colloidal nanoparticles. The authors observed a magneto-optical transition at the wavelength of LSPR of the plasmonic component of the gold moiety. They concluded that such feature originates from the magnetite moiety, but it is too weak to be observed in plain magnetite nanoparticles. A similar type of effect has been reported for Ag-CoFe₂O₄ heterodimers [66]. On the other hand, no reports have appeared so far in the literature for enhancements of magnetic field modulation of LSPR. This is probably due to the fact that magnetic oxides are bad conductors, and they exhibit poor mixing with the electronic structure of the plasmonic material, and thus do not participate to LSPR in any way, as in the case of metallic magnets (see Section 6.5.1). Pineider et al. underlined the importance of the chemical nature of the magnetic moiety with a synchrotron-based X-ray magnetic circular dichroism study at the Au edge [67]. They compared two gold-iron oxide core@shell nanostructures, of which one featured fully oxidized magnetite (γ -Fe₂O₃), and the other had a thicker shell containing a mixture of magnetite (Fe₃O₄) and wustite (FeO), surrounding the gold core. They found no signature of a transfer of magnetic moment to the gold core in the former, and a sizeable magnetic moment in gold in the latter. They concluded that in the first case the magnetic and plasmonic components are orthogonal, while in the second case some degree of hybridization occurs. This is probably due to the fact that the slightly conducting magnetite/wustite system can mediate interaction with gold, thus making the system a potential candidate for the observation of magnetoplasmonic effects. Unfortunately, LSPR was completely damped on this sample, due to the strong absorption of the iron oxide shell, and no magneto-optical study could be carried out to confirm this hypothesis.

6.5.3 Plasmonic Metals/Magnetic Molecules

The last class of magnetic-plasmonic architectures reviewed here is that of molecule-plasmonic nanoantenna hybrids. In these materials, the plasmonic part consists of classic systems, i.e., gold nanostructures, while the counterpart is an assembly of molecules. Plasmonic-molecular hybrids are extremely promising, thanks to the wide tuneability of molecules both in terms of optical and magnetic properties. However, to date, very scarce literature can be found on the subject. An interesting report was given by Melnikau et al., who coupled nonmagnetic JC-1 dye molecules to gold nanorods and studied this hybrid structure with MCD [29]. The molecule assembles around the gold nanorods to form J-aggregates, which exhibit excitonic coupling (i.e., an excited state delocalized over a large number of molecular units), which in turn

undergoes strong coupling with the longitudinal LSPR of the nanorods. Strong coupling can take place when two optical resonances are spatially and energetically close; in this regime, instead of overlapping resonances, a noncrossing behavior is observed, and the two modes are hybridized. Thus, the two noncrossing peaks share both molecular and plasmonic nature.

In MCD, the signal from JC-1 dye molecule is negligible, while the plasmon resonance of the gold nanorods has a distinct MCD response (see Section 6.4.1). Leveraging on this effect, the authors showed that part of the MCD response of the plasmonic structure is carried onto the molecular side of the resonance. The authors claimed that with this method it is in principle possible to use MO techniques to detect nonmagnetic molecules that are magneto-optically silent. A further observation by the authors is that, when decreasing the energy overlap between the resonance of the J-aggregate and the LSPR of nanorods (achieved by changing nanorod aspect ratio), the strength of the MCD signal from the molecular side of the resonance decreases. This is coherent with the fact that also the degree coupling between the molecular and plasmonic modes decreases, thus decreasing mode hybridization and, finally, the plasmonic character of the molecular resonance.

Another description of plasmon-molecule interaction in MCD was given by Pineider et al. [68]. In this case, the plasmonic structure is an array of gold nanodisks supported on glass, and the molecule is TbPc₂, a rare earth-based single-molecule magnet. This molecule is not known to form J-aggregates and does not exhibit excitonic resonances. On the other hand, its magnetic properties are well known, since it can retain magnetic memory up to relatively high temperature (~ 10 K). The molecule was deposited as a 2-nm thin film over the plasmonic nanostructure and studied with optical and MCD spectroscopies. The authors found that this hybrid structure can be described by the weak coupling regime (i.e., molecular resonance and LSPR does not hybridize) and found that the MCD response of TbPc₂ is amplified of a factor 5 by the plasmonic structure, which in fact acts as a nanoantenna for magneto-optics. Previous reports on plasmon-enhanced magneto-optics are scarce (see Section 6.5.2), and not always very clear for what concerns the amplification factor and its origin. In this work, the authors showed for the first time that the increase in the MCD signal is a direct consequence of the plasmon antenna effect taking place at the optical level. They were able to draw this conclusion also thanks to an in-depth analysis of the MCD contribution from the Au nanodisks, which is usually considered negligible compared to that of magnetic species. This is in general a poor approximation, and with very reduced amounts of magnetic material like in this case, it is not possible to correctly interpret the MCD spectrum without explicitly taking into account the LSPR contribution to the MCD spectrum. This very promising experiment shows that plasmon-enhanced magneto-optics can be a very powerful tool to study magnetic materials in very low concentration, even down to the monolayer. On the other hand, the onset of strong coupling between a magnetic molecule and a nanoantenna could show interesting hybridization effects that might lead to the development of novel optoelectronic devices.

6.6 Conclusion

To summarize, magnetoplasmonics is now a mature field of research. We hope that the survey of materials and their properties presented here could convey to the reader a clear picture of the current status of this field. Several different approaches have been devised, realized, and tested by several research groups around the globe. It appears clear that current approaches have demonstrated their conceptual validity: in order to bring them to actual applicability, energies must be spent toward their optimization, to maximize field responsivity of LSPR while maintaining sharp, well-defined optical resonances. On the other hand, radically new approaches, like the use of nonmetallic conductors, could open the way to a completely different approach to magnetoplasmonics, adding several precious degrees of freedom.

Acknowledgment

This work has been supported by the European Union's Horizon2020 Research and Innovation program under Grant agreement No. 737709 (FEMTOTERABYTE <http://www.physics.gu.se/femtoterabyte>).

References

- [1] B.C. Stipe, T.C. Strand, C.C. Poon, H. Balamane, T.D. Boone, J.A. Katine, J.-L. Li, V. Rawat, H. Nemoto, A. Hirotsune, O. Hellwig, R. Ruiz, E. Dobisz, D.S. Kercher, N. Robertson, T.R. Albrecht, B.D. Terris, Magnetic recording at 1.5 Pb m^{-2} using an integrated plasmonic antenna, *Nat. Photonics* 4 (2010) 484–488.
- [2] V.V. Temnov, G. Armelles, U. Woggon, D. Guzatov, A. Cebollada, A. Garcia-Martin, J.-M. Garcia-Martin, T. Thomay, A. Leitenstorfer, R. Bratschitsch, Active magneto-plasmonics in hybrid metal–ferromagnet structures, *Nat. Photonics* 4 (2010) 107–111.
- [3] S. Lal, S. Link, N. Halas, Nano-optics from sensing to waveguiding, *Nat. Photonics* 1 (2007) 641–648.
- [4] K.M. Mayer, J.H. Hafner, Localized surface plasmon resonance sensors, *Chem. Rev.* 111 (2011) 3828–3857.
- [5] A.V. Krasavin, N.I. Zheludev, Active plasmonics: controlling signals in Au/Ga waveguide using nanoscale structural transformations, *Appl. Phys. Lett.* 84 (2004) 1416–1418.
- [6] K.F. MacDonald, Z.L. Samson, M.I. Stockman, N. Zheludev, Ultrafast active plasmonics, *Nat. Photonics* 3 (2009) 55–58.
- [7] N. Jiang, X. Zhuo, J. Wang, Active plasmonics: principles, structures, and applications, *Chem. Rev.* 118 (2018) 2882–2926.
- [8] G. Armelles, A. Cebollada, A. García-Martín, M.U. González, Magnetoplasmonics: combining magnetic and plasmonic functionalities, *Adv. Opt. Mater.* 1 (2013) 10–35.
- [9] F. Pineider, G. Campo, V. Bonanni, J. Fernandez Cde, G. Mattei, A. Caneschi, D. Gatteschi, C. Sangregorio, Circular magnetoplasmonic modes in gold nanoparticles, *Nano Lett.* 13 (2013) 4785–4789.
- [10] N. Maccaferri, K.E. Gregorczyk, T.V. de Oliveira, M. Kataja, S. van Dijken, Z. Pirzadeh, A. Dmitriev, J. Åkerman, M. Knez, P. Vavassori, Ultrasensitive and label-free molecular-level detection enabled by light phase control in magnetoplasmonic nanoantennas, *Nat. Commun.* 6 (2015) 6150.
- [11] J.N. Anker, W.P. Hall, O. Lyandres, N.C. Shah, J. Zhao, R.P.V. Duyne, Biosensing with plasmonic nanosensors, *Nat. Mater.* 7 (2008) 442–453.
- [12] A. Buckingham, P. Stephens, Magnetic optical activity, *Annu. Rev. Phys. Chem.* 17 (1966) 399–432.
- [13] M.I. Stockman, The physics beyond the applications, *Phys. Today* 64 (2011) 39–44.

- [14] J. Homola, Surface plasmon resonance sensors for detection of chemical and biological species, *Chem. Rev.* 108 (2008) 462–493.
- [15] S. Kim, N. Cheng, J.-R. Jeong, S.-G. Jang, S.-M. Yang, W.T.S. Huck, Localized surface plasmon resonance (LSPR) sensitivity of Au nanodot patterns to probe solvation effects in polyelectrolyte brushes, *Chem. Commun.* 211 (2008) 3666–3668.
- [16] N.N. Jiang, L. Shao, J.F. Wang, (Gold nanorod core)/(polyaniline shell) plasmonic switches with large plasmon shifts and modulation depths, *Adv. Mater.* 26 (2014) 3282–3289.
- [17] J. Gosciniaik, S.I. Bozhevolnyi, T.B. Andersen, V.S. Volkov, J. Kjelstrup-Hansen, L. Markey, A. Dereux, Thermo-optic control of dielectric-loaded plasmonic waveguide components, *Opt. Express* 18 (2010) 1207–2016.
- [18] J.A. Dionne, K. Diest, L.A. Sweatlock, H.A. Atwater, PlasMOSStor: a metal – Oxide – Si field effect plasmonic modulator, *Nano Lett.* 9 (2009) 897–902.
- [19] A. Agrawal, C. Susut, G. Stafford, U. Bertocci, B. McMorran, H.J. Lezec, A.A. Talin, An integrated electrochromic nanoplasmonic optical switch, *Nano Lett.* 11 (2011) 2774–2778.
- [20] G. Armelles, A. Cebollada, A. García-Martín, J.M. García-Martín, M.U. González, J.B. González-Díaz, E. Ferreiro-Vila, J. Torrado, Magnetoplasmonic nanostructures: systems supporting both plasmonic and magnetic properties, *J. Opt. A Pure Appl. Opt.* 11 (2009) 114023.
- [21] V. Amendola, M. Meneghetti, O.M. Bakr, P. Riello, S. Polizzi, D.H. Anjum, S. Fiameni, P. Arosio, T. Orlando, C. de Julian Fernandez, F. Pineider, C. Sangregorio, A. Lascialfari, Coexistence of plasmonic and magnetic properties in Au₈₉Fe₁₁ nanoalloys, *Nanoscale* (12) (2013) 5611–5619.
- [22] M.A. Zaitoun, W.R. Mason, C.T. Lin, Magnetic circular dichroism spectra for colloidal gold nanoparticles in Xerogels at 5.5 K, *J. Phys. Chem. B* 105 (2001) 6780–6784.
- [23] W. Roy Mason, *A Practical Guide to Magnetic Circular Dichroism Spectroscopy*, Wiley Interscience, Hoboken, NJ, 2007.
- [24] M. Artemyev, R. Krutokhvostov, D. Melnikau, V. Oleinikov, A. Sukhanova, I. Nabiev, in: *Low-field magnetic circular dichroism in silver and gold colloidal nanoparticles of different sizes, shapes, and aggregation states*, *SPIE NanoScience + Engineering* (International Society for Optics and Photonics), 2012, pp. 845710–845729.
- [25] I. Mayergoyz, P. McAvoy, G. Lang, D. Bowen, C. Krafft, Excitation and dephasing of circularly polarized plasmon modes in spherical nanoshells for application in all-optical magnetic recording, *J. Appl. Phys.* 105 (2009) 07B904.
- [26] Y. Gu, K.G. Kornev, Plasmon enhanced direct and inverse faraday effects in non-magnetic nanocomposites, *J. Opt. Soc. Am. B* 27 (2010) 2165–2173.
- [27] B. Sepúlveda, J.B. González-Díaz, A. García-Martín, L.M. Lechuga, G. Armelles, Plasmon-induced magneto-optical activity in nanosized gold disks, *Phys. Rev. Lett.* 104 (2010) 147401.
- [28] H. Fredriksson, Y. Alaverdyan, A. Dmitriev, C. Langhammer, D.S. Sutherland, M. Zäch, B. Kasemo, Hole-mask colloidal lithography, *Adv. Mater.* 19 (2007) 4297–4302.
- [29] D. Melnikau, D. Savateeva, A. Susha, A.L. Rogach, Y.P. Rakovich, Strong plasmon-exciton coupling in a hybrid system of gold nanostars and J-aggregates, *Nanoscale Res. Lett.* 8 (2013) 134.
- [30] B. Han, X. Gao, L. Shi, L.Y. Zheng, K. Hou, J. Lv, J. Guo, W. Zhang, Z. Tang, Geometry-modulated magnetoplasmonic optical activity of Au nanorod-based nanostructures, *Nano Lett.* 17 (2017) 6083–6089.
- [31] G.V. Naik, V.M. Shalaev, A. Boltasseva, Alternative plasmonic materials: beyond gold and silver, *Adv. Mater.* 25 (2013) 3264–3294.
- [32] J.A. Faucheaux, A.L.D. Stanton, P.K. Jain, Plasmon resonances of semiconductor nanocrystals: physical principles and new opportunities, *J. Phys. Chem. Lett.* 5 (2014) 976–985.
- [33] U. Kreibig, M. Vollmer, *Optical Properties of Metal Clusters*, Springer Series in Materials Science, vol. 25, Springer, Berlin, 1995.
- [34] G. Weick, D. Weinmann, Lifetime of the surface magnetoplasmons in metallic nanoparticles, *Phys. Rev. B* 83 (2011) 125405.

- [35] K.H. Hartstein, A.M. Schimpf, M. Salvador, D.R. Gamelin, Cyclotron splittings in the plasmon resonances of electronically doped semiconductor nanocrystals probed by magnetic circular dichroism spectroscopy, *J. Phys. Chem. Lett.* 8 (2017) 1831–1836.
- [36] J. Chen, P. Albella, Z. Pirzadeh, P. Alonso-González, F. Huth, S. Bonetti, V. Bonanni, J. Åkerman, J. Nogués, P. Vavassori, Plasmonic nickel nanoantennas, *Small* 7 (2011) 2341–2347.
- [37] J.B. González-Díaz, A. García-Martín, G. Armelles, Unusual magneto-optical behavior induced by local dielectric variations under localized surface plasmon excitations, *Nanoscale Res. Lett.* 6 (2011) 408.
- [38] V. Bonanni, S. Bonetti, T. Pakizeh, Z. Pirzadeh, J. Chen, J. Nogués, P. Vavassori, R. Hillenbrand, J. Åkerman, A. Dmitriev, Designer magnetoplasmonics with nickel nanoferrimagnets, *Nano Lett.* 11 (2011) 5333–5338.
- [39] N. Maccaferri, J.B. González-Díaz, S. Bonetti, A. Berger, M. Kataja, S. Van Dijken, J. Nogués, V. Bonanni, Z. Pirzadeh, A. Dmitriev, Polarizability and magnetoplasmonic properties of magnetic general nanoellipsoids, *Opt. Express* 21 (2013) 9875–9889.
- [40] N. Maccaferri, M. Kataja, V. Bonanni, S. Bonetti, Z. Pirzadeh, A. Dmitriev, S. van Dijken, J. Åkerman, P. Vavassori, Effects of a non-absorbing substrate on the magneto-optical Kerr response of plasmonic ferromagnetic nanodisks, *Phys. Status Solidi* 211 (2014) 1067–1075.
- [41] N. Maccaferri, A. Berger, S. Bonetti, V. Bonanni, M. Kataja, Q.H. Qin, S. van Dijken, Z. Pirzadeh, A. Dmitriev, J. Nogués, J. Åkerman, P. Vavassori, Tuning the magneto-optical response of nanosize ferromagnetic Ni disks using the phase of localized plasmons, *Phys. Rev. Lett.* 111 (2013) 167401.
- [42] K. Lodewijks, N. Maccaferri, T. Pakizeh, R.K. Dumas, I. Zubritskaya, J. Åkerman, P. Vavassori, A. Dmitriev, Magnetoplasmonic design rules for active magneto-optics, *Nano Lett.* 14 (2014) 7207–7214.
- [43] E.T. Papaioannou, V. Kapaklis, P. Patoka, M. Giersig, P. Fumagalli, A. García-Martín, E. Ferreiro-Vila, G. Ctistis, Magneto-optic enhancement and magnetic properties in Fe antidot films with hexagonal symmetry, *Phys. Rev. B* 81 (2010) 054424.
- [44] E.T. Papaioannou, V. Kapaklis, E. Melander, B. Hjörvarsson, S.D. Pappas, P. Patoka, M. Giersig, P. Fumagalli, A. Garcia-Martin, G. Ctistis, Surface plasmons and magneto-optic activity in hexagonal Ni anti-dot arrays, *Opt. Express* 19 (2011) 23867–23877.
- [45] V.K. Valev, A.V. Silhanek, W. Gillijns, Y. Jeyaram, H. Paddubrouskaya, A. Volodin, C.G. Biris, N.C. Panoiu, B.D. Clercq, M. Ameloot, O.A. Aktsipetrov, V.V. Moshchalkov, T. Verbiest, Plasmons reveal the direction of magnetization in nickel nanostructures, *ACS Nano* 5 (2011) 91–96.
- [46] S. Stafford, R. Serrano Garcia, Y.K. Gun'ko, Multimodal magnetic-plasmonic nanoparticles for biomedical applications, *Appl. Sci.* 8 (2018) 97–112.
- [47] M. Ravichandran, G. Oza, S. Velumani, J.T. Ramirez, F. Garcia-Sierra, N.B. Andrade, A. Vera, L. Leija, M. A. Garza-Navarro, Plasmonic/magnetic multifunctional nanoplatform for cancer theranostics, *Sci. Rep.* 6 (2016) 34874.
- [48] K.C.-F. Leung, S. Xuan, X. Zhu, D. Wang, C.-P. Chak, S.-F. Lee, W.K.-W. Ho, B.C.-T. Chung, Gold and iron oxide hybrid nanocomposite materials, *Chem. Soc. Rev.* 41 (2012) 1911–1928.
- [49] M.G. Manera, E. Ferreiro-Vila, J.M. Garcia-Martin, A. GarciaMartin, R. Rella, Enhanced antibody recognition with a magneto optic surface plasmon resonance (MO-SPR) sensor, *Biosens. Bioelectron.* 58 (2014) 114–120.
- [50] J.B. González-Díaz, A. García-Martín, J.M. García-Martín, A. Cebollada, G. Armelles, B. Sepúlveda, Y. Alaverdyan, M. Käll, Plasmonic Au/Co/Au nanosandwiches with enhanced magneto-optical activity, *Small* 4 (2008) 202–205.
- [51] L. Wang, K. Yang, C. Clavero, A. Nelson, K. Carroll, E. Carpenter, R. Lukaszew, Localized surface plasmon resonance enhanced magneto-optical activity in core-shell Fe–Ag nanoparticles, *J. Appl. Physiol.* 107 (2010) 09B303.
- [52] L. Wang, C. Clavero, Z. Huba, K.J. Carroll, E.E. Carpenter, D. Gu, R.A. Lukaszew, Plasmonics and enhanced magneto-optics in core-shell Co-Ag nanoparticles, *Nano Lett.* 11 (2011) 1237–1240.
- [53] P. Varty, N. Stefanou, A. Christofi, N. Papanikolaou, Strong circular dichroism of core-shell magnetoplasmonic nanoparticles, *J. Opt. Soc. Am. B* 32 (2015) 1063–1069.

- [54] D. Meneses-Rodríguez, E. Ferreiro-Vila, P. Prieto, J. Anguita, M.U. González, J.M. García-Martín, A. Cebollada, A. García-Martín, G. Armelles, Probing the electromagnetic field distribution within a metallic nanodisk, *Small* 7 (2011) 3317–3323.
- [55] G. Armelles, J.B. González-Díaz, A. García-Martín, J.M. García-Martín, A. Cebollada, M.U. González, S. Acimovic, J. Cesario, R. Quidant, G. Badenes, Localized surface plasmon resonance effects on the magneto-optical activity of continuous Au/Co/Au trilayers, *Opt. Express* 16 (2008) 16104–16112.
- [56] G. Armelles, A. Cebollada, A. García-Martín, M.U. González, F. García, D. Meneses-Rodríguez, N. de Sousa, L. Froufe-Pérez, Mimicking electromagnetically induced transparency in the magneto-optical activity of magnetoplasmonic nanoresonators, *Opt. Express* 21 (2013) 27356–27370.
- [57] N. de Sousa, L. Froufe-Pérez, G. Armelles, A. Cebollada, M. González, F. García, D. Meneses-Rodríguez, A. García-Martín, Interaction effects on the magneto-optical response of magnetoplasmonic dimers, *Phys. Rev. B* 89 (2014) 205419.
- [58] B. Toal, M. McMillen, A. Murphy, W. Hendren, M. Arredondo, R. Pollard, Optical and magneto-optical properties of gold core cobalt shell magnetoplasmonic nanowire arrays, *Nanoscale* 6 (2014) 12905–12911.
- [59] G. Armelles, B. Caballero, P. Prieto, F. García, A. Cebollada, M.U. González, A. García-Martín, Magnetic field modulation of chiroptical effects in magnetoplasmonic structures, *Nanoscale* 6 (2014) 3737–3741.
- [60] G. Armelles, B. Caballero, A. Cebollada, A. Garcia-Martín, D. Meneses-Rodríguez, Magnetic field modification of optical magnetic dipoles, *Nano Lett.* 15 (2015) 2045–2049.
- [61] M. Hentschel, T. Weiss, S. Bagheri, H. Giessen, Babinet to the half: coupling of solid and inverse plasmonic structures, *Nano Lett.* 13 (2013) 4428–4433.
- [62] S. Tomita, K. Takeshi, T. Shigeru, I. Satoshi, F. Minoru, H. Shinji, Magneto-optical Kerr effects of yttrium-iron garnet thin films incorporating gold nanoparticles, *Phys. Rev. Lett.* 96 (2006) 167402.
- [63] E. Umut, F. Pineider, P. Arosio, C. Sangregorio, M. Corti, F. Tabak, A. Lascialfari, P. Ghigna, Magnetic, optical and relaxometric properties of organically coated gold-magnetite (Au-Fe₃O₄) hybrid nanoparticles for potential use in biomedical applications, *J. Magn. Magn. Mater.* 324 (2012) 2373–2379.
- [64] G. Shemer, G. Markovich, Enhancement of magneto-optical effects in magnetite nanocrystals near gold surfaces, *J. Phys. Chem. B* 106 (2002) 9195–9197.
- [65] P.K. Jain, Y. Xiao, R. Walsworth, A.E. Cohen, Surface plasmon resonance enhanced magneto-optics (SuPREMO): faraday rotation enhancement in gold-coated iron oxide nanocrystals, *Nano Lett.* 9 (2009) 1644–1650.
- [66] Y. Li, Q. Zhang, A.V. Nurmikko, S. Sun, Enhanced magneto-optical response in dumbbell-like Ag-CoFe₂O₄ nanoparticle pairs, *Nano Lett.* 5 (2005) 1689–1692.
- [67] F. Pineider, C. de Julian Fernandez, V. Videtta, E. Carlino, A. Al Hourani, F. Wilhelm, A. Rogalev, P. D. Cozzoli, P. Ghigna, C. Sangregorio, Spin-polarization transfer in colloidal magnetic-plasmonic Au/iron oxide hetero-nanocrystals, *ACS Nano* 7 (2013) 857–866.
- [68] F. Pineider, A. Mekonnen, M. Serri, E. Pedrueza Villalmanzo, E. Smetanina, V. Bonanni, G. Campo, M. Mannini, C. de Julián Fernández, C. Sangregorio, M. Gurioli, A. Dmitriev, R. Sessoli, Magnetoplasmonics with single-molecule magnets and optical antennas. Manuscript in preparation.

Highly Responsive Magnetoactive Elastomers

Mikhail Shamonin^{*}, Elena Yu. Kramarenko^{†,‡}

^{*}*Ostbayerische Technische Hochschule Regensburg, Regensburg, Germany*, [†]*Faculty of Physics, Lomonosov Moscow State University, Moscow, Russia*, [‡]*A.N. Nesmeyanov Institute for Organoelement Compounds RAS, Moscow, Russia*

7.1 Introduction

The idea to combine polymers with magnetic materials is not new. Conventional rigid (Young's modulus is about 1–50 MPa) magnetic rubbers are known for a long time. They are widely used nowadays as fixing or sealing elements (e.g., flexible rubber materials) and magnet cores. Look, for example, on the sealing element (gasket) on the door of your fridge. Rigid magnetic rubbers do not belong to “smart” or “intelligent” materials in a sense that their physical properties cannot be significantly changed in a controlled fashion by external magnetic fields. Recently, a new class of intelligent magnetic polymer materials known as magnetoactive elastomers (MAEs) became the subject of intensive investigations, because of the plentitude of unconventional physical phenomena and promising industrial applications [1–8]. The striking difference to conventional materials is that magnetic filler particles are embedded into highly compliant matrices (Young's modulus is below 100 kPa), where they can easily change their positions and orientations due to the forces and torques appearing in the presence of external magnetic fields (Fig. 7.1) because of magnetic polarization of the particles. Driven by these forces, filler particles bound to the polymer network can change their spatial positions and the compliant polymer matrix will follow them [9–12]. As a result, the internal mechanical stresses arise in the polymer matrix and the sample may be significantly deformed.

MAEs are solid analogs to magnetorheological (MR) fluids, where the μm -sized magnetic particles are embedded into a soft elastomer matrix rather than in a carrier fluid [1,13]. Ferrofluids differ from MR fluids by the size of the particles. Ferrofluids consist of nanoparticles suspended by Brownian motion, which prevents sedimentation under normal conditions. The μm -scale particles in MR fluids are too heavy for Brownian motion to maintain suspension, and thus will settle over time because of the inherent density difference between particle and carrier fluid. Specific efforts (in particular, particle surface modification) are

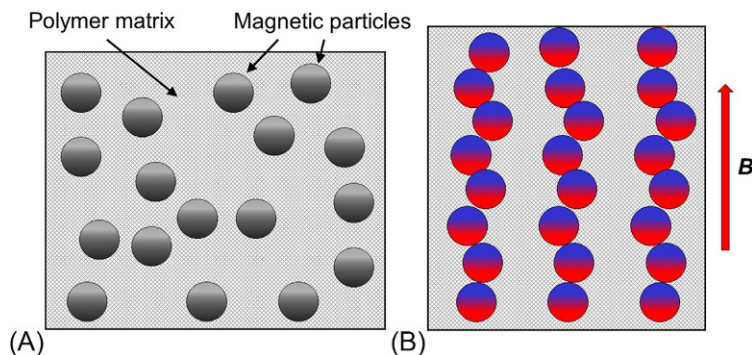


Fig. 7.1

Schematic representation of (A) an MAE with an isotropic distribution of magnetic filler particles in a polymer matrix at zero magnetic field and (B) structuring of magnetic filler particles in a homogeneous magnetic field.

needed to stabilize MR fluid suspensions. In MAEs, particle sedimentation after curing is prevented by polymer matrix.

To summarize: The new generation of magnetic polymer materials benefits from the softness of polymer matrix giving particles some freedom to move but simultaneously limiting this freedom by elastic forces. It is well known that the physical properties of a composite material depend on its microstructure [14]. In a magnetic field, the particles are magnetized, commence to interact and to form mesoscopic structures dependent on magnetic field. Such a behavior gives rise to high responsiveness of these composite materials to magnetic fields. Highly responsive MAEs are an emerging field of applied and fundamental research.

We do not pretend that the list of references in this chapter is complete. The citations have been selected in such a way that the reader may refer to some representative publications in order to follow the logic of our exposition. For a more comprehensive list of publications, the reader is referred to reviews [1–8].

7.2 Constitutive Materials

Obviously, MAEs are composite materials. Two main components are the polymer matrix and the magnetic filler. One can tune properties of MAEs by varying the type of polymer matrix, the type of magnetic filler and their proportions (filler concentration p) within the resulting materials.

7.2.1 Polymer Matrix

In general, any highly compliant matrix can be used. The most popular are silicone (PDMS) matrices [15–18]; however, others are also used, in particular, different rubbers [19–22], polyurethane [23–25], silicone/polyurethane blends [26,27], thermoplastic materials [28,29], elastomers [30,31], etc. [32–34].

The overall magnetoelastic coupling can be characterized by the relative stiffness of the elastomer phase to the magnetic saturation of the inclusions, which may be quantified by the nondimensional parameter [35].

$$\kappa \approx \frac{\mu_0 M_s^2}{G}, \quad (7.1)$$

where G is the shear modulus of the polymer matrix and M_s is the saturation magnetization of the composite material and μ_0 is the vacuum permeability.

To obtain highly responsive MAE, one has to decrease the shear modulus of the polymer matrix or to increase the saturation magnetization M_s because larger matrix deformations will be required to equilibrate the elastic and magnetic forces acting between magnetic particles. It is well known [36] that the modulus of a polymer network is defined by the density ν of mechanically active subchains, $G = \nu kT$, where k is the Boltzmann constant, T is the absolute temperature. From this formula, it follows that one can decrease the modulus by reducing ν , i.e., by increasing the molecular mass of network subchains. However, there is a lower limit of the modulus reduction due to the presence of chain entanglements that behave as topological crosslinks. Thus, the modulus due to entanglements is then defined as $G_e = \nu_e kT$, where ν_e is the number density of entanglements. The value of the modulus G_e for polymer melts is varied in the range of 10^5 – 10^6 Pa [36–38]. Therefore, to make softer elastomers with a modulus lower than 10^5 Pa solvents are usually employed. In case of silicone elastomers the solvent or plasticizer is silicone oil, in case of hydrogels it is usually water.

A very important perspective from the point of view of reducing the modulus without using any solvent are the recently developed so-called bottlebrush networks [39–41]. They are prepared from bottlebrush macromolecules, i.e., polymers with densely grafted side chains. The brush-like architecture expands the diameter of the polymer chains, diluting their entanglements without markedly increasing stiffness. It has been demonstrated that bottlebrush elastomers exhibit a useful combination of low elastic modulus (~ 100 Pa), high tensile strength ($\sim 1000\%$), and extraordinary elasticity.

The choice of polymer matrix is obviously defined by envisaged applications. Soft MAEs, being highly responsive, cannot withstand heavy loads and large strains. Thus, they could be more promising for some biological applications where high responsiveness is needed without considerable mechanical stresses and strains. A fine balance between elastic and magnetic properties of the resulting MAEs is required to obtain materials with large initial modulus (in the range of several or even tens of MPa), for example, for damping applications, which could still demonstrate some control of their properties by magnetic fields.

7.2.2 Filler Particles

The factors influencing magnetic interactions are magnetic properties of the filler, the size, and the shape of the particles as well as their spatial density (i.e., the average concentration of magnetic filler particles as well as their volume distribution). Since the polymer matrix is

nonmagnetic, these must be the filler particles that can respond to magnetic fields. Iron is a ferromagnetic material and it is the most popular filler. It is characterized by high permeability (typical initial permeability of pure iron ≈ 300 – 500 , maximum permeability ≈ 3500 – 6000) and high saturation magnetization ($\mu_0 M_s \approx 2.16$ T). Moreover, it is commercially available in various particle sizes and rather inexpensive. Magnetite (Fe_3O_4) is a ferrimagnetic material, which is also easily available and possesses considerable magnetic properties.

Iron and magnetite are magnetically soft materials that are characterized by small values of coercive force (< 1 kA/m) and small remanent magnetization. Usually magnetically soft materials have a narrow magnetic hysteresis, i.e., small amount of dissipated energy during magnetization cycle, it means that they can easily magnetized and easily demagnetized upon switching off magnetic field. Thus, magnetically soft composites could be actively operated with magnetic field, since magnetization of magnetically soft fillers is directly controlled by magnetic fields. Up to now the majority of publications focused on MR effect have reported results obtained with magnetically soft composites mainly based on iron particles (statistical analysis of relevant publications can be found in a recent review in Ref. [4]).

Recently, MAEs were obtained on the basis of magnetically hard materials, in particular, NdFeB alloy [42–45]. Magnetically hard materials have a high coercive force (> 100 kA/m), a wide magnetic hysteresis loop and need quite a lot of energy to be magnetized. Contrary to magnetically soft particles, magnetically hard particles keep the magnetic moments fixed upon magnetization. Thus, application of an external magnetic field to magnetically hard composites causes one-time switching of their properties (a kind of a passive control). Furthermore, the nonzero moment of MAEs after magnetization leads to very unusual properties of these materials even in the absence of any external magnetic field, as it will be described in [Section 7.3.2](#).

Mixing magnetically soft and magnetically hard fillers within MAEs provides the materials combining possibilities of passive and active control of their properties [44].

One should also distinguish between magnetic properties of nano- and microparticles.

Nanoparticles are usually monodomain carrying a constant magnetic moment that is proportional to the magnetic core volume and depends on the saturation magnetization of the material [46,47]. Thus, nanoparticles interact via magnetic forces even in the absence of any magnetic field. Magnetic interactions force nanoparticles to form aggregates, and particular care should be taken to stabilize nm-sized particles from aggregation in the course of MAE synthesis.

Micrometer-sized particles usually consist of a large number of domains whose magnetic moments are randomly oriented in such a way that the total magnetic moment of the particle almost vanishes. There are also some challenges of preventing μm -sized particles from aggregation. However, for microparticles, there is even more severe challenge of obtaining homogeneous precompositions, namely, particle sedimentation due to the high-density

mismatch between dispersive medium and filler. Heavy particles easily precipitate due to the gravitational force. This undesirable process is more significant for compositions with low concentration of the magnetic filler.

While conventional polymeric composites are usually based on nanoparticles (e.g., carbon black or silica), MAEs are mainly synthesized with microparticles.

Iron and magnetite particles are usually almost spherical. Deviation of the magnetic particle's form from the spherical shape leads to the appearance of the magnetic shape anisotropy with certain directions in which the particles can be magnetized more easily (magnetic easy axis). In this case, the torque on a nonspherical particle should be expected in applied magnetic field leading to stronger internal and possibly external deformation of the sample. In our opinion, the effect of the particle shape has not been fully explored yet.

7.2.3 Filler-Filler Interactions in Magnetic Fields

One further possibility to influence the properties of MAEs is to introduce anisotropy in the arrangement of filler particles. For this purpose, the composite material is placed into a constant magnetic field during crosslinking. The particles can move in the polymer solution and try to arrange themselves along the magnetic field lines forming chain-like aggregates along the field lines. When the crosslinking process is completed, the particles remain fixed in their positions.

Fig. 7.2 compares the distribution of filler particles in an isotropic MAE with the distribution of particles in an anisotropic MAE. It is seen that particles in anisotropic MAE are indeed aligned in chains. This alignment induces some anisotropy of material properties in directions parallel and perpendicular to internal structure orientation [48], see also Section 7.3.2. It should also be mentioned that the application of an external magnetic field during MAE curing

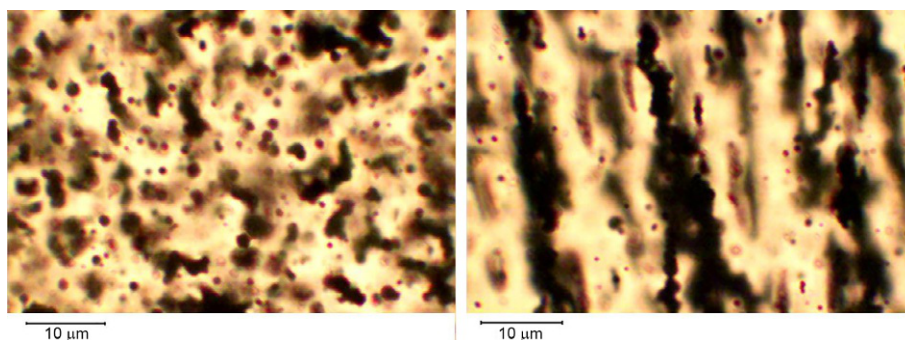


Fig. 7.2

Illustration of magnetic particle displacements under the action of the external magnetic field: photos obtained with the help of optical microscope in through-passing light demonstrate displacements of magnetic particles under the action of the external magnetic field; (left) in magnetic field of 0.02 T; (right) without field [48].

helps to solve the problem of particle sedimentation in the course of polymerization since magnetic forces can to a large extent overcome gravitation.

7.3 Mechanical Properties in Homogeneous Magnetic Fields

From the practical point of view, mechanical properties are the most interesting. Therefore, majority of research has concentrated on investigation of how mechanical properties of MAEs are influenced by external magnetic fields.

7.3.1 Magnetostriction

Since MAEs comprise ferromagnetic particles, the resulting composite materials are also ferromagnetic and the associated physical phenomenon, namely, magnetostriction, is observed in them [35,49–54]. Fig. 7.3 shows the dependence of elongation (positive magnetostriction) of an MAE sample on the external homogeneous magnetic flux density. It is seen that the resulting deformation (strain $\sim 10^{-2}$ – 10^{-1}) is several orders of magnitude larger than the magnetostriction of inclusions (strain $\sim 10^{-6}$ – 10^{-7}). Clearly, the physical origin of the magnetostriction in MAEs is different from conventional magnetostrictive materials. For typical inclusion materials, such as carbonyl iron, the particles are effectively rigid, and the principal mechanisms are magnetic torques and magnetic interactions between particles [52]. Because these torques are induced through the direct interaction of the particles with the applied magnetic field, their magnitudes are of order of the particles' concentration p (as opposed to p^2 for the dipolar interactions), which means that significant field-induced effects may be achieved at relatively small particle concentrations, before the effective elastic modulus of

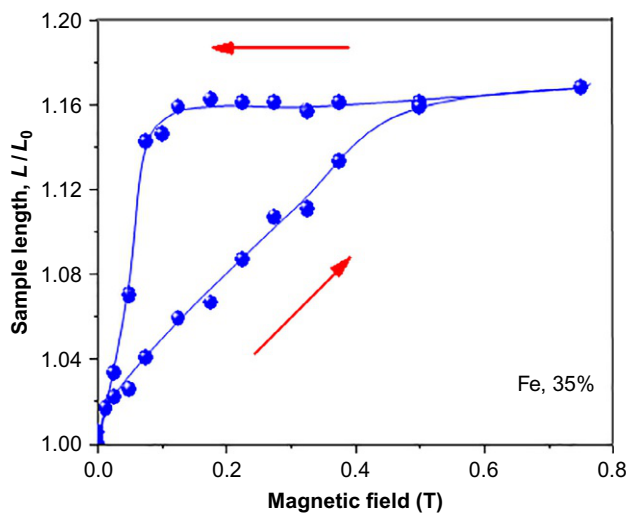


Fig. 7.3

Deformation of an MAE under the influence of a homogeneous magnetic field [15].

the composite material will significantly increase [35]. The numerical simulations of 2D systems in Ref. [55] have shown that magnetodeformation could be indeed large (area shrinkage $\sim 20\%$), although dipolar interactions were irrelevant for investigated models.

It has been also pointed out by several authors that a number of magnetomechanical phenomena are caused by magnetomechanical coupling [55], and they all are related. Magnetostriction is one possible circumstance. One more magnetomechanical phenomenon, the MR or field-stiffening effect will be discussed in the next subsection. In the framework of a simple 2D model, it was shown that an external magnetic field acts with torques on magnetic filler particles, creates mechanical stresses in the vicinity of inclusions, induces shear strain, and increases the effective shear modulus of MAE materials [10]. Raikher and Stolbov proposed a very simple estimation of the magnetostriction in MAEs. Assume that an MAE sample of the length l is placed into a homogeneous magnetic field H . It is also assumed that the magnetization of the MAE in such a field is M . The magnetostrictive effect is determined by the balance of magnetic and elastic contributions to the energy density of the sample: $\mu_0 M^2 \approx G(\Delta l/l)^2$ [56]. Assuming the shear modulus of the material $G \approx 10$ kPa, magnetic field intensity $H \approx 10^5$ A/m, magnetization $M \approx 10^4$ A/m, it is easily obtained that $\Delta l/l \approx 0.1$.

Two aspects of magnetostrictive phenomena have been intensively discussed in the literature. First question is how to increase the magnitude of the magnetostriction. Obviously, the magnetostriction will grow if the compliance of the matrix increases. The next way to increase the magnetostriction is to play with the shape of particles, for example, by employing oblate ellipsoidal particles instead of spherical inclusions. Galipeau and Ponte Castañeda proposed a new class of MAEs with doubly layered, herringbone-type microstructures capable of generating large field-induced strains of up to 100% [35].

The second challenge is the sign of magnetostrictive effect, namely, if the sample shrinks or elongates in external magnetic field. Consider the deformation of the spherical MAE sample in a homogeneous magnetic field. If the sample is assumed to be made of a *homogeneous* material (effective medium approximation), the theory predicts elongation of the sphere along the magnetic field lines. However, if the microstructure of the sample is taken into account (Raikher and Stolbov figuratively called such a representation the “watermelon-with-seeds” model [56]), one may come to the conclusion that interacting dipoles will lead to the shrinking of the sample in the direction of applied magnetic field. This seeming discrepancy means that both simplified models are not entirely correct and the resulting magnetostriction is the interplay of the shape magnetostriction as described by the continuum model and the mesoscopic magnetostriction determined by the short-range order in the magnetic subsystem. Usually, real MAE samples comprising high concentrations of soft-magnetic particles elongate in external magnetic fields as it has been shown theoretically [57].

Finally, it should be noted that the magnetostriction phenomenon manifests itself in the growth of the normal force in the case when the MAE dimensions perpendicular to the applied magnetic field are fixed and the sample elongation is impossible. The change of the normal

force with magnetic field has been studied in Ref. [31,58–61]. Usually the normal force is measured on a rheometer simultaneously with the components of the dynamic modulus under shear oscillations. Presence of an oscillating mechanical load in addition to the magnetic field enables filler particles to form stronger structures along the field lines leading to an increase in normal force under cyclic loading [61].

7.3.2 Magnetorheological Effect

Magnetorheological effect is manifested as an increase in viscoelastic properties of MAE on the application of a magnetic field. This effect is one of the most widely studied in MAEs. The first publications in the end of 1990s reported up to 60% maximum increase in Young's modulus [1,2]; this result was considered to be quite large. However, a notable progress in the magnitude of the MR effect has been made achieved very fast, namely, 1000% increase has been gained in Ref. [62], while recently a colossal MR effect ($>10^6\%$) of the shear storage modulus has been observed in moderate magnetic fields of 500 mT, see Fig. 7.4 [63].

During last 15 years, viscoelastic properties of MAEs in magnetic fields have been studied by various experimental techniques. In particular, the elastic modulus has been measured in static experiments under static elongation [64,65], compression [2,15,66], or shear [62].

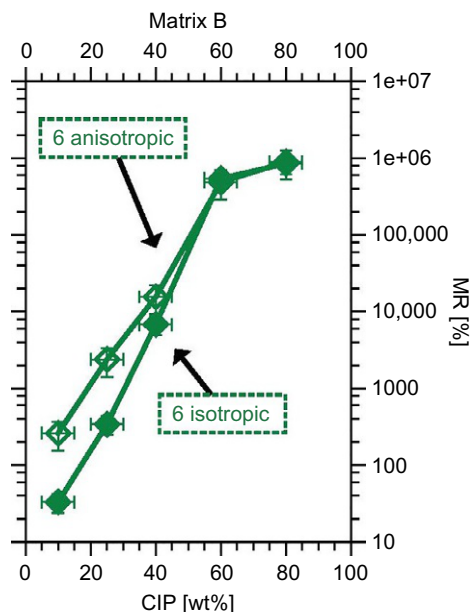


Fig. 7.4

Relative MR effect dependent on the CIP content for a particular matrix composition after curing on the hot plate. The lines connecting the experimental points serve as a guide to the eye [63].

The main objectives of these studies were ascertaining the MR effect in MAEs manifested in a stiffening of the samples (increase in the elastic modulus) and elucidating the influence of MAE composition on the extent of this effect. Static experiments have also demonstrated the appearance of a considerable nonlinearity in stress-strain dependences in magnetic fields, huge mechanical hysteresis, and large residual deformations [15,66].

As an example, Fig. 7.5 demonstrates typical stress-strain dependences for MAEs in a magnetic field. One can see, that, indeed, they are strongly nonlinear, the hysteresis area increases with the field, and so does Young's modulus of the material, which can be found as the initial slope of the stress-strain curves. Furthermore, it has been shown that highly filled MAE samples can keep their deformed state in a magnetic field (field-induced plasticity). Nonzero deformations after reducing the load down to zero are clearly seen in Fig. 7.5. Samples return to the initial shape only after the field is switched off, i.e., a kind of a shape memory effect has been revealed in MAEs [15,64]. Both effects have been explained by strong magnetic interactions between magnetic particles, which cannot be overcome by elastic forces of the matrix unless the magnetic field is decreased [67].

Dynamic modulus of MAEs is usually determined by means of oscillation tests [45,68–72]. In this type of experiments, the shear storage modulus G' and the shear loss modulus G'' describing the rheological properties of viscoelastic media are obtained. Storage modulus G' shows the amount of stored energy during shearing and refers to the elastic properties of the material while the loss modulus G'' expresses how much energy was dissipated in a cycle of deformation in the form of heat and quantifies the viscous properties of the material. Dynamic experiments demonstrated an increase of both storage and loss modulus values upon

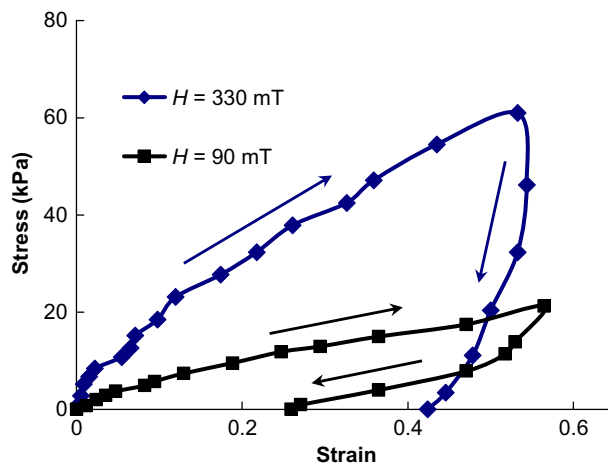


Fig. 7.5

Loading-unloading curves of a MAE sample measured in the magnetic field of various intensities (arrows show the experimental procedure: loading and subsequent unloading) [48].

increase of DC magnetic field; this result is consistent with the conclusions made from static experiments.

The MR effect itself can be quantified by the absolute increase $\Delta G'$ and relative increase $\Delta G'_r$ of the storage modulus, which are defined as

$$\Delta G' = G'_{\max} - G'_0$$

$$\Delta G'_r = (G'_{\max} - G'_0) / G'_0$$

where G'_0 is the initial value of the modulus in the absence of magnetic field, G'_{\max} is the modulus in the maximum magnetic field. The absolute and relative MR effects could be tuned by MAE composition in a wide range.

In particular, at a similar polymer/magnetic phase proportions composites based on iron show a higher MR effect in comparison with iron oxides. Magnetic interactions obviously increase with the amount of filling particles. To get a large absolute MR effect, composite materials with rather high volume fraction of magnetic particles (up to 25–35 vol%) are usually fabricated. Since the initial modulus G'_0 of the composite also increases with the filling degree, the relative MR effect could be finely tuned by decreasing the modulus of the pure elastomer while increasing concentration of magnetic particles. In general, the absolute value of the MR effect increases with the filling degree while the maximum relative MR effect could be reached at some optimal fractions of magnetic particles, which are small enough not to increase considerably the initial modulus of the material but are high enough to strengthen considerably the material in a magnetic field. The most effective way to reach large values of $\Delta G'_r$ is to decrease the modulus of the polymer matrix itself as has been discussed in the previous section.

Recently, it has been shown that the storage modulus of the magnetic network formed by carbonyl iron particles in a fluid carrier at 20–30 vol% could reach several MPa [73]. In a fluid, magnetic particles can move easily to form a strong magnetic network. Similar rearrangements in MAEs are possible only if the polymer matrix is soft enough; however, in an elastic matrix, any rearrangements are accompanied by local matrix deformations that could give an additional contribution to the material strengthening in magnetic fields. In particular, MR fluids and MAEs filled with the same magnetic iron particles of 3–5 μm in diameter at the similar concentration of 82–83 mass% demonstrate the storage modulus of 1 and 5 MPa, respectively.

The size of magnetic particles plays a crucial role in magnetorheological response of MAEs. At the same filler volume fraction, nano- and microparticles have different surface area; thus, they could differently interact with polymer matrix. In particular, it has been shown that small filler particles increase the initial modulus of the composite, thus decreasing the relative MR effect. Moreover, there exists an additional length scale defined by the polymer network mesh size. While nanoparticle size could be comparable with the network mesh size, microparticles are always much larger. Thus, even in the absence of strong adsorption of

polymer on the particle surface, they become built into the matrix due to polymer chemical crosslinks. Due to these additional effects, the magnetorheological effect differs for MAEs based on nano- or microparticles even at the same volume fraction of the particles. It has been shown that larger particles usually provide higher magnetorheological effect [74,75]. Majority of synthesized MAEs are nowadays based on iron particles with sizes from 3 to 7 μm , which seems to be an optimum at the present stage of technology. Recently, submillimeter-sized particles have shown to provide two orders of magnitude increase of elastic modulus [76].

It has recently been shown that it could be advantageous to use mixtures of small and large particles [68,77–79]. The effect is two-fold: first, there is better dispersion in a sense that small particles help larger particles to disperse more homogeneously and, second, better close packing conditions for particle chain aggregates formed in magnetic field are reached. As a result, there is a higher magnetic response in such mixtures. One can mix particles of the same chemical nature, i.e., iron particles of various sizes [77–79], or one can use submicrometer or nanosized magnetite together with iron microparticles [68]. Using bimodal filler particles, it was possible to tailor various MR properties, which can be useful for different target applications. In particular, either absolute or relative magnetorheological effects could be tuned.

Nonmagnetic particles can be added to the magnetic filler as well. Although such particles do not themselves participate in magnetic interactions, they facilitate fabrication of homogeneously distributed composite materials and enhance both absolute and relative MR effects. The growth of elastic moduli in an external magnetic field has been attributed to the stress transfer by additional chains of magnetic particles via nonmagnetic particles [80,81].

Distribution of magnetic filler particles within a polymer matrix also plays an important role in MR effect. The structuring of magnetic filler during synthesis results in anisotropy of properties along and perpendicular to chain aggregates. At small concentrations of filler particles ($p < 0.2$), anisotropic composites show larger MR effect than isotropic composite materials with the same filler concentration and the polymer matrix (cf. Fig. 7.4). The reason is probably the easier arrangement of filler particles in chain-like aggregates if there are already existing chains. At high filler concentrations ($p \approx 0.3$, which corresponds to approximately 70 wt%), this advantage practically disappears. Possible explanation is that there is not much space for magnetic-field-induced rearrangement of particles due to pure geometrical constraints [82].

Some specific MR properties are demonstrated by magnetically hard MAEs. Being magnetized, they retain nonzero magnetization; thus, their mechanical behavior in the absence of any external magnetic field is similar to that of magnetically soft MAEs in a magnetic field. The storage and loss moduli of the material increase with an increase of magnetizing field, magnetization causes large nonlinearity in stress-strain dependences with large residual deformations [42,83]. Moreover, the storage and loss moduli of magnetically hard MAEs can either increase or decrease depending on the direction of the external magnetic field. If the

directions of the field and sample magnetization coincide, the magnetic field strengthens the internal magnetic structure and the moduli grow with the increasing field. If the vectors of the external magnetic field and internal magnetization are opposite, the external magnetic field reorients magnetic particles with disruption of filler structures and the moduli decrease with the field, i.e., the negative MR effect can be observed in magnetically hard MAEs [42].

It should be also mentioned that after initial magnetization, magnetically hard MAEs cannot be easily demagnetized because magnetized filler particles prefer to rotate in an opposite magnetic field rather than decrease their magnetization level [10,43].

7.3.3 Filler-Matrix Interactions in Magnetic Fields: Payne Effect

The Payne effect is known to be a particular feature of the stress-strain behavior of rubber composites containing fillers, in particular, carbon black [84]. It is manifested as a dependence of the storage and loss moduli on the amplitude of the applied strain. Above some critical strain amplitude, the storage modulus decreases rapidly with increasing amplitude saturating at rather large deformations, while the loss modulus shows a maximum in the region where the storage modulus decreases. The Payne effect depends on the filler content of the material and vanishes for unfilled elastomers.

A large amount of work in theoretical interpretation of the experimental results has been done in the field of rubber with embedded active fillers like carbon black or silica [85–87]. It has been shown that spherical particles form clusters with a fractal structure joining into a network at high particle concentrations. It is important to note that this fractal network is not stable but breaks into smaller units with increasing mechanical strain. It is widely accepted that it is the formation of filler network that is responsible for the nonlinear viscoelastic behavior of filled rubbers. The Payne effect is interpreted as a dynamical break-up of the filler network.

In Ref. [88], the term “magnetic Payne effect” was coined for MR gels to emphasize their strain softening. As an example, Fig. 7.6 shows the strain amplitude dependences of the storage and loss moduli of the MAE based on silicone polymer containing 70 mass% of iron particles with the average diameter of 4.5 μm . The moduli are measured in various magnetic fields produced by the drive current, I , of an electromagnet. Magnetic field increases almost linearly with I reaching the maximum value of approximately 600 mT at $I = 5\text{A}$. One can see in Fig. 7.6 that at zero magnetic field the MAE behaves as a conventional filled rubber demonstrating slight (several times) decrease of G' and a maximum of G'' at $\gamma \sim 0.2\%$. When a magnetic field is applied, not only considerable growth of the moduli takes place (MR effect) but also the Payne effect becomes much more pronounced. More than an order of magnitude change of the moduli with γ is observed. This “magnetic Payne effect” is explained by strongly increased activity of magnetic filler particles interacting via magnetic interactions in magnetic fields, which are long-ranged and by far exceed van der Waals and hydrodynamic interactions

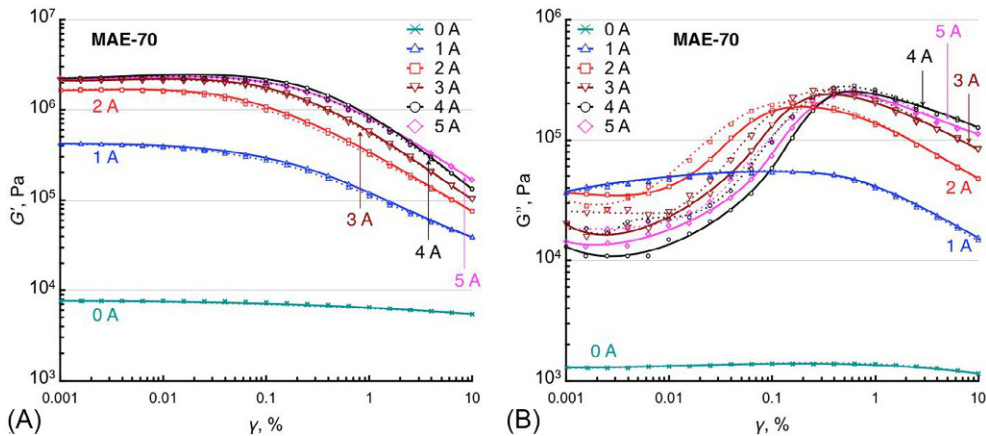


Fig. 7.6

Storage modulus (A) and loss modulus (B) vs. strain amplitude, γ , measured in various magnetic fields (driving currents $I=0, 1, 2, 3, 4, 5$). Solid and dotted lines show the moduli values obtained under increasing and decreasing γ , respectively.

responsible for conventional Payne effect in nonmagnetic filled rubbers. Magnetic interactions enhance with magnetic field and a larger strain is needed to destroy magnetic filler structures; as a result, the linear viscoelastic regime where G' remains nearly constant broadens with the drive current I .

The model of Kraus is commonly applied in the elastomer industry for the evaluation of the strain sweep characteristics of filled rubbers [87]. It describes rather well experimental data and is useful for the practical applications. The strain dependences of the dynamic moduli were derived using the assumption of the de-agglomeration/re-agglomeration mechanism for “assemblage” of filler clusters [89]:

$$G' = G'_\infty + \frac{G'_0 - G'_\infty}{1 + \left(\frac{\gamma}{\gamma_0}\right)^\beta}, \quad (7.2)$$

$$G'' = G''_\infty + \frac{2(G''_{max} - G''_\infty)}{1 + \left(\frac{\gamma}{\gamma_0}\right)^\beta} \cdot \left(\frac{\gamma}{\gamma_0}\right)^{\frac{\beta}{2}}, \quad (7.3)$$

where $G'_0 = G'(\gamma=0)$, $G'_\infty = G'(\gamma \rightarrow \infty)$, $G''_\infty = G''(\gamma \rightarrow \infty)$, and G''_{max} is the value of the local maximum of the loss modulus at the characteristic value $\gamma = \gamma_0$.

In rubbers with carbon black or silica fillers, the exponent β in the dependences (7.2) and (7.3) can be estimated via simple theoretical considerations. The model using the connectivity

parameter for fractal aggregates [90] gives $\beta \approx 1.2$, while an Ising model yields $\beta \approx 1.0$ [87]. These theoretical values of b reasonably agree with experimental values.

Recently, the Kraus model has been applied to interpret experimental results on MAEs [91]. Experiments suggest that at small deformation amplitudes, the exponent β of the Kraus model changes in an externally applied magnetic field because of the rearrangement (structuring) of ferromagnetic particles [91]. There is an optimum network microstructure in a particular magnetic field. At large deformation amplitudes, the exponent β of the Kraus model seems to be independent of the external magnetic field [91]. Since the exponent β is related to the mass fractal dimension of the filler network and connectivity exponent C of the filler aggregates, the proposed approach could indirectly give some information about magnetic filler structure evolution with magnetic field. This is especially important since at the present stage of technology direct methods (optical or X-ray tomography) do not work reliably at high filling degrees where all the effects are the most pronounced in MAE.

The rubber-magnetic-particle interactions can be controlled by the modification of the particles' surface, for example, by using different kinds of silane coupling agents acting on iron particles [92].

7.3.4 Hysteretic Behavior

The mechanical hysteresis of filled elastomers means that the dependence of the strain of a material depends not only on the instantaneous value of the stress but also on the previous history of mechanical loading. The origin of mechanical hysteresis is the energy dissipated as internal friction during the loading, which cannot be recovered on unloading. The hysteresis losses are represented by the area between the loading and the relaxation curves. Quite often, some particulate filler, comprising small solid particles on the nm or μm scale, is dispersed in the elastic matrix for reinforcement of the elastomer material. It is well known that such fillers increase hysteresis losses.

In the preceding section, we described the effect of magnetostriction in MAEs. The physical reason for the magnetostriction is the forces acting on magnetized particles. In this sense, the application of a magnetic field has a similar effect to mechanical loading; therefore, it can be expected that there would be hysteresis as a function of sample elongation in the magnetic field, and it is clearly seen in Fig. 7.3. A theoretical model for the hysteresis of magnetostriction has been proposed in Ref. [93].

If an MAE sample is mechanically or magnetically loaded, the internal microstructure of the filler depends on the loading history. Therefore, the hysteresis is an intrinsic property of MAEs and it can be observed in several effective properties of the MAEs, in particular, the stress-strain curves (Fig. 7.5), shear modulus (Fig. 7.6), or dielectric permittivity (Fig. 7.8).

Talking about hysteresis, we cannot ignore the problem of time dependence of MAE responses to magnetic fields, which is highly important for industrial applications of these materials, where, for example, the stiffness of the MR element should be controlled in time. Investigations of transient rheological behavior of MAEs under dynamic torsion at a fixed oscillation frequency in temporally stepwise changing magnetic fields and oscillation amplitudes have shown that three exponential functions are required to reasonably describe the time response of the storage shear modulus over long time scales ($>10^3$ s) [94]. The characteristic time constants τ_i of the corresponding rearrangement processes of the filler network differ approximately by one order of magnitude ($\tau_i \sim 10, 10^2, 10^3$) depending on MAE composition, strain amplitude, and magnetic field.

In spite of the presence of long-time relaxation processes in MAEs, the storage modulus under periodic switching of the magnetic field between the “on” and “off” states could be reproduced rather well in active phases, which is important for MAE applications.

Iron microparticles used as a filler in MAEs are soft magnetic. Their magnetic hysteresis loops are negligibly small [10]. However, significant magnetic hysteresis is found in such materials due to restructuring of the filler [10,95]. Biller et al. considered an interaction of two magnetically soft particles embedded into a polymer and showed theoretically the appearance of the magnetomechanical hysteresis [96]. As is to be expected, magnetic hysteresis is also observed in MAEs filled with hard magnetic particles [43]. However, there is additional contribution to hysteresis caused by rotation of magnetically hard particles when the direction of an external magnetic field is reversed [97]. It has been suggested to apply the first-order reversal curve (FORC) analysis to magnetic hysteresis in MAEs in order to extract information about relative proportions of reversible and irreversible components of the magnetization of a material [12,98].

The conducted research on hysteretic behavior of physical properties of MAEs leads to the conclusion that hysteresis is an intrinsic property of MAEs, both in the dependence on an external magnetic field and on the mechanical loading in the presence of magnetization.

7.3.5 Magnetodeformation in Inhomogeneous Fields

As described in Section 7.3.1, in homogeneous magnetic fields, considerable changes of MAE sample dimensions (up to 20%) can take place due to the structuring of magnetic filler particles trying to minimize magnetic energy. In gradient magnetic fields even larger deformations become possible; 200%–300% elongation of MAE samples were observed in Refs. [53,64,99]. The physical reason is the presence of magnetic force acting on magnetic particles, which is defined by the field gradient. This force drives the particles into the areas with the maximum magnetic flux density, and the particles move together with compliant polymer matrix resulting in sample deformation. Local stress distributions within a MAE sample in a gradient

magnetic field are spatially nonhomogeneous depending on the local magnetic field gradient counterbalanced by elastic forces.

Various shape changes could be induced in gradient magnetic fields depending on the field configuration [2]. The elongation occurs if the maximum field is reached in the vicinity of MAE sample free edge (Fig. 7.7A), while contraction takes place if the maximum field is realized within the sample volume (Fig. 7.7B). Special magnetic field distributions could provide rather complex bending of MAE samples whose shape could follow the magnetic field line configurations. It is important the MAEs completely restore their initial shape when the magnetic field is turned off. Switching between different field configurations could even induce directional movement of MAE specimen.

Since gradient magnetic fields are easily producible, magnetodeformation phenomenon is of even more perspective for various applications than magnetostriction. You can play with the shape of MAEs by means of common NdFeB magnets, provided the MAE matrix is compliant enough.

It is also possible to apply alternating magnetic fields; in this case, MAE sample can repeatedly change its shape with time following AC magnetic field alterations [2,99]. However, MAE responsiveness crucially depends on the field frequency. It has been shown that the working frequencies f do not exceed 40–50 Hz. At higher f , MAE shape alterations cannot get in time with the field.

Giant magnetodeformation in MAEs paves the way for a design of seals or various kinds of manipulators and even artificial muscles operated by tunable magnetic fields.

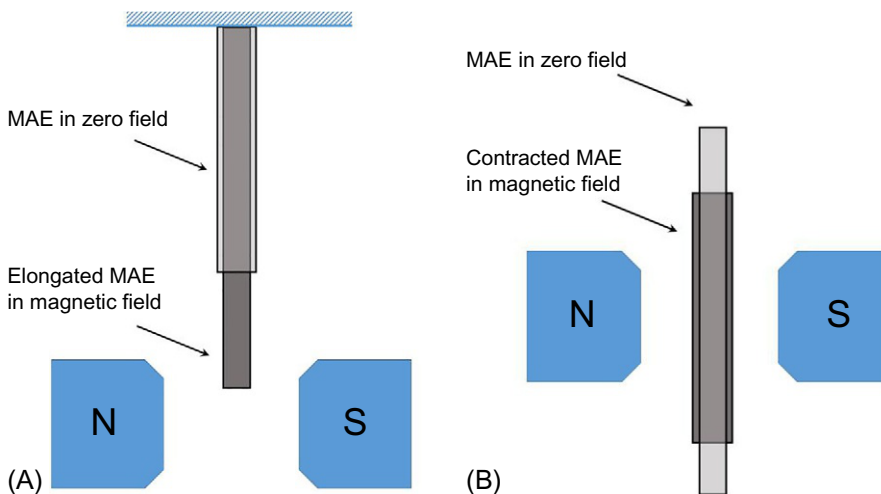


Fig. 7.7

Schematic representation of different types of MAE deformation in gradient magnetic field: (A) elongation; (B) compression.

7.4 Electromagnetic and Acoustic Properties

It has been previously discussed that considerable changes of mechanical and viscoelastic properties of MAEs in magnetic fields are mainly caused by strong interactions between magnetic filler particles and their restructuring. One could expect that not only rheological response but any other physical property of MAEs that depends on magnetic particle distribution could also be controlled by external magnetic field. In particular, electromagnetic properties of MAE are influenced by external magnetic fields as well [100].

A strong magnetodielectric effect (MDE) characterized by up to 150% increase of the relative dielectric permittivity ϵ in the magnetic field of 1 T has been reported in Ref. [101] for MAEs based on magnetically hard NdFeB microparticles. The effective permittivity has been obtained by measuring the capacitance of a plane capacitor containing the MAE sample as a core material under an applied magnetic field. Special care has been taken to exclude the effect of magnetostriction by fixing the distance between the capacitor planes. It has been shown that effective permittivity depends essentially on the direction of external magnetic field. Considerable increase of ϵ is observed if magnetic field is oriented perpendicular to the capacitor plane, in parallel magnetic field ϵ is practically field independent (Fig. 7.8). It should be noted that the field dependence of permittivity is nonlinear and tends to saturate in a large magnetic field.

MDE was shown to enhance with growing concentration of magnetic filler, and it is also bigger for softer elastomer matrices giving more freedom for particles to rearrange in magnetic field

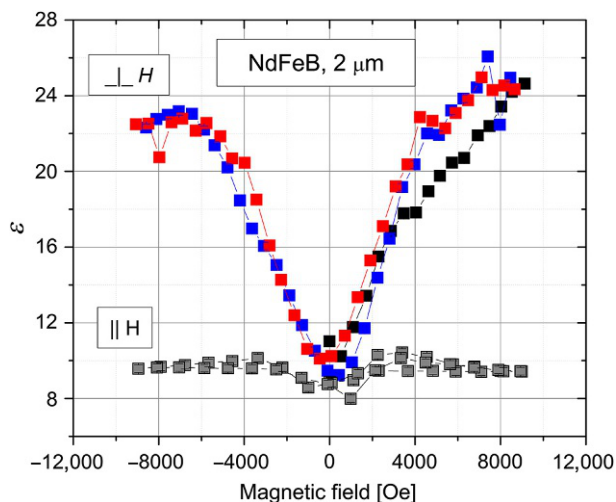


Fig. 7.8

Field dependence of the effective permittivity for an NdFeB-based MAE. Mass concentration of the filler is 75%. Two directions of an external magnetic field are shown: parallel and perpendicular to the capacitor's plane. Several magnetization-demagnetization curves are shown [101].

[102]. To our knowledge, up to now, the biggest MDE of approximately 1500% was achieved in very soft MAEs (with the shear modulus of 2kP) based on iron microparticles [102].

It should be noted that magnetodielectric effect is also characterized by a considerable hysteresis (see Fig. 7.8) and pronounced time dependence. The transient response of MDE to a step magnetic field excitations was reported to be quite complex. In small magnetic field the effective permittivity of MAE grows monotonically with time, while in large magnetic field steps (>0.3 T) an overshoot has been observed. Rather large settling times ~ 1000 s were reported in Ref. [102], which characterize restructuring processes under the influence of magnetic field. Similar characteristic times have been found in rheological studies; however, during shear modulus measurements, the internal filler structure is affected not only by magnetic field but also by the shear. MDE transient behavior reflects filler reorganization without any mechanical disturbance.

Effect of an external magnetic field on MAE resistivity has been studied in [103–106]. 300-fold decrease of resistivity of MAEs containing 14% of carbonyl iron particles in the magnetic field of 1T has been found in Ref. [104] while the resistivity of highly filled anisotropic MAEs based on hard-magnetic NdFeB particles has shown to fall by 4 orders of magnitude in the magnetic field of only 300 mT [103]. Measurements of MAE resistivity in repeatedly increasing-decreasing magnetic field demonstrate considerable hysteresis [103].

Application of external stress could also affect the internal magnetic arrangements changing the interparticle distances, thus influencing MRE, MDE, and magnetoresistance of MAEs.

Recently, the effect of magnetic field on the propagation of bulk acoustic waves (BAW) through MAEs has been investigated [107]. It has been shown that the velocity of longitudinal BAW increases with increasing applied magnetic field. The maximum change in velocity due to external magnetic field of 1T was equal to 1.75% for structured samples (synthesized in magnetic field). The analysis has also shown that the longitudinal BAW velocity in the structured samples of MAE changes stronger due to an external magnetic field than in the nonstructured (isotropic) samples.

7.5 Prospects of Research and Development

The subject of MAEs is flourishing now. What are the reasons for that success? MAEs come into the focus of research interest from engineering not from fundamental science. The Oxford Dictionary defines engineering as “the branch of science and technology concerned with the design, building, and use of engines, machines, and structures.”[108] This is the reason. MAEs can do something useful. They have been developed as an alternative to MR fluids, because MR elastomers are eventually free of their disadvantages, such as deposition, sealing issues, and environmental contamination [3]. Therefore, most of applied research has concentrated on utilization of magnetomechanical properties of these materials. Most current applications

utilize the MR or field-stiffening properties of MAEs. Examples are vibration absorbers and isolators. Soft actuators (e.g., controllable valve [109] or Kashima's [110] actuators) relying on magnetodeformation have been proposed as well. The review [3] provides a comprehensive overview of MAE devices. However, one can observe that not many magnetomechanical devices relying on MAEs have found their way into industrial applications or daily life. One reason is probably that there exist alternative technologies, which can solve similar problems in a more effective way. Two such disadvantages of MAEs are relatively large power consumption, from tens watts to hundreds watts, and large device size due to necessity of magnetic circuit [3]. It seems to be challenging to overcome these limitations in conventional applications. So what is our subjective opinion? First, we believe that MAEs may find their unique place in "niche" applications, where there are no alternative technical solutions. One such field could be biomedical engineering [111,112]. Second, more progress has to be done in understanding the material behavior. It turns out that the behavior of MAEs is more complex than it appeared at the beginning—e.g., explanation of the sign of magnetostriction, or prediction of how to design a sample with given sign and value of magnetostriction, remains a great challenge.

In this Chapter, we practically did not touch a wide field of theoretical research in the area of MAE. For >15 years, various theoretical approaches have been developed; however, they have mainly proposed either too simplified models based on dipole-dipole interactions and linear approximations, which do not work for highly filled MAEs where maximum effects are observed, or they are too complex for the practice. Furthermore, there is still a need for development of controlled strategies [4] for successful implementation of MAE-based devices. The effective medium approach has not been fully explored yet [10].

Hitherto, most of research is done on bulk properties of MAEs. Structuring of magnetic filler along magnetic field lines takes place not only within the bulk of MAEs but also on the surface resulting in formation of needle-like "mountains" [113,114]. The characteristic height of these mountains and their separation depend on the MAE composition and external magnetic field. Thus, application of the field could tune not only the rigidity of MAE films, but also the structure of their surface profile providing a new way to control its wettability and adhesion properties. It is plausible that new interesting application will emerge from the high surface responsiveness of MAEs.

7.6 Conclusion

In this Chapter, we provided a brief review of the composition and magnetic-field dependent properties of novel intelligent MAEs combining useful properties of polymers and magnetic materials. Starting from the 1990s, the field of MAEs has been growing tremendously with the total amount of publications exceeding one thousand. During these years, new materials and new technologies have been developed for the synthesis of MAEs; furthermore,

considerable amount of new effects has been found in MAEs. While in the beginning the main focus was on mechanical and viscoelastic properties of these fascinating materials, nowadays, it has been realized that there is a complex of new phenomena, in particular, magnetodielectric and magnetoresistive effects, and MAEs could be legitimately called highly responsive multifunctional materials. The reason for the high responsivity is the significant restructuring of magnetizable filler particles due to the softness of the polymer matrix.

We have hopefully persuaded the readers that MAEs will enjoy a bright future and encouraged interested scientists and engineers to do further research in the field of MAEs.

Acknowledgements

E.Yu.K. gratefully acknowledges the financial support by the Russian Foundation for Basic Research (project No. 16-29-05276). M.S. gratefully acknowledges financial support by the OTH Regensburg in the framework of cluster funding.

References

- [1] J.D. Carlson, M.R. Jolly, MR fluid, foam and elastomer devices, *Mechatronics* 10 (2000) 555–569.
- [2] G. Filipcsei, I. Csetneki, A. Szilágyi, M. Zrínyi, Magnetic field-responsive smart polymer composites, *Adv. Polym. Sci.* 206 (2007) 137–189.
- [3] Y. Li, J. Li, W. Li, H. Du, A state-of-the-art review on magnetorheological elastomer devices, *Smart Mater. Struct.* 23 (2014). 123001.
- [4] Ubaidillah, J. Sutrisno, A. Purwanto, S.A. Mazlan, Recent progress on magnetorheological solids: materials, fabrication, testing, and applications, *Adv. Eng. Mater.* 17 (2015) 563–597.
- [5] A.M. Menzel, Tuned, driven, and active soft matter, *Phys. Rep.* 554 (2015) 1–45.
- [6] S. Odenbach, Microstructure and rheology of magnetic hybrid materials, *Arch. Appl. Mech.* 86 (2016) 269–279.
- [7] M. Lopez-Lopez, J.D. Durán, L.Y. Iskakova, A.Y. Zubarev, Mechanics of magnetopolymer composites: a review, *J. Nanofluids* 5 (2016) 479–495.
- [8] M.A. Cantera, M. Behrooz, R.F. Gibson, F. Gordaninejad, Modeling of magneto-mechanical response of magnetorheological elastomers (MRE) and MRE-based systems: a review, *Smart Mater. Struct.* 26 (2) (2017). 023001.
- [9] H.-N. An, S.J. Picken, E. Mendes, Direct observation of particle rearrangement during cyclic stress hardening of magnetorheological gels, *Soft Matter* 8 (2012). 11995.
- [10] G.V. Stepanov, D.Y. Borin, Y.L. Raikher, P.V. Melenev, N.S. Perov, Motion of ferroparticles inside the polymeric matrix in magnetoactive elastomers, *J. Phys. Condens. Matter* 20 (2008). 204121.
- [11] V.M. Kalita, A.A. Snarskii, M. Shamonin, D. Zorinets, Effect of single-particle magnetostriction on the shear modulus of compliant magnetoactive elastomers, *Phys. Rev. E* 95 (3) (2017). 032503.
- [12] J.M. Linke, D.Y. Borin, S. Odenbach, First-order reversal curve analysis of magnetoactive elastomers, *RSC Adv.* 6 (2016). 100407.
- [13] J. de Vicente, D.J. Klingenberg, R. Hidalgo-Alvarez, Magnetorheological fluids: a review, *Soft Matter* 7 (2011) 3701–3710.
- [14] A.A. Snarskii, I.V. Bezudnov, V.A. Sevryukov, A. Morozovskiy, J. Malinsky, *Transport Processes in Macroscopically Disordered Media: From Mean Field Theory to Percolation*, Springer, Berlin, 2016.

- [15] S. Abramchuk, E. Kramarenko, G. Stepanov, L.V. Nikitin, G. Filipcsei, A.R. Khokhlov, M. Zrinyi, Novel highly elastic magnetic materials for dampers and seals: part I. Preparation and characterization of the elastic materials, *Polym. Adv. Technol.* 18 (11) (2007) 883–890.
- [16] D. Borin, D. Günther, C. Hintze, G. Heinrich, S. Odenbach, The level of cross-linking and the structure of anisotropic magnetorheological elastomers, *J. Magn. Magn. Mater.* 324 (21) (2012) 3452–3454.
- [17] W.H. Li, M. Nakano, Fabrication and characterization of PDMS based magnetorheological elastomers, *Smart Mater. Struct.* 22 (5) (2013). 055035.
- [18] T.F. Tian, X.Z. Zhang, W.H. Li, G. Alici, J. Ding, Study of PDMS based magnetorheological elastomers, *J. Phys. Conf. Ser.* 412 (1) (2013). 012038.
- [19] H.J. Choi, S.A. Mazlan, F. Imaduddin, Fabrication and viscoelastic characteristics of waste tire rubber based magnetorheological elastomer, *Smart Mater. Struct.* 25 (11) (2016)115026.
- [20] L. Ge, X. Gong, Y. Fan, S. Xuan, Preparation and mechanical properties of the magnetorheological elastomer based on natural rubber/rosin glycerin hybrid matrix, *Smart Mater. Struct.* 22 (11) (2013). 115029.
- [21] L.V. Nikitin, G.V. Stepanov, L.S. Mironova, A.N. Samus, Properties of magnetoelastics synthesized in external magnetic field, *J. Magn. Magn. Mater.* 258 (2003) 468–470.
- [22] Y. Wang, Y. Hu, H. Deng, X. Gong, P. Zhang, W. Jiang, Z. Chen, Magnetorheological elastomers based on isobutylene-isoprene rubber, *Polym. Eng. Sci.* 46 (3) (2006) 264–268.
- [23] J. Wu, X. Gong, L. Chen, H. Xia, Z. Hu, Preparation and characterization of isotropic polyurethane magnetorheological elastomer through in situ polymerization, *J. Appl. Polym. Sci.* 114 (2) (2009) 901–910.
- [24] J. Wu, X. Gong, Y. Fan, H. Xia, Improving the magnetorheological properties of polyurethane magnetorheological elastomer through plasticization, *J. Appl. Polym. Sci.* 123 (4) (2012) 2476–2484.
- [25] Y. Kimura, S. Kanauchi, M. Kawai, T. Mitsumata, S. Tamesue, T. Yamauchi, Effect of plasticizer on the magnetoelastic behavior for magnetic polyurethane elastomers, *Chem. Lett.* 44 (2) (2015) 177–178.
- [26] Y. Hu, Y.L. Wang, X.L. Gong, X.Q. Gong, X.Z. Zhang, et al., New magnetorheological elastomers based on polyurethane/Si-rubber hybrid, *Polym. Test.* 24 (3) (2005) 324–329.
- [27] C. Lian, K.H. Lee, C.H. Lee, Friction and wear characteristics of magneto-rheological elastomers based on silicone/polyurethane hybrid, *J. Tribol.* 137 (3) (2015). 031607.
- [28] X. Qiao, X. Lu, W. Li, J. Chen, X. Gong, T. Yang, et al., Microstructure and magnetorheological properties of the thermoplastic magnetorheological elastomer composites containing modified carbonyl iron particles and poly(styrene-*b*-ethylene-ethylene-propylene-*b*-styrene) matrix, *Smart Mater. Struct.* 21 (11) (2012). 115028.
- [29] J. Kaleta, M. Królewicz, D. Lewandowski, Magnetomechanical properties of anisotropic and isotropic magnetorheological composites with thermoplastic elastomer matrices, *Smart Mater. Struct.* 20 (8) (2011). 085006.
- [30] S. Xuan, Y. Xu, T. Liu, X. Gong, Recent progress on the magnetorheological plastomers, *Int. J. Smart Nano Mater.* 6 (2) (2015) 135–148.
- [31] T. Liu, Y. Xu, X. Gong, H. Pang, S. Xuan, Magneto-induced normal stress of magnetorheological plastomer, *AIP Adv.* 3 (8) (2013). 082122.
- [32] P.V. Rao, S. Maniprakash, S.M. Srinivasan, A.R. Srinivasa, Functional behavior of isotropic magnetorheological gels, *Smart Mater. Struct.* 19 (8) (2010). 085019.
- [33] M.J. Wilson, A. Fuchs, F. Gordaninejad, Development and characterization of magnetorheological polymer gels, *J. Appl. Polym. Sci.* 84 (14) (2002) 2733–2742.
- [34] N. Golinelli, A. Spaggiari, E. Dragoni, Mechanical behaviour of magnetic silly putty: viscoelastic and magnetorheological properties, *J. Intell. Mater. Syst. Struct.* 28 (8) (2017) 953–960.
- [35] E. Galipeau, P. Ponte Castañeda, Giant field-induced strains in magnetoactive elastomer composites, *Proc. R. Soc. A* 469 (2158) (2013). 20130385.
- [36] A.R. Khokhlov, A.Y. Grosberg, *Statistical Physics of Macromolecules*, AIP Press, New York, USA, 1997.
- [37] S.K. Patel, S. Malone, C. Cohen, J.R. Gillmor, R.H. Colby, Elastic modulus and equilibrium swelling of poly(dimethylsiloxane) networks, *Macromolecules* 25 (1992) 5241–5251.

- [38] R. Everaers, Entanglement effects in defect-free model polymer networks, *New J. Phys.* 1 (1999) 12.1–12.54.
- [39] W.F.M. Daniel, J. Burdynska, M. Vatankeh-Varnoosfaderani, K. Matyjaszewski, J. Paturej, M. Rubinstein, A.V. Dobrynin, S.S. Sheiko, Solvent-free, supersoft and superelastic bottlebrush melts and networks, *Nat. Mater.* 15 (2016) 183–189.
- [40] L.-H. Cai, T.E. Kodger, R.E. Guerra, A.F. Pegoraro, M. Rubinstein, D.A. Weitz, Soft poly(dimethylsiloxane) elastomers from architecture driven entanglement free design, *Adv. Mater.* 27 (2015) 5132–5140.
- [41] Z. Cao, W.F.M. Daniel, M. Vatankeh-Varnoosfaderani, S.S. Sheiko, A.V. Dobrynin, Dynamics of bottlebrush networks, *Macromolecules* 49 (2016) 8009–8017.
- [42] G.V. Stepanov, A.V. Chertovich, E.Y. Kramarenko, Magnetorheological and deformation properties of magnetically controlled elastomers with hard magnetic filler, *J. Magn. Magn. Mater.* 324 (2012) 3448–3451.
- [43] E.Y. Kramarenko, A.V. Chertovich, G.V. Stepanov, A.S. Semisalova, L.A. Makarova, N.S. Perov, A. R. Khokhlov, Magnetic and viscoelastic response of elastomers with hard magnetic filler, *Smart Mater. Struct.* 24 (3) (2015). 035002.
- [44] G.V. Stepanov, D.Y. Borin, A.V. Bakhtiarov, P.A. Storozhenko, Magnetic properties of hybrid elastomers with magnetically hard fillers: rotation of particles, *Smart Mater. Struct.* 26 (3) (2017). 035060.
- [45] Q. Wen, Y. Wang, X. Gong, The magnetic field dependent dynamic properties of magnetorheological elastomers based on hard magnetic particles, *Smart Mater. Struct.* 26 (2017). 075012.
- [46] N.A. Spaldin, *Magnetic Materials: Fundamentals and Applications*, Cambridge University Press, Cambridge, 2010.
- [47] S.P. Gubin (Ed.), *Magnetic nanoparticles*, Wiley-VCH Verlag GmbH & Co. KGaA, Weinheim, Germany, 2009.
- [48] G.V. Stepanov, S.S. Abramchuk, D.A. Grishin, L.V. Nikitin, E.Y. Kramarenko, A.R. Khokhlov, Effect of a homogeneous magnetic field on the viscoelastic behavior of magnetic elastomers, *Polymer* 48 (2) (2007) 488–495.
- [49] S. Bednarek, The giant linear magnetostriction in elastic ferromagnetic composites within a porous matrix, *J. Magn. Magn. Mater.* 301 (2006) 200.
- [50] X. Guan, X. Dong, J. Ou, Magnetostrictive effect of magnetorheological elastomer, *J. Magn. Magn. Mater.* 320 (2008) 158.
- [51] K. Danas, S.V. Kankanala, N. Triantafyllidis, Experiments and modeling of iron-particle-filled magnetorheological elastomers, *J. Mech. Phys. Solids* 60 (2012) 120.
- [52] E. Galipeau, P. Ponte Castañeda, The effect of particle shape and distribution on the macroscopic behavior of magnetoelastic composites, *Int. J. Solids Struct.* 49 (1) (2012) 17.
- [53] G.V. Stepanov, E.Y. Kramarenko, D.A. Semerenko, Magnetodeformational effect of the magnetoactive elastomer and its possible applications, *J. Phys. Conf. Ser.* 412 (2013). 012031.
- [54] R. Weeber, S. Kantorovich, C. Holm, Deformation mechanisms in 2d magnetic gels studied by computer simulations, *Soft Matter* 8 (2012) 9923.
- [55] Y. Han, A. Mohla, X. Huang, W. Hong, L.E. Faidley, Magnetostriction and field stiffening of magneto-active elastomers, *Int. J. Appl. Mech.* 7 (2015). 1550001.
- [56] Yu.L. Raikher, O.V. Stolbov, <https://www.icmm.ru/nauka/sborniki/680-etyudy-o-mekhanike> (in Russian), 2017.
- [57] A. Zubarev, D.Y. Borin, Effect of particle concentration on ferrogel magnetodeformation, *J. Magn. Magn. Mater.* 377 (2015) 373–377.
- [58] G. Liao, X. Gong, S. Xuan, C. Guo, L. Zong, Magnetic-field-induced normal force of magnetorheological elastomer under compression status, *Ind. Eng. Chem. Res.* 51 (8) (2012) 3322–3328.
- [59] G. Liao, X. Gong, S. Xuan, Influence of shear deformation on the normal force of magnetorheological elastomer, *Mater. Lett.* 106 (2013) 270–272.
- [60] B. Ju, M. Yu, J. Fu, X. Zheng, S. Liu, Magnetic field-dependent normal force of magnetorheological gel, *Ind. Eng. Chem. Res.* 52 (33) (2013) 11583–11589.
- [61] V.V. Sorokin, G.V. Stepanov, M. Shamonin, G.J. Monkman, A.R. Khokhlov, E.Y. Kramarenko, Hysteresis of the viscoelastic properties and the normal force in magnetically and mechanically soft magnetoactive elastomers: effects of filler composition, strain amplitude and magnetic field, *Polymer* 76 (2015) 191–202.

- [62] A.V. Chertovich, G.V. Stepanov, E.Y. Kramarenko, A.R. Khokhlov, New composite elastomers with giant magnetic response, *Macromol. Mater. Eng.* 295 (4) (2010) 336–341.
- [63] A. Stoll, M. Mayer, G.J. Monkman, M. Shamonin, Evaluation of highly compliant magneto-active elastomers with colossal magnetorheological response, *J. Appl. Polym. Sci.* 131 (2) (2014).
- [64] L.V. Nikitin, G.V. Stepanov, L.S. Mironova, A.I. Gorbunov, Magnetodeformational effect and effect of shape memory in magnetoelastics, *J. Magn. Magn. Mater.* 272–276 (2004) 2072.
- [65] L.V. Nikitin, D.G. Korolev, G.V. Stepanov, L.S. Mironova, Experimental study of magnetoelastics, *J. Magn. Magn. Mater.* 300 (2006) e234–e238.
- [66] S.S. Abramchuk, D.A. Grishin, E.Y. Kramarenko, G.V. Stepanov, A.R. Khokhlov, Effect of homogeneous magnetic field on the mechanical behavior of soft magnetic elastomers under compression, *Polym. Sci., Ser. A* 48 (2) (2006) 138–145.
- [67] P. Melenev, Y. Raikher, G. Stepanov, V. Rusakov, L. Polygalova, Modeling of the field-induced plasticity of soft magnetic elastomers, *J. Intell. Mater. Syst. Struct.* 22 (6) (2011) 531–538.
- [68] V.V. Sorokin, G.V. Stepanov, M. Shamonin, G.J. Monkman, E.Y. Kramarenko, Magnetorheological behavior of magnetoactive elastomers filled with bimodal iron and magnetite particles, *Smart Mater. Struct.* 26 (3) (2017). 035019.
- [69] H. Böse, R. Röder, Magnetorheological elastomers with high variability of their mechanical properties, *J. Phys. Conf. Ser.* 149 (1) (2009). 012090.
- [70] W.H. Li, Y. Zhou, T.F. Tian, Viscoelastic properties of MR elastomers under harmonic loading, *Rheol. Acta* 49 (7) (2010) 733–740.
- [71] H. An, S.J. Picken, E. Mendes, Enhanced hardening of soft self-assembled copolymer gels under homogeneous magnetic fields, *Soft Matter* 6 (18) (2010) 4497–4503.
- [72] Y. Xu, X. Gong, S. Xuan, W. Zhang, Y. Fan, A high-performance magnetorheological material: preparation, characterization and magnetic-mechanic coupling properties, *Soft Matter* 7 (11) (2011) 5246–5254.
- [73] V. Vasiliev, N. Sheremetyeva, M. Buzin, D. Turenko, V. Papkov, I. Klepikov, I.V. Razumovskaya, A. M. Muzafarov, E.Y. Kramarenko, Magnetorheological fluids based on a hyperbranched polycarbosilane matrix and iron microparticles, *Smart Mater. Struct.* 25 (2016). 055016.
- [74] Q. Jin, Y. Xu, Y. Di, H. Fan, Influence of the particle size on the rheology of magnetorheological elastomer, *Mater. Sci. Forum* 809–810 (2015) 757–763.
- [75] A. Boczkowska, S. Awietjan, Microstructure and properties of magnetorheological elastomers, Chapter 6, in: A. Boczkowska (Ed.), *Advanced Elastomers—Technology, Properties and Applications*, InTech, London, United Kingdom, ISBN: 978-953-51-0739-2, 2012. 412 pp.
- [76] N. Chiba, K. Yamamoto, T. Hojo, M. Kawai, T. Mitsumata, Wide-range modulation of dynamic modulus and loss tangent for magnetic elastomers containing submillimeter magnetic particles, *Chem. Lett.* 42 (3) (2013) 253–254.
- [77] P. von Lockette, J. Kadlowec, J.H. Koo, In: *Particle mixtures in magnetorheological elastomers (MREs)*, Proc. SPIE 6170, 2006. 61700T.
- [78] S. Aloui, M. Klüppel, Magneto-rheological response of elastomer composites with hybrid magnetic fillers, *Smart Mater. Struct.* 24 (2014). 025016.
- [79] P.R. von Lockette, S.E. Lofland, J.-H. Koo, J. Kadlowec, M. Dermond, Dynamic characterization of bimodal particle mixtures in silicone rubber magnetorheological materials, *Polym. Test.* 27 (2008) 931–935.
- [80] K. Nagashima, S. Kanauchi, M. Kawai, T. Mitsumata, S. Tamesue, T. Yamauchi, Nonmagnetic particles enhance magnetoelastic response of magnetic elastomers, *J. Appl. Phys.* 118 (2015). 024903.
- [81] T. Mitsumata, S. Otori, N. Chiba, M. Kawai, Enhancement of magnetoelastic behavior of bimodal magnetic elastomers by stress transfer via nonmagnetic particles, *Soft Matter* 9 (2013) 10108–10116.
- [82] D. Romeis, V.P. Toshchevnikov, M. Saphiannikova, Elongated micro-structures in magneto-sensitive elastomers: a dipolar mean field model, *Soft Matter* 12 (2016) 9364–9376.
- [83] G.V. Stepanov, D.Y. Borin, E.Y. Kramarenko, V.V. Bogdanov, D.A. Semerenko, P. A. Storozhenko, Magnetoactive elastomer based on magnetically hard filler: synthesis and study of viscoelastic and damping properties, *Polym. Sci., Ser. A* 56 (5) (2014) 603–613.

- [84] A.R. Payne, The dynamic properties of carbon black-loaded natural rubber vulcanizates. Part I, *J. Appl. Polym. Sci.* 6 (19) (1962) 57–63.
- [85] A. Lion, Phenomenological modelling of strain-induced structural changes in filler-reinforced elastomers, a time domain formulation of the Kraus model, *KGK, Kautsch. Gummi Kunstst.* 58 (2005) 157–162.
- [86] M. Arora, G. Carlesso, J.M. Davidson, A.J. Domb, G. Heinrich, M. Klüppel, et al., *Filled Elastomers Drug Delivery Systems*, *Advances in Polymer Science*, vol. 160, Springer Verlag, Berlin, 2002.
- [87] G. Heinrich, T.A. Vilgis, A statistical mechanical approach to the Payne effect in filled rubbers, *Express Polym Lett* 9 (2015) 291–299.
- [88] H.-N. An, S.J. Picken, E. Mendes, Nonlinear rheological study of magneto responsive soft gels, *Polymer* 53 (2012) 4164–4170.
- [89] A.D. Drozdov, A. Dorfmann, The Payne effect for particle-reinforced elastomers, *Polym. Eng. Sci.* 42 (2002) 591–604.
- [90] G. Huber, T.A. Vilgis, G. Heinrich, Universal properties in the dynamical deformation of filled rubbers, *J. Phys. Condens. Matter* 8 (1996) 409–412.
- [91] V.V. Sorokin, I.A. Belyaeva, M. Shamonin, E.Y. Kramarenko, Magnetorheological response of highly filled magnetoactive elastomers from perspective of mechanical energy density: fractal aggregates above the nanometer scale? *Phys. Rev. E* 95 (6) (2017). 062501.
- [92] Y. Wang, Y. Hu, L. Chen, X. Gong, W. Jiang, P. Zhang, Z. Chen, Effects of rubber/magnetic particle interactions on the performance of magnetorheological elastomers, *Polym. Test.* 25 (2) (2006) 262–267.
- [93] A. Zubarev, D. Chirikov, G. Stepanov, D. Borin, Hysteresis of ferrogels magnetostriction, *J. Magn. Magn. Mater.* 431 (2017) 120–122.
- [94] I.A. Belyaeva, E.Y. Kramarenko, G.V. Stepanov, V.V. Sorokin, D. Stadler, M. Shamonin, Transient magnetorheological response of magnetoactive elastomers to step and pyramid excitations, *Soft Matter* 12 (2016) 2901–2913.
- [95] A.Y. Zubarev, D.N. Chirikov, D.Y. Borin, G.V. Stepanov, Hysteresis of the magnetic properties of soft magnetic gels, *Soft Matter* 12 (30) (2016) 6473–6480.
- [96] A. Biller, O. Stolbov, Y.L. Raikher, Mesoscopic magnetomechanical hysteresis in a magnetorheological elastomer, *Phys. Rev. E* 92 (2015). 023202.
- [97] G.V. Stepanov, D.Y. Borin, P.A. Storozhenko, Rotation of magnetic particles inside the polymer matrix of magnetoactive elastomers with a hard magnetic filler, *J. Magn. Magn. Mater.* 431 (2017) 138–140.
- [98] M.V. Vaganov, J. Linke, S. Odenbach, Y.L. Raikher, Model FORC diagrams for hybrid magnetic elastomers, *J. Magn. Magn. Mater.* 431 (2017) 130–133.
- [99] S. Abramchuk, E. Kramarenko, D. Grishin, G. Stepanov, L.V. Nikitin, G. Filipcsei, A. R. Khokhlov, M. Zrinyi, Novel highly elastic magnetic materials for dampers and seals II.: material behaviour in a magnetic field, *Polym. Adv. Technol.* 18 (7) (2007) 513–518.
- [100] I. Bica, Y.D. Liu, H.J. Choi, Magnetic field intensity effect on plane electric capacitor characteristics and viscoelasticity of magnetorheological elastomer, *Colloid Polym. Sci.* 290 (2012) 1115–1122.
- [101] A.S. Semisalova, N.S. Perov, G.V. Stepanov, E.Y. Kramarenko, A.R. Khokhlov, Strong magnetodielectric effect in magnetorheological elastomers, *Soft Matter* 9 (2013) 11318–11324.
- [102] I.A. Belyaeva, E. Yu. Kramarenko, M. Shamonin, Magnetodielectric effect in magnetoactive elastomers: transient response and hysteresis, *Polymer* 127 (2017) 119–128.
- [103] G.V. Stepanov, D.A. Semerenko, A.V. Bakhtiarov, P.A. Storozhenko, Magnetoresistive effect in magnetoactive elastomers, *J. Supercond. Novel Magn.* 26 (2016) 1055–1059.
- [104] I. Bica, The influence of hydrostatic pressure and transverse magnetic field on the electric conductivity of the magnetorheological elastomers, *J. Ind. Eng. Chem.* 18 (2012) 483–486.
- [105] I. Bica, Influence of the magnetic field on the electric conductivity of magnetorheological elastomers, *J. Ind. Eng. Chem.* 16 (2010) 359–363.
- [106] M. Yu, P. Yang, J. Fu, S. Liu, S.-B. Choi, A theoretical model for the field-dependent conductivity of magneto-rheological gels and experimental verification, *Sens. Actuat. A* 245 (2016) 127–134.

- [107] I.E. Kuznetsova, B.D. Zaitsev, A.M. Shikhabudinov, I.A. Borodina, E. Yu. Kramarenko, V.V. Kolesov, G.V. Stepanov, The influence of the external magnetic field on acoustic properties of magnetic elastomers, in: *Proceedings of IEEE Ultrasonics Symposium*, July 21–26, 2013, pp. 492–495, Prague, Czech Republic.
- [108] Available at: <https://en.oxforddictionaries.com/definition/engineering>. Accessed on 26.09.2017.
- [109] H. Böse, R. Rabindranath, J. Ehrlich, Soft magnetorheological elastomers as new actuators for valves, *J. Intell. Mater. Syst. Struct.* 23 (2012) 989–994.
- [110] S. Kashima, F. Miyasaka, K. Hirata, Novel soft actuator using magnetorheological elastomer, *IEEE Trans. Magn.* 48 (2012) 1649–1652.
- [111] M. Mayer, R. Rabindranath, J. Börner, E. Hörner, A. Bentz, J. Salgado, et al., Ultra-soft PDMS-based magnetoactive elastomers as dynamic cell culture substrata *PLoS ONE* 8 (10) (2013) e76196.
- [112] L.A. Makarova, T.A. Nadzharyan, J.A. Alekhina, G.V. Stepanov, E.G. Kazimirova, N.S. Perov, E. Yu. Kramarenko, Magnetoactive elastomer as an element of a magnetic retina fixator, *Smart Mater. Struct.* 26 (2017) 095054.
- [113] S. Lee, C. Yim, W. Kim, S. Jeon, Magnetorheological elastomer films with tunable wetting and adhesion properties, *ACS Appl. Mater. Interf.* 7 (35) (2015) 19853–19856.
- [114] V. V. Sorokin, B. O. Sokolov, G. V. Stepanova, E. Yu. Kramarenko, Controllable hydrophobicity of magnetoactive elastomer coatings, *J. Magn. Magn. Mater.* (In press), <https://doi.org/10.1016/j.jmmm.2017.10.074>.

This page intentionally left blank

Neel Effect: Exploiting the Nonlinear Behavior of Superparamagnetic Nanoparticles for Applications in Life Sciences up to Electrical Engineering

Luc Lenglet*, Laurence Motte†

*Normafin, Levallois-Perret, France, †Inserm, U1148, Laboratory for Vascular Translational Science, UFR SMBH, Université Paris 13, Sorbonne Paris Cité, Bobigny, France.

8.1 Louis Néel, Superparamagnetism, and Neel Effect®

Louis Néel was a French physicist who won Nobel Prize for Physics in 1970 for his pioneering studies of the magnetic properties of solids. Inventor of antiferromagnetism in the 30s and ferrimagnetism in the 40s, he has also given an explanation of the weak magnetism of certain rocks, unveiling the history of Earth's magnetic field. He elected the magnetism of fine grains, superparamagnetism, as one of his favorite research topics [1]. Paradoxically, whereas Néel was instrumental in the development of improved computer memory units, superparamagnetism remains for most people this unbeatable barrier toward reduction in the size of memories. And superparamagnetic materials, so far, have a limited number of applications, e.g., ferrofluids for audio speakers or seals supplied by Ferrotec (Japan), beads for cell sorting and other magnetic separations like Dynabeads® supplied by Thermo Fisher Scientific (USA), MACS® MicroBeads by Miltenyi Biotec (Germany), or Estapor® Magnetic Microspheres by Merck (Germany). However, emerging applications of magnetic nanoparticles (NPs), be it superparamagnetic or slightly hysteretic, are flourishing in life sciences, and beyond, with the ongoing development of particle-based contrast agents for medical imaging, magnetic hyperthermia agents for cancer therapies, magnetic labels for bioassays, etc.

This chapter will focus on Neel Effect, a special feature of nonlinear magnetic NPs, which has been recently implemented in breakthrough analytical techniques and instruments. Neel Effect appears when magnetic NPs, most often superparamagnetic, are placed in a two-frequency magnetic field, thus generating an array of recordable signals at linear combinations of incident

frequencies. Frequency mixing is a well-known technique for extracting nonlinear characteristics of materials or electronic devices [2]. In the present case, it is the nonlinear magnetization of NPs, which, upon magnetic excitation at two distinct frequencies, generates response signals at combinatorial frequencies.

The principle is displayed in Fig. 8.1. The magnetization $M(H)$ of superparamagnetic NPs is nonhysteretic and strongly nonlinear, while approaching a saturation value for large magnetic fields (see Fig. 8.1C). The time trace of a magnetic field $H(t)$ consisting of two spectral components, a high-frequency component f_1 and a low-frequency component f_2 , is displayed in

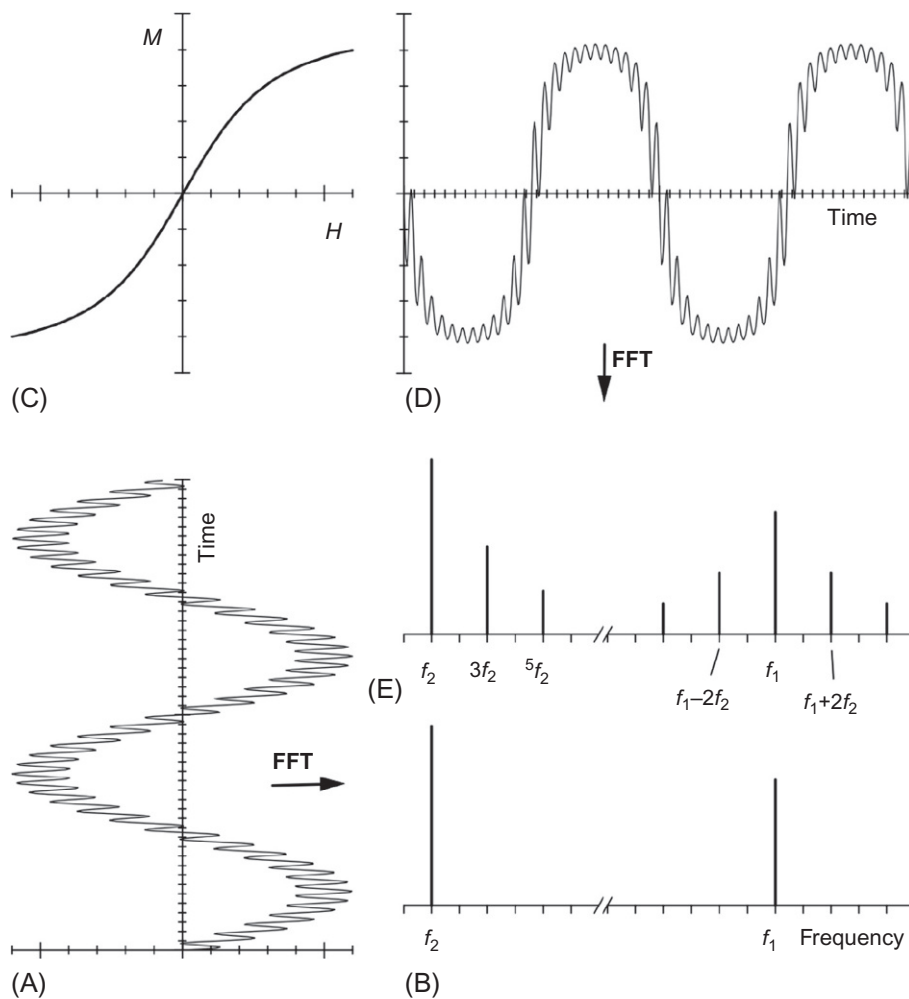


Fig. 8.1

(A) Time trace of a two-frequency magnetic field. (B) Fourier-transformed spectrum of a two-frequency magnetic field with two distinct lines. (C) nonlinear magnetization curve of superparamagnetic NPs. (D) Resulting time-dependent magnetization. (E) Higher harmonics and frequency mixing components in the Fourier-transformed response signal (© 2006 Elsevier).

Fig. 8.1A. The Fourier spectrum simply consists of two discrete lines as shown in Fig. 8.1B. When NPs are exposed to such magnetic field, it leads to a time-varying magnetization according to Fig. 8.1D. Magnetization exhibits flattened extrema but still has strong variations for lower field values. The Fourier transform of this distorted magnetization response, schematically depicted in Fig. 8.1E., exhibits lines at linear combinations of initial frequencies, $mf_1 + nf_2$, straight harmonics or mixing terms. Due to symmetry, only uneven harmonics, $3f_1, 5f_1, \dots, 3f_2, 5f_2, \dots$, and such mixing terms as $f_1 \pm 2f_2, f_1 \pm 4f_2, \dots$, are effectively present besides f_1 and f_2 . Such findings can be retrieved through the math, assuming the Langevin function for $M(H)$ and a two-frequency sinusoidal magnetic field.

On a technical standpoint, implementing frequency mixing for analytical purposes is straightforward. Indeed, Faraday's law of induction teaches the relationship between magnetic flux time variations through a wire loop and the electromotive force thus generated. Measuring the voltage at the terminals of a detection coil containing nonlinear magnetic material exposed to a two-frequency magnetic field will hence provide a faithful image of the magnetic flux density B , and the magnetization M , through $B = M + \mu_0 H$. More specifically, these frequency combinations will be directly retrieved in voltage spectra.

Neel Effect can be implemented in two different strategies, either for particle sensing, or for magnetic field sensing. Particle sensors will feature a two-frequency excitation field. Measuring selected intermodulation products in the presence of unknown magnetic NPs will allow for the detection, quantification, and characterization of said NPs. Magnetic field sensors will feature a transducer consisting of a superparamagnetic core excited by a one-frequency magnetic field. Measuring selected intermodulation products when the transducer is exposed to an unknown magnetic field will allow for determining the components of said magnetic field, both direct and/or alternating.

8.2 Neel Effect for Particle Sensing

8.2.1 Magnetic Immunoassays

Magnetic immunoassay (MIA) is a novel type of diagnostic immunoassay using magnetic beads as labels in lieu of conventional enzymes (ELISA), radioisotopes (RIA), or fluorescent dyes (FIA). This assay involves the specific binding of an antibody to its antigen, where a magnetic label is conjugated to one element of the pair. The measurement of the quantity of magnetic beads combined with a test-specific calibration curve allows for retrieving the amount of analyte (e.g., virus, toxin, bacteria, cardiac marker) in the initial sample. The rationale for using magnetic beads as labels in bioassays is numerous. Magnetic NPs are not affected by reagent chemistry or photobleaching and are therefore stable over time, unlike many colored or fluorescent labels. Magnetic compounds in a biological sample are usually absent, thus have limited background signal. Moreover, magnetic fields have the

capability to pass unaltered through plastic, water, blood, nitrocellulose, and other materials, thereby allowing for a comprehensive exploration of the whole probe volume, not only of its surface, be it turbid, colored, naturally fluorescent. But the most important may be that magnetic beads are easily manipulated remotely by magnetic fields. They are hence widely used in life sciences for concentration, separation, or mixing purpose, and already widely used as reagents in bioassays. The same beads can then provide both functions, magnetic handling and magnetic labeling.

Conventional magnetic detection techniques encompass susceptometry and relaxometry. Susceptometry measures the magnetic susceptibility, an extensive property of any material, by magnetic lock-in detection of the response to a magnetic oscillating excitation, by means of different magnetic field sensors. However, susceptometry lacks selectivity, as water, sample holders, cuvettes, etc., would contribute to the overall susceptibility, and make it very difficult to detect small concentrations of magnetic particles in biological samples. Therefore, delicate and tedious referencing techniques must be employed. Relaxometry is based on recording the time transient of the magnetic response of the particles during the off-time of a pulsed excitation field. It even allows to make a distinction between bound and unbound magnetic particles! Since the relaxometric signals are typically very small, magnetometers with excellent sensitivity such as superconducting quantum interference devices (SQUIDs) must be utilized. Cumbersome, they are costly and uneasy to operate since they require complicated cooling instrumentation. Less conventional sensors include giant magnetoresistive resistance sensors, anisotropic magnetoresistive rings, spin valves, and piezoresistive cantilevers. However, for numerous reasons, none of these detection methods are widely used in *in vitro* diagnostics (IVD) systems. Either they are incorporated in instruments that feature moving parts, or they require expensive consumables, embedded electronics, liquid-nitrogen refrigeration, connections, or microfluidics.

The first implementation of Neel Effect for magnetic immunoassays was patented in 2000 by P.I. Nikitin team from the General Physics Institute in Moscow [3]. They disclosed in 2003 a prototype reader for the first time [4]. The two-frequency magnetic excitation was generated by a double electrical coil. It featured an additional DC magnetic field in the probe zone to help saturate magnetic NPs at lower current driver. This allowed for a battery-operated handheld device with a high signal-to-noise ratio, able to measure a relative change of magnetic susceptibility at the level of up to 10^{-8} , with a measure at $f_1 + 2f_2$ strictly proportional to the quantity of magnetic NPs over five orders of magnitude.

In 2007, P.I. Nikitin et al. disclosed sensitivity results on a variety of biological targets, e.g., 0.1 ng/mL of F1 capsular antigen of *Yersinia pestis*, 0.1 ng/mL for soluble lipopolysaccharides from *Francisella tularensis*, 10^3 cell/mL of *Salmonella typhimurium* [5,6]. Initial results were obtained with MIAflo[®], a flow-through cartridge. The solid phase of the sandwich immunoassay is a three-dimensional millimetric filter sealed inside a tip or directly in a syringe. The filter is coated with antibodies specific for the target antigen. The sample, magnetic

reagent, and washing solutions are passed through the filter either manually with a syringe or pipette, or with any automated dispenser. In this way, the filter is used simultaneously as a media for immunoconcentration, for the filtration of the sample, and as the solid phase for the assay in a unique single-dose cartridge. Preliminary results were also presented with an alternate solid phase, a multicapillary glass structure (otherwise used as photonic crystal). Structures of 2.5 mm in diameter contain 1500 capillaries, each 40 μm in diameter, which can be coated with well-known methods.

2007 was a busy year for magnetic immunoassays based on frequency mixing. Meyer from Philipps-Universität Marburg (Germany) together with Krause from Forschungszentrum Jülich (Germany) also disclosed a series of results with a consumable based on an ABICAP[®] polyethylene column, similar in principle to MIAflo[®]. They demonstrated a 25-to-2500 ng/mL linear detection range for the c-reactive protein (CRP), a 115-kDa protein, once much more sensitive than reference high-sensitivity ELISA assays. They also could detect *F. tularensis* lipopolysaccharides between 10^4 and 10^6 colony-forming units. With *Y. pestis*, they demonstrated a linear detection range of 25–300 ng/mL and a detection limit of 2.5 ng/mL for the antigen F1 in buffer and human blood serum [7–9].

Again in 2007, Krause et al. issued a comprehensive and excellent theoretical study for the design of frequency-mixing sensors, also providing insights on the optimization of the detection coil and the setup/optimization of readout electronics [10].

New results were disclosed more recently with the flow-through format. For example, Orlov et al. [11] proved the capability of the flow-through format to accommodate large, unprepared, samples, in the tens of milliliters. The method has demonstrated near-linear dose-response curves within a range of three decades while assaying staphylococcal enterotoxin A (SEA) and toxic shock syndrome toxin (TSST) in unprepared milk samples. Limits of detection (LoD) as low as 4 and 10 pg/mL for TSST and SEA, respectively, were obtained in 2 h with 30 mL samples. LoDs of 0.1 and 0.3 ng/mL were reached for the same toxins in 25 min with 150- μL samples. Also, the flow-through format was adapted by Hong et al. [12] for the detection of influenza virus based on a nitrocellulose membrane as a solid phase instead of a filter as described here to reduce the nonspecific binding of magnetic beads. Most probably further developments should be expected that will extensively tap into the potential of magnetic detection, that is, the accommodation of large, unprepared, samples.

Magnetic labels were then adapted to the most widespread immunoassay format, that is, lateral flow immunoassay on a strip, which features a multifunctional strip, reagent reservoir, immunoaggregation reactor, separation medium, solid phase, all at once. This format was made popular by the pregnancy test (Fig. 8.2). This is the most widespread format, by far the cheapest, for near-patient in vitro diagnostics, but not the most trustworthy, as it lacks reproducibility and most often only provides a Yes/No result, which is hardly acceptable on a regulatory standpoint.

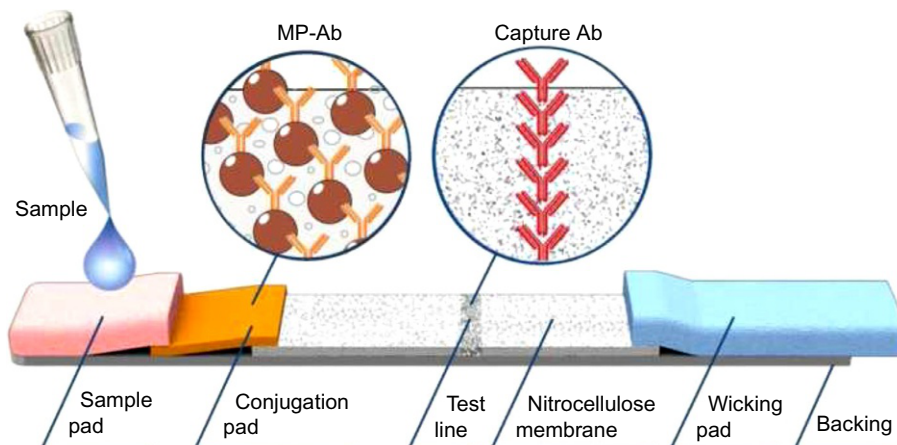


Fig. 8.2

Lateral flow immunochromatographic strip adapted with magnetic NPs (MP) as labels (© American Chemical Society).

Colored or fluorescent labels are simply replaced by magnetic beads. Unlike conventional labels “read” by the operator’s eye, magnetic labels are detected by a magnetic reader, allowing for a quantified result. Moreover, the reader can count all NPs, even those buried in the lower part of the nitrocellulose membrane, unattainable by optical methods. Finally, unlike conventional susceptometric methods, the frequency-mixing method is insensitive to the slight interbatch variations due to the usage of variable natural raw materials (cellulose).

Results with lateral flow immunochromatographic strips were disclosed by several teams in France, Russia, Korea, Germany, on a variety of targets, e.g., hCG β [13], *Alexandrium minutum* [14], botulinum toxins [15]. Interestingly, Gas et al. were the first to report the detection of unprepared whole cells as large as 10 μm in diameter, i.e., *A. minutum*, by means of a quantitative lateral flow magnetic immunoassay. *A. minutum* is a marine dinoflagellate producing paralytic toxins very detrimental to shellfish aquaculture industry and fisheries. The test was shown to be highly specific for *A. minutum* and able to detect reproducibly 10^5 cells/L within 30 min in unprepared environmental samples. No significant difference was observed with conventional light microscopy counting, the extraordinarily tedious reference method. Orlov et al. have displayed an amazing multiplex quantitative lateral flow assay for the simultaneous on-site detection of botulinum neurotoxin (BoNT) types A, B, and E in complex matrices. More generally, multiplexing on-site assays is key to forensics, environmental testing, warfare agent detection, etc. The approach is original compared to conventional multiline multiplex lateral flow assays while multiplexing is realized via joining an on-demand set of single-plex lateral flow strips into a miniature cylinder cartridge. The cartridge is read out by a portable multichannel magnetic reader, which offers an unmatched 60-zmol detection limit and 7-order linear dynamic range. The proposed multiplex assay has demonstrated LoDs

of 0.22, 0.11, 0.32 ng/mL for BoNT-A, -B, and -E. These figures are noticeably comparable to the figures of each single-plex component unlike conventional multiline multiplex lateral flow assays. As for commercial developments, Magnisense (France) claims to release soon an emergency kit for cardiovascular situations based on their lateral flow magnetic immunoassays, MIAstrip[®].

Besides conventional immunoassays, Motte's team (France) has used magnetic readers as routine benchtop tools in their research on multifunctional magnetic NPs. For example, they monitored the cellular uptake of NPs coated with an oligonucleotide targeting the signal transducer and activator of transcription 3 (STAT3, a key regulator of cell survival and proliferation) in order to optimize functionalization parameters. The stability of magnetic labels has allowed for monitoring over 24 h, whereas quenching and bleaching of fluorescent labels in the same conditions were disturbing measurements. Similar conclusions were reached with both ALEXA and TARMA dyes in a variety of setups, oligonucleotide or peptide labeling, SW480 colon carcinoma cells or RAW 264.7 cells, allowing for better understanding uptake and metabolism mechanisms [16–18]. Benchtop monitoring was also instrumental to the development of a bimodal contrast agent targeting tumors (for both fluorescence observation and MRI) [19].

Shipunova et al. [20] have developed a rapid method called MPQ-cytometry implementing magnetic particle quantification (MPQ) to quantify interactions between magnetically labeled NPs and living cells (Fig. 8.3). MPQ-cytometry features a LoD of 0.33 ng of NPs. Each measurement takes only a few seconds, and no complicated sample preparation or data processing is required. The method was demonstrated by measuring the quantity of NPs that specifically recognized the HER2/neu marker on human cancer cell surface, the specificity of interaction permitting the detection of HER2/neu positive cells in a cell mixture.

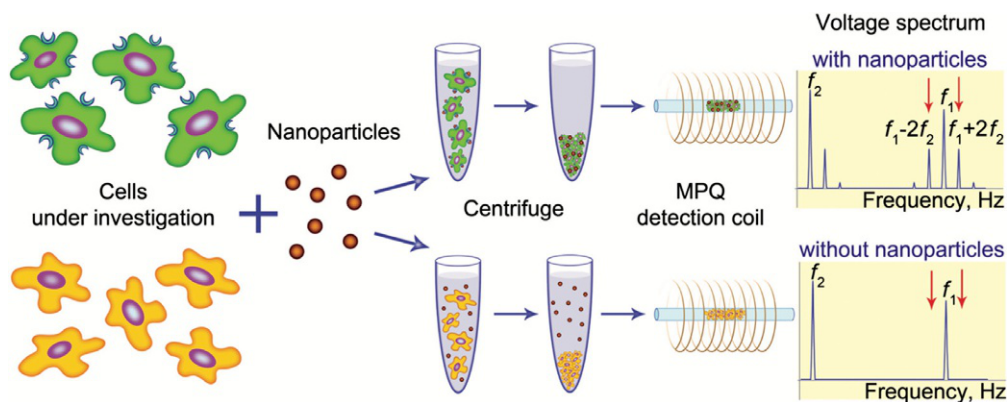


Fig. 8.3

MPQ-cytometry to quantify interactions between magnetically labeled nanoparticles and living cells (©2016 The Royal Society of Chemistry).

Potential applications encompass quantifying cell-bound NPs or estimating the expression level of cell surface antigens, at no expensive sophisticated equipment or highly skilled personnel, even under field conditions.

There might still be room for improvement as a recent patent discloses an optimized design for the transducer (driving and geometry) claiming bettered portability and performance [21]. The Holy Grail in these matters is the smartphone format!

8.2.2 Magnetic Particle Imaging

The physical principle initially disclosed for immunoassays by P.I. Nikitin was implemented shortly after for imaging by Gleich [22] from Philips Research Hamburg (Germany). Named magnetic particle imaging (MPI), Gleich's invention proved to be cornerstone to a new tomographic imaging method capable of 3D dynamic imaging of magnetic tracers. While implementing frequency mixing, the method realizes spatial encoding by means of a tunable static magnetic field, saturating the magnetic material almost everywhere in the sample except in the vicinity of a special point, called the field-free point (FFP). Only in this area will magnetic NPs exhibit Neel Effect, whereas they are not fully saturated. Additional homogeneous oscillating magnetic fields (drive fields) will allow for evaluating the quantity of magnetic NPs at the FFP by frequency mixing. Resolved images can hence be obtained by moving the FFP over the sample. It should be noticed that the FFP movement itself can be used as a modulation driver. Interestingly, MPI can accommodate common tracers as iron-oxide-based magnetic NPs, which have a long history as contrast agents in magnetic resonance imaging (MRI). In MRI, magnetic NPs yield a negative contrast, making it difficult to distinguish tissue from the magnetic NPs. Furthermore, quantification of NPs within tissues is challenging. Conversely, MPI provides simultaneously a positive contrast, no background, and direct quantification.

Philips progressed quite far ahead. In 2005, dynamic 2D experiments were published in *Nature* [23]. In 2007, they presented simulations of a scanner large enough to accept human bodies [24]. In 2009, first in vivo 3D real-time MPI scans were presented revealing details of a beating mouse heart using a clinically approved concentration of a commercially available MRI contrast agent. A temporal resolution of 21.5 ms was achieved at a 3D field of view of 5 cm³ with a spatial resolution sufficient to resolve all heart chambers [25]. With these abilities, MPI had taken a huge step toward medical application. Allowing for a spatial resolution in the submillimeter range, the method had proven to be flexible enough to allow for a well-balanced choice of acquisition speed, sensitivity, and resolution, or for the maximization of either one of them. In addition, MPI does not apply ionizing radiation and is therefore potentially safe for patient and medical staff if the applied magnetic fields do not exceed safety limits.

MPI PreClinical, the first MPI-based scanner ever released, was announced in 2013 as the result of Bruker's collaboration with Philips. It combines Bruker's leadership in preclinical imaging

with Philips' strength in medical imaging. In 2014, the first commercial unit was installed at the University Medical Center Hamburg-Eppendorf (Germany) for in vivo imaging of small animals in translational research. More recently, a startup company, Magnetic Insight (USA), was founded by one of the leading research groups in the field of MPI from UC Berkeley [26], in collaboration with General Electric (USA). They collaborated with Stanford School of Medicine (USA) for solving challenges in cell therapy and vascular imaging with magnetic particle imaging. They have developed the Momentum™ MPI System, also available for sale.

Gleich's initial publication triggered the interest of more than 20 research groups all around the world, e.g., Berkeley (USA), Braunschweig (Germany), Dartmouth (USA), Lübeck (Germany), Seattle (USA), Tokyo (Japan), and Würzburg (Germany). Hundreds of papers have been published since then, displaying improvements in signal generation, spatial encoding and/or signal detection, and in both hardware and software. And with the availability of the first two commercial MPI systems, preclinical results have started piling up. The historical focus has been on vascular imaging for the diagnosis of stenosis, vascular occlusions, internal bleeding and aneurysms, and on device imaging during an intervention. More recently, interest in targeted imaging has been raised, implementing an amazing variety of modalities, e.g., cellular-specific NPs, stem cells loaded with NPs, or even nebulized NPs for lung imaging. Finally, hyperthermia applications could also be addressed with MPI, combining diagnostic imaging and therapy in a unified framework. In 2015, the MPI community even started its own scientific research journal, the *International Journal on Magnetic Particle Imaging*, under the guidance of Knopp from the University Medical Center Hamburg-Eppendorf, who has gathered a thorough view of MPI principles, historical developments, and medical potentialities [27].

8.2.3 Real-Time Monitoring

One most promising applications for a portable, cheap, easy-to-operate, room-temperature, magnetometer device is the monitoring of chemical processes involving NPs, starting from synthesis downward to stabilization, purification, functionalization, and downwards implementation by final users. Pr. Thanh, University College of London insists that the best control of conditions and critical parameters during these steps is mandatory for manufacturing scale-up; hence, further development of magnetic particles in life sciences and moreover clinical applications submitted to demanding regulations are needed [28]. One key success factor will be transitioning laboratory batch process toward well-reproducible continuous-flow industrial processes, at least for the upstream steps. Indeed, "millifluidic" or microfluidic reactors for continuous synthesis provide more control of the reaction time (via residence time), mixing times, heating stages, reaction pressure, and the separation of nucleation and growth, with precision that is difficult to achieve with batch techniques. Motte et al. have implemented a Neel Effect reader to monitor in line the nucleation and growth of NPs obtained by coprecipitation of ferrous chloride and ammonium hydroxide in water (Fig. 8.4). Recording in

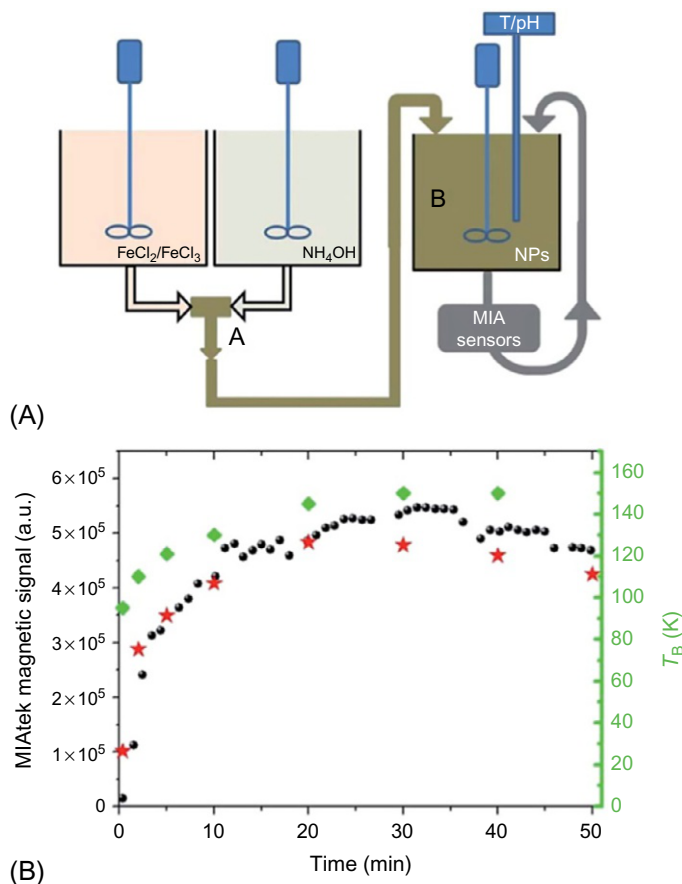


Fig. 8.4

(A) Two-stage synthesis setup: a continuous-flow nucleation; B batch growth reactor. (B) Magnetic measurements by MIAtek (*black* in situ; *star* ex situ) and VSM (losange) (© The Royal Society of Chemistry).

real time the magnetic signal during the reaction allows to monitor reaction progress, to identify deviations, but also, as exemplified by Milosevic et al. [29], to better understand involved mechanisms. This portable device showed to be comparable to far less portable reference techniques such as VSM or SQUID.

Eventually, final users of NPs might find useful to monitor their processes in, e.g., flow cytometers, IVD automates, biomagnetic separation equipments.

Prior to process monitoring, M.P. Nikitin had used a similar setup for the in vivo monitoring of magnetic particles injected in rats (Fig. 8.5). A derivation of the rat's blood flow was passing through the measuring device by means of a catheter. The magnetic signal was continuously recorded in the circulating blood, hence monitoring the concentration of particles after injection. The same device was used to evaluate the particle distribution between rat's organs and its sensitivity was found equal to the detection of radioactive ^{59}Fe -labeled particles.

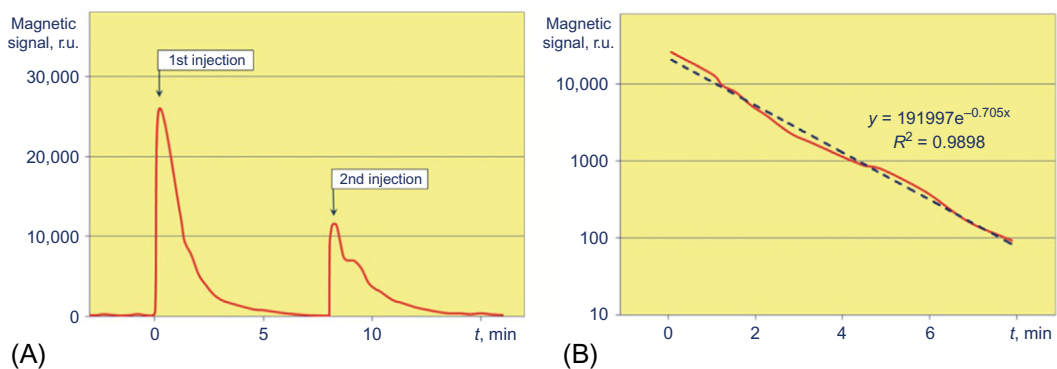


Fig. 8.5

Magnetic monitoring of particle concentration in a mouse tail: (A) after two sequential bead injections of 1 and 0.5 mg; (B) exponential fitting of the first decay curve (100 r.u. = 30 ng particles) (© American Institute of Physics).

These experiments showed that *in vivo* dynamics of injected particles strongly depend on particle type (size, composition, coating, etc.), site of injection, and dose. In an amazingly straightforward setup, he has simply immobilized a mouse, placed its tail inside the coil of the reader, injected 500-nm magnetic beads near its eye (retro-orbital injection), and recorded a magnetic signal in its tail's veins and arteries with time resolution of 2 s. This measurement directly provides half-life of particles in blood circulation and other pharmacokinetic key parameters [30–32].

Building on high sensitivity and absence of background signal from linear diamagnetic living organisms, these experiments pave the way to cheap and portable monitoring of magnetic particle usages in translational research, e.g., optimization of doses for hyperthermia of tumors, evaluation of efficiency of magnetic drug delivery or magnetofection, *in vivo* magnetic immunoassays.

8.2.4 Magnetic Colorization

There is a wide variety of magnetic behaviors across magnetic NPs, based on their size, composition, shape, crystalline structure, dispersity, etc. While magnetic NPs usages are growing, this suggests room for multiplexing, more specifically for life sciences applications wherein it is a key trend.

In 2007, Lenglet first disclosed the upgrade of frequency mixing for the detection, discrimination, and quantification of particles of two kinds when mixed together. Each kind of particle is characterized by a specific magnetic signature based on the shape of the second derivative of its magnetization $M(H)$ at low field, i.e., between -30 kA m^{-1} and $+30 \text{ kA m}^{-1}$ (Fig. 8.6). Appropriate data processing of the signature measured on a mixture of both particles compared to the specific signatures of each particle allows for retrieving the amount of each particle. This paves the way to multiparametric magnetic immunoassays [33,34].

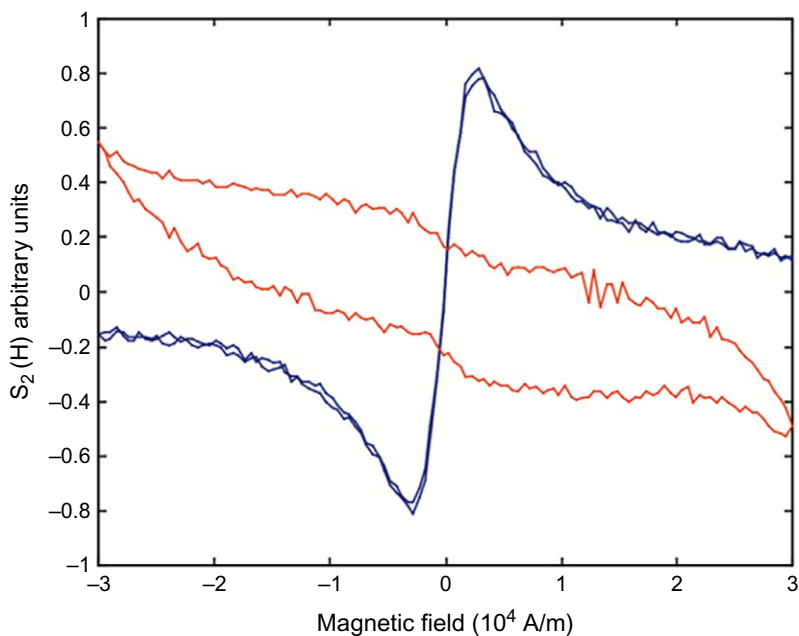


Fig. 8.6

Magnetic signatures of NPs, superparamagnetic (*superimposable back-and-forth curves*), hysteretic (*non-superimposable roundtrip*) (© 2009 Elsevier).

Motte's group experienced a portable reader recording such signatures, MIAplex[®], which was developed by Magnisense (France), for the characterization of a variety of magnetic particles, their potential as labels for multiparametric immunoassays, and moreover the study of their interactions through the alteration of their signature.

They found that the signatures of particles varying in size at similar composition and crystalline structure were different enough to allow discrimination by MIAplex thus providing a reservoir of candidates for labels in magnetic multiparametric assays. They also showed the impact of polydispersity of NPs on their signatures. MIAplex, an easy-to-use benchtop device, provides results comparable to the far more tedious and cumbersome low magnetic field SQUID (LMF SQUID). Sample volume, in the microliters, is about 1000 times smaller; acquisition of the whole signature only requires seconds, about 100 times less than SQUID [35–37]. Besides size, they also explored the potential of particle shape as a differentiator, comparing nanospheres, nanohexagons, nanocubes, and nanorods, all coated with caffeic acid to allow stabilization in physiological conditions. Experimental results were successfully compared to Monte Carlo simulations [38,39].

MIAplex also allows to report particle interactions through their impact on magnetization. Yet, the colloidal stability of NPs is of primary importance for all scientists and engineers working with magnetic NPs. For example, magnetosomes, which are larger, hysteretic NPs, produced by *Magnetospirillum magneticum*, were evaluated under two arrangements, in chains

of tens of particles as extracted from bacteria, and as individual particles after removing the phospholipidic membrane, which ensures chain cohesion. Both arrangements differing by their interactions were easily discriminated by MIAplex [40]. More generally, this benchtop tool can help all those eager to coat/functionalize NPs. For example, the catalytical activity of nano-organocatalysts based on magnetic NPs—which enable easy magnetic recovery—strongly depends on their colloidal status. MIAplex was used to report particle aggregation across various functionalization strategies for enantioselective L-proline organocatalysis based on 10-nm maghemite NPs [41]. Caffeic acid coating and SiO₂ shell passivation are two different strategies leading to stable aqueous ferrofluids from iron oxide NPs. Magnetization second derivatives demonstrated that they are actually differing due to nanoparticle interactions, which alter their magnetic behavior at low magnetic field [42].

Distinguishing bound and unbound NPs in samples, multiplexing assays, measuring in situ the temperature of NPs, those are challenges, which together with MPI developments, have triggered the interest of several academic groups around magnetic particle spectroscopy (MPS), i.e., measuring all an array of harmonics and mixed frequencies, hence generalizing MIAplex, which simply measures the second harmonics of a slowly moving static field.

Based on their simulation works on the frequency distribution of NP magnetization in 2008 [43], Weaver et al., in 2009 were the first to disclose an experimental application for MPS, the in situ estimation of the temperature of magnetic NPs, based on the ratio of the fifth and third harmonics of magnetization in a sinusoidal field. The accuracy was 0.3 K between 20° and 50°. Thanks to the implementation of a calibration curve, the method was found independent of NP concentration and NP size distribution [44]. Far from being anecdotal, the application field is wide, from monitoring in hyperthermia therapies to voxel information enrichment in imaging.

In 2010, they also applied spectroscopic measurement to monitor molecular binding of NPs and quantify the bound fraction. Beyond potential applications already mentioned, it was plausible that MPS could be used to measure binding in vivo, e.g., to aid target imaging [45]. Finally, the same year, they also experimentally proved to be able to quantify simultaneously up to three different magnetic NPs [46], offering alternate strategies for multiparametric assays or multimodal imaging. Since changes in the binding state of NPs or the viscosity of the surrounding medium mainly affect the contribution of Brownian relaxation to the spectrum, they have termed this approach magnetic spectroscopy of nanoparticle Brownian motion.

And finally, in 2015, Philips disclosed the first experimental evidence of the feasibility of multicolor magnetic particle imaging [47]. They were able to reconstruct separate images for different particles obtained from their preclinical demonstrator system and to combine them into a single color-coded image.

Other teams have explored further these potentialities, e.g., magnetic particle colorization [48], temperature measurement [49], measurement of magnetic NPs bound to cancer cells [50].

8.3 Neel Effect for Magnetic Field Sensing

8.3.1 Current Sensors

Current sensors can be split into two categories: shunt resistors, which directly measure current through a voltage drop; and magnetic field sensors, which measure current-induced magnetic fields to retrieve the original current. While galvanic insulated, protected against overcurrent spikes, and sparsely dissipating, the latter have been the focus of considerable development efforts with a wide offer, ranging from conventional current transformers and Hall effect sensors to innovative fluxgate or giant magnetoresistive (GMR) sensors. Of those, Rogowski sensors are well known for measuring alternating current (AC) such as high-speed transient, pulsed currents, or power frequency sinusoidal currents. They comprise an air-cored coil placed around the conductor in a toroidal shape. Simple to retrofit, the clip-around Rogowski coil sensor is thin, lightweight, flexible, and robust. The main drawback of Rogowski coil technology is that it only measures AC currents.

Initially patented by Lenglet in 2005, Neel Effect magnetic field sensors and derived current sensors, while sharing the same user-friendly design as Rogowski coils, allow for measuring DC currents [51]. Unlike magnetic particle sensors, which implement two-frequency excitation coils as transducer to probe unknown magnetic NPs, magnetic field sensors based on Neel Effect rely on a one-frequency excitation coil stuffed with a superparamagnetic core. In presence of an unknown magnetic field, intermodulation-demodulation with the excitation frequency will allow for retrieving the magnetic field components, both constant and harmonic.

The superparamagnetic core is a composite material comprising magnetic NPs, the nonlinear magnetic behavior of which carries the mixing Neel Effect, and of a polymeric matrix, which maintains NPs independent from each other and carries the required mechanical properties. The matrix can be thermoplastic, e.g., a polypropylene/polyethylene copolymer, or thermoset, e.g., an epoxy resin. NP-loaded PP-PE copolymer can be extruded into flexible rods, around which the excitation/pick-up coil is wound, thus providing flexibility to the transducer, which can be clipped around the conductor. Varying the features of the NPs embedded in the composite, i.e., their chemical composition, their shape, their average size and size distribution, allows for adapting the sensor to operating conditions, e.g., sensitivity requirements, immunity to crosstalk.

Neel Effect current sensors were further explored and optimized through a collaboration between Neology (France) and ENS Cachan (Fig. 8.7) [52–55].

Neel Effect current sensors got commercial in 2012 for test and measurement applications, i.e., benchwork at R&D laboratories, quality control in manufacturing plants, diagnostics of electrical equipment, windmills, solar farms, or for embedded energy metering. They usually combine a Rogowski coil together with the Neel Effect coil in order to provide DC/AC measurements over a wide range of frequencies. By design, Rogowski coils don't provide DC measurements. They are also known to be poor sensors in the low frequencies, e.g., 50 Hz. Unexpectedly it was found that there is a synergistic effect while combining both technologies.

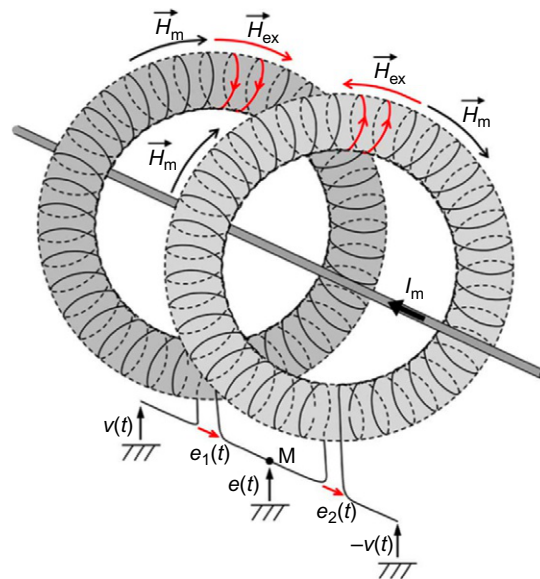


Fig. 8.7

Current sensor topology implementing two cores featuring homogeneous windings wound in opposite directions and connected in series (© 2012 IEEE).

The measurements in the low frequencies are far better than expected if one would simply add the performance of each coil.

In 2015, breakthrough patent applications filed by Cima [56] and Augais [57] disclosed dramatically optimized driving and transducer geometry, thus allowing for compact, cheap, battery-based, very sensitive DC/AC sensors with low crosstalk. This paves the way to a breakthrough design, the shunt-like sensor. While still galvanic insulated, this one can be mounted inside the conductor, for example a busbar, instead of clipped around. It even can be integrated as a part of a connector, into a multifunctional smart connector.

Applications of Neel Effect current sensors in aircraft power systems are most promising whereas “more electrical” aircrafts (MEA) require new, both contactless and lightweight, current sensors for control and command. The MEA concept provides for the utilization of electric power for all nonpropulsive systems. Traditionally these nonpropulsive systems are driven by a combination of different secondary power sources such as hydraulic, pneumatic, mechanical, and electrical. Recent technological advances in the field of power electronics, fault-tolerant architecture, electrohydrostatic actuators, flight control systems, high-density electric motors, power generation, and conversion systems have ushered the era of the MEA. Neel Effect sensors have been evaluated within CleanSky, the largest European research program aimed at reducing CO₂, gas emissions and noise levels produced by aircraft [58].

Beyond aircrafts given as an example here, the demand for DC current sensors is raising very fast with DC spreading wide over all industrial fields. First, fast-growing renewable power sources are intrinsically DC with photovoltaic generation, and even with windmills, which most often require a DC phase before connection to the grid. Both request embedded DC monitoring for control-command and optimization purpose. Second, DC distribution enjoys a spectacular revival, driven by HVDC electric power transmission (also called power super highway), and lately ultra-HVDC with, e.g., a coming land link in China featuring a 1100-kV voltage, a 3000-km length and 12 GW of power. Allowing transmission between unsynchronized AC grids, HVDC links allow power exchanges, hence optimization, at continental scale. They also allow power transmission from sunny or windy remote production locations to consumers, e.g., North Sea or Mediterranean region. And, finally, DC consumptions are flourishing with the replacement of traditional AC consumers such as lighting or TV sets, the plugging of billions of electronic devices, and moreover electrical mobility. The latter will request building a brand-new side-system carefully monitored to avoid breaking down the main. These trends all commend a variety of new sensors, from the cheapest due in every downstream converter, to the most sophisticated for the control-command of IGBTs or the detection of hazardous DC leakages in AC networks. There is a wide potential of applications for Neel Effect current sensors.

8.3.2 Position Sensors

Besides current sensors, magnetic measurements are widely used in position sensors to report the position of a moving part. A patent by Lenglet [59] discloses the implementation of Neel Effect for such purpose.

MIAPlex[®], MIAtek[®], MIAstrip[®] and MIAflo[®] are trademarks owned by Magnisense (France). Neel Effect[®] is a trademark owned by Neelogy (France).

References

- [1] L. Néel, Théorie du traînage magnétique des ferromagnétiques en grains fins avec application aux terres cuites, *Ann. Géophys.* 5 (1949) 99–136.
- [2] T. Paoli, J. Svacek, Derivative measurement by frequency mixing, *Rev. Sci. Instrum.* 47 (9) (1976) 1016–1019.
- [3] P.I. Nikitin, P.M. Vetoshko, Analysis of biological and/or chemical mixtures using magnetic particles, 2000. Russian Patent 2,166,751.
- [4] P.I. Nikitin, P.M. Vetoshko, M.V. Valeiko, Book of Abstracts of Eurosensors XVII Conference, Guimaraes, Portugal, 2003, pp. 140–141. Available from: <https://repositorium.sdum.uminho.pt/handle/1822/4837>.
- [5] P.I. Nikitin, P.M. Vetoshko, T.I. Ksenevich, New type of biosensor based on magnetic nanoparticle detection, *J. Magn. Magn. Mater.* 311 (1) (2007) 445–449.
- [6] P.I. Nikitin, P.M. Vetoshko, T.I. Ksenevich, Magnetic immunoassays, *Sens. Lett.* 5 (1) (2007) 296–299.
- [7] M.H.F. Meyer, M. Hartmann, H.J. Krause, G. Blankenstein, B. Mueller-Chorus, J. Oster, P. Miethe, M. Keusgen, CRP determination based on a novel magnetic biosensor, *Biosens. Bioelectron.* 22 (2007) 973–979.

- [8] M.H.F. Meyer, H.J. Krause, M. Hartmann, P. Miethe, J. Oster, M. Keusgen, *Francisella tularensis* detection using magnetic labels and a magnetic biosensor based on frequency mixing, *J. Magn. Magn. Mater.* 311 (1) (2007) 259–263.
- [9] M.H.F. Meyer, M. Stehr, S. Bhujji, H.J. Krause, M. Hartmann, P. Miethe, M. Singh, M. Keusgen, Magnetic biosensor for the detection of *Yersinia pestis*, *J. Microbiol. Methods* 68 (2) (2007) 218–224.
- [10] H.J. Krause, N. Wolters, Y. Zhang, A. Offenhäusser, P. Miethe, M.H.F. Meyer, M. Hartmann, M. Keusgen, Magnetic particle detection by frequency mixing for immunoassay applications, *J. Magn. Magn. Mater.* 311 (1) (2007) 436–444.
- [11] A.V. Orlov, J.A. Khodakova, M.P. Nikitin, A.O. Shepelyakovskaya, F.A. Brovko, A.G. Laman, E.V. Grishin, P.I. Nikitin, Magnetic immunoassay for detection of staphylococcal toxins in complex media, *Anal. Chem.* 85 (2) (2013) 1154–1163.
- [12] H.B. Hong, H.J. Krause, K.B. Song, C.J. Choi, M.A. Chung, S.W. Sona, A. Offenhäusser, Detection of two different influenza A viruses using a nitrocellulose membrane and a magnetic biosensor, *J. Immunol. Methods* 365 (1–2) (2011) 95–100.
- [13] L. Aldaz-Carroll, S. Richon, V. Dangles-Marie, M. Cocquebert, T. Fournier, F. Troalen, D. Stevens, B. Guery, A. M. Hersant, J. Guibourdenche, A. Nordor, A. Pecking, D. Bellet, Specific detection of type II human chorionic gonadotropin beta subunit produced by trophoblastic and neoplastic cells, *Clin. Chim. Acta* 444 (2015) 92–100.
- [14] F. Gas, B. Baus, J. Queré, A. Chapelle, C. Dreanno, Rapid detection and quantification of the marine toxic algae, *Alexandrium minutum*, using a super-paramagnetic immunochromatographic strip test, *Talanta* 147 (2016) 581–589.
- [15] A.V. Orlov, S.L. Znoyko, V.R. Cherkasov, M.P. Nikitin, P.I. Nikitin, Multiplex biosensing based on highly sensitive magnetic nanolabel quantification: rapid detection of botulinum neurotoxins a, B, and E in liquids, *Anal. Chem.* 88 (21) (2016) 10419–10426.
- [16] F. Geinguenaud, I. Souissi, R. Fagard, L. Motte, Y. Lalatonne, Electrostatic assembly of a DNA superparamagnetic nano-tool for simultaneous intracellular delivery and in situ monitoring, *Nanomedicine: NBM* 8 (2012) 1106–1115.
- [17] F. Geinguenaud, I. Souissi, R. Fagard, Y. Lalatonne, L. Motte, Easily controlled grafting of oligonucleotides on $\gamma\text{Fe}_2\text{O}_3$ nanoparticles: physicochemical characterization of DNA organization and biological activity studies, *J. Phys. Chem. B* 118 (2014) 1535–1544.
- [18] F. Geinguenaud, C. Banissi, F. Carpentier, L. Motte, Iron oxide nanoparticles coated with a phosphorothioate oligonucleotide and a cationic peptide: exploring four different ways of surface functionalization, *Nano* 5 (2015) 1588–1609.
- [19] S. Richard, M. Boucher, A. Saric, A. Herbet, Y. Lalatonne, P.X. Petit, S. Mériaux, D. Boquet, L. Motte, Optimization of pegylated iron oxide nanoplatfoms for antibody coupling and bio-targeting, *J. Mater. Chem. B* 5 (2017) 2896–2907.
- [20] V.O. Shipunova, M.P. Nikitin, P.I. Nikitin, S.M. Deyeva, MPQ-cytometry: a magnetism-based method for quantification of nanoparticle-cell interactions, *Nano* 8 (2016) 12764–12772.
- [21] T. Augais, French Patent FR 3,038,060, in: Appareil de mesure d'une quantité de matériau superparamagnétique, 2015.
- [22] B. Gleich, Verfahren zur Ermittlung der räumlichen Verteilung magnetischer Partikel, 2001. German Patent DE 10,151,778.
- [23] B. Gleich, J. Weizenecker, Tomographic imaging using the nonlinear response of magnetic particles, *Nature* 435 (2005) 1214–1217.
- [24] J. Weizenecker, J. Borgert, B. Gleich, A simulation study on the resolution and sensitivity of magnetic particle imaging, *Phys. Med. Biol.* 52 (2007) 6363–6374.
- [25] J. Weizenecker, B. Gleich, J. Rahmer, H. Dahnke, J. Borgert, Three-dimensional real-time *in vivo* magnetic particle imaging, *Phys. Med. Biol.* 54 (5) (2009) L1–L10.
- [26] E. Saritas, P. Goodwill, L. Croft, J. Konkle, K. Lu, B. Zheng, S. Conolly, Magnetic particle imaging (MPI) for NMR and MRI researchers, *J. Magn. Magn. Mater.* 229 (2013) 116–126.
- [27] T. Knopp, N. Gdaniec, M. Möddel, Magnetic particle imaging: from proof of principle to preclinical applications, *Phys. Med. Biol.* 62 (2017) R124–R178.

- [28] A. LaGrow, M. Besenhard, R. Hachani, N.T.K. Thanh, Experimental considerations for magnetic nanoparticle synthesis and surface functionalization for clinical applications, in: N.T.K. Thanh (Ed.), *Clinical Applications of Magnetic Nanoparticles*, CRC Press, Taylor & Francis, Boca Raton, London, New York, 2018. <https://www.ncbi.nlm.nih.gov/nlmcatalog/101713332>.
- [29] I. Milosevic, F. Warmont, Y. Lalatonne, L. Motte, Magnetic metrology for iron oxide nanoparticle scaled-up synthesis, *RSC Adv.* 4 (2014) 49086–49089.
- [30] M.P. Nikitin, M. Torno, H. Chen, A. Rosengart, P.I. Nikitin, Quantitative real-time *in vivo* detection of magnetic nanoparticles by their non-linear magnetization, *J. Appl. Phys.* 103 (7) (2008). 07A304.
- [31] M.P. Nikitin, P.M. Vetoshko, N.A. Brusentsov, P.I. Nikitin, Highly sensitive room-temperature method of non-invasive *in vivo* detection of magnetic nanoparticles, *J. Magn. Mater.* 321 (10) (2009) 1658–1661.
- [32] M.P. Nikitin, M. Yuriev, N. Brusentsov, P. Vetoshko, P.I. Nikitin, Non-invasive *in vivo* mapping and long-term monitoring of magnetic nanoparticles in different organs of animals, *AIP Conf. Proc.* 1311 (2010) 452–457.
- [33] L. Lenglet, Dispositif et procédé de mesure de la masse de matériau magnétique, appareil d'analyse incorporant ce dispositif, 2007. French Patent FR 2,914,060.
- [34] L. Lenglet, Multi-parametric magnetic immunoassays utilizing non-linear signatures of magnetic labels, *J. Magn. Mater.* 321 (10) (2009) 1639–1643.
- [35] Y. Lalatonne, F. Benyettou, D. Bonnin, N. Lièvre, P. Monod, M. Lecouvey, P. Weinmann, L. Motte, Characterization of magnetic labels for bioassays, *J. Magn. Mater.* 321 (10) (2009) 1653–1657.
- [36] C. de Montferrand, Y. Lalatonne, D. Bonnin, N. Lièvre, M. Lecouvey, P. Monod, V. Russier, L. Motte, Size-dependent nonlinear weak-field magnetic behavior of maghemite nanoparticles, *Small* 8 (12) (2012) 1945–1956.
- [37] C. de Montferrand, Y. Lalatonne, D. Bonnin, L. Motte, P. Monod, Non-linear magnetic behavior around zero field on a assembly of superparamagnetic nanoparticles, *Analyst* 137 (2012) 2304–2308.
- [38] C. de Montferrand, L. Hu, I. Milosevic, V. Russier, D. Bonnin, L. Motte, A. Brioude, Y. Lalatonne, Iron oxide nanoparticles with size, shape and composition resulting in different magnetization signatures as potential labels for multiparametric detection, *Acta Biomater.* 9 (4) (2012) 6150–6157.
- [39] V. Russier, C. de Montferrand, Y. Lalatonne, L. Motte, Magnetization of densely packed interacting magnetic nanoparticles with cubic and uniaxial anisotropies: a Monte Carlo study, *J. Appl. Phys.* 114 (2013). 143904 (11 pages).
- [40] E. Alphandéry, L. Lijeour, Y. Lalatonne, L. Motte, Different signatures between chemically and biologically synthesized nanoparticles in a magnetic sensor: a new technology for multi parametric detection, *Sensors Actuators* 147 (2) (2010) 786–790.
- [41] E. Nehlig, L. Motte, E. Guénin, Nano-organocatalyst synthesis: Boc vs Fmoc protection, *Catal. Today* 208 (2013) 90–96.
- [42] C. de Montferrand, L. Hu, Y. Lalatonne, N. Lièvre, D. Bonnin, A. Brioude, L. Motte, SiO₂ versus chelating agent@ iron oxide nanoparticles: interactions effect in nanoparticles assemblies at low magnetic field, *J. Sol-Gel Sci. Technol.* 75 (3) (2015) 572–579.
- [43] J. Weaver, A. Rauwerdink, C. Sullivan, I. Baker, Frequency distribution of the nanoparticle magnetization in the presence of a static as well as a harmonic magnetic field, *Med. Phys.* 35 (2008) 1988–1994.
- [44] J.B. Weaver, A.M. Rauwerdink, E.W. Hansen, Magnetic nanoparticle temperature estimation, *Med. Phys.* 36 (5) (2009) 1822–1829.
- [45] A.M. Rauwerdink, J.B. Weaver, Measurement of molecular binding using the Brownian motion of magnetic nanoparticle probes, *Appl. Phys. Lett.* 96 (3) (2010). 033702.
- [46] A.M. Rauwerdink, A.J. Giustini, J.B. Weaver, Simultaneous quantification of multiple magnetic nanoparticles, *Nanotechnology* 21 (2010). 455101 (5 pages).
- [47] J. Rahmer, A. Halkola, B. Gleich, I. Schmale, J. Borgert, First experimental evidence of the feasibility of multi-color magnetic particle imaging, *Phys. Med. Biol.* 60 (2015) 1775–1791.
- [48] L. Tu, K. Wu, T. Klein, J.P. Wang, Magnetic nanoparticles colourization by a mixing-frequency method, *J. Phys. D: Appl. Phys.* 47 (15) (2014)155001 (6 pages).
- [49] E. Garaio, J.M. Collantes, J.A. Garcia, F. Plazaola, O. Sandre, Harmonic phases of the nanoparticle magnetization: an intrinsic temperature probe, *Appl. Phys. Lett.* 107 (2015)123103.

- [50] B. Ficko, C. NDong, P. Giacometti, K. Griswold, S. Diamond, A feasibility study of nonlinear spectroscopic measurement of magnetic nanoparticles targeted to cancer cells, *IEEE Trans. Biomed. Eng.* 64 (5) (2017).
- [51] L. Lenglet, Capteurs de champ magnétique et de courant, procédé de commande et noyau magnétique pour ces capteurs, (2005) French Patent FR 2,891,917.
- [52] L. Cima, Y. Maniouloux, Capteur de circulation de champ magnétique et capteur de courant mettant en œuvre un tel capteur, (2008) French Patent FR 2,931,945.
- [53] E. Vourc'h, P.Y. Joubert, G. Cinquin, Y. Maniouloux, L. Cima, Novel magnetic field and current sensors based on superparamagnetic transducers, *Sens. Lett.* 7 (3) (2009) 1–6.
- [54] E. Vourc'h, P.Y. Joubert, L. Cima, Analytical and numerical analyses of a current sensor using non-linear effect in a flexible magnetic transducer, *Prog. Electromagn. Res.* 99 (2009) 323–338.
- [55] E. Vourc'h, Y. Wang, P.Y. Joubert, B. Revol, A. Couderette, L. Cima, Neel effect toroidal current sensor, *IEEE Trans. Magn.* 49 (1) (2013) 81–84.
- [56] L. Cima, Capteur de courant et de tension DC isolé à faible diaphonie, 2015. French Patent FR 3,034,526.
- [57] T. Augais, Appareil pour mesurer un champ magnétique, 2015. French Patent FR 3,038,063.
- [58] A. Bouzourene, T. Bensalah, L. Cima, A. Couderette, in: Investigation of Neel effect technology for current sensors in next-generation aeronautical applications, Proceedings of the 2011 14th European Conference on Power Electronics and Applications, IEEE, 2011.
- [59] L. Lenglet, Dispositif et procédé de mesure de la position d'une pièce mobile, 2006. French Patent FR 2,909,169.

This page intentionally left blank

Ferrimagnetic Heterostructures for Applications in Magnetic Recording

Florin Radu, Jaime Sánchez-Barriga¹

Helmholtz-Zentrum Berlin für Materialien und Energie, Berlin, Germany

¹*Corresponding author: jaime.sanchez-barriga@helmholtz-berlin.de*

9.1 Magnetic Recording: Fundamentals and Perspectives

The computers and electronic devices have become indispensable companions in our everyday life through an abundance of applications in education, medicine, automotive industry, and all the way to space industry. Most important material traits involved in these devices at the atomic and nanometer scales are the electron's charge and spin, which may couple to each other through direct and indirect interactions, all building up a rather new field of research called "spintronics" [1, 2]. The functionality of all these interactions manifests itself in storing and removing information on physical devices, encoding and decoding transferred information, sensing properties to external stimuli, and imaging technologies of biological and hard matter, as well as in the prospected interfacing between life and machines. The most fascinating property of matter continues to be magnetism because its natural ability to sense and interact with external magnetic fields. A ground-breaking example of the early days is the development of the compass, where a magnet orients in the rather weak Earth's magnetic field. Similarly, the incorporation of magnetic media in currently existing technologies for information transfer and storage is one of the most far-reaching developments of our modern era.

Since more than a half century, extensive research activities have been devoted to understanding unique properties of magnetic materials. The discovery of interlayer exchange coupling (IEC) [3] and giant magnetoresistance (GMR) [4, 5] has led to an unprecedented technological advance in storage media, read-out sensors, and nonvolatile magnetic random access memories. In consequence, magnetic recording holds 90% of all storage media technology that is available today. On the research front, the discovery of IEC and GMR triggered fundamental understanding of spin-dependent transport properties in magnetic thin films and multilayers. For spin-valve systems, which typically consist of two ferromagnetic layers separated by a nonmagnetic spacer, the crucial role of IEC manifests in both the sign and strength of the coupling following a damped oscillatory behavior as a function of the spacer

thickness. Equally important, the GMR effect, observed for the first time in Fe/Cr [4] and Fe/Cr/Fe multilayers [5], manifests as a large change in resistivity when switching the magnetization of the ferromagnetic layers from an antiparallel configuration at zero magnetic field to a parallel configuration in an applied magnetic field. Both IEC and GMR effects are widely employed nowadays in magnetic recording technologies, and represent prominent examples of the long-term benefit of industrial applications from fundamental research.

Only a decade after the discovery of the GMR, hard-disk read heads essentially based on this effect became the first generation of spintronic devices that revolutionized the industry of magnetic storage. The impact of GMR-based devices on the underlying technology, where the information is stored as a sequence of magnetic *bits* or domains, can be seen in Fig. 9.1A by the time evolution of the areal bit density since the first commercial magnetic hard-disk drive became available in the late 1950s. The areal bit density describes how many bits can be stored per surface area. We clearly see various stages that changed the annual growth rate of storage density (CGR). After the introduction of the first magnetoresistive read head in 1992, initially based on the anisotropic magnetoresistance (AMR) effect in thin films [6], the CGR increased up to $\sim 60\%$. At this stage, the thickness of the films used in the magnetic head itself but also in the track-recording medium within the disk where several ~ 100 nm in thickness. Subsequently, after the implementation of the first hard-disk read heads based on the GMR effect in 1998, the advancing technology reached a stage with a CGR of 100%, which impressively means about 50 million times increase in the areal bit density with respect to the starting technology in the 1950s. At this point, the hard drives were exclusively operated using the so-called longitudinal magnetic recording (LMR) technology [7], which means that

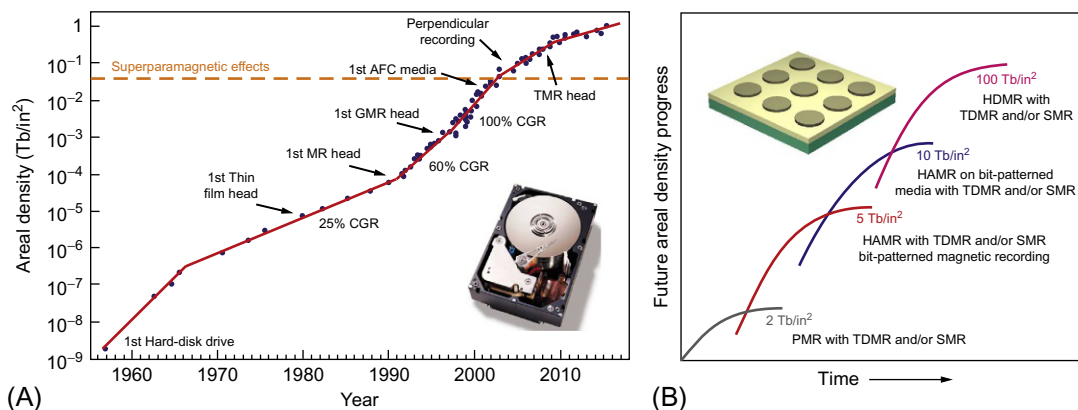


Fig. 9.1

(A) Time evolution of the areal bit density since the first commercial magnetic hard drive disk became available in the late 1950s. The *inset* shows a top view of the IMB hard drive Ultrastar 36ZX with the cover removed. This model was developed in 1999 using GMR head technology, and reached an areal density of 3.5×10^{-3} Tb/in². (B) Future progress of the areal density, which is expected to continuously increase well beyond 10 Tb/in² due to emergent new technologies (see text). *Inset*: Sketch of bit-patterned recording media.

the in-plane orientation of the bit magnetization within the recording medium is parallel to the surface of the disk.

9.1.1 Perpendicular Magnetic Recording and Superparamagnetism

Of particular importance in the evolution toward higher areal densities is the transition from longitudinal to perpendicular magnetic recording (PMR) [8], where differently from LMR the out-of-plane orientation of the bit magnetization is perpendicular to the surface of the disk. One of the fundamental advantages of PMR is that it allows to reach higher magnetic write fields as compared to LMR, and thus to use materials with higher magnetic anisotropy K_u . The possibility of using high- K_u materials is critically important to maintain the stability of the magnetic bits against superparamagnetic effects [8–12], which eventually might cause the bit magnetization to flip due to thermal fluctuations and hence lead to information loss. Because of this reason, the transition to PMR has been accompanied by a change in the choice of materials for the magnetic recording medium, which evolved from traditional recording materials such as FePd [13], MnAl [14–16], or CoCrPt [17] to materials with high magneto-crystalline anisotropy such as FePt [18–20], CoPt [21–23], or SmCo₅ [24–26] to name a few examples. In practice, the magnetic recording layer is in reality replaced by a stack of layers to ensure uniformly sized and well-oriented magnetic grains with out-of-plane magnetization. In addition, a soft-magnetic underlayer is introduced to channel the magnetic flux of the write head back into the pole of the read head, allowing sensitivity to the magnetic state of individual bits through smaller stray fields that do not affect the magnetization of written bits. In general terms, the transition to PMR technology allowed to achieve areal densities substantially larger than the established superparamagnetic limit of magnetic recording. Indeed, as one can see in Fig. 9.1A, at present the areal density approaches the 1 Tb/in² density point, which means that each individual bit, despite being composed by several magnetic grains, is only ~ 25 nm² in size. A second aspect concerning superparamagnetic effects is related to the bit volume V , because the time between fluctuations of the bit magnetization is essentially proportional to $K_u V$ [12]. This quantity determines the nonvolatility of the magnetic medium. Therefore, to further decrease the bit volume, for example, by using materials with smaller grains, it is in principle necessary to accordingly increase K_u [27]. This implies that the higher magnetic fields provided by PMR are required for the write process.

9.1.2 Future Areal Density Progress and Emergent Technologies

If we now look in Fig. 9.1B at the expected future progress of the areal bit density, we anticipate a remarkable increase by at least two orders of magnitude within the next 10 years due to the continuous development of emergent technologies such as heat-assisted magnetic recording (HAMR) [28–30] and bit-patterned magnetic recording [30–34]. It is also expected that further

increase of the areal density will result from the combination of these technologies with shingled magnetic recording (SMR) [35, 36] and/or two-dimensional magnetic recording (TDMR) [37, 38]. SMR is an extension of current PMR technology that writes new magnetic tracks that overlap with part of the previously written tracks. This allows to utilize narrower tracks and thus to increase the areal density. TDMR, on the other hand, uses an array of heads to read data from either one, or several nearby tracks. This method allows to minimize intertrack interference effects due cross-talk between neighboring magnetic tracks [39] and, similar to SMR, to further increase the areal density by accessing the magnetic information from narrower tracks. Hence, it is expected that the nearest-future increase in the areal density will be caused at first by a progressive evolution from PMR-based technology into one that combines TDMR and/or SMR with HAMR on high-anisotropy granular media.

9.1.3 Heat-Assisted Magnetic Recording

HAMR takes advantage of thermal laser heating of the magnetic medium to write data using moderate recording fields, which in practical applications of today's recording technology are limited to about 2.4 Tesla because of several technological challenges [40]. The applied magnetic field combined with a focused laser spot allows to reverse the magnetization of the grains within the heated area, and the process is fundamentally distinct from conventional LMR and PMR technologies (see Fig. 9.2). In consequence, the overall HAMR process allows to use materials with even smaller grain size and much higher coercivity at room temperature, which not only improves the long-term stability of the magnetic information but also

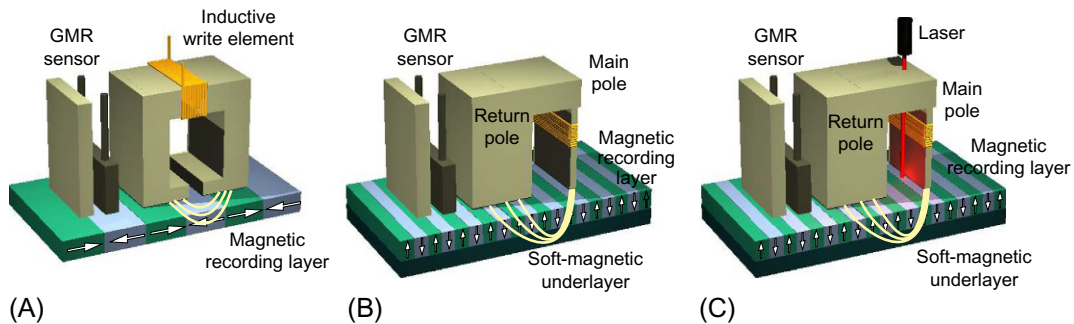


Fig. 9.2

Sketches comparing (A) longitudinal magnetic recording (LMR), (B) perpendicular magnetic recording (PMR), and (C) heat-assisted magnetic recording (HAMR) technologies. In LMR and PMR, the data bits are aligned parallel and perpendicular to the surface of the disk, respectively. The latter configuration reduces the repelling forces between bits and enables higher write magnetic fields, allowing higher areal recording densities. HAMR uses thermal laser heating of the magnetic medium to write data at high temperatures, enabling the use of smaller write magnetic fields and thus magnetic recording layers with smaller grain size and higher anisotropy. This not only improves the long-term stability of the magnetic information but also allows to further increase the areal bit density.

allows writing bits on a much smaller area than before. Moreover, as the writing process occurs at elevated temperature, a potential advantage of HAMR is that there is much less compromise between the room temperature high saturation bit magnetization and the maximum possible magnetic field that can be applied using conventional writing heads.

At the same time, during the HAMR process the magnetic recording medium needs to be heated to temperatures above its Curie temperature T_C , which for high-anisotropy HAMR materials such as FePt, CoPt, or SmCo₅ lies in a high-temperature range between ~ 750 to ~ 1000 K [28]. The idea behind is to substantially reduce the magnetic coercivity of the recording medium during the writing process, so that it is possible to use as small as possible write magnetic fields to induce a new magnetic state during the cooling process. Engineering challenges are thus the incorporation of small laser diodes in recording heads, achieving high enough temperatures with tightly focused laser beams, as well as efficient control of heat dissipation. In this context, there have been also attempts to reduce the high T_C of the recording layers with doping. In one example, Ni was used as doping to reduce the T_C of FePt; however, at the same time the anisotropy decreases [41]. While the HAMR process can be seen as an analog of magneto-optical recording [42, 43], the very first generation of commercially available HAMR hard drives are expected to take advantage of a magnetoresistive element for the readout of magnetic information, as sketched in Fig. 9.2C. The technical feasibility of HAMR using this approach was first demonstrated in 2006 [44]. This was followed by a demonstration of a storage density of ~ 1 Tb/in² and a working prototype of noncommercial HAMR hard drive in 2013 [45]. Most recently, HAMR recording at an areal density of about 1.4 Tb/in² was achieved using plasmonic near-field transducers and high anisotropy granular FePt media [29]. It should be mentioned that other approaches of energy-assisted magnetic recording besides HAMR, such as microwave-assisted magnetic recording (MAMR), are currently being explored at the fundamental level [46, 47]. The key idea behind MAMR is to replace laser heating by an AC magnetic field of high frequency applied on the recording layer, and in this way increase the effectiveness of the writing process by promoting reversal of the bit magnetization [48, 49].

9.1.4 Heat-Assisted Magnetic Recording on Bit-Patterned Media

On the other hand, as recent advances in plasmonics and near-field optics pave the way for focusing and transmitting optical energy down to laser spot sizes beyond the diffraction limit of current optics [28, 50, 51], the combination of HAMR and bit-patterned media emerges as one of the most promising magnetic recording technologies of the nearest future (see Fig. 9.3). Bit-patterned magnetic recording uses a uniform array of nanometer-sized magnetic islands [52], usually grown in the form of lithographically defined magnetic dots [53–55], each of which stores 1 bit of information. This is in contrast to current granular media where each bit is composed by hundreds of magnetic grains, and thus stored in a much larger area. Moreover, while in granular media the energy barrier to overcome the effect of superparamagnetism is proportional to the grain volume, in bit-patterned media the energy

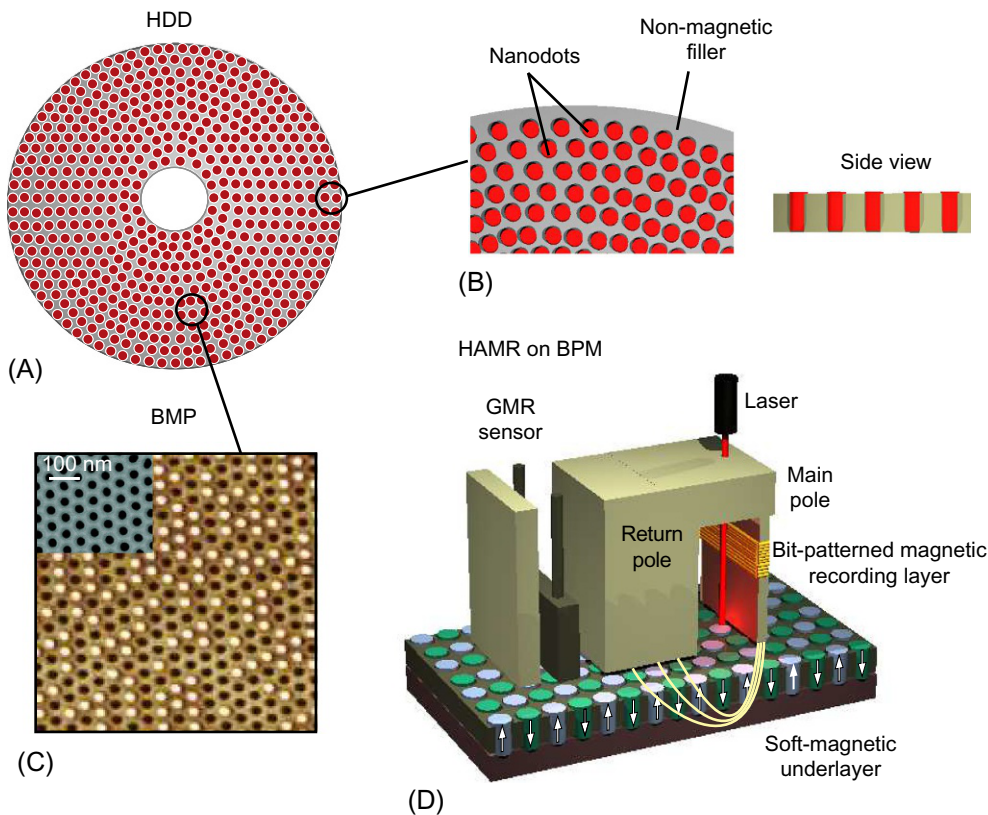


Fig. 9.3

(A) Schematics of hard-disk drive (HDD) patterned with circular tracks of magnetic nanodots. (B) Zoom-in showing a sketch of the nanodot array, which is embedded in a nonmagnetic template. On the *right*, the corresponding side view is shown. (C) Magnetic force microscopy (MFM) image of bit-patterned media. *Dark and white dots* represent opposite magnetization directions. *Inset*: Scanning electron microscopy (SEM) image of a patterned alumina membrane. The *period between dots* is about 100 nm, and the *nominal dot radius* about 24 nm. (D) Sketch illustrating the combination of heat-assisted magnetic recording (HAMR) and bit-patterned media. (Taken from M. Albrecht, G. Hu, A. Moser, O. Hellwig, B.D. Terris, *Magnetic dot arrays with multiple storage layers*, *J. Appl. Phys.* 97 (10) (2005) 103910, <https://doi.org/10.1063/1.1904705>.)

barrier ultimately depends on the strong lateral exchange coupling between magnetic grains within each island [52, 55]. In other words, due to the strong exchange coupling, the energy barrier to overcome superparamagnetic effects in bit-patterned media becomes proportional to the island volume, rather than to the volume of individual grains within each island. As a result, with this alternative technology, it is possible to further increase the areal bit density by substantially reducing the diameter of the islands and at the same time maintain their thermal stability [30–34, 52, 55].

Bit-patterned magnetic recording thus replaces the previously unpatterned hard-disk drive of granular media by a disk that contains an array of nanometer-sized dots, possibly arranged along circular tracks, and with each dot containing a well-defined magnetic state, as shown in Fig. 9.3a–c. In this context, the ultimate challenge of the near-future recording technology is to achieve the so-called heated-dot magnetic recording (HDMR), which aims at focusing the laser spot down to a size of the order of the dot dimensions, so that only a single dot is heated in every writing step (see sketch in Fig. 9.3d). This is not an impossible challenge if we assume that the incorporation of near-field optics and plasmonics in near-future magnetic recording technology will allow to focus the laser spot down to sizes well below $25\text{--}50\text{ nm}^2$ in operation conditions [28, 50, 51, 56].

9.1.5 Spin-Valve Systems for Magnetic Read Heads

Coming back to the time evolution of the areal bit density shown in Fig. 9.1A, another critically important aspect that has marked the continuous increase of the areal density up to the present date concerns the use of antiferromagnetically coupled (AFC) media [57, 58] and the substitution in 2005 of GMR read heads by spin-valve sensors based on the tunneling magnetoresistance [59, 60]. This takes advantage of spin-dependent tunneling effects across a thin insulating barrier that replaces the nonmagnetic metallic spacer of conventional spin valves. To capture this evolution in more detail, in Fig. 9.4 several basic coupling mechanisms for the realization of spin valves for the read heads of storage devices are depicted.

The original aim was to orient two ferromagnetic layers in a parallel or antiparallel manner in order to create a binary basis for the AMR reading. To this end, one can consider splitting a ferromagnetic film into two parts by using an imaginary vacuum layer. For a weak in-plane

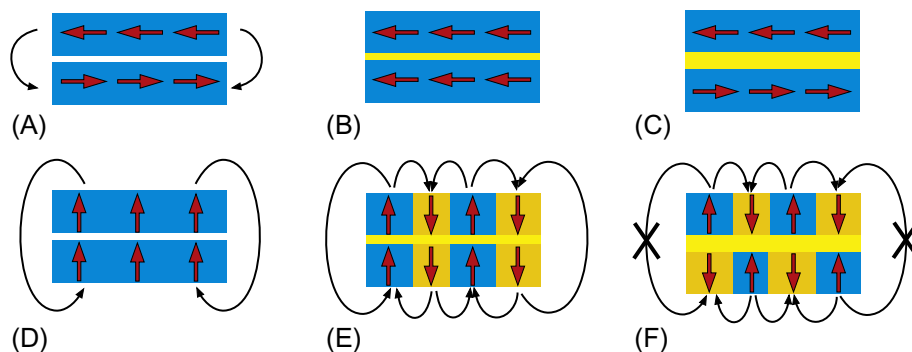


Fig. 9.4

Schematics of several basic coupling mechanisms for the realization of spin valves for the read heads of storage devices. (A) Dipolar coupling, (B) ferromagnetic coupling, and (C) antiferromagnetic coupling for a spin-valve system with in-plane magnetic anisotropy. (D) Stray-field coupling, (E) ferromagnetic coupling, and (F) antiferromagnetic coupling for a spin-valve system with out-of-plane magnetic anisotropy.

magnetic anisotropy of the film, one would expect that an antiparallel ground-state orientation will occur due to the dipolar coupling between both layers. This antiparallel orientation can then be turned parallel by applying external magnetic fields.

In practice, separating two ferromagnetic layers is achieved by introducing a nonmagnetic metallic layer during the sample growth. In doing so, the observation is that not only an AF orientation can take place, but also that the layers can stay parallel oriented. This is due to the IEC [3], which is stronger with respect to the dipolar coupling for extended films. Note that by reducing the lateral dimensions, the dipolar coupling becomes stronger and may effectively overcome the IEC leading to an antiparallel ground state of the layers. The thickness of the interlayer plays a crucial role because the IEC mechanism exhibits a decaying oscillatory behavior as a function of interlayer thickness, as discussed earlier, but also depends on the choice of material. As such, by choosing the optimum material and tuning the thickness of the interlayer one can achieve the AF orientation required for the realization of the spin valve. The implementation of such a spin-valve system in GMR sensors of read-head devices is considered another important technological breakthrough, which made possible the fabrication of the first magnetic hard-disk drive using LMR depicted in Fig. 9.2A. Besides the GMR sensor, the read head contains an inductive element, which can change locally the orientation of the magnetic moments of the writing media by generating external magnetic fields.

The reading process occurs by detection of the stray fields at the border of opposite magnetized regions (bits) written by the inductive write element. As such, the magnetic layer of the spin-valve system, which lies in the proximity of the storage media (at about 2–10 nm distance) will ideally reverse its orientation and become parallel- or antiparallel-oriented with respect to the second magnetic layer of the spin valve, thereby leading to the highest possible read-back GMR signal. In Fig. 9.5 we show several types of GMR spin valves [61], which have been subject to intensive research after the discovery of the GMR effect. The *multilayer spin valve* shown in Fig. 9.5A and the *bilayer spin valve* shown in Fig. 9.5B consist of two ferromagnetic layers, which are separated by nonmagnetic spacer layer providing an antiferromagnetic coupling of the adjacent ferromagnetic layers. The magnetoresistance exhibits enhanced values (giant as compared to the typical AMR values) when the ferromagnetic layers are antiparallel oriented with respect to each other, and low values when the layers are ferromagnetic aligned. By tuning the magnetic properties, it is possible to optimize the magnetic response toward highest magnetoresistance contrast, allowing to achieve the two possible bit states, namely “0” for an antiferromagnetic orientation and “1” for a ferromagnetic alignment. The GMR of multilayer spin valves is much higher than its bilayer version because in the latter there are more interfaces contributing to spin-dependent electron scattering events. Epitaxial growth of these two types of spin-valve systems allows to achieve an orientation of their in-plane magnetic anisotropies, which is well-defined by their crystallographic axes. In this respect, it should be noted that the GMR effect can also be obtained in polycrystalline samples grown by less-demanding processes such as sputtering techniques [62].

nonmagnetic spacer layer does not need to be tuned for providing an antiferromagnetic coupling. Instead, it should be tuned to sufficiently large values to properly decouple the ferromagnetic layers.

The use of the exchange bias effect leads actually to a possible simplification of the magnetic sensors, by giving away the free layer. The so-called AMR-based sensor includes essentially a ferromagnetic layer coupled to an antiferromagnetic layer. The AMR effect causes a variation of the resistivity depending on the relative angle between the electrical current flow direction and the orientation of the magnetization in a ferromagnet. The magnitude of magnetoresistance will be higher when the current is perpendicular to the magnetization direction, and minimum when magnetization and the electrical current flow directions are parallel to each other. Therefore, the magnetization must be well aligned toward an anisotropy axis and easy to rotate, which implies a reduced magnetic stiffness. The best performance can then be achieved by stabilizing the magnetization of the ferromagnetic layer through the proximity of an antiferromagnetic layer. The development of this sensor is still pursued today. Basic elements most commonly used are NiFe as ferromagnet, IrMn as antiferromagnet and an additional top Mg layer which plays a role in optimizing the noise level. The performance of this type of sensors is actually reflected by a superior signal-to-noise ratio and moderate read-back signal, which is characterized by nearly a 60% increase in peak-to-peak output voltages [70].

Yet, there is another way to realize opposite orientation of the magnetization in the top ferromagnetic layer by making use of the *pseudo spin valve* [71, 72] depicted in Fig. 9.5D. To ensure that the magnetizations of the top and bottom layers are opposite, one can use materials that provide different coercive fields of their individual hysteresis loops, thereby achieving plateaus in the macroscopic hysteresis loops when the magnetization of the layers is opposite. Different coercive fields can also be achieved by using the same materials but with different thickness and/or interfacial roughness. In this case, the nonmagnetic interlayer needs to be optimized toward weak coupling values to achieve sufficient decoupling between the ferromagnetic layers. In a more controlled way, a hard magnetic layer can be introduced to provide a high coercive field through stronger coupling to a third layer (as in the case of the spin valve), while the top layer would be a soft magnetic layer with low coercive field. This soft magnetic layer can then be quasi-independently rotated with respect to the hard layer by exposing it to external magnetic fields which are lower as compared to the coercive field of the hard layer.

9.1.6 Tunneling Magnetoresistance

The discovery of the GMR has also led to increased interest on another effect which results in enhanced magnetoresistance values, namely the aforementioned tunneling magnetoresistance (TMR) [59, 60]. Based on the previous development of the GMR spin valves, the incorporation of an insulating barrier replacing the nonmagnetic conducting layer of the exchange bias spin valve and the pseudo spin valves was easily approachable because of

less constrains posed by the eventual AF coupling. The effect was initially discovered in 1975 by Jullière [59], who observed that the tunneling conductance between Fe and Co separated by a Ge artificial layer was dependent on the relative orientation of the ferromagnetic electrodes of the tunnel junction. At the electronic level, the origin of TMR arises from the difference in the electronic density of states at the Fermi level between spin-up and spin-down electrons [59]. The spin-up electrons can only tunnel in the electronic band which has the same spin orientation as its own spin. As a result the TMR will depend on the spin polarization of the ferromagnetic layers and on their relative orientation [59]: $TMR = \frac{R_{AP}-R_P}{R_P} = \frac{R_{AP}-R_P}{R_P} = \frac{2P_1P_2}{1-P_1P_2}$, where R_P and R_{AP} are the resistances measured for parallel and antiparallel orientations of the magnetization, respectively, and P_1 and P_2 are the polarization factors at the Fermi energy. As such, intensive research was conducted to identify materials with high spin polarization at the Fermi energy (e.g., ideally 100% spin polarization predicted for Heusler alloys) and to optimize tunnel barriers and interfaces. One important breakthrough in obtaining significant values for the TMR was achieved in 1995 by the observation of a significant TMR at room temperature equal to 15% for AlOx tunnel barriers [60]. The development of these alumina tunnel junction has led to a steady progress in the increase of the TMR ratio reaching a 70% for a CoFe/AlOx/CoFe sputtered junction [73]. It was soon realized that, also due to the amorphous structure of the AlOx barrier, the spin-dependent scattering of electrons within this barrier might cause depolarization effects, limiting the achievement of TMR ratios sufficiently close to maximum possible theoretical limit. The impact of this limitation can also be seen in the time evolution of the TMR ratio for magnetic tunnel junctions using AlOx barriers, as shown in Fig. 9.6A [60, 73–87].

Theoretical predictions published in 2001 [88, 89] suggested that a large TMR ratio can be achieved in epitaxial tunnel junctions using MgO tunnel barriers. These studies were motivated by previous experimental observations establishing the occurrence of TMR in Fe/MgO/Fe(001) junctions for a thickness of MgO of only five atomic layers [74]. More than 1000% TMR ratio was expected to be measured for Fe(100)/MgO(100)/Fe(100) bilayers and for a thickness of 20 MgO monolayers [89]. Soon afterwards a significant high TMR of 220% was achieved experimentally in epitaxial CoFe/MgO/CoFe tunnel junctions, overcoming the performance of the AlOx-based junctions, as seen in Fig. 9.6A. Using an annealing procedure, the epitaxial properties were further improved over the years, until a record measurement of 604% TMR in the MgO-based tunnel junction, namely on CoFeB/MgO/CoFeB stacks, was reported [87] (see Fig. 9.6B). With this result, the theoretical TMR limit was achieved (the TMR at 5 K was measured to be higher than 1100% in close agreement with the theoretical prediction which was done for a temperature equal to 0 K), and therefore the performance of the MgO tunnel junction became very attractive for magnetic random access memories (MRAMs).

The MRAM [90] has the potential of establishing itself as the sole memory device of the future, since among several properties it has important advantages concerning nonvolatility, that is, the magnetic information can be preserved for very long time after turning off the device power. Moreover, MRAMs take advantage of an array of spin valves arranged in a high-density matrix,

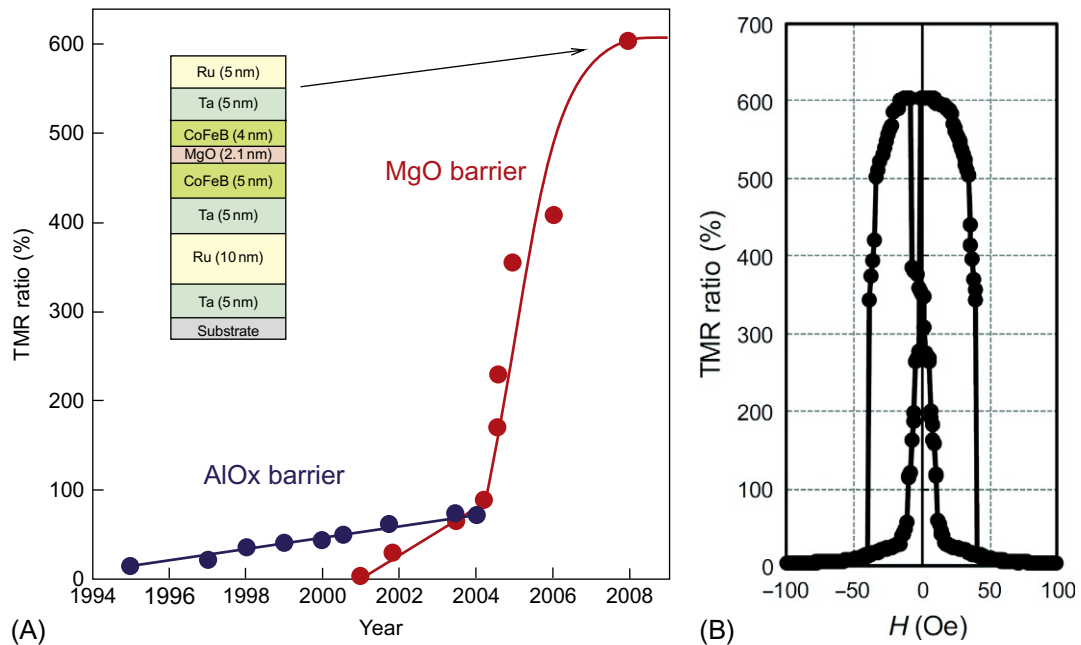


Fig. 9.6

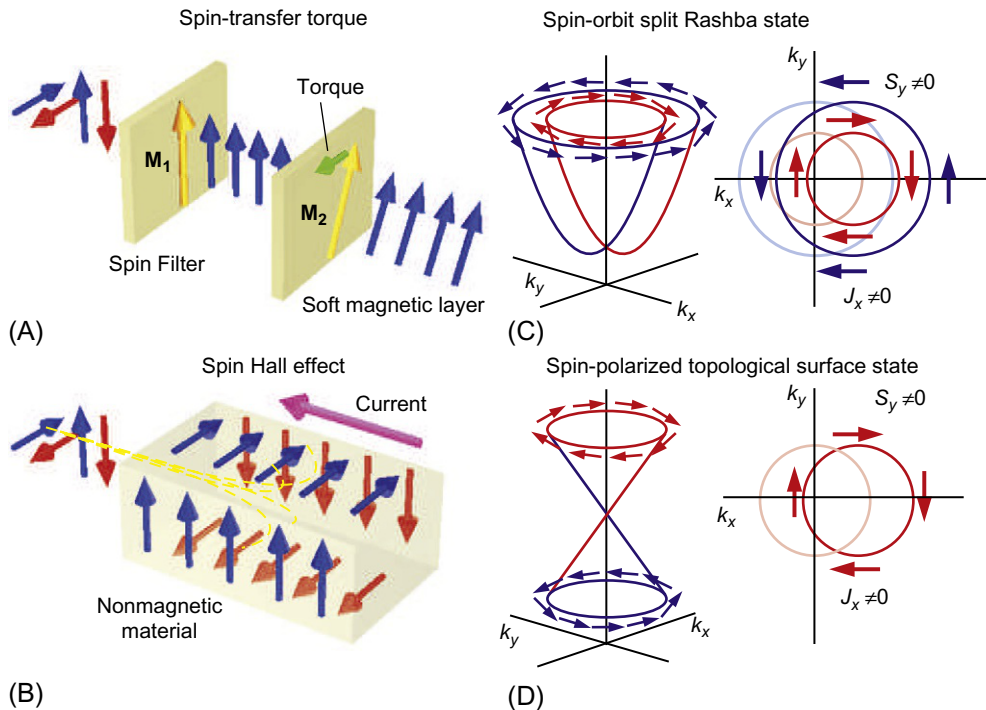
(A) Time evolution of the tunneling magnetoresistance (TMR) ratio for magnetic tunnel junctions based on AlOx [blue (dark)] and MgO barriers [red (light)]. The data are collected from TMR ratios reported in the literature [60, 73–87]. The maximum TMR ratio of 604% reported in 2008 at room temperature [87] extrapolates to the theoretical limit at 0 K. *Inset*: Sketch of the magnetic tunnel junction used to achieve 604% TMR ratio [87]. (B) Magnetoresistance loop at room temperature for the magnetic tunnel junction is shown in the *inset* of panel A. (Adapted from S. Ikeda, J. Hayakawa, Y. Ashizawa, Y.M. Lee, K. Miura, H. Hasegawa, M. Tsunoda, F. Matsukura, H. Ohno, Tunnel magnetoresistance of 604% at 300 K by suppression of Ta diffusion in CoFeB/MgO/CoFeB pseudo-spin-valves annealed at high temperature, *Appl. Phys. Lett.* 93 (8) (2008) 082508, <https://doi.org/10.1063/1.2976435>.)

which can be used to store and read magnetic information much more efficiently than conventional devices by simply using magnetic fields and resistance reading through multiple bit lines.

9.1.7 Spin-Transfer Torque Effect

Interestingly, in these MRAM cells the writing can be performed not only by magnetic fields and electric currents but also by making use of the so-called spin-transfer torque (STT) effect [91–97]. By passing an electric current through a magnetic film, a torque will act on the domain wall causing it to move along the electric current direction. Oppositely, when the direction of the current reverses, the torque will also reverse making the domain wall to move along the opposite direction. Switching the magnetization by spin currents has been predicted in 1996 [98, 99] and it is based on the conservation of the angular momentum. Generally, when an

electric current passes through a ferromagnetic material, the s -electrons will align with the d -electrons of the majority and minority spin subbands. This is a quantum-mechanical effect, which aligns the spin quantization axis of the electron cloud to the magnetic field. In doing so, the s -electrons lose angular momentum, which is in turn transferred to the d -electrons. As such, the magnetization of the film can feel a torque which, when high enough, can lead to its rotation. In case that the electric current is fully unpolarized, the torque will average out. However, injecting polarized electric currents into a ferromagnetic state, which makes an angle between s - and d -electrons, can lead to a full reversal of the magnetization for injected high s -electron densities. This effect is exploited in the so-called STT-MRAM cells [1, 2, 100–102], where instead of magnetic fields, spin currents are used to reverse the magnetization. Note that the torque acting on the ferromagnetic state requires an angle between the polarization direction of the injected electrons and the magnetization direction of the ferromagnet, otherwise the torque will be vanishing. The torque is usually maximized by utilizing a hard magnetic layer with a fixed direction of the magnetization acting as a spin filter, as sketched in Fig. 9.7A. Due to spin-dependent scattering, only injected electrons whose spin is aligned with the


Fig. 9.7

Various mechanisms for generating spin currents to exert torques on the magnetization of ferromagnets. (A) Schematics of the spin-transfer torque effect. (B–D) Mechanisms of generating spin currents through the spin-orbit interaction. Schematics of (B) the spin Hall effect, (C) the Rashba-Edelstein effect, and (D) its extension to the case of topological insulators.

magnetization of this layer will pass through the system and be transferred into a soft magnetic layer. The spin-polarized current generated in this way will exert a torque on the soft-layer magnetization, which in the ground state is oriented in an angle with respect to the one of the spin filter.

9.1.8 Spin Hall and Rashba-Edelstein Effects

As shown in Fig. 9.7B–D, there are alternative ways for generating spin currents by making use of spin-orbit coupling (SOC). These are the spin Hall effect (SHE) [103–107] and the Rashba-Edelstein effect [108–112], which can also be extended to the case of topological insulators [113–116]. Let us focus on the SHE in nonmagnetic layers, as sketched in Fig. 9.7B. In this case an unpolarized electron current is injected into heavy elements like Pt [104] or Ta [105], which results into a positive metal ion current flowing along the opposite direction. Due to the relativistic effects arising from SOC, in the reference frame of the electron this is equivalent to an effective magnetic field acting on its spin. In consequence, the injected electrons split their trajectories depending on the orientation of their spin quantization axis and accumulate on the opposite surfaces of the material. Due to the spin imbalance between opposite surfaces, spin currents are generated toward the two orthogonal directions with respect to the current flow direction. There are various contributions to the SHE. One of them is skew or asymmetric scattering on nonmagnetic impurities, which exhibit strong spin-orbit interaction [107]. This is an inelastic scattering effect, which causes the electrons to acquire different velocities. Another contribution is the so-called side jumps [106], which also occur at the impurity site, but are an elastic effect. Both skew scattering and side jumps are extrinsic contributions to the SHE [107]. Nevertheless, since for the present purpose of generating large spin torques in ferromagnets the nonmagnetic metal must share a common interface with a soft magnetic layer, a magnetic proximity effect leading to an induced magnetic moment in the nonmagnetic layer should also be taken into account. This effect can be seen as an intrinsic contribution to the SHE [107]. Note that by changing the direction of the current flow through the nonmagnetic layer, the spin currents polarized orthogonal to the current flow will reverse their polarization, and in consequence the direction of the torque in the soft magnetic layer will also reverse. For sufficiently high current densities, the generated torque can also lead to a full reversal of the magnetization in the soft magnetic layer. A natural extension of the SHE is anomalous Hall effect [117], which also takes advantage of SOC, but uses a magnetic layer instead.

For the other case, namely the Rashba-Edelstein effect [108–112], the torque in the soft magnetic layer is induced by spin currents originating from Rashba-type spin-orbit interaction. The Rashba effect is due to SOC and it is generated by an electric field in a system with broken inversion symmetry at the 2D interface [118, 119]. As shown on the left panel of Fig. 9.7C, the spin subbands forming spin-orbit split Rashba surface states are shifted in opposite directions along the electron momentum axis, and the spin-orbit splitting is proportional to the magnitude

of the electric field. The spin subbands form a Fermi surface that is characterized by two concentric circles with opposite spin textures, where the spins are perpendicular to the electron momentum [120–125]. When an in-plane current flows in the surface state, both spin subbands shift rigidly in the same direction along the electron momentum axis, leading to preferential population of one of the spin subbands (see right panel of Fig. 9.7C). As a result, spins with a preferential orientation become accumulated at the interface, generating a spin current that exerts a torque on the magnetization of the ferromagnetic overlayer. In the case of topological insulators, as shown in Fig. 9.7D, the mechanism that underlies the generation of spin current is rather similar. However, the energy-momentum band dispersion of topological surface states (left panel of Fig. 9.7D) is fundamentally different from the one of conventional Rashba states. Topological insulators are characterized by an insulating bulk energy gap that is inverted due to strong SOC, and by a metallic surface with gapless spin-polarized Dirac-cone surface states with an helical spin texture [126–136]. This peculiar spin texture is believed to play a central role in inducing exotic quantum phenomena, realizing novel magnetic-spin physics, as well as in the generation and manipulation of dissipationless spin currents [137–142]. As shown on the right panel of Fig. 9.7D, when an in-plane current flows in the Dirac-cone surface state of a topological insulator, the Fermi surface shifts along the electron momentum axis. Due to the helical locking between the electron spin and momentum in the surface state, the flow of charge is accompanied by a nonequilibrium surface spin accumulation. As the Fermi surface is composed by a single circular contour with a well-defined helical spin texture and large spin polarization, the spin accumulation can couple much more efficiently to an adjacent ferromagnetic film, so that the flow of spin angular momentum will exert a considerably large spin-transfer torque on its magnetization. In fact, recent experiments have revealed that the size of the torque induced by a topological insulator on a soft ferromagnetic overlayer can be greater than the one induced by any other material so far [113].

9.1.9 All-Optical Switching and Topological Skyrmions

Yet, the magnetization cannot only be reversed by magnetic fields or spin currents, it can also be reversed by nonmagnetic stimuli as for instance laser beams only. A very promising route to achieve this is all-optical magnetic recording, which utilizes circularly polarized femtosecond laser pulses to induce a reversal of the magnetization without any applied magnetic field, as shown for a ferrimagnetic $\text{Gd}_2\text{Fe}_{74.6}\text{Co}_{3.4}$ sample in Fig. 9.8 [143]. This method is a very efficient way for writing magnetic bits on femtosecond timescales and at record-breaking speeds, that is, much faster than currently available write heads where the writing speeds are in the order of hundreds of nanoseconds. In this context, the use of femtosecond laser pulses for generating and controlling magnetic skyrmions and their dynamics in ferrimagnets is also being explored at the fundamental level [144, 145].

Skyrmions [146] are topologically protected nanometer-sized objects that can be stabilized at room temperature in, for example, ultrathin bilayers of a ferromagnet and a heavy metal [147–149], and are potential candidates for future spintronic devices [150]. Due to the

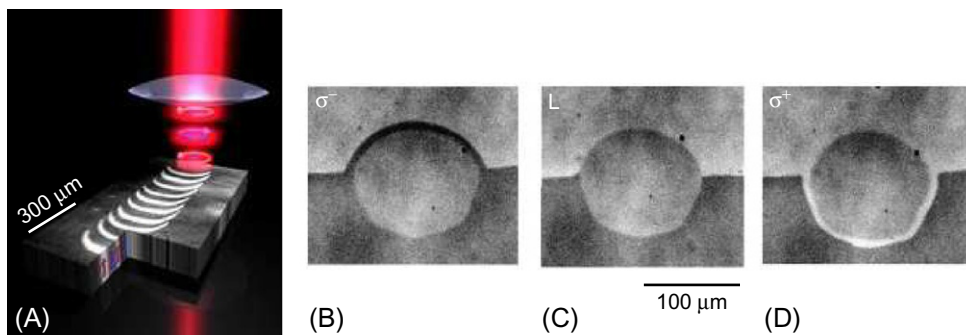


Fig. 9.8

All-optical magnetic recording with circularly polarized light. (A) Effect of scanning a circularly polarized laser beam across a $\text{Gd}_{22}\text{Fe}_{74.6}\text{Co}_{3.4}$ sample. By simultaneously modulating the helicity of the circular light polarization from positive to negative, compact all-optical recording of magnetic bits is achieved. (B–D) Magneto-optical images of the domain patterns in the region of the laser spot focused onto a domain wall for (B) circular negative, (C) linear and (D) circular positive laser light polarization. For circularly polarized excitation the magnetic contrast reverses on the perimeter of the excited area, where the temperature is just below the Curie temperature. (Adapted from C.D. Stanciu, F. Hansteen, A.V. Kimel, A. Kirilyuk, A. Tsukamoto, A. Itoh, T. Rasing, *All-optical magnetic recording with circularly polarized light*, *Phys. Rev. Lett.* 99 (2007) 047601, <https://doi.org/10.1103/PhysRevLett.99.047601>.)

interfacial Dzyaloshinskii-Moriya interaction [151, 152], skyrmions are characterized by an exotic spin texture with a fixed chirality in real space, which can be utilized to efficiently drive current densities at the nanoscale while simultaneously suppressing scattering effects with natural pinning sites [153–155]. Comprehensive reviews on this emergent field of research can be found in Refs. [156–158].

On the material research front, other important efforts are being devoted to the investigation of magnetic properties of half-metallic ferromagnets [159–162], multiferroics [163–165], and carbon-based materials [166–169]. At present, *ferrimagnetic* materials can be considered as very promising candidates for applications in spintronics, as we will discuss following. This not only concerns dynamical processes of the magnetization or all-optical switching using ferrimagnets (such as the example shown in Fig. 9.8), but also the incorporation of thin ferrimagnetic layers in magnetic recording media, the development of ferrimagnetic spin valves for magnetic read heads, or the use of ferrimagnetic nanostructures as bit-patterned media. These are all aspects that are close to real applications in magnetic recording and take advantage of the unique properties of ferrimagnetic systems. Therefore, in the following sections, we would like to focus our attention on key fundamental properties of ferrimagnetic heterostructures, which represent a very exciting research field with continuously advancing potential for applications in future information technology. In particular, we will discuss important properties of ferrimagnetic thin films and nanostructures, as well as new functionalities that might lead to their incorporation into established concepts of magnetic recording.

9.2 Ferrimagnetism

The ferromagnetic, antiferromagnetic, and ferrimagnetic traits of thin films are part of the same class of magnetic ordering based on the exchange interaction, which couples the magnetic spins of the lattice leading to preferred orientations of individual magnetic moments along certain direction, which defines the anisotropy axis. While all three cases of magnetic ordering are characterized by an onset of spontaneous sublattice magnetization at a certain temperature, that is, Curie temperature T_C for ferromagnets and ferrimagnets and Néel temperature for antiferromagnets, they differ in some essential general aspects as depicted in Fig. 9.9.

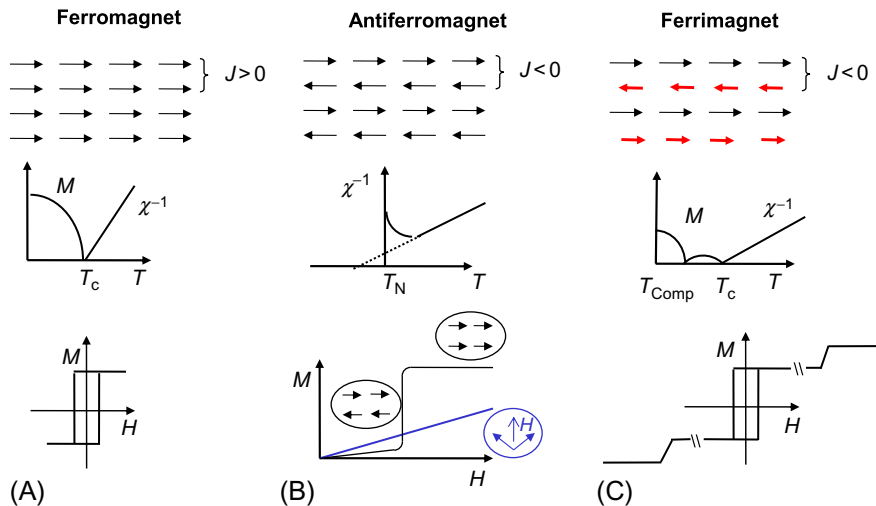


Fig. 9.9

General overview of macroscopic properties of the ferro-, antiferro-, and ferrimagnetic state.

(A) The *top sketch* shows a basic state of a ferromagnetic thin film, which is characterized by an onset of a spontaneous magnetization leading to a parallel orientation of the spins along the anisotropy axis.

The temperature behavior of the magnetization above and below T_C is shown in the *middle panel*.

The hysteresis loop along the anisotropy axis is *rectangular* as shown in the *bottom panel*.

(B) The *top sketch* shows an antiferromagnetic state, which is characterized by an antiparallel orientation of the spins leading to a vanishing macroscopic magnetization in zero field. The temperature

dependence exhibits an onset of a spontaneous sublattice magnetization below the Néel temperature.

The field response shown in the *bottom panel* exhibits a linear dependence when the field is applied perpendicular to the easy axis, and a spin-flip when the field is applied parallel to the easy axis.

A spin-flop can also take place before saturation at high fields. (C) The ferrimagnetic state is characterized by an antiparallel orientation of the spins, but each sublattice has different magnetization. This is achieved when, for instance, the sublattice is made of different elements.

A typical temperature response is shown in the *middle panel* for a case in which the compensation

of the sublattices occurs at a temperature below the ordering temperature. The response to an

external field shown in the *bottom panel* exhibits a hysteresis loop at low fields and a boost of the magnetization at very high fields. Similar to antiferromagnets, a spin-flop can also occur at

intermediate fields (not shown).

For instance, a ferromagnet exhibits a macroscopic magnetization in all the temperature range below the ordering temperature, whereas the magnetization of the sublattices in an antiferromagnet is fully compensated for all temperatures below the Néel temperature. For the ferrimagnetic state, the total magnetization can be uncompensated as similar to the ferromagnets but it can also be fully compensated for one certain temperature, depending on the stoichiometry of the constituent elements. Moreover, the ferromagnet can be easily aligned with external magnetic fields, whereas for aligning the magnetic moments of an antiferromagnet, very large magnetic fields are required, generally of the order of up to hundreds of Teslas. In these very high external magnetic fields, the antiferromagnet can be driven through spin-flip and spin-flop transitions when the magnetic field is applied along the anisotropy axis, or its total magnetization can be linearly increased as a function of the external magnetic field when applied perpendicular to the anisotropy axis. A ferrimagnet can be easily aligned with external field similar to the ferromagnet, and for higher magnetic fields [170] spin-flip and spin-flop transitions can also occur leading to a boost of the total magnetization value. Moreover, differently from antiferromagnets, a linear change of magnetization as a function of the magnetic field cannot be achieved outside the magnetic compensation.

The ferromagnetic materials are extensively used for applications due to their high magnetization, low anisotropy, relatively high polarization at the Fermi energy, and abundance in nature. Nevertheless, optimization and control of their properties are by now somewhat limited. For instance, a perpendicular magnetic orientation is difficult to be maintained for single films because the demagnetization fields which are directed against the magnetization direction are much stronger in the perpendicular direction as compared to the ones which are virtually missing for the in-plane configuration. Stabilizing an out-of-plane anisotropy can be achieved for multilayers systems like Co/Pt or Co/Pd by using thin Co and Pd layers. This is also possible for ultrathin magnetic films with optimized interface anisotropy through Dzyaloshinskii-Moriya interaction, interlayer coupling, exchange bias effect, and strain-induced interactions. Also, the magnetization can be tuned at room temperature by the right choice of materials or by doping. The strength of the anisotropy is generally rather low because the orbital moments are nearly quenched, leaving the crystal field splitting as the major source of anisotropy. As such, an intrinsic control of anisotropy is rather limited. In Table 9.1 we show the orbital and the spin moment of Fe, Co, and Ni. The orbital moments are below $0.2 \mu_B$ which amounts to about 10% of the full moment.

Table 9.1 Spin and orbital moments for Fe, Co, and Ni

	Spin Moment (μ_B)	Orbital Moment (μ_B)
Fe	2.2	0.07
Co	1.7	0.11
Ni	0.6	0.05

The antiferromagnetic materials, instead, exhibit a vanishing macroscopic magnetization and generally high anisotropy. Therefore, the control of the magnetic states requires very high magnetic fields of order of several tens of Teslas, field cooling through the ordering temperature in high magnetic fields, or field cooling in the proximity of ferromagnetic materials. Nevertheless, antiferromagnetic materials are an integral part of spintronic devices because they can mediate magnetic stability through induced anisotropies in ferromagnetic materials. More recently, it has been shown that antiferromagnets can also be functionalized by making use of spin currents [173].

An alternative route for controlling magnetic properties of materials can be achieved by combining ferromagnetic transition metals (TM) with rare-earth (RE) elements to form ferrimagnetic alloys. The RE materials have specific characteristics which are of high interest in this respect. In Table 9.2 we show the magnetic moments of the lanthanide series compiled and updated based on Refs. [171, 172]. The magnetism of RE materials is largely given by the 4f shells. These shells are localized closer to the atom, at about 10% of the atomic radii, being outwards screened by the d and s shells. As such the magnetic moment of the RE is more localized [174], with its single-ion anisotropy caused by the electrostatic interaction of the nonspherical charge distribution of the 4f electron with the local electric field of the surrounding atoms. This implies that the SOC is the main source of anisotropy, with crystal fields considered as a perturbation [171].

The exchange interaction between the localized moment of the RE with the 3d itinerant magnetic moments of the TM was suggested [175] to be mediated by the d-shell of the RE. The electron spin on the f-shell creates a positive local moment on the d shell through an ordinary exchange which further couples to the d-shell of the TM. For Fe, Co, and Ni, the exchange interaction is negative leading to an antiferromagnetic ground state of these TM and RE ions.

In Table 9.2 we show the calculated spin and orbital moments of the RE elements. This is instructive when choosing the material for achieving certain properties of the RE-TM ferrimagnets. For instance, the orbital moments are quite high in most cases except for the Gd ion which is expected to exhibit a vanishing orbital moment. As such, films with low anisotropy can be easily achieved by combining Gd with the TM. Note that divalent Eu (ground state: $^8S_{7/2}$) exhibits also a pure spin moment ($L = 0, S = 7/2$), therefore magnetic anisotropy of Eu²⁺-based ferrimagnets and antiferromagnets should exhibit soft magnetic properties. Instead, for films which are required to exhibit high anisotropy, the RE elements that have high orbital moments, like Dy, Tb, Sm, Nd, are preferred [176]. An exception is the Terfenol-D ($\text{Tb}_x\text{Dy}_{1-x}\text{Fe}_2$), a material which in spite of containing Dy and Tb elements exhibits soft magnetic properties, probably due to a high degree of oxidation [177]. Another interesting variable is the total moment of the RE. This can also be tuned by the right choice of elements.

Table 9.2 Orbital, spin, total, and experimental moments for the trivalent rare-earth elements

Ion 3+	GS	NE	L	S	J	g	μ_l (μ_B)	μ_s (μ_B)	μ_t (μ_B)	μ_{exp} (μ_B)
La	1S_0	0	0	0	0	—	—	—	—	0
Ce	$^2F_{5/2}$	1	3	1/2	5/2	6/7	3.381	-0.845	2.535	2.3–2.5
Pr	3H_4	2	5	1	4	4/5	5.367	-1.789	3.578	3.4–3.6
Nd	$^4I_{9/2}$	3	6	3/2	9/2	8/11	6.332	-2.714	3.618	3.5–3.6
Pm	5I_4	4	6	2	4	3/5	6.261	-3.578	2.683	—
Sm	$^6H_{5/2}$	5	5	5/2	5/2	2/7	5.071	-4.226	0.845	1.4–1.7
Eu	7F_0	6	3	3	0	—	3.464	-3.464	0	3.3–3.5
Gd	$^8S_{7/2}$	7	0	7/2	7/2	2	0	7.937	7.937	7.9–8.0
Tb	7F_6	8	3	3	6	3/2	3.240	6.481	9.721	9.5–9.8
Dy	$^6H_{15/2}$	9	5	5/2	15/2	4/3	5.323	5.323	10.646	10.4–10.6
Ho	5I_8	10	6	2	8	5/4	6.364	4.243	10.607	10.4–10.7
Er	$^4I_{15/2}$	11	6	3/2	15/2	6/5	6.387	3.194	9.581	9.4–9.6
Tm	3H_6	12	5	1	6	7/6	5.401	2.160	7.561	7.1–7.6
Yb	$^2F_{7/2}$	13	3	1/2	7/2	8/7	3.402	1.134	4.536	4.3–4.9
Lu	1S_0	14	0	0	0	—	—	—	—	0

Notes: The values have been calculated based on Hund's rules as described in Ref. [171]. GS and NE refer to ground state and number of unpaired electrons, respectively.

The experimental moments are reproduced from *Lanthanide Magnetism*, Available from: https://www.radiochemistry.org/periodictable/la_series/L8.html, Accessed 24 July 2017.

For the first part of the series (Ce to Eu), the spin and orbital moments are opposite oriented leading to a reduced total moment, whereas for the second part of the series (Gd to Yb), the orbital and the spin moments are parallel oriented leading to a higher moment for the RE ion. This is a consequence of the Hund's rules, which dictate the occupation of the available state in the 4f shell. One interesting element in this respect is trivalent Eu, which is expected to exhibit equal spin and orbital moments of opposite sign in the ground state. This leads to an interesting paradox, namely the existence of an ordered magnetic material, which exhibits a zero total magnetic moment, so macroscopically it appears as being nonmagnetic. This situation has been actually achieved on an Sm-based material, which behaves intrinsically similar to a ferrimagnet due to the compensation of the spin and orbital moments [178].

The stoichiometry of the chosen material plays also a crucial role in opening an effective and easy way to tune the total magnetization of the RE-TM alloy for a certain temperature, usually close to room temperature. Due to the antiparallel orientation of the RE and TM ions, the total magnetization can vanish at temperatures below the ordering temperature when the relative stoichiometry of the RE-TM leads to an equal amount of net magnetic moments for each sublattice. This is called magnetization compensation temperature.

9.3 Selected Examples of Ferrimagnetic Thin Films

In Fig. 9.10 we show a timely exemplary case of DyFe and TbFe films [179]. The films were prepared by RF cosputtering technique from an Fe target covered by small Tb or Dy plates in order to provide a variation of stoichiometry. For a certain relative composition the total magnetic moment vanishes at room temperature, whereas away of the magnetic compensation point the total magnetization reaches values of up to 200 Gauss for DyFe and up to 400 Gauss for FeTb. This is correlated with the ordering temperature which is higher for the FeTb film. This has been confirmed in more recent experiments and for a wider choice of materials for basic research [180–191]. Apart of the demonstration of the occurrence of magnetization compensation as a function of stoichiometry, one remarkable observation is that both films exhibit perpendicular magnetic anisotropy at room temperature. This is a great advantage for applications, and it is naturally a property of nearly all RE-TM films around the magnetic compensation point. However, away of the compensation point, as the total magnetization becomes stronger, the demagnetization fields become also stronger. This leads to a peculiar magnetic hysteresis loop indicating the formation of stripe domains for the regions II and IV, similar to the hysteresis loops of the archetypal Co/Pt multilayers [192]. When the total

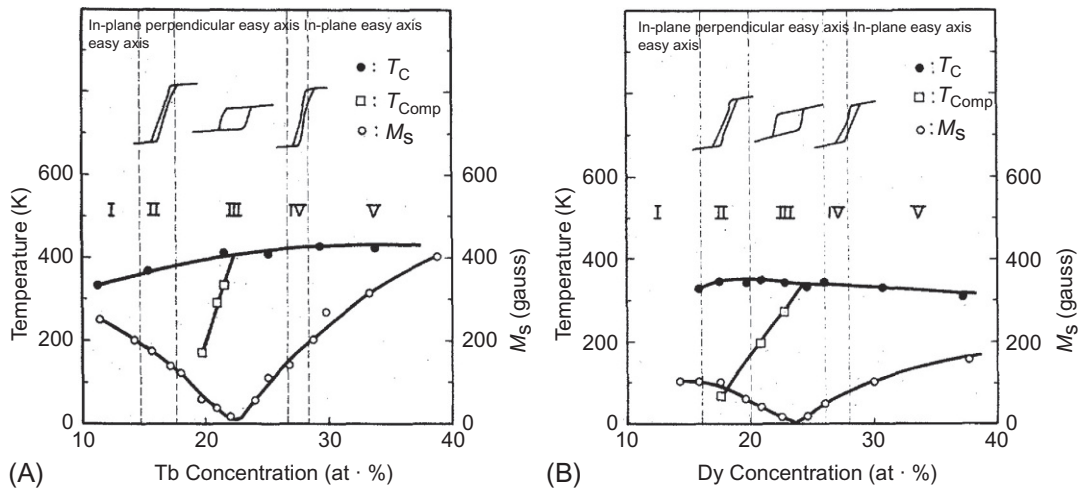


Fig. 9.10

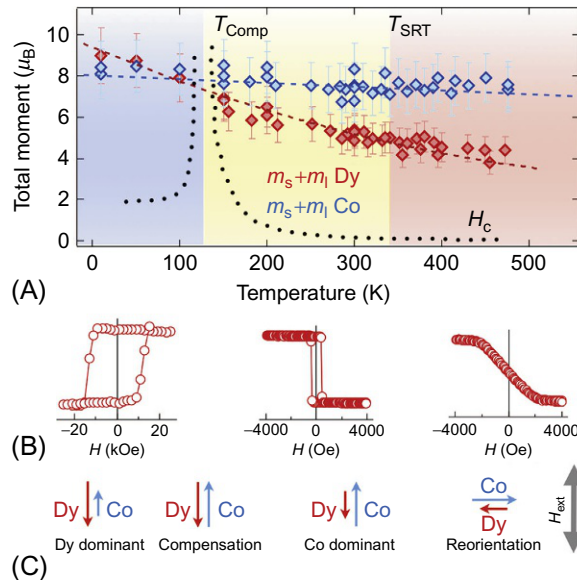
Curie temperature T_C , compensation temperature T_{Comp} , saturation magnetization M_S , and hysteresis loops as a function of composition for amorphous (A) Tb-Fe and (B) Dy-Co films. (From Y. Mimura, N. Imamura, T. Kobayashi, *Magnetic properties and curie point writing in amorphous metallic films*, *IEEE Trans. Magn.* 12 (6) (1976) 779–781, ISSN 0018-9464, <https://doi.org/10.1109/TMAG.1976.1059199>.)

magnetization of the films becomes even higher, the perpendicular anisotropy cannot anymore withstand the demagnetization energy, leading to a preferred in-plane orientation of the magnetic moments. This reorientation of the anisotropy as a function of stoichiometry originates from increased demagnetization energy, and the phenomenon might resemble the spin-reorientation in single RE-TM crystals. In such single crystals like some of the RE-TM5, the spins easy axis may rotate at certain temperature from a specific crystallographic direction to an orthogonal one. Note that the demagnetization is also proportional to the film thickness, therefore engineering RE-TM with a clean perpendicular behavior of the magnetization requires tuning of the thickness and stoichiometry as well as proper choice of the magnetic elements to be used.

A magnetic compensation for the RE-TM alloys occurs also as a function of temperature for certain ranges of stoichiometry. This effect occurs only in ferrimagnets and it is related to the different temperature dependence of the magnetization of the individual sublattices. The temperature dependence of saturation magnetization, magnetic anisotropy, and compensation temperatures of amorphous alloys has been studied in detail using laboratory-based sources [180], leading to an advanced understanding of the magnetic properties of these class of materials.

However, with the advance of soft X-ray spectroscopy techniques, such as X-ray magnetic circular dichroism (XMCD), new insights are made possible because of the possibility of performing element-specific measurements. These type of measurements allow to separate not only the contribution from the magnetic moments of individual species but also their orbital from their spin moments. In following, we highlight a recent experimental and theoretical study of DyCo₅ [193].

As single crystal DyCo₅ is a part of the ReCo₅ intermetallics, which exhibit a plethora of interesting properties, including compensation temperature, reorientation, and high magnetic anisotropy [194]. In the form of thin films, these properties are largely preserved with the advantage of attaining a perpendicular orientation of the magnetization without the need of controlling accurately the structure. In Fig. 9.11 the experimental temperature dependence of the sublattice magnetizations for Dy and Co is shown for a DyCo₅ film grown by magnetron sputtering on an Si₃N₄ membrane substrate and at room temperature. As such, the films can either be polycrystalline or even amorphous. The measurements were performed at Co L_{3,2} and Dy M_{5,4} absorption edges by reversing the magnetic field at each energy point. The XMCD and the absorption curves were then subjected to the sum rules analysis which delivered the orbital and spin moments for each magnetic atom, separately. For the particular case of RE elements, this appears to be the first time when the measured magnetic moment of the Dy is closest to the theoretical expectation (compare the experimental moment of 9.5 μ_B /atom to the theoretical value of 10 μ_B /atom), demonstrating that this analysis reached its maturity also for


Fig. 9.11

(A) Temperature dependence of the total Dy and Co magnetic moments as a function of temperature of a DyCo_5 sample. The orbital and spin magnetic moments of Dy and Co extracted from XMCD measurements were added and weighted by their relative stoichiometry. The coercive field of the sample is also shown to indicate the occurrence of the compensation temperature at its diverging region. (B) Characteristic magnetic hysteresis loops. (C) Schematic orientation of the elemental Dy and Co moments is shown for the *three colored regions* in panel A. On the *right*, the incoming X-ray beam and the external applied magnetic field are depicted. (From A. Donges, S. Khmelevskiy, A. Deak, R.-M. Abrudan, D. Schmitz, I. Radu, F. Radu, L. Szunyogh, U. Nowak, *Magnetization compensation and spin reorientation transition in ferrimagnetic DyCo_5 : multiscale modeling and element-specific measurements*, *Phys. Rev. B* 96 (2017) 024412, <https://doi.org/10.1103/PhysRevB.96.024412>.)

the RE materials. The temperature dependence of each sublattice clearly demonstrates the origin of a compensation temperature: the sublattice magnetization of the RE decreases faster as compared to the magnetization of the TM. Therefore, when the stoichiometry is appropriate, the intersection between the sublattice magnetization curves will lead to a vanishing net magnetic moment at the corresponding temperature. This leads to a divergent coercive field behavior in this compensation region, because the coercive field is inverse proportional to the net magnetization. With respect to compensation, we distinguish two regions, one below the compensation temperature where the sublattice magnetization of the RE is dominant, causing this sublattice to align parallel to the external fields; and another region above the compensation temperature where the TM sublattice is dominant with this lattice being parallel

aligned to the external field. Note that for both regions the antiparallel alignment of the RE and TM sublattices with respect to each other is preserved irrespective of the orientation of moderate external fields.

The temperature dependence of the Dy and Co sublattices has been considered theoretically within an *ab initio* approach. The self-consistent field calculation performed in terms of the Korringa-Kohn-Rostoker (KKR) method within the atomic sphere approximation [195, 196] and the local spin-density approximation with Perdew-Wang parameterization demonstrates that a ferrimagnetic ground state is energetically more favorable than a ferromagnetic arrangement for this system. Moreover, using a relativistic LDA + U method employed within the KKR formalism [197, 198], the magnetocrystalline anisotropy could be calculated establishing the easy axis of magnetization. The temperature dependence of the magnetic properties of DyCo₅ was further calculated by numerical integration of the stochastic LLG equation [199]. In Fig. 9.12, the theoretical results are summarized in terms of the temperature dependence of the elemental sublattice magnetization. Not only the compensation temperature but also the Curie and reorientation temperatures are consistent with the experiment.

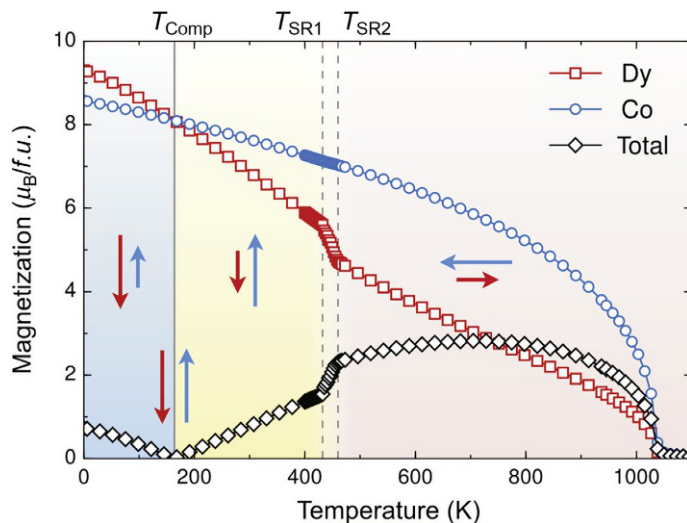


Fig. 9.12

Sublattice resolved magnetization as a function of temperature from atomistic simulations. The *solid vertical line* shows the magnetization compensation point $T_{\text{Comp}} = 164$ K. The SRT region is indicated by the *dashed lines*, with starting point $T_{\text{SR1}} = 432$ K and end point $T_{\text{SR2}} = 460$ K, clearly visible by the steep slope of the magnetization in this temperature range. (From A. Donges, S. Khmelevskiy, A. Deak, R.-M. Abrudan, D. Schmitz, I. Radu, F. Radu, L. Szunyogh, U. Nowak, Magnetization compensation and spin reorientation transition in ferrimagnetic DyCo₅: multiscale modeling and element-specific measurements, *Phys. Rev. B* 96 (2017) 024412, <https://doi.org/10.1103/PhysRevB.96.024412>.)

In addition to the compensation temperature, a spin reorientation temperature takes place. In single crystals, it is observed experimentally and theoretically that the spin axis turns from the basal plane to perpendicular to it in a temperature range bordered by two well-defined temperatures referred to as SR1 and SR2 [200]. These characteristic temperatures are revealed by measuring equilibrium states, namely the spontaneous magnetization in a vanishing external field. This leads to the observation of rotating magnetic moments as a function of temperature, and therefore it is referred to as spin-reorientation temperature. In thin films, it is often that magnetic hysteresis loops are measured as a function of temperature. For this case, the observation is that the magnetic anisotropy turns from the perpendicular direction to an in-plane direction, therefore this temperature is referred to as the anisotropy-reorientation temperature [201, 202]. In Ref. [193] this appears to be reconciled by suggesting that the relative anisotropy energies of the RE and TM sublattices are approximately compensated close to the spin reorientation because the RE loses its magnetic order faster. By increasing the temperature, it appears to be energetically favorable for the system to align in the easy direction along the TM axis, resulting in a spin reorientation. Note that not only the temperature dependence of the RE moment contributes the characteristics of the anisotropy reorientation, but also the absolute value of the RE anisotropy influences the temperature interval which accommodates the spin reorientation [203]. The theory predicts even one more effect for this reorientation, namely a discontinuity of the RE magnetic moment as a function of temperature. This reflects the occurrence of a noncollinear state referred to as easy cone across the reorientation temperature where the RE and the TM sublattices no longer align perfectly collinear, but have a finite canting which can reach up to 5°C. This noncollinear state still needs to be considered experimentally in thin films, which is well within the sensitivity of soft X-ray spectroscopy today.

When reducing the thickness of the films, new effects might take place due to interface effects and finite-size effects. In thin films one needs to consider that at least two interfaces, namely bottom substrate/film and top surface/vacuum or capping layer. At the surface, the top most layer exhibits a coordination deficiency which leads in general to modifications of the exchange parameters and thereby to a change of the magnetic moments, anisotropies and even of the exchange stiffness. Also, the strain effects and growth morphology caused by the bottom interface will influence the magnetic properties. As a result, the surface of the film is expected to have different properties with respect to the bulk. When reducing the thickness of such films, then the surface might play an important role for the macroscopic behavior of the film. For the particular case of RE-TM alloys, this can play a crucial role especially close to the compensation temperature, as described further below. Note that the length scales for these low-dimensional effects in ferrimagnets might be higher than the corresponding ones in ferromagnetic and antiferromagnetic systems, also due to a lower magnetic stiffness which is by one order of magnitude smaller for ferrimagnets as compared to ferromagnets [176, 203]. This allows for noncollinear states which manifest as fanning

cones, sperimagnetism, and even spin-flop configurations [204]. Also, it is remarkable that the compensation temperature exhibits a thickness dependence saturating at several tens of nanometers [182].

To this end we highlight the case of a 50 nm thick DyCo₄ with perpendicular anisotropy [187], which shows a novel field transition [205] that occurs close to the compensation temperature. In Fig. 9.14 the hysteresis loops for Dy and Co are shown separately. This is made possible by involving soft X-ray spectroscopy in transmission which allows to distinguish the magnetic moments of Dy and Co due to its element specificity. The hysteresis loops of each lattice exhibit a nearly rectangular shape away from the compensation point. The hysteresis loops perpendicular to the surface develop peculiar shapes close to the compensation temperature which is equal to 250 K as measured by the divergence of the coercive field. This compensation temperature is characteristic for the whole film. Particularly, above the compensation point the hysteresis loops exhibit side wings which appear to be shifted with respect to the magnetic-field axis. The characteristic hysteresis loop at 270 K provides indication of domain wall formation. One important observation is that the loops of Dy and Co appear to be inverted with respect to each other. This rules out a spin-flop transition as the origin of this effect. Note that a spin-flop state is characterized by a large angle between the RE and TM elements which is not observed here.

In order to shed light on the mechanism behind this observation, one can make use of the surface sensitivity of soft X-ray spectroscopy. By measuring hysteresis loops and registering the drain current, that is, the so-called total electron yield (TEY), sensitivity to a surface layer of about 6 nm is naturally provided due to the reduced escape length of the photoelectrons. Thereby it is possible through simultaneous measurements to probe the surface magnetism by means of TEY and the bulk magnetic properties by means of transmission measurements. This allows to obtain a separate measure of the bulk and surface properties while preserving the element-specific trait. The data shown in Fig. 9.13 reveal that the surface with respect to bulk magnetization curves is markedly different: While the central part of the hysteresis loop is similar for the bulk as compared to the surface, the hysteresis wings in Fig. 9.14 exhibit different saturation points, labeled as S_{6T} and B_{6T} . The surface magnetization appears to be nearly fully reversed, whereas the bulk part shows smaller saturating value. This is consistent with a domain wall winding top-down through the film. As such, a noncollinear state which should also show an in-plane component of magnetization will be present at high fields. Certainly, further measurements involving X-ray magnetic linear dichroism to reveal directly a noncollinearity as indicative for a domain wall formation will help even further to obtain deeper understanding of the reversal process. Nevertheless, the shift of the wings with respect to the field axis can be understood qualitatively as an “atomic exchange effect,” which exhibits record values characterized by shifts of several Tesla.

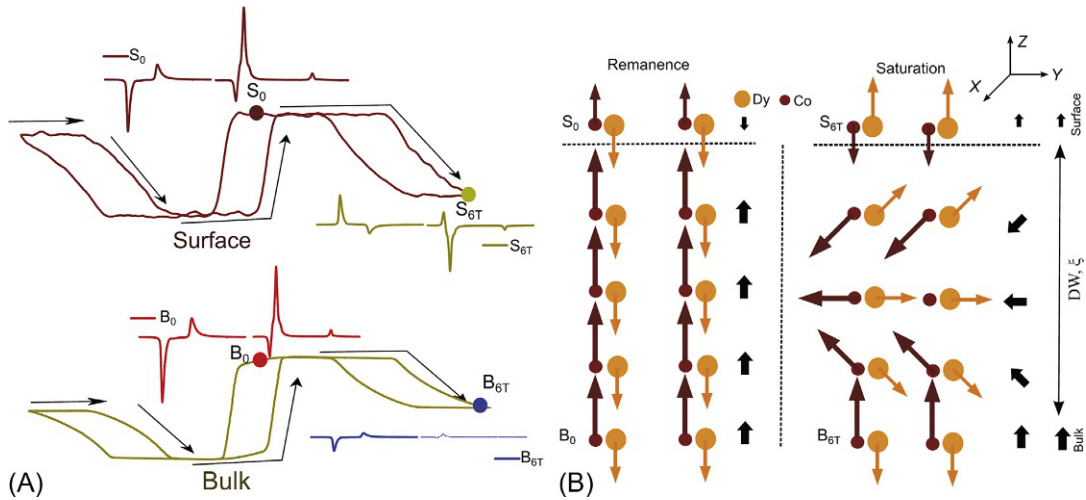


Fig. 9.13

(A) Surface and bulk magnetic hysteresis loops of Dy at 270 K. XMCD of Dy and Co at the four states of S_0 , S_{6T} , B_0 , and B_{6T} marked in the hysteresis are also shown. For an external magnetic field equal up to 6 T, side hysteresis loops are observed, which indicates a magnetic field transition. (B) Sketch of the spin structure of $DyCo_4$ at 270 K for the remanent and saturation state with an out of plane magnetic domain wall from the surface to the bulk. (From K. Chen, D. Lott, F. Radu, F. Choueikani, E. Otero, P. Ohresser, *Observation of an atomic exchange bias effect in $DyCo_4$ film*, *Sci. Rep.* 5 (18377) (2015), <https://doi.org/10.1038/srep18377>.)

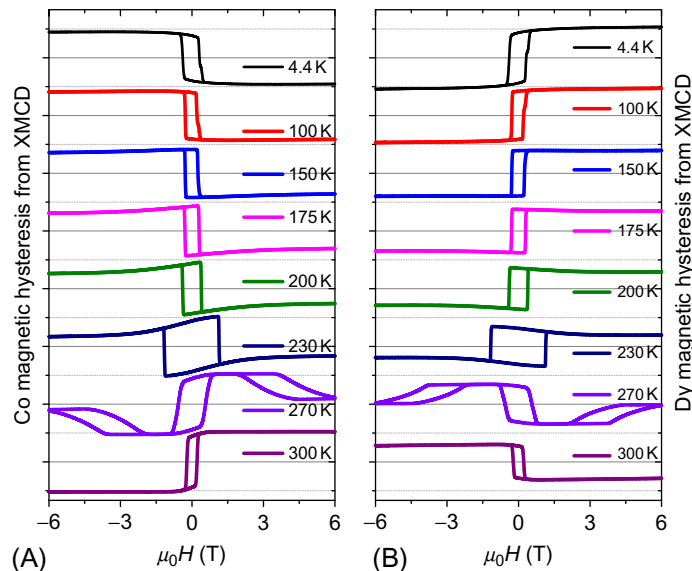


Fig. 9.14

Magnetic hysteresis derived from XMCD for Co (A) and Dy (B) of a $DyCo_4$ film as a function of temperature ranging from 4.4 to 300 K. The bulk magnetic hysteresis loops of Co and Dy have similar shape but opposite sign, this indicates that an antiferromagnetic orientation between Co and Dy which further excludes the occurrence of a spin-flop state. The shape of the magnetic hysteresis loops exhibits peculiar shapes around above and below the compensation temperature, showing also the atomic exchange bias effect at 270 K [187].

The analogy to the mechanisms of exchange bias is motivated by the similarity to the Mauri model which considers the formation of domain walls at the interface between an antiferromagnetic and a ferromagnetic layer [206]. Similarly, for the case of a ferrimagnetic film with vertically varying magnetic compensation one can consider a two-component model where the top part of the film has, in average, a different compensation temperature as compared to bottom part of the layer. As such, between these two compensation temperatures the system is in a frustrated state. The fact that the surface part of the layer has a higher compensation temperature has been clearly demonstrated by analyzing the XMCD spectra of the surface and bulk involving the sum rules analysis. The results show that the magnetic moments of the surface are lower as compared to the bulk which can be a result of the surface coordination deficiency. Other reports suggest that the surface may exhibit different magnetic moments also due to a possible lateral inhomogeneity and/or migration of the RE atoms as described in Refs. [207–209]. Nevertheless, the fact that the surface and the bulk part exhibit different compensation temperature leads to a distinct scenario for the magnetization reversal. After applying a high negative external field and decreasing the field beyond the coercive field of the film, the following magnetic state takes place: The bottom part of the film has the TM moment aligned parallel to the field, and this represents a stable state that is also maintained by further decreasing the field. The top part of the film is, however, in a frustrated state. Such frustrated state of the surface is caused by the competition between the direct exchange with the bottom film, causing the magnetization of each sublattice to stay parallel oriented with respect to each other. Note that the external field tends to align the magnetization of the top Dy lattice opposite to the one of the bottom layer. This is due to the fact that the top part of the film is RE dominated in this temperature range. Therefore, we encounter a situation similar to a magnetically hard bottom layer coupled to a soft top layer. The latter can be rotated by the influence of an external field in the presence of a strong exchange coupling to a stable magnetic medium. This is observed as the side wings of the magnetization curve, which exhibits a shift of the hysteresis loop with an asymmetric shape characteristic of the exchange bias effect. Note that outside the compensation temperature of the bulk and the surface, this effect does not occur. However, it is interesting to observe that in nanostructures, a decrease of magnetization emerges at high fields indicating partial domain formation (see, e.g., Fig. 9.20). This further strengthens the case of a reduced magnetic stiffness at the surface of thin films and nanostructures, which allows for enhanced nonlinearity at the border of the RE-TM alloys. Seemingly, these effects appear to be present in more thin ferrimagnetic alloys and for a larger combination of materials as it has been recently confirmed by soft X-rays spectroscopy on other alloys. It will be of interest to consider these effects also in connection with all-optical switching of ferrimagnetic alloys [210].

9.3.1 Ferrimagnetic Spin Valves

In the following we describe a possible realization of a ferrimagnetic spin valve for possible applications in magnetic memory media. Based on the opportunity to engineer films with desired properties by combining REs and TMs one can engineer spin valves with perpendicular anisotropy which also exhibit the exchange bias effect. This has materialized in a magnetically hard/soft bilayer with tunable exchange bias field and perpendicular anisotropy. At the fundamental level it has been suggested that the interface between the ferrimagnetic alloys can exhibit vanishing frustration [201, 211, 212]. This can be achieved in a temperature range above or below the compensation of both layers. For a temperature range between the compensation of both layers, the system would exhibit a frustrated state which can be used as a model to investigate the field transition described earlier.

As an exemplary demonstration we present the case of FeGd/Ta/DyCo₅ ferrimagnetic spin valve. Due to its strong anisotropy, high Curie temperature, and rectangular shape of the hysteresis loop at room temperature, the DyCo₅ was chosen as a hard layer. The soft layer was a FeGd film designed to have a low compensation temperature, and a rectangular shape of the perpendicular magnetization loop. Its soft nature is assured by the use of Gd which is expected to have a vanishing orbital moment. Note that designing the magnetic properties of each single layer is not sufficient to achieve a shift of the hysteresis loop when they share a common interface. As shown in Fig. 9.15, if the layers are in direct contact, both layers reverse together. This is a consequence of the strong coupling characteristic of the ferrimagnetic alloys. Thus, to achieve an exchange bias effect an additional decoupling mechanism needs to be introduced. This can be realized by introducing a spacer layer in order to decrease the interfacial coupling. For this particular case, a Ta layer which is thicker than about 3 Å reduces the IEC and in this way the layers begin to reverse independently. The coupling across the Ta layer is still present, but it diminishes when the Ta layer becomes thicker. This demonstrates a typical exponential decay of the IEC as a function of the interlayer Ta thickness.

Past this interlayer critical thickness one can achieve a shift of the soft layer with respect to the hard layer as shown in Fig. 9.16. The hysteresis loop of FeGd, which acts as the soft layer due to its reduced anisotropy, can be shifted and the orientation of the shift can even be reversed without involving a field-cooling procedure. In the left column of Fig. 9.16, the measured data corresponding to the sample with a Ta interlayer thickness of 5 Å is shown. When the hysteresis loop is measured between -900 to +900 Oe and backwards, both hysteresis loops of the DyCo₅ and FeGd layers are centered with respect to the external field. However, after saturating the system in a positive field higher than the coercive field of hard ferrimagnetic layer and measuring the hysteresis loop of the FeGd layer from -300 to 300 Oe and backwards, a shift of the hysteresis loop occurs revealing the presence of an unidirectional anisotropy. The right panel of Fig. 9.16 shows the same scenario, but with a higher thickness of the spacer layer. This demonstrates that the unidirectional anisotropy can be easily tuned by varying the interlayer

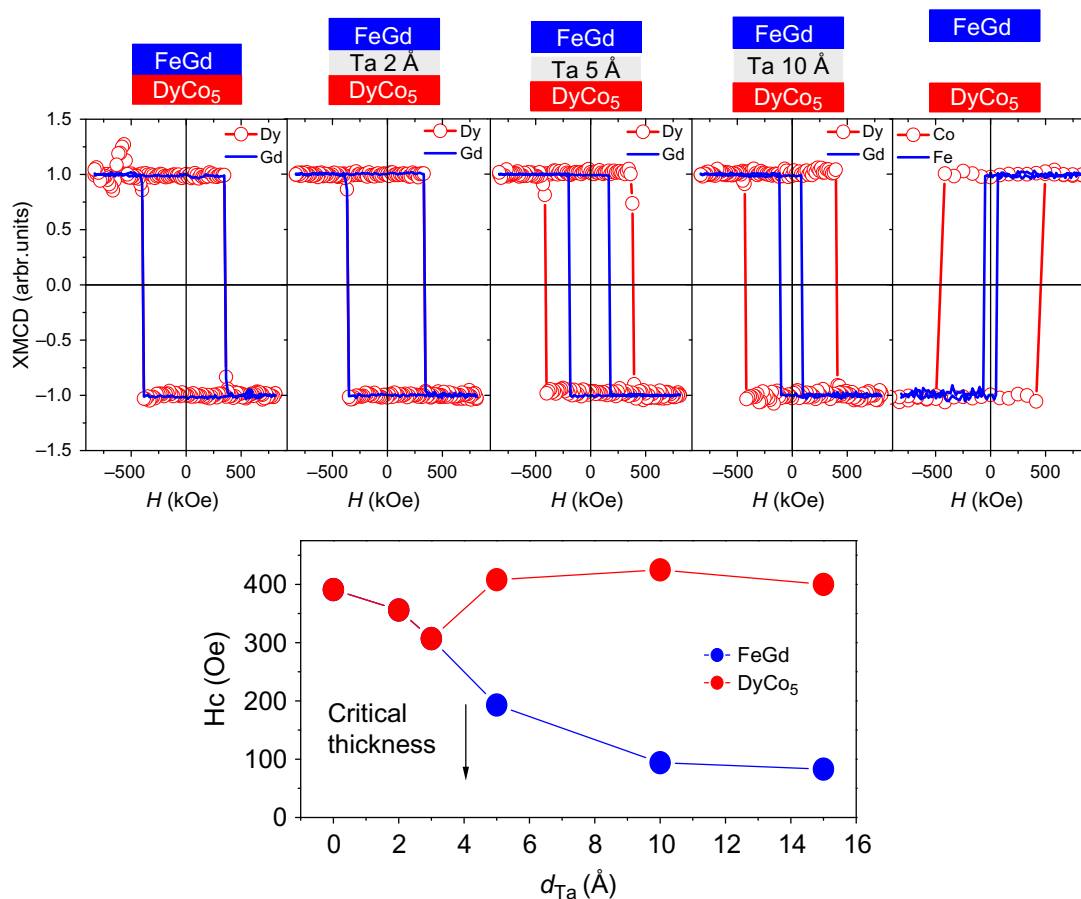


Fig. 9.15

The *top panel* shows the hysteresis loops of the soft and hard layers for different Ta interlayer thicknesses. In the *bottom panel*, the coercive fields for the FeGd and DyCo₅ layers extracted from the hysteresis loops are plotted as a function of the interlayer thickness. These show a critical thickness of about 3 Å the Ta interlayer spacer for which the films will decouple. (From F. Radu, R. Abrudan, I. Radu, D. Schmitz, H. Zabel, *Perpendicular exchange bias in ferrimagnetic spin valves*, *Nat. Commun.* 3 (2012) 715, <https://doi.org/10.1038/ncomms1728>.)

spacer. Another advantage of the ferrimagnetic spin valve is that the shift of the hysteresis loop is stable, opposite to most of the exchange bias systems which show training effects.

In the context of all-optical switching, this type spin valve can be functionalized also as an *ultrafast ferrimagnetic spin valve*. Since the thickness of the soft layer can be varied as to contain nearly all the laser pumping energy, the magnetization of the top layer can be switched while maintaining the magnetization of the bottom layer unaffected. Interestingly, this concept has been attempted in Ref. [213] for a Tb₂₂Co₅Fe₇₃/Pr₆O₁₁/Tb₁₉Co₅Fe₇₆ tunnel junction

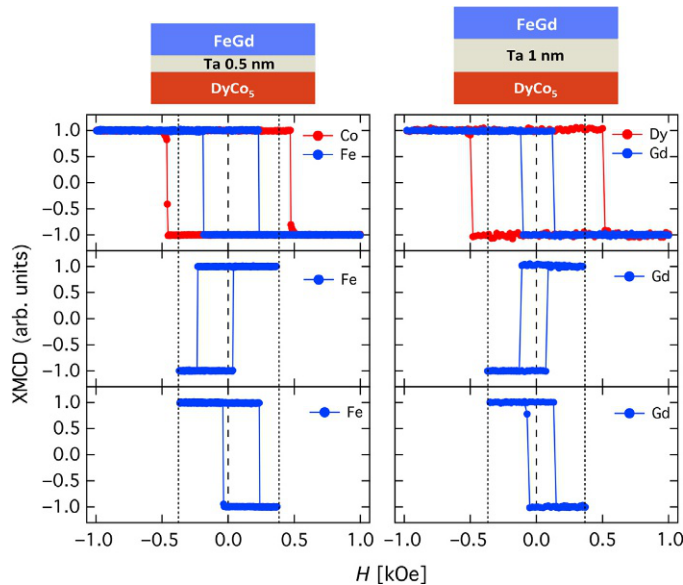


Fig. 9.16

Left column: (A–C) Hysteresis loops measured for a sample with a 5 Å Ta interlayer spacer. (A) Hysteresis loops of the DyCo₅ and FeGd films were measured from –900 to +900 Oe. (B) The system was saturated in a positive field of +3000 Oe and consecutively a hysteresis loop was measured between +300 and –300 Oe. (C) The system was saturated in a negative field of –3000 Oe and consecutively a hysteresis loop was measured between –300 and +300 Oe. The dotted vertical lines mark the +300 and –300 Oe fields [201]. *Right column:* (D–F) Similar results as (A)–(C) but after increasing the Ta interlayer thickness to 10 Å. (Taken from F. Radu, R. Abrudan, I.

Radu, D. Schmitz, H. Zabel, *Perpendicular exchange bias in ferrimagnetic spin valves*, *Nat. Commun.* 3 (2012) 715, <https://doi.org/10.1038/ncomms1728>.)

which exhibits a fairly large TMR value equal to 70% at room temperature. The magnetization switching of one ferrimagnetic layer is achieved using a pulsed laser with about 80 ps time duration [213].

The ultrafast ferrimagnetic spin valves have the advantage of versatile tuning of magnetic properties (anisotropy, magnetization, interfacial coupling) through stoichiometry variation and material choices. Through careful engineering, rectangular magnetization loops with perpendicular anisotropy can be achieved. Also, by using oxide interlayers a fairly high TMR was demonstrated [201, 213].

9.4 Ferrimagnetic Nanostructures for Magnetic Memory Bits

The research on engineered spintronic materials in the form of ordered arrays of magnetic nanostructures has experienced a tremendous boost due to the versatility of their applications in magnetic recording technology [30–34, 52, 55, 214]. Due to their reduced atomic coordination

and modified density of states, magnetic nanostructures often exhibit unique properties that do not exist in their bulk counterparts [214–216]. One of the main reasons is that the surface to volume ratio becomes very large due to the reduced dimensionality, leading to a modification of the magnetic properties such as surface and shape anisotropies, as well as strain-induced magnetic anisotropies. Moreover, the shell of individual nanostructures often exhibits distinct magnetic properties as compared to their inner core, leading to interesting effects such as spin-glass behavior [217], diluted antiferromagnetic behavior [218, 219], or even a complete loss of net magnetization. These effects are often triggered by the breaking of inversion symmetry at the surface as well as by the incorporation of surface defects.

Another phenomenon of general importance in all types of magnetic nanostructures concerns finite-size effects, because they lead to a scaling of the intrinsic magnetic properties such as the magnetic ordering temperature and the magnetic anisotropy. For instance, in antiferromagnetic materials, which play a crucial role in exchange-bias systems, finite-size effects lead to reduced magnetic anisotropy K_{AF} and decreased magnetic stiffness, as well as to a scaling of the corresponding Néel temperature [220]. Similarly, in ferromagnetic materials, finite-size effects cause a scaling of the Curie temperature (T_C) and a modification of the magnetic anisotropy K_F [221–223]. On the other hand, the extrinsic magnetic properties critically depend on the details of the shape, geometry, and preparation conditions of the nanostructure assembly. In particular, control of the shape magnetic anisotropy can be achieved depending on the geometry of the nanobjects [224]. All these effects taken as a whole are relevant in various magnetic systems of low dimensionality such as artificially grown ferromagnetic nanostructures [225, 226], magnetic nanodot arrays [227, 228], nanowires [229–231], antidot arrays [232], or self-organized magnetic nanoparticles [227] to name a few examples.

It should be emphasized that to increase the magnetic data recording density even further, it is important not only to reduce the size of the individual memory elements of a magnetic recording layer, but also to employ magnetic materials with temperature-dependent functionalities. In this respect, arrays of ordered *ferrimagnetic* nanostructures are ideal candidates for this purpose, as they allow for unprecedented control of their magnetic properties with temperature and/or doping [202, 233]. Due to the antiparallel alignment between the magnetic moments of the two (or more) sublattices forming the ferrimagnet, the magnetic dipolar interaction between neighboring ferrimagnetic nanostructures within the array can be substantially suppressed. Decreasing the magnetic dipolar interaction is essential to achieve superior control of the bit stability and a fully controllable magnetic state of individual bits. This is because the dipolar interaction often manifests as a stray field that ultimately reverses the magnetization of neighboring bits [52, 234, 235]. This situation is typically encountered in arrays of ferromagnetic nanostructures [236–238], where in contrast to ferrimagnets, the dipolar interaction eventually causes a loss of magnetic information in storage media thereby affecting the lifetime of the stored information.

Another advantage of ferrimagnetic nanostructures concerns the tunability of the magnetic anisotropy, which can be increased with respect to the one using ferromagnets by factors of up to $\times 50$. This can be achieved by proper tuning of composition, in particular by taking advantage of RE elements with high orbital moment, as discussed in [Section 9.2](#). As the energy barrier to overcome the effect of superparamagnetism is proportional to $K_u V$ [12] (see [Sections 9.1.1](#) and [9.1.4](#)), significantly increasing the magnetic anisotropy allows to further decrease the bit volume V . Thus, ferrimagnetic nanostructures in principle allow to achieve even higher areal bit densities without the need of large magnetic fields during the write process. This is also accompanied by the possibility of controlling the direction of the magnetic anisotropy near room temperature [201, 202], which for instance can be relevant in HAMR, as we will discuss in [Section 9.4.2](#).

More generally, the incorporation of bit-patterned media into hard-disk drives requires preparation of arrays of nanostructures of high quality and within extremely small tolerances [34, 52]. In addition, reducing the size of the nanoelements well below the 100 nm range requires a high level of precision in the bit pattern positioning, possibly below 1 nm [52]. Other technological issues standing on the way toward mass production are, for example, the nonplanar disk topography or the need of an absolute write synchronization [34, 52]. However, many of these challenges can be overcome by combining accurate nanofabrication methods with strategies such as, for example, planarization of the patterned disk or incorporation of write clocks to reach the required timing accuracy during information processing [34]. Current advances in lithographic methods pave the way for the integration of bit-patterned media with existing hard-disk drive technology in the nearest future. In [Fig. 9.17](#), we summarize various steps involved in the fabrication of bit-patterned media using conventional methods such as electron-beam lithography [239], anodization of Al [240], and nanoimprint lithography [241–243]. In [Fig. 9.18](#) we show few-selected scanning electron microscopy (SEM) images of state-of-the-art magnetic nanostructure arrays prepared using these methods [34, 244].

Fabrication of bit-patterned media by means of electron-beam lithography (see [Fig. 9.17A](#)) usually involves several steps of deposition and lift-off processes [239], and requires a fully controlled growth of the magnetic recording layer and underlayer using techniques such as molecular-beam epitaxy or magnetron sputtering. The overall process shown in [Fig. 9.17A](#) is a bottom-up approach, which allows to obtain well-ordered arrays of magnetic nanodots with a resolution of the order of ~ 10 nm, which is mostly limited by the resist resolution, writing time, proximity effects, and stitching errors [52]. Alternatively, a magnetic thin film can be directly patterned which represents a top-bottom approach which is typically followed by ion ball milling through the magnetic layer and strip of the residual mask materials. Note that to achieve an areal bit density beyond 1 Tb/in^2 would require a bit length below 25 nm, a value that pushes the current limits of electron-beam lithography [239]. It has been shown that approaches such as blankerless writing, multiple pass exposure, and cold ultrasonic developing [245] substantially expand the capabilities of electron-beam lithography. In particular, these

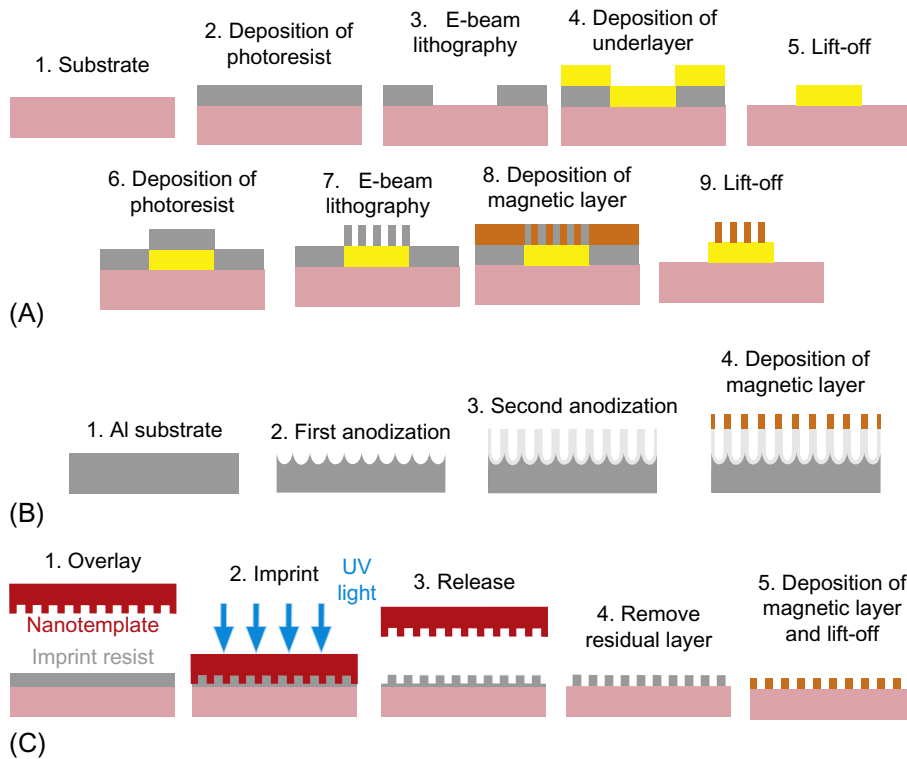
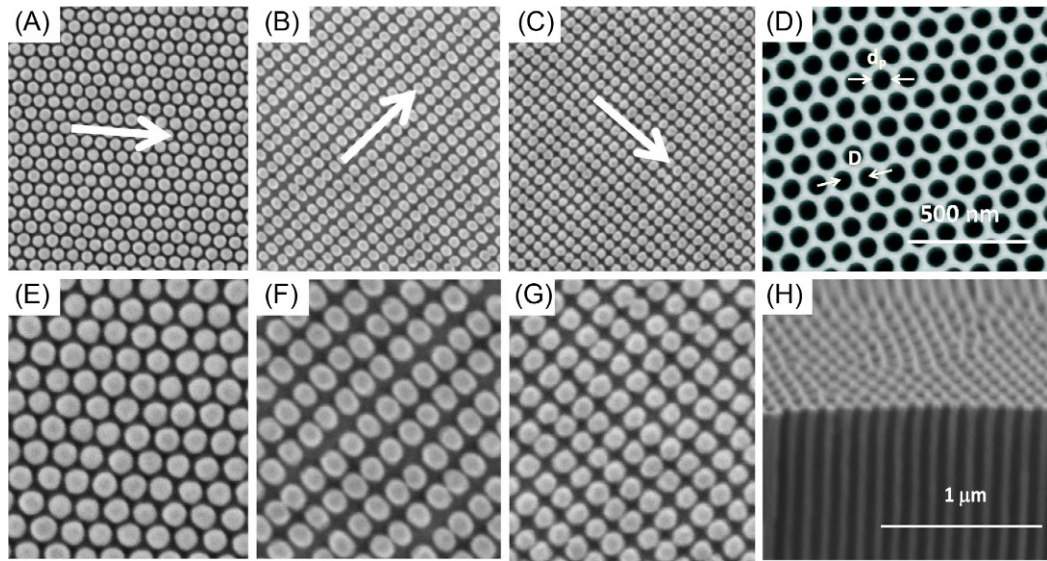


Fig. 9.17

Sketches depicting various steps involved in the fabrication of bit-patterned media using (A) electron-beam lithography, (B) anodization of Al, and (C) nanoimprint lithography.

approaches have been useful to increase writing speeds, optimize tolerances in nanostructure positioning, and improve the overall resolution, respectively. In this way, areal densities as high as 4.5 Tb/in^2 have been achieved using electron-beam lithography [239]. However, in practical applications, the existing requirements in nanostructure positioning and nanodot uniformity for mass production of hard-disk drives based on bit-patterned media limit electron-beam lithography to $\sim 1 \text{ Tb/in}^2$ [34, 52].

Anodization of Al (Fig. 9.17B) represents an alternative and less expensive technique for the fabrication of arrays of magnetic nanostructures. It is usually performed in a two-step electrochemical process and allows to generate highly ordered and self-organized nanohole arrays exhibiting closely packed honeycomb structures [240]. Typical nanohole diameters prepared by this method are in the range of 10–100 nm, and interhole distances are usually between 50 and 400 nm. The geometrical properties of the nanohole array strongly depend on the electrolyte used, growth temperature, and electrochemical potential applied during the anodization process. A full description of the chemical and physical processes involved during the anodization can be found in Refs. [246, 247]. Nanohole arrays grown in this way can be used


Fig. 9.18

Few-selected scanning electron microscopy images of arrays of nanostructures. (A–C) State-of-the-art CoCrPt magnetic nanodot arrays fabricated by nanoimprint lithography in combination with magnetron sputtering. (A) 27.3 nm hexagonal array, (B) 27 nm circumferential \times 20.5 nm radial rectangular array, and (C) 22 nm circumferential \times 18.5 nm radial rectangular array. The *arrows* indicate the down-track direction. (D) Permalloy antidot arrays grown by magnetron sputtering on anodic alumina. Nanohole diameters and interhole distances are 70 and 105 nm, respectively. (E–G) Higher magnification images of the nanodot arrays are shown in A–C, respectively.

(H) Corresponding cross-section of the antidot array is shown in D. (Panels A–C and E–G are taken from T.R. Albrecht, H. Arora, V. Ayanoor-Vitikkate, J.M. Beaujour, D. Bedau, D. Berman, A.L. Bogdanov, Y.A. Chapuis, J. Cushen, E.E. Dobisz, G. Doerk, H. Gao, M. Grobis, B. Gurney, W. Hanson, O. Hellwig, T. Hirano, P.O. Jubert, D. Kercher, J. Lille, Z. Liu, C.M. Mate, Y. Obukhov, K.C. Patel, K. Rubin, R. Ruiz, M. Schabes, L. Wan, D. Weller, T.W. Wu, E. Yang, *Bit-patterned magnetic recording: theory, media fabrication, and recording performance*, *IEEE Trans. Magn.* 51 (5) (2015) 1–42, <https://doi.org/10.1109/TMAG.2015.2397880>, Available from: <http://ieeexplore.ieee.org/abstract/document/7029109/>, and panels D and H are adapted from K.J. Merazzo, *Ordered magnetic antidot arrays*, Ph.D. thesis, Universidad Autónoma de Madrid, 2012, Available from: <http://hdl.handle.net/10486/11761>.)

to fabricate a negative replication or antipattern of the original structure, resulting in a nanotemplate with desired composition and geometrical properties. Alumina templates are also widely employed in fundamental studies to produce hexagonally ordered magnetic nanowire arrays of high vertical aspect-ratio [248, 249]. Alternatively, as shown in Fig. 9.17B, honeycomb structures in anodic alumina can be used to fabricate arrays of self-assembled magnetic antidots [202, 244]. Magnetic antidot arrays can be described as a continuous magnetic thin film containing spatially ordered nonmagnetic defects at the nanoscale, and thus represent the counterpart of magnetic nanodot structures. Fig. 9.18D and H shows SEM images of permalloy ($\text{Fe}_{20}\text{Ni}_{80}$) antidot arrays of high quality [244]. In these images, the deposited

magnetic material can be distinguished by the bright (white) color contrast. Besides the high ordering degree of nanoholes, the images reveal a narrow distribution of nanohole diameters and interhole distances. It can also be seen that the magnetic material is only deposited on the nanotemplate surface while not deeper inside the nanoholes or at the bottom of the nanotemplate. This type of nanostructures pave the way for novel applications in magnetic recording due to their enhanced magnetic properties. In [Section 9.4.2](#), we will focus our attention on the magnetic properties of ferrimagnetic antidot arrays.

Fabrication of nanotemplates with high level of precision is critically important to produce bit-patterned media with high areal densities by nanoimprint lithography ([Fig. 9.17C](#)). Nanoimprint lithography is one of the most suitable techniques for the fabrication and replication of bit-patterned media, and probably the technique of choice for mass production of nanopatterned hard-disk drives without stitching [[241–243](#)]. Among currently available nanoimprinting methods, ultraviolet-cure nanoimprint lithography is most promising for low-cost high-volume replication of nanopatterns due to its high imprint uniformity [[34](#)]. As shown in [Fig. 9.17C](#), the process initially requires precise overlay between nanotemplate and substrate. This step is followed by controlled resist dispensing (for instance, by using spin coating or ink jet nozzles), accurate conformal contact between nanotemplate and substrate, exposure to ultraviolet light (which typically takes few seconds), and separation of substrate and nanotemplate. Note that the overall strategy takes advantage of the generation of a master pattern ideally with an areal density well beyond 1 Tb/in² prior to nanoimprinting. To achieve this within very small tolerances, as required for mass production, guided self-assembly of block copolymers for the fabrication of nanotemplates is at present the most important route to achieve sublithographic resolution [[250](#)]. In particular, it has been shown that when combined with nanoimprint lithography, the use of block copolymers allows to generate well-ordered arrays of magnetic nanostructures with feature sizes close to the sub-10 nm range [[34](#)]. In addition, block copolymers allow unprecedented control of the features shape, size, and their separation with extreme precision, for instance, when combined with self-aligned double nanoimprint lithography [[34](#)]. State-of-the-art magnetic nanostructures prepared in this way, as shown in [Fig. 9.18A–C](#) and [E–F](#), are a unique platform to achieve superior accuracy in controlling the fabrication of bit-patterned media, and thus much higher areal densities than what conventional nanofabrication methods can achieve.

Yet, there are other routes for nanoimprinting such as focused electron beam induced deposition (FEBID) [[251](#)], which is an emerging direct-write technique for the fabrication of complex magnetic systems with resolution of a few tens of nanometers [[252](#), [253](#)]. However, at present FEBID is still being explored to scale the growth to larger areas, possibly exploiting new strategies. Other routes to simplify the growth of magnetic nanostructures have been also proposed, such as the use of percolated magnetic media. Among various methods, percolated magnetic nanostructures can be fabricated by direct growth of the magnetic material on the nanotemplate surface. While this method leaves a trench material between

individual nanostructures [254], it does not require nanoimprinting. In fact, a number of studies show that percolated ferromagnetic nanostructures exhibit a unique potential for applications in magnetic recording technology [255–257].

Conversely, the magnetic properties of ferrimagnetic nanostructure arrays have remained largely unexplored in the context of applications. In the following sections, we will focus our attention on the magnetic properties of patterned ferrimagnetic nanostructures. In particular, in [Section 9.4.1](#) we will explore the magnetic properties of ferrimagnetic Fe-Tb nanodot arrays. In [Section 9.4.2](#), we will examine the potential of ferrimagnetic DyCo₅ antidot arrays for HAMR. Finally, [Section 9.4.3](#) will be devoted to technologically relevant processes of laser-induced magnetization switching in ferrimagnetic FeGdCo nanostructures.

9.4.1 Magnetic Properties of FeTb Nanodots

As discussed in previous section, the use of percolated media is a promising approach for the development of future hard-disk drive technology [254–258, 258–261]. One of the main difference with respect to conventional magnetic nanostructure arrays is the presence of a trench material, which plays a role in the magnetic interaction between nanostructures. Controlling this interaction is important to achieve high signal-to-noise ratios during information processing. Under appropriate conditions, the trench material can be beneficial to achieve higher thermal stability of individual bits. This is because in percolated media the film is continuous and through exchange interaction the magnetic coupling between nanostructures can be principally tuned by taking advantage of the trench material.

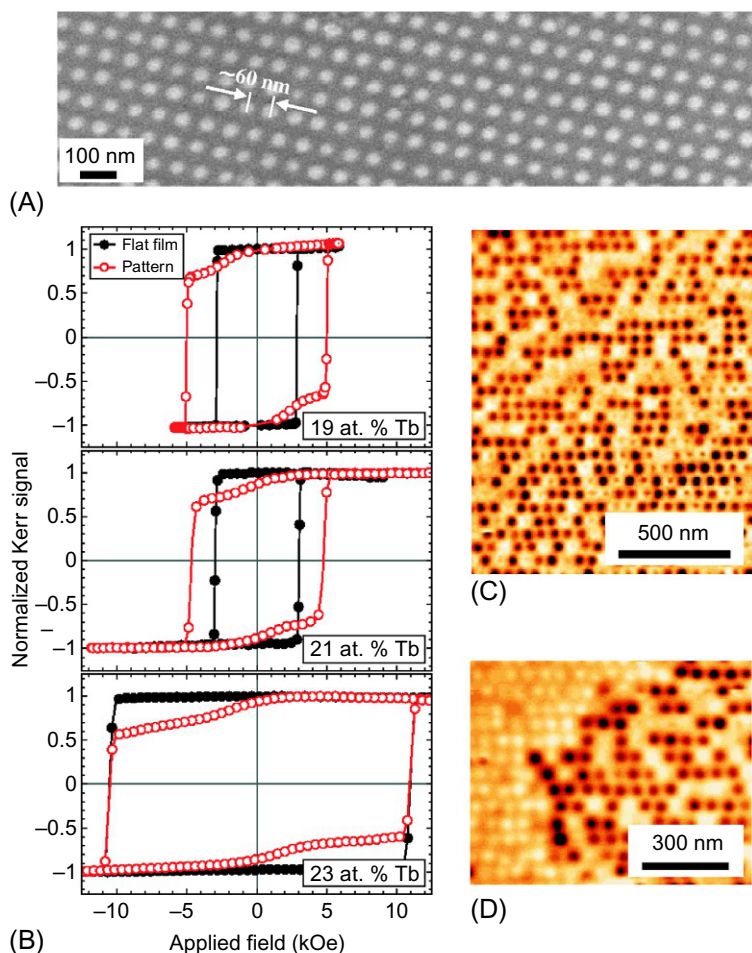
Percolated magnetic media is usually prepared by growing a continuous film on a prepatterned substrate, for example, a nonmagnetic nanotemplate containing an array of nanoislands with desired geometrical properties [254, 259, 260]. The substrate is typically fabricated by using techniques such as the ones described in the discussion preceding this section. In more general terms, the definition of percolated magnetic media also covers magnetic thin films containing dense and evenly distributed nonmagnetic entities with lateral dimensions of few nanometers. Such nonmagnetic entities act as pinning centers for the propagation of the domain walls [257, 260], and thus represent an additional knob for controlling magnetization reversal of individual bits. Thus, magnetic antidot arrays are commonly included within the definition of percolated magnetic media [261]. Nevertheless, a basic property of all types of percolated magnetic media is the fact that the magnetic grains are percolated at the nanoscale, and hence magnetically coupled.

Percolated ferromagnetic media with strong perpendicular magnetic anisotropy, commonly known as percolated perpendicular media, enable several advantages for applications in magnetic recording. These advantages are exemplified by a lower transition noise, higher thermal stability of magnetic bits, and unprecedented control of the magnetic coercivity of the

recording medium without affecting the thermal stability of individual bits. This approach is particularly successful when the size of the pinning sites remains in the range of the domain wall width [255–257]. For ferrimagnetic materials, on the other hand, comprehensive knowledge about the influence of the pinning sites on the magnetization reversal processes as well as on the thermal stability of the percolated medium has remained elusive at the fundamental level. In this respect, ferrimagnetic materials are important as they enable the possibility of reducing the intrinsic exchange stiffness and saturation magnetization which play an essential role in the pinning effect of the domain wall at nonmagnetic defects. This in principle allows independent switching of the trench material and nanostructure magnetization, paving the way for further control. In addition, the effect is expected to be accompanied by a concomitant decrease of the dipolar magnetic interaction between individual nanostructures while retaining all the advantages of percolated ferromagnetic systems.

An ideal platform to investigate these properties is the ferrimagnetic alloy $\text{Fe}_{1-x}\text{Tb}_x$, which in the form of thin film is amorphous and exhibits the required magnetic properties: Weak exchange stiffness, high perpendicular magnetic anisotropy, and low saturation magnetization [262–264]. In addition, proper tuning of the Tb content x allows to reach a magnetic compensation point between the Fe and Tb sublattices near room temperature. To this end, the magnetic properties of percolated $\text{Fe}_{1-x}\text{Tb}_x$ nanodot arrays close to the magnetic compensation point were investigated in Ref. [233]. Using magneto-optical Kerr effect and magnetic force microscopy (MFM), in that work it was shown that this type of ferrimagnetic nanostructures exhibits excellent magnetic properties. Specifically, the Fe-Tb nanodot arrays of Ref. [233] were prepared by nanoimprint lithography. First, the structure of the imprinted resist was transferred via chemical etching into a 30 nm-thick Ta layer. This layer was then used as a hard mask to transfer the whole structure into a Si wafer using reactive plasma etching, leading to well-ordered Si nanodots with about 30 nm diameter, 16 nm height, and 60 nm center-to-center distance. The high quality of the samples fabricated in this way can be evidenced by the SEM image shown in Fig. 9.19A [233]. The magnetic material was grown by magnetron sputtering directly on the patterned Si wafer and capped with a 5 nm-thick Pt layer to prevent oxidation in air.

Fig. 9.19B–D displays few-selected results of the magnetic characterization for various Tb contents x . All the samples exhibit perpendicular magnetic anisotropy for the selected compositions, as deduced from the high remanence values and sharp reversal branches under an out-of-plane applied magnetic field. Moreover, as seen in Fig. 9.19B, there are important differences between the hysteresis loops of the patterned substrate (red open symbols) and its flat film counterpart (black solid symbols). The hysteresis loops of the patterned substrate exhibit pronounced shoulders that are due to the reversal of the magnetization in the Fe-Tb nanodot caps, while the sharp reversal at higher magnetic fields can be attributed to the trench material. This is in contrast to the case of thin reference films of the same composition, which exhibits square-like hysteresis loops and coercive fields that become smaller than the corresponding coercive fields of the trench material when the Tb content x decreases.


Fig. 9.19

(A) SEM image of Si nanodots with 30 nm diameter and 60 nm pitch fabricated by nanoimprint lithography. (B) Normalized magnetization hysteresis loops of ferrimagnetic $\text{Fe}_{1-x}\text{Tb}_x$ nanodots [red (light) open symbols] and its flat film counterpart [black (dark) solid symbols] as a function of Tb content x .

(C and D) Corresponding MFM images for $x = 21\%$ revealing that the nanodot caps are in a single magnetic-domain state. (Taken from C. Schubert, *Percolated $\text{Fe}_{100-x}\text{Tb}_x$ nanodot arrays: exchange interaction and magnetization reversal*, in: *Magnetic Order and Coupling Phenomena: A Study of Magnetic Structure and Magnetization Reversal Processes in Rare-Earth-Transition-Metal Based Alloys and Heterostructures*, Springer International Publishing, Cham, ISBN 978-3-319-07106-0, 2014, pp. 77–86, https://doi.org/10.1007/978-3-319-07106-0_7.)

For $x = 19\%$, the coercivity difference between the trench material and reference film is largest, as can be seen in the top panel of Fig. 9.19B. This difference can be attributed to pinning effects caused by the magnetostatic interaction at the nonmagnetic pillars of the substrate, as the nanodot sizes are in the order of the domain wall width which for Fe-Tb is about 10 nm [265, 266]. Thus, for this composition the depinning field dominates the magnetization reversal

in the trench material. On the other hand, for Tb content of $x = 23\%$, which is closest to the magnetic compensation point [262–264], there is no appreciable difference between the coercive field of the trench material and the corresponding reference film. This is due to the fact that near the compensation point the net magnetization substantially decreases, and in consequence the intrinsic coercivity overcomes the depinning field. In other words, by proper tuning of the composition toward the magnetic compensation point, the coercivity of the trench material becomes progressively determined by the coercivity rather than by the depinning field.

Remarkably, the hysteresis loops clearly demonstrate that the magnetization of the coupled Fe-Tb nanodot caps can be rotated independently from the magnetization of the trench material for all investigated compositions. The magnetic switching field distribution is relatively broad, indicating that nucleation-dominated processes play the most important role in the magnetization reversal of individual Fe-Tb caps. This picture was shown to be also consistent with measurements of the angular dependence of the switching field distribution [233], which qualitatively follows the Stoner-Wohlfarth model [267]. Moreover, as revealed by the MFM images shown in Fig. 9.19C and D, the magnetization of the Fe-Tb nanodot caps resides in a single-domain state. Differently from this, the trench material revealed larger magnetic-domain structures characterized by domain walls following the arrangement of the nanodots [233]. One part of such type of domain walls can be seen in Fig. 9.19D. The observation of single magnetic-nanodomain states at the Fe-Tb caps is in principle consistent with the weak exchange stiffness of Fe-Tb alloy films. The observed magnetic properties of this percolated ferrimagnetic medium taken as a whole open up interesting paths toward applications in magnetic recording.

9.4.2 DyCo₅ Antidots for Heat-Assisted Magnetic Recording

As briefly discussed earlier, nano-patterned magnetic films such as antidot arrays are another example of percolated magnetic media which can be described as a continuous thin film containing an array of well-ordered nanoholes, which act as pinning centers for the domain wall propagation [202]. This effect ultimately allows further control of the magnetic properties depending on the interhole distances and nanohole dimensions. For instance, the magnetic properties of ferromagnetic antidots can be widely tuned depending on the nanoholes diameter and magnetic layer thickness while keeping the same distance between their centers [268]. The pinning effect of the domain wall also influences the magnetization reversal mechanisms in the regions between nanoholes [269, 270], and generally causes an increase of the magnetic coercivity when compared to unpatterned thin films. In turn, by continuously increasing the nanoholes diameter [271], the coercivity of magnetic antidots can be in principle enhanced to desired values [272], as in this case the domain wall movement becomes progressively harder [273]. On the other hand, if the size of the antidots is sufficiently small, the easy directions for domain wall propagation can be controlled depending on the symmetry of the nanohole lattice [274–276]. This leads to a spatially dependent local magnetic anisotropy in the

regions around the nanoholes, and thus to other advantages with respect to magnetic thin films. One of them is the possibility of achieving much more stable magnetic domain configurations within these nanoscopic regions, and thus to substantially suppress the effects of superparamagnetism. All these attributes taken together make magnetic antidot arrays promising candidates for ultra-high-density magnetic storage media.

Recently, the magnetic properties of ferrimagnetic DyCo₅ antidot arrays grown on hexagonally ordered alumina templates have been investigated in Ref. [202] (see Fig. 9.20). The main idea was to explore the potential of this type of ferrimagnetic nanostructures for

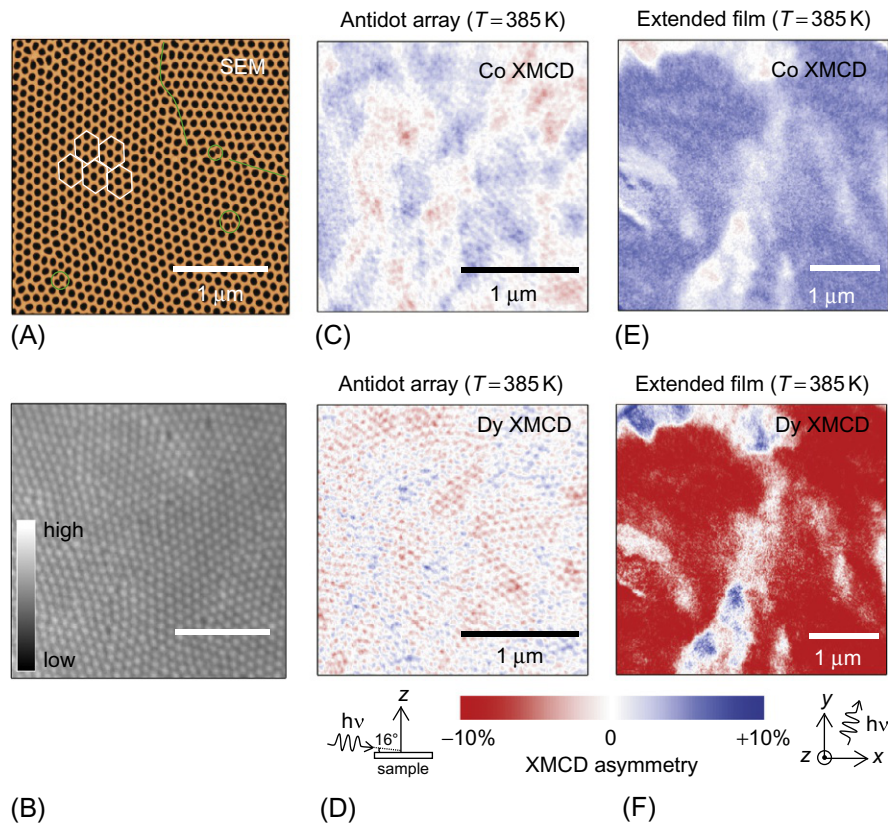


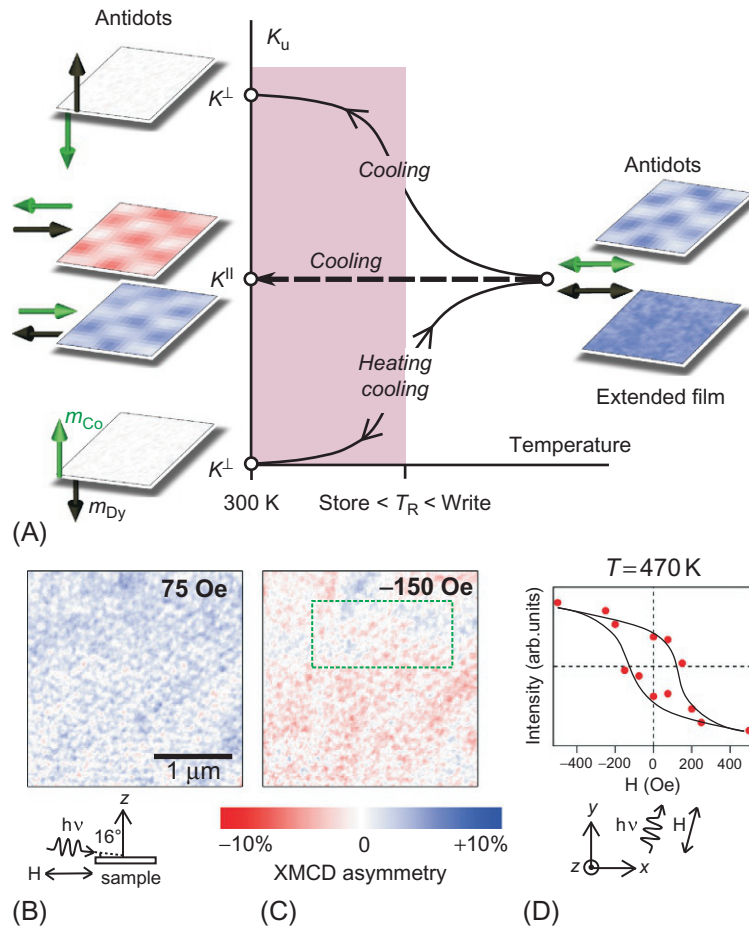
Fig. 9.20

(A) SEM and (B) X-ray photoelectron emission microscopy images of hexagonally ordered DyCo₅ antidots with 68 nm diameter and 105 nm separation. (C-F) XMCD-PEEM images from (C, D) DyCo₅ antidot array and (E, F) its extended thin film counterpart. The images were obtained at a temperature of 385 K and at the (C, E) Co-L₃ and (D, F) Dy-M₅ edges. Blue (dark) [red (light)] contrast indicates in-plane magnetization parallel (antiparallel) to the projection of the incident X-rays on the sample surface. On the bottom right, the color scale depicting the magnitude of the XMCD contrast and a sketch of the experimental geometry are shown. (From A.A. Únal, S. Valencia, F. Radu, D. Marchenko, K.J. Merazzo, M. Vázquez, J. Sánchez-Barriga, *Ferrimagnetic DyCo₅ nanostructures for bits in heat-assisted magnetic recording*, *Phys. Rev. Appl.* 5 (2016) 064007, <https://doi.org/10.1103/PhysRevApplied.5.064007>.)

temperature-dependent functionalities. To this end, DyCo₅ is a suitable alloy system as it possesses a magnetic anisotropy reorientation temperature (T_R) of ~ 350 K, above which the magnetization rotates from out-of-plane to in-plane [200, 201]. At room temperature, the Dy-Co alloy acts as a hard ferrimagnetic material with relatively low coercive field and perpendicular magnetic anisotropy. These properties render DyCo₅ an interesting material for applications in high-density magnetic recording. The DyCo₅ antidots were grown by magnetron sputtering from independent Co and Dy targets keeping the nano-patterned substrate at room temperature. For comparison purposes, a DyCo₅ extended film was grown simultaneously on top of an unpatterned alumina substrate under the same conditions. The thickness of the films was ~ 25 nm. A magnetic field of 0.5 T was applied perpendicular to the surface of the samples prior to magnetic characterization. The magnetic properties were investigated by means of X-ray circular dichroism (XMCD) in combination with photoelectron emission microscopy (PEEM) [277]. XMCD-PEEM is an ideal tool for this purpose as it exploits the element and magnetic sensitivity of XMCD together with the high spatial resolution of PEEM.

Fig. 9.20A and B shows SEM and X-ray absorption microscopy images of the DyCo₅ antidot array, respectively. Lines and circles on the SEM image indicate several punctual defects and structural domains that appear during the self-assembling process of the substrate. The nanoholes diameter is ~ 68 nm with a separation between their borders of ~ 37 nm, corresponding to a spacing between the nanohole centers of ~ 105 nm. At a temperature of 385 K, just above $T_R = 350$ K, the XMCD-PEEM contrast shown in Fig. 9.20C–F demonstrates ferrimagnetic ordering between Co and Dy sublattices. This manifests as a direct correspondence between the red (blue) regions of the Co XMCD images and the blue (red) regions of the Dy XMCD images, which appears due to the antiparallel alignment between the Co and Dy magnetic moments. Comparing the XMCD-PEEM images of the antidot array (Fig. 9.20C and D) and its extended film counterpart (Fig. 9.20E and F) reveals remarkable differences in the size of the magnetic domains. While the antidots exhibit nanometer-sized domains separated from each other by white color contrast, the extended film contains magnetic domains of several micrometers. This difference can be attributed to the above-mentioned pinning effect in the nano-patterned sample, which stabilizes magnetic nanodomains that are separated from each other according to the symmetry of the antidot lattice. As such pinning centers are absent in the extended film, the small nucleation centers that initiate magnetization reversal are likely responsible for the appearance of the large magnetic domains. From the XMCD-PEEM images of the antidots we deduce magnetic information repeating every 45–50 nm, which is in fair agreement with the difference between the nominal center-to-center nanohole distance and diameter.

In Fig. 9.21A we summarize key experimental results of the temperature dependence of the DyCo₅ antidot sample as compared with the extended film. Here we show a schematic representation of the magnetic anisotropy of the samples K_u as a function of temperature, along


Fig. 9.21

(A) Schematic representation of the heat-assisted magnetic recording processes and magnetic anisotropy reorientation observed with XMCD-PEEM on DyCo₅ antidot arrays and extended films. A selection of images summarizes the experimental results. The images on the left are taken at the Co-L₃ edge and correspond to the antidot array. (B, C) XMCD-PEEM images obtained at 470 K under an in-plane applied magnetic field of (B) 75 and (D) -150 Oe. (D) Hysteresis loop extracted from the region marked by a green (light) dashed rectangle in panel C. In bottom of figure, the experimental geometry and the XMCD asymmetry are indicated. (From A.A. Ünal, S. Valencia, F. Radu, D. Marchenko, K.J. Merazzo, M. Vázquez, J. Sánchez-Barriga, *Ferrimagnetic DyCo₅ nanostructures for bits in heat-assisted magnetic recording*, *Phys. Rev. Appl.* 5 (2016) 064007, <https://doi.org/10.1103/PhysRevApplied.5.064007>.)

with several channels for writing and storing information. In the initial state at room temperature, the magnetization of both samples is pointing perpendicular to the surface plane. Due to the shallow incidence angle of the X-ray beam with respect to the sample surface (see experimental geometry depicted at the bottom of Figs. 9.20 and 9.21), our XMCD-PEEM measurements are mainly sensitive to the in-plane magnetization. Therefore, a faint color

contrast is observed in the XMCD-PEEM images corresponding to states with out-of-plane anisotropy K^\perp shown on the left-hand side of Fig. 9.21A. Differently from this, a clear magnetic contrast emerges when the samples are heated above T_R , as it can be seen in the XMCD-PEEM images displayed on the right-hand side of Fig. 9.21A. This is due to the fact that with increasing temperature, the easy axis of magnetization rotates from out-of-plane to in-plane. Thus, the magnetic configurations above T_R are represented by states of in-plane magnetic anisotropy K^\parallel where the spins of the Co and Dy sublattices are aligned antiparallel to each other in the surface plane. Cooling the extended film back to room temperature in the absence of an external magnetic field leads to either one of the two possible out-of-plane anisotropy configurations. However, the antidot sample exhibits more options upon cooling: It can decay through four different channels corresponding to two out-of-plane and two in-plane magnetic anisotropy orientations. Consistent with results of micromagnetic simulations [202], we attribute the appearance of the in-plane channels to the landscape of pinning potentials created by the nanoholes within the whole structure.

By applying a weak external magnetic field during the cooling procedure it is possible to obtain a well-defined and stable magnetic state at room temperature, leading to HAMR [28–30]. The magnitude of the applied magnetic field should be smaller than the anisotropy field above T_R . From the spatially resolved hysteresis loop at 470 K shown in Fig. 9.21D, we estimate a local field distribution centered around 100 Oe. Fig. 9.22 shows schematically the overall HAMR process using ferrimagnetic DyCo₅ antidots when the external magnetic field is applied perpendicular to the surface. At room temperature, the magnetic moments are stable against the weak applied magnetic field (Fig. 9.22A). Moderate heating from a focused laser increases the temperature of individual bits above T_R and rotates the bit magnetization into the plane (Fig. 9.22B). The applied external magnetic field is also considerably smaller than the anisotropy field above T_R . (C) The magnetic moment is subsequently overwritten by the weak magnetic field upon cooling to room temperature.

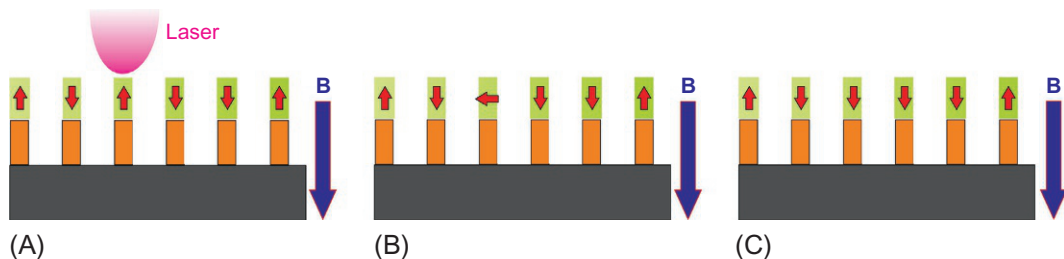


Fig. 9.22

Schematics of heat-assisted magnetic recording process using ferrimagnetic DyCo₅ antidots. (A) The magnetic moments are perpendicular to the plane and stable against a small out-of-plane external magnetic field B (denoted with blue (dark) arrows). A focused laser pulse can be used to locally increase the temperature of individual bits. (B) Moderate laser heating above the magnetic anisotropy reorientation temperature of $T_R = 370$ K rotates the magnetic moment associated with a single bit into the plane. The applied external magnetic field is also considerably smaller than the anisotropy field above T_R . (C) The magnetic moment is subsequently overwritten by the weak magnetic field upon cooling to room temperature.

(Fig. 9.22B). Upon cooling back to room temperature, the bit is overwritten by the out-of-plane magnetic field (Fig. 9.22C). Note that the critical temperature of the overall process is not the Curie temperature as in the case of conventional HAMR materials such as FePt [18–20, 28], but the much smaller anisotropy reorientation temperature T_R . Moreover, the switching process is done under relatively weak write fields, in strong contrast to conventional perpendicular media. The lower writing temperature also circumvents other problems associated with heat dissipation, requires lower power consumption, and diminishes the risk of damaging the magnetic recording medium. These properties open an alternative route toward a very efficient HAMR process, and thus it would be interesting to incorporate bit-patterned ferrimagnetic nanostructures within the currently existing HAMR technology.

9.4.3 Laser-Induced Switching of FeGdCo Nanostructures

In Section 9.1.9, we have briefly introduced the possibility of switching the magnetization with a focused laser beam and without an external applied magnetic field. This method was shown to be efficient for ferrimagnets in the pioneering work of Stanciu et al. [143], where the net magnetization of an amorphous $\text{Fe}_{74.6}\text{Co}_{3.4}\text{Gd}_{22}$ ferrimagnetic alloy was switched in a deterministic way by the helicity of the incoming circularly polarized fs-laser pulses (see Fig. 9.8). In this way, a magnetic bit pattern could be created at the nanoscale by scanning the laser beam across the sample while continuously modulating its helicity between left- and right-circular pulses (Fig. 9.8A). This effect is commonly referred to as all-optical helicity-dependent switching [278], and has also been observed in ferromagnetic materials such as granular L1_0 FePt in a C matrix and Co/Pt multilayers [279]. However, the detailed processes responsible for the deterministic switching of the magnetization are currently under debate.

First, theoretical attempts to explain the origin of helicity-dependent switching were based on the assumption that circularly polarized fs-laser pulses induce a transient magnetic field via the inverse Faraday effect [281, 282]. For ferromagnetic materials, simulations show that a laser-induced effective magnetic field of about 20 T would be at least required to achieve a deterministic switching of the magnetization [282]. Probably due to this reason, helicity-dependent switching has not been reported for single-element bulk ferromagnets so far. In thin films, there is also the possibility that the strong spin-orbit interaction at the interface plays a crucial role in enhancing the inverse Faraday effect; however, this proposal is at present subject of fundamental studies [283].

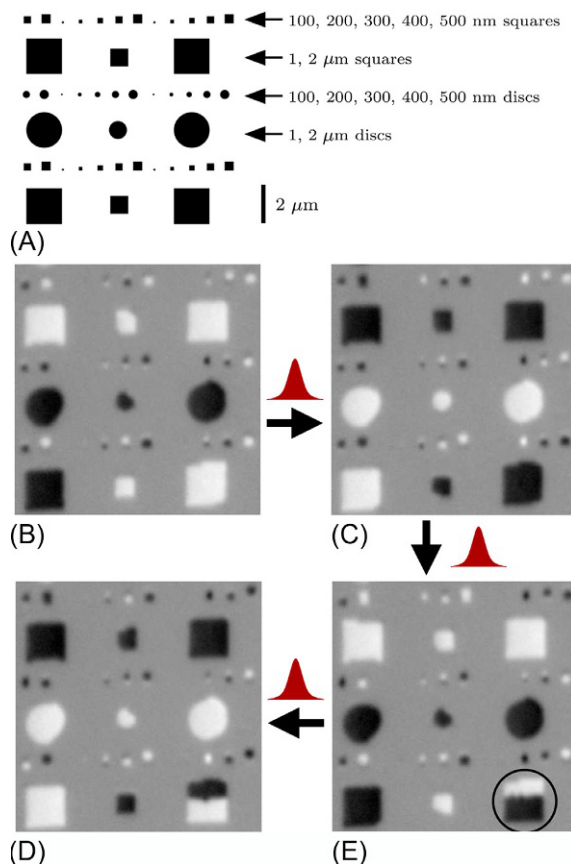
By contrast, for ferrimagnetic materials, helicity-dependent switching is so efficient that an energy lower than 10 fJ is in principle sufficient to switch the magnetization within a $20 \times 20 \text{ nm}^2$ area. Experimental works [263, 264, 278, 278, 284–286] focused on ferrimagnetic alloys and heterostructures, as well as on synthetic ferrimagnets, are consistent with this picture. Although ferrimagnetic heterostructures have a well-defined Curie temperature T_C , helicity-dependent switching is commonly observed in a narrow composition range [287],

being more effective when the starting temperature of the process is close to the compensation temperature T_{Comp} of the ferrimagnet. Hence, helicity-dependent switching in ferrimagnets is likely connected to the different temperature dependencies of the two or more sublattices forming the ferrimagnet, as shown for the exemplary case of DyCo₅ in Figs. 9.11 and 9.12 [193]. In other words, optically induced ultrafast processes are relevant for the deterministic switching of the magnetization, and we will come back to this point below.

At present, helicity-dependent switching of individual ferrimagnetic nanostructures in bit-patterned media still remains not only a fundamental but also a technological challenge. The process is limited by the spot size of the laser, which is too large to fulfill the requirements of ultrahigh areal bit densities. In this respect, the use of plasmonic Au nanoantennas patterned on magnetic thin films to reduce the laser spot size to the bit dimensions has been shown a promising approach to circumvent this problem [51]. For instance, this method has been employed to investigate all-optical switching at a spot size of 50 nm in ferrimagnetic Tb-Fe-Co thin films [288]. In fact, the implementation of plasmonic nanoantennas in well-ordered arrays of ferrimagnetic nanostructures might be one of the ideal alternatives to achieve single-dot helicity-dependent switching in bit-patterned media.

Another phenomenon that is fundamentally distinct from helicity-dependent switching is the so-called thermally induced magnetization switching (TIMS). This effect is purely thermally driven and helicity independent [289], and sometimes referred to as helicity-independent toggle switching. TIMS has been shown to be feasible with only a single femtosecond laser pulse, in contrast to helicity-dependent switching which usually requires multiple laser pulses. Moreover, in TIMS deterministic reversal of the magnetization is even achieved for linearly polarized laser light [289], and the efficiency of the process as well as its dynamics has been investigated in lithographically defined ferrimagnetic nanostructures [280]. A prominent example is shown in Fig. 9.23, where deterministic switching of the magnetization in ferrimagnetic FeCoGd nanostructures of different sizes is achieved via TIMS with single laser pulses of 50 fs duration. The effect appears to be similar in other ferrimagnetic systems of different compositions.

The underlying processes giving rise to the deterministic switching of the magnetization are likely related to the different dynamics of the magnetic moments within each sublattice on ultrafast time scales [290]. These processes are also relevant at the nanoscale. In this respect, time-resolved experiments in FeCoGd thin films demonstrate that following optical excitation the sublattice dominated by Fe and Co 3*d* electrons demagnetizes faster than the one dominated by Gd 4*f* electrons [290]. The faster demagnetization is due to the strong ferromagnetic exchange interaction between the magnetic moments in the Fe-Co sublattice. This leads to a transient out-of-equilibrium state where only the Gd magnetic moments are hardly demagnetized. Subsequently, due to the angular momentum transfer between the Fe-Co and Gd sublattices, a transient ferromagnetic-like state where the Fe-Co and Gd magnetic moments are parallel to each other emerges during the relaxation process. The relaxation dynamics is then


Fig. 9.23

Laser-induced magnetization switching in $\text{Fe}_{66.1}\text{Co}_{9.4}\text{Gd}_{24.5}$ nanostructures observed by XMCD-PEEM. (A) Sketch of the imaged structures depicting their sizes and shapes. (B–E) Sequence of XMCD-PEEM images acquired after applying a single linearly polarized fs-laser pulse between each image. *Black and white color contrast corresponds to opposite directions of the out-of-plane magnetization, recorded at the Fe L_3 edge.* The *arrows* indicate the order in which the pulses and images were acquired, and the *circle* in (D), a region where the switching is not complete. (Results taken from L. Le Guyader, S. El Moussaoui, M. Buzzi, R.V. Chopdekar, L.J. Heyderman, A. Tsukamoto, A. Itoh, A. Kirilyuk, T. Rasing, A.V. Kimel, F. Nolting, *Demonstration of laser induced magnetization reversal in GdFeCo nanostructures*, *Appl. Phys. Lett.* 101 (2) (2012) 022410, <https://doi.org/10.1063/1.4733965>.)

followed by a recovery of the Gd magnetic moments which now point in the opposite direction due to the weaker exchange interaction between the two sublattices. This would result in a final state where the net sample magnetization is reversed with respect to the one before optical excitation.

Recent theoretical studies [291, 292] indicate that TIMS is a specific phenomenon for ferrimagnetic materials. Computational approaches based on spin model simulations reveal that by varying the temperature and the initial magnetization of the RE-dominated sublattice

leads to different regimes where either the magnetization switches completely in the final state or backswitches into its initial state after a first transient reversal during the relaxation process [291]. The accessibility of one regime or another also depends on the laser fluence, and the material needs to be heated close to its Curie temperature T_C . Atomistic spin dynamics modeling of TIMS shows that while the existence of a transient ferromagnetic-like state seems a necessary precondition to achieve deterministic switching, the presence of a magnetization compensation point or going through it is not ultimately required [291, 292]. The modeling also reveals a decrease in the efficiency of TIMS with increasing laser pulse duration, establishing the boundaries outside which TIMS becomes a fully stochastic phenomenon. From the model calculations it is also concluded that deterministic switching shall be achieved with pulse durations Δt on the time scale of the antiferromagnetic exchange interaction (note that for $\Delta t = 50$ fs, $\Delta E \sim \hbar/2\Delta t = 10^{-21}$ J which is in the order of the energy of the antiferromagnetic exchange interaction).

In the context of applications, both helicity-dependent switching and TIMS on ferrimagnetic bit-patterned media may lead to unprecedented technological breakthroughs in HAMR at ultrahigh areal bit densities in the near future. Although the recording process requires control of heat dissipation, it proceeds on ultrafast time scales and without an applied magnetic field. Thus, the method represents a fundamentally distinct alternative to the HAMR process across the magnetic anisotropy-reorientation temperature in ferrimagnetic DyCo₅ antidots discussed in [Section 9.4.2](#).

9.5 Conclusion and Outlook

To summarize, we have presented the current status of magnetic recording media showing that maturity has been achieved for magnetic-based memory devices including tunnel junctions, spin valves, and spin-transfer torque effects. We have provided insight on the fundamental properties of emergent ferrimagnetic systems, and have shown and discussed key aspects in the research field of ferrimagnetic thin films and nanostructures. Recent achievements demonstrate that advanced understanding of the basic properties of these systems allows a versatile control of their intrinsic magnetic properties. We have emphasized unique properties of ferrimagnetic heterostructures, which are important for the prospect of incorporating ferrimagnetic-based recording media and sensors in future information technology. One of the most interesting properties of ferrimagnetic-based devices is the demonstration of ultrafast control of their magnetic states. In this respect, efficient all-optical switching using ferrimagnets, which is directly connected to dynamical effects of the magnetization on sup-picosecond time scales, emerges as one of the attractive routes for even higher performance of future spintronic devices. We have also highlighted nanostructuring of ferrimagnetic alloys as a prospective route toward ultrahigh-density magnetic recording. To this end, we have provided an overview on the status of the field of ferrimagnetic nanostructures, which holds

the potential for an unprecedented boost in the development of magnetic recording technology. Finally, we have discussed some technological challenges to overcome for the successful incorporation of ferrimagnetic bit patterned media into emergent technologies, such as HAMR, HDMR, and single-dot helicity-dependent switching. Future directions require sustained fundamental research on spin-orbitronics and plasmonics to achieve deterministic control of spin and orbital degrees of freedom. Understanding the role of topological properties of skyrmion lattices in ferrimagnetic systems emerges as a unique field of research awaiting for exciting discoveries.

References

- [1] S.A. Wolf, D.D. Awschalom, R.A. Buhrman, J.M. Daughton, S. von Molnár, M.L. Roukes, A. Y. Chtchelkanova, D.M. Treger, Spintronics: a spin-based electronics vision for the future, *Science* 294 (5546) (2001) 1488–1495, <https://doi.org/10.1126/science.1065389>, <http://science.sciencemag.org/content/294/5546/1488>.
- [2] I. Žutić, J. Fabian, S. Das Sarma, Spintronics: fundamentals and applications, *Rev. Mod. Phys.* 76 (2004) 323–410, <https://doi.org/10.1103/RevModPhys.76.323>.
- [3] P. Grünberg, R. Schreiber, Y. Pang, M.B. Brodsky, H. Sowers, Layered magnetic structures: evidence for antiferromagnetic coupling of Fe layers across Cr interlayers, *Phys. Rev. Lett.* 57 (19) (1986) 2442, <https://doi.org/10.1103/PhysRevLett.57.2442>.
- [4] M.N. Baibich, J.M. Broto, A. Fert, F.N. Van Dau, F. Petroff, P. Etienne, G. Creuzet, A. Friederich, J. Chazelas, Giant magnetoresistance of (001)Fe/(001)Cr magnetic superlattices, *Phys. Rev. Lett.* 61 (1988) 2472–2475, <https://doi.org/10.1103/PhysRevLett.61.2472>.
- [5] G. Binasch, P. Grünberg, F. Saurenbach, W. Zinn, Enhanced magnetoresistance in layered magnetic structures with antiferromagnetic interlayer exchange, *Phys. Rev. B* 39 (1989) 4828–4830, <https://doi.org/10.1103/PhysRevB.39.4828>.
- [6] T. McGuire, R. Potter, Anisotropic magnetoresistance in ferromagnetic 3D alloys, *IEEE Trans. Magn.* 11 (4) (1975) 1018–1038, <https://doi.org/10.1109/TMAG.1975.1058782>, <http://ieeexplore.ieee.org/document/1058782/>.
- [7] D. Weller, M.F. Doerner, Extremely high-density longitudinal magnetic recording media, *Annu. Rev. Mater. Sci.* 30 (1) (2000) 611–644, <https://doi.org/10.1146/annurev.matsci.30.1.611>.
- [8] S. Khizroev, D. Litvinov, *Perpendicular Magnetic Recording*, Springer Science & Business Media, New York, NY, 2006, <https://doi.org/10.1007/1-4020-2723-0>.
- [9] C.P. Bean, J.D. Livingston, Superparamagnetism, *J. Appl. Phys.* 30 (4) (1959) S120–S129, <https://doi.org/10.1063/1.2185850>.
- [10] W.F. Brown, Thermal fluctuations of a single-domain particle, *Phys. Rev.* 130 (1963) 1677–1686, <https://doi.org/10.1103/PhysRev.130.1677>.
- [11] H.N. Bertram, *Theory of Magnetic Recording*, Cambridge University Press, Cambridge, MA, 1994, <https://doi.org/10.1017/CBO9780511623066.001>.
- [12] D. Weller, A. Moser, Thermal effect limits in ultrahigh-density magnetic recording, *IEEE Trans. Magn.* 35 (6) (1999) 4423–4439, <https://doi.org/10.1109/20.809134>, <http://ieeexplore.ieee.org/document/809134/>.
- [13] T. Klemmer, D. Hoydick, H. Okumura, B. Zhang, W.A. Soffa, Magnetic hardening and coercivity mechanisms in L10 ordered FePd ferromagnets, *Scr. Met. Mater.* 33 (10) (1995) 1793–1805, [https://doi.org/10.1016/0956-716X\(95\)00413-P](https://doi.org/10.1016/0956-716X(95)00413-P), <http://www.sciencedirect.com/science/article/pii/0956716X9500413P>.
- [14] T. Sands, J.P. Harbison, M.L. Leadbeater, S.J. Allen Jr, G.W. Hull, R. Ramesh, V.G. Keramidis, Epitaxial ferromagnetic t-MnAl films on GaAs, *Appl. Phys. Lett.* 57 (24) (1990) 2609–2611, <https://doi.org/10.1063/1.103826>.

- [15] A. Morisako, M. Matsumoto, M. Naoe, Sputtered Mn-Al-Cu films for magnetic recording media, *IEEE Trans. Magn.* 23 (5) (1987) 2470–2472, <https://doi.org/10.1109/TMAG.1987.1065673>. <http://ieeexplore.ieee.org/abstract/document/1065673/>.
- [16] M. Hosoda, M. Oogane, M. Kubota, T. Kubota, H. Saruyama, S. Iihama, H. Naganuma, Y. Ando, Fabrication of L10-MnAl perpendicularly magnetized thin films for perpendicular magnetic tunnel junctions, *J. Appl. Phys.* 111 (7) (2012) 07A324, <https://doi.org/10.1063/1.3676428>.
- [17] P. Glijer, K. Sin, J.M. Sivertsen, J.H. Judy, Structural design of CoCrPt(Ta,B)/Cr magnetic thin film media for ultra high density longitudinal magnetic recording, *Scr. Met. Mater.* 33 (10) (1995) 1575–1584, [https://doi.org/10.1016/0956-716X\(95\)00402-H](https://doi.org/10.1016/0956-716X(95)00402-H). <http://www.sciencedirect.com/science/article/pii/0956716X9500402H>.
- [18] J.S. Chen, B.C. Lim, J.F. Hu, Y.K. Lim, B. Liu, G.M. Chow, High coercivity L10 FePt films with perpendicular anisotropy deposited on glass substrate at reduced temperature, *Appl. Phys. Lett.* 90 (4) (2007) 042508, <https://doi.org/10.1063/1.2430910>.
- [19] J.S. Chen, B.C. Lim, J.F. Hu, B. Liu, G.M. Chow, G. Ju, Low temperature deposited L10 FePt-C (001) films with high coercivity and small grain size, *Appl. Phys. Lett.* 91 (13) (2007) 132506, <https://doi.org/10.1063/1.2789790>.
- [20] A. Perumal, Y.K. Takahashi, K. Hono, L10 FePt-C nanogranular perpendicular anisotropy films with narrow size distribution, *Appl. Phys. Express* 1 (10) (2008) 101301. <http://stacks.iop.org/1882-0786/1/i=10/a=101301>.
- [21] R.A. Ristau, K. Barmak, L.H. Lewis, K.R. Coffey, J.K. Howard, On the relationship of high coercivity and L10 ordered phase in CoPt and FePt thin films, *J. Appl. Phys.* 86 (8) (1999) 4527–4533, <https://doi.org/10.1063/1.371397>.
- [22] J.A. Christodoulides, Y. Huang, Y. Zhang, G.C. Hadjipanayis, I. Panagiotopoulos, D. Niarchos, CoPt and FePt thin films for high density recording media, *J. Appl. Phys.* 87 (9) (2000) 6938–6940, <https://doi.org/10.1063/1.372892>.
- [23] M. Yu, Y. Liu, D.J. Sellmyer, Nanostructure and magnetic properties of composite CoPt:C films for extremely high-density recording, *J. Appl. Phys.* 87 (9) (2000) 6959–6961, <https://doi.org/10.1063/1.372899>.
- [24] J. Sayama, K. Mizutani, T. Asahi, T. Osaka, Thin films of SmCo₅ with very high perpendicular magnetic anisotropy, *Appl. Phys. Lett.* 85 (23) (2004) 5640–5642, <https://doi.org/10.1063/1.1829792>.
- [25] J. Sayama, K. Mizutani, T. Asahi, J. Ariake, K. Ouchi, S. Matsunuma, T. Osaka, Magnetic properties and microstructure of SmCo₅ thin film with perpendicular magnetic anisotropy, *J. Magn. Magn. Mater.* 287 (2005) 239–244, <https://doi.org/10.1016/j.jmmm.2004.10.039>. <http://www.sciencedirect.com/science/article/pii/S0304885304011175>.
- [26] Y.K. Takahashi, T. Ohkubo, K. Hono, Microstructure and magnetic properties of SmCo₅ thin films deposited on Cu and Pt underlayers, *J. Appl. Phys.* 100 (5) (2006) 053913, <https://doi.org/10.1063/1.2266247>.
- [27] G. Bertotti, *Hysteresis in Magnetism*, Academic Press, San Diego, CA, 1998, <https://doi.org/10.1016/B978-0-12-093270-2.50071-4><http://www.sciencedirect.com/science/book/9780120932702>.
- [28] M.H. Kryder, E.C. Gage, T.W. McDaniel, W.A. Challener, R.E. Rottmayer, G. Ju, Y.T. Hsia, M.F. Erden, Heat assisted magnetic recording, *Proc. IEEE* 96 (11) (2008) 1810–1835, <https://doi.org/10.1109/JPROC.2008.2004315>. <http://ieeexplore.ieee.org/document/4694026/>.
- [29] G. Ju, Y. Peng, E.K.C. Chang, Y. Ding, A.Q. Wu, X. Zhu, Y. Kubota, T.J. Klemmer, H. Amini, L. Gao, Z. Fan, T. Rausch, P. Subedi, M. Ma, S. Kalarickal, C.J. Rea, D.V. Dimitrov, P.W. Huang, K. Wang, X. Chen, C. Peng, W. Chen, J.W. Dykes, M.A. Seigler, E.C. Gage, R. Chantrell, J.U. Thiele, High density heat-assisted magnetic recording media and advanced characterization—progress and challenges, *IEEE Trans. Magn.* 51 (11) (2015) 1–9, <https://doi.org/10.1109/TMAG.2015.2439690>. <http://ieeexplore.ieee.org/document/7115916/>.
- [30] C. Vogler, C. Abert, F. Bruckner, D. Suess, D. Praetorius, Heat-assisted magnetic recording of bit-patterned media beyond 10 Tb/in², *Appl. Phys. Lett.* 108 (10) (2016) 102406, <https://doi.org/10.1063/1.4943629>.
- [31] M. Albrecht, G. Hu, A. Moser, O. Hellwig, B.D. Terris, Magnetic dot arrays with multiple storage layers, *J. Appl. Phys.* 97 (10) (2005) 103910, <https://doi.org/10.1063/1.1904705>.
- [32] H.J. Richter, A.Y. Dobin, R.T. Lynch, D. Weller, R.M. Brockie, O. Heinonen, K.Z. Gao, J. Xue, R.J.M. van de Veerdonk, P. Asselin, M.F. Erden, Recording potential of bit-patterned media, *Appl. Phys. Lett.* 88 (22) (2006) 222512, <https://doi.org/10.1063/1.2209179>.

- [33] H.J. Richter, A.Y. Dobin, O. Heinonen, K.Z. Gao, R.J.M. van de Veerdonk, R.T. Lynch, J. Xue, D. Weller, P. Asselin, M.F. Erden, R.M. Brockie, Recording on bit-patterned media at densities of 1 Tb/in² and beyond. *IEEE Trans. Magn.* 42 (10) (2006) 2255–2260, <https://doi.org/10.1109/TMAG.2006.878392>. <http://ieeexplore.ieee.org/document/1704265/>.
- [34] T.R. Albrecht, H. Arora, V. Ayanoor-Vitikkate, J.M. Beaujour, D. Bedau, D. Berman, A.L. Bogdanov, Y.A. Chapuis, J. Cushen, E.E. Dobisz, G. Doerk, H. Gao, M. Grobis, B. Gurney, W. Hanson, O. Hellwig, T. Hirano, P.O. Jubert, D. Kercher, J. Lille, Z. Liu, C.M. Mate, Y. Obukhov, K.C. Patel, K. Rubin, R. Ruiz, M. Schabes, L. Wan, D. Weller, T.W. Wu, E. Yang, Bit-patterned magnetic recording: theory, media fabrication, and recording performance, *IEEE Trans. Magn.* 51 (5) (2015) 1–42, <https://doi.org/10.1109/TMAG.2015.2397880>. <http://ieeexplore.ieee.org/abstract/document/7029109/>.
- [35] S. Greaves, Y. Kanai, H. Muraoka, Shingled magnetic recording on bit patterned media, *IEEE Trans. Magn.* 46 (6) (2010) 1460–1463, <https://doi.org/10.1109/TMAG.2010.2043221>. <http://ieeexplore.ieee.org/document/6559316/>.
- [36] S. Wang, Y. Wang, R.H. Victora, Shingled magnetic recording on bit patterned media at 10 rm Tb/in², *IEEE Trans. Magn.* 49 (7) (2013) 3644–3647, <https://doi.org/10.1109/TMAG.2012.2237545>. <http://ieeexplore.ieee.org/document/5467475/>.
- [37] R. Wood, M. Williams, A. Kavcic, J. Miles, The feasibility of magnetic recording at 10 terabits per square inch on conventional media, *IEEE Trans. Magn.* 45 (2) (2009) 917–923, <https://doi.org/10.1109/TMAG.2008.2010676>. <http://ieeexplore.ieee.org/abstract/document/4782114/>.
- [38] E. Hwang, R. Negi, B.V.K.V. Kumar, Signal processing for near 10 Tbit/in² density in two-dimensional magnetic recording (TDMR), *IEEE Trans. Magn.* 46 (6) (2010) 1813–1816, <https://doi.org/10.1109/TMAG.2010.2041531>. <http://ieeexplore.ieee.org/abstract/document/5467383/>.
- [39] W. Chang, J.R. Cruz, Inter-track interference mitigation for bit-patterned magnetic recording, *IEEE Trans. Magn.* 46 (11) (2010) 3899–3908, <https://doi.org/10.1109/TMAG.2010.2056926>. <http://ieeexplore.ieee.org/abstract/document/5467383/>.
- [40] H. Wang, T. Katayama, K.S. Chan, Y. Kanai, Z. Yuan, S. Shafidah, Optimal write head design for perpendicular magnetic recording, *IEEE Trans. Magn.* 51 (11) (2015) 1–4, <https://doi.org/10.1109/TMAG.2015.2436433>. <http://ieeexplore.ieee.org/abstract/document/7112167/>.
- [41] J.U. Thiele, K.R. Coffey, M.F. Toney, J.A. Hedstrom, A.J. Kellock, Temperature dependent magnetic properties of highly chemically ordered Fe_{55-x}Ni_xPt₄₅L₁₀ films, *J. Appl. Phys.* 91 (10) (2002) 6595–6600, <https://doi.org/10.1063/1.1470254>.
- [42] H. Awano, N. Ohta, Magneto-optical recording technology toward 100 Gb/in², *IEEE J. Sel. Top. Quantum Electron.* 4 (5) (1998) 815–820, <https://doi.org/10.1109/2944.735766>. <http://iopscience.iop.org/article/10.1088/0022-3727/34/17/201/meta>.
- [43] S. Tsunashima, Magneto-optical recording, *J. Phys. D. Appl. Phys.* 34 (17) (2001) R87, <https://doi.org/10.1088/0022-3727/34/17/201>. <http://stacks.iop.org/0022-3727/34/i=17/a=201>.
- [44] J.G. Zhu, X. Zhu, Y. Tang, Thermally assisted magnetic recording, *Fujitsu Sci. Tech. J.* 42 (1) (2006) 158–167. <http://www.fujitsu.com/global/about/resources/publications/fstj/archives/vol42-1.html>.
- [45] A.Q. Wu, Y. Kubota, T. Klemmer, T. Rausch, C. Peng, Y. Peng, D. Karns, X. Zhu, Y. Ding, E.K. Chang, Y. Zhao, H. Zhou, K. Gao, J.U. Thiele, M. Seigler, G. Ju, E. Gage, HAMR areal density demonstration of 1+ Tbps on spindisk, *IEEE Trans. Magn.* 49 (2) (2013) 779–782, <https://doi.org/10.1109/TMAG.2012.2219513>. <http://ieeexplore.ieee.org/document/6417009/>.
- [46] J.G. Zhu, X. Zhu, Y. Tang, Microwave assisted magnetic recording, *IEEE Trans. Magn.* 0018-946444 (1) (2008) 125–131, <https://doi.org/10.1109/TMAG.2007.911031>. <http://ieeexplore.ieee.org/abstract/document/4407618/>. ISSN.
- [47] Y. Wang, Y. Tang, J.G. Zhu, Media damping constant and performance characteristics in microwave assisted magnetic recording with circular AC field, *J. Appl. Phys.* 105 (7) (2009) 07B902, <https://doi.org/10.1063/1.3067839>.
- [48] Y. Nozaki, K. Tateishi, S. Taharazako, M. Ohta, S. Yoshimura, K. Matsuyama, Microwave-assisted magnetization reversal in 0.36-μm-wide Permalloy wires, *Appl. Phys. Lett.* 91 (12) (2007) 122505, <https://doi.org/10.1063/1.2786593>.

- [49] Y. Nozaki, N. Narita, T. Tanaka, K. Matsuyama, Microwave-assisted magnetization reversal in a Co/Pd multilayer with perpendicular magnetic anisotropy, *Appl. Phys. Lett.* 95 (8) (2009) 082505, <https://doi.org/10.1063/1.3213559>.
- [50] T.W. McDaniel, Areal density limitation in bit-patterned, heat-assisted magnetic recording using FePtX media, *J. Appl. Phys.* 112 (9) (2012) 093920, <https://doi.org/10.1063/1.4764336>.
- [51] B.C. Stipe, T.C. Strand, C.C. Poon, H. Balamane, T.D. Boone, J.A. Katine, J.L. Li, V. Rawat, H. Nemoto, A. Hirotsune, O. Hellwig, R. Ruiz, E. Dobisz, D.S. Kercher, N. Robertson, T.R. Albrecht, B. D. Terris, Magnetic recording at 1.5 Pb m^{-2} using an integrated plasmonic antenna, *Nat. Photonics* 4 (1) (2010) 484–488, <https://doi.org/10.1038/nphoton.2010.90>.
- [52] T.R. Albrecht, O. Hellwing, R. Ruiz, M.E. Schabes, B.D. Terris, X.Z. Wu, Bit-patterned magnetic recording: nanoscale magnetic islands for data storage, in: *Nanoscale Magnetic Materials and Applications* Springer US, New York, NY, 2009, , pp. 237–274, https://doi.org/10.1007/978-0-387-85600-1_9.
- [53] B.D. Terris, T. Thomson, G. Hu, Patterned media for future magnetic data storage, *Microsyst. Technol.* 13 (2) (2007) 189–196, <https://doi.org/10.1007/s00542-006-0144-9>.
- [54] V. Sundar, X. Yang, Y. Liu, Z. Dai, B. Zhou, J. Zhu, K. Lee, T. Chang, D. Laughlin, J.-G.J. Zhu, Fabrication of bit patterned media using templated two-phase growth, *APL Mater.* 5 (2) (2017) 026106, <https://doi.org/10.1063/1.4974866>.
- [55] P. Krone, D. Makarov, T. Schrefl, M. Albrecht, Exchange coupled composite bit patterned media, *Appl. Phys. Lett.* 97 (8) (2010) 082501, <https://doi.org/10.1063/1.3481668>.
- [56] W.A. Challener, C. Peng, A.V. Itagi, D. Karns, W. Peng, Y. Peng, X.M. Yang, X. Zhu, N.J. Gokemeijer, Y.T. Hsia, G. Ju, R.E. Rottmayer, M.A. Seigler, E.C. Gage, Heat-assisted magnetic recording by a near-field transducer with efficient optical energy transfer, *Nat. Photonics* 3 (2009) 220–224, <https://doi.org/10.1038/nphoton.2009.26>.
- [57] E.E. Fullerton, D.T. Margulies, N. Supper, H. Do, M. Schabes, A. Berger, A. Moser, Antiferromagnetically coupled magnetic recording media, *IEEE Trans. Magn.* 39 (2) (2003) 639–644, <https://doi.org/10.1109/TMAG.2003.808985>. <http://ieeexplore.ieee.org/document/1190077/>.
- [58] V. Skumryev, S. Stoyanov, Y. Zhang, G. Hadjipanayis, D. Givord, J. Nogues, Beating the superparamagnetic limit with exchange bias, *Nature* 423 (2003) 850–853, <https://doi.org/10.1038/nature01687>.
- [59] M. Jullière, Tunneling between ferromagnetic films, *Phys. Lett. A* 54 (3) (1975) 225–226, [https://doi.org/10.1016/0375-9601\(75\)90174-7](https://doi.org/10.1016/0375-9601(75)90174-7). <http://www.sciencedirect.com/science/article/pii/0375960175901747>.
- [60] J.S. Moodera, L.R. Kinder, T.M. Wong, R. Meservey, Large magnetoresistance at room temperature in ferromagnetic thin film tunnel junctions, *Phys. Rev. Lett.* 74 (1995) 3273–3276, <https://doi.org/10.1103/PhysRevLett.74.3273>.
- [61] B. Dieny, Giant magnetoresistance in spin-valve multilayers, *J. Magn. Magn. Mater.* 136 (3) (1994) 335–359, [https://doi.org/10.1016/0304-8853\(94\)00356-4](https://doi.org/10.1016/0304-8853(94)00356-4). <http://www.sciencedirect.com/science/article/pii/0304885394003564>.
- [62] S.S.P. Parkin, N. More, K.P. Roche, Oscillations in exchange coupling and magnetoresistance in metallic superlattice structures: Co/Ru, Co/Cr, and Fe/Cr, *Phys. Rev. Lett.* 64 (1990) 2304–2307, <https://doi.org/10.1103/PhysRevLett.64.2304>.
- [63] W.H. Meiklejohn, C.P. Bean, New magnetic anisotropy, *Phys. Rev.* 105 (1957) 904–913, <https://doi.org/10.1103/PhysRev.105.904>.
- [64] J. Nogués, I.K. Schuller, Exchange bias, *J. Magn. Magn. Mater.* 0304-8853192 (2) (1999) 203–232, [https://doi.org/10.1016/S0304-8853\(98\)00266-2](https://doi.org/10.1016/S0304-8853(98)00266-2). <http://www.sciencedirect.com/science/article/pii/S0304885398002662>. ISSN.
- [65] A. Berkowitz, K. Takano, Exchange anisotropy: a review, *J. Magn. Magn. Mater.* 0304-8853200 (1) (1999) 552–570, [https://doi.org/10.1016/S0304-8853\(99\)00453-9](https://doi.org/10.1016/S0304-8853(99)00453-9). <http://www.sciencedirect.com/science/article/pii/S0304885399004539>. ISSN.
- [66] R.L. Stamps, Mechanisms for exchange bias, *J. Phys. D. Appl. Phys.* 33 (23) (2000) R247. <http://stacks.iop.org/0022-3727/33/i=23/a=201>.
- [67] M. Kiwi, Exchange bias theory, *J. Magn. Magn. Mater.* 0304-8853234 (3) (2001) 584–595, [https://doi.org/10.1016/S0304-8853\(01\)00421-8](https://doi.org/10.1016/S0304-8853(01)00421-8). <http://www.sciencedirect.com/science/article/pii/S0304885301004218>. ISSN.

- [68] F. Radu, H. Zabel, Exchange bias effect of ferro-/antiferromagnetic heterostructures, in: H. Zabel, S.D. Bader (Eds.), *Magnetic Heterostructures: Advances and Perspectives in Spinstructures and Spintransport*, Springer, Berlin, Heidelberg, 2008, ISBN 978-3-540-73462-8, pp. 97–184, https://doi.org/10.1007/978-3-540-73462-8_3.
- [69] P.K. Manna, S.M. Yusuf, Two interface effects: exchange bias and magnetic proximity, *Phys. Rep.* 0370-1573535 (2) (2014) 61–99, <https://doi.org/10.1016/j.physrep.2013.10.002>. <http://www.sciencedirect.com/science/article/pii/S0370157313003773>. ISSN.
- [70] Y. Guo, Y. Ouyang, N. Sato, C.C. Ooi, S.X. Wang, Exchange-biased anisotropic magnetoresistive field sensor, *IEEE Sensors J.* 17 (11) (2017) 3309–3315, <https://doi.org/10.1109/JSEN.2017.2695238>. <http://ieeexplore.ieee.org/document/7904678/>.
- [71] R.R. Katti, Current-in-plane pseudo-spin-valve device performance for giant magnetoresistive random access memory applications (invited), *J. Appl. Phys.* 91 (10) (2002) 7245–7250, <https://doi.org/10.1063/1.1456037>.
- [72] R.R. Katti, Giant magnetoresistive random-access memories based on current-in-plane devices, *Proc. IEEE* 91 (5) (2003) 687–702, <https://doi.org/10.1109/JPROC.2003.811805>. <http://ieeexplore.ieee.org/document/1200122/>.
- [73] D. Wang, C. Nordman, J.M. Daughton, Z. Qian, J. Fink, 70 CoFeB as free and reference layers, *IEEE Trans. Magn.* 0018-946440 (4) (2004) 2269–2271, <https://doi.org/10.1109/TMAG.2004.830219>. <http://ieeexplore.ieee.org/abstract/document/1325474/>. ISSN.
- [74] W. Wulfhekel, M. Klaua, D. Ullmann, F. Zavaliche, J. Kirschner, R. Urban, T. Monchesky, B. Heinrich, Single-crystal magnetotunnel junctions, *Appl. Phys. Lett.* 78 (4) (2001) 509–511, <https://doi.org/10.1063/1.1342778>.
- [75] T. Miyazaki, T. Yaoui, S. Ishio, Large magnetoresistance effect in 82Ni-Fe/Al-Al₂O₃/Co magnetic tunneling junction, *J. Magn. Mater.* 98 (1) (1991) L7–L9, [https://doi.org/10.1016/0304-8853\(91\)90417-9](https://doi.org/10.1016/0304-8853(91)90417-9). <http://www.sciencedirect.com/science/article/pii/0304885391904179>.
- [76] T.S. Plaskett, P.P. Freitas, N.P. Barradas, M.F. da Silva, J.C. Soares, Magnetoresistance and magnetic properties of NiFe/oxide/Co junctions prepared by magnetron sputtering, *J. Appl. Phys.* 76 (10) (1994) 6104–6106, <https://doi.org/10.1063/1.358319>.
- [77] R.C. Sousa, J.J. Sun, V. Soares, P.P. Freitas, A. Kling, M.F. da Silva, J.C. Soares, Large tunneling magnetoresistance enhancement by thermal anneal, *Appl. Phys. Lett.* 73 (22) (1998) 3288–3290, <https://doi.org/10.1063/1.122747>.
- [78] S. Cardoso, V. Gehanno, R. Ferreira, P.P. Freitas, Ion beam deposition and oxidation of spin-dependent tunnel junctions, *IEEE Trans. Magn.* 35 (5) (1999) 2952–2954, <https://doi.org/10.1109/20.801044>. <http://ieeexplore.ieee.org/abstract/document/801044/>.
- [79] J.S. Moodera, J. Nassar, G. Mathon, Spin-tunneling in ferromagnetic junctions, *Annu. Rev. Mater. Sci.* 29 (1) (1999) 381–432, <https://doi.org/10.1146/annurev.matsci.29.1.381>.
- [80] M. Bowen, V. Cros, F. Petroff, A. Fert, C.M. Boubeta, J.L. Costa-Krämer, J.V. Anguita, A. Cebollada, F. Briones, J.M. de Teresa, L. Morellón, M.R. Ibarra, F. Güell, F. Peiró, A. Cornet, Large magnetoresistance in Fe/MgO/FeCo(001) epitaxial tunnel junctions on GaAs(001), *Appl. Phys. Lett.* 79 (11) (2001) 1655–1657, <https://doi.org/10.1063/1.1404125>.
- [81] J.H. Yu, H.M. Lee, Y. Ando, T. Miyazaki, Electron transport properties in magnetic tunnel junctions with epitaxial NiFe (111) ferromagnetic bottom electrodes, *Appl. Phys. Lett.* 82 (26) (2003) 4735–4737, <https://doi.org/10.1063/1.1587271>.
- [82] J. Faure-Vincent, C. Tiusan, E. Jouguelet, F. Canet, M. Sajieddine, C. Bellouard, E. Popova, M. Hehn, F. Montaigne, A. Schuhl, High tunnel magnetoresistance in epitaxial Fe/MgO/Fe tunnel junctions, *Appl. Phys. Lett.* 82 (25) (2003) 4507–4509, <https://doi.org/10.1063/1.1586785>.
- [83] S.S.P. Parkin, C. Kaiser, A. Panchula, P.M. Rice, B. Hughes, M. Samant, S.-H. Yang, Giant tunnelling magnetoresistance at room temperature with MgO (100) tunnel barriers, *Nat. Mater.* 3 (2004) 862–867, <https://doi.org/10.1038/nmat1256>.
- [84] S. Yuasa, T. Nagahama, A. Fukushima, Y. Suzuki, K. Ando, Giant room-temperature magnetoresistance in single-crystal Fe/MgO/Fe magnetic tunnel junctions, *Nat. Mater.* 3 (2004) 868–871, <https://doi.org/10.1038/nmat1257>.
- [85] S. Yuasa, T. Katayama, T. Nagahama, A. Fukushima, H. Kubota, Y. Suzuki, K. Ando, Giant tunneling magnetoresistance in fully epitaxial body-centered-cubic Co/MgO/Fe magnetic tunnel junctions, *Appl. Phys. Lett.* 87 (22) (2005) 222508, <https://doi.org/10.1063/1.2138355>.

- [86] S. Yuasa, A. Fukushima, H. Kubota, Y. Suzuki, K. Ando, Giant tunneling magnetoresistance up to 410% at room temperature in fully epitaxial Co/MgO/Co magnetic tunnel junctions with BCC Co(001) electrodes, *Appl. Phys. Lett.* 89 (4) (2006) 042505, <https://doi.org/10.1063/1.2236268>.
- [87] S. Ikeda, J. Hayakawa, Y. Ashizawa, Y. M. Lee, K. Miura, H. Hasegawa, M. Tsunoda, F. Matsukura, H. Ohno, Tunnel magnetoresistance of 604% at 300 K by suppression of Ta diffusion in CoFeB/MgO/CoFeB pseudo-spin-valves annealed at high temperature, *Appl. Phys. Lett.* 93 (8) (2008) 082508, <https://doi.org/10.1063/1.2976435>.
- [88] W.H. Butler, X.G. Zhang, T.C. Schulthess, J.M. MacLaren, Spin-dependent tunneling conductance of Fe[MgO]Fe sandwiches, *Phys. Rev. B* 63 (2001) 054416, <https://doi.org/10.1103/PhysRevB.63.054416>.
- [89] J. Mathon, A. Umerski, Theory of tunneling magnetoresistance of an epitaxial Fe/MgO/Fe(001) junction, *Phys. Rev. B* 63 (2001) 220403, <https://doi.org/10.1103/PhysRevB.63.220403>.
- [90] S. Bhatti, R. Sbiaa, A. Hirohata, H. Ohno, S. Fukami, S.N. Piramanayagam, Spintronics based random access memory: a review, *Mater. Today* 1369-7021(2017)<https://doi.org/10.1016/j.mattod.2017.07.007> <http://www.sciencedirect.com/science/article/pii/S1369702117304285>. ISSN.
- [91] G. Tatara, H. Kohno, Theory of current-driven domain wall motion: spin transfer versus momentum transfer, *Phys. Rev. Lett.* 92 (2004) 086601, <https://doi.org/10.1103/PhysRevLett.92.086601>.
- [92] Z. Li, S. Zhang, Domain-wall dynamics and spin-wave excitations with spin-transfer torques, *Phys. Rev. Lett.* 92 (2004) 207203, <https://doi.org/10.1103/PhysRevLett.92.207203>.
- [93] A. Thiaville, Y. Nakatani, J. Miltat, Y. Suzuki, Micromagnetic understanding of current-driven domain wall motion in patterned nanowires, *EPL (Europhys. Lett.)* 69 (6) (2005) 990.
- [94] D.C. Ralph, M.D. Stiles, Spin transfer torques, *J. Magn. Mater.* 320 (7) (2008) 1190–1216, <https://doi.org/10.1016/j.jmmm.2007.12.019>. <http://www.sciencedirect.com/science/article/pii/S0304885307010116>.
- [95] J.Z. Sun, D.C. Ralph, Magnetoresistance and spin-transfer torque in magnetic tunnel junctions, *J. Magn. Mater.* 320 (7) (2008) 1227–1237, <https://doi.org/10.1016/j.jmmm.2007.12.008>. <http://www.sciencedirect.com/science/article/pii/S0304885307010177>.
- [96] A. Manchon, S. Zhang, Theory of spin torque due to spin-orbit coupling, *Phys. Rev. B* 79 (2009) 094422, <https://doi.org/10.1103/PhysRevB.79.094422>.
- [97] J. Park, D.C. Ralph, R.A. Buhrman, Fast deterministic switching in orthogonal spin torque devices via the control of the relative spin polarizations, *Appl. Phys. Lett.* 103 (25) (2013) 252406, <https://doi.org/10.1063/1.4851855>.
- [98] L. Berger, Emission of spin waves by a magnetic multilayer traversed by a current, *Phys. Rev. B* 54 (1996) 9353–9358, <https://doi.org/10.1103/PhysRevB.54.9353>.
- [99] J.C. Slonczewski, Current-driven excitation of magnetic multilayers, *J. Magn. Mater.* 0304-8853/159 (1) (1996) L1–L7, [https://doi.org/10.1016/0304-8853\(96\)00062-5](https://doi.org/10.1016/0304-8853(96)00062-5). <http://www.sciencedirect.com/science/article/pii/0304885396000625>. ISSN.
- [100] A. Fert, Nobel lecture: origin, development, and future of spintronics, *Rev. Mod. Phys.* 80 (2008) 1517–1530, <https://doi.org/10.1103/RevModPhys.80.1517>.
- [101] S.A. Wolf, J. Lu, M.R. Stan, E. Chen, D.M. Treger, The promise of nanomagnetism and spintronics for future logic and universal memory, *Proc. IEEE* 0018-9219/98 (12) (2010) 2155–2168, <https://doi.org/10.1109/JPROC.2010.2064150>. ISSN.
- [102] A.D. Kent, D.C. Worledge, A new spin on magnetic memories, *Nat. Nanotechnol.* 10 (2015) 187–191, <https://doi.org/10.1038/nnano.2015.24>.
- [103] J. Sinova, S.O. Valenzuela, J. Wunderlich, C.H. Back, T. Jungwirth, Spin Hall effects, *Rev. Mod. Phys.* 87 (2015) 1213–1260, <https://doi.org/10.1103/RevModPhys.87.1213>.
- [104] G.Y. Guo, S. Murakami, T.W. Chen, N. Nagaosa, Intrinsic spin Hall effect in platinum: first-principles calculations, *Phys. Rev. Lett.* 100 (2008) 096401, <https://doi.org/10.1103/PhysRevLett.100.096401>.
- [105] L. Liu, C.-F. Pai, Y. Li, H.W. Tseng, D.C. Ralph, R.A. Buhrman, Spin-torque switching with the giant spin Hall effect of tantalum, *Science* 336 (6081) (2012) 555–558, <https://doi.org/10.1126/science.1218197>. <http://science.sciencemag.org/content/336/6081/555>.
- [106] L. Berger, Side-jump mechanism for the hall effect of ferromagnets, *Phys. Rev. B* 2 (1970) 4559–4566, <https://doi.org/10.1103/PhysRevB.2.4559>.

- [107] Y. Niimi, Y. Otani, Reciprocal spin Hall effects in conductors with strong spin-orbit coupling: a review, *Rep. Prog. Phys.* 78 (2015) 124501, <https://doi.org/10.1088/0034-4885/78/12/124501>.
- [108] V.M. Edelstein, Spin polarization of conduction electrons induced by electric current in two-dimensional asymmetric electron systems, *Solid State Commun.* 73 (3) (1990) 233–235, [https://doi.org/10.1016/0038-1098\(90\)90963-C](https://doi.org/10.1016/0038-1098(90)90963-C). <http://www.sciencedirect.com/science/article/pii/003810989090963C>.
- [109] I.M. Miron, G. Gaudina, S. Auffret, B. Rodmacq, A. Schuhl, S. Pizzini, J. Vogel, P. Gambardella, Current-driven spin torque induced by the Rashba effect in a ferromagnetic metal layer, *Nat. Mater.* 9 (2010) 230–234, <https://doi.org/10.1038/nmat2613>.
- [110] I.M. Miron, T. Moore, H. Szambolics, L.D. Buda-Prejbeanu, S. Auffret, B. Rodmacq, S. Pizzini, J. Vogel, M. Bonfim, A. Schuhl, G. Gaudin, Fast current-induced domain-wall motion controlled by the Rashba effect, *Nat. Mater.* 10 (2011) 419–423, <https://doi.org/10.1038/nmat3020>.
- [111] J.C. Rojas-Sánchez, L. Vila, G. Desfonds, S. Gambarelli, J.P. Attané, J.M.D. Teresa, C. Magén, A. Fert, Spin-to-charge conversion using Rashba coupling at the interface between non-magnetic materials, *Nat. Commun.* 4 (2013) 2944, <https://doi.org/10.1038/ncomms3944>.
- [112] W. Zhang, M.B. Jungfleisch, W. Jiang, J.E. Pearson, A. Hoffmann, Spin pumping and inverse Rashba-Edelstein effect in NiFe/Ag/Bi and NiFe/Ag/Sb, *J. Appl. Phys.* 117 (17) (2015) 17C727, <https://doi.org/10.1063/1.4915479>.
- [113] A.R. Mellnik, J.S. Lee, A. Richardella, J.L. Grab, P.J. Mintun, M.H. Fischer, A. Vaezi, A. Manchon, E. A. Kim, N. Samarth, D.C. Ralph, Spin-transfer torque generated by a topological insulator, *Nature* 511 (2014) 449–451, <https://doi.org/10.1038/nature13534>.
- [114] Y. Fan, P. Upadhyaya, X. Kou, M. Lang, S. Takei, Z. Wang, J. Tang, L. He, L. T. Chang, M. Montazeri, G. Yu, W. Jiang, T. Nie, R.N. Schwartz, Y. Tserkovnyak, K.L. Wang, Magnetization switching through giant spin-orbit torque in a magnetically doped topological insulator heterostructure, *Nat. Mater.* 13 (2014) 699–704, <https://doi.org/10.1038/nmat3973>.
- [115] J.C. Rojas-Sánchez, S. Oyarzún, Y. Fu, A. Marty, C. Vergnaud, S. Gambarelli, L. Vila, M. Jamet, Y. Ohtsubo, A. Taleb-Ibrahimi, P. Le Fèvre, F. Bertran, N. Reyren, J.M. George, A. Fert, Spin to charge conversion at room temperature by spin pumping into a new type of topological insulator: α -Sn films, *Phys. Rev. Lett.* 116 (2016) 096602, <https://doi.org/10.1103/PhysRevLett.116.096602>.
- [116] H. Wang, J. Kally, J.S. Lee, T. Liu, H. Chang, D.R. Hickey, K. A. Mkhoyan, M. Wu, A. Richardella, N. Samarth, Surface-state-dominated spin-charge current conversion in topological-insulator ferromagnetic-insulator heterostructures, *Phys. Rev. Lett.* 117 (2016) 076601, <https://doi.org/10.1103/PhysRevLett.117.076601>.
- [117] N. Nagaosa, J. Sinova, S. Onoda, A.H. MacDonald, N.P. Ong, Anomalous Hall effect, *Rev. Mod. Phys.* 82 (2010) 1539–1592, <https://doi.org/10.1103/RevModPhys.82.1539>.
- [118] Y.A. Bychkov, E.I. Rashba, Properties of a 2D electron gas with lifted spectral degeneracy, *JETP Lett.* 39 (1984) 78–81. http://www.jetpletters.ac.ru/ps/1264/article_19121.shtml.
- [119] G. Bihlmayer, O. Rader, R. Winkler, Focus on the Rashba effect, *New J. Phys.* 17 (5) (2015) 050202. <http://stacks.iop.org/1367-2630/17/i=5/a=050202>.
- [120] S. LaShell, B.A. McDougall, E. Jensen, Spin splitting of an Au(111) surface state band observed with angle resolved photoelectron spectroscopy, *Phys. Rev. Lett.* 77 (1996) 3419–3422, <https://doi.org/10.1103/PhysRevLett.77.3419>.
- [121] E. Rotenberg, J.W. Chung, S.D. Kevan, Spin-orbit coupling induced surface band splitting in Li/W(110) and Li/Mo(110), *Phys. Rev. Lett.* 82 (1999) 4066–4069, <https://doi.org/10.1103/PhysRevLett.82.4066>.
- [122] M. Hochstrasser, J.G. Tobin, E. Rotenberg, S.D. Kevan, Spin-resolved photoemission of surface states of W(110)–(1 × 1)H, *Phys. Rev. Lett.* 89 (2002) 216802, <https://doi.org/10.1103/PhysRevLett.89.216802>.
- [123] O. Krupin, G. Bihlmayer, K. Starke, S. Gorovikov, J.E. Prieto, K. Döbrich, S. Blügel, G. Kaindl, Rashba effect at magnetic metal surfaces, *Phys. Rev. B* 71 (2005) 201403, <https://doi.org/10.1103/PhysRevB.71.201403>.
- [124] A. Varykhalov, D. Marchenko, M.R. Scholz, E.D.L. Rienks, T.K. Kim, G. Bihlmayer, J. Sánchez-Barriga, O. Rader, Ir(111) surface state with giant Rashba splitting persists under graphene in air, *Phys. Rev. Lett.* 108 (2012) 066804, <https://doi.org/10.1103/PhysRevLett.108.066804>.

- [125] J. Sánchez-Barriga, G. Bihlmayer, D. Wortmann, D. Marchenko, O. Rader, A. Varykhalov, Effect of structural modulation and thickness of a graphene overlayer on the binding energy of the Rashba-type surface state of Ir(111), *New J. Phys.* 15 (11) (2013) 115009. <http://stacks.iop.org/1367-2630/15/i=11/a=115009>.
- [126] M.Z. Hasan, C.L. Kane, Colloquium, *Rev. Mod. Phys.* 82 (2010) 3045–3067, <https://doi.org/10.1103/RevModPhys.82.3045>.
- [127] J.E. Moore, The birth of topological insulators, *Nature* 464 (2010) 194–198, <https://doi.org/10.1038/nature08916>.
- [128] L. Fu, C.L. Kane, E.J. Mele, Topological insulators in three dimensions, *Phys. Rev. Lett.* 98 (2007) 106803, <https://doi.org/10.1103/PhysRevLett.98.106803>.
- [129] D. Hsieh, Y. Xia, L. Wray, D. Qian, A. Pal, J.H. Dil, J. Osterwalder, F. Meier, G. Bihlmayer, C.L. Kane, Y.S. Hor, R.J. Cava, M.Z. Hasan, Observation of unconventional quantum spin textures in topological insulators, *Science* 323 (5916) (2009) 919–922, <https://doi.org/10.1126/science.1167733>. <http://science.sciencemag.org/content/323/5916/919>.
- [130] D. Hsieh, Y. Xia, D. Qian, L. Wray, J.H. Dil, F. Meier, J. Osterwalder, L. Patthey, J.G. Checkelsky, N.P. Ong, A.V. Fedorov, H. Lin, A. Bansil, D. Grauer, Y.S. Hor, R.J. Cava, M.Z. Hasan, A tunable topological insulator in the spin helical Dirac transport regime, *Nature* 460 (2009) 1101–1105, <https://doi.org/10.1038/nature08234>.
- [131] C. Jozwiak, Y.L. Chen, A.V. Fedorov, J.G. Analytis, C.R. Rotundu, A.K. Schmid, J.D. Denlinger, Y.D. Chuang, D.H. Lee, I.R. Fisher, R.J. Birgeneau, Z.X. Shen, Z. Hussain, A. Lanzara, Widespread spin polarization effects in photoemission from topological insulators, *Phys. Rev. B* 84 (2011) 165113, <https://doi.org/10.1103/PhysRevB.84.165113>.
- [132] Z.H. Pan, E. Vescovo, A.V. Fedorov, G.D. Gu, T. Valla, Persistent coherence and spin polarization of topological surface states on topological insulators, *Phys. Rev. B* 88 (2013) 041101, <https://doi.org/10.1103/PhysRevB.88.041101>.
- [133] J. Sánchez-Barriga, A. Varykhalov, J. Braun, S.Y. Xu, N. Alidoust, O. Kornilov, J. Minár, K. Hummer, G. Springholz, G. Bauer, R. Schumann, L.V. Yashina, H. Ebert, M.Z. Hasan, O. Rader, Photoemission of Bi_2Se_3 with circularly polarized light: probe of spin polarization or means for spin manipulation?, *Phys. Rev. X* 4 (2014) 011046, <https://doi.org/10.1103/PhysRevX.4.011046>.
- [134] J. Sánchez-Barriga, M.R. Scholz, E. Golias, E. Rienks, D. Marchenko, A. Varykhalov, L.V. Yashina, O. Rader, Anisotropic effect of warping on the lifetime broadening of topological surface states in angle-resolved photoemission from Bi_2Te_3 , *Phys. Rev. B* 90 (2014) 195413, <https://doi.org/10.1103/PhysRevB.90.195413>.
- [135] J. Sánchez-Barriga, A. Varykhalov, G. Springholz, H. Steiner, R. Kirchschrager, G. Bauer, O. Caha, E. Schierle, E. Weschke, A.A. Ünal, S. Valencia, M. Dunst, J. Braun, H. Ebert, J. Minár, E. Golias, L. V. Yashina, A. Ney, V. Holý, O. Rader, Nonmagnetic band gap at the Dirac point of the magnetic topological insulator $(\text{Bi}_{1-x}\text{Mn}_x)_2\text{Se}_3$, *Nat. Commun.* 7 (2016) 10559, <https://doi.org/10.1038/ncomms10559>.
- [136] J. Sánchez-Barriga, M. Battiato, M. Krivenkov, E. Golias, A. Varykhalov, A. Romualdi, L. V. Yashina, J. Minár, O. Kornilov, H. Ebert, K. Held, J. Braun, Subpicosecond spin dynamics of excited states in the topological insulator Bi_2Te_3 , *Phys. Rev. B* 95 (2017) 125405, <https://doi.org/10.1103/PhysRevB.95.125405>.
- [137] A.M. Essin, J.E. Moore, D. Vanderbilt, Magnetoelectric polarizability and axion electrodynamics in crystalline insulators, *Phys. Rev. Lett.* 102 (2009) 146805, <https://doi.org/10.1103/PhysRevLett.102.146805>.
- [138] R. Li, J. Wang, X.L. Qi, S.C. Zhang, Dynamical axion field in topological magnetic insulators, *Nat. Phys.* 6 (2010) 284–288, <https://doi.org/10.1038/nphys1534>.
- [139] X.-L. Qi, R. Li, J. Zang, S.-C. Zhang, Inducing a magnetic monopole with topological surface states, *Science* 323 (5918) (2009) 1184–1187, <https://doi.org/10.1126/science.1167747>. <http://science.sciencemag.org/content/323/5918/1184>.
- [140] J.W. McIver, D. Hsieh, H. Steinberg, P. Jarillo-Herrero, N. Gedik, Control over topological insulator photocurrents with light polarization, *Nat. Nanotechnol.* 7 (2012) 96, <https://doi.org/10.1038/nnano.2011.214>.
- [141] C. Kastl, C. Karmetzky, H. Karl, A.W. Holleitner, Ultrafast helicity control of surface currents in topological insulators with near-unity fidelity, *Nat. Commun.* 6 (2015) 6617, <https://doi.org/10.1038/ncomms7617>.

- [142] A. Dankert, J. Geurs, M.V. Kamalakar, S. Charpentier, S.P. Dash, Room temperature electrical detection of spin polarized currents in topological insulators, *Nano Lett.* 15 (12) (2015) 7976–7981, <https://doi.org/10.1021/acs.nanolett.5b03080>.
- [143] C.D. Stanciu, F. Hansteen, A.V. Kimel, A. Kirilyuk, A. Tsukamoto, A. Itoh, T. Rasing, All-optical magnetic recording with circularly polarized light, *Phys. Rev. Lett.* 99 (2007) 047601, <https://doi.org/10.1103/PhysRevLett.99.047601>.
- [144] M. Finazzi, M. Savoini, A. R. Khorsand, A. Tsukamoto, A. Itoh, L. Duò, A. Kirilyuk, T. Rasing, M. Ezawa, Laser-induced magnetic nanostructures with tunable topological properties, *Phys. Rev. Lett.* 110 (2013) 177205, <https://doi.org/10.1103/PhysRevLett.110.177205>.
- [145] W. Koshibae, N. Nagaosa, Creation of skyrmions and antiskyrmions by local heating, *Nat. Commun.* 5 (2014) 5148, <https://doi.org/10.1038/ncomms6148>.
- [146] T.H.R. Skyrme, A unified field theory of mesons and baryons, *Nucl. Phys.* 31 (1962) 556–569, [https://doi.org/10.1016/0029-5582\(62\)90775-7](https://doi.org/10.1016/0029-5582(62)90775-7). <http://www.sciencedirect.com/science/article/pii/0029558262907757>.
- [147] W. Jiang, P. Upadhyaya, W. Zhang, G. Yu, M.B. Jungfleisch, F.Y. Fradin, J.E. Pearson, Y. Tserkovnyak, K. L. Wang, O. Heinonen, S.G.E. te Velthuis, A. Hoffmann, Blowing magnetic skyrmion bubbles, *Science* 349 (6245) (2015) 283–286, <https://doi.org/10.1126/science.aaa1442>. <http://science.sciencemag.org/content/349/6245/283>.
- [148] G. Yu, P. Upadhyaya, X. Li, W. Li, S.K. Kim, Y. Fan, K.L. Wong, Y. Tserkovnyak, P.K. Amiri, K. L. Wang, Room-temperature creation and spin-orbit torque manipulation of skyrmions in thin films with engineered asymmetry, *Nano Lett.* 16 (3) (2016) 1981–1988, <https://doi.org/10.1021/acs.nanolett.5b05257>.
- [149] S. Woo, K. Litzius, B. Krüger, M.Y. Im, L. Caretta, K. Richter, M. Mann, A. Krone, R. M. Reeve, M. Weigand, P. Agrawal, I. Lemesch, M.A. Mawass, P. Fischer, M. Kläui, G.S.D. Beach, Creation of skyrmions and antiskyrmions by local heating, *Nat. Mater.* 15 (2016) 501–506, <https://doi.org/10.1038/nmat4593>.
- [150] A. Fert, V. Cros, J. Sampaio, Skyrmions on the track, *Nat. Nanotechnol.* 8 (2013) 152–156, <https://doi.org/10.1038/nnano.2013.29>.
- [151] I.E. Dzyaloshinskii, Theory of helicoidal structures in antiferromagnets, *Sov. Phys. JETP* 19 (1964) 960. <http://www.jetp.ac.ru/cgi-bin/e/index/e/19/4/p960?a=list>.
- [152] A. Thiaville, S. Rohart, E. Jué, V. Cros, A. Fert, Dynamics of Dzyaloshinskii domain walls in ultrathin magnetic films, *Europhys. Lett.* 100 (2012) 57002. <http://stacks.iop.org/0295-5075/100/i=5/a=57002>.
- [153] N. Romming, C. Hanneken, M. Menzel, J.E. Bickel, B. Wolter, K. von Bergmann, A. Kubetzka, R. Wiesendanger, Writing and deleting single magnetic skyrmions, *Science* 341 (6146) (2013) 636–639, <https://doi.org/10.1126/science.1240573>. <http://science.sciencemag.org/content/341/6146/636>.
- [154] S. Mühlbauer, B. Binz, F. Jonietz, C. Pfleiderer, A. Rosch, A. Neubauer, R. Georgii, P. Böni, Skyrmion lattice in a chiral magnet, *Science* 323 (5916) (2009) 915–919, <https://doi.org/10.1126/science.1166767>. <http://science.sciencemag.org/content/323/5916/915>.
- [155] N. Nagaosa, Y. Tokura, Topological properties and dynamics of magnetic skyrmions, *Nat. Nanotechnol.* 8 (2013) 899–911, <https://doi.org/10.1038/nnano.2013.243>.
- [156] R. Wiesendanger, Nanoscale magnetic skyrmions in metallic films and multilayers: a new twist for spintronics, *Nat. Rev. Mater.* 1 (2016) 16044, <https://doi.org/10.1038/natrevmats.2016.44>.
- [157] A. Fert, N. Reyren, V. Cros, Magnetic skyrmions: advances in physics and potential applications, *Nat. Rev. Mater.* 2 (2017) 17031, <https://doi.org/10.1038/natrevmats.2017.31>.
- [158] W. Jiang, G. Chen, K. Liu, J. Zang, S.G.E. te Velthuis, A. Hoffmann, Skyrmions in magnetic multilayers, *Phys. Rep.* 704 (2017) 1–49, <https://doi.org/10.1016/j.physrep.2017.08.001>. <http://www.sciencedirect.com/science/article/pii/S0370157317302934>.
- [159] R.A. de Groot, F.M. Mueller, P.G. van Engen, K.H.J. Buschow, New class of materials: half-metallic ferromagnets, *Phys. Rev. Lett.* 50 (1983) 2024–2027, <https://doi.org/10.1103/PhysRevLett.50.2024>.
- [160] J.H. Park, E. Vescovo, H.J. Kim, C. Kwon, R. Ramesh, T. Venkatesan, Half-metallic ferromagnets: from band structure to many-body effects, *Nature* 392 (1998) 794–796, <https://doi.org/10.1038/33883>.

- [161] M.I. Katsnelson, V.Y. Irkhin, L. Chioncel, A.I. Lichtenstein, R.A. de Groot, Half-metallic ferromagnets: from band structure to many-body effects, *Rev. Mod. Phys.* 80 (2008) 315–378, <https://doi.org/10.1103/RevModPhys.80.315>.
- [162] S.M. Griffin, J.B. Neaton, Prediction of a new class of half-metallic ferromagnets from first principles, *Phys. Rev. Mater.* 1 (2017) 044401, <https://doi.org/10.1103/PhysRevMaterials.1.044401>.
- [163] R. Ramesh, N.A. Spaldin, Multiferroics: progress and prospects in thin films, *Nat. Mater.* 6 (2007) 21–29, <https://doi.org/10.1038/nmat1805>.
- [164] H. Béa, M. Gajek, M. Bibes, A. Barthélémy, Spintronics with multiferroics, *J. Phys. Condens. Matter* 20 (43) (2008) 434221, <https://doi.org/10.1088/0953-8984/20/43/434221>.
- [165] M. Fiebig, T. Lottermoser, D. Meier, M. Trassin, The evolution of multiferroics, *Nat. Rev. Mater.* 1 (2016) 16046, <https://doi.org/10.1038/natrevmats.2016.46>.
- [166] L. Hueso, J.M. Pruneda, V. Ferrari, G. Burnell, J.P. Valdes-Herrera, B.D. Simons, P.B. Littlewood, E. Artacho, A. Fert, N.D. Mathur, Transformation of spin information into large electrical signals using carbon nanotubes, *Nature* 445 (2007) 410–413, <https://doi.org/10.1038/nature05507>.
- [167] A.H. Castro Neto, F. Guinea, N.M.R. Peres, K.S. Novoselov, A.K. Geim, The electronic properties of graphene, *Rev. Mod. Phys.* 81 (2009) 109–162, <https://doi.org/10.1103/RevModPhys.81.109>.
- [168] A. Varykhalov, J. Sánchez-Barriga, D. Marchenko, P. Hlawenka, P.S. Mandal, O. Rader, Tunable Fermi level and hedgehog spin texture in gapped graphene, *Nat. Commun.* 6 (2015) 7610, <https://doi.org/10.1038/ncomms8610>.
- [169] W. Yan, L.C. Phillips, M. Barbone, S.J. Hämäläinen, A. Lombardo, M. Ghidini, X. Moya, F. Maccherozzi, S. van Dijken, S.S. Dhesi, A.C. Ferrari, N.D. Mathur, Long spin diffusion length in few-layer graphene flakes, *Phys. Rev. Lett.* 117 (2016) 147201, <https://doi.org/10.1103/PhysRevLett.117.147201>.
- [170] A.E. Clark, E. Callen, Néel ferrimagnets in large magnetic fields, *J. Appl. Phys.* 39 (13) (1968) 5972–5982, <https://doi.org/10.1063/1.1656100>.
- [171] J. Jensen, A. Mackintosh, *Rare Earth Magnetism: Structures and Excitations*, Clarendon Press, 1991. ISBN 9780198520276 <https://books.google.de/books?id=LbTvAAAAMAAJ>.
- [172] Lanthanide Magnetism, Available from: https://www.radiochemistry.org/periodictable/la_series/L8.html, Accessed 24 July 2017.
- [173] P. Wadley, B. Howells, J. Železný, C. Andrews, V. Hills, R.P. Champion, V. Novák, K. Olejník, F. Maccherozzi, S.S. Dhesi, S.Y. Martin, T. Wagner, J. Wunderlich, F. Freimuth, Y. Mokrousov, J. Kuneš, J.S. Chauhan, M.J. Grzybowski, A.W. Rushforth, K.W. Edmonds, B.L. Gallagher, T. Jungwirth, Electrical switching of an antiferromagnet, *Science* 0036-8075351 (6273) (2016) 587–590, <https://doi.org/10.1126/science.aab1031>. <http://science.sciencemag.org/content/351/6273/587>. ISSN.
- [174] W.C. Koehler, Magnetic properties of rare-earth metals and alloys, *J. Appl. Phys.* 36 (3) (1965) 1078–1087, <https://doi.org/10.1063/1.1714108>.
- [175] I.A. Campbell, Indirect exchange for rare earths in metals, *J. Phys. F* 2 (3) (1972) L47. <http://stacks.iop.org/0305-4608/2/i=3/a=004>.
- [176] R. Lemaire, R. Pauthenet, J. Schweizer, Magnetism of rare earth alloys, *IEEE Trans. Magn.* 0018-94646 (2) (1970) 153–157, <https://doi.org/10.1109/TMAG.1970.1066815>. ISSN.
- [177] H. Taz, T. Sakhivel, N.K. Yamoah, C. Carr, D. Kumar, S. Seal, R. Kalyanaraman, Transparent ferromagnetic and semiconducting behavior in Fe-Dy-Tb based amorphous oxide films, *Sci. Rep.* 2045-23226 (2016) 27869, <https://doi.org/10.1038/srep27869>. <http://www.ncbi.nlm.nih.gov/pmc/articles/PMC4906280/>. 27298196[pmid] ISSN.
- [178] H. Adachi, H. Ino, A ferromagnet having no net magnetic moment, *Nature* 0028-0836401 (6749) (1999) 148–150, <https://doi.org/10.1038/43634>. ISSN.
- [179] Y. Mimura, N. Imamura, T. Kobayashi, Magnetic properties and curie point writing in amorphous metallic films, *IEEE Trans. Magn.* 0018-946412 (6) (1976) 779–781, <https://doi.org/10.1109/TMAG.1976.1059199>. ISSN.
- [180] P. Hansen, C. Clausen, G. Much, M. Rosenkranz, K. Witter, Magnetic and magneto-optical properties of rare-earth transition-metal alloys containing Gd, Tb, Fe, Co, *J. Appl. Phys.* 66 (2) (1989) 756–767, <https://doi.org/10.1063/1.343551>.

- [181] T.A. Ostler, R.F.L. Evans, R.W. Chantrell, U. Atxitia, O. Chubykalo-Fesenko, I. Radu, R. Abrudan, F. Radu, A. Tsukamoto, A. Itoh, A. Kirilyuk, T. Rasing, A. Kimel, Crystallographically amorphous ferrimagnetic alloys: comparing a localized atomistic spin model with experiments, *Phys. Rev. B* 84 (2011) 024407, <https://doi.org/10.1103/PhysRevB.84.024407>.
- [182] B. Hebler, A. Hassdenteufel, P. Reinhardt, H. Karl, M. Albrecht, Ferrimagnetic Tb-Fe alloy thin films: composition and thickness dependence of magnetic properties and all-optical switching, *Front. Mater.* 3 (2016) 8, <https://doi.org/10.3389/fmats.2016.00008>.
- [183] S. Alebrand, M. Gottwald, M. Hehn, D. Steil, M. Cinchetti, D. Lacour, E. Fullerton, M. Aeschlimann, S. Mangin, Light-induced magnetization reversal of high-anisotropy TbCo alloy films, *Appl. Phys. Lett.* 101 (16) (2012) 162408, <https://doi.org/10.1063/1.4759109>.
- [184] L. Gierster, A.A. Ünal, Laser induced magnetization switching in a TbFeCo ferrimagnetic thin film: discerning the impact of dipolar fields, laser heating and laser helicity by XPEEM, *Ultramicroscopy* 0304-3991159 (2015) 508–512, <https://doi.org/10.1016/j.ultramic.2015.05.016>. <http://www.sciencedirect.com/science/article/pii/S0304399115001278>. Special Issue: LEEM-PEEM 9 ISSN.
- [185] K. Chen, D. Lott, F. Radu, F. Choueikani, E. Otero, P. Ohresser, Temperature-dependent magnetic properties of ferrimagnetic DyCo₃ alloy films, *Phys. Rev. B* 91 (024409) (2015), <https://doi.org/10.1103/PhysRevB.91.024409>.
- [186] S.V. Kozhevnikov, Y.N. Khaydukov, T. Keller, F. Ott, F. Radu, Polarized neutron channeling as a tool for the investigations of weakly magnetic thin films, *JETP Lett.* 103 (1) (2016) 36–40, <https://doi.org/10.1134/S0021364016010082>.
- [187] K. Chen, D. Lott, F. Radu, F. Choueikani, E. Otero, P. Ohresser, Observation of an atomic exchange bias effect in DyCo₄ film, *Sci. Rep.* 5 (18377) (2015) <https://doi.org/10.1038/srep18377>.
- [188] I. Radu, C. Stamm, A. Eschenlohr, F. Radu, R. Abrudan, K. Vahaplar, T. Kachel, N. Pontius, R. Mitzner, K. Hollmack, A. Föhlisch, T.A. Ostler, J.H. Mentink, R.F.L. Evans, R. W. Chantrell, A. Tsukamoto, A. Itoh, A. Kirilyuk, A.V. Kimel, T. Rasing, Ultrafast and distinct spin dynamics in magnetic alloys, *SPIN* 5 (3) (2015) 1550004, <https://doi.org/10.1142/S2010324715500046>.
- [189] A. Arora, M.-A. Mawass, O. Sandig, C. Luo, A.A. Ünal, F. Radu, S. Valencia, F. Kronast, Spatially resolved investigation of all optical magnetization switching in TbFe alloys, *Sci. Rep.* 2045-23227 (1) (2017) 9456, <https://doi.org/10.1038/s41598-017-09615-1>. ISSN.
- [190] N. Berggaard, A. Mougin, M. Izquierdo, E. Fonda, F. Sirotti, Correlation between structure, electronic properties, and magnetism in CoxGd1-x thin amorphous films, *Phys. Rev. B* 96 (2017) 064418, <https://doi.org/10.1103/PhysRevB.96.064418>.
- [191] T. Seifert, U. Martens, S. Günther, M.A.W. Schoen, F. Radu, X.Z. Chen, I. Lucas, R. Ramos, M.H. Aguirre, P. A. Algarabel, A. Anadón, H.S. Körner, J. Walowski, C. Back, M.R. Ibarra, L. Morellón, E. Saitoh, M. Wolf, C. Song, K. Uchida, M. Münzenberg, I. Radu, T. Kampfrath, Terahertz spin currents and inverse spin Hall effect in thin-film heterostructures containing complex magnetic compounds, *SPIN* 7 (3) (2017) 1740010, <https://doi.org/10.1142/S2010324717400100>.
- [192] O. Hellwig, A. Berger, J.B. Kortright, E.E. Fullerton, Domain structure and magnetization reversal of antiferromagnetically coupled perpendicular anisotropy films, *J. Magn. Magn. Mater.* 0304-8853319 (1) (2007) 13–55, <https://doi.org/10.1016/j.jmmm.2007.04.035>. <http://www.sciencedirect.com/science/article/pii/S030488530700649X>. ISSN.
- [193] A. Donges, S. Khmelevskiy, A. Deak, R.-M. Abrudan, D. Schmitz, I. Radu, F. Radu, L. Szunyogh, U. Nowak, Magnetization compensation and spin reorientation transition in ferrimagnetic DyCo₅: multiscale modeling and element-specific measurements, *Phys. Rev. B* 96 (2017) 024412, <https://doi.org/10.1103/PhysRevB.96.024412>.
- [194] Z. Tie-Song, J. Han-Min, G. Guang-Hua, H. Xiu-Feng, C. Hong, Magnetic properties of R ions in RCo₅ compounds (R=Pr, Nd, Sm, Gd, Tb, Dy, Ho, and Er), *Phys. Rev. B* 43 (1991) 8593–8598, <https://doi.org/10.1103/PhysRevB.43.8593>.
- [195] I.A. Abrikosov, H.L. Skriver, Self-consistent linear-muffin-tin-orbitals coherent-potential technique for bulk and surface calculations: Cu-Ni, Ag-Pd, and Au-Pt random alloys, *Phys. Rev. B* 47 (1993) 16532–16541, <https://doi.org/10.1103/PhysRevB.47.16532>.

- [196] A.V. Ruban, H.L. Skriver, Calculated surface segregation in transition metal alloys, *Comput. Mater. Sci.* 15 (2) (1999) 119–143, [https://doi.org/10.1016/S0927-0256\(99\)00003-8](https://doi.org/10.1016/S0927-0256(99)00003-8). <http://www.sciencedirect.com/science/article/pii/S0927025699000038>.
- [197] H. Ebert, A. Perlov, S. Mankovsky, Incorporation of the rotationally invariant LDA+U scheme into the SPR-KKR formalism: application to disordered alloys, *Solid State Commun.* 127 (6) (2003) 443–446, [https://doi.org/10.1016/S0038-1098\(03\)00455-1](https://doi.org/10.1016/S0038-1098(03)00455-1). <http://www.sciencedirect.com/science/article/pii/S0038109803004551>.
- [198] L. Oroszlány, A. Deák, E. Simon, S. Khmelevskiy, L. Szunyogh, Magnetism of gadolinium: a first-principles perspective, *Phys. Rev. Lett.* 115 (2015) 096402, <https://doi.org/10.1103/PhysRevLett.115.096402>.
- [199] U. Nowak, Classical spin models, in: *Handbook of Magnetism and Advanced Magnetic Materials* John Wiley & Sons, Ltd, New York, NY, 2007. ISBN 9780470022184, <https://doi.org/10.1002/9780470022184.hmm205>.
- [200] T. Tsushima, M. Ohokoshi, Spin reorientation in DyCo₅, *J. Magn. Magn. Mater.* 0304-885331–34 (1983) 197–198, [https://doi.org/10.1016/0304-8853\(83\)90213-5](https://doi.org/10.1016/0304-8853(83)90213-5). <http://www.sciencedirect.com/science/article/pii/0304885383902135>. ISSN.
- [201] F. Radu, R. Abrudan, I. Radu, D. Schmitz, H. Zabel, Perpendicular exchange bias in ferrimagnetic spin valves, *Nat. Commun.* 3 (2012) 715, <https://doi.org/10.1038/ncomms1728>.
- [202] A.A. Ünal, S. Valencia, F. Radu, D. Marchenko, K.J. Merazzo, M. Vázquez, J. Sánchez-Barriga, Ferrimagnetic DyCo₅ nanostructures for bits in heat-assisted magnetic recording, *Phys. Rev. Appl.* 5 (2016) 064007, <https://doi.org/10.1103/PhysRevApplied.5.064007>.
- [203] V.V. Kelarev, V.V. Chuev, A.N. Pibogov, S.K. Sidoeov, Anisotropy and exchange effects in heavy rare-earth-cobalt compounds of the RCo₅ type, *Phys. Status Solidi A* 1521-396X79 (1) (1983) 57–66, <https://doi.org/10.1002/pssa.2210790104>. ISSN.
- [204] U.K. Röbller, A.N. Bogdanov, Reorientation in antiferromagnetic multilayers: spin-flop transition and surface effects, *Phys. Status Solidi C* 1610-16421 (12) (2004) 3297–3305, <https://doi.org/10.1002/pssc.200405441>. ISSN.
- [205] A.K. Zvezdin, Field induced phase transitions in ferrimagnets (Chapter 4), in: *Handbook of Magnetic Materials*, vol. 9, Elsevier, Amsterdam, 1995, , pp. 405–543, [https://doi.org/10.1016/S1567-2719\(05\)80008-3](https://doi.org/10.1016/S1567-2719(05)80008-3). <http://www.sciencedirect.com/science/article/pii/S1567271905800083>.
- [206] D. Mauri, H.C. Siegmann, P.S. Bagus, E. Kay, Simple model for thin ferromagnetic films exchange coupled to an antiferromagnetic substrate, *J. Appl. Phys.* 62 (7) (1987) 3047–3049, <https://doi.org/10.1063/1.339878>.
- [207] M. Amatsu, S. Honda, T. Kusuda, Anomalous hysteresis loops and domain observation in Gd-Fe co-evaporated films, *IEEE Trans. Magn.* 0018-946413 (5) (1977) 1612–1614, <https://doi.org/10.1109/TMAG.1977.1059620>. ISSN.
- [208] S. Esho, Anomalous magneto-optical hysteresis loops of sputtered Gd-Co films, *Jpn J. Appl. Phys.* 15 (S1) (1976) 93. <http://stacks.iop.org/1347-4065/15/i=S1/a=93>.
- [209] H. Ratajczak, I. Gocianska, Hall hysteresis loops in the vicinity of compensation temperature in amorphous HoCo films, *Phys. Status Solidi A* 1521-396X62 (1) (1980) 163–168, <https://doi.org/10.1002/pssa.2210620118>. ISSN.
- [210] C. Xu, Z. Chen, D. Chen, S. Zhou, T. Lai, Origin of anomalous hysteresis loops induced by femtosecond laser pulses in GdFeCo amorphous films, *Appl. Phys. Lett.* 96 (9) (2010) 092514, <https://doi.org/10.1063/1.3339878>.
- [211] S. Romer, M.A. Marioni, K. Thorwarth, N.R. Joshi, C.E. Corticelli, H.J. Hug, S. Oezer, M. Parlinska-Wojtan, H. Rohrmann, Temperature dependence of large exchange-bias in TbFe-Co/Pt, *Appl. Phys. Lett.* 101 (22) (2012) 222404, <https://doi.org/10.1063/1.4767142>.
- [212] C. Schubert, B. Hebler, H. Schletter, A. Liebig, M. Daniel, R. Abrudan, F. Radu, M. Albrecht, Interfacial exchange coupling in Fe-Tb/[Co/Pt] heterostructures, *Phys. Rev. B* 87 (2013) 054415, <https://doi.org/10.1103/PhysRevB.87.054415>.
- [213] M. Krupa, A. Korostil, Pulsed laser impact on ferrimagnetic nanostructures, *Int. J. Phys.* 1 (2) (2013) 28–40, <https://doi.org/10.12691/ijp-1-2-2>. <http://pubs.sciepub.com/ijp/1/2/2>.
- [214] A. Fernández-Pacheco, R. Streubel, O. Fruchart, R. Hertel, P. Fischer, R.P. Cowburn, Three-dimensional nanomagnetism, *Nat. Commun.* 8 (2017) 15756, <https://doi.org/10.1038/ncomms15756>.

- [215] D. Sander, S.O. Valenzuela, D. Makarov, C.H. Marrows, E.E. Fullerton, P. Fischer, J. McCord, P. Vavassori, S. Mangin, P. Pirro, B. Hillebrands, A.D. Kent, T. Jungwirth, O. Gutfleisch, C.G. Kim, A. Berger, The 2017 magnetism roadmap, *J. Phys. D: Appl. Phys.* 50 (36) (2017) 363001. <http://stacks.iop.org/0022-3727/50/i=36/a=363001>.
- [216] K. Bennemann, Magnetic nanostructures, *J. Phys. Condens. Matter* 22 (24) (2010) 243201. <http://stacks.iop.org/0953-8984/22/i=24/a=243201>.
- [217] R. Skomski, D. Leslie-Pelecky, Cooperative freezing in spin glasses and magnetic nanostructures, *J. Appl. Phys.* 89 (11) (2001) 7036–7038, <https://doi.org/10.1063/1.1358337>.
- [218] M.J. Benitez, O. Petravic, E.L. Salabas, F. Radu, H. Tüysüz, F. Schüth, H. Zabel, Evidence for core-shell magnetic behavior in antiferromagnetic Co₃O₄ nanowires, *Phys. Rev. Lett.* 101 (2008) 097206, <https://doi.org/10.1103/PhysRevLett.101.097206>.
- [219] M.J. Benitez, O. Petravic, H. Tüysüz, F. Schüth, H. Zabel, Fingerprinting the magnetic behavior of antiferromagnetic nanostructures using remanent magnetization curves, *Phys. Rev. B* 83 (2011) 134424, <https://doi.org/10.1103/PhysRevB.83.134424>.
- [220] M. Molina-Ruiz, A.F. Lopeandía, F. Pi, D. Givord, O. Bourgeois, J. Rodríguez-Viejo, Evidence of finite-size effect on the Néel temperature in ultrathin layers of CoO nanograins, *Phys. Rev. B* 83 (2011) 140407, <https://doi.org/10.1103/PhysRevB.83.140407>.
- [221] I.M.L. Billas, A. Châtelain, W.A. de Heer, Magnetism from the atom to the bulk in iron, cobalt, and nickel clusters, *Science* 265 (5179) (1994) 1682–1684, <https://doi.org/10.1126/science.265.5179.1682>. <http://science.sciencemag.org/content/265/5179/1682>.
- [222] L. Sun, P.C. Searson, C.L. Chien, Finite-size effects in nickel nanowire arrays, *Phys. Rev. B* 61 (2000) R6463–R6466, <https://doi.org/10.1103/PhysRevB.61.R6463>.
- [223] P. Gambardella, S. Rusponi, M. Veronese, S.S. Dhesi, C. Grazioli, A. Dallmeyer, I. Cabria, R. Zeller, P.H. Dederichs, K. Kern, C. Carbone, H. Brune, Giant magnetic anisotropy of single cobalt atoms and nanoparticles, *Science* 300 (5622) (2003) 1130–1133, <https://doi.org/10.1126/science.1082857>. <http://science.sciencemag.org/content/300/5622/1130>.
- [224] D. Sander, The magnetic anisotropy and spin reorientation of nanostructures and nanoscale films, *J. Phys. Condens. Matter* 16 (2004) R603. <http://stacks.iop.org/0953-8984/16/i=20/a=R01>.
- [225] C. Desvaux, C. Amiens, P. Fejes, P. Renaud, M. Respaud, P. Lecante, E. Snoeck, B. Chaudret, Multimillimetre-large superlattices of air-stable iron-cobalt nanoparticles, *Nat. Mater.* 4 (2004) 750–753, <https://doi.org/10.1038/nmat1480>.
- [226] C.A. Ross, Patterned magnetic recording media, *Annu. Rev. Mater. Res.* 31 (1) (2001) 203–235, <https://doi.org/10.1146/annurev.matsci.31.1.203>.
- [227] S. Sun, C.B. Murray, D. Weller, L. Folks, A. Moser, Monodisperse FePt nanoparticles and ferromagnetic FePt nanocrystal superlattices, *Science* 287 (5460) (2000) 1989–1992, <https://doi.org/10.1126/science.287.5460.1989>. <http://science.sciencemag.org/content/287/5460/1989>.
- [228] J.I. Martízn, J. Nogués, K. Liu, J.L. Vicent, I.K. Schuller, Ordered magnetic nanostructures: fabrication and properties, *J. Magn. Magn. Mater.* 0304-8853256 (1) (2003) 449–501, [https://doi.org/10.1016/S0304-8853\(02\)00898-3](https://doi.org/10.1016/S0304-8853(02)00898-3). <http://www.sciencedirect.com/science/article/pii/S0304885302008983>. ISSN.
- [229] A.J. Yin, J. Li, W. Jian, A.J. Bennett, J.M. Xu, Fabrication of highly ordered metallic nanowire arrays by electrodeposition, *Appl. Phys. Lett.* 79 (7) (2001) 1039–1041, <https://doi.org/10.1063/1.1389765>.
- [230] J. Sánchez-Barriga, M. Lucas, F. Radu, E. Martin, M. Multigner, P. Marin, A. Hernando, G. Rivero, Interplay between the magnetic anisotropy contributions of cobalt nanowires, *Phys. Rev. B* 80 (2009) 184424, <https://doi.org/10.1103/PhysRevB.80.184424>.
- [231] J. Sánchez-Barriga, M. Lucas, G. Rivero, P. Marin, A. Hernando, Magneto-electrolysis of Co nanowire arrays grown in a track-etched polycarbonate membrane, *J. Magn. Magn. Mater.* 0304-8853312 (1) (2007) 99–106, <https://doi.org/10.1016/j.jmmm.2006.09.020>. <http://www.sciencedirect.com/science/article/pii/S0304885306010973>. ISSN.
- [232] Z.L. Xiao, C.Y. Han, U. Welp, H.H. Wang, V.K. Vlasko-Vlasov, W.K. Kwok, D.J. Miller, J.M. Hiller, R. E. Cook, G.A. Willing, G.W. Crabtree, Nickel antidot arrays on anodic alumina substrates, *Appl. Phys. Lett.* 81 (15) (2002) 2869–2871, <https://doi.org/10.1063/1.1512993>.

- [233] C. Schubert, Percolated Fe_{100-x}Tb_x nanodot arrays: exchange interaction and magnetization reversal, in: *Magnetic Order and Coupling Phenomena: A Study of Magnetic Structure and Magnetization Reversal Processes in Rare-Earth-Transition-Metal Based Alloys and Heterostructures* Springer International Publishing, Cham, 2014, . ISBN 978-3-319-07106-0, pp. 77–86, https://doi.org/10.1007/978-3-319-07106-0_7.
- [234] O. Hellwig, L.J. Heyderman, O. Petravic, H. Zabel, Competing interactions in patterned and self-assembled magnetic nanostructures, in: *Magnetic Nanostructures: Spin Dynamics and Spin Transport* Springer, Berlin, Heidelberg, 2013, . ISBN 978-3-642-32042-2, pp. 189–234, https://doi.org/10.1007/978-3-642-32042-2_6.
- [235] M.V. Lubarda, S. Li, B. Livshitz, E.E. Fullerton, V. Lomakin, Reversal in bit patterned media with vertical and lateral exchange, *IEEE Trans. Magn.* 0018-9464/7 (1) (2011) 18–25, <https://doi.org/10.1109/TMAG.2010.2089610>. ISSN.
- [236] V. Repain, J.P. Jamet, N. Vernier, M. Bauer, J. Ferré, C. Chappert, J. Gierak, D. Maily, Magnetic interactions in dot arrays with perpendicular anisotropy, *J. Appl. Phys.* 95 (5) (2004) 2614–2618, <https://doi.org/10.1063/1.1645973>.
- [237] H.J. Jang, P. Eames, E.D. Dahlberg, M. Farhoud, C.A. Ross, Magnetostatic interactions of single-domain nanopillars in quasistatic magnetization states, *Appl. Phys. Lett.* 86 (2) (2005) 023102, <https://doi.org/10.1063/1.1846150>.
- [238] N. Eibagi, J.J. Kan, F.E. Spada, E.E. Fullerton, Role of dipolar interactions on the thermal stability of high-density bit-patterned media, *IEEE Magn. Lett.* 1949-307X/3 (2012) 4500204, <https://doi.org/10.1109/LMAG.2012.2211864>. 4500204 ISSN.
- [239] X. Yang, S. Xiao, W. Wu, Y. Xu, K. Mountfield, R. Rottmayer, K. Lee, D. Kuo, D. Weller, Challenges in 1 Teradot/in² dot patterning using electron beam lithography for bit-patterned media, *J. Vac. Sci. Technol. B: Microelectron. Nanometer Struct.-Process. Meas. Phenom.* 25 (6) (2007) 2202–2209, <https://doi.org/10.1116/1.2798711>.
- [240] H. Masuda, K. Fukuda, Ordered metal nanohole arrays made by a two-step replication of honeycomb structures of anodic alumina, *Science* 268 (5216) (1995) 1466–1468, <https://doi.org/10.1126/science.268.5216.1466>. <http://science.sciencemag.org/content/268/5216/1466>.
- [241] S.Y. Chou, P.R. Krauss, P.J. Renstrom, Imprint lithography with 25-nanometer resolution, *Science* 272 (5258) (1996) 85–87, <https://doi.org/10.1126/science.272.5258.85>. <http://science.sciencemag.org/content/272/5258/85>.
- [242] M. Colburn, S.C. Johnson, M.D. Stewart, S. Damle, T.C. Bailey, B. Choi, M. Wedlake, T.B. Michaelson, S.V. Sreenivasan, J.G. Ekerdt, C.G. Willson, Step and flash imprint lithography: a new approach to high-resolution patterning, *Proc. SPIE* 3676 (1999) 379–389, <https://doi.org/10.1117/12.351155>.
- [243] G.M. Schmid, M. Miller, C. Brooks, N. Khusnatdinov, D. LaBrake, D.J. Resnick, S. V. Sreenivasan, G. Gauzner, K. Lee, D. Kuo, D. Weller, X. Yang, Step and flash imprint lithography for manufacturing patterned media, *J. Vac. Sci. Technol. B: Microelectron. Nanometer Struct.-Process. Meas. Phenom.* 27 (2) (2009) 573–580, <https://doi.org/10.1116/1.3081981>.
- [244] K.J. Merazzo, Ordered magnetic antidot arrays, Ph.D. thesis, Universidad Autónoma de Madrid, 2012, Available from: <http://hdl.handle.net/10486/11761>.
- [245] S. Yasin, D.G. Hasko, H. Ahmed, Fabrication of <5 nm width lines in poly(methylmethacrylate) resist using a water:isopropyl alcohol developer and ultrasonically-assisted development, *Appl. Phys. Lett.* 78 (18) (2001) 2760–2762, <https://doi.org/10.1063/1.1369615>.
- [246] M.P. Proenca, C.T. Sousa, D.C. Leitao, J. Ventura, J.B. Sousa, J.P. Araujo, Nanopore formation and growth in phosphoric acid Al anodization, *J. Non-Cryst. Solids* 354 (47) (2008) 5238–5240, <https://doi.org/10.1016/j.jnoncrysol.2008.04.055>. <http://www.sciencedirect.com/science/article/pii/S0022309308006819>.
- [247] C.T. Sousa, D.C. Leitao, M.P. Proenca, J. Ventura, A.M. Pereira, J.P. Araujo, Nanoporous alumina as templates for multifunctional applications, *Appl. Phys. Rev.* 1 (3) (2014) 031102, <https://doi.org/10.1063/1.4893546>.
- [248] C.T. Sousa, D.C. Leitão, M.P. Proenca, A. Apolinário, J.G. Correia, J. Ventura, J.P. Araújo, Tuning pore filling of anodic alumina templates by accurate control of the bottom barrier layer thickness, *Nanotechnology* 22 (31) (2011) 315602. <http://stacks.iop.org/0957-4484/22/i=31/a=315602>.

- [249] L.G. Vivas, J. Escrib, D.G. Trabada, G.A. Badini-Confalonieri, M. Vázquez, Magnetic anisotropy in ordered textured Co nanowires, *Appl. Phys. Lett.* 100 (25) (2012) 252405, <https://doi.org/10.1063/1.4729782>.
- [250] C.A. Ross, K.K. Berggren, J.K. Cheng, Y.S. Jung, J.B. Chang, Three-dimensional nanofabrication by block copolymer self-assembly, *Adv. Mater.* 1521-409526 (25) (2014) 4386–4396, <https://doi.org/10.1002/adma.201400386>. ISSN.
- [251] I. Utke, P. Hoffmann, J. Melngailis, Gas-assisted focused electron beam and ion beam processing and fabrication, *J. Vac. Sci. Technol. B: Microelectron. Nanometer Struct.-Process. Meas. Phenom.* 26 (4) (2008) 1197–1276, <https://doi.org/10.1116/1.2955728>.
- [252] I. Utke, P. Hoffmann, R. Berger, L. Scandella, High-resolution magnetic Co supertips grown by a focused electron beam, *Appl. Phys. Lett.* 80 (25) (2002) 4792–4794, <https://doi.org/10.1063/1.1489097>.
- [253] A. Fernández-Pacheco, L. Serrano-Ramón, J.M. Michalik, M.R. Ibarra, J.M. De Teresa, L. O'Brien, D. Petit, J. Lee, R.P. Cowburn, Three dimensional magnetic nanowires grown by focused electron-beam induced deposition, *Sci. Rep.* 3 (2013) 1492, <https://doi.org/10.1038/srep01492>.
- [254] O. Hellwig, A. Moser, E. Dobisz, Z.Z. Bandic, H. Yang, D.S. Kercher, J.D. Risner-Jamtgaard, D. Yaney, E.E. Fullerton, Suppression of magnetic trench material in bit patterned media fabricated by blanket deposition onto prepatterned substrates, *Appl. Phys. Lett.* 93 (19) (2008) 192501, <https://doi.org/10.1063/1.3013857>.
- [255] D.E. Laughlin, Y. Peng, Y.L. Qin, M. Lin, J.G. Zhu, Fabrication, microstructure, magnetic, and recording properties of percolated perpendicular media, *IEEE Trans. Magn.* 43 (2007) 693–697, <https://doi.org/10.1109/TMAG.2006.888237>. <http://ieeexplore.ieee.org/document/4069040/>.
- [256] M.T. Rahman, N.N. Shams, Y.C. Wu, C.H. Lai, D. Suess, Magnetic multilayers on porous anodized alumina for percolated perpendicular media, *Appl. Phys. Lett.* 91 (13) (2007) 132505, <https://doi.org/10.1063/1.2790788>.
- [257] C. Schulze, M. Faustini, J. Lee, H. Schletter, M.U. Lutz, P. Krone, M. Gass, K. Sader, A.L. Bleloch, M. Hietschold, M. Fuger, D. Suess, J. Fidler, U. Wolff, V. Neu, D. Grosso, D. Makarov, M. Albrecht, Magnetic films on nanopatterned templates: a route towards percolated perpendicular media, *Nanotechnology* 21 (49) (2010) 495701. <http://stacks.iop.org/0957-4484/21/i=49/a=495701>.
- [258] J.G. Zhu, Y. Tang, A medium microstructure for high area density perpendicular recording, *J. Appl. Phys.* 99 (8) (2006) 08Q903, <https://doi.org/10.1063/1.2172205>.
- [259] M.T. Rahman, C.H. Lai, D. Vokoun, N.N. Shams, A simple route to fabricate percolated perpendicular magnetic recording media, *IEEE Trans. Magn.* 43 (6) (2007) 2133–2135, <https://doi.org/10.1109/TMAG.2007.893142>. <http://ieeexplore.ieee.org/abstract/document/4202887/>.
- [260] M. Grobis, C. Schulze, M. Faustini, D. Grosso, O. Hellwig, D. Makarov, M. Albrecht, Recording study of percolated perpendicular media, *Appl. Phys. Lett.* 98 (19) (2011) 192504, <https://doi.org/10.1063/1.3587635>.
- [261] M. Krupinski, D. Mitin, A. Zarzycki, A. Szkudlarek, M. Giersig, M. Albrecht, M. Marszalek, Magnetic transition from dot to antidot regime in large area Co/Pd nanopatterned arrays with perpendicular magnetization, *Nanotechnology* 28 (8) (2017) 085302. <http://stacks.iop.org/0957-4484/28/i=8/a=085302>.
- [262] Y. Mimura, N. Imamura, T. Kobayashi, A. Okada, Y. Kushiuro, Magnetic properties of amorphous alloy films of Fe with Gd, Tb, Dy, Ho, or Er, *J. Appl. Phys.* 49 (3) (1978) 1208–1215, <https://doi.org/10.1063/1.325008>.
- [263] A. Hassdenteufel, B. Hebler, C. Schubert, A. Liebig, M. Teich, M. Helm, M. Aeschlimann, M. Albrecht, R. Bratschitsch, Thermally assisted all-optical helicity dependent magnetic switching in amorphous Fe_{100-x}Tb_x alloy films, *Adv. Mater.* 1521-409525 (22) (2013) 3122–3128, <https://doi.org/10.1002/adma.201300176>. ISSN.
- [264] B. Hebler, A. Hassdenteufel, P. Reinhardt, H. Karl, M. Albrecht, Ferrimagnetic Tb-Fe alloy thin films: composition and thickness dependence of magnetic properties and all-optical switching, *Front. Mater.* 3 (2016) 8, <https://doi.org/10.3389/fmats.2016.00008>.
- [265] H. Kronmüller, K.D. Durst, M. Sagawa, Analysis of the magnetic hardening mechanism in RE-FeB permanent magnets, *J. Magn. Magn. Mater.* 74 (1988) 291–302, [https://doi.org/10.1016/0304-8853\(88\)90202-8](https://doi.org/10.1016/0304-8853(88)90202-8). <http://www.sciencedirect.com/science/article/pii/0304885388902028>.

- [266] B. Lanchava, H. Hoffmann, Magnetic domains and demagnetizing fields in FeTb thin films, *J. Phys. D. Appl. Phys.* 31 (16) (1998) 1991, <https://doi.org/10.1088/0022-3727/31/16/008>. <http://stacks.iop.org/0022-3727/31/i=16/a=008>.
- [267] E.C. Stoner, E.P. Wohlfarth, A mechanism of magnetic hysteresis in heterogeneous alloys, *Philos. Trans. R. Soc. Lond. A* 240 (826) (1948) 599–642, <https://doi.org/10.1098/rsta.1948.0007>. <http://rsta.royalsocietypublishing.org/content/240/826/599>.
- [268] K.J. Merazzo, R.P. del Real, A. Asenjo, M. Vázquez, Dependence of magnetization process on thickness of Permalloy antidot arrays, *J. Appl. Phys.* 109 (7) (2011) 07B906, <https://doi.org/10.1063/1.3544483>.
- [269] J.M. Gonzalez, O.A. Chubykalo-Fesenko, F. Garcia-Sanchez, J.M.T. Bruna, J. Bartolome, L.M. G. Vinuesa, Reversible magnetization variations in large field ranges associated to periodic arrays of antidots, *IEEE Trans. Magn.* 41 (10) (2005) 3106–3108, <https://doi.org/10.1109/TMAG.2005.854890>. <http://ieeexplore.ieee.org/document/1519222/>.
- [270] K.J. Merazzo, D.C. Leitao, E. Jiménez, J.P. Araujo, J. Camarero, R.P. del Real, A. Asenjo, M. Vázquez, Geometry-dependent magnetization reversal mechanism in ordered Py antidot arrays, *J. Phys. D. Appl. Phys.* 44 (50) (2011) 505001, <https://doi.org/10.1088/0022-3727/44/50/505001>. <http://stacks.iop.org/0022-3727/44/i=50/a=505001>.
- [271] K.R. Pirota, P. Prieto, A.M.J. Neto, J.M. Sanz, M. Knobel, M. Vázquez, Coercive field behavior of permalloy antidot arrays based on self-assembled template fabrication, *J. Magn. Magn. Mater.* 320 (14) (2008) e235–e238, <https://doi.org/10.1016/j.jmmm.2008.02.146>. <http://www.sciencedirect.com/science/article/pii/S0304885308001480>.
- [272] I. Ruiz-Feal, L. López-Díaz, A. Hirohata, J. Rothman, C.M. Guertler, J.A.C. Bland, L.M. Garcia, J.M. Torres, J. Bartolomé, F. Bartolomé, M. Natali, D. Decanini, Y. Chen, Geometric coercivity scaling in magnetic thin film antidot arrays, *J. Magn. Magn. Mater.* 242 (Part 1) (2002) 597–600, [https://doi.org/10.1016/S0304-8853\(01\)01108-8](https://doi.org/10.1016/S0304-8853(01)01108-8). <http://www.sciencedirect.com/science/article/pii/S0304885301011088>.
- [273] R.P. Cowburn, A.O. Adeyeye, J.A.C. Bland, Magnetic domain formation in lithographically defined antidot Permalloy arrays, *Appl. Phys. Lett.* 70 (17) (1997) 2309–2311, <https://doi.org/10.1063/1.118845>.
- [274] C.C. Wang, A.O. Adeyeye, N. Singh, Magnetic antidot nanostructures: effect of lattice geometry, *Nanotechnology* 17 (6) (2006) 1629, <https://doi.org/10.1088/0957-4484/17/6/015>. <http://stacks.iop.org/0957-4484/17/i=6/a=015>.
- [275] P. Vavassori, G. Gubbiotti, G. Zangari, C.T. Yu, H. Yin, H. Jiang, G.J. Mankey, Lattice symmetry and magnetization reversal in micron-size antidot arrays in Permalloy film, *J. Appl. Phys.* 91 (10) (2002) 7992–7994, <https://doi.org/10.1063/1.1453321>. <http://aip.scitation.org/doi/abs/10.1063/1.1453321>.
- [276] N.G. Deshpande, M.S. Seo, X.R. Jin, S.J. Lee, Y.P. Lee, J.Y. Rhee, K.W. Kim, Tailoring of magnetic properties of patterned cobalt antidots by simple manipulation of lattice symmetry, *Appl. Phys. Lett.* 96 (12) (2010) 122503, <https://doi.org/10.1063/1.3368691>.
- [277] F. Kronast, J. Schlichting, F. Radu, S.K. Mishra, T. Noll, H.A. Dürr, Spin-resolved photoemission microscopy and magnetic imaging in applied magnetic fields, *Surf. Interface Anal.* 1096–991842 (10–11) (2010) 1532–1536, <https://doi.org/10.1002/sia.3561>. ISSN.
- [278] S. Mangin, M. Gottwald, C.H. Lambert, D. Steil, V. Uhlir, L. Pang, M. Hehn, S. Alebrand, M. Cinchetti, G. Malinowski, Y. Fainman, M. Aeschlimann, E.E. Fullerton, Engineered materials for all-optical helicity-dependent magnetic switching, *Nat. Mater.* 13 (2014) 286–292, <https://doi.org/10.1038/nmat3864>.
- [279] C.H. Lambert, S. Mangin, B.S.D.C.S. Varaprasad, Y.K. Takahashi, M. Hehn, M. Cinchetti, G. Malinowski, K. Hono, Y. Fainman, M. Aeschlimann, E.E. Fullerton, All-optical control of ferromagnetic thin films and nanostructures, *Science* 345 (6202) (2014) 1337–1340, <https://doi.org/10.1126/science.1253493>. <http://science.sciencemag.org/content/345/6202/1337>.
- [280] L. Le Guyader, S. El Moussaoui, M. Buzzi, R.V. Chopdekar, L.J. Heyderman, A. Tsukamoto, A. Itoh, A. Kirilyuk, T. Rasing, A.V. Kimel, F. Nolting, Demonstration of laser induced magnetization reversal in GdFeCo nanostructures, *Appl. Phys. Lett.* 101 (2) (2012) 022410, <https://doi.org/10.1063/1.4733965>.
- [281] K. Vahaplar, A.M. Kalashnikova, A.V. Kimel, D. Hinzke, U. Nowak, R. Chantrell, A. Tsukamoto, A. Itoh, A. Kirilyuk, T. Rasing, Ultrafast path for optical magnetization reversal via a strongly nonequilibrium state, *Phys. Rev. Lett.* 103 (2009) 117201, <https://doi.org/10.1103/PhysRevLett.103.117201>.

- [282] K. Vahaplar, A.M. Kalashnikova, A.V. Kimel, S. Gerlach, D. Hinzke, U. Nowak, R. Chantrell, A. Tsukamoto, A. Itoh, A. Kirilyuk, T. Rasing, All-optical magnetization reversal by circularly polarized laser pulses: experiment and multiscale modeling, *Phys. Rev. B* 85 (2012) 104402, <https://doi.org/10.1103/PhysRevB.85.104402>.
- [283] G.P. Zhang, Y.H. Bai, T.F. George, Switching ferromagnetic spins by an ultrafast laser pulse: emergence of giant optical spin-orbit torque, *EPL (Europhys. Lett.)* 115 (5) (2016) 57003. <http://stacks.iop.org/0295-5075/115/i=5/a=57003>.
- [284] S. Alebrand, M. Gottwald, M. Hehn, D. Steil, M. Cinchetti, D. Lacour, E.E. Fullerton, M. Aeschlimann, S. Mangin, Light-induced magnetization reversal of high-anisotropy TbCo alloy films, *Appl. Phys. Lett.* 101 (16) (2012) 162408, <https://doi.org/10.1063/1.4759109>.
- [285] S. Alebrand, U. Bierbrauer, M. Hehn, M. Gottwald, O. Schmitt, D. Steil, E.E. Fullerton, S. Mangin, M. Cinchetti, M. Aeschlimann, Subpicosecond magnetization dynamics in TbCo alloys, *Phys. Rev. B* 89 (2014) 144404, <https://doi.org/10.1103/PhysRevB.89.144404>.
- [286] A. Hassdenteufel, C. Schubert, B. Hebler, H. Schultheiss, J. Fassbender, M. Albrecht, R. Bratschitsch, All-optical helicity dependent magnetic switching in Tb-Fe thin films with a MHz laser oscillator, *Opt. Express* 22 (8) (2014) 10017–10025, <https://doi.org/10.1364/OE.22.010017>. <http://www.opticsexpress.org/abstract.cfm?URI=oe-22-8-10017>.
- [287] A. Kirilyuk, A.V. Kimel, T. Rasing, Laser-induced magnetization dynamics and reversal in ferrimagnetic alloys, *Rep. Prog. Phys.* 76 (2) (2013) 026501. <http://stacks.iop.org/0034-4885/76/i=2/a=026501>.
- [288] T.M. Liu, T. Wang, A.H. Reid, M. Savoini, X. Wu, B. Koene, P. Granitzka, C.E. Graves, D. J. Higley, Z. Chen, G. Razinskas, M. Hantschmann, A. Scherz, J. Stöhr, A. Tsukamoto, B. Hecht, A. V. Kimel, A. Kirilyuk, T. Rasing, H.A. Dürr, Nanoscale confinement of all-optical magnetic switching in TbFeCo—competition with nanoscale heterogeneity, *Nano Lett.* 15 (10) (2015) 6862–6868, <https://doi.org/10.1021/acs.nanolett.5b02743>.
- [289] T.A. Ostler, J. Barker, R.F.L. Evans, R.W. Chantrell, U. Atxitia, O. Chubykalo-Fesenko, S. El Moussaoui, L. Le Guyader, E. Mengotti, L.J. Heyderman, F. Nolting, A. Tsukamoto, A. Itoh, D. Afanasiev, B. A. Ivanov, A.M. Kalashnikova, K. Vahaplar, J. Mentink, A. Kirilyuk, T. Rasing, A.V. Kimel, Ultrafast heating as a sufficient stimulus for magnetization reversal in a ferrimagnet, *Nat. Commun.* 3 (2012) 666, <https://doi.org/10.1038/ncomms1666>.
- [290] I. Radu, K. Vahaplar, C. Stamm, T. Kachel, N. Pontius, H.A. Dürr, T.A. Ostler, J. Barker, R.F.L. Evans, R.W. Chantrell, A. Tsukamoto, A. Itoh, A. Kirilyuk, T. Rasing, A.V. Kimel, Transient ferromagnetic-like state mediating ultrafast reversal of antiferromagnetically coupled spins, *Nature* 472 (2011) 205–208, <https://doi.org/10.1038/nature09901>.
- [291] R. Moreno, T.A. Ostler, R.W. Chantrell, O. Chubykalo-Fesenko, Conditions for thermally induced all-optical switching in ferrimagnetic alloys: modeling of TbCo, *Phys. Rev. B* 96 (2017) 014409, <https://doi.org/10.1103/PhysRevB.96.014409>.
- [292] S. Gerlach, L. Oroszlany, D. Hinzke, S. Sievering, S. Wienholdt, L. Szunyogh, U. Nowak, Modeling ultrafast all-optical switching in synthetic ferrimagnets, *Phys. Rev. B* 95 (2017) 224435, <https://doi.org/10.1103/PhysRevB.95.224435>.

This page intentionally left blank

Nanomagnetic-Supported Catalysts

Vincent Terrasson, Erwann Guénin

Sorbonne Universités, Université de Technologie de Compiègne, Integrated Transformations of Renewable Matter Laboratory (EA TIMR 4297 UTC-ESCOM), Compiègne, France

10.1 Introduction

During the past decades, due to public environmental concerns, the chemical industry has been pushed to reconsider its business strategies in terms of energy resources, impact on the environment, and sustainability [1–3]. The development of green chemical processes is thus becoming one of the main challenges [4]. The use of a catalyst to promote a reaction is one of the twelve green chemistry principles established by Anastas and Warner [5,6]. Nowadays, catalysts play a crucial role in chemical industries since 90% of industrial chemicals are obtained using catalysis at least at one point in the synthetic process [7,8]. There are two main types of catalysis: homogeneous catalysts, where both catalysts and reactants are in the same phase, are often more efficient and selective than heterogeneous ones, but have the advantages to be easily retrievable from the reaction medium and so can be recycled [9,10]. This latter feature is becoming important as over the last decades, catalytic systems based on expensive and critical noble transition metals have been extensively developed. Hence, durability and recyclability are fundamental aspects to take into account in the development of new greener catalysts. In the quest for more eco-compatible and less expensive catalysts, the use of nanomaterials as support in heterogeneous catalysis is a growing field of research [11–21]. Due to their high surface/volume ratio, nanoparticles (NPs) as a supporting material provide the benefit of an increased active surface area, which allows for increasing reaction rates. NPs are now often considered as a bridge between heterogeneous and homogeneous catalyses [22,23] reuniting advantages of both methodologies in one catalyst. In this area, magnetic nanoparticles (mNPs) appear as an ultimate nanosupport due to their ease of recovery [24–34]. Hence, the simple use of an external magnet allows the rapid recovery of the catalyst without the need for filtration or centrifugation. Nevertheless, synthesis of mNPs with a precise control over their size and magnetic properties is not a trivial process. The attachment of the catalytic entity on the surface of the NPs is also a key feature of this methodology. Affording stable colloidal solution or controlled nanocomposites is a crucial part of the development of such nanomagnetic catalysts.

In this chapter, we will go back to the fundamentals of the existing synthesis methodologies of the mNPs and present an overview of the preparation of nanomagnetic catalysts focusing on the NPs coating. Then we will give pertinent literature examples of the various types of catalysts that can be immobilized onto nanomagnetic support as well as the different applications in chemical synthesis of such nanomagnetic catalysts. To conclude, we will present limitations and recent outlooks for these new objects.

10.2 Synthesis and Property of Magnetic Nanoparticles

Magnetic nanoparticles (mNPs) have attracted lot of interest in recent years in a wide range of disciplines due to their unique properties. They have been studied for example as nanofluids, in environmental remediation, in targeted drug delivery, in sensor applications, in imaging, in hyperthermia, and of course in catalysis [35–44]. The term mNP covers a large variety of different compositions and phases—from magnetic iron-oxide (maghemite and magnetite), ferromagnet (MFe_2O_4 with $M = Ni, Mn, Zn, Co$, etc.) to zero-valence metals (iron and cobalt) and alloys (with noble metals, for example). Though all these compositions can be theoretically (and have been for most of them practically) utilized as magnetic support for catalysis, the most commonly used are iron oxide NPs [34]. Zero-valent metallic NPs are intrinsically chemically highly active and therefore easily oxidized in air, which renders synthesis more difficult and has limited their use without highly efficient surface protection [45,46]. Moreover, oxidation of the surface generally diminished their magnetic properties and their dispersibility. As far as the ferromagnets are concerned, while their synthesis is fairly well described and assessable, their use can be limited by the presence of reactive and potentially toxic metals in their structure. But on other hand, these metals can also be a catalytic entity as we will see further in the chapter. Nevertheless, as presented in the following sections, several examples of pure metallic and ferromagnet nanosupports have been described. The relatively inert nature of iron oxide, the ease of synthesis, and the nontoxic character for environment as well as for human body probably explain the preference for these nanosupports, and we will, therefore, mainly focus on iron oxide synthesis in this part. It must be noted that most of the synthesis described for the iron oxide is applicable for mixed ferrites (MFe_2O_4).

Control over synthesis is highly important for mNPs as their magnetic properties are directly related to their composition and size [47]. Magnetic materials are characterized by their reaction to a magnetic field and all substances are categorized into the following main categories: diamagnetic, paramagnetic, ferromagnetic, antiferromagnetic, and ferrimagnetic. With rare exception, diamagnetics' magnetic behavior is not significant. Paramagnetics possess weak magnetic field in the direction of an applied one and therefore are not interesting in nanomagnetic catalysis. Antiferromagnetics such as hematite (in bulk) have a null magnetic moment. On the other hand, ferromagnetics such as iron or ferrimagnetics such as maghemite or magnetite have significant magnetic properties that can be applied for the development of

nanomagnetic catalysts. At the nanometric level, ferro- or ferrimagnetic particles (>20 nm) turn to a single domain structure and become superparamagnetic acquiring high saturation magnetization in response to an external magnetic field but without any remanent magnetization. Fig. 10.1 (from Kolhatkar et al. [47]) shows the properties of the different types of magnetic materials when placed under a magnetic field. The important values given by these curves are the saturation magnetization (M_s , maximum induced magnetization) the remanent magnetization (M_r , induced magnetization remaining after an applied field is removed), and coercivity (H_c , the intensity of an external coercive field needed to force the magnetization to zero).

M_s and M_r are critical parameters not often discussed in literature that describes the design of nanomagnetic catalyst. In fact, the nanosupport must exhibit as little magnetization as possible when in colloidal solution because if remanent magnetization exists NPs agglomeration will occur during the catalysis step, thus diminishing the reactive surface and impairing catalytic activity. However, when placed under a magnetic field during the purification step, the nanomagnetic catalyst should have a saturation magnetization in order to be efficiently retrieved from the medium. Hence, the activity of the nanomagnetic material is a difficult balance between high dispersibility in the catalysis medium and easy recovery owing to its magnetic property. That is also why maghemite and magnetite superparamagnetic NPs offering all these assets are often favored in literature.

Several methods exist for the iron oxide synthesis that mainly differs from the control in the size and shape of the particles, which could in turn affect their magnetic properties [48]. Another important aspect is the conditions and the scalability of the process as that could impair further development of the catalyst. Generally, methods for iron oxide NP synthesis are classified as aqueous (A) or nonaqueous processes (NA) [49]. Among the different methodologies the main ones are coprecipitation (A), thermal decomposition (NA), micelle synthesis (direct or indirect) (A), hydrothermal synthesis (NA), Sol-gel reactions, and polyol methods (NA). Generally, the nonaqueous routes are described to yield iron oxide NPs with a better control over size and crystallinity and therefore a better control over their magnetic

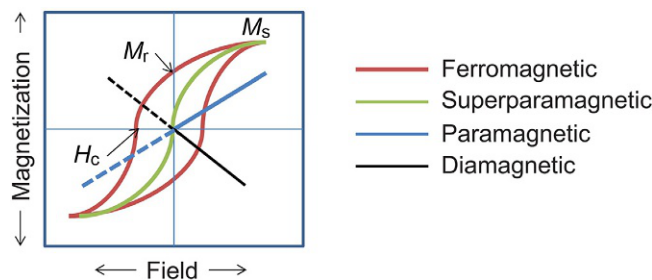


Fig. 10.1

Properties of different types of materials when placed under a magnetic field.

property. But they suffer from various disadvantages: the use of high temperature for the reaction (and in certain cases high pressure) or the use of a calcination step, in some cases (sol gel) multistep phase preparation, the use of costly metal precursors for some, and the obtaining in most cases of iron oxide NPs dissolved in polar solvent due to the presence of organic ligands that will need to be replaced for aqueous dispersion. The latter is not true for polyol methods as iron oxide is obtained with hydrophilic ligands at their surface allowing water dispersion. On the other hand, aqueous routes are described to yield iron oxide NPs with a broader size distribution and less crystallinity. Nevertheless, micelle methodologies are proposed to have a better control over the NP size, but with the use of a surfactant, which will need important washing steps.

For some biological applications where high-quality mNPs are needed some of these protocols will be favored, but for nanomagnetic catalysis applications more emphasis will be put on the robustness of the protocol allowing for reproducible reactions that are easily scalable. The latter asset has recently been particularly developed for coprecipitation methodology as several authors have shown that this synthesis mode could be scaled up to gram scale in appropriate batch reactors or using continuous flow [50,51]. Moreover, one of the driving forces of nanocatalysis is the will to produce more eco-compatible catalysts; therefore, aqueous methods are often preferred in this area. It should also be pointed out that recently the synthesis of iron oxide in water has achieved important advances that permit reduction of polydispersibility [49]. New methods such as laser pyrolysis of aerosols can also lead to reduction of polydispersity [52]. Finally, sonochemical or microwave-based synthesis has also been implemented the last years for iron oxide synthesis by modifying crystal growth kinetics, thus increasing the rate of reaction and reducing reaction time [53,54]. These new methods are therefore considered as attractive for fabrication of large-scale and size-controllable iron oxide NPs.

10.3 Preparation of NanoMagnetic-Supported Catalysts

10.3.1 Uncoated Nanoparticles

Though mNPs are described as prone to aggregation when uncoated, several authors have prepared magnetic nanocatalysts by using directly bare iron oxide or ferrite NPs to support catalytic metal salts or metallic NPs. In this approach, impregnation methodology represents the oldest and simplest way to prepare a supported catalyst. It consists of evaporation of the catalyst precursor solution over the mNPs' surface. Salts of catalytic metals such as Pd [55–62], Ru [63,64], Rh [65], Au [66–73], Co [74], Ni [75], Cu [76,77], or multimetals [78] were therefore deposited on mNPs. In certain cases, post reduction treatment was performed to produce metallic NP at the mNPs' surface [56,57,62,74,75]. The main disadvantage of this procedure is the inability to control salt or particle distribution over the mNPs as well as the interaction with the iron oxide surface [79]. Nevertheless, the latter is also often cited to have a

beneficial effect on catalysis efficiency. Finally, the control over the active species on the surface is also difficult and prone to difficult characterization [30].

As previously seen in ferrite NPs, MFe_2O_4 are one of the magnetic supports that can also be utilized to produce magnetic nanocatalysts. However, they also can be directly used owing to catalysis properties of their constitutive metal M. For example, ferrites containing manganese [80], nickel and cobalt [81–83], or copper [84–86] have been prepared for catalytic purposes in different organic reactions. In a similar manner, Pd- Fe_3O_4 heterodimers nanocrystals can be prepared by thermolysis of a mixture of iron and palladium precursor salts [87–89]. The resulting heterodimers represent a robust catalyst for pallado-catalyzed classical C—C coupling reactions such as Suzuki-Miyaura or Sonogashira. Nevertheless, in these diverse examples, catalysis loading utilized was quite high, probably reflecting the decreased stability of these magnetic nanocatalysts in the reaction medium. Lipshutz and collaborators recently proposed an alternative by running such catalysts in the presence of a surfactant to enhance their catalysis aptitude in aqueous media [90–92].

10.3.2 Nanoparticle Coating

NP coating is generally a crucial step for the development of a nanomagnetic-supported catalyst [93]. In fact, as other NPs, mNPs have the disadvantage of being prone to aggregation, to form large clusters [37,94], and consequently to lose their unique surface area associated with high catalytic efficiency. Depending on the synthetic route chosen to prepare the mNPs, their surface will be different but their stability will be limited. For example, when prepared via coprecipitation methodology, mNPs will possess hydroxyl groups at their surface and be stable only in aqueous suspensions at acid or basic pH. Whereas when prepared by thermal decomposition, the as-synthesized mNPs will be stabilized by organic surfactants such as oleic acid stabilizing the mNPs in nonpolar media but not in a sufficient manner to proceed with harsh reaction conditions. Therefore, for catalytic applications (as for biomedicine ones), the mNPs needed to be coated with specific organic or inorganic materials to prevent their aggregation and conserve their catalytic properties [95,96].

High stability of the magnetic nanocatalyst as well as its robustness is a prerequisite to develop an economically viable industrial process. The coating must confer high stability in the catalytic medium, be sufficiently stable at high temperature or pressure often required in catalytic reactions, and allow for repeating and recycling processes to be conducted. Moreover, the coating will have to present functional groups that permit the conjugation of the catalytic species [97]. This latter aspect is important, as it will define the loading capability of catalysts onto the magnetic nanosupport. Control over the number of functional groups and consecutively number of catalytic entities on the support is of crucial importance. Control over the functionalization methodology is also of importance [98], as for example some catalysts such as enzymes possess catalytic sites that cannot be altered when attached to the

magnetic support. Finally, to ensure good recyclability of the nanocatalysts, a control over the leaching is necessary, especially when anchoring metals or metal complexes. All this is only performed by considering proper functionalization methodologies.

Several ways to immobilize catalysts at the surface of mNPs have been explored. They range from simple organic molecules to complex polymer or inorganic shells [99–101]. We will here give a quick overview of the three principal strategies utilized to stabilize the mNP-based catalysts.

10.3.2.1 Silica shell

Owing to its stability, compatibility, low cost, and theoretical control over thickness and porosity, the formation of silica shell over the mNPs appears as a very convenient way to protect the NP surface [102]. Using the well-described Stöber synthesis or microemulsion methodology, uniformed silica shells are produced around the magnetic core without formation of silica NPs (Fig. 10.2). Moreover, the possibility to silanize the surface with functional

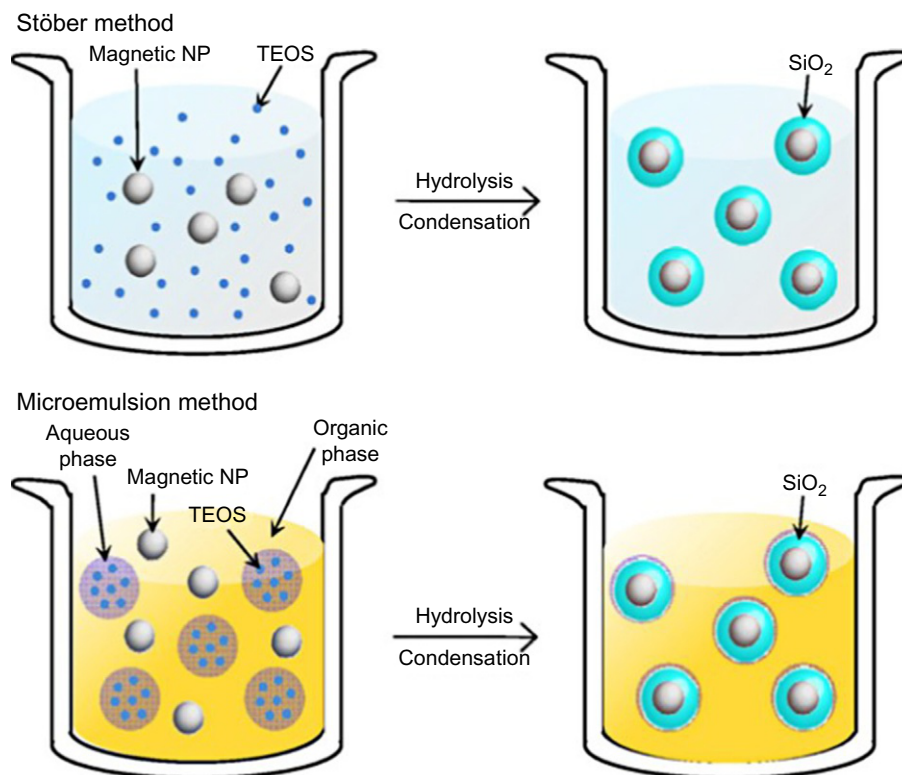


Fig. 10.2
Silica coating from Lim et al. [24].

organosilanes opens up the opportunity to further modify the mNPs with a wide range of chemical functions. While this strategy remains the most used to prepare magnetic nanocatalysts [103–110], the main drawback is that it remains difficult to obtain a reproducible homogeneous distribution of mNPs in silica shell. Thus, larger-sized aggregates could be obtained by decreasing the specific surface of the catalysts and their stability.

10.3.2.2 Polymer coating

When considering the coating of mNPs by polymers, two strategies can be utilized: grafting to or grafting from methodologies. In the grafting to methodology, the polymer is presynthesized and added to the mNPs (Fig. 10.3). Generally, this methodology is based on ionic interactions between the surface and the polymer as in polyelectrolyte films [111]. Several polymers have been described for the obtaining of such catalysts mainly based on amine-containing polymers: polyethylene imine (PEI) [112,113], polyaniline [114], polypyrrole [115,116], polydopamine [117], or biopolymers such as chitosan [118]. The latter example, describing the use of an eco-friendly and naturally abundant compound for coating of mNPs, is stirring great interest to produce more eco-compatible catalysts [119,120].

In the second strategy (grafting from), small molecules bearing a polymerizable function are added to the surface prior to in situ polymerization [121–123]. This approach is similar to the formation of silica shell from organosilicates and affords dendrimerization on the mNPs [122,124,125]. Such formation of dendrimer at the surface of the mNPs, which enables to entrap the catalyst, was also studied by Rosario-Amorin et al. [126,127] but by adding grafting to methodology.

10.3.2.3 Small-molecule coating

The last important method to coat mNPs is the use of small organic molecules [128,129]. In contrast to the silica shell formation or polymer coating, in this strategy, each mNP is theoretically coated individually and the resulting nanocatalyst as a limited size is close to the

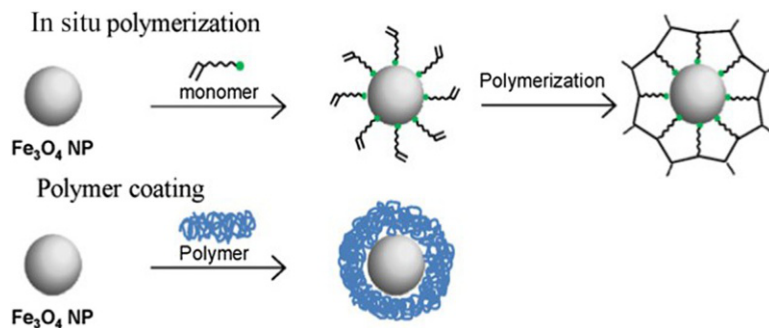


Fig. 10.3

Polymer-coating strategies from Lim et al. [24].

nanocrystal one. These small molecules usually present a chelating function that is able to strongly bind the iron oxide surface and a second functionality that will ensure the post functionalization and for example the binding of the catalytic entity. Several chelating moieties are able to bind iron oxide (Fig. 10.4) [99]. Among them, two families are especially studied for mNP functionalization in catalytic applications as well as in biomedical applications [101]. The first one is the derivative bearing a catechol moiety often referred to as the mussel-inspired ligands [130] that are found in several supported magnetic nanocatalysts [31,131–134]. The second family corresponds to molecules containing one or several phosphonic acid functionalities known to interact strongly with metal oxides. [135,136] This type of linkage, widely utilized for biomedical applications of mNPs [137–139], was also used to stabilize mNPs bearing various catalysts [134,140–142].

A possible concern associated with the coating with small molecule is the strength of their linkage to the surface and the possible release of these small molecules in the reaction media and thus release of the catalyst. However, authors usually report low leaching of catalyst when using these systems. Another concern could also be the possible interactions with the close NP surface during the catalysis, as it cannot be considered completely inert and in some case may interact with the reaction [134,143].

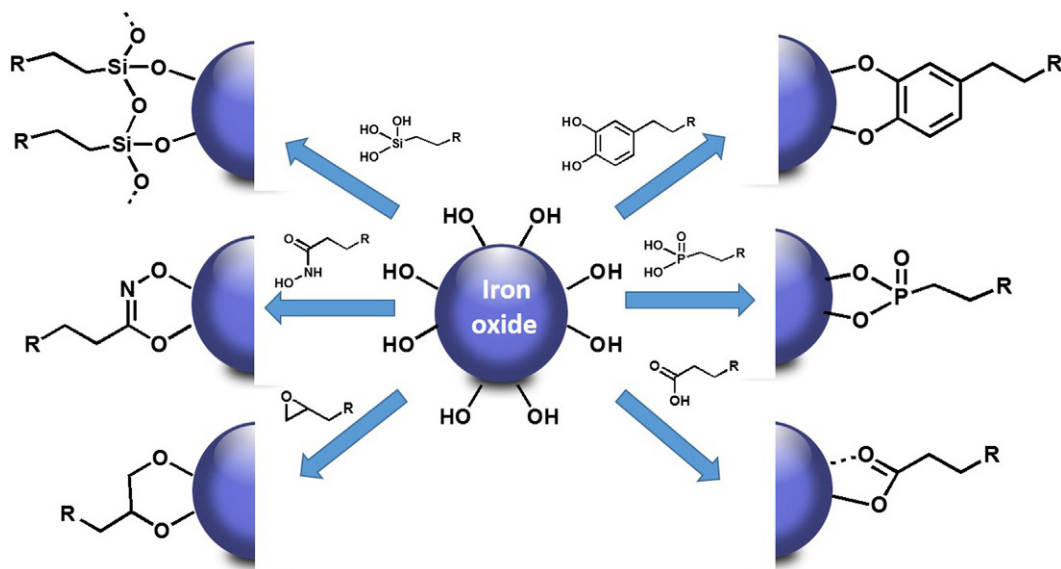


Fig. 10.4

Small molecules able to bind metal oxide surface from Pujari et al. [99].

10.4 Different Types of Catalysts Immobilized Onto Nanomagnetic Support

Virtually all catalysts could be immobilized onto mNPs as far as the right coating is used to stabilize the mNPs and the right chemistry procedure is chosen to link the catalyst to the surface. Catalysis has played an important role in synthetic chemistry in the last decades. Though catalysts have been designed to be increasingly more efficient and selective, the Graal for all researcher is to be able to compete with enzyme activity in nature. Immobilizing a catalyst onto NPs surface is somewhat adding an active site onto an object of few nanometers corresponding to the approximate size of all enzymes [100]. This related size of nano-object and proteins in nature is one of the principles at the base of the incredible development of nanomedicine. Therefore, nanocatalysts can be considered as artificial enzymes and nanomagnetic-supported catalysis participates in the development of bioinspired catalysis [144,145].

In general, the catalyst grafted onto magnetic nanosupport can be divided into three categories: mNPs bearing small organic catalysts, i.e., organocatalysts; mNPs bearing metallic catalysts under the form of organometallic complexes or under the form of metallic NPs; and, because enzymes still sometime outperformed the synthetic catalyst, mNPs bearing enzymes. We will here describe these three categories.

10.4.1 Immobilization of Enzymes

Thanks to several scientific advances, fast and cheap sequencing, bioinformatics, gene expression, etc. production of enzymes of reliable quality on a larger scale is nowadays possible. Moreover, protein engineering allows the design of enzymes with controlled properties. These various advances concurred to the successful development of biocatalysis [146], and nowadays enzymatic catalysis is useful to a plethora of industrial and manufacturing processes among which are pharmaceutical and biofuel production, environmental monitoring, and disease diagnostics [147,148]. Nevertheless, enzymes remain biological material that are prone to degradation and that are thus difficult to handle and recycle compared to pure synthesized catalysts. That is why for enhancing enzyme stability, simplifying the separation and recycling process enzymes can be immobilized on a surface and used in heterogeneous catalysis. In order to circumvent the negative effects of enzymes immobilization on surfaces, NPs appear as an ideal carrier owing to their enhanced active surface, and mNPs owing to their magnetic properties are the ideal recyclable support. Several enzymes from hydrolases, oxydoreductases, or transferases superfamily have been successfully immobilized onto mNPs [149]. Various coatings were studied for the mNP stabilization (Fig. 10.5), but mainly formation of a silica shell [150–152] (or use of small silane molecule) and a polymer shell (chitosan [153], cellulose [154], polyglycerol [155], etc.) were the most-studied strategies. The immobilization of the enzyme is most of the time done by covalently coupling amine or carboxylic functions present at the surface with enzyme residues through glutaraldehyde [150,151] or carbodiimide [156,157] coupling. Though this type of chemistry cannot permit

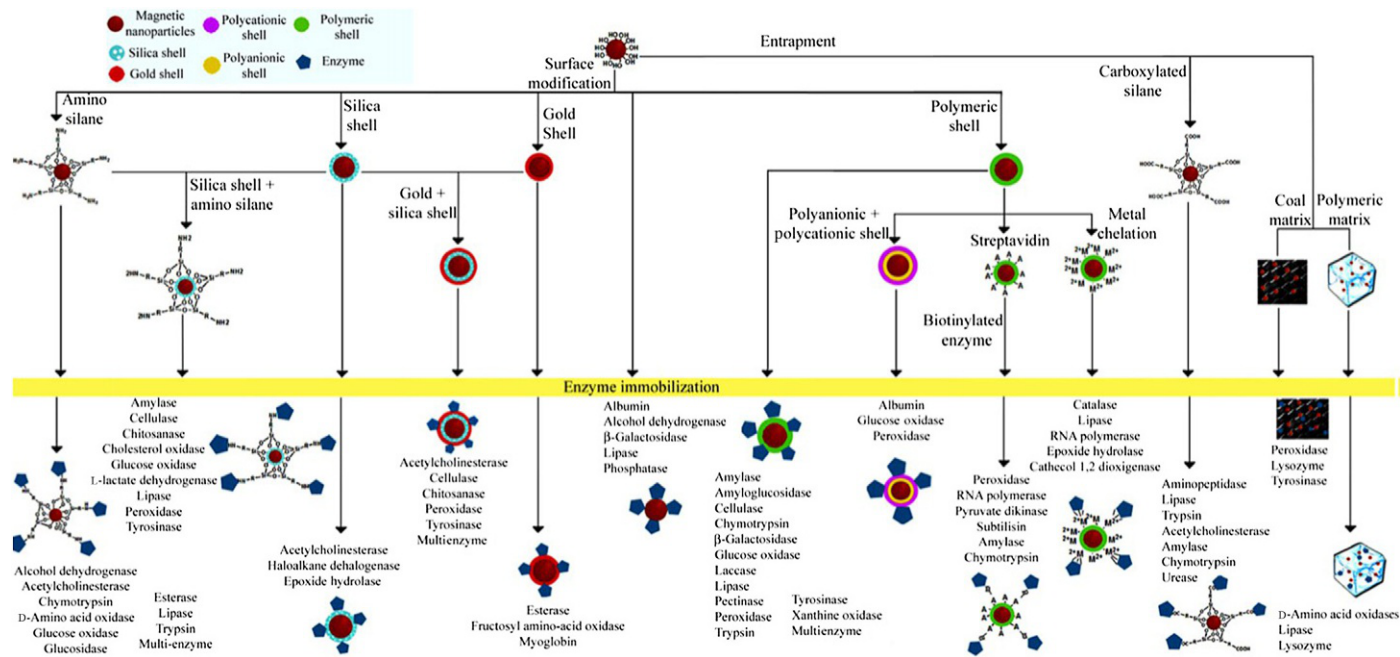


Fig. 10.5 Summary of supports and respective immobilized enzymes from Netto et al. [149].

any chemoselectivity, statistically some of the active sites will remain unaltered by the coupling. Another approach to graft the enzyme on the mNP surface is to apply high-affinity binding such as affinity of Histidine Tag (often used for the purification process of proteins) for metal [158,159] or affinity peptides [152] or biotin streptavidin interaction [160].

Reviewing the literature clearly shows that though not all the enzyme-mNPs biocatalysts show increase activity, most of the time these magnetic nanocatalysts are more efficient and show improved stability and good recyclability [148,161,162]. This appears highly dependent on the controlled conjugation of the enzyme bound to mNPs. Finally, further interest in immobilizing enzymes at the surface of mNPs is the ability to coimmobilize different enzymes on the same surface to achieve a multicatalytic system [147].

10.4.2 Immobilization of Organocatalysts

Most of the catalysts utilized in fine chemistry usually contain metals, but half of the enzymes in nature do not contain any metals in their active site. It is based on this simple principle that researchers started to design small chiral organic molecules that could complete the toolbox of catalysis. Such use of nonmetallic catalysts for the acceleration of reactions has been described for more than a century. But it is only recently after reports from list [163] and Ahrendt et al. [164] that the organocatalysis rush has begun [165,166]. Organocatalysis and especially chiral organocatalysis evolved quite spectacularly over the past 15 years with lots of applications in various domains [167] and especially in medicinal chemistry [168]. Organocatalysts have several advantages: they are usually robust, nontoxic, and are often readily accessible from small biological molecules such as for example amino acids. Unfortunately, one of the main drawbacks of using small organic molecules as a catalyst in an organic synthesis is the separation and recyclability of the system. Thus, the formation of heterogeneous organocatalysis has been rapidly studied and, once again, the nanomaterials and especially mNPs appear as a support of choice [31,169,170]. The first report of the evaluation of an mNP-supported organocatalyst was given by O'Dalaigh et al. [171], and since then several types of organocatalysts have been immobilized on the surface of mNPs: various bases [172–176], acids [124,177], oxidants [21,140]. The first example of asymmetric catalysis was reported by Jiang et al. [178], and the following research mainly focused on the utilization of amino acids or small peptides [134,179–182] or biomolecules such as quinine derivatives [142,143,183] grafted onto mNPs. When comparing the properties of the immobilized chiral organocatalysts with the parent catalysts, most of the authors described retention of the enantio or/and dia stereoselectivity properties, but some showed that problems could be linked to interaction with the surface of the nanomaterial [134,143].

10.4.3 Immobilization of Organometallic Catalysts or Metal Nanoparticles

Organometallic catalysis is long known to be highly efficient and has been utilized in numerous industrial processes [9,184]. Among the organometallic catalysts, the platinum metal group complexes have achieved outstanding performance in several synthetic methods. This is demonstrated by the obtaining of three consecutive Nobel prizes in this area since the beginning of the 21st century (W.S. Knowles, R. Noyori, and K.B. Sharpless in 2001; Y. Chauvin, R.H. Grubbs, and R.R. Schrock in 2005; and R.F. Heck, E. Negishi, and A. Suzuki in 2010) [185,186]. The high efficiency of these organometallic catalysts, however, is not without cost. The transition metals that are used are expensive, toxic, and considered as critical raw materials due to their extensive use and the low quantity of natural stockpiles [187]. Moreover, in certain applications such as OLED technology, contamination (even in small quantities) of the product with metals could greatly impair the properties. Therefore, for both economic and environmental reasons, the industry has been pushed to consider a way to recycle these metals without losing their catalytic potencies. Thus, heterogeneous catalysis has emerged as a promising solution to obtain selective and reusable catalysts. With the concomitant development of nanomaterials, it rapidly appears that immobilizing these organometallic catalysts onto nanomaterials can therefore allow for conservation of their efficiency and selectivity.

Organometallic catalysts immobilized onto mNPs have been widely developed since the beginning of the last century. They represent the most important part of the literature concerning nanomagnetic-supported catalysts [16,22,24,25,28–31]. A great part of this literature concerns platinum group metals catalysts (Pt, Pd, Ru, Rh) or gold catalysts, but less expensive and critical metals such as Ni or Cu have also been studied a lot. For some of these catalysts, reviews already exist (Pd [188] or Ru [189]) and can be even found for some particular reactions conducted with these catalysts [27,190,191]. The metals are generally immobilized in two different forms. In the first approach, the organometallic complexes used in homogeneous catalysis simply mimic at the surface of the mNP support. Ligands of various kinds (phosphines [123,127,192–198], amino acids [131,199], N-heterocyclic carbens [200–203], bipyridines or salen [204–207]) are grafted onto the surface of the mNPs (via polymers, silica, or small molecules), and the organometallic complex is reproduced by adding the metal salts to the magnetic support. Exact formation of the complex is claimed by the authors but usually difficult to assess. The second strategy is relatively similar in its preparation but after immobilization of the metal salt on the support, an extra reduction is conducted to afford the formation of small metallic NPs at the surface of the mNPs. However, when immobilizing the metal salts without a reduction step, small NPs are also formed and could be characterized by XPs or XRD analysis. Activities of the obtained supported organometallic catalysts are usually very good whatever be the strategy chosen. Owing to the high active

surface, in some cases, the reaction occurred with ppm quantities of the organometallic catalyst [90,92,203,208,209]. When considering the catalysis by small metallic NPs, it is debatable whether the catalysis occurred at the surface of the NPs or by leaching the metal atom from the surface [210]. The leaching of the metals from the mNP catalyst is an important aspect that is not always informed. Most of the results found in the literature nevertheless show that these magnetic nanocatalysts can be easily recycled owing to their magnetic properties and therefore reused several times.

10.5 Application of Magnetic Nanocatalysts

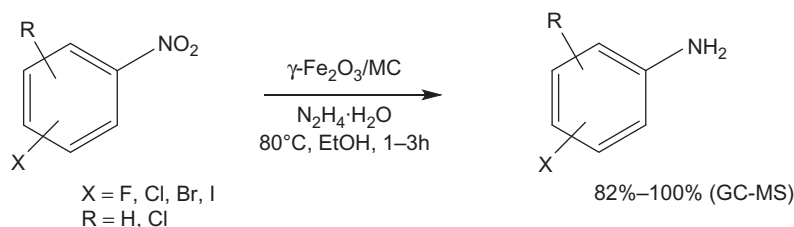
Magnetic nanocatalysts present several advantages when compared to the corresponding nonsupported catalysts. Apart from the ease of their magnetical separation from the reaction medium, they have very often demonstrated higher efficiency (higher TOF), better selectivity, and greater stability. All these reasons explain why they have been used in a wide range of catalytic reactions, including C—C and C-heteroatom bond formation, oxidation, reduction, or cycloaddition through metal or organocatalysis [16,26,29,31].

10.5.1 Reduction Reactions

Magnetically recyclable nanocatalysts have been extensively used in reductions of organic compounds such as reduction of nitroaromatics, hydrogenation of alkenes, or hydrogen transfer to carbonyl groups.

Reduction of nitroaromatics into functionalized anilines, valuable intermediates in the synthesis of biologically active compounds or pigments, have been developed with magnetic nanocatalysts involving different metals. Indeed, Au [211–214], Ni [215,216], Pd [118,217,218], Pt [219–221], or Ag [222–224] catalysts have been reported for this application. As an example, Au-functionalized SiO₂ NPs coated with a double-layered shell of Fe₃O₄ and carbon have shown a high catalytic efficiency in the reduction of 4-nitrophenol using NaBH₄ in water [225]. The recyclability of the catalyst seems to be excellent, as it can be used for at least nine cycles of reaction/magnetic separation. More recently, a low-cost catalyst consisting of γ -Fe₂O₃ NPs encapsulated in a mesoporous carbon structure was applied to the hydrogenation of various halogenated nitrobenzenes using hydrazine as the reductant in ethanol (Scheme 10.1) [226]. A very high selectivity was observed as products from dehalogenation were almost never formed and the recyclability was tested five times without any significant loss of activity.

Magnetic nanocatalysts have also been applied to the hydrogenation of olefins. Very efficient catalysts, based on Pd [227], Rh [228], or Ru [229], were developed for the conversion of

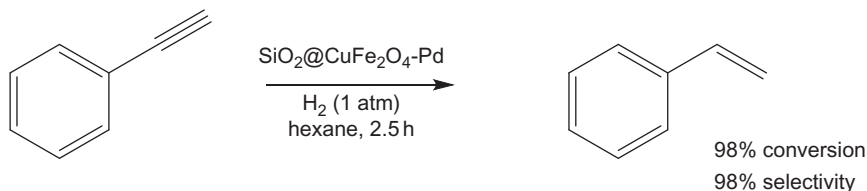
**Scheme 10.1**

Hydrogenation of halogenated nitrobenzenes.

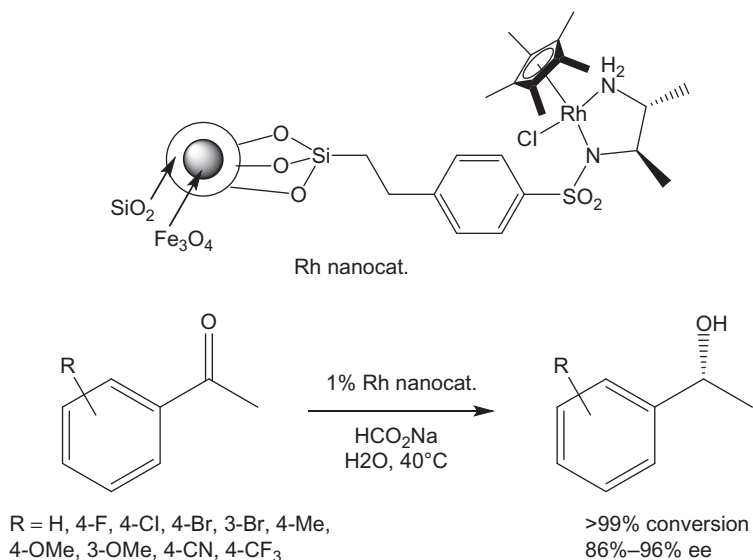
simple alkenes like cyclohexene with excellent TOF. For example, with palladium NPs stabilized by terpyridine ligands linked to $\text{Fe}_3\text{O}_4@\text{SiO}_2$ mNPs, a TOF of over 50000 h^{-1} (as moles of the substrate transformed per mole of surface Pd) was obtained at 75°C under 6 atm of H_2 [230].

Selective hydrogenation of alkynes to alkenes was also studied. In this case, magnetic nanocatalysts showed better conversion and selectivity than with the commercial Lindlar catalyst. With CuFe_2O_4 and Pd-NPs encapsulated in mesoporous silica, a 98% conversion of phenylacetylene was achieved in 2.5 h under 1 atm of H_2 with over 98% selectivity toward styrene, compared to 82% conversion and 92% selectivity employing the commercial catalyst under the same conditions (Scheme 10.2) [231]. Iron NPs, as an alternative to potentially high cost noble metals, were also reported with good activities and recyclability using an external magnetic field [232,233].

Asymmetric reduction of carbonyl compounds by hydrogen transfer catalysis was described using rhodium-based catalysts attached to silica-coated Fe_3O_4 NPs [234–236]. With a ligand derived from chiral 1,2-diphenylethane-1,2-diamine, a wide range of substituted acetophenones were successfully reduced in water to the corresponding chiral alcohols with quantitative conversion and excellent enantioselectivity (up to 96% ee) [236]. Recycling of the magnetic nanocatalyst was performed 10 times without any significant loss in activity or enantioselectivity (Scheme 10.3).

**Scheme 10.2**

Selective hydrogenation of alkyne to alkene.

**Scheme 10.3**

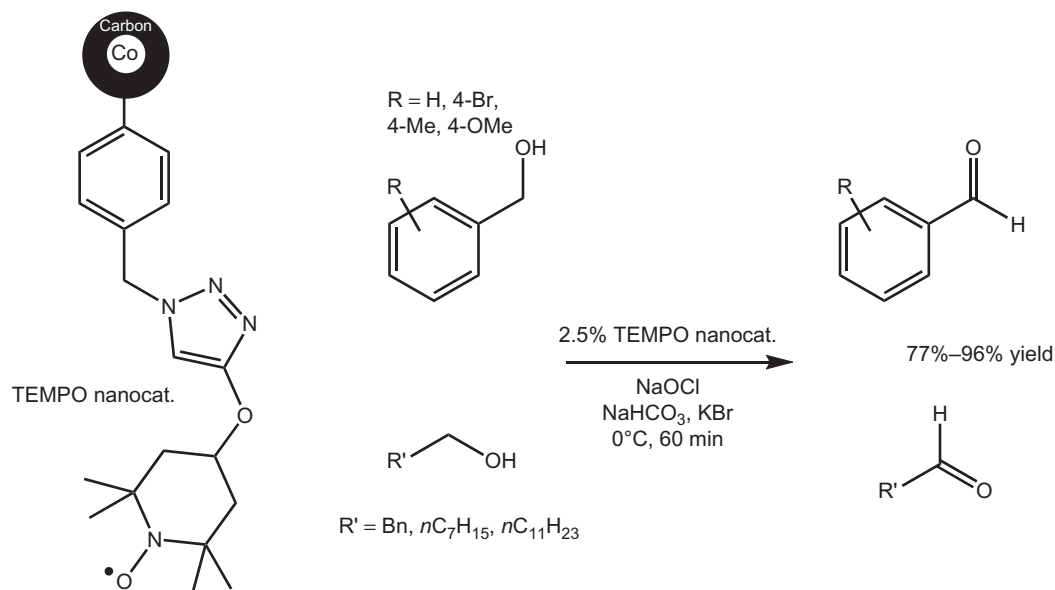
Asymmetric reduction of acetophenones by hydrogen transfer.

10.5.2 Oxidation Reactions

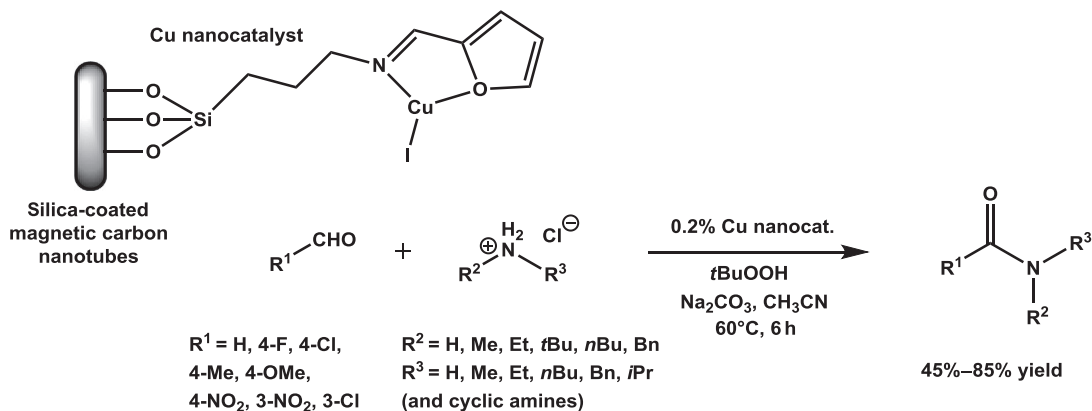
Oxidation reactions are essential transformations in industrial chemistry. In the effort to develop more environment-friendly conditions and use more green chemistry principles, magnetic nanocatalysts have proven to be very useful tools. Oxidation of alcohols to aldehydes or ketones is the most commonly described reaction in this field. Very different magnetic nanocatalysts were used for this transformation from unfunctionalized Fe₂O₃ NPs [237] to Ru [63,229] or Pd-based [238,239] catalysts. In organocatalysis, highly chemoselective oxidation of alcohols to carbonyl compounds was also reported employing recyclable TEMPO-coated mNPs (Scheme 10.4) [140,240]. Oxidation nanocatalysts were additionally evaluated for the aerobic oxidation of amines to imines with good conversions and selectivity [241].

Oxidation of aldehydes to amides in the presence of amines salt was developed with a copper catalyst supported on silica-coated magnetic carbon nanotubes [242]. Various amides were successfully synthesized through this one-pot procedure starting from substituted benzaldehydes, and the catalyst could be magnetically recycled five times without significant loss of activity (Scheme 10.5).

Epoxidation of olefins is another oxidation reaction, which could easily be catalyzed by magnetic nanocatalysts. Using a Cu(II)-phthalocyanine complex immobilized through an ion-pair on silica-coated Fe₃O₄ NPs (Scheme 10.6), the expected epoxides were obtained with high yields (generally over 90%) [243]. The same catalyst was efficiently used for the oxidation of sulfides. In this case, sulfoxides or sulfones could be selectively obtained just by adjusting the

**Scheme 10.4**

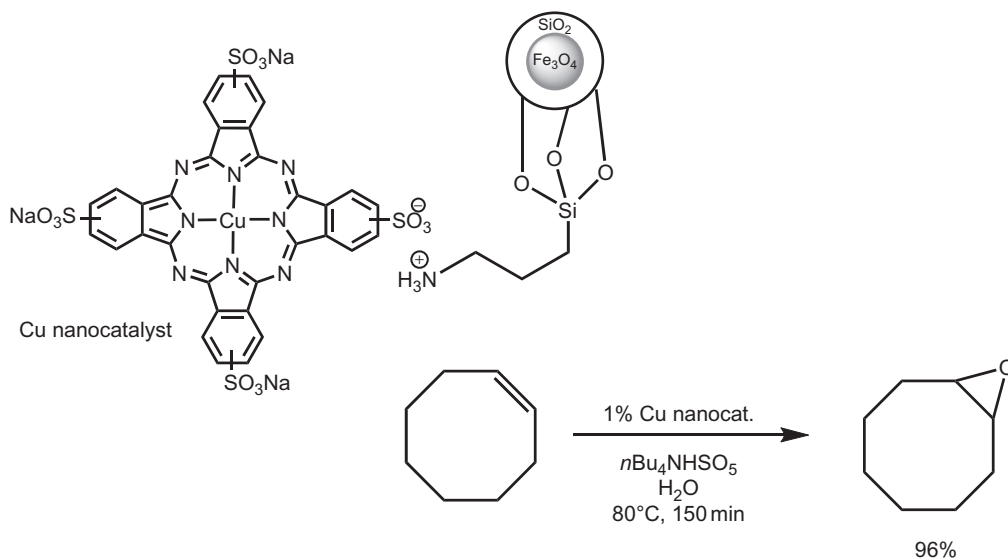
Oxidation of alcohols to carbonyl employing recyclable TEMPO-coated mNPs.

**Scheme 10.5**

Oxidation of aldehydes to amides with a copper catalyst supported on silica-coated magnetic carbon nanotubes.

nature of the solvent and the quantity of the oxidant. Manganese catalysts have equally been reported for the same type of oxidation with comparable results [244].

Alkanes as less easily oxidizable substrates were also studied. With stoichiometric amounts of CoFe₂O₄ nanocrystals as recyclable heterogeneous phase, aerobic oxidation of cyclohexane to form cyclohexanol and cyclohexanone occurred with around 16% conversion, which is a better



Scheme 10.6

Epoxidation of olefins with Cu(II)-phthalocyanine complex immobilized on silica-coated Fe₃O₄ NPs.

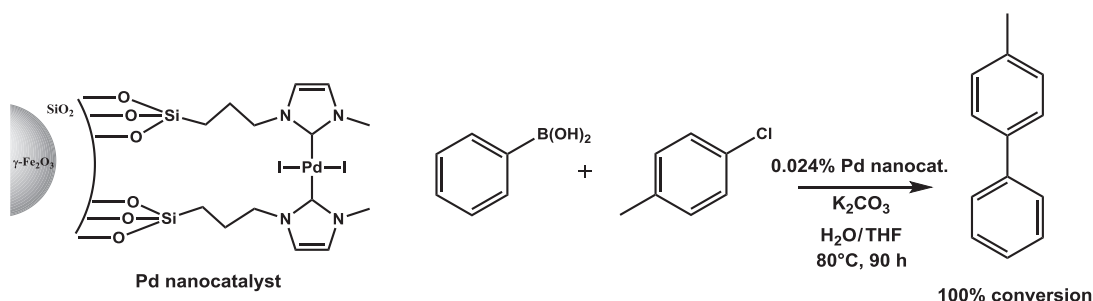
result than with cobalt- or iron-based homogeneous salt [245]. Benzylic positions of various alkanes were oxidized to ketone with a copper catalyst [243].

10.5.3 C—C Bond Formation

10.5.3.1 Metal catalysis

C—C bond formation is a crucial transformation in synthetic chemistry. Transition-metal-catalyzed crosscoupling reactions have received considerable attention as an efficient strategy to create new C—C bonds. To overcome the problem of the removal of the leached metals and ligands from the product, magnetic nanocatalysts have attracted much interest during the past few years. Suzuki-Miyaura, Heck, Sonogashira, or Hiyama reactions have been reported with this type of catalysts [246].

The Suzuki-Miyaura crosscoupling reaction is one of the most powerful ways to prepare biaryl molecules. A wide range of magnetic palladium-based nanocatalysts, with different types of ligands, has been developed for this reaction. N-heterocyclic carbenes, immobilized on the surface of γ -Fe₂O₃ NPs [202], proved to be very efficient ligands: both activated and deactivated aryl bromides could react in quantitative yields and the palladium catalyst could be recycled several times with no loss of catalytic activity (Scheme 10.7). In fact, the magnetic catalyst was found to be more active than the analogue supported on polystyrene [200]. With β -oxoiminato ligand supported on SiO₂/Fe₃O₄ NPs, excellent results were obtained for the coupling of aryl chlorides (even with electron-rich or sterically hindered ones) in water and in

**Scheme 10.7**

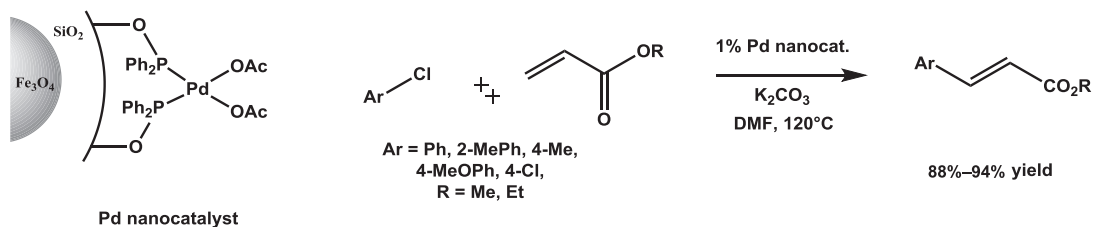
γ -Fe₂O₃ NPs with Pd immobilized through N-heterocyclic carbenes for Suzuki-Miyaura reaction.

the presence of an additional phase-transfer catalyst [247]. More traditional phosphine ligands were obviously tested when supported on polymer or SiO₂-coated NPs, providing good yields of biaryl compounds with low catalyst loading [22,127]. Amine ligands were also described [106,248,249].

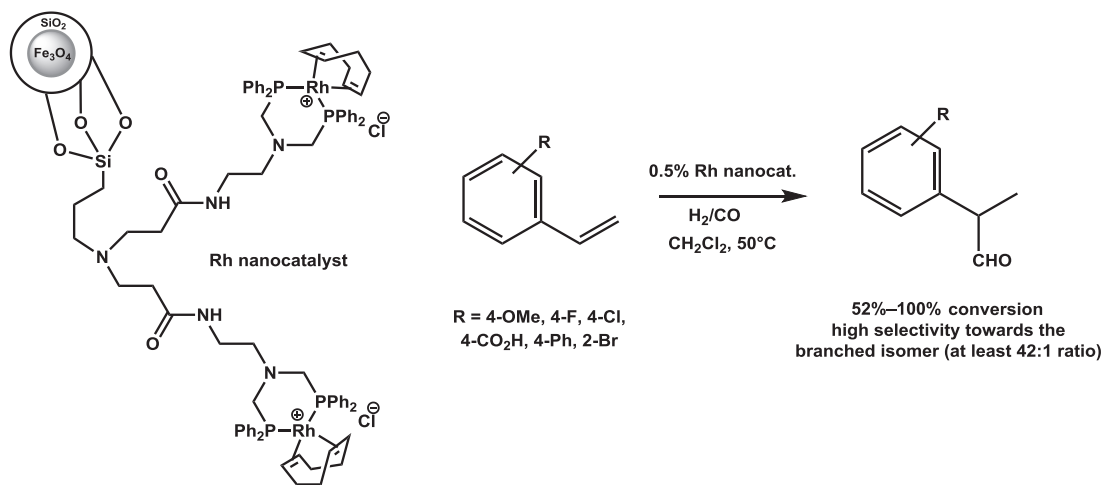
mNPs were also useful in Heck reactions [59,250]. The catalytic systems generally proved to be noticeably efficient even when compared to classic homogeneous systems. As an example, with simple diphenylphosphine ligands supported on silica-coated Fe₃O₄ particles (Scheme 10.8), excellent yields of trans-arylated olefins were obtained even with deactivated aryl chlorides. [194] ICP analysis revealed that less than 1% of palladium was released from the catalyst explaining its good recyclability over four cycles.

Several magnetically retrievable nanocatalysts were additionally reported in Sonogashira reactions between terminal alkynes and aryl halides [251,252]. Magnetic nanocatalysts also proved to be efficient in Hiyama reaction starting from arylsilanes [253,254].

Other metal-catalyzed reactions creating C—C bond were described with magnetic nanocatalysts, including Rh-catalyzed hydroformylation of alkenes with excellent regioselectivity [255–257] (Scheme 10.9) or metathesis of unsaturated fatty acid esters with a supported second-generation Hoveyda-Grubbs Ru-catalyst [258].

**Scheme 10.8**

Heck reaction catalyzed by Pd diphenylphosphine complex supported on silica-coated Fe₃O₄ particles.

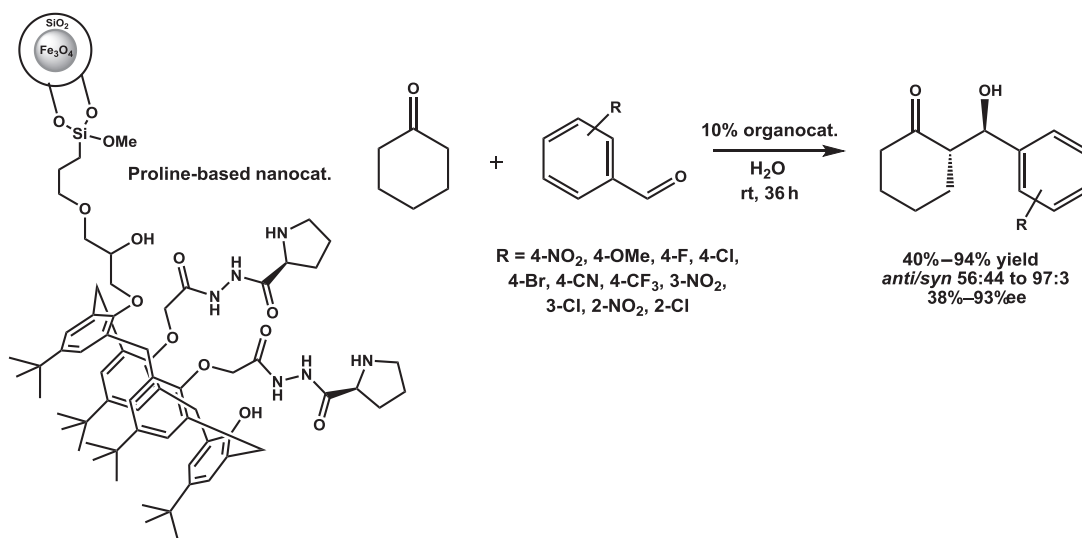


Scheme 10.9

Rh-catalyzed hydroformylation with a magnetic nanocatalyst.

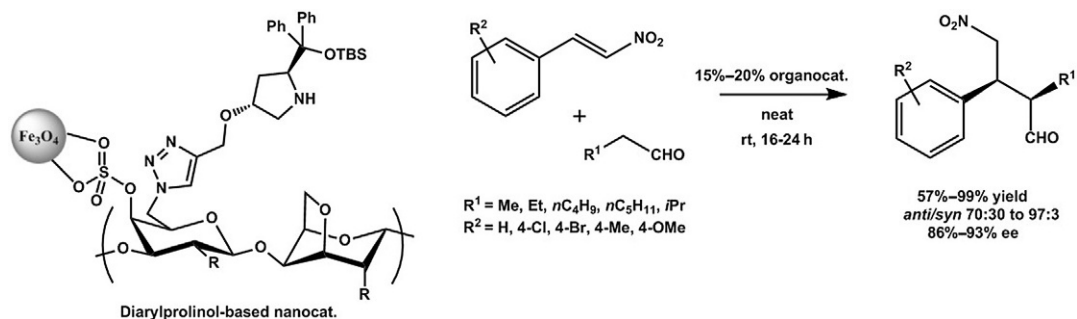
10.5.3.2 Asymmetric organocatalysis

New C—C bonds can also be created without metals but with the intervention of an organocatalyst. Organocatalysis is a fast-growing area of research and new organocatalysts supported on mNPs were naturally developed in order to improve the recyclability of the catalysts [169,170]. L-Proline is without a doubt one of the simplest chiral organocatalysts. Many examples of mNPs functionalized with L-proline derivatives were reported (Scheme 10.10).



Scheme 10.10

Example of proline-based magnetic nanocatalyst for aldol condensation.



Scheme 10.11

Diarylprolinol-based nanocatalyst for asymmetric Michael addition of aldehydes to nitroalkenes.

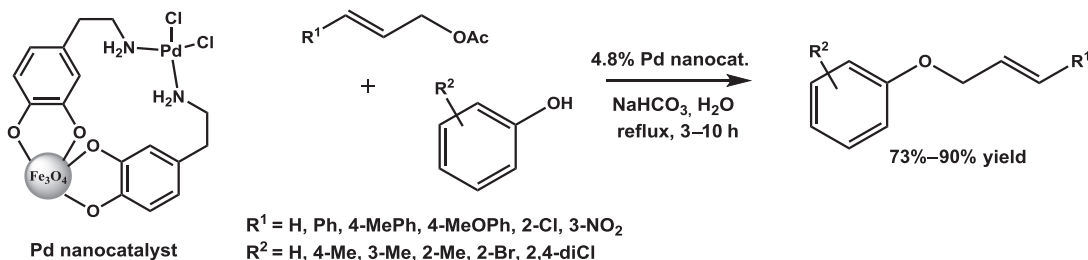
They were generally used in asymmetric aldol reactions in water or without solvent providing good results in terms of yield and enantiomeric excess and showing good recyclability (for at least five cycles) [181,182,259–261]. Asymmetric aldol reactions have also been performed with supported organocatalysts based on natural cinchona alkaloids [142], chiral cyclohexanediamine [262], or oligopeptides [178].

Diarylprolinol derivatives, a widely described family of powerful organocatalysts, were immobilized on mNPs too. Their catalytic activity was tested in asymmetric Michael addition of aldehydes to nitroalkenes (Scheme 10.11). These supported organocatalysts gave results comparable to the corresponding nonsupported diarylprolinols, but their recyclability was not perfect due to some leaching: after three or four cycles, the catalytic activity decreased substantially [263–266]. Magnetic nanocatalysts based on enantiopure imidazolidinones were also described and evaluated in asymmetric Friedel-Crafts alkylation of pyrroles or indoles [267]. Many other organocatalyzed C—C bond formations have been studied with magnetically retrievable nanocatalysts, including Morita-Baylis-Hillman [176] or Mannich reactions [268].

Organocatalysts acting as Brønsted acids were also developed on magnetic nanosupport [177,269,270].

10.5.4 C-Heteroatom Bond Formation

C—O, C—S, or C—N bond formations were reported under catalysis with mNPs. The C—O bond for example could be created by Tsuji-Trost palladium catalysis for the O-allylation of phenols (Scheme 10.12). In this case, a dopamine-Pd complex supported on Fe₃O₄ NPs proved to be efficient under ambient conditions and could be reused six times without losing its activity [132]. Cinchona-functionalized mNPs have been described for the asymmetric syn-dihydroxylation of styrene with OsO₄ and K₃Fe(CN)₆ as oxidants proving to be almost as efficient as the unsupported corresponding catalyst for at least eight cycles [271]. C—O bond formations could also be catalyzed by phase-transfer catalysis without metal. A series of quaternary ammonium and phosphonium salts were immobilized on mNPs and evaluated in the



Scheme 10.12

Tsuji-Trost palladium catalysis for the O-allylation of phenols.

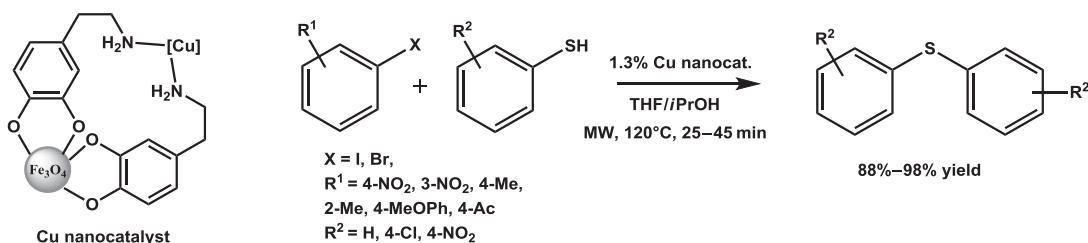
alkylation of PhONa [272]. The catalytic activity was similar to the unsupported quaternary salts with the added advantage that the NPs were easily retrievable and reusable without significant loss of activity. The same strategy was also applied to the immobilization of crown ethers with the same results [273].

Similarly for the creation of C—S bonds, Ullmann coupling has been reported for the S-arylation of thiols with aryl halides catalyzed by copper-containing mNPs (Scheme 10.13) [274,275]. Ullmann coupling with magnetically retrievable catalysts has also been developed for the N-arylation of nitrogen heterocycles like imidazoles, pyrazoles, or indoles [276,277]. Another copper nanocatalyst proved to be efficient in the N-alkylation of anilines or benzylamines using aliphatic alcohols as electrophiles and giving the expected amines with excellent yields generally higher than 95% [278].

C—N bond creation was also described via organocatalysis. Glutathione-functionalized mNPs promoted aza-Michael reaction, Paal-Knorr pyrrole synthesis, and pyrazole ring formation under microwaves [279].

10.5.5 Cycloaddition Reactions

Cycloaddition reactions, which enabled the concerted formations of at least two C—C or C—heteroatom bonds, have been studied with magnetic nanocatalysts. For example, Diels-Alder cycloaddition between cyclopentadiene and α,β -unsaturated aldehydes [133]

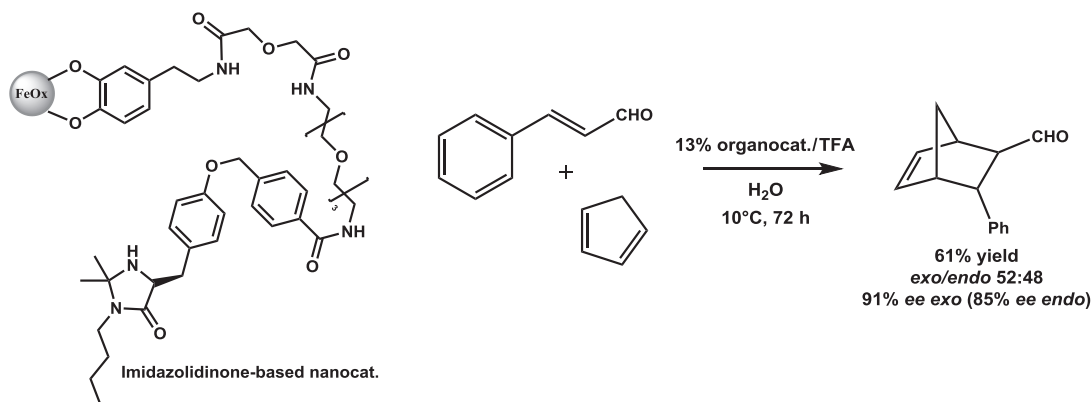


Scheme 10.13

Ullmann coupling catalyzed by copper-containing mNPs.

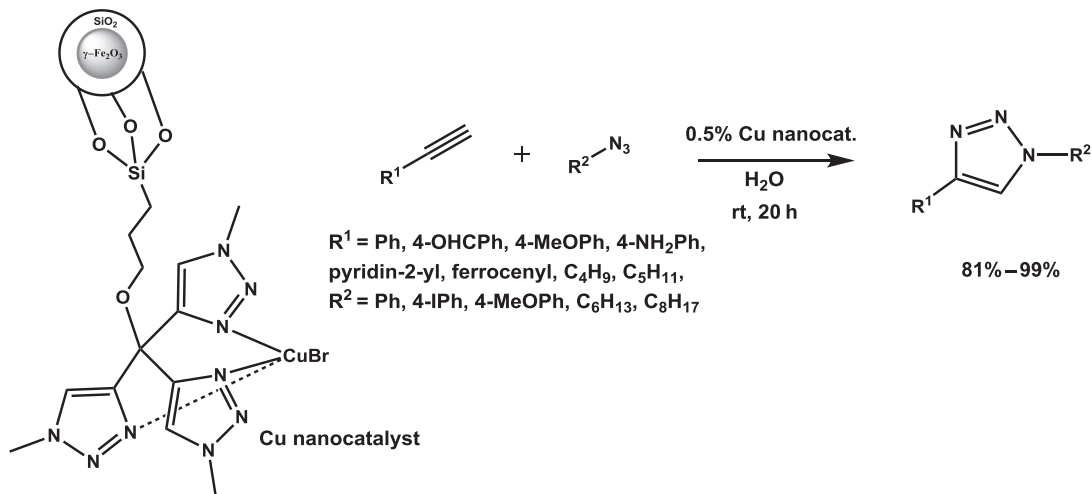
was described with a recoverable chiral imidazolidinone organocatalyst (Scheme 10.14). Using the same family of organocatalysts, asymmetric 1,3-dipolar cycloaddition of nitrones was also reported [280].

Ruthenium [281] or copper-based [282–284] magnetic nanocatalysts have also been evaluated in the 1,3-dipolar cycloaddition between azides and alkynes (click chemistry) to synthesize 1,2,3-triazoles (Scheme 10.15).



Scheme 10.14

Recoverable chiral imidazolidinone organocatalyst for Diels-Alder cycloaddition reaction.



Scheme 10.15

Copper-based magnetic nanocatalysts for the 1,3-dipolar cycloaddition.

10.5.6 C—H Activation

Magnetically recyclable catalysts could be used in C—H activation reactions both on C(sp²) of heterocycles and C(sp³) in benzylic positions [285,286]. For example, copper-ferrite NPs could promote the direct arylation of benzothiazoles with diversely substituted aryl bromides and conserve their catalytic activity after at least four cycles (Scheme 10.16) [84].

10.5.7 Hydrolysis

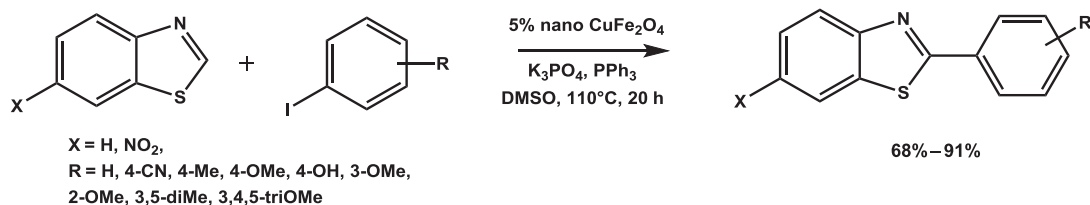
Enzymes are very efficient catalysts for hydrolysis reactions. Immobilized enzymes on mNPs generally showed a catalytic activity as high as the free enzyme and sometimes even higher. The immobilization on nanoparticles seemed to play a protective role since the enzymes proved to be more thermally or pH stable [147,161]. Hydrolysis of oligosaccharides or lipids was evaluated with enzymes supported on magnetically recoverable NPs providing excellent results [154,155,287,288].

Selective hydrolysis of nitriles to the corresponding amides was reported under microwave irradiations using a ruthenium catalyst supported on silica-coated Fe₃O₄ NPs [289,290].

10.5.8 Kinetic Resolution by Esterification

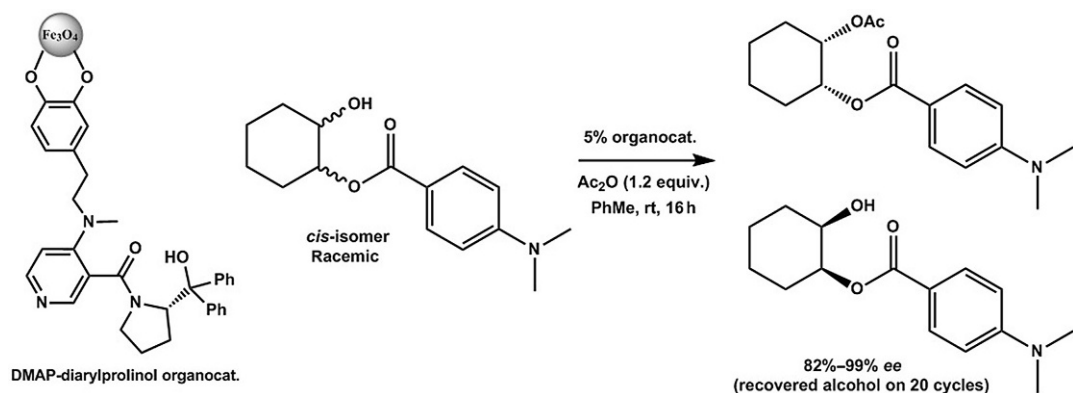
A diarylprolinol-based organocatalyst supported on mNPs was evaluated in the kinetic resolution of several secondary alcohols with acetic anhydride. Excellent results were obtained with enantiomeric excesses up to 99%, and the catalyst could be recycled more than 30 times without significant loss of activity (Scheme 10.17) [143,179].

Other results in this field included the kinetic resolution of 1,2-diols with a copper catalyst [291], meso succinic anhydrides in methanol catalyzed by a supported cinchona alkaloid [143], or racemic carboxylic acids using an immobilized lipase [292].



Scheme 10.16

Copper-ferrite NPs promoting the direct arylation of benzothiazoles.



Scheme 10.17

Kinetic resolution using a diarylprolinol-based organocatalyst supported on mNPs.

10.6 Limitations and Outlooks

Most of the examples we gave in this chapter reported increased selectivities and efficiencies achieved by magnetic nanocatalysts compared to conventional reactions. But Hübner et al. [293] in their critical review on industrial use of heterogeneous catalyst explained that in order to see supported catalysts used in industry, “the immobilization specialist must start producing catalysts of enhanced productivity.” So TON and TOF have to be measured and compared with the best homogeneous catalyst available for the considered reaction (which is not often the case). Moreover, the evaluation of these numbers has to be done in industrial conditions for example in high-concentration conditions to be meaningful. Understanding the effects of the immobilization of catalysts onto the magnetic support is also highly important, and particularly the effect on kinetics of the reaction is crucial for the development of such catalysts. Few authors have discussed the influence of the iron oxide support on the catalytic reaction [134,143]. It was found in these reports that the magnetic nanosupport should not be considered as completely inert for the catalytic reaction.

Another beneficial aspect also put forward by some authors is the high stability increase of the catalyst supported onto mNPs, but this phenomenon (linked to possible poisoning of active sites as well as the influence of leaching) is often scarcely documented and studied. In the case of organometallic catalysis, the difference between immobilization of catalytic metallic complexes and immobilization of small metallic NPs is another aspect to be studied. The compared stability and activity should be more evaluated as well as the process of growth of the metallic NPs onto the magnetic support that is of crucial importance [210].

One of the interests in mNPs-supported catalysis is its potential use in green chemistry [49]. As mNPs can be synthesized through aqueous methodology, some catalysts are elaborated in pure water and therefore can be used to realize organic reaction in aqueous media without the use of organic solvents [26]. In some cases, conjugation of a nanocatalyst together with the use of

micelles technology can afford efficient organic catalysis in water, thus reducing wastes [90–92]. Using such nanocatalytic processes, which replace organic solvents by water, is in accordance with the green chemistry principles [11]. Moreover, the opportunity to utilize magnetic nanocatalysts that render laborious separation steps unnecessary is also beneficial in terms of sustainability. This aspect is especially of importance when using immobilized organometallic catalysts composed of platinum group metals for which the price has increased significantly since the year 2000. Therefore, the recovery and reuse of such expensive precious metal catalysts is advisable and enhances their sustainability.

Several nanomaterial-based catalysts are used in industry [294,295], and with the beneficial aforementioned properties of mNPs-supported catalysts, they without doubt present a high industrial potency. However, to be usable on large-scale reactions, robust and perfectly reproducible synthesis of the mNP support needs to be implemented. It is essential that properties of the formed catalysts are identical batch to batch. Fortunately, much progress has been made on intensification protocols for NP synthesis. Scale up of batch synthesis has been proposed with good control over size, dispersion, and properties [296,297]. The application of continuous-flow processes to the mNPs synthesis has also been studied and shows good promise [51,298–303]. This technology is also potent for the realization of the catalysis reaction in itself and authors have started to implement continuous-flow protocols using mNPs-supported catalysts [291,304,305]. Moreover, the applicability of these protocols opens up new horizons by taking into account the intrinsic properties of magnetic materials. In fact, magnetic heating (hyperthermia) modalities of NPs (i.e., applying an alternative magnetic field to heat the vicinity of the magnetic nanomaterial) have been largely exploited in nanomedicine and opened the way to extensive works for thermal therapies and drug delivery [306]. However, it is only recently that this highly potent concept has been evaluated to boost the catalytic efficiency of mNP catalysts [307–310]. This represents another sustainable optimization of mNPs-supported catalysts as it could lead to the development of more energy-efficient heating procedure.

Thus, it appears that catalysts supported on mNPs show great premises; nevertheless, with the increasing concerns of NP-related risks on civil society, scientists working in the nanoscience domain should asked themselves important questions such as: How can the NP-related risks be assessed? Though iron oxide NPs are described as nontoxic material [294], we must remember that considering NPs inherent hazards are not dictated solely by their nature but depend greatly on their surface functionalization [295]. One answer will be to conduct life cycle assessment on these new catalysts and study their real full impact on environment.

Acknowledgements

This work was done within the framework of the Chair “Green Chemistry and Processes” sponsored by the European Union, the Région Haut de France, the Ecole Supérieure de Chimie Organique et Minérale, and the Université de Technologie de Compiègne through FEDER funding.

References

- [1] B.W. Cue, J. Zhang, Green process chemistry in the pharmaceutical industry, *Green Chem. Lett. Rev.* 2 (4) (2009) 193–211.
- [2] H.K. Chan, Green process and product design in practice, *Procedia. Soc. Behav. Sci.* 25 (2011) 398–402.
- [3] I.D. Paul, G.P. Bhole, J.R. Chaudhari, A review on green manufacturing: it's important, methodology and its application, *Procedia Mater. Sci.* 6 (2014) 1644–1649.
- [4] P.J. Dunn, The importance of green chemistry in process research and development, *Chem. Soc. Rev.* 41 (4) (2012) 1452–1461.
- [5] P.T. Anastas, J.C. Warner, *Green Chemistry: Theory and Practice*, Oxford University Press, New York, 1998.
- [6] P.T. Anastas, M.M. Kirchhoff, T.C. Williamson, Catalysis as a foundational pillar of green chemistry, *Appl. Catal. A Gen.* 221 (1) (2001) 3–13.
- [7] I. Chorkendorff, J.W. Niemantsverdriet (Eds.), *Introduction to catalysis*, In: *Concepts of Modern Catalysis and Kinetics*, Wiley-VCH Verlag GmbH & Co. KGaA, Weinheim, FRG, 2003. <https://doi.org/10.1002/3527602658.ch1>.
- [8] E. Roduner, Understanding catalysis, *Chem. Soc. Rev.* 43 (24) (2014) 8226–8239.
- [9] I. Fecheté, Y. Wang, J.C. Védrine, The past, present and future of heterogeneous catalysis, *Catal. Today* 189 (1) (2012) 2–27.
- [10] R. Schlögl, Heterogeneous catalysis, *Angew. Chem. Int. Ed.* 54 (11) (2015) 3465–3520.
- [11] N. Yan, C. Xiao, Y. Kou, Transition metal nanoparticle catalysis in green solvents, *Coord. Chem. Rev.* 254 (9) (2010) 1179–1218.
- [12] S. Chaturvedi, P.N. Dave, N.K. Shah, Applications of nano-catalyst in new era, *J. Saudi Chem. Soc.* 16 (3) (2012) 307–325.
- [13] P. Munnik, P.E. de Jongh, K.P. de Jong, Recent developments in the synthesis of supported catalysts, *Chem. Rev.* 115 (14) (2015) 6687–6718.
- [14] H. Cong, J.A. Porco, Chemical synthesis of complex molecules using nanoparticle catalysis, *ACS Catal.* 2 (1) (2012) 65–70.
- [15] N. Sharma, et al., Preparation and catalytic applications of nanomaterials: a review, *RSC Adv.* 5 (66) (2015) 53381–53403.
- [16] R.S. Varma, Nano-catalysts with magnetic core: sustainable options for greener synthesis, *Sustainable Chem. Processes* 2 (1) (2014) 11.
- [17] F. Zaera, Nanostructured materials for applications in heterogeneous catalysis, *Chem. Soc. Rev.* 42 (7) (2013) 2746–2762.
- [18] L.L. Chng, N. Erathodiyil, J.Y. Ying, Nanostructured catalysts for organic transformations, *Acc. Chem. Res.* 46 (8) (2013) 1825–1837.
- [19] J. Fan, Y. Gao, Nanoparticle-supported catalysts and catalytic reactions—a mini-review, *J. Exp. Nanosci.* 1 (4) (2006) 457–475.
- [20] G. Centi, S. Perathoner, Creating and mastering nano-objects to design advanced catalytic materials, *Coord. Chem. Rev.* 255 (13) (2011) 1480–1498.
- [21] A. Schätz, O. Reiser, W.J. Stark, Nanoparticles as semi-heterogeneous catalyst supports, *Chem. Eur. J.* 16 (30) (2010) 8950–8967.
- [22] S. Shylesh, V. Schünemann, W.R. Thiel, Magnetically separable nanocatalysts: bridges between homogeneous and heterogeneous catalysis, *Angew. Chem. Int. Ed.* 49 (20) (2010) 3428–3459.
- [23] D. Astruc, F. Lu, J.R. Aranzas, Nanoparticles as recyclable catalysts: the frontier between homogeneous and heterogeneous catalysis, *Angew. Chem. Int. Ed.* 44 (48) (2005) 7852–7872.
- [24] C.W. Lim, I.S. Lee, Magnetically recyclable nanocatalyst systems for the organic reactions, *Nano Today* 5 (5) (2010) 412–434.
- [25] J. Govan, et al., Recent advances in the application of magnetic nanoparticles as a support for homogeneous catalysts, *Nanomaterials* 4 (2) (2014) 222.
- [26] T. Cheng, et al., Magnetically recoverable nanoparticles as efficient catalysts for organic transformations in aqueous medium, *Green Chem.* 16 (7) (2014) 3401–3427.

- [27] B. Karimi, F. Mansouri, H.M. Mirzaei, Recent applications of magnetically recoverable nanocatalysts in C-C and C-X coupling reactions, *ChemCatChem* 7 (12) (2015) 1736–1789.
- [28] M.B. Gawande, R. Luque, R. Zboril, The rise of magnetically recyclable nanocatalysts, *ChemCatChem* 6 (12) (2014) 3312–3313.
- [29] D. Wang, D. Astruc, Fast-growing field of magnetically recyclable nanocatalysts, *Chem. Rev.* 114 (14) (2014) 6949–6985.
- [30] M.B. Gawande, P.S. Branco, R.S. Varma, Nano-magnetite (Fe_3O_4) as a support for recyclable catalysts in the development of sustainable methodologies, *Chem. Soc. Rev.* 42 (8) (2013) 3371–3393.
- [31] R.B.N. Baig, R.S. Varma, Magnetically retrievable catalysts for organic synthesis, *Chem. Commun.* 49 (8) (2013) 752–770.
- [32] D. Zhang, et al., Magnetically recyclable nanocatalysts (MRNCs): a versatile integration of high catalytic activity and facile recovery, *Nanoscale* 4 (20) (2012) 6244–6255.
- [33] V. Polshettiwar, et al., Magnetically recoverable nanocatalysts, *Chem. Rev.* 111 (5) (2011) 3036–3075.
- [34] L.M. Rossi, et al., Magnetic nanomaterials in catalysis: advanced catalysts for magnetic separation and beyond, *Green Chem.* 16 (6) (2014) 2906–2933.
- [35] M. Colombo, et al., Biological applications of magnetic nanoparticles, *Chem. Soc. Rev.* 41 (11) (2012) 4306–4334.
- [36] J. Gao, H. Gu, B. Xu, Multifunctional magnetic nanoparticles: design, synthesis, and biomedical applications, *Acc. Chem. Res.* 42 (8) (2009) 1097–1107.
- [37] A.-H. Lu, E.L. Salabas, F. Schüth, Magnetic nanoparticles: synthesis, protection, functionalization, and application, *Angew. Chem. Int. Ed.* 46 (8) (2007) 1222–1244.
- [38] A. Hervault, N.T.K. Thanh, Magnetic nanoparticle-based therapeutic agents for thermo-chemotherapy treatment of cancer, *Nanoscale* 6 (20) (2014) 11553–11573.
- [39] J.H. Jung, J.H. Lee, S. Shinkai, Functionalized magnetic nanoparticles as chemosensors and adsorbents for toxic metal ions in environmental and biological fields, *Chem. Soc. Rev.* 40 (9) (2011) 4464–4474.
- [40] S.-Z. Guo, et al., Nanofluids containing $\gamma\text{-Fe}_2\text{O}_3$ nanoparticles and their heat transfer enhancements, *Nanoscale Res. Lett.* 5 (7) (2010) 1222.
- [41] Y. Pan, et al., Magnetic nanoparticles for the manipulation of proteins and cells, *Chem. Soc. Rev.* 41 (7) (2012) 2912–2942.
- [42] L.H. Reddy, et al., Magnetic nanoparticles: design and characterization, toxicity and biocompatibility, pharmaceutical and biomedical applications, *Chem. Rev.* 112 (11) (2012) 5818–5878.
- [43] W. Wu, C.Z. Jiang, V.A.L. Roy, Designed synthesis and surface engineering strategies of magnetic iron oxide nanoparticles for biomedical applications, *Nanoscale* 8 (47) (2016) 19421–19474.
- [44] C. Yang, J. Wu, Y. Hou, Fe_3O_4 nanostructures: synthesis, growth mechanism, properties and applications, *Chem. Commun.* 47 (18) (2011) 5130–5141.
- [45] S. Cheong, et al., Simple synthesis and functionalization of iron nanoparticles for magnetic resonance imaging, *Angew. Chem. Int. Ed.* 50 (18) (2011) 4206–4209.
- [46] K. Gharbi, et al., Alkyl phosphonic acid-based ligands as tools for converting hydrophobic iron nanoparticles into water soluble iron-iron oxide core-shell nanoparticles, *New J. Chem.* 41 (20) (2017) 11898–11905.
- [47] A. Kolhatkar, et al., Tuning the magnetic properties of nanoparticles, *Int. J. Mol. Sci.* 14 (8) (2013) 15977.
- [48] S. Laurent, et al., Magnetic iron oxide nanoparticles: synthesis, stabilization, vectorization, physicochemical characterizations, and biological applications, *Chem. Rev.* 108 (6) (2008) 2064–2110.
- [49] W. Wu, et al., Recent progress on magnetic iron oxide nanoparticles: synthesis, surface functional strategies and biomedical applications, *Sci. Technol. Adv. Mater.* 16 (2) (2015) 023501.
- [50] L. Maurizi, et al., One step continuous hydrothermal synthesis of very fine stabilized superparamagnetic nanoparticles of magnetite, *Chem. Commun.* 47 (42) (2011) 11706–11708.
- [51] N. Hassan, V. Cabuil, A. Abou-Hassan, Continuous multistep microfluidic assisted assembly of fluorescent, plasmonic, and magnetic nanostructures, *Angew. Chem. Int. Ed.* 52 (7) (2013) 1994–1997.
- [52] A.J. Gröhn, et al., Scale-up of nanoparticle synthesis by flame spray pyrolysis: the high-temperature particle residence time, *Ind. Eng. Chem. Res.* 53 (26) (2014) 10734–10742.

- [53] M. Baghbanzadeh, et al., Microwave-assisted synthesis of colloidal inorganic nanocrystals, *Angew. Chem. Int. Ed.* 50 (48) (2011) 11312–11359.
- [54] J.H. Bang, K.S. Suslick, Applications of ultrasound to the synthesis of nanostructured materials, *Adv. Mater.* 22 (10) (2010) 1039–1059.
- [55] J. Liu, et al., Magnetically separable Pd catalyst for carbonylative sonogashira coupling reactions for the synthesis of α,β -alkynyl ketones, *Org. Lett.* 10 (18) (2008) 3933–3936.
- [56] S.R. Borhade, S.B. Waghmode, Studies on Pd/NiFe₂O₄ catalyzed ligand-free Suzuki reaction in aqueous phase: synthesis of biaryls, terphenyls and polyaryls, *Beilstein J. Org. Chem.* 7 (2011) 310–319.
- [57] U. Laska, et al., Easy-separable magnetic nanoparticle-supported Pd catalysts: kinetics, stability and catalyst re-use, *J. Catal.* 268 (2) (2009) 318–328.
- [58] R. Cano, D.J. Ramón, M. Yus, Impregnated palladium on magnetite, a new catalyst for the ligand-free cross-coupling Suzuki–Miyaura reaction, *Tetrahedron* 67 (30) (2011) 5432–5436.
- [59] J.M. Perez, et al., Palladium(ii) oxide impregnated on magnetite as a catalyst for the synthesis of 4-arylcoumarins via a Heck-arylation/cyclization process, *RSC Adv.* 6 (43) (2016) 36932–36941.
- [60] A.S. Singh, U.B. Patil, J.M. Nagarkar, Palladium supported on zinc ferrite: a highly active, magnetically separable catalyst for ligand free Suzuki and Heck coupling, *Catal. Commun.* 35 (2013) 11–16.
- [61] S. Zhou, M. Johnson, J.G.C. Veinot, Iron/iron oxide nanoparticles: a versatile support for catalytic metals and their application in Suzuki–Miyaura cross-coupling reactions, *Chem. Commun.* 46 (14) (2010) 2411–2413.
- [62] Z. Gao, et al., Pd-loaded superparamagnetic mesoporous NiFe₂O₄ as a highly active and magnetically separable catalyst for Suzuki and Heck reactions, *J. Mol. Catal. A Chem.* 336 (1) (2011) 51–57.
- [63] M. Kotani, et al., Ruthenium hydroxide on magnetite as a magnetically separable heterogeneous catalyst for liquid-phase oxidation and reduction, *Green Chem.* 8 (8) (2006) 735–741.
- [64] R. Cano, D.J. Ramón, M. Yus, Impregnated ruthenium on magnetite as a recyclable catalyst for the N-alkylation of amines, sulfonamides, sulfinamides, and nitroarenes using alcohols as electrophiles by a hydrogen autotransfer process, *J. Org. Chem.* 76 (14) (2011) 5547–5557.
- [65] U. Laska, et al., Rhodium containing magnetic nanoparticles: effective catalysts for hydrogenation and the 1,4-addition of boronic acids, *Catal. Lett.* 122 (1) (2008) 68–75.
- [66] T. Akita, Y. Maeda, M. Kohyama, Low-temperature CO oxidation properties and TEM/STEM observation of Au/ γ -Fe₂O₃ catalysts, *J. Catal.* 324 (2015) 127–132.
- [67] L.A. Aronica, et al., Solvated gold atoms in the preparation of efficient supported catalysts: correlation between morphological features and catalytic activity in the hydrosilylation of 1-hexyne, *J. Catal.* 266 (2) (2009) 250–257.
- [68] S.T. Daniells, et al., The mechanism of low-temperature CO oxidation with Au/Fe₂O₃ catalysts: a combined Mössbauer, FT-IR, and TAP reactor study, *J. Catal.* 230 (1) (2005) 52–65.
- [69] M. Khoudiakov, M.C. Gupta, S. Deevi, Au/Fe₂O₃ nanocatalysts for CO oxidation: a comparative study of deposition–precipitation and coprecipitation techniques, *Appl. Catal. A Gen.* 291 (1) (2005) 151–161.
- [70] J. Mizera, et al., Au/FeOx catalysts of different degree of iron oxide reduction, *Catal. Today* 187 (1) (2012) 20–29.
- [71] S. Najafshirtari, et al., The effect of Au domain size on the CO oxidation catalytic activity of colloidal Au–FeOx dumbbell-like heterodimers, *J. Catal.* 338 (2016) 115–123.
- [72] M.M. Schubert, et al., CO oxidation over supported gold catalysts—“inert” and “active” support materials and their role for the oxygen supply during reaction, *J. Catal.* 197 (1) (2001) 113–122.
- [73] A.M. Visco, et al., Catalytic oxidation of carbon monoxide over Au/Fe₂O₃ preparations, *React. Kinet. Catal. Lett.* 61 (2) (1997) 219–226.
- [74] M.B. Gawande, et al., A recyclable ferrite–co magnetic nanocatalyst for the oxidation of alcohols to carbonyl compounds, *ChemPlusChem* 77 (10) (2012) 865–871.
- [75] M.B. Gawande, et al., Regio- and chemoselective reduction of nitroarenes and carbonyl compounds over recyclable magnetic Ferrite–Nickel nanoparticles (Fe₃O₄–Ni) by using glycerol as a hydrogen source, *Chem. Eur. J.* 18 (40) (2012) 12628–12632.

- [76] R. Cano, D.J. Ramón, M. Yus, Impregnated copper on magnetite as recyclable catalyst for the addition of alkoxy diboron reagents to C–C double bonds, *J. Org. Chem.* 75 (10) (2010) 3458–3460.
- [77] M.J. Aliaga, D.J. Ramon, M. Yus, Impregnated copper on magnetite: an efficient and green catalyst for the multicomponent preparation of propargylamines under solvent free conditions, *Org. Biomol. Chem.* 8 (1) (2010) 43–46.
- [78] R. Cano, M. Yus, D.J. Ramón, Impregnated copper or palladium–copper on magnetite as catalysts for the domino and stepwise Sonogashira-cyclization processes: a straightforward synthesis of benzo[b]furans and indoles, *Tetrahedron* 68 (5) (2012) 1393–1400.
- [79] J.F. Lambert, M. Che, The molecular approach to supported catalysts synthesis: state of the art and future challenges, *J. Mol. Catal. A Chem.* 162 (1) (2000) 5–18.
- [80] J.-I. Lai, et al., Mixed iron-manganese oxide nanoparticles, *Prepr. Pap. Am. Chem. Soc., Div. Fuel Chem.* 48 (2) (2003) 729–730.
- [81] P.B. Bhat, B.R. Bhat, Magnetically retrievable nickel hydroxide functionalised AFe_2O_4 ($\text{A} = \text{Mn, Ni}$) spinel nanocatalyst for alcohol oxidation, *Appl. Nanosci.* 6 (3) (2016) 425–435.
- [82] Q. Li, et al., Tailoring a magnetically separable NiFe_2O_4 nanoparticle catalyst for Knoevenagel condensation, *Tetrahedron* 72 (50) (2016) 8358–8363.
- [83] F.M. Moghaddam, G. Tavakoli, A. Aliabadi, Application of nickel ferrite and cobalt ferrite magnetic nanoparticles in C–O bond formation: a comparative study between their catalytic activities, *RSC Adv.* 5 (73) (2015) 59142–59153.
- [84] G. Satish, et al., Direct C–H arylation of benzothiazoles by magnetically separable nano copper ferrite, a recyclable catalyst, *Tetrahedron Lett.* 56 (34) (2015) 4950–4953.
- [85] B.S.P. Anil Kumar, et al., Magnetically separable CuFe_2O_4 nano particles catalyzed multicomponent synthesis of 1,4-disubstituted 1,2,3-triazoles in tap water using ‘click chemistry’, *Tetrahedron Lett.* 53 (34) (2012) 4595–4599.
- [86] A.S. Kumar, et al., Magnetically recoverable CuFe_2O_4 nanoparticles: catalyzed synthesis of aryl azides and 1,4-diaryl-1,2,3-triazoles from boronic acids in water, *Eur. J. Org. Chem.* 2013 (21) (2013) 4674–4680.
- [87] Y. Jang, et al., Simple synthesis of $\text{Pd-Fe}_3\text{O}_4$ heterodimer nanocrystals and their application as a magnetically recyclable catalyst for Suzuki cross-coupling reactions, *Phys. Chem. Chem. Phys.* 13 (7) (2011) 2512–2516.
- [88] J. Chung, et al., Heck and Sonogashira cross-coupling reactions using recyclable $\text{Pd-Fe}_3\text{O}_4$ heterodimeric nanocrystal catalysts, *Tetrahedron Lett.* 54 (38) (2013) 5192–5196.
- [89] H. Woo, et al., A new hybrid nanocatalyst based on Cu-doped $\text{Pd-Fe}_3\text{O}_4$ for tandem synthesis of 2-phenylbenzofurans, *J. Mater. Chem. A* 3 (42) (2015) 20992–20998.
- [90] S. Handa, et al., Sustainable Fe–ppm Pd nanoparticle catalysis of Suzuki–Miyaura cross-couplings in water, *Science* 349 (6252) (2015) 1087–1091.
- [91] J. Feng, et al., Safe and selective nitro group reductions catalyzed by sustainable and recyclable Fe/ppm Pd nanoparticles in water at room temperature, *Angew. Chem. Int. Ed.* 55 (31) (2016) 8979–8983.
- [92] A. Adenot, et al., Fe/ppm Cu nanoparticles as a recyclable catalyst for click reactions in water at room temperature, *Green Chem.* 19 (11) (2017) 2506–2509.
- [93] P. Majewski, B. Thierry, Functionalized magnetite nanoparticles—synthesis, properties, and bio-applications, *Crit. Rev. Solid State Mater. Sci.* 32 (3–4) (2007) 203–215.
- [94] F. Gambinossi, S.E. Mylon, J.K. Ferri, Aggregation kinetics and colloidal stability of functionalized nanoparticles, *Adv. Colloid Interf. Sci.* 222 (Supplement C) (2015) 332–349.
- [95] W.R. Algar, et al., The controlled display of biomolecules on nanoparticles: a challenge suited to bioorthogonal chemistry, *Bioconjug. Chem.* 22 (5) (2011) 825–858.
- [96] S. Bagheri, N.M. Julkapli, Modified iron oxide nanomaterials: functionalization and application, *J. Magn. Mater.* 416 (Supplement C) (2016) 117–133.
- [97] V. Biju, Chemical modifications and bioconjugate reactions of nanomaterials for sensing, imaging, drug delivery and therapy, *Chem. Soc. Rev.* 43 (3) (2014) 744–764.
- [98] T. Perrier, P. Saulnier, J.-P. Benoit, Methods for the functionalisation of nanoparticles: new insights and perspectives, *Chem. Eur. J.* 16 (38) (2010) 11516–11529.

- [99] S.P. Pujari, et al., Covalent surface modification of oxide surfaces, *Angew. Chem. Int. Ed.* 53 (25) (2014) 6322–6356.
- [100] R.A. Sperling, W.J. Parak, Surface modification, functionalization and bioconjugation of colloidal inorganic nanoparticles, *Philos. Trans. R. Soc. A Math. Phys. Eng. Sci.* 368 (1915) (2010) 1333–1383.
- [101] K. Turcheniuk, et al., Recent advances in surface chemistry strategies for the fabrication of functional iron oxide based magnetic nanoparticles, *Nanoscale* 5 (22) (2013) 10729–10752.
- [102] Y. Piao, et al., Designed fabrication of silica-based nanostructured particle systems for nanomedicine applications, *Adv. Funct. Mater.* 18 (23) (2008) 3745–3758.
- [103] A. Khazaei, M. Khazaei, M. Nasrollahzadeh, Nano-Fe₃O₄@SiO₂ supported Pd(0) as a magnetically recoverable nanocatalyst for Suzuki coupling reaction in the presence of waste eggshell as low-cost natural base, *Tetrahedron* 73 (38) (2017) 5624–5633.
- [104] Z. Arabpoor, H.R. Shaterian, L-Leucine supported on superparamagnetic silica-encapsulated γ -Fe₂O₃ nanoparticles: design, characterization, and application as a green catalyst for highly efficient synthesis of thiazoloquinolines, *RSC Adv.* 6 (50) (2016) 44459–44468.
- [105] F. Dehghani Firuzabadi, Z. Asadi, F. Panahi, Immobilized NNN Pd-complex on magnetic nanoparticles: efficient and reusable catalyst for Heck and Sonogashira coupling reactions, *RSC Adv.* 6 (103) (2016) 101061–101070.
- [106] R.R.G. Guerra, et al., Factorial design evaluation of the Suzuki cross-coupling reaction using a magnetically recoverable palladium catalyst, *Tetrahedron Lett.* 58 (10) (2017) 903–908.
- [107] X. Le, et al., Palladium nanoparticles immobilized on core-shell magnetic fibers as a highly efficient and recyclable heterogeneous catalyst for the reduction of 4-nitrophenol and Suzuki coupling reactions, *J. Mater. Chem. A* 2 (46) (2014) 19696–19706.
- [108] M. Rajabzadeh, et al., Generation of Cu nanoparticles on novel designed Fe₃O₄@SiO₂/EP.EN.EG as reusable nanocatalyst for the reduction of nitro compounds, *RSC Adv.* 6 (23) (2016) 19331–19340.
- [109] H. Eshghi, et al., Nanomagnetic organic–inorganic hybrid (Fe@Si-Gu-Prs): a novel magnetically green catalyst for the synthesis of tetrahydropyridine derivatives at room temperature under solvent-free conditions, *Tetrahedron* 71 (3) (2015) 436–444.
- [110] S. Mukherjee, A. Kundu, A. Pramanik, A new and efficient synthesis of pyrazole-fused isocoumarins on the solid surface of magnetically separable Fe₃O₄@SiO₂-SO₃H nanoparticles, *Tetrahedron Lett.* 57 (19) (2016) 2103–2108.
- [111] Y. Wang, J.-K. Lee, Recyclable nano-size Pd catalyst generated in the multilayer polyelectrolyte films on the magnetic nanoparticle core, *J. Mol. Catal. A Chem.* 263 (1) (2007) 163–168.
- [112] F. Zou, et al., Magnetically recyclable catalytic activity of spiky magneto-plasmonic nanoparticles, *RSC Adv.* 5 (70) (2015) 56653–56657.
- [113] A.J. Amali, R.K. Rana, Stabilisation of Pd(0) on surface functionalised Fe₃O₄ nanoparticles: magnetically recoverable and stable recyclable catalyst for hydrogenation and Suzuki-Miyaura reactions, *Green Chem.* 11 (11) (2009) 1781–1786.
- [114] S. Xuan, et al., Preparation, characterization, and catalytic activity of core/shell Fe₃O₄@polyaniline@Au nanocomposites, *Langmuir* 25 (19) (2009) 11835–11843.
- [115] W. Guo, et al., Controllable synthesis of core-satellite Fe₃O₄@polypyrrole/Pd nanoarchitectures with aggregation-free Pd nanocrystals confined into polypyrrole satellites as magnetically recoverable and highly efficient heterogeneous catalysts, *RSC Adv.* 5 (124) (2015) 102210–102218.
- [116] H. Zhang, et al., Fe₃O₄/polypyrrole/Au nanocomposites with core/shell/shell structure: synthesis, characterization, and their electrochemical properties, *Langmuir* 24 (23) (2008) 13748–13752.
- [117] J. Manna, S. Akbayrak, S. Ozkar, Palladium(0) nanoparticles supported on polydopamine coated Fe₃O₄ as magnetically isolable, highly active and reusable catalysts for hydrolytic dehydrogenation of ammonia borane, *RSC Adv.* 6 (104) (2016) 102035–102042.
- [118] T. Parandhaman, et al., Metal nanoparticle loaded magnetic-chitosan microsphere: water dispersible and easily separable hybrid metal nano-biomaterial for catalytic applications, *ACS Sustain. Chem. Eng.* 5 (1) (2017) 489–501.

- [119] M. Gholinejad, et al., Green synthesis of carbon quantum dots from vanillin for modification of magnetite nanoparticles and formation of palladium nanoparticles: efficient catalyst for Suzuki reaction, *Tetrahedron* 73 (38) (2017) 5585–5592.
- [120] A. Pourjavadi, et al., Magnetic starch nanocomposite as a green heterogeneous support for immobilization of large amounts of copper ions: heterogeneous catalyst for click synthesis of 1,2,3-triazoles, *RSC Adv.* 6 (23) (2016) 19128–19135.
- [121] W. Wang, et al., Recyclable nanobiocatalyst for enantioselective sulfoxidation: facile fabrication and high performance of chloroperoxidase-coated magnetic nanoparticles with iron oxide core and polymer shell, *J. Am. Chem. Soc.* 131 (36) (2009) 12892–12893.
- [122] Q.M. Kainz, O. Reiser, Polymer- and dendrimer-coated magnetic nanoparticles as versatile supports for catalysts, scavengers, and reagents, *Acc. Chem. Res.* 47 (2) (2014) 667–677.
- [123] A. Schätz, et al., Immobilization on a nanomagnetic Co/C surface using ROM polymerization: generation of a hybrid material as support for a recyclable palladium catalyst, *Adv. Funct. Mater.* 20 (24) (2010) 4323–4328.
- [124] A. Pourjavadi, et al., Magnetic nanoparticles coated by acidic functionalized poly(amidoamine) dendrimer: effective acidic organocatalyst, *Catal. Commun.* 28 (Supplement C) (2012) 86–89.
- [125] M. Zakeri, et al., Synthesis and characterization of a host (a new thiol based dendritic polymer)-guest (Pd nanoparticles) nanocomposite material: an efficient and reusable catalyst for C-C coupling reactions, *RSC Adv.* 6 (106) (2016) 104608–104619.
- [126] D. Rosario-Amorin, et al., Metallo-dendritic grafted core-shell γ -Fe₂O₃ nanoparticles used as recoverable catalysts in Suzuki C-C coupling reactions, *Chem. Eur. J.* 18 (11) (2012) 3305–3315.
- [127] D. Rosario-Amorin, et al., Dendron-functionalized core-shell superparamagnetic nanoparticles: magnetically recoverable and reusable catalysts for Suzuki C-C cross-coupling reactions, *Chem. Eur. J.* 15 (46) (2009) 12636–12643.
- [128] S. Mallakpour, M. Madani, A review of current coupling agents for modification of metal oxide nanoparticles, *Prog. Org. Coat.* 86 (Supplement C) (2015) 194–207.
- [129] M.-A. Neouze, U. Schubert, Surface modification and functionalization of metal and metal oxide nanoparticles by organic ligands, *Monatsh. Chem.* 139 (3) (2008) 183–195.
- [130] M. Krogsgaard, V. Nue, H. Birkedal, Mussel-inspired materials: self-healing through coordination chemistry, *Chem. Eur. J.* 22 (3) (2016) 844–857.
- [131] E. Nehlig, et al., Immobilized Pd on magnetic nanoparticles bearing proline as a highly efficient and retrievable Suzuki-Miyaura catalyst in aqueous media, *Dalton Trans.* 44 (2) (2015) 501–505.
- [132] A. Saha, J. Leazer, R.S. Varma, *O*-Allylation of phenols with allylic acetates in aqueous media using a magnetically separable catalytic system, *Green Chem.* 14 (1) (2012) 67–71.
- [133] S. Mondini, et al., Magnetic nanoparticles conjugated to chiral imidazolidinone as recoverable catalyst, *J. Nanopart. Res.* 15 (11) (2013) 2025.
- [134] E. Nehlig, L. Motte, E. Guenin, Magnetic nano-organocatalysts: impact of surface functionalization on catalytic activity, *RSC Adv.* 5 (127) (2015) 104688–104694.
- [135] C. Queffelec, et al., Surface modification using phosphonic acids and esters, *Chem. Rev.* 112 (7) (2012) 3777–3807.
- [136] A. Cattani-Scholz, Functional organophosphonate interfaces for nanotechnology: a review, *ACS Appl. Mater. Interfaces* 9 (31) (2017) 25643–25655.
- [137] B. Basly, et al., Dendronized iron oxide nanoparticles as contrast agents for MRI, *Chem. Commun.* 46 (6) (2010) 985–987.
- [138] R. Torres Martin de Rosales, et al., 99mTc-bisphosphonate-iron oxide nanoparticle conjugates for dual-modality biomedical imaging, *Bioconjug. Chem.* 22 (3) (2011) 455–465.
- [139] J. Bolley, et al., Carbodiimide versus click chemistry for nanoparticle surface functionalization: a comparative study for the elaboration of multimodal superparamagnetic nanoparticles targeting $\alpha\beta$ 3 integrins, *Langmuir* 29 (47) (2013) 14639–14647.
- [140] A.K. Tucker-Schwartz, R.L. Garrell, Simple preparation and application of TEMPO-coated Fe₃O₄ superparamagnetic nanoparticles for selective oxidation of alcohols, *Chem. Eur. J.* 16 (42) (2010) 12718–12726.

- [141] E. Nehlig, L. Motte, E. Guénin, Nano-organocatalysts synthesis: Boc vs Fmoc protection, *Catal. Today* 208 (2013) 90–96.
- [142] J. Wan, et al., Facile one-pot fabrication of magnetic nanoparticles (MNPs)-supported organocatalysts using phosphonate as an anchor point through direct co-precipitation method, *RSC Adv.* 4 (72) (2014) 38323–38333.
- [143] O. Gleeson, et al., The immobilisation of chiral organocatalysts on magnetic nanoparticles: the support particle cannot always be considered inert, *Org. Biomol. Chem.* 9 (22) (2011) 7929–7940.
- [144] P.J. Deuss, et al., Bioinspired catalyst design and artificial metalloenzymes, *Chem. Eur. J.* 17 (17) (2011) 4680–4698.
- [145] E. Kuah, et al., Enzyme mimics: advances and applications, *Chem. Eur. J.* 22 (25) (2016) 8404–8430.
- [146] U.T. Bornscheuer, Biocatalysis: successfully crossing boundaries, *Angew. Chem. Int. Ed.* 55 (14) (2016) 4372–4373.
- [147] S.A. Ansari, Q. Husain, Potential applications of enzymes immobilized on/in nano materials: a review, *Biotechnol. Adv.* 30 (3) (2012) 512–523.
- [148] S. Ding, et al., Increasing the activity of immobilized enzymes with nanoparticle conjugation, *Curr. Opin. Biotechnol.* 34 (Supplement C) (2015) 242–250.
- [149] C.G.C.M. Netto, H.E. Toma, L.H. Andrade, Superparamagnetic nanoparticles as versatile carriers and supporting materials for enzymes, *J. Mol. Catal. B Enzym.* 85 (Supplement C) (2013) 71–92.
- [150] C.C.S. Fortes, et al., Optimization of enzyme immobilization on functionalized magnetic nanoparticles for laccase biocatalytic reactions, *Chem. Eng. Process. Process Intensif.* 117 (Supplement C) (2017) 1–8.
- [151] S. Rouhani, A. Rostami, A. Salimi, Preparation and characterization of laccases immobilized on magnetic nanoparticles and their application as a recyclable nanobiocatalyst for the aerobic oxidation of alcohols in the presence of TEMPO, *RSC Adv.* 6 (32) (2016) 26709–26718.
- [152] A.K. Johnson, et al., Novel method for immobilization of enzymes to magnetic nanoparticles, *J. Nanopart. Res.* 10 (6) (2008) 1009–1025.
- [153] K. Pospiskova, I. Safarik, Low-cost, easy-to-prepare magnetic chitosan microparticles for enzymes immobilization, *Carbohydr. Polym.* 96 (2) (2013) 545–548.
- [154] M. Namdeo, S.K. Bajpai, Immobilization of α -amylase onto cellulose-coated magnetite (CCM) nanoparticles and preliminary starch degradation study, *J. Mol. Catal. B Enzym.* 59 (1) (2009) 134–139.
- [155] A. Landarani-Isfahani, et al., Xylanase immobilized on novel multifunctional hyperbranched polyglycerol-grafted magnetic nanoparticles: an efficient and robust biocatalyst, *Langmuir* 31 (33) (2015) 9219–9227.
- [156] G.K. Kouassi, J. Irudayaraj, G. McCarty, Examination of cholesterol oxidase attachment to magnetic nanoparticles, *J. Nanobiotechnol.* 3 (1) (2005) 1.
- [157] Y.K. Sim, et al., Facile preparation of recyclable biocatalyst-decorated magnetic nanobeads in aqueous media, *Tetrahedron Lett.* 52 (9) (2011) 1041–1043.
- [158] W. Wang, D.I.C. Wang, Z. Li, Facile fabrication of recyclable and active nanobiocatalyst: purification and immobilization of enzyme in one pot with Ni-NTA functionalized magnetic nanoparticle, *Chem. Commun.* 47 (28) (2011) 8115–8117.
- [159] S.Y. Lee, et al., Enzyme-magnetic nanoparticle conjugates as a rigid biocatalyst for the elimination of toxic aromatic hydrocarbons, *Chem. Commun.* 47 (36) (2011) 9989–9991.
- [160] Ó.A. Loaiza, et al., Disposable magnetic DNA sensors for the determination at the attomolar level of a specific enterobacteriaceae family gene, *Anal. Chem.* 80 (21) (2008) 8239–8245.
- [161] E.P. Cipolatti, et al., Nanomaterials for biocatalyst immobilization—state of the art and future trends, *RSC Adv.* 6 (106) (2016) 104675–104692.
- [162] D. Zhang, et al., Laccase immobilized on magnetic nanoparticles by dopamine polymerization for 4-chlorophenol removal, *Green Energy Environ.* 2 (4) (2017) 393–400.
- [163] B. List, R.A. Lerner, C.F. Barbas, Proline-catalyzed direct asymmetric aldol reactions, *J. Am. Chem. Soc.* 122 (10) (2000) 2395–2396.
- [164] K.A. Ahrendt, C.J. Borths, D.W.C. MacMillan, New strategies for organic catalysis: the first highly enantioselective organocatalytic Diels–Alder reaction, *J. Am. Chem. Soc.* 122 (17) (2000) 4243–4244.

- [165] P.I. Dalko, L. Moisan, In the golden age of organocatalysis, *Angew. Chem. Int. Ed.* 43 (39) (2004) 5138–5175.
- [166] L. Albrecht, H. Jiang, K.A. Jørgensen, A simple recipe for sophisticated cocktails: organocatalytic one-pot reactions—concept, nomenclature, and future perspectives, *Angew. Chem. Int. Ed.* 50 (37) (2011) 8492–8509.
- [167] S. Bertelsen, K.A. Jørgensen, Organocatalysis—after the gold rush, *Chem. Soc. Rev.* 38 (8) (2009) 2178–2189.
- [168] J. Aleman, S. Cabrera, Applications of asymmetric organocatalysis in medicinal chemistry, *Chem. Soc. Rev.* 42 (2) (2013) 774–793.
- [169] R. Mrowczynski, A. Nan, J. Liebscher, Magnetic nanoparticle-supported organocatalysts—an efficient way of recycling and reuse, *RSC Adv.* 4 (12) (2014) 5927–5952.
- [170] V. Angamuthu, D.-F. Tai, Asymmetric reactions of chiral organo-magnetic nanoparticles, *Appl. Catal. A Gen.* 506 (Supplement C) (2015) 254–260.
- [171] C. O' Dalaigh, et al., A magnetic-nanoparticle-supported 4-N,N-dialkylaminopyridine catalyst: excellent reactivity combined with facile catalyst recovery and recyclability, *Angew. Chem. Int. Ed.* 46 (23) (2007) 4329–4332.
- [172] H.-J. Xu, et al., Magnetic nano-Fe₃O₄-supported 1-Benzyl-1,4-dihydropyridinamide (BNAH): synthesis and application in the catalytic reduction of \hat{I}^{\pm} , $\hat{I}^{\pm 2}$ -epoxy ketones, *Org. Lett.* 14 (5) (2012) 1210–1213.
- [173] A. Rostami, B. Atashkar, D. Moradi, Synthesis, characterization and catalytic properties of magnetic nanoparticle supported guanidine in base catalyzed synthesis of \hat{I}^{\pm} -hydroxyphosphonates and \hat{I}^{\pm} -acetoxyposphonates, *Appl. Catal. A Gen.* 467 (0) (2013) 7–16.
- [174] P. Rattanaburi, B. Khumraksa, M. Pattarawarapan, Synthesis and applications of Fe₃O₄-diisopropylaminoacetamide as a versatile and reusable magnetic nanoparticle supported N,N-diisopropylethylamine equivalent, *Tetrahedron Lett.* 53 (22) (2012) 2689–2693.
- [175] R. Abu-Reziq, H. Alper, Magnetically separable base catalysts: heterogeneous catalysis vs. quasi-homogeneous catalysis, *Appl. Sci.* 2 (2) (2012) 260–276.
- [176] S. Luo, et al., Magnetic nanoparticle-supported Morita–Baylis–Hillman catalysts, *Adv. Synth. Catal.* 349 (16) (2007) 2431–2434.
- [177] M.Z. Kassaee, H. Masrouri, F. Movahedi, Sulfamic acid-functionalized magnetic Fe₃O₄ nanoparticles as an efficient and reusable catalyst for one-pot synthesis of \hat{I}^{\pm} -amino nitriles in water, *Appl. Catal. A Gen.* 395 (1–2) (2011) 28–33.
- [178] Y. Jiang, et al., Asymmetric aldol addition by oligopeptide immobilized on magnetic particles through an ionic liquids spacer, *Ind. Eng. Chem. Res.* 47 (23) (2008) 9628–9635.
- [179] O. Gleeson, et al., The first magnetic nanoparticle-supported chiral DMAP analogue: highly enantioselective acylation and excellent recyclability, *Chem. Eur. J.* 15 (23) (2009) 5669–5673.
- [180] M.B. Gawande, et al., A facile synthesis of cysteine-ferrite magnetic nanoparticles for application in multicomponent reactions—a sustainable protocol, *RSC Adv.* 2 (15) (2012) 6144–6149.
- [181] H. Yang, et al., Core-shell silica magnetic microspheres supported proline as a recyclable organocatalyst for the asymmetric aldol reaction, *J. Mol. Catal. A Chem.* 363–364 (2012) 404–410.
- [182] Y. Kong, et al., l-Proline supported on ionic liquid-modified magnetic nanoparticles as a highly efficient and reusable organocatalyst for direct asymmetric aldol reaction in water, *Green Chem.* 15 (9) (2013) 2422–2433.
- [183] P. Demay-Drouhard, et al., Nanoparticles under the light: click functionalization by photochemical thiol-yne reaction, towards double click functionalization, *Chem. Eur. J.* 19 (26) (2013) 8388–8392.
- [184] M. Picquet, Organometallics as catalysts in the fine chemical industry, *Platin. Met. Rev.* 57 (4) (2013) 272–280.
- [185] T.J. Colacot, The 2010 Nobel Prize in chemistry: palladium-catalysed cross-coupling, *Platin. Met. Rev.* 55 (2) (2011) 84–90.
- [186] C.C.C. Johansson Seechurn, et al., Palladium-catalyzed cross-coupling: a historical contextual perspective to the 2010 Nobel Prize, *Angew. Chem. Int. Ed.* 51 (21) (2012) 5062–5085.
- [187] P. Fröhlich, et al., Valuable metals—recovery processes, current trends, and recycling strategies, *Angew. Chem. Int. Ed.* 56 (10) (2017) 2544–2580.

- [188] P. Taladriz-Blanco, P. Hervés, J. Pérez-Juste, Supported Pd nanoparticles for carbon–carbon coupling reactions, *Top. Catal.* 56 (13) (2013) 1154–1170.
- [189] D. Wang, D. Astruc, Magnetically recoverable ruthenium catalysts in organic synthesis, *Molecules* 19 (4) (2014) 4635.
- [190] A. Fihri, et al., Nanocatalysts for Suzuki cross-coupling reactions, *Chem. Soc. Rev.* 40 (10) (2011) 5181–5203.
- [191] D. Pla, M. Gómez, Metal and metal oxide nanoparticles: a lever for C–H functionalization, *ACS Catal.* 6 (6) (2016) 3537–3552.
- [192] S. Shylesh, L. Wang, W.R. Thiel, Palladium(II)-phosphine complexes supported on magnetic nanoparticles: filtration-free, recyclable catalysts for Suzuki–Miyaura cross-coupling reactions, *Adv. Synth. Catal.* 352 (2–3) (2010) 425–432.
- [193] P. Li, et al., Magnetic nanoparticles-supported palladium: a highly efficient and reusable catalyst for the Suzuki, Sonogashira, and Heck reactions, *Adv. Synth. Catal.* 354 (7) (2012) 1307–1318.
- [194] A. Khalafi-Nezhad, F. Panahi, Phosphine-functionalized magnetic nanoparticles (PFMN) as a magnetic recyclable phosphorus ligand: preparation of its palladium(II) complex for Heck reaction of chloroarenes, *J. Organomet. Chem.* 741–742 (2013) 7–14.
- [195] F. González de Rivera, et al., A general approach to fabricate Fe₃O₄ nanoparticles decorated with Pd, Au, and Rh: magnetically recoverable and reusable catalysts for Suzuki C–C cross-coupling reactions, hydrogenation, and sequential reactions, *Chem. Eur. J.* 19 (36) (2013) 11963–11974.
- [196] D. Astruc, Palladium catalysis using dendrimers: molecular catalysts versus nanoparticles, *Tetrahedron Asymmetry* 21 (9–10) (2010) 1041–1054.
- [197] K.-I. Fujita, H. Hattori, Suzuki–Miyaura reaction catalyzed by a dendritic phosphine–palladium complex, *Tetrahedron* 72 (11) (2016) 1485–1492.
- [198] N.J.S. Costa, et al., A single-step procedure for the preparation of palladium nanoparticles and a phosphine-functionalized support as catalyst for Suzuki cross-coupling reactions, *J. Catal.* 276 (2) (2010) 382–389.
- [199] R.B. Nasir Baig, R.S. Varma, A highly active magnetically recoverable nano ferrite–glutathione–copper (nano-FGT–Cu) catalyst for Huisgen 1,3-dipolar cycloadditions, *Green Chem.* 14 (3) (2012) 625–632.
- [200] Y. Zheng, P.D. Stevens, Y. Gao, Magnetic nanoparticles as an orthogonal support of polymer resins: applications to solid-phase Suzuki cross-coupling reactions, *J. Organomet. Chem.* 71 (2) (2006) 537–542.
- [201] P.D. Stevens, et al., Superparamagnetic nanoparticle-supported catalysis of Suzuki cross-coupling reactions, *Org. Lett.* 7 (11) (2005) 2085–2088.
- [202] F. Martínez-Olíd, et al., Magnetically recoverable catalysts based on mono- or bis-(NHC) complexes of palladium for the Suzuki–Miyaura reaction in aqueous media: two NHC–Pd linkages are better than one, *Dalton Trans.* 45 (29) (2016) 11633–11638.
- [203] T. Begum, et al., An immobilized symmetrical bis-(NHC) palladium complex as a highly efficient and recyclable Suzuki–Miyaura catalyst in aerobic aqueous media, *Dalton Trans.* 46 (2) (2017) 539–546.
- [204] Q. Zhang, et al., “Click” magnetic nanoparticle-supported palladium catalyst: a phosphine-free, highly efficient and magnetically recoverable catalyst for Suzuki–Miyaura coupling reactions, *Cat. Sci. Technol.* 3 (1) (2013) 235–243.
- [205] M. Pirhayati, H. Veisi, A. Kakanejadifard, Palladium stabilized by 3,4-dihydropyridine-functionalized magnetic Fe₃O₄ nanoparticles as a reusable and efficient heterogeneous catalyst for Suzuki reactions, *RSC Adv.* 6 (32) (2016) 27252–27259.
- [206] G. Lv, et al., Immobilization of dipyrityl complex to magnetic nanoparticle via click chemistry as a recyclable catalyst for Suzuki cross-coupling reactions, *Synlett* 2008 (09) (2008) 1418–1422.
- [207] X. Jin, et al., Magnetite nanoparticles immobilized Salen Pd (II) as a green catalyst for Suzuki reaction, *Catal. Commun.* 26 (Supplement C) (2012) 199–203.
- [208] Z. Wang, et al., A magnetically separable palladium catalyst containing a bulky N-heterocyclic carbene ligand for the Suzuki–Miyaura reaction, *Green Chem.* 17 (1) (2015) 413–420.
- [209] C. Wang, et al., An efficient parts-per-million α -Fe₂O₃ nanocluster/graphene oxide catalyst for Suzuki–Miyaura coupling reactions and 4-nitrophenol reduction in aqueous solution, *Chem. Commun.* 53 (3) (2017) 644–646.

- [210] Y. Wu, D. Wang, Y. Li, Nanocrystals from solutions: catalysts, *Chem. Soc. Rev.* 43 (7) (2014) 2112–2124.
- [211] Y. Zhu, et al., Multifunctional magnetic composite microspheres with in situ growth Au nanoparticles: a highly efficient catalyst system, *J. Phys. Chem. C* 115 (5) (2011) 1614–1619.
- [212] J. Zheng, et al., In situ loading of gold nanoparticles on Fe₃O₄@SiO₂ magnetic nanocomposites and their high catalytic activity, *Nanoscale* 5 (11) (2013) 4894–4901.
- [213] H. Zhang, X.-L. Yang, Magnetic polymer microsphere stabilized gold nanocolloids as a facilely recoverable catalyst, *Chin. J. Polym. Sci.* 29 (3) (2011) 342–351.
- [214] Y. Wu, et al., A facile approach to Fe₃O₄@Au nanoparticles with magnetic recyclable catalytic properties, *Mater. Res. Bull.* 45 (4) (2010) 513–517.
- [215] M.H. Rashid, M. Raula, T.K. Mandal, Polymer assisted synthesis of chain-like cobalt-nickel alloy nanostructures: magnetically recoverable and reusable catalysts with high activities, *J. Mater. Chem.* 21 (13) (2011) 4904.
- [216] Z. Ji, et al., Reduced graphene oxide/nickel nanocomposites: facile synthesis, magnetic and catalytic properties, *J. Mater. Chem.* 22 (8) (2012) 3471.
- [217] A. Guarnizo, et al., 4-Mercaptophenyldiphenylphosphine as linker to immobilize Pd onto the surface of magnetite nanoparticles. Excellent catalytic efficiency of the system after partial linker removal, *RSC Adv.* 5 (111) (2015) 91340–91348.
- [218] A. Guarnizo, et al., Highly water-dispersible magnetite-supported Pd nanoparticles and single atoms as excellent catalysts for Suzuki and hydrogenation reactions, *RSC Adv.* 6 (73) (2016) 68675–68684.
- [219] S. Wu, et al., Recoverable platinum nanocatalysts immobilized on magnetic spherical polyelectrolyte brushes, *Ind. Eng. Chem. Res.* 51 (15) (2012) 5608–5614.
- [220] K. Mori, et al., Catalytically active, magnetically separable, and water-soluble FePt nanoparticles modified with cyclodextrin for aqueous hydrogenation reactions, *Green Chem.* 11 (9) (2009) 1337.
- [221] B. Dong, D.L. Miller, C.Y. Li, Polymer single crystal as magnetically recoverable support for nanocatalysts, *J. Phys. Chem. Lett.* 3 (10) (2012) 1346–1350.
- [222] X. Zhang, et al., Sonochemical synthesis and characterization of magnetic separable Fe₃O₄/Ag composites and its catalytic properties, *J. Alloys Compd.* 508 (2) (2010) 400–405.
- [223] K.S. Shin, et al., Facile synthesis and catalytic application of silver-deposited magnetic nanoparticles, *Catal. Lett.* 133 (1–2) (2009) 1–7.
- [224] Y. Chi, et al., Synthesis of Fe₃O₄@SiO₂-Ag magnetic nanocomposite based on small-sized and highly dispersed silver nanoparticles for catalytic reduction of 4-nitrophenol, *J. Colloid Interface Sci.* 383 (1) (2012) 96–102.
- [225] T. Zeng, et al., A double-shelled yolk-like structure as an ideal magnetic support of tiny gold nanoparticles for nitrophenol reduction, *J. Mater. Chem. A* 1 (38) (2013) 11641.
- [226] M. Tian, et al., Efficient chemoselective hydrogenation of halogenated nitrobenzenes over an easily prepared γ -Fe₂O₃-modified mesoporous carbon catalyst, *Green Chem.* 19 (6) (2017) 1548–1554.
- [227] L.M. Rossi, et al., Superparamagnetic nanoparticle-supported palladium: a highly stable magnetically recoverable and reusable catalyst for hydrogenation reactions, *Green Chem.* 9 (4) (2007) 379.
- [228] M.J. Jacinto, et al., Recoverable rhodium nanoparticles: synthesis, characterization and catalytic performance in hydrogenation reactions, *Appl. Catal. A Gen.* 338 (1–2) (2008) 52–57.
- [229] M.J. Jacinto, et al., Preparation of recoverable Ru catalysts for liquid-phase oxidation and hydrogenation reactions, *Appl. Catal. A Gen.* 360 (2) (2009) 177–182.
- [230] M. Guerrero, et al., Taking advantage of a terpyridine ligand for the deposition of Pd nanoparticles onto a magnetic material for selective hydrogenation reactions, *J. Mater. Chem. A* 1 (4) (2013) 1441–1449.
- [231] K.H. Lee, et al., Dual Pd and CuFe₂O₄ nanoparticles encapsulated in a core/shell silica microsphere for selective hydrogenation of arylacetylenes, *Chem. Commun. (Camb.)* 48 (37) (2012) 4414–4416.
- [232] R. Hudson, et al., Iron-iron oxide core-shell nanoparticles are active and magnetically recyclable olefin and alkyne hydrogenation catalysts in protic and aqueous media, *Chem. Commun. (Camb.)* 48 (27) (2012) 3360–3362.
- [233] D.L. Huber, Synthesis, properties, and applications of iron nanoparticles, *Small* 1 (5) (2005) 482–501.

- [234] Y. Sun, et al., Magnetically recoverable SiO₂-coated Fe₃O₄ nanoparticles: a new platform for asymmetric transfer hydrogenation of aromatic ketones in aqueous medium, *Chem. Commun. (Camb.)* 47 (9) (2011) 2583–2585.
- [235] G. Liu, et al., Magnetically recoverable nanoparticles: highly efficient catalysts for asymmetric transfer hydrogenation of aromatic ketones in aqueous medium, *Adv. Synth. Catal.* 353 (8) (2011) 1317–1324.
- [236] X. Gao, et al., Phenylene-coated magnetic nanoparticles that boost aqueous asymmetric transfer hydrogenation reactions, *Chem. Eur. J.* 20 (6) (2014) 1515–1519.
- [237] F. Shi, et al., Tuning catalytic activity between homogeneous and heterogeneous catalysis: improved activity and selectivity of free nano-Fe₂O₃ in selective oxidations, *Angew. Chem. Int. Ed. Eng.* 46 (46) (2007) 8866–8868.
- [238] M. Zhang, et al., Ni/MWCNT-supported palladium nanoparticles as magnetic catalysts for selective oxidation of benzyl alcohol, *Aust. J. Chem.* 66 (2013) 564–571.
- [239] L. Zhang, et al., Palladium supported on magnetic core-shell nanoparticles: an efficient and reusable catalyst for the oxidation of alcohols into aldehydes and ketones by molecular oxygen, *ChemPlusChem* 79 (2) (2014) 217–222.
- [240] A. Schatz, et al., TEMPO supported on magnetic C/Co-nanoparticles: a highly active and recyclable organocatalyst, *Chem. Eur. J.* 14 (27) (2008) 8262–8266.
- [241] L. Aschwanden, et al., Magnetically separable gold catalyst for the aerobic oxidation of amines, *ChemCatChem* 1 (1) (2009) 111–115.
- [242] D. Saberi, A. Heydari, Oxidative amidation of aromatic aldehydes with amine hydrochloride salts catalyzed by silica-coated magnetic carbon nanotubes (MagCNTs@SiO₂)-immobilized imine-Cu(I), *Appl. Organomet. Chem.* 28 (2) (2014) 101–108.
- [243] A. Rezaeifard, et al., Aqueous heterogeneous oxygenation of hydrocarbons and sulfides catalyzed by recoverable magnetite nanoparticles coated with copper(ii) phthalocyanine, *Green Chem.* 14 (12) (2012) 3386.
- [244] A. Rezaeifard, et al., Nanomagnet-supported partially brominated manganese-porphyrin as a promising catalyst for the selective heterogeneous oxidation of hydrocarbons and sulfides in water, *Eur. J. Inorg. Chem.* 2012 (33) (2012) 5515–5524.
- [245] J. Tong, et al., Magnetic CoFe₂O₄ nanocrystal: a novel and efficient heterogeneous catalyst for aerobic oxidation of cyclohexane, *J. Mol. Catal. A Chem.* 307 (1–2) (2009) 58–63.
- [246] M.O. Sydnes, Use of nanoparticles as catalysts in organic synthesis–cross-coupling reactions, *Curr. Org. Chem.* 18 (3) (2014) 312–326.
- [247] M.J. Jin, D.H. Lee, A practical heterogeneous catalyst for the Suzuki, Sonogashira, and Stille coupling reactions of unreactive aryl chlorides, *Angew. Chem. Int. Ed. Eng.* 49 (6) (2010) 1119–1122.
- [248] A. Ghorbani-Choghamarani, B. Tahmasbi, P. Moradi, Palladium-S-propyl-2-aminobenzothioate immobilized on Fe₃O₄magnetic nanoparticles as catalyst for Suzuki and Heck reactions in water or poly(ethylene glycol), *Appl. Organomet. Chem.* 30 (6) (2016) 422–430.
- [249] A. Ghorbani-Choghamarani, M. Norouzi, Palladium supported on modified magnetic nanoparticles: a phosphine-free and heterogeneous catalyst for Suzuki and Stille reactions, *Appl. Organomet. Chem.* 30 (3) (2016) 140–147.
- [250] F. Panahi, N. Zarnaghash, A. Khalafi-Nezhad, Phosphanamine-functionalized magnetic nanoparticles (PAFMNP): an efficient magnetic recyclable ligand for the Pd-catalyzed Heck reaction of chloroarenes, *New J. Chem.* 40 (2) (2016) 1250–1255.
- [251] N.T.S. Phan, H.V. Le, Superparamagnetic nanoparticles-supported phosphine-free palladium catalyst for the Sonogashira coupling reaction, *J. Mol. Catal. A Chem.* 334 (1–2) (2011) 130–138.
- [252] M. Esmaeilpour, A.R. Sardarian, J. Javidi, Synthesis and characterization of Schiff base complex of Pd(II) supported on superparamagnetic Fe₃O₄@SiO₂ nanoparticles and its application as an efficient copper- and phosphine ligand-free recyclable catalyst for Sonogashira–Hagihara coupling reactions, *J. Organomet. Chem.* 749 (2014) 233–240.

- [253] L. Zhang, et al., A recyclable magnetic nanoparticles supported palladium catalyst for the Hiyama reaction of aryltrialkoxysilanes with aryl halides, *Cat. Sci. Technol.* 2 (9) (2012) 1859.
- [254] B. Sreedhar, A. Kumar, D. Yada, Magnetically recoverable Pd/Fe₃O₄-catalyzed Hiyama cross-coupling of aryl bromides with aryl siloxanes, *Synlett* 2011 (08) (2011) 1081–1084.
- [255] T.-J. Yoon, et al., Magnetic nanoparticles as a catalyst vehicle for simple and easy recycling, *New J. Chem.* 27 (2) (2003) 227–229. Electronic supplementary information (ESI) available: XRD and FT-IR data, as well as the detailed experimental conditions for the catalytic hydroformylation reactions. See, <http://www.rsc.org/suppdata/nj/b2/b209391j>.
- [256] M.N. Shaikh, et al., Magnetic nanoparticle-supported ferrocenylphosphine: a reusable catalyst for hydroformylation of alkene and Mizoroki–Heck olefination, *RSC Adv.* 6 (48) (2016) 41687–41695.
- [257] R. Abu-Reziq, et al., Metal supported on dendronized magnetic nanoparticles: highly selective hydroformylation catalysts, *J. Am. Chem. Soc.* 128 (15) (2006) 5279–5282.
- [258] Z. Yinghuai, et al., Magnetic nanoparticle supported second generation hoveyda-grubbs catalyst for metathesis of unsaturated fatty acid esters, *Adv. Synth. Catal.* 351 (16) (2009) 2650–2656.
- [259] X. Zheng, et al., Magnetic nanoparticle supported polyoxometalates (POMs) via non-covalent interaction: reusable acid catalysts and catalyst supports for chiral amines, *Chem. Commun. (Camb.)* 47 (45) (2011) 12325–12327.
- [260] Z. Yacob, A. Nan, J. Liebscher, Proline-functionalized magnetic core-shell nanoparticles as efficient and recyclable organocatalysts for aldol reactions, *Adv. Synth. Catal.* 354 (17) (2012) 3259–3264.
- [261] E. Akceylan, et al., Calixarene-proline functionalized iron oxide magnetite nanoparticles (Calix-Pro-MN): an efficient recyclable organocatalyst for asymmetric aldol reaction in water, *Appl. Catal. A Gen.* 499 (2015) 205–212.
- [262] S. Luo, X. Zheng, J.P. Cheng, Asymmetric bifunctional primary aminocatalysis on magnetic nanoparticles, *Chem. Commun. (Camb.)* (44) (2008) 5719–5721.
- [263] B.G. Wang, et al., Superparamagnetic nanoparticle-supported (s)-diphenylprolinol trimethylsilyl ether as a recyclable catalyst for asymmetric Michael addition in water, *Adv. Synth. Catal.* 352 (17) (2010) 2923–2928.
- [264] P. Riente, C. Mendoza, M.A. Pericás, Functionalization of Fe₃O₄ magnetic nanoparticles for organocatalytic Michael reactions, *J. Mater. Chem.* 21 (20) (2011) 7350.
- [265] C.A. Mak, et al., Hybrid magnetic materials (Fe₃O₄-κ-carrageenan) as catalysts for the Michael addition of aldehydes to nitroalkenes, *Tetrahedron* 70 (36) (2014) 6169–6173.
- [266] M. Keller, et al., Dendrimers or nanoparticles as supports for the design of efficient and recoverable organocatalysts? *Adv. Synth. Catal.* 355 (9) (2013) 1748–1754.
- [267] P. Riente, J. Yadav, M.A. Pericas, A click strategy for the immobilization of MacMillan organocatalysts onto polymers and magnetic nanoparticles, *Org. Lett.* 14 (14) (2012) 3668–3671.
- [268] H. Zhu, et al., Highly enantioselective synthesis of N-protected β-amino malonates catalyzed by magnetically separable heterogeneous rosin-derived amino thiourea catalysts: a stereocontrolled approach to β-amino acids, *ChemCatChem* 5 (8) (2013) 2187–2190.
- [269] E. Kolvari, N. Koukabi, O. Armandpour, A simple and efficient synthesis of 3,4-dihydropyrimidin-2-(1H)-ones via Biginelli reaction catalyzed by nanomagnetic-supported sulfonic acid, *Tetrahedron* 70 (6) (2014) 1383–1386.
- [270] M. Hajjami, B. Tahmasbi, Synthesis and characterization of glucosulfonic acid supported on Fe₃O₄ nanoparticles as a novel and magnetically recoverable nanocatalyst and its application in the synthesis of polyhydroquinoline and 2,3-dihydroquinazolin-4(1H)-one derivatives, *RSC Adv.* 5 (73) (2015) 59194–59203.
- [271] D. Lee, et al., Filtration-free recyclable catalytic asymmetric dihydroxylation using a ligand immobilized on magnetic mesocellular mesoporous silica, *Adv. Synth. Catal.* 348 (1–2) (2006) 41–46.
- [272] M. Kawamura, K. Sato, Magnetically separable phase-transfer catalysts, *Chem. Commun. (Camb.)* (45) (2006) 4718–4719.
- [273] M. Kawamura, K. Sato, Magnetic nanoparticle-supported crown ethers, *Chem. Commun.* (32) (2007) 3404.

- [274] N. Panda, A.K. Jena, S. Mohapatra, Heterogeneous magnetic catalyst for S-arylation reactions, *Appl. Catal. A Gen.* 433–434 (2012) 258–264.
- [275] R.B.N. Baig, R.S. Varma, A highly active and magnetically retrievable nanoferrite-DOPA-copper catalyst for the coupling of thiophenols with aryl halides, *Chem. Commun.* 48 (20) (2012) 2582–2584.
- [276] R. Zhang, et al., Magnetic nanoparticles of ferrite complex oxides: a cheap, efficient, recyclable catalyst for building the C–N bond under ligand-free conditions, *ChemCatChem* 4 (6) (2012) 824–830.
- [277] G. Chouhan, D. Wang, H. Alper, Magnetic nanoparticle-supported proline as a recyclable and recoverable ligand for the CuI catalyzed arylation of nitrogen nucleophiles, *Chem. Commun. (Camb.)* (45) (2007) 4809–4811.
- [278] R.K. Sharma, et al., Magnetite (Fe₃O₄) silica based organic–inorganic hybrid copper(ii) nanocatalyst: a platform for aerobic N-alkylation of amines, *Green Chem.* 15 (10) (2013) 2800.
- [279] V. Polshettiwar, R.S. Varma, Nano-organocatalyst: magnetically retrievable ferrite-anchored glutathione for microwave-assisted Paal-Knorr reaction, aza-Michael addition, and pyrazole synthesis, *Tetrahedron* 66 (5) (2010) 1091–1097.
- [280] S. Pagoti, D. Dutta, J. Dash, A magnetoclick imidazolidinone nanocatalyst for asymmetric 1,3-dipolar cycloadditions, *Adv. Synth. Catal.* 355 (18) (2013) 3532–3538.
- [281] D. Wang, et al., A recyclable ruthenium(II) complex supported on magnetic nanoparticles: a regioselective catalyst for alkyne-azide cycloaddition, *Chem. Commun. (Camb.)* 49 (62) (2013) 6956–6958.
- [282] D. Wang, et al., A highly active and magnetically recoverable tris(triazolyl)-Cu(I) catalyst for alkyne-azide cycloaddition reactions, *Chem. Eur. J.* 20 (14) (2014) 4047–4054.
- [283] R. Hudson, C.-J. Li, A. Moores, Magnetic copper–iron nanoparticles as simple heterogeneous catalysts for the azide–alkyne click reaction in water, *Green Chem.* 14 (3) (2012) 622.
- [284] R.B.N. Baig, R.S. Varma, A highly active magnetically recoverable nano ferrite–glutathione–copper (nano-FGT-Cu) catalyst for Huisgen 1,3-dipolar cycloadditions, *Green Chem.* 14 (3) (2012) 625–632.
- [285] H. Yang, et al., Iron-catalyzed direct alkenylation of sp³(C–H) bonds via decarboxylation of cinnamic acids under ligand-free conditions, *Green Chem.* 15 (4) (2013) 976.
- [286] J. Lee, et al., Direct catalytic C–H arylation of imidazo[1,2-a]pyridine with aryl bromides using magnetically recyclable Pd–Fe₃O₄ nanoparticles, *Tetrahedron* 69 (27–28) (2013) 5660–5664.
- [287] R.S. Prakasham, et al., Novel synthesis of ferric impregnated silica nanoparticles and their evaluation as a matrix for enzyme immobilization, *J. Phys. Chem. C* 111 (10) (2007) 3842–3847.
- [288] S.H. Huang, M.H. Liao, D.H. Chen, Direct binding and characterization of lipase onto magnetic nanoparticles, *Biotechnol. Prog.* 19 (3) (2003) 1095–1100.
- [289] V. Polshettiwar, R.S. Varma, Nanoparticle-supported and magnetically recoverable ruthenium hydroxide catalyst: efficient hydration of nitriles to amides in aqueous medium, *Chem. Eur. J.* 15 (7) (2009) 1582–1586.
- [290] R.B. Baig, R.S. Varma, A facile one-pot synthesis of ruthenium hydroxide nanoparticles on magnetic silica: aqueous hydration of nitriles to amides, *Chem. Commun. (Camb.)* 48 (50) (2012) 6220–6222.
- [291] A. Schätz, M. Hager, O. Reiser, Cu(II)-azabis(oxazoline)-complexes immobilized on superparamagnetic magnetite@silica-nanoparticles: a highly selective and recyclable catalyst for the kinetic resolution of 1,2-diols, *Adv. Funct. Mater.* 19 (13) (2009) 2109–2115.
- [292] H.M. Gardimalla, et al., Superparamagnetic nanoparticle-supported enzymatic resolution of racemic carboxylates, *Chem. Commun. (Camb.)* (35) (2005) 4432–4434.
- [293] S. Hübner, J.G. de Vries, V. Farina, Why does industry not use immobilized transition metal complexes as catalysts? *Adv. Synth. Catal.* 358 (1) (2016) 3–25.
- [294] S. Oliveira, S.P. Forster, S. Seeger, Nanocatalysis: academic discipline and industrial realities, *J. Nanotechnol.* 2014 (2014) 19.
- [295] W.J. Stark, et al., Industrial applications of nanoparticles, *Chem. Soc. Rev.* 44 (16) (2015) 5793–5805.
- [296] J. Park, et al., Ultra-large-scale syntheses of monodisperse nanocrystals, *Nat. Mater.* 3 (12) (2004) 891–895.
- [297] Y.V. Kolen'ko, et al., Large-scale synthesis of colloidal Fe₃O₄ nanoparticles exhibiting high heating efficiency in magnetic hyperthermia, *J. Phys. Chem. C* 118 (16) (2014) 8691–8701.
- [298] C.-X. Zhao, et al., Nanoparticle synthesis in microreactors, *Chem. Eng. Sci.* 66 (7) (2011) 1463–1479.

- [299] M. Simmons, et al., The preparation of magnetic iron oxide nanoparticles in microreactors, *J. Flow Chem.* 3 (1) (2013) 7–10.
- [300] F. Haseidl, B. Müller, O. Hinrichsen, Continuous-flow synthesis and functionalization of magnetite: intensified process for tailored nanoparticles, *Chem. Eng. Technol.* 39 (11) (2016) 2051–2058.
- [301] L. Gonzalez-Moragas, et al., Scale-up synthesis of iron oxide nanoparticles by microwave-assisted thermal decomposition, *Chem. Eng. J.* 281 (Supplement C) (2015) 87–95.
- [302] W. Glasgow, et al., Continuous synthesis of iron oxide (Fe_3O_4) nanoparticles via thermal decomposition, *Particuology* 26 (2016) 47–53.
- [303] A. Abou Hassan, et al., Synthesis of iron oxide nanoparticles in a microfluidic device: preliminary results in a coaxial flow millichannel, *Chem. Commun.* (15) (2008) 1783–1785.
- [304] D. Cantillo, C.O. Kappe, Immobilized transition metals as catalysts for cross-couplings in continuous flow—a critical assessment of the reaction mechanism and metal leaching, *ChemCatChem* 6 (12) (2014) 3286–3305.
- [305] T.H. Rehm, et al., Proof of concept: magnetic fixation of dendron-functionalized iron oxide nanoparticles containing palladium nanoparticles for continuous-flow Suzuki coupling reactions, *ACS Appl. Mater. Interfaces* 7 (49) (2015) 27254–27261.
- [306] R. Hudson, Coupling the magnetic and heat dissipative properties of Fe_3O_4 particles to enable applications in catalysis, drug delivery, tissue destruction and remote biological interfacing, *RSC Adv.* 6 (5) (2016) 4262–4270.
- [307] A. Meffre, et al., Complex nano-objects displaying both magnetic and catalytic properties: a proof of concept for magnetically induced heterogeneous catalysis, *Nano Lett.* 15 (5) (2015) 3241–3248.
- [308] H.J. Kim, et al., Alternating magnetic field mediated micro reaction system for palladium-catalyzed coupling reactions, *RSC Adv.* 7 (59) (2017) 37181–37184.
- [309] L. Gao, et al., The effect of external magnetic fields on the catalytic activity of Pd nanoparticles in Suzuki cross-coupling reactions, *Nanoscale* 8 (15) (2016) 8355–8362.
- [310] S. Ceylan, et al., Inductive heating with magnetic materials inside flow reactors, *Chem. Eur. J.* 17 (6) (2011) 1884–1893.

This page intentionally left blank

Spin and Charge Tunneling Transport in Magnetic Tunnel Junctions With Embedded Nanoparticles

Artur Useinov^{*}, Chih-Huang Lai[†], Niazbeck Kh. Useinov[‡], Lenar R. Tagirov^{‡,§,¶}

^{*}National Chiao Tung University, Hsinchu, Taiwan, [†]National Tsing Hua University, Hsinchu, Taiwan, [‡]Kazan Federal University, Kazan, Russia, [§]E. K. Zavoisky Physical-Technical Institute of RAS, Kazan, Russia, [¶]Institute for Advanced Studies of ASRT, Kazan, Russia

11.1 Introduction

Various multilayer systems such as magnetic tunnel junctions (MTJs) and their modifications attract attention due to their promising applications: magnetic field sensors, magnetic memory, memristors, nano spin-valves, and resistance generators. The current progress in studying giant magnetoresistance (GMR), tunnel magnetoresistance (TMR), and spin-transfer torque (STT) can provide successful solutions of the problems related to energy consumption and thermal stability factor of magnetic random access memory (MRAM, STT MRAM). Moreover, spintronic devices have a unique advantage against semiconductor devices that they are nonvolatile. In addition, they are expected to be more scalable than semiconductor-based devices, because magnetic nano-domain is much more stable groundwork for the information storage in contrast to a charged micro-capacitor. It is well-known that the leakage current rapidly increases with a capacitor dimension reduced down to the nano-scale.

In this review we show how quasiclassical theory for point-like contacts can be adapted for spintronic device physics explaining mean free path and GMR effects in nano-scale heterocontacts, asymmetric voltage dependences of TMR in MTJs, as well as applied to modeling of zero bias TMR anomalies in MTJs with embedded nanoparticles (NPs). The dependence of in-plane component of STT on the applied voltage for various size of NPs in the case of the different barrier asymmetry can be also calculated.

GMR is a change in electric resistance of a magnetically inhomogeneous material when an applied magnetic field modifies magnetic configurations in the system. The magnetically inhomogeneous system usually consists of a magnetic multilayer in which the layers are

typically a few nanometers in thickness. It is useful and customary to divide GMR into two major types: current in plane (CIP) GMR and current perpendicular to plane (CPP) GMR. The physics of these two types of GMR is quite different.

In CIP GMR the electrons travel along the layer planes, so the spin-dependent channeling plays a major role in determining the CIP resistance of the multilayer. So matching of the electronic band structures of the spin channels plays an important role in CIP GMR, and in CPP GMR as well [1]. For example, the first observation of CIP GMR was in Fe-Cr multilayers [2, 3]. It turned out that Fe and Cr have very similar minority spin bands whereas their majority spin bands are quite different. An important implementation of spin valves used in magnetic field sensors is based on layers of Cu and Co, or materials similar to Co, in the majority channel.

In CPP GMR the electrons travel perpendicular to magnetic layers. It is relatively easy to see in a qualitative picture that if the majority or minority bands of two ferromagnetic layers match the spacer layer, electrons in one of the spin channels can easily pass through the layers when the magnetic moments are aligned. The opposite can be also true if the moments are antialigned. Furthermore, some magnetic alloys, for example, Ni alloys containing Co and Fe, conduct spin-up electrons with very little scattering while the spin-down electrons can hardly travel more than interatomic distance before they scatter [1]. CPP GMR is difficult to measure because the resistance of a thin film (a few nanometers) across its thickness is usually very tiny. The thickness must remain small compared with the distance over which the electrons conserve their spin projection, and which is of the order of dozen nanometers for magnetic materials. For this reason, the first CPP-GMR measurements were performed using superconducting leads [4].

TMR is geometrically similar to CPP GMR and considered in [Section 11.3](#). The difference is that the nonmagnetic metallic spacer layer is replaced by an insulator or semiconductor. Apparently, the band matching between one of the spin channels and the spacer layer (the origin of CPP GMR) cannot longer occur because there are no conduction bands at the Fermi energy in an insulator. For this reason, the original theory of TMR was based on the Fermi energy density of states (DOS) of ferromagnetic electrodes [5]. In this case, it turns out that a new and different kind of band matching can occur, and this can be used to achieve a very large ratio of tunneling conductance between parallel (P) and antiparallel (AP) alignments of magnetic moments.

In [Section 11.4](#), we consider STT phenomenon. It was predicted independently by Joan Slonczewski and Luc Berger in 1996 year [6, 7]. In a sense, it is an inverse to the GMR and TMR effects in which the transport of electrons between two ferromagnetic layers is affected by the relative alignment of their magnetic moments. In STT, the currents flowing through ferromagnetic layers can change the relative alignment of their magnetic moments. The spin-polarized currents have been observed to cause precession of magnetic moments and switching the magnetic configurations from AP to P and vice versa.

11.2 Giant Magnetoresistance in Ferromagnetic Heteronanocontacts

Metallic nano-scale point contact is considered within the model of circular conducting orifice, which is embedded into an insulating membrane. The insulator separates a metallic bulk on two half-spaces (see Fig. 11.1A). The charge current through the orifice cross-section can be calculated according to the following equation, which was derived in assumption that the electron energy is equal to E_F , and $E_F \gg k_B T$ [8–10] (k_B is the Boltzmann constant, T is the temperature):

$$I_s = \frac{e^2 k_{F,s,\min}^2 a^2 V}{2\pi\hbar} \int_0^\infty dk \frac{J_1^2(ka)}{k} F_s(k, D_s, l_s), \quad (11.1)$$

$$F_s(k, D_s, l_s) = F_s^{bal}(D_s) + F_s^{df'}(k, D_s, l_s) + F_s^{df''}(k, D_s, l_s), \quad (11.2)$$

where e and l_s are electron charge and mean free path, respectively; a is the radius of the orifice contact and $s = \uparrow, \downarrow$ is the spin index. The k is momentum in the orifice conjugated to the radial variable ρ of the coordinate of electron in the contact plane; $J_1(x)$ is the Bessel function. $k_{F,s,\min}$ is the Fermi wavenumber which has to be minimal (min) of two wavenumbers, $k_{F,s}^L$ and $k_{F,s}^R$, where the superscripts $L(R)$ denote left and right sides of the contact. $F_s(k, D_s, l_s)$ contains integration over $\theta_{c,s}$ which is an angle between z -axis and direction of the electron velocity, the index $c = L(R)$ determines the contact side. The z -axis is chosen as a normal to the orifice plane passing through its center of symmetry. The transmission coefficient D_s is usually a function of the electron wavenumbers, $\theta_{c,s}$, applied voltage V and other possible variables. These variables have been defined from specification of the considered problems, where

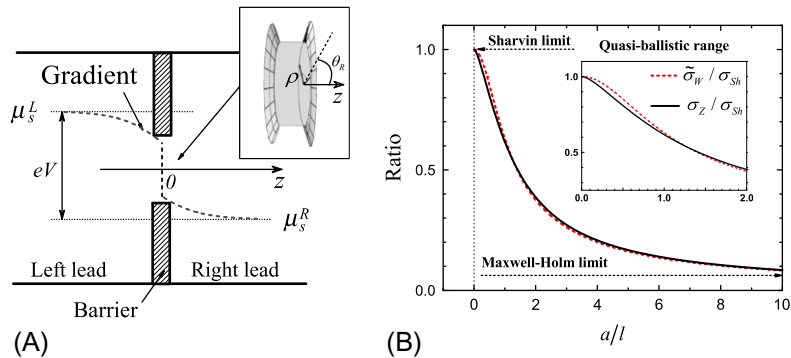


Fig. 11.1

(A) Schematic plot of the point-like contact which is considered as an orifice in the insulating membrane (a -spot model); $\mu_s^{L(R)}$ is the chemical potential. (B) Numerical solution of the present model for σ_z/σ_{sh} (solid line) and refined Wexler's ratio $\tilde{\sigma}_w/\sigma_{sh}$ (dash line) as a function of a/l .

(The original figure (A) is published in A.N. Useinov, C.H. Lai, Tunnel magnetoresistance and temperature related effects in magnetic tunnel junctions with embedded nanoparticles, SPIN 6 (1) (2016) 165000, <https://doi.org/10.1142/S2010324716500016>.)

the point-contact area can be replaced by a quantum object whose transmission properties can be quantified using conventional quantum mechanics.

The total current is a sum of the both spin components of the charge current, $I = I_{\uparrow} + I_{\downarrow}$. The complete form of the first and second terms in expression (11.2) can be accessed in Refs. [10, 12]. The first term has a simple view, $F_s^{bal} = \langle \cos(\theta_{L,s}) D_s \rangle_{\theta_L}$, and is responsible for ballistic (or tunnel) transport: $l_{\uparrow}, l_{\downarrow} \gg a$, while $F_s^{df'}$ (k, D_s, l_s) and $F_s^{df''}$ (k, D_s, l_s) correspond to the quasiballistic ($l_{\uparrow}, l_{\downarrow} \approx a$) and diffusive Ohmic regimes ($l_{\uparrow}, l_{\downarrow} \ll a$).

It is worthy to note that expression (11.2) for the spin-polarized current allows to simplify the numerical calculations of the spin-dependent conductivity and magnetoresistance in structures like MTJ when only the tunnel (ballistic) term is sufficient to take into account, see, for example, Ref. [13]. The magnetic point-like heterocontact model containing the two terms, $F_s^{bal}(D_s)$ and $F_s^{df'}$ (k, D_s, l_s), is considered in Useinov et al. [9]. The more general case of the magnetic point-like heterocontact when $l \sim a$ is studied with the use of the term $F_s^{df''}$ (k, D_s, l_s) in Refs. [12, 14]. All three terms in expression (11.2) are solutions of the system for the quasiclassical Green functions with quantum boundary conditions.

It is also worthy to notice that F_s^{bal} is independent of l_s and k . When we consider the ballistic or tunnel transport, $F_s(k, D_s, l_s) = F_s^{bal}(D_s)$, then Eq. (11.1) can be simplified since $\int_0^{\infty} J_1^2(x)/x dx = 1/2$, and

$$\sigma_s = I_s/V = \frac{e^2}{h} \frac{(k_{F,s}^L)^2 a^2}{2} \langle \cos(\theta_{L,s}) D_s \rangle_{\theta_L}, \quad (11.3)$$

where $\langle \dots \rangle_{\theta_L}$ is the solid-angle averaging, and $\cos(\theta_{L,s})$ is a cosine of the incidence angle on the L -side ferromagnet.

In the case of symmetric nonmagnetic point-like metallic contact: $k_F^L = k_F^R$, $\sigma_{\uparrow} = \sigma_{\downarrow}$, $D_{\uparrow} = D_{\downarrow} \rightarrow 1$, $F_s^{bal} = \langle \cos(\theta_{L,s}) \rangle_{\theta_L} = 1/2$, the conductance $\sigma_Z = \sigma_{\uparrow} + \sigma_{\downarrow} = (2e^2/h)(k_F^2 a^2/4)$ coincides with the Sharvin limit σ_{Sh} [15–17]. Thus, Eq. (11.3) is extension of the Sharvin conduction limit, so that ballistic transport through a contact of two nonidentical and nonmagnetic metals can be described within this approach. The ballistic conductance is fully determined by quantum mechanical transmission coefficient of the interface between two metals.

In the case of nonballistic transport, all three terms in Eq. (11.2) have to be included. In the case of a contact of two identical metals, a straightforward analytical evaluation of all integrals in Eqs. (11.1), (11.2) results in a simple expression valid for the arbitrary ratio of the mean free path to the orifice radius [12]:

$$\sigma_Z = 4\sigma_{Sh} \left(\frac{1}{4} - \int_0^{\infty} \frac{dx}{x} \frac{J_1^2(x)}{1 + (xK)^2 + \sqrt{1 + (xK)^2}} \right), \quad (11.4)$$

where $K = l/a$ is the Knudsen number. In the limit $K \rightarrow \infty$ ($a/l \rightarrow 0$), the integral in Eq. (11.4) vanishes and the conductance transforms to σ_{Sh} . For $K \rightarrow 0$ ($a/l \rightarrow \infty$):

$$\lim_{K \rightarrow 0} \int_0^\infty \frac{dx}{x} \frac{J_1^2(x)}{1 + (xK)^2 + \sqrt{1 + (xK)^2}} = \frac{1}{4} - \frac{2}{3\pi}K, \quad (11.5)$$

it is easy to obtain the exact diffusive solution in the form of the Maxwell-Holm limit: $\sigma_Z \rightarrow \sigma_M$, $\sigma_M = (8K/3\pi)\sigma_{Sh} = 2a/\rho_V$, where $\rho_V = \hbar k_F / e^2 n l = 3\pi^2 \hbar^3 / e^2 p_F^2 l$ is resistivity in volume (Ωm). Here $n = k_F^3/3\pi^2$ is the electron density in a metal and $p_F = \hbar k_F$ is the Fermi momentum. The numerical σ_Z/σ_{Sh} dependence on K is close to the Wexler solution [16],

$$\tilde{\sigma}_W / \sigma_{Sh} = \left(\frac{3\pi}{8K} \gamma(K) + 1 \right)^{-1},$$

with Mikrajuddin's corrections [17, 18], where

$$\gamma(K) \approx \frac{2}{\pi} \int_0^\infty e^{-K \cdot x} \text{sinc}(x) dx.$$

Fig. 11.1B shows the matching between the Wexler-Mikrajuddin's and σ_Z solutions in the entire range from ballistic to diffusive limits.

The experimental discovery of ultra-high magnetoresistance (MR) in ferromagnetic nanocontacts is still attracting for its potential applications in magnetoresistive sensors [19–25] and other spintronic devices. Two mechanisms of GMR in magnetic nanocontacts were proposed to explain the experimental data: one is enhancement of the impurity scattering within a domain wall (DW) [20, 22], and the second one is the scattering of electrons by DW potential landscape [8, 26, 27]. Both mechanisms assume abrupt domain wall profile which is localized in a narrow contact area [28–31]. The DW electron scattering theory [8] is general enough to admit spin asymmetry of the bulk impurity scattering. It also accounts for the spin-dependent mean free path of the conduction electron which can be relatively different by length in five to seven times [32, 33]. Spin asymmetry of the contact interface resistance for different magnetic materials may also add valuable impact on the MR value.

Spin bands in the left and right sides of the contacting FMs are split by exchange interaction. It allows to classify the contacts on three types according to the spin-split conduction subband bottoms against the common equilibrium Fermi level. Magnetization reversal, which occurs inside the contact area at the AP alignment, can be simulated by linear scattering potential within the model of the linear DW. It is worthy to notice that the sloping energy potential profile for the P state can also be used as an approach for the simulation of interface scattering in heterocontacts due to mismatch of their conduction band's bottoms. The angular- and spin-dependent quantum-mechanical transmission D^{SL} for the linear energy profile is obtained as follows [9, 34]:

$$D^{SL}(\cos(\theta_L), L) = \frac{4}{\pi^2} \frac{p_M p_m t^2(L)}{(p_M \beta - p_m \gamma)^2 + (p_M p_m \alpha + \chi)^2}, \quad (11.6)$$

where

$$\begin{aligned} \alpha &= \text{Ai}(q_1 L) \text{Bi}(q_2 L) - \text{Bi}(q_1 L) \text{Ai}(q_2 L), \\ \beta &= t(L) \{ \text{Ai}(q_1 L) \text{Bi}'(q_2 L) - \text{Bi}(q_1 L) \text{Ai}'(q_2 L) \}, \\ \gamma &= t(L) \{ \text{Ai}'(q_1 L) \text{Bi}(q_2 L) - \text{Bi}'(q_1 L) \text{Ai}(q_2 L) \}, \\ \chi &= t^2(L) \{ \text{Ai}'(q_1 L) \text{Bi}'(q_2 L) - \text{Bi}'(q_1 L) \text{Ai}'(q_2 L) \}. \end{aligned}$$

Here we have omitted the spin indices for simplicity. In the earlier formulas L is the DW width, $\text{Ai}(z)$, $\text{Bi}(z)$ and $\text{Ai}'(z)$, $\text{Bi}'(z)$ are the Airy functions and their derivatives. In addition to this, the following abbreviations have been used:

$$\begin{aligned} t(L) &= [2mE_{\text{ex}}/L]^{1/3}, \\ E_{\text{ex}} &= (p_{FM}^2 - p_m^2)/2m, \\ q_1 &= -p_{FM}^2 t(L)/2mE_{\text{ex}}, \\ q_2 &= -p_m^2 t(L)/2mE_{\text{ex}}, \end{aligned}$$

where E_{ex} is the exchange energy. The normal components of the Fermi momentum $p_m = p_{FM} \cos(\theta_m)$ and $p_M = p_{FM} \cos(\theta_M)$ are determined for every spin projections of the *minority* and *majority* subbands, respectively. The quantum-mechanical expression for the transmission coefficient through the abrupt, or step-like DW,

$$D^{\text{Step}}(\cos(\theta_L)) = 4p_M p_m / (p_M + p_m)^2,$$

can be retrieved at $L \rightarrow 0$ from Eq. (11.6). The magnetoresistance of a magnetic nanocontact is determined as $\text{MR} = (\sigma^P - \sigma^{AP})/\sigma^{AP}$, where $\sigma^{\text{P(AP)}} = \sigma_{\uparrow}^{\text{P(AP)}} + \sigma_{\downarrow}^{\text{P(AP)}}$ is conductance for the P(AP) magnetic configuration.

The calculated MR for Fe-Fe and Co-Co junctions is shown in Fig. 11.2. The spin-subbands of Fe and Co metals are reversed with respect to their macroscopic magnetic moment: the densities of states, $N(E)$, are shown in right-hand side plots of Fig. 11.2. It is worthy to notice that the calculated results are similar for these junctions due to the symmetry with respect to complete spin inversion.

The MR in heterojunctions can be positive or negative depending on the junction design and size (a/l ratio). The negative MR becomes possible in the case when scattering in the contact area for AP configuration is less (interface transparency is higher) compared with the P case due to particular combination of the relative shifts of the conduction band bottoms [34].

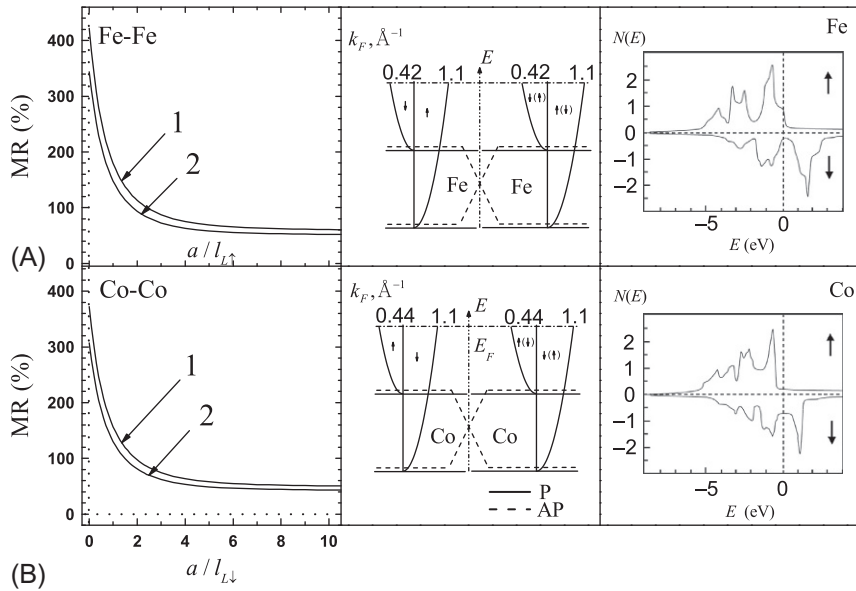


Fig. 11.2

(A) MR versus $a/l_{L\uparrow}$ for Fe-Fe junction at $l_{L\downarrow}/l_{L\uparrow} = 2.0$, $l_{L\uparrow}/l_{R\uparrow} = 1.0$, $l_{R\downarrow}/l_{R\uparrow} = 2.0$. (B) The same for Co-Co junctions at $l_{L\downarrow}/l_{L\uparrow} = 0.5$, $l_{L\uparrow}/l_{R\uparrow} = 1.0$, $l_{R\downarrow}/l_{R\uparrow} = 0.5$. MR curves 1 and 2 are derived at $L = 2 \text{ \AA}$ and $L = 10 \text{ \AA}$, respectively. The *middle windows* show the model potential energy profiles of the junction, and the *right-hand side windows* show DOS for the related metals in the bulk [35].

(The original figure is published in A.N. Useinov, L.R. Tagirov, R.G. Deminov, N.K. Useinov, *Giant magnetoresistance of nanoscale ferromagnetic heterocontacts*, Kazan. Gos. Univ. Uchen. Zap. Ser. Fiz. Mater. Nauki 149 (3) (2007) 5–30.)

To the authors knowledge, there are a few reports showing MR measurements in Mumetal-Ni ferromagnetic heterocontacts [22, 36]. The Mumetal ($\text{Ni}_{77}\text{Fe}_{14}\text{Cu}_5\text{Mo}_4$) is close to permalloy ($\text{Ni}_{79}\text{Fe}_{21}$) by physical properties. Thus, the material parameters for permalloy and nickel [22, 32, 36–38] are quite suitable for the trial MR simulations. The results of these simulation for Mumetal-Ni junction are shown in Fig. 11.3. The MR magnitude for a ballistic case ($a/l_{L\downarrow} \ll 1.0$) is varied in the range of 100–132% for $L = 10.0 \text{ \AA}$ down to $L = 1.0 \text{ \AA}$, respectively. These values agree with the experimental MR values in 78–132% range, quoted in Table 1 of Ref. [36] and Fig. 2 in Ref. [22]. The MR and conductance values are beyond the scope of the presented approach for $a/l_{L\downarrow} \geq 15$, since the DW profile is suspected to be out of the contact area at these conditions.

In summary, the analysis has shown that the most optimal conditions for the maximal MR amplitude in terms of the spin asymmetry are implemented in symmetric (homo) junctions (such as Co-Co, Fe-Fe, etc.) rather than in heterojunctions due to the largest contrast between spin subbands.

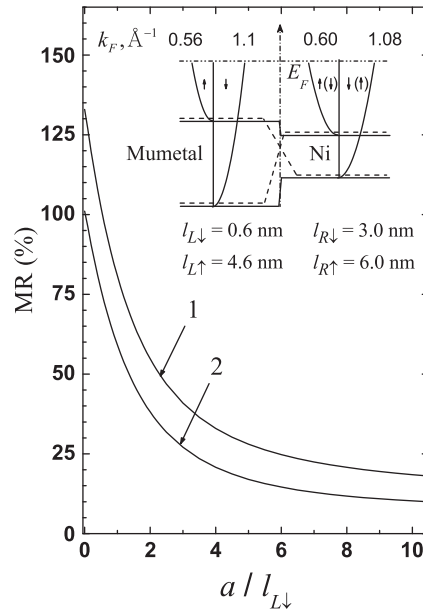


Fig. 11.3

MR dependence on the contact size for the parameters close to Mumetal-Ni heterocontact. MR curves 1 and 2 are derived at $L = 1.0 \text{ \AA}$ and $L = 10.0 \text{ \AA}$, respectively. (Adapted from A. Useinov, R. Deminov, L. Tagirov, G. Pan, Giant magnetoresistance in nanoscale ferromagnetic heterocontacts, *J. Phys. Condens. Matter* 19 (2007) 196215, <https://doi.org/10.1088/0953-8984/19/19/196215>.)

11.3 Tunnel Magnetoresistance in Single- and Double-Barrier MTJ

Previously, we reviewed a theory of electronic transport through a nanosized domain wall inside the contact between ferromagnetic homo- and hetero-electrodes in a point-like geometry. This theory utilizes quasiclassical equations to describe the transport phenomena in the ferromagnetic metals, and quantum-mechanical equations for modeling the electron transmission through the domain wall, which was approximated by the sloping potential. In this section, we apply the previously derived Eq. (11.1) for the current replacing the transmission through a domain wall by the tunneling transmission through single- or double-barrier systems. The tunnel transmissions for the single- and double-barrier MTJ (SMTJ and DMTJ) were calculated analytically in Useinov et al. [9, 13], respectively. The inhomogeneous $F_s^{df}(k, D_s, l_s)$ and $F_s^{d'f}(k, D_s, l_s)$ terms, which are responsible for the point-like geometry and diffusive transport, were neglected due to their small contributions into the tunnel transport. The approach corresponds to the case of high Fermi energies ($\gtrsim 4 \text{ eV}$), accounting for the dependence of the electron transmission on the trajectory angle and the conduction band spin-splitting. It was also assumed that the electron spin state is conserved during the ballistic tunneling, and the model of free-electron parabolic dispersion relation is maintained as well.

The normalized TMR, considering a single-band model, can be determined as follows:

$$\text{TMR} = \frac{(J^{\text{P}} - J^{\text{AP}})}{J^{\text{AP}}} \times (\text{TMR}_{\text{max}}^{-1}), \quad (11.7)$$

where $J^{\text{P(AP)}} = J_{\uparrow}^{\text{P(AP)}} + J_{\downarrow}^{\text{P(AP)}}$ is the sum of spin-up and spin-down current densities for the P (or AP) magnetic moments alignment, and TMR_{max} is the maximal TMR amplitude for the SMTJ, for example, $\text{TMR}_{\text{max}} = \text{TMR}(V_a \rightarrow 0)$. Within the ballistic approximation, which is a suitable assumption when the MTJ dimensions are comparable with the mean free path of electrons, a simplified solution for the tunnel current densities was derived by Useinov et al. [13, 39]. The current density for the $\text{FM}^L/\text{I}/\text{FM}^R$ and $\text{FM}^L/\text{I}/\text{FM}^M/\text{I}/\text{FM}^R$ junctions is proportional to the product of the transmission coefficient and the cosine of the incidence angle $\theta_{L,s}$, $\cos(\theta_{L,s}) \equiv x_s$ of the quasiclassical electron trajectory. It is contribution of the single electron trajectory averaged over the solid angle Ω_L :

$$J_s^{\text{P(AP)}} = \frac{e^2 (k_{F,s}^L)^2 V_a}{4\pi^2 \hbar} \left\langle x_s D_s^{\text{P(AP)}} \right\rangle_{\Omega_L}, \quad (11.8)$$

where $k_{F,s}^L$ is the Fermi wave vector of the left-hand side electrode. Furthermore, $D_s^{\text{P(AP)}}$ can be a transmission coefficient for a single or double barrier, which is a function of the barrier geometry, the applied voltage and values of the spin-dependent Fermi wave vectors $k_{F,s}^j$ ($j=L,R$, or L,M,R). There is no difference between all in-plane or all out-of-plane-oriented magnetizations: the transmission does not depend on the choice of the common quantization axis since the anisotropy effects such as voltage-induced screening or crystallographic dependence of the DOS in FM layers were not included in the model. Eq. (11.8) is applied for the positive values of the applied voltage V_a ($V_a = V$ in the case of SMTJ, or $V_a = 2V$ in the case of symmetrical DMTJ, where the barrier width $L_1 = L_2$), while solution for the negative V_a is derived using symmetry relations for the system, that is, the parameters of the electronic states of the contact electrodes must be reversed $k_{F,\uparrow\text{maj}}^{L(R)} \rightarrow k_{F,\uparrow\text{maj}}^{R(L)}$ and $k_{F,\downarrow\text{min}}^{L(R)} \rightarrow k_{F,\downarrow\text{min}}^{R(L)}$.

The D_s is defined as a ratio of the transmitted probability density in FM^R to the incident one in FM^L . Analytical solution for the transmission D_s is accessed in Ref. [39] for SMTJ and in Ref. [13] for DMTJ. It is a function of the quasiclassical electron trajectory angle $\theta_{L,s}$ and projections of the wave vectors, which are perpendicular to the plane of the contact interfaces. The related components for SMTJ are:

$$k_{\perp,s}^L = k_{F,s}^L \cos(\theta_{L,s}) \quad \text{and} \quad k_{\perp,s}^R = k_{F,s}^R(V) \cos(\theta_{R,s}),$$

where

$$k_{F,s}^R(V) = \sqrt{(k_{F,s}^R)^2 + (2m_R e / \hbar^2) V}$$

is the voltage-dependent absolute value of the Fermi wave vectors in FM^R . Additional assumption has been made for the middle layer of DMTJ:

$$k_{\perp,s}^M = k_{F,s}^M(V) \cos(\theta_{M,s}),$$

where

$$k_{F,s}^M(V) = \sqrt{(k_{F,s}^M)^2 + (2m_M e/\hbar^2)V},$$

and m_j is the effective electron mass for FM^j , $m_{L(R)}$ values are close to those for the free electron mass m_0 .

The system of linear equations for the wave functions of the single- and double-barrier structures was derived using the matrix method proposed by Kane [40]. This method represents the wave functions derived from the Schrödinger equation in the matrix form, including also their continuity conditions, and following transmission probabilities. The term $\langle \dots \rangle_{\Omega_L}$ in Eq. (11.8) (and also in Eq. 11.3) is obtained by the solid angle integration:

$$\langle x_s D_s^{\text{P(AP)}} \rangle_{\Omega_L} = \frac{1}{2\pi} \int_0^{\theta_{\min}} \sin(\theta_{L,s}) d\theta_{L,s} \int_0^{2\pi} d\varphi(\dots) = \int_{X_{CR}}^{1.0} x_s D_s^{\text{P(AP)}} dx_s, \quad (11.9)$$

where the lower limit X_{CR} for SMTJ is the critical restriction, which is equal to zero when electrons tunnel in the whole sector of incidence angle $\theta_{L,s} \in [0, \pi/2]$ and

$$X_{CR} = \sqrt{1 - \left(k_{F,\text{maj}}^L/k_{F,\text{min}}^R\right)^2},$$

when the electron tunnels from the majority into the minority subband and there are slanting trajectories undergoing full specular reflection [39]. In the case of DMTJ, $X_{CR} = \cos(\theta_{\min})$ with $\theta_{\min} = \min\{\theta_1, \theta_2\}$, where

$$\theta_1 = \arccos \left(\sqrt{\left| 1 - \left(k_{F,\text{maj}}^L/k_{F,\text{min}}^M\right)^2 \right|} \right),$$

$$\theta_2 = \arccos \left(\sqrt{\left| 1 - \left(k_{F,\text{maj}}^L/k_{F,\text{min}}^R\right)^2 \right|} \right).$$

These conditions are derived from the conservation laws for the Fermi wave vector projection parallel to the junction plane:

$$k_{\parallel,s}^L = k_{F,s}^L \sin(\theta_{L,s}) = k_{F,s}^R(V) \sin(\theta_{R,s})$$

for SMTJ and

$$k_{\parallel,s}^L = k_{F,s}^L \sin(\theta_{L,s}) = k_{F,s}^M(V) \sin(\theta_{M,s}) = k_{F,s}^R(V) \sin(\theta_{R,s})$$

for DMTJ.

Fig. 11.4 shows normalized TMR- V_a curve for the SMTJ with the potential energy profile depicted in Fig. 11.5. The normalized TMR- V_a curve fits clearly the experimental data, which were obtained for CoFeB/MgO/CoFeB in Ref. [41]. The asymmetric voltage behavior at positive and negative V_a (Fig. 11.4, see the *inset*) occurs due to the slight difference of the FM^L and FM^R magnetic properties. The TMR- V_a asymmetry was used for more accurate wave

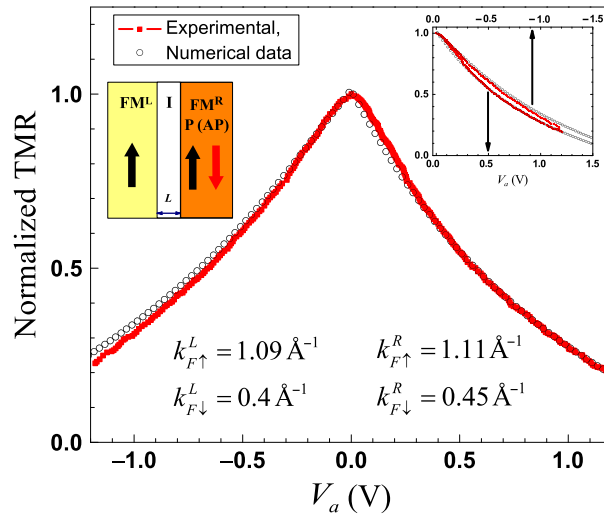


Fig. 11.4

TMR versus voltage in comparison with the experimental data [41] for SMTJ, $U_B = 1.8$ eV, $m_B = m_{L(R)} = m_0$. (Reproduced from A. Useinov, J. Kosel, *Spin asymmetry calculations of the TMR-V curves in single and double-barrier magnetic tunnel junctions*, *IEEE Trans. Magn.* 47 (10) (2011) 2724–2727, <https://doi.org/10.1109/TMAG.2011.2153182>.)

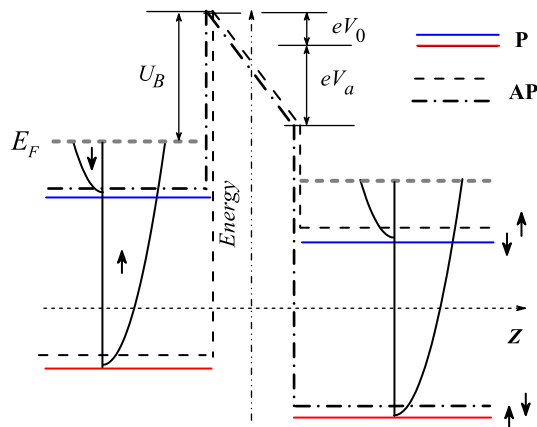


Fig. 11.5

Schematic energy diagram for SMTJ at parallel (P) and antiparallel (AP) magnetic configurations.

vectors assignment in the numerical calculations [42, 43]. The thickness of the insulating barrier $L = 18.0 \text{ \AA}$, which was used in simulations, is the same for the experimental data. The experimental data were normalized to their maximal amplitude 230%.

The potential energy profile for DMTJ is shown in Fig. 11.6. The conduction electron spin channels passing through minority or majority subbands are determined by tunneling trajectories with conserved spin orientation. In Fig. 11.7, the TMR is shown as a function of the middle ferromagnetic layer thickness L_M at the applied voltage $V_a = 0.5 \text{ V}$. Some resonant features of the TMR curves are of particular interest: first, the TMR as a function of L_M shows well-defined peaks, where the height of the peaks decreases monotonously with increasing L_M ; and second, the background TMR between the peaks increases with increasing the electron effective masses of the insulating barriers $m_{1(2)}$. Moreover, the TMR peaks are repeated periodically every 3.1 \AA . The first TMR peak has a significant maximum amplitude of about 1300% and corresponds to $m_{1(2)} = m_0$ and $L_M \approx 4 \text{ \AA}$.

Fig. 11.8A shows the resonant TMR dependence on V_a the shape of which is influenced by

$$\delta_{L(R)} = k_{F,\min}^{L(R)} / k_{F,\text{maj}}^{L(R)}$$

In the case of $\delta_{L(R)} = 0.38$, the resonant TMR arises as a flat-dome bump between $0.22 < V_a < 0.72 \text{ V}$ with the amplitude of 290% against nonresonant background of 135%. The rise of the flat-dome TMR curve ($\delta_{L(R)} = 0.38$), Fig. 11.8A, coincides with the voltage of the first resonant peak location in Fig. 11.8B for the transmission co-efficient $D_s(V_a)$ at the first

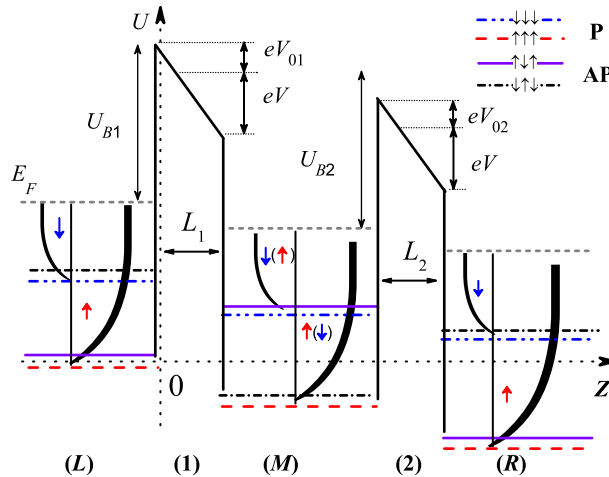
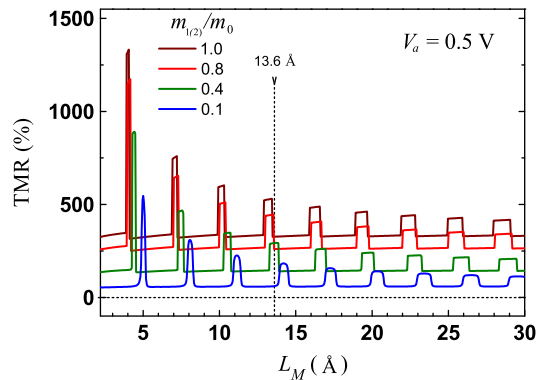


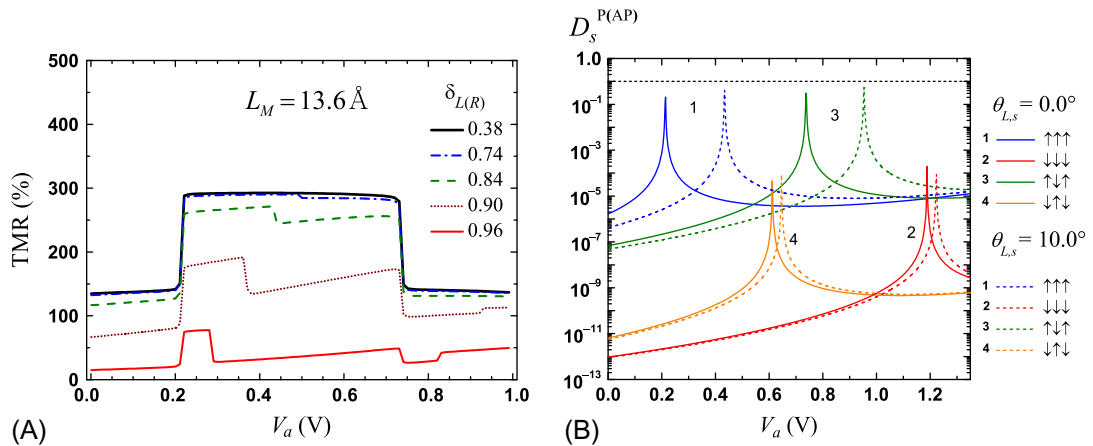
Fig. 11.6

Schematic energy diagram for the DMTJ, the V is the voltage drop on the first and second barriers ($V_a = 2V$). The eV_{01} and eV_{02} are intrinsic potential shifts induced by the interfaces matching. (Reprinted from A. Useinov, J. Kosel, N.K. Useinov, L.R. Tagirov, Resonant tunnel magnetoresistance in double-barrier planar magnetic tunnel junctions, *Phys. Rev. B* 84 (2011) 085424, <https://doi.org/10.1103/PhysRevB.84.085424>.)


Fig. 11.7

TMR as a function of the middle ferromagnetic layer thickness L_M . The four curves correspond to different electron effective masses $m_{1(2)}$ in the insulating barriers. Other parameters are as follows: $L_{1(2)} = 12 \text{ \AA}$, $L_M = 13.6 \text{ \AA}$, $U_{B1(2)} = 1.8 \text{ eV}$, $V_{01(2)} = 0.1 \text{ eV}$, and $m_{1(2)} = 0.4m_0$, $\delta_{L(R)} = 0.38$, $\delta_M = 0.96$.

(Reprinted from A. Useinov, J. Kosel, N.K. Useinov, L.R. Tagirov, Resonant tunnel magnetoresistance in double-barrier planar magnetic tunnel junctions, *Phys. Rev. B* 84 (2011) 085424, <https://doi.org/10.1103/Phys-RevB.84.085424>.)


Fig. 11.8

(A) Resonant, flat-dome TMR behavior in DMTJ for different $\delta_{L(R)}$ ($\delta_R = \delta_L$) and fixed $\delta_M = 0.96$. The other parameters are the same as in Fig. 11.6. (B) Transmission versus V_a for two fixed trajectory angles: $\theta_{L,s} = 0.0$ degrees (solid lines) and $\theta_{L,s} = 10.0$ degrees (dash lines). The conduction channels assume four configurations at P and AP states, depicted in the right. Other parameters are the same as in Fig. 11.7. (Reprinted from A. Useinov, J. Kosel, N.K. Useinov, L.R. Tagirov, Resonant tunnel magnetoresistance in double-barrier planar magnetic tunnel junctions, *Phys. Rev. B* 84 (2011) 085424, <https://doi.org/10.1103/PhysRevB.84.085424>.)

channel: $V_a \approx 0.22$ V, $\theta_{L,s} = 0.0$ degrees in the P case. The drop edge of this flat-dome feature corresponds to the voltage of the AP resonant peak located at $V_a \approx 0.72$ V and denoted as a third transmission channel. The example shows that the resonant tunneling is the physical origin of the flat-dome features in TMR of DMTJ. Moreover, the resonant TMR- V_a dependence may have more complicated shape upon increasing $\delta_{L(R)}$ because of overlapping bumps caused by the resonant transmission peaks in $D_s(V_a)$, Fig. 11.8A.

In the case of ferromagnetic middle FM^M layer, the TMR behavior depends on magnetic configurations and couplings in the system of FM layers. Fig. 11.9A shows simulations of the nonresonant TMR in DMTJ with magnetic and nonmagnetic middle FM^M at $L_M = 18.2$ Å. The TMR at $V_a \rightarrow 0$ (TMR_0) reaches 122% (curve 1) and 92% (curve 2). The vertical dash line shows a voltage, $V_a = 50$ mV, suitable for measurements, and used to adjust the material parameters for calculations. Curve 1 is drawn for the configuration (a) (see Fig. 11.9B and the figure caption for notations) and $k_{F,\uparrow}^M = 0.542$ Å⁻¹ and $k_{F,\downarrow}^M = 0.538$ Å⁻¹. Curve 2 is drawn for the configuration (b) and $k_{F,\uparrow}^M = 0.538$ Å⁻¹, $k_{F,\downarrow}^M = 0.542$ Å⁻¹. Curve 3 shows the case of nonmagnetic middle FM^M layer and $k_F^M = 0.54$ Å⁻¹. The other parameters were taken as follows: $k_{F,\uparrow} = 1.09$ Å⁻¹, $k_{F,\downarrow} = 0.421$ Å⁻¹, $L_{1(2)} = 10.0$ Å, $U_B = 1.2$ eV, the effective masses: $m_M = 0.8 m_0$ for FM^M , $m_{1(2)} = 0.4 m_0$ for the barriers, and $m_{L(R)} = m_0$ for the $FM^{L(R)}$.

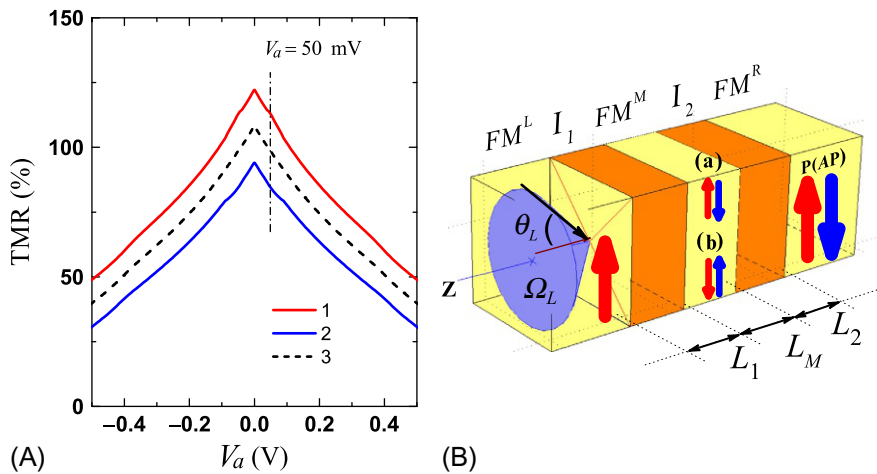


Fig. 11.9

(A) TMR versus voltage dependence in DMTJ (simulation results). The calculation parameters are as follows: $k_{F,\uparrow}^{L(R)} = 1.01$ Å⁻¹, $k_{F,\downarrow}^{L(R)} = 0.45$ Å⁻¹, $k_{F,\uparrow}^M = 0.542$ Å⁻¹, $k_{F,\downarrow}^M = 0.538$ Å⁻¹, the magnetic configuration (a) for curve 1; the configuration (b) for curve 2; nonmagnetic middle FM^M with $k_F^M = 0.54$ Å⁻¹ for curve 3. (B) The scheme of magnetic configurations in DMTJ: the configuration (a) is $\uparrow - \uparrow (\downarrow) - \uparrow (\downarrow)$; the configuration (b) is $\uparrow - \downarrow (\uparrow) - \uparrow (\downarrow)$ (see arrows in the draw).

(Plot (A) is adapted from A.N. Useinov, L.X. Ye, N.K. Useinov, T.H. Wu, C.H. Lai, Anomalous tunnel magnetoresistance and spin transfer torque in magnetic tunnel junctions with embedded nanoparticles, *Sci. Rep.* 5 (2015) 18026, [https://doi.org/10.1038/srep18026\(2015\)](https://doi.org/10.1038/srep18026(2015)).)

As a result, the TMR amplitude depends on the aligned or antialigned coupling of the FM^M and FM^R magnetic moments. The difference in 0.004 \AA^{-1} between $k_{F,\uparrow}^M$ and $k_{F,\downarrow}^M$ in the middle FM^M layer is caused by the presence of external magnetic field. The case of nonmagnetic middle FM^M layer is considered for $k_F^M = 0.54 \text{ \AA}^{-1}$ (curve 3). The spin-resolved $k_{F,s}^M$ opens additional spin-dependent electron scattering in FM^M layer that alters the tunnel transparencies for the spin-up and spin-down electrons. At the same time, there are always several reasons in a real system, which reduce the theoretically estimated TMR magnitudes: the charge screening effect, interface and internal disorder, spin-flip scattering, domains in the layers, etc.

Details for the case of nonresonant tunneling will be presented in the next section, where the TMR versus the applied voltage V_a dependence for MTJ with embedded NPs (np-MTJ) of the size $d \lesssim 3.5 \text{ nm}$ will be mapped onto the DMTJ model with a thin, $L_M \lesssim 3.5 \text{ nm}$, middle FM^M layer.

The I - V curves in DMTJ with small $k_{F,\uparrow(\downarrow)}^M < 0.5 \text{ \AA}^{-1}$ behave more complicated at low temperature and can be attributed to the quantized conductance regime [44, 45]. This additional feature essentially modifies the I - V characteristics of np-MTJ against DMTJ.

11.4 Spin-Transfer Torque, Size Distribution, and Temperature-Related Effects in MTJs With Embedded Nanoparticles

The goals of this section are simulations of the TMR behavior as well as STT in np-MTJ at finite temperature taking into account size distribution of the NPs, Fig. 11.10A. These np-MTJs are equivalent to double-barrier junctions. Two experimental works [46, 48] were considered

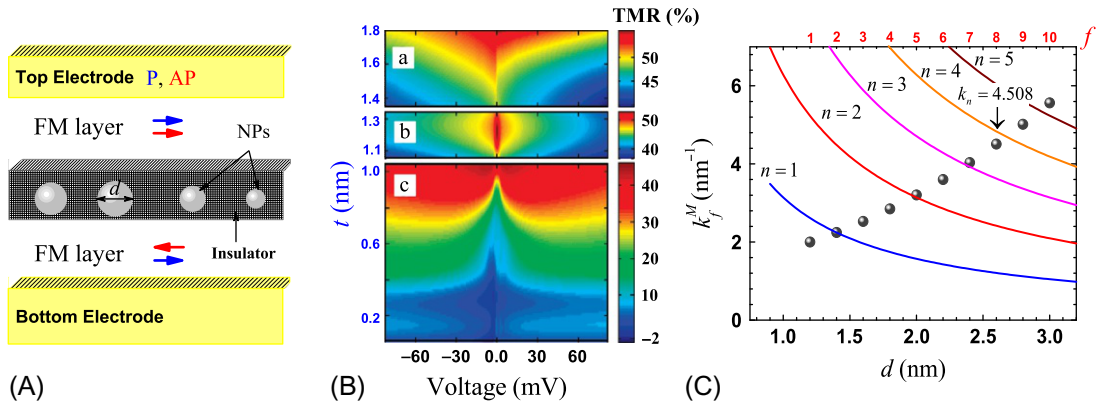


Fig. 11.10

(A) Schematic model of np-MTJ. Blue and dark arrows show parallel (P) and antiparallel (AP) magnetic configurations, respectively. Barrier thicknesses $L_{1(2)} = 10.0 \text{ \AA}$ are fixed. (B) The experimental data by Yang et al. [46] at $T = 250 \text{ mK}$. (C) The dark beads show initial distribution over k_f^M . Solid curves show ideal quantum well solution for $n = 1$ to $n = 5$ [47].

as a data source for the comparison with our numerical results. The first mentioned reference considers np-MTJ with the in-plane magnetic anisotropy on the basis of $\text{SiO}_2/\text{Ta}(10)/\text{Ir}_{22}\text{Mn}_{78}(25)/\text{Co}_{70}\text{Fe}_{30}(3.5)/\text{Mg}(0.8)/\text{MgO}(2.5)/\text{Co}_{70}\text{Fe}_{30}(t)/\text{Mg}(0.8)/\text{MgO}(2.5)/\text{Co}_{70}\text{Fe}_{30}(7)/\text{Ir}_{22}\text{Mn}_{78}(15)/\text{Ta}(10)$ structure (thicknesses in nm), which contains encapsulated $\text{Co}_{70}\text{Fe}_{30}$ NPs inside MgO barrier. This structure is characterized by the nominal FM^M thickness $t \sim 0.25\text{--}0.75$ nm which corresponds to the average NP diameters 1.53 ± 0.4 to 3.2 ± 0.7 nm, respectively. Parameter t is assigned with ideal deposition conditions of the flat homogeneous FM^M , while formation of NPs and their dispersion are results of clusterization. The experimental TMR- V_a data obtained at $T = 250$ mK are shown in Fig. 11.10B. The size dispersion is controlled by deposition rates, materials, annealing conditions, etc. The simplest way to find the NP size distribution is to make scanning tunnel microscope images of the front interface and cross-section of the middle layer.

According to the tunneling model, discussed in detail by Ciudad et al. [48], the tunneling conductance can be represented as a sum of three terms: $\sigma = \alpha\sigma_D + \beta(\sigma_E + \sigma_K)$, where $\alpha + \beta = 1$; σ_K is the conductance through NPs, which reveal Kondo behavior: σ_D and σ_E are the direct tunneling between electrodes through the dielectric barrier, and the elastic conductance through the NPs without spin flips, respectively.

The relative weight for α and β depends on the fractional population of clusters on one hand, and temperature on the other. The relationship between α and β changes also with the nominal FM^M thickness: it assumes $\alpha > \beta$ for thin layers since very few clusters are within the barrier, and direct tunneling between electrodes through the barrier dielectric dominates. When the intermediate FM^M layer thickness increases, it may become $\beta > \alpha$ since number and size of the clusters increase thus increasing the contribution of the current through NPs against the direct tunneling.

The relationship between σ_E and σ_K , and TMR as a consequence, depends on the layers thickness and temperature. If σ_K dominates, the TMR is reduced. If σ_E dominates, the TMR is enhanced at low temperatures because of cotunneling. The transitions are smooth, and crossover of the regimes, if any, depends on the sample design and temperature.

As a result, the consecutive, Kondo-assisted cotunneling and Coulomb blockade models, neglecting the direct tunneling, were used by Yang et al. and Ciudad et al. to explain anomalous TMR behaviors shown in Fig. 11.10B. On the contrary, it was theoretically shown recently that the regime of quantized conductance, which is observed in the range of ballistic (direct tunneling, $\alpha = 1$) transport, can be a main reason of anomalous TMR behaviors in np-MTJs [44, 45].

In these studies, np-MTJs were simulated as tunneling cells (TunCs) connected in parallel, where TunC is equivalent to the double-barrier junction containing one NP as a part of the middle layer, Fig. 11.10A. For simulations, the total amount of NPs was distributed over

10 fractions with the NP's diameters d_f , and the whole amount of NPs is $N_{\text{tot}} = \sum_f i_f = 100$, where i_f is the amount of NPs in the fraction f . The fraction is defined as a set of the TunCs with the same size of NPs (the spin or fraction index can be omitted for the presentation simplicity). In this model, we considered only coherent tunneling, $\alpha = 1$, where the current for each TunC or double-barrier subsystem is defined as follows:

$$I_{s,f} = \frac{e^2 k_{F,s}^2 d_f^2 V_a}{h} \times \int_{X_1}^{X_2} dx \int_0^{\theta_{\min}} \sin(\theta_s) \cos(\theta_s) D_s(\theta_s, k_{s,f}^M + x) d\theta_s, \quad (11.10)$$

where V_a is the applied voltage, and θ_{\min} is the angle constraint for θ_s , which arises from conservation of the parallel to the interface projections of the k -vectors;

$X_{1(2)} = \mp \sqrt{2m_{\text{eff}} k_B T / \hbar^2}$, and m_{eff} , k_B , and T are the effective electron mass, Boltzmann constant, and temperature, respectively; Eq. (11.3) was adapted for integration over the top incident electron angle θ_s , and $k_{F,s}$ is taken as a Fermi wavenumber of the top FM layer for positive voltage.

The transmission coefficient of the double-barrier system is a function of $k_{F,s}$ and θ_s , it is defined in Ref. [13] according to the standard definition of quantum mechanics. The consideration of the transmission coefficient at finite T is important when the electron energy $E = \hbar^2 (k_f^M)^2 / 2m_{\text{eff}}$ is comparable with $k_B T$. The modified quantum-ballistic approach (Eqs. 11.3, 11.10) can be used for description of the direct electron tunneling at finite T [11, 49]. The transverse wave number in NP, $k_{s,f}^M$, has deviation x , which is responsible for additional temperature-induced conduction band broadening. The $k_{s,f}^M$ is a key parameter, since the result of the integration in Eq. (11.10) is very sensitive to its value.

Among different insulating materials, MgO barrier is quite complex one due to complicated band structure [50, 51]. Single crystalline MgO induces enhancement of the spin polarization of the tunneling current, the filtering mostly affects $k_{F,\downarrow}$ and the related wave functions [1, 52]. In the present work, the band structure or the complex k -vector behavior for the barriers was not considered; however, $k_{F,s}^{L(R)}$ are assumed as effective, taking into account an impact of the MgO spin-filtering properties. In particular, $k_{F,\downarrow}$ value is reduced against the real one. The experimental and theoretical estimations for the k -values are accessed in Himpfel et al. [53] and Tagirov and García [54], respectively. The following simplified definition for the spin polarization, $P = (k_{F,\uparrow} - k_{F,\downarrow}) / (k_{F,\uparrow} + k_{F,\downarrow})$, was used to obtain $P = 0.443$ from the initial parameters: $k_{F,\uparrow}^{L(R)} = 1.09 \text{ \AA}^{-1}$, $k_{F,\downarrow}^{L(R)} = 0.421 \text{ \AA}^{-1}$.

The additional spin-filtering effect in the case of Al_2O_3 -based MTJ is absent. It assumes a decreased P , for example, $P = 0.27$ at $k_{F,\downarrow}^{L(R)} = 0.621 \text{ \AA}^{-1}$ for the same $k_{F,\uparrow}^{L(R)} = 1.09 \text{ \AA}^{-1}$. The low TMR amplitude with the maximum around 10–24% has been observed in Ref. [48] that was also confirmed by our calculations with $d = 2.63 \text{ nm}$ obtaining TMR around 16%. Nevertheless, the TMR- V_a and T behaviors as well as related quantum effects are similar to that for the MgO-based junctions.

The main results were found according to TMR definition

$$\text{TMR} = (I^P - I^{\text{AP}})/I^{\text{AP}},$$

where $I^{\text{P(AP)}} = \sum i_f (I_{\uparrow,f}^{\text{P(AP)}} + I_{\downarrow,f}^{\text{P(AP)}})$ and the $I_{s,f}^{\text{P(AP)}}$ were calculated making use of Eq. (11.10). The conductance σ of the system is defined as $\sigma^{\text{P(AP)}} = I^{\text{P(AP)}}/V_a$. The TMR at zero voltage is denoted by TMR_0 . The tunneling current, which passes through an insulator between NPs, was considered having negligible impact.

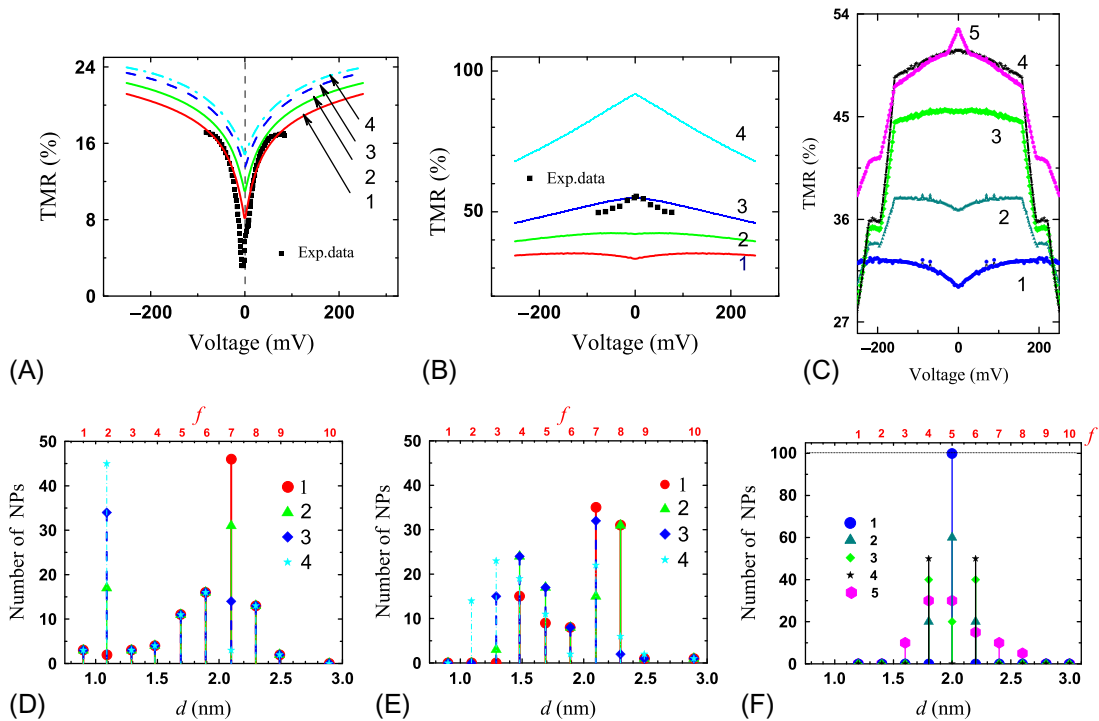
One of the important dynamic MTJ properties is the STT [55–57]. STT is determined by a vector which consists of parallel T_{\parallel} and perpendicular T_{\perp} components with respect to the interfaces. The parallel component T_{\parallel} vanishes at zero voltage, while at finite voltage it lies in the plane of the FM^L interface triggering additional magnetization fluctuation. The value of T_{\perp} is determined by the interlayer exchange interaction, which does not vanish at zero voltage, $T_{\perp} \neq 0$. Only T_{\parallel} component will be considered below, since we assume in our case $T_{\parallel} \gg T_{\perp}$. The parallel STT component is calculated as a difference between the spin current densities $\mathcal{J}^{\text{P(AP)}}$ [56, 57]:

$$T_{\parallel} = \frac{\sin(\gamma)}{2} (\mathcal{J}^P - \mathcal{J}^{\text{AP}}), \quad (11.11)$$

where $\mathcal{J}^{\text{P(AP)}} = \hbar (J_{\uparrow}^{\text{P(AP)}} - J_{\downarrow}^{\text{P(AP)}})/2e$, and γ is an angle between FMs magnetizations; $J_s^{\text{P(AP)}} = I_s^{\text{P(AP)}}/S_{\varphi}$ is the charge current density, and, finally, $S_{\varphi} = \frac{\pi}{4} \sum_{f=1 \dots 10} i_f d_f^2$ is the total active cross-section area of the np-MTJ. We continue our discussion starting with TMR.

The experimental data fitting for the dip-like TMR behavior [46] made according to the presented approach (11.10) and the quantum well (QW) quantization rule $k_{s,f}^M = n\pi/d_f - \Phi_f$ is shown in Fig. 11.11A and B, where the deviation Φ_f from the ideal QW solution was neglected. Fig. 11.11A and D demonstrates how NP size distribution influences the qualitative TMR versus voltage behavior: for example, in distribution 1 (Fig. 11.11D) the fraction $f = 7$ containing 47% of NPs with $d_{f=7} = 2.098$ nm dominates over the fraction $f = 2$ (3% of NPs), while in distribution 4 (Fig. 11.11D) the fraction $f = 2$ containing 45% of NPs with $d_{f=2} = 1.09$ nm dominates over the fraction $f = 7$ (3% of NPs). Correspondingly, distribution 1 with lowest k_f^M and largest d produces lowest TMR with dip-like feature (Fig. 11.11A curve 1). Thus, the suppressed TMR_0 is a result of low k_f^M with quantization $n = 1$. Moreover, the TunCs with the largest NPs by size and thinnest barriers provide most significant contribution to the total ballistic current.

Tunneling magnetoresistance as a function of the applied voltage is strongly modified at $n = 2$ (Fig. 11.11B). The gradual TMR variations show initially suppressed TMR at low voltages (curve 1) or dome-like behavior (curve 4) that depends on the size distributions (i_f , Fig. 11.11E). Fig. 11.11E represents the distributions of NPs with relatively small ($d < 1.7$ nm) and middle size (1.7–2.5 nm) NP fractions dominating. All initial $k_{f,s}^M$ are different for the each fraction


Fig. 11.11

TMR versus voltage in the presence of size distributions. Panel (A) shows four TMR- V_a curves for different NP size distributions depicted below in the window (D). The ideal QW approach is used for calculations, the initial values $k_f^M = n\pi/d_f$ at $n = 1$. (B) The TMR- V_a curves for $n = 2$ and distributions given below in window (E). (C) TMR- V_a curves for the system at $d_{av} = 2.0$ nm with different distributions are shown in window (F). (D), (E), and (F) windows represent the NP size distributions for the curves depicted in windows (A), (B), and (C), respectively. Experimental data at $t = 0.45$ nm and $t = 1.79$ nm obtained from Ref. [46] are shown in (A) and (B), respectively. All presented data were simulated within the low-temperature approach or measured at low temperatures. (*Adapted from A. Useinov, H.H. Lin, C.H. Lai, Symmetric and asymmetric magnetic tunnel junctions with embedded nanoparticles: effects of size distribution and temperature on tunneling magnetoresistance and spin transfer torque, Sci. Rep. 7 (2017) 8357, <https://doi.org/10.1038/s41598-017-08354-7>.*)

according to the quantization rule. The formation of the lowest TMR_0 , with the dip-like behavior, refers to the fraction with smallest k_f^M (curve 1) that is similar to the case of $n = 1$. The small k_f^M values correspond to NPs distribution with largest average NP size, $d_{av} = N_{tot}^{-1} \sum i_f d_f$. The calculated TMR curves satisfactorily reproduce experimental data for this case, for example, Figs. 4 and S6 from Ref. [46]; however, TMR behavior (with respect to the parameter t) is opposite to the experimental observations for $d_{av} > 1.8$ nm. Thus, it might be more rational explanation when k_f^M increases with increase of d_f too. It is assumed that there is a size threshold at $d_{av} \approx 1.8$ nm ($t \approx 0.8$ nm) between quasi-0D and bulk-assisted states in the middle conducting layer, and thus, QW quantization rule has to be changed.

To reproduce the experimental data more precisely as a matter of correlation between the growing thickness t of the middle layer and the TMR response, an initial k_f^M distribution with the low quantization degree was considered in a range of weak parabolic dependence for $1.1 \text{ nm} < d < 3.5 \text{ nm}$ (dark beads in Fig. 11.10C). Nevertheless, this distribution can be also treated as QW quantization corrected by Φ_f .

The result of the TMR- V_a behavior at different NP size distributions for the fixed $d_{av} = 2.0 \text{ nm}$ is shown in Fig. 11.11C, where curve 1 corresponds to the dip-like behavior with relatively small $k_f^M = 3.2 \text{ nm}^{-1}$. Curve 1 shows similar behavior to the experimental data depicted in the region **c**, Fig. 11.10B. The peak-like TMR enhancement at low voltages has been observed when fraction with critical parameters of the quantized (step-like) conductance becomes a part of the distribution (i.e., curve 5, Fig. 11.11C). At the same time, the maximal TMR_0 value is formed by the distribution No. 5, which is less uniform, Fig. 11.11F. It is worthy to notice that the most valuable impact on the I - V curves and TMR amplitude is exerted by TunCs with largest k_f^M values, which correspond to the fractions with largest d , according to the related distribution of the k -values versus d . As a result, it means that homogeneously deposited middle layer between barriers, which has the maximal thickness to perform the coherent tunneling, is an important condition for the highest TMR in a double-barrier system. The fraction $f = 8$ satisfies the critical conditions to observe the quantum conductance. The TMR peaks ($4.504 \text{ nm}^{-1} < k_f^M < 4.509 \text{ nm}^{-1}$ for $d = 2.6 \text{ nm}$) or TMR dips ($k_f^M < 4.0 \text{ nm}^{-1}$) highlighted on Fig. 11.12A correspond to the steps of conductance shown in Fig. 11.12B. Such kind of behavior is a consequence of quantized conductance regime of the electron motion in the confined conditions. The rapid growth of the system transparency at the threshold voltage is caused by opening of additional sectors of angles for the electron trajectories to transmit, as well as transmission enhancement itself due to gradual growth of k_f^M with the voltage. The conductance steps are localized at the regions of the small voltages or the finite critical voltages in the cases of peak- or dip-like TMR behaviors, respectively.

Fig. 11.12C shows TMR- V_a dependencies with consecutive increasing of the NPs size without distribution, while Fig. 11.12D demonstrates the modified TMR curves according to valuable impacts from the nearest fractions. The squares, stars, and circles in Fig. 11.12C and D show extracted experimental data of **a**, **b**, and **c** regions in Fig. 11.10B, respectively.

According to the results, curves 2, 3, 5 in Fig. 11.12C and 1–4 in Fig. 11.12D fit the region **c**. Curves 6 and 7 in Fig. 11.12D are similar to curve 8 in Fig. 11.12C, which corresponds to the region **b**. Finally, curve 9 in Fig. 11.12C and curves 8, 9 in Fig. 11.12D are assigned to the region **a**. Similar experimental behaviors for all these regions can be found in Ref. [48] too. As a result, the presented theoretical model is able to reproduce experimental TMR behaviors with respect to NPs size and k_f^M distributions. The reduced experimental TMR values with respect to the theoretical ones might be related to uncounted spin-flip leakages as well as nonideally oriented magnetizations of magnetic domains.

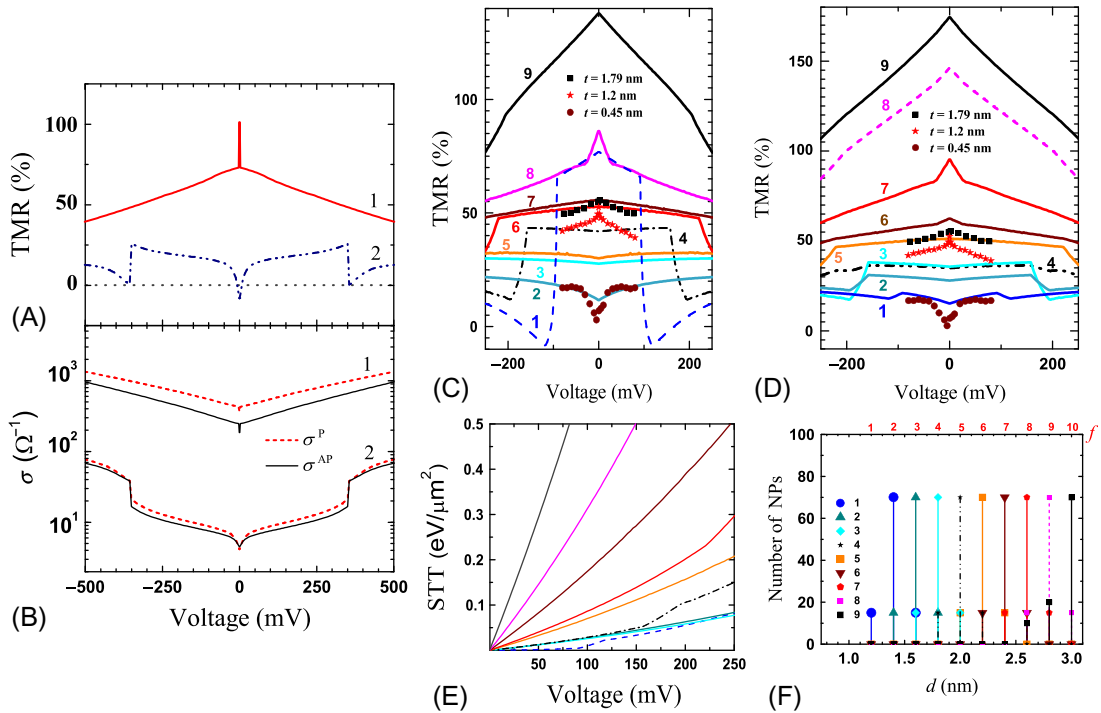


Fig. 11.12

The peak- and dip-like TMR within the extended voltage range. (A) Curve 1 shows clear impact of the peak-like TMR for $i_{f=8} = 100$, $k_f^M = 4.08 \text{ nm}^{-1}$; Curve 2 shows TMR₀ = -8% at $V_a \rightarrow 0$, $T \rightarrow 0$, $k_f^M = 1.15 \text{ nm}^{-1}$. (B) The step-like quantized conductance with the voltage thresholds according to Ref. [44]. (C) TMR- V_a in the case of low degree of quantization for $i_{f=1\dots 9} = N_{\text{tot}}$, curves 1 to 9.

(D) TMR- V_a modifications due to impact from the nearest fractions. (E) Spin transfer torque simulations for the related curves with low degree of quantization (identified by line types).

(F) shows the size distributions for the TMR curves from (D). Squares, stars, and circles are the experimental data extracted from Fig. 11.10B. (Panels (C) and (D) are adapted from A. Useinov, H.H. Lin, C.H. Lai, Symmetric and asymmetric magnetic tunnel junctions with embedded nanoparticles: effects of size distribution and temperature on tunneling magnetoresistance and spin transfer torque, *Sci. Rep.* 7 (2017) 8357, <https://doi.org/10.1038/s41598-017-08354-7>.)

The simulation predicts the step-like quantized TMR and STT behaviors derived at low temperature. The threshold voltages corresponding to the step-like TMR behaviors are obtained as follows: curves 2–5 at $V_a \approx 170\text{--}190 \text{ mV}$ in Fig. 11.11C, or curve 4 in Fig. 11.12C. The voltage threshold occurs by cause of quantum confinement and related conditions for the quantized conductance, the additionally opened conduction channels abruptly change mutual weights of σ^P and σ^{AP} at the threshold.

Moreover, the reason of the step-like TMR, curve 1 in Fig. 11.12C, is assumed to be different and related to the k_f^M threshold. The electron wave function shows deficiency of any quantum

interference for $d_{f=1} = 1.2$ nm at $V_a \approx 0.1-100$ mV, because k_f^M becomes too small. Conduction electrons are involved only in single-barrier tunneling, because electron wavelength is large enough. The conditions of tunneling drastically change regarding k_f^M and $k_{F,s}^R$ behaviors with applied voltage. The double-barrier direct tunneling arises at $|V_a| > 100$ mV again, shifting the TMR magnitude into the negative range. Similar TMR behavior is weakly highlighted in Fig. 11.10B at $t < 0.2$ nm, where the single-barrier tunneling voltage range is a few mV, and it is much smaller compared with theoretical curve 1 (Fig. 11.12C) which might be due to intermixing of the possible impacts from nearest fractions.

The in-plane STT components shown in Fig. 11.12E were calculated for $i_{f=1\dots 10} = N_{\text{tot}}$ (no distribution at the every case). The kinks on STT curves correlate with the TMR curves in Fig. 11.12C, which may have abrupt steps due to the mentioned thresholds. The STT steps potentially can be used in spintronic devices for the voltage control of magnetic states. Moreover, STT has a strong dependence on d , for example, the STT amplitude rapidly increases by order of magnitude, from ~ 0.1 to 1.0 eV μm^{-2} at $V_a = 250$ mV (see Fig. 11.12E), when growing NP size in the range given by Fig. 11.12F.

The model can be also adapted for TMR simulations in asymmetric np-MTJs when the voltage drops are proportional to the nonequal barrier widths. Examples of the asymmetric TMR curves are shown in Fig. 11.13A and B for $L_1 = 1.0$ nm, $L_2 = 0.9$ nm ($d_{\text{av}} = 1.45$ nm) and $L_1 = 0.9$ nm, $L_2 = 1.0$ nm ($d_{\text{av}} = 2.63$ nm), respectively. The negative and positive TMR- V_a curves reproduce asymmetric TMR behaviors, which are highlighted for experimental data in Fig. 11.10B at $t \approx 0.2$ nm, $t \approx 0.5$ nm (region c) and $t \approx 1.6$ nm (region a). The quantization rule is kept as the weak parabolic dependence denoted by black beads in Fig. 11.10C, the related size distribution is shown in Fig. 11.13C. The barriers' width scatter in real structures is a result of the lattice defects and nonideal NPs' shapes: even 1 Å of difference in the barriers' width gives significant impact. Fig. 11.13D shows TMR evolution with T in symmetric np-MTJ at $d_{\text{av}} = 1.45$ nm. A transition from the dip-like to the weak dome-like behavior occurs due to T variation from 250 mK to 300 K, respectively. The derived temperature dependence correlates with the experimental results, whereas TMR₀ dip was observed only at low T [46]. The dependence is strong enough, because related $k_{f=1\dots 3}^M$ values are relatively small compared with the other case $d_{\text{av}} = 2.63$ nm, Fig. 11.13B. Moreover, the peak-like TMR (e.g., curve 5 in Fig. 11.11C and curve 8 in Fig. 11.12C) and step-like TMR behaviors (e.g., curves 2–5, Fig. 11.11C) in the case of room temperature will be strongly averaged, having the dome-like shapes.

Thereafter, an induced in-plane STT was calculated for the different cases of barrier asymmetry in the bottom FM^L at low temperature, Fig. 11.14. In particular, curve 3 shows valuable difference of the STT voltage dependence for the negative and positive voltage branches, for example, the ratio of the STT values is $T_{\parallel}(V_a = -20 \text{ mV})/T_{\parallel}(V_a = +20 \text{ mV}) \approx 5$, which grows up to ≈ 6 at $|V_a| > 250$ mV due to weak nonlinear behavior. The STT curves were simulated at $d_{\text{av}} = 2.63$ nm for the NP size distribution shown in Fig. 11.13C. All STT curves in the present work were derived at $\gamma = \pi/2$ see Eq. (11.11), where the STT amplitude is maximal.

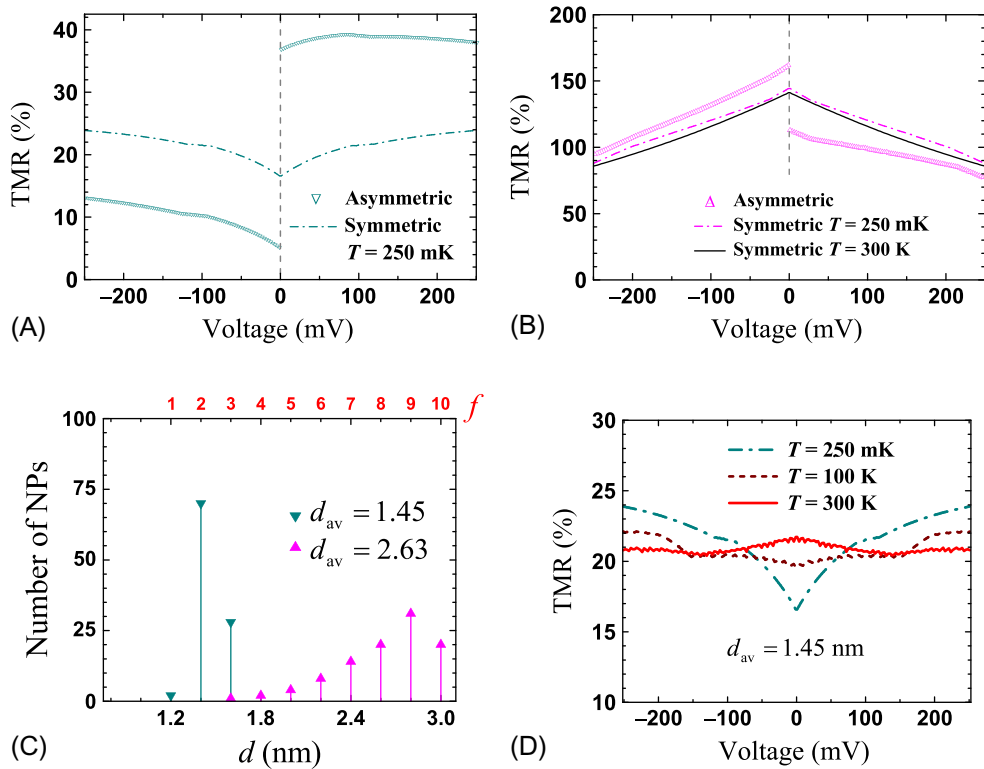


Fig. 11.13

TMR versus voltage in its dependence on the NP size distributions, temperature, and barrier asymmetry. (A) Symmetric ($L_1 = L_2 = 1.0$ nm) and asymmetric ($L_1 = 1.0$ nm, $L_2 = 0.9$ nm) TMR at low temperature and NP size distribution depicted on the panel (C) and containing fractions $f = 1, 2, 3$ with $d_{av} = 1.45$ nm. (B) Symmetric ($L_1 = L_2 = 1.0$ nm) and asymmetric ($L_1 = 0.9$ nm, $L_2 = 1.0$ nm)

TMR at low and room temperatures and NP size distribution depicted on the panel (C) and containing fractions $f = 5-10$ with $d_{av} = 2.63$ nm. Asymmetric curves reproduce the experimental data from Fig. 11.10B for the regions with high t (a) and low t (c), respectively. (D) The evolution of the symmetric TMR- V curve, depicted on the panel (A), with temperature. (Adapted from A. Useinov, H.H. Lin, C.H. Lai, *Symmetric and asymmetric magnetic tunnel junctions with embedded nanoparticles: effects of size distribution and temperature on tunneling magnetoresistance and spin transfer torque*, *Sci. Rep.* 7 (2017) 8357, <https://doi.org/10.1038/s41598-017-08354-7>.)

11.5 Conclusions

The enhanced model of nanoscale point contacts, which is demonstrated here, allows to find I - V curves and MR values of various magnetically and electrically inhomogeneous systems (domain walls, tunnel junctions, point-like contacts, np-MTJ, etc.). The model is based on calculation of conductance, which is fully determined by quantum mechanical transmission of the contact area. The complete equation for the conductance includes ballistic and diffusive

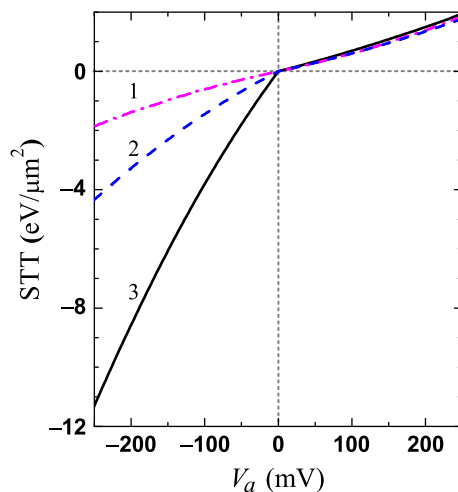


Fig. 11.14

Symmetric and asymmetric STT voltage dependence at $T = 250$ mK. Curves 1, 2, and 3 correspond to $L_1 = 1.0$ nm, $L_2 = 0.9$ nm, and $L_2 = 0.8$ nm for the fixed $L_2 = 1.0$ nm, respectively. (Adapted from A. Useinov, H.H. Lin, C.H. Lai, *Symmetric and asymmetric magnetic tunnel junctions with embedded nanoparticles: effects of size distribution and temperature on tunneling magnetoresistance and spin transfer torque*, *Sci. Rep.* 7 (2017) 8357, <https://doi.org/10.1038/s41598-017-08354-7>.)

regimes as well as transition between them without rudiment terms. In a case of point-like contacts, the optimal condition to obtain maximal MR was found for symmetric magnetic junctions. Furthermore, the methodology was successfully extended from single-barrier to double-barrier MTJs, explaining details of the tunneling magnetoresistance for different conditions and showing the reasonable fitting to the experimental data.

Additional complicated problem such as np-MTJ was formulated in terms of parallel connection of TunCs. The TunC by itself is equivalent to a double-barrier junction from one hand, it approaches the point-like contact from the other hand when NP touches the both FM leads. The TMR effects were studied at low voltage in terms of various NPs size distributions, which become important for the np-MTJs. The dimensional quantization of conducting properties is observed in these systems. In terms of TMR efficiency, the case of the uniform middle layer with maximal thickness, which allows the coherent tunneling only, provides the largest TMR in comparison to any other size distributions. It was demonstrated that TMR and in-plane STT dependencies on voltage may have quantized step-like features at low temperatures.

Finally, the calculated np-MTJ asymmetries and temperature impacts are in accordance with the TMR- V_a characteristics observed experimentally. Moreover, it was found that barrier asymmetry is very promising route for applications, since STT becomes highly sensitive to the voltage polarity. The derived results may potentially reveal an additional hidden origins of the

spin dynamics in np-MTJs, for example, utilizing the spin-torque magnetic resonance technique for superparamagnetic NPs in MgO-based MTJs by using spin-torque diode effect [58]. Asymmetric STT effect may improve possible MRAM benefits, which can be fabricated as a system of uniform DMTJ or np-MTJ cells. The demonstrated asymmetry can be used to write a bit or initiate magnetization state switching by negative voltage pulse, since STT is large, while it is more convenient to read a bit in a positive voltage range, where STT is small.

Acknowledgments

N.Kh. Useinov and L.R. Tagirov acknowledge partial support by the Program of Competitive Growth of Kazan Federal University.

References

- [1] W.H. Butler, Tunneling magnetoresistance from a symmetry filtering effect, *Sci. Technol. Adv. Mater.* 9 (2008) 014106, <https://doi.org/10.1088/1468-6996/9/1/014106>.
- [2] M.N. Baibich, J.M. Broto, A. Fert, F.N. Van Dau, F. Petroff, P. Eitenne, G. Greuzet, A. Friederich, J. Chazelas, Giant magnetoresistance of (001)Fe/(001)Cr magnetic superlattices, *Phys. Rev. Lett.* 61 (1988) 2472, <https://doi.org/10.1103/PhysRevLett.61.2472>.
- [3] G. Binash, P. Grünberg, F. Saurenbach, W. Zinn, Enhanced magnetoresistance in layered magnetic structures with antiferromagnetic interlayer exchange, *Phys. Rev. B.* 39 (1989) 4828(R), <https://doi.org/10.1103/PhysRevB.39.4828>.
- [4] W.P. Pratt, S.F. Lee Jr., J.M. Slaughter, R. Loloee, P.A. Schroeder, J. Bass, Perpendicular giant magnetoresistances of Ag/Co multilayers, *Phys. Rev. Lett.* 66 (1991) 3060, <https://doi.org/10.1103/PhysRevLett.66.3060>.
- [5] M. Julliere, Tunneling between ferromagnetic films, *Phys. Lett. A* 54 (1975) 225–226, [https://doi.org/10.1016/0375-9601\(75\)90174-7](https://doi.org/10.1016/0375-9601(75)90174-7).
- [6] J.C. Slonczewski, Current-driven excitation of magnetic multilayers, *J. Magn. Magn. Mater.* 159 (1996) L1–L7, [https://doi.org/10.1016/0304-8853\(96\)00062-5](https://doi.org/10.1016/0304-8853(96)00062-5).
- [7] L. Berger, Emission of spin waves by a magnetic multilayer traversed by a current, *Phys. Rev. B* 54 (1996) 9353, <https://doi.org/10.1103/PhysRevB.54.9353>.
- [8] L.R. Tagirov, B.P. Vodopyanov, K.B. Efetov, Ballistic versus diffusive magnetoresistance of a magnetic point contact, *Phys. Rev. B* 63 (2001) 104468, <https://doi.org/10.1103/PhysRevB.63.104428>.
- [9] A. Useinov, R. Deminov, L. Tagirov, G. Pan, Giant magnetoresistance in nanoscale ferromagnetic heterocontacts, *J. Phys. Condens. Matter* 19 (2007) 196215, <https://doi.org/10.1088/0953-8984/19/19/196215>.
- [10] N.K. Useinov, Semiclassical Green's functions of magnetic point contacts, *Theor. Math. Phys.* 183 (2015) 705–714, <https://doi.org/10.4213/tmf8786>.
- [11] A.N. Useinov, C.H. Lai, Tunnel magnetoresistance and temperature related effects in magnetic tunnel junctions with embedded nanoparticles, *SPIN* 6 (1) (2016) 165000, <https://doi.org/10.1142/S2010324716500016>.
- [12] A. Useinov, H.H. Lin, N. Useinov, L.R. Tagirov, Quantum point contact: a case of spin-resolved electron transport, 2017 pp. 1–20, e-Print, ArXiv: 1710.00496v1.
- [13] A. Useinov, J. Kosel, N.K. Useinov, L.R. Tagirov, Resonant tunnel magnetoresistance in double-barrier planar magnetic tunnel junctions, *Phys. Rev. B* 84 (2011) 085424, <https://doi.org/10.1103/PhysRevB.84.085424>.
- [14] R.G. Deminov, N.K. Useinov, L.R. Tagirov, Magnetic and superconducting heterostructures in spintronics, *Magn. Reson. Solids Electron. J.* 16 (2014) 14209.
- [15] Y.V. Sharvin, A possible method for studying Fermi surfaces, *Sov. Phys. JETP* 21 (1965) 655–656.

- [16] G. Wexler, The size effect and the non-local Boltzmann transport equation in orifice and disk geometry, *Proc. Phys. Soc.* 89 (1966) 927–941, <https://doi.org/0370-1328/89/4/316>.
- [17] R.S. Timsit, Electrical conduction through small contact spots, in: *Proceedings of the 50th IEEE Holm Conference on Electrical Contacts and the 22nd International Conference on Electrical Contacts*, 2004, pp. 184–191.
- [18] A. Mikrajuddin, F. Shi, H. Kim, K. Okuyama, Size-dependent electrical constriction resistance for contacts of arbitrary size: from Sharvin to Holm limits, *Mater. Sci. Semicond. Process.* 2 (1999) 321–327, [https://doi.org/10.1016/S1369-8001\(99\)00036-0](https://doi.org/10.1016/S1369-8001(99)00036-0).
- [19] N. García, M. Muñoz, Y.W. Zhao, Magnetoresistance in excess of 200% in ballistic Ni nanocontacts at room temperature and 100 Oe, *Phys. Rev. Lett.* 82 (14) (1999) 2923, <https://doi.org/10.1103/PhysRevLett.82.2923>.
- [20] G. Tataru, Y.W. Zhao, M. Muñoz, N. García, Domain wall scattering explains 300% ballistic magnetoconductance of nanocontacts, *Phys. Rev. Lett.* 83 (10) (1999) 2030, <https://doi.org/10.1103/PhysRevLett.83.2030>.
- [21] N. García, M. Muñoz, Y.W. Zhao, Ballistic magnetoresistance in transition-metal nanocontacts: the case of iron, *Appl. Phys. Lett.* 76 (18) (2000) 2586, <https://doi.org/10.1063/1.126416>.
- [22] Y.W. Zhao, M. Muñoz, G. Tataru, N. García, From ballistic to non-ballistic magnetoresistance in nanocontacts: theory and experiments, *J. Magn. Magn. Mater.* 223 (2001) 169–174, [https://doi.org/10.1016/S0304-8853\(00\)00750-2](https://doi.org/10.1016/S0304-8853(00)00750-2).
- [23] N. García, M. Muñoz, G.G. Qian, H. Rohrer, I.G. Saveliev, Y.W. Zhao, Ballistic magnetoresistance in a magnetic nanometer sized contact: an effective gate for spintronics, *Appl. Phys. Lett.* 79 (2001) 4550, <https://doi.org/10.1063/1.1427152>.
- [24] M.R. Sullivan, D.A. Boehm, D.A. Ateya, S.Z. Hua, H.D. Chopra, Ballistic magnetoresistance in nickel single-atom conductors without magnetostriction, *Phys. Rev. B* 71 (2005) 024412, <https://doi.org/10.1103/PhysRevB.71.024412>.
- [25] H.D. Chopra, M.R. Sullivan, J.N. Armstrong, S.Z. Hua, The quantum spin-valve in cobalt atomic point contacts, *Nat. Mater.* 4 (2005) 832–837, <https://doi.org/10.1038/nmat1510>.
- [26] H. Imamura, N. Kobayashi, S. Takahashi, S. Maekawa, Conductance quantization and magnetoresistance in magnetic point contacts, *Phys. Rev. Lett.* 84 (2000) 1003, <https://doi.org/10.1103/PhysRevLett.84.1003>.
- [27] A.K. Zvezdin, A.F. Popkov, Effect of domain boundary on the electrical conductivity of a magnetic nanocontact, *JETP Lett.* 71 (2000) 209–212, <https://doi.org/10.1134/1.568317>.
- [28] P. Bruno, Geometrically constrained magnetic wall, *Phys. Rev. Lett.* 83 (1999) 2425, <https://doi.org/10.1103/PhysRevLett.83.2425>.
- [29] L.L. Savchenko, A.K. Zvezdin, A.F. Popkov, K.A. Zvezdin, Magnetic configurations in the region of a nanocontact between ferromagnetic bars, *Phys. Solid State* 43 (2001) 1509, <https://doi.org/10.1134/1.1395092>.
- [30] V.A. Molyneux, V.V. Osipov, E.V. Ponizovskaya, Stable two- and three-dimensional geometrically constrained magnetic structures: the action of magnetic fields, *Phys. Rev. B* 65 (2002) 184425, <https://doi.org/10.1103/PhysRevB.65.184425>.
- [31] Y. Labaye, L. Berger, J.M.D. Coey, Domain walls in ferromagnetic nanoconstriction, *J. Appl. Phys.* 91 (2002) 5341, <https://doi.org/10.1063/1.1461065>.
- [32] B.A. Gurney, V.S. Speriosu, J.P. Nozieres, H. Lefakis, D.R. Wilhoit, O.U. Need, Direct measurement of spin-dependent conduction-electron mean free paths in ferromagnetic metals, *Phys. Rev. Lett.* 71 (1993) 4023, <https://doi.org/10.1103/PhysRevLett.71.4023>.
- [33] B.J. Dieny, Giant magnetoresistance in spin-valve multilayers, *J. Magn. Magn. Mater.* 136 (1994) 335–359, [https://doi.org/10.1016/0304-8853\(94\)00356-4](https://doi.org/10.1016/0304-8853(94)00356-4).
- [34] A.N. Useinov, L.R. Tagirov, R.G. Deminov, Y. Zhou, G. Pan, Mean-free path effects in magnetoresistance of ferromagnetic nanocontacts, *Eur. Phys. J. B* 60 (2007) 187–192, <https://doi.org/10.1140/epjb/e2007-00335-8>.
- [35] J. Mathon, Phenomenological theory of giant magnetoresistance, in: M. Ziese, M.J. Thornton (Eds.), *Spin Electronics 2001*, Springer-Verlag, Berlin, Heidelberg, 2001, p. 569, <https://doi.org/10.1007/3-540-45258-3>.

- [36] N. García, Y.W. Zhao, M. Muñoz, I.G. Saveliev, Magnetoresistance in ballistic nanocontacts and its manipulation in electrodeposited nanometric Ni contacts, *IEEE Trans. Magn.* 36 (2000) 2833, <https://doi.org/10.1109/20.908602>.
- [37] D.Y. Petrovykh, K.N. Altmann, H. Hochst, M. Laubscher, S. Maat, G.J. Mankey, F.J. Himpsel, Spin-dependent band structure, Fermi surface, and carrier lifetime of permalloy, *Appl. Phys. Lett.* 73 (1998) 3459, <https://doi.org/10.1063/1.122796>.
- [38] K.N. Altmann, N. Gilman, J. Hayoz, R.F. Willis, F.J. Himpsel, Effect of magnetic doping on the electronic states of Ni, *Phys. Rev. Lett.* 87 (2001) 137201, <https://doi.org/10.1103/PhysRevLett.87.137201>.
- [39] A.N. Useinov, R.G. Deminov, N.K. Useinov, L.R. Tagirov, Tunneling magnetoresistance in ferromagnetic planar hetero-nanojunctions, *Phys. Status Solidi B* 247 (2010) 1797–1801, <https://doi.org/10.1002/pssb.200945565>.
- [40] E.O. Kane, Basic concepts of tunneling, in: E. Burstein, S. Lundqvist (Eds.), *Tunneling Phenomena in Solids*, Plenum Press, New York, NY, 1969, pp. 1–11.
- [41] D. Djayaprawira, K. Tsunekawa, M. Nagai, H. Maehara, S. Yamagata, N. Watanabe, S. Yuasa, Y. Suzuki, K. Ando, 230% room-temperature magnetoresistance in CoFeB/MgO/CoFeB magnetic tunnel junctions, *Appl. Phys. Lett.* 86 (2005) 092502, <https://doi.org/10.1063/1.1871344>.
- [42] A. Useinov, J. Kosel, Spin asymmetry calculations of the *TMR-V* curves in single and double-barrier magnetic tunnel junctions, *IEEE Trans. Magn.* 47 (10) (2011) 2724–2727, <https://doi.org/10.1109/TMAG.2011.2153182>.
- [43] A. Useinov, O. Mryasov, J. Kosel, Output voltage calculations in double barrier magnetic tunnel junctions with asymmetric voltage behavior, *J Magn. Magn. Mater.* 324 (2012) 2844–2848, <https://doi.org/10.1016/j.jmmm.2012.04.025>.
- [44] A.N. Useinov, L.X. Ye, N.K. Useinov, T.H. Wu, C.H. Lai, Anomalous tunnel magnetoresistance and spin transfer torque in magnetic tunnel junctions with embedded nanoparticles, *Sci. Rep.* 5 (2015) 18026, [https://doi.org/10.1038/srep18026\(2015\)](https://doi.org/10.1038/srep18026(2015)).
- [45] A.N. Useinov, N.K. Useinov, L.X. Ye, T.H. Wu, C.H. Lai, Tunnel magnetoresistance in magnetic tunnel junctions with embedded nanoparticles, *IEEE Trans. Magn.* 51 (11) (2015) 4401404, <https://doi.org/10.1109/TMAG.2015.2451705>.
- [46] H. Yang, S.H. Yang, S.S. Parkin, Crossover from Kondo-assisted suppression to co-tunneling enhancement of tunneling magnetoresistance via ferromagnetic nanodots in MgO tunnel barriers, *Nano Lett.* 8 (1) (2008) 340–344, <https://doi.org/10.1021/nl072930n>.
- [47] A. Useinov, H.H. Lin, C.H. Lai, Symmetric and asymmetric magnetic tunnel junctions with embedded nanoparticles: effects of size distribution and temperature on tunneling magnetoresistance and spin transfer torque, *Sci. Rep.* 7 (2017) 8357, <https://doi.org/10.1038/s41598-017-08354-7>.
- [48] D. Ciudad, Z.C. Wen, A.T. Hindmarch, E. Negusse, D.A. Arena, X.F. Han, C.H. Marrows, Competition between cotunneling, Kondo effect, and direct tunneling in discontinuous high-anisotropy magnetic tunnel junctions, *Phys. Rev. B* 85 (11) (2012) 214408, <https://doi.org/10.1103/PhysRevB.85.214408>.
- [49] A. Useinov, L.X. Ye, C.L. Yang, N. Useinov, H.H. Lin, C.H. Lai, Calculation of tunnel magnetoresistance in magnetic tunnel junctions with particle size dispersion, *IEEE Magn. Lett.* 7 (2016) 3108203, <https://doi.org/10.1109/LMAG.2016.2614801>.
- [50] K.D. Belashchenko, J. Velev, E.Y. Tsymbal, Effect of interface states on spin-dependent tunneling in Fe/MgO/Fe tunnel junctions, *Phys. Rev. B* 72 (2005) 140404(R), <https://doi.org/10.1103/PhysRevB.72.140404>.
- [51] E.Y. Tsymbal, I. Žutić, *Handbook of Spin Transport and Magnetism*, Taylor and Francis Group, LLC, London, 2012.
- [52] X.G. Zhang, W.H. Butler, Large magnetoresistance in bcc Co/MgO/Co and FeCo/MgO/FeCo tunnel junctions, *Phys. Rev. B* 70 (2004) 172407, <https://doi.org/10.1103/PhysRevB.70.172407>.
- [53] F.J. Himpsel, K.N. Altmann, G.J. Mankey, J.L. Ortega, D.Y. Petrovykh, Electronic states in magnetic nanostructures, *J. Magn. Magn. Mater.* 200 (1999) 456–469, [https://doi.org/10.1016/S0304-8853\(99\)00349-2](https://doi.org/10.1016/S0304-8853(99)00349-2).

- [54] L.R. Tagirov, N. García, Quasiclassical boundary conditions for a contact of two metals, *Superlattices Microstruct.* 41 (2007) 152–162, <https://doi.org/10.1016/j.spmi.2006.08.002>.
- [55] D.C. Ralph, M.D. Stiles, Spin transfer torques, *J. Magn. Magn. Mater.* 320 (2008) 1190–1216, <https://doi.org/10.1016/j.jmmm.2007.12.019>.
- [56] I. Theodonis, N. Kioussis, A. Kalitsov, M. Chshiev, W.H. Butler, Anomalous bias dependence of spin torque in magnetic tunnel junctions, *Phys. Rev. Lett.* 97 (2006) 237205, <https://doi.org/10.1103/PhysRevLett.97.237205>.
- [57] A. Kalitsov, W. Silvestre, M. Chshiev, J.P. Velev, Spin torque in magnetic tunnel junctions with asymmetric barriers, *Phys. Rev. B* 88 (2013) 104430, <https://doi.org/10.1103/PhysRevB.88.104430>.
- [58] S. Miwa, S. Park, S. Kim, Y. Jo, N. Mizuochi, T. Shinjo, Y. Suzuki, Enhancement of spin diode signals from Fe nanoparticles in MgO-based magnetic tunnel junctions, *Appl. Phys. Express* 5 (2012) 123001, <https://doi.org/10.1143/APEX.5.123001>.

Further Reading

- [1] A.N. Useinov, L.R. Tagirov, R.G. Deminov, N.K. Useinov, Giant magnetoresistance of nanoscale ferromagnetic heterocontacts, *Kazan. Gos. Univ. Uchen. Zap. Ser. Fiz. Mater. Nauki* 149 (3) (2007) 5–30.

An Overview of Spin Crossover Nanoparticles[☆]

David J. Harding

Walailak University, Nakhon Si Thammarat, Thailand

12.1 Introduction to Spin Crossover

Spin crossover (SCO) compounds are among the best-studied molecular switches. Their switchability arises from the presence of two magnetic states, termed high spin (HS) and low spin (LS), which are close in energy [1–4]. A particular advantage of SCO compounds is that a range of different stimuli can be used to interconvert between the two spin states, including temperature [5–7], pressure [8,9], light [10,11], or application of a magnetic field [12] (Fig. 12.1). The movement of the electrons from the t_{2g} to the e_g set, or vice versa, causes significant changes in the structural, magnetic, optical, spectroscopic, and mechanical properties of the material. This allows a wide range of potential applications for SCO materials [13,14].

Although SCO may occur in any *pseudo*-octahedral transition metal compound with a $3d^A-3d^7$ electron configuration [15–19], most studies concern Fe(II) [20–25], and this will be the focus of the following discussion. Structural changes associated with SCO are usually studied by X-ray crystallography with the Fe-ligand bond lengths shorter in the LS state than the HS state by *ca.* 0.20 Å [26,27]. The coordination sphere also becomes more regular with the molecular volume shrinking by on average 10%. The change in the number of unpaired electrons can be monitored by magnetometric techniques with SQUID (superconducting quantum interference device) and VSM (vibrating sample magnetometry) being the most common. Studies have shown that the SCO can take various forms, including abrupt, gradual, and stepped profiles (Fig. 12.2). In systems where the spin centers are coupled, either through coordination bonds or supramolecular contacts [28], the SCO may occur with hysteresis conferring a memory effect on the system.

☆ Dedicated to the memory of His Majesty, the late King Bhumibol Adulyadej of Thailand.

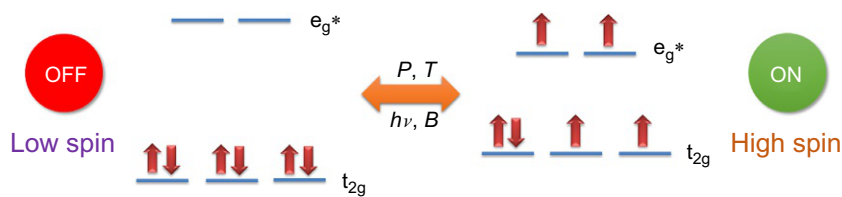


Fig. 12.1

The HS and LS states for the d^6 electron configuration showing binary encoding of these two magnetic states.

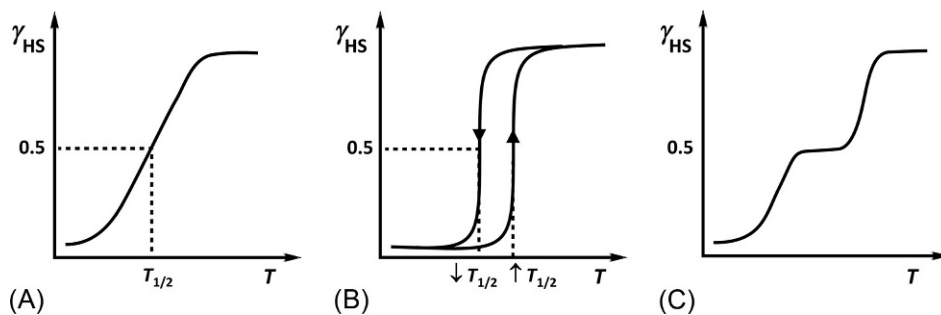


Fig. 12.2

Common SCO transitions, (A) gradual, (B) abrupt with hysteresis, and (C) stepped.

The activation of SCO molecules by light is called light-induced excited spin state trapping or LIESST. This involves excitation from a suitable $d-d$ or charge-transfer band using either visible or near-infrared light [29,30]. This produces an excited state that relaxes through intersystem crossing to a metastable HS state that at sufficiently low temperatures, typically $<50\text{K}$, can be stable for many days. The efficiency of LIESST is strongly dependent on the system involved and is much more common for Fe(II) than it is for Fe(III). The increase in magnetism caused by light irradiation is typically measured in a SQUID magnetometer.

While molecular SCO systems are well developed, SCO nanomaterials have only really been explored in the last 15 years [12,31–39]. Moreover, much of the work has involved only two SCO systems, Fe(II) triazole, $[\text{Fe}(\text{Htrz})_3][\text{A}]_2$ or $[\text{Fe}(\text{Htrz})_2(\text{trz})][\text{A}]$ (Htrz = triazole, trz = triazolate, A = anion) [40] and Hofmann networks $[\text{Fe}(\text{pyrazine})\{\text{M}(\text{CN})_4\}]$ (M = Ni, Pd, Pt). Early studies focused principally on size effects and the synthetic challenges inherent in making nanomaterials. These studies revealed that, in general, as the nanomaterials become smaller the hysteresis reduces and the proportion of molecules trapped in the HS state also increases. This is thought to be due to the increase in the proportion of the surface area of the nanoparticle, which remains in the HS state, relative to the internal volume.

The last comprehensive review of SCO nanomaterials was in 2013 by Ruben et al. [41]. Consequently, this chapter will focus on papers reported since then referring back to earlier work only when this is required to put the current work in context. We include in the review

only systems where at least one of the dimensions of the materials is in the nano-realm. The exception are the SCO devices where both molecular and nanomaterials have been used but are very similar and therefore best discussed together.

12.2 Nanoparticles and Nanocrystals

12.2.1 Triazole Systems

The Fe(II) triazoles are among the most well-studied SCO nanomaterials. The synthesis of $[\text{Fe}(\text{Htrz})_2(\text{trz})]\text{BF}_4$ nanoparticles was first reported by Coronado et al. in 2007 [42]. The nanoparticles were prepared using a reverse micelle synthesis involving combining separate microemulsions of Fe(II) and triazole in water in *n*-octane and ethanol in *n*-octane, respectively, stabilized by a surfactant (Fig. 12.3). The nanoparticles produced are *ca.* 15 nm in size and despite their small size still maintain a hysteresis of 41 K, similar to the bulk material. More recently, Coronado et al. have revisited this synthesis and found that the crucial parameter is the water-to-surfactant ratio, ω_0 [43]. Varying ω_0 from 5 to 10 allows control of the size of nanomaterials from 4 to 18 nm with even the smaller nanomaterials exhibiting a hysteresis of 24 K. However, there was no simple correlation between ω_0 and the size of the nanomaterials.

At about the same time, Roubeau et al. reported that the nanomaterials produced from this synthesis are actually nanorods as evidenced by TEM (transmission electron microscopy) studies [44]. They also found that there is significant variation in the length and width of the nanorods. Decreasing the concentration of the behenic acid cosurfactant resulted in a decrease in the size of the nanoparticles, in particular their width. It is interesting to note that in all cases the nanorods produced were far larger than those reported by Coronado and coworkers. Moreover, Roubeau et al. found that washing of the nanorods reduces the hysteresis of the nanomaterials to *ca.* 20 K. The two reports emphasize that the synthesis suffers from poor reproducibility and that each sample needs to be screened prior to use.

The issue of surfactant has been addressed by Daro, Guionneau et al. who used a neutral surfactant in the synthesis of $[\text{Fe}(\text{Htrz})_2(\text{trz})]\text{BF}_4$ [45]. They explored temperature and time

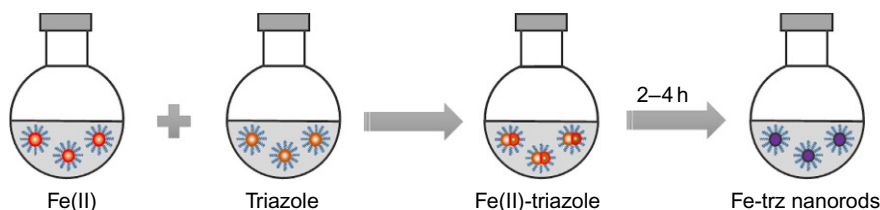


Fig. 12.3

Representation of the reverse micelle synthesis of Fe(II) triazole nanorods.

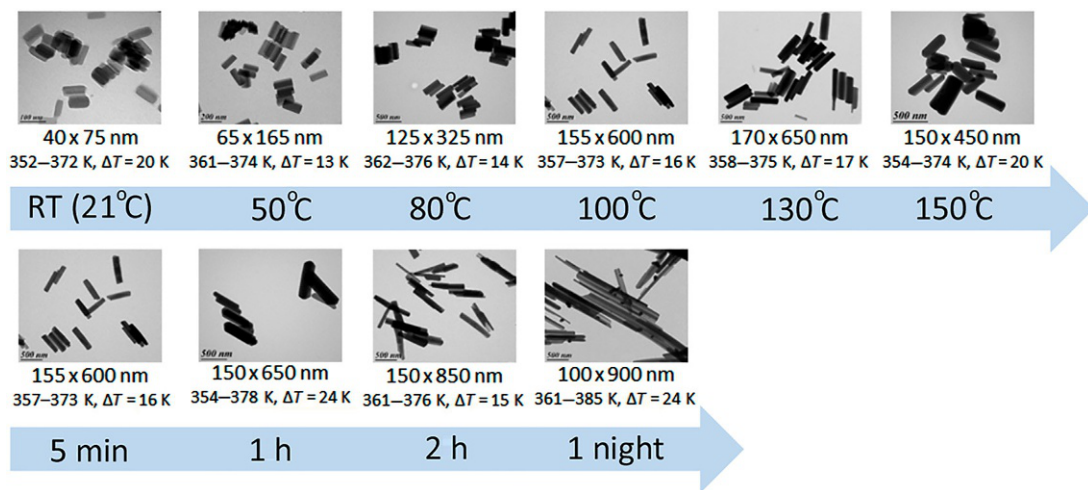


Fig. 12.4

View of the size and morphology of $[\text{Fe}(\text{Htrz})_2(\text{trz})]\text{BF}_4$ nanoparticles as TEM images, produced using a neutral surfactant. Modified from L. Moulet, N. Daro, C. Etrillard, J.-F. Létard, A. Grosjean, P. Guionneau, *Magnetochemistry 2* (2016) 10.

finding that higher temperatures and longer reaction times resulted in larger nanorods. In this case, the authors were able to control the size of the nanorods from 80 to 1000 nm (Fig. 12.4). While all samples underwent SCO, the hysteresis varied from 13 to 36 K being generally wider for the larger particles. Once again, it is evident that the synthetic procedure is crucial and even if the morphology and size of the nanoparticles are identical the magnetic response may not be.

It is obvious that surfactant can have a significant effect on the nanomaterials produced and in seeking to address these concerns Bousseksou, Salmon, and coworkers devised a matrix-free synthesis. $[\text{Fe}(\text{Htrz})_3][\text{CF}_3\text{SO}_3]_2 \cdot 1.2\text{H}_2\text{O}$ is isolated after slow evaporation over 2 months from a mixture of $\text{Fe}(\text{CF}_3\text{SO}_3)_2$ and triazole in the presence of triflic acid [46]. The products are actually microrods but following dehydration produce a strongly hysteretic SCO of 50 K centered at room temperature. The same authors have shown that $[\text{Fe}(\text{Htrz})_2(\text{trz})]\text{BF}_4$ can be prepared in a similar way this time producing nano- and microrods from 0.1 to 40 μm [47]. The disadvantage of the technique is that long evaporation times are required to produce the nanomaterials. In another approach, Ren and colleagues simply mixed amino-triazole ($\text{NH}_2\text{-trz}$) suspended in an aqueous solution of sodium dodecylsulfonate (doe) with $\text{Fe}(\text{BF}_4)_2$ in the same surfactant to give spherical nanoparticles of $[\text{Fe}(\text{NH}_2\text{-trz})_3][\text{doe}]_2$ [48]. The nanoparticles were between 200 and 300 nm and gave a hysteresis of 13 K slightly above room temperature. This compares well with the bulk $[\text{Fe}(\text{NH}_2\text{-trz})_3][\text{A}]_2$ ($\text{A} = \text{anion}$) material.

In a proof of concept, Guionneau and coworkers have shown that spray-drying can be used to prepare $[\text{Fe}(\text{NH}_2\text{-trz})_3][\text{A}]_2$ ($\text{A} = \text{Br}, \text{BF}_4$) nanoparticles [49]. Interestingly, the morphology in most cases is spherical rather than the more common nanorods. The samples are also less

crystalline and this impacts the abruptness of SCO and the hysteresis, both being poorer compared to the bulk material. In another synthetic approach, Robertson et al. have reported the preparation of $[\text{Fe}(\text{Htrz})_2(\text{trz})]\text{BF}_4$ using flow chemistry [50]. The microrods (1100 nm) closely mirror those produced in an identical batch process with a hysteresis of 44 K. Given the flexibility of microfluidic systems, this may prove to be a valuable methodology in the production of nanoparticles of repeatable size, morphology, and more importantly magnetic behavior.

The impact of SCO on the structure of $[\text{Fe}(\text{Htrz})_2(\text{trz})]\text{BF}_4$ nanorods has been explored by Molnár and Bousseksou [51]. Using in situ AFM (atomic force microscopy) imaging, they found that the nanorods are actually aggregates of small nanocrystals that expand and separate upon SCO. They also noted other irreversible changes in the morphology of the nanorods, which explain the narrowing of the hysteresis upon repeated cycling in $[\text{Fe}(\text{Htrz})_2(\text{trz})]\text{BF}_4$. In a similar study, Freysz et al. have shown how the change in the refractive index due to SCO in $[\text{Fe}(\text{NH}_2\text{-trz})_3][\text{Br}]_2$ nanoparticles can be related to the dielectric constant opening the door to a myriad of applications with these nanomaterials [52].

12.2.2 Hofmann Systems

Hofmann networks are constructed from cyanometallates, Fe(II), and a coligand often having the general formula $[\text{Fe}(\text{pz})\{\text{M}(\text{CN})_4\}]$ (pz = pyrazine; M = Ni, Pd, Pt). As mentioned in the introduction, it was long believed that as nanomaterials became smaller, hysteresis would ultimately disappear and SCO would become less abrupt. In 2014, Salmon, Bousseksou, and coworkers showed in a study of $[\text{Fe}(\text{pz})\{\text{Ni}(\text{CN})_4\}]$ that this is not true [53]. While between 107 and 12 nm the SCO does become progressively less abrupt, as the size of the nanoparticles drops below 10 nm, the SCO changes and cooperativity reappears at 2 nm. The reason for the reappearance of hysteresis is that the smaller nanoparticles exhibit a change in their stiffness related to the strain induced on the surface of the ultra-small nanoparticles.

The lattice dynamics of $[\text{Fe}(\text{pz})\{\text{Ni}(\text{CN})_4\}]$ have also been investigated using nuclear inelastic scattering [54]. The authors were able to show that a range of different parameters, specific heat, entropy, and Debye temperature are spin state dependent. A particularly large change in the sound velocity was observed, which is important in understanding the propagation of SCO through a solid.

In a remarkable study, Zewail et al. were able to determine the impact of SCO on a single nanoparticle of $[\text{Fe}(\text{pz})\{\text{Pt}(\text{CN})_4\}]$ [55]. This involved using 4D-electron microscopy and allowed the visualization of the impact of SCO on a single nanoparticle in real time (Fig. 12.5). The authors found that the single nanoparticle switched far more quickly than the nanoparticle ensemble, <15 ns compared to 29 ± 3 ns.

Size effects of light-induced SCO in $[\text{Fe}(\text{pz})\{\text{Pt}(\text{CN})_4\}]$ have also been explored by Sagar, Jimenez, and coworkers [56]. They found that smaller nanocrystals (*ca.* 100 nm, 5–10 ps)

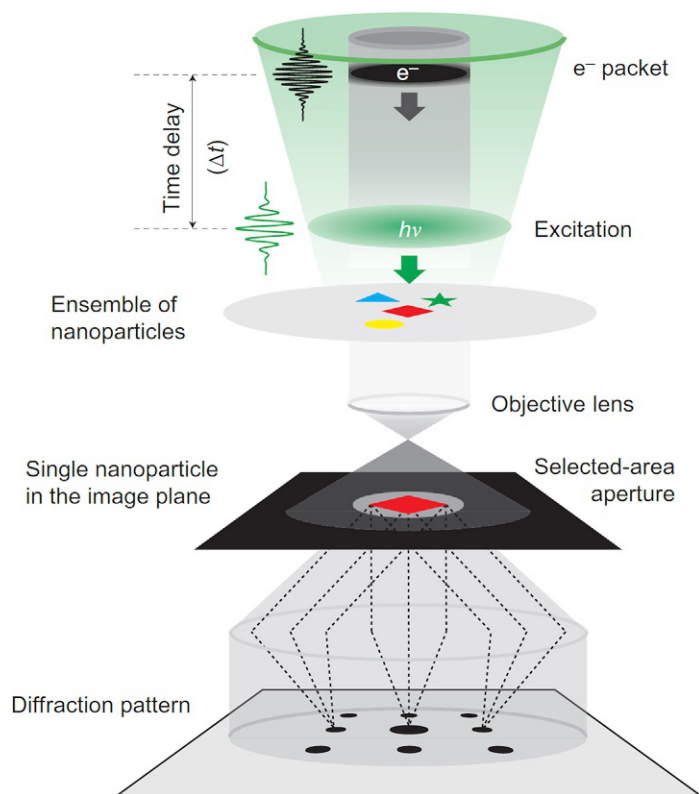


Fig. 12.5

View of the 4D-electron microscopy set-up used to visualize nanoparticle of $[\text{Fe}(\text{pz})\{\text{Pt}(\text{CN})_4\}]$.
 Reproduced from R.M. van der Veen, O.-H. Kwon, A. Tissot, A. Hauser, A.H. Zewail, *Nat. Chem.* 5 (2013) 395–402 with permission of the Nature Publishing Group, 2013.

exhibit a faster LS to HS transition compared to larger nanocrystals (375 nm, 20 ps). They ascribed this difference to the greater abundance of the LS state in the smaller nanocrystals. It is interesting to note that the twofold difference in switching times mirrors that found by Zewail et al. in their 4D-electron microscopy study.

12.2.3 Molecular Systems

While Fe(II) triazole and Hofmann nanomaterials are well explored, these represent only a fraction of the SCO systems reported. This necessarily limits the materials that can be made as both the transition temperature and the hysteresis are fixed. The vast majority of SCO systems are molecular and in the last 5 years there has been a more concerted effort to explore the possibility of using molecular compounds to make nanocrystals. $[\text{Fe}(\text{NCS})_2(\text{phen})_2]$ is the archetypal SCO compound. Nanomaterials have been made by rapid precipitation and the reverse micelle procedure. In the former, a methanolic solution of $[\text{Fe}(\text{NCS})_2(\text{phen})_2]$ is added

to a BuOH solution to give microcrystals [57]. These are then redispersed in a BuOH solution containing polyethylene glycol (PEG) at 80°C before cooling to 0°C to give 650-nm nanocrystals. Smaller nanocrystals are only accessible by heat treatment of $[\text{Fe}(\text{phen})_3][\text{NCS}]_2$ at 180°C, redispersion in a BuOH-PEG solution, filtration through a 0.2- μm PTFE membrane, and cooling to 0°C, which produces nanocrystals between 20 and 30 nm in size. As the nanocrystals become smaller, $T_{1/2}$ moves from 179 to 168 K and the SCO becomes more gradual. In contrast, using the reverse micelle approach, nanocrystals from $200 \times 200 \times 100$ nm to $140 \times 140 \times 70$ nm can be made, which have very high crystallinity [58]. In these nanomaterials, the hysteresis is actually greater than the bulk material being between 6 and 8 K. This highlights that the synthetic procedure is just as important as the size of the nanomaterials (Fig. 12.6).

The rapid precipitation method has also been used to make $[\text{Fe}(\text{AP-Mesal})_2]$ {AP-Mesal = 2-hydroxy-3-methyl-*N'*-((pyridin-2-yl)ethylidene)benzohydrazide} with PEG-400 used as the surfactant [59]. Microcubes (1–4 μm) and nanospheres (30–50 nm) can be made, and as with $[\text{Fe}(\text{NCS})_2(\text{phen})_2]$ the hysteresis increases as the particle size decreases reaching 10 K for the smallest nanospheres. Remarkably, the bulk material exhibits little or no hysteresis and it's clear that the response of an individual material to size reduction cannot be predicted. $[\text{Fe}(\text{NCSe})_2(\text{Me}_2\text{-bipy})_2]$ is prepared in a similar way this time with poly(methylmethacrylate) (PMMA) as the confining polymer [60]. Unusually, the size of the nanoparticles does not influence the magnetic properties possibly because the SCO of $[\text{Fe}(\text{NCSe})_2(\text{Me}_2\text{-bipy})_2]$ is not cooperative.

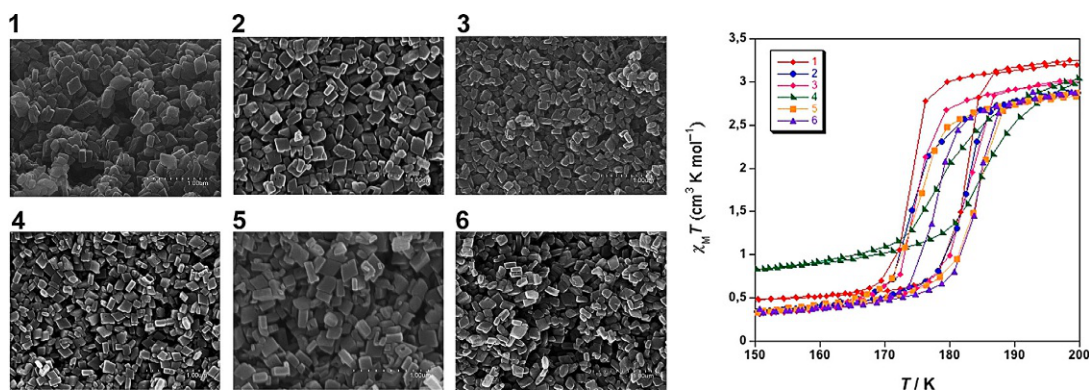


Fig. 12.6

View of the nanocrystals of $[\text{Fe}(\text{NCS})_2(\text{phen})_2]$ produced by reverse micelle synthesis and SCO properties. Samples 1–6 are nanocrystals prepared using an Fe(II) concentration of 0.10, 0.15, 0.2, 0.3, 0.4, and 0.5 mol/L, respectively. Reproduced slightly modified with permission from F.J. Valverde-Muñoz, A.B. Gaspar, S.I. Shylin, V. Ksenofontov, J.A. Real, *Inorg. Chem.* 54 (2015) 7906–7914. Copyright, 2015, American Chemical Society.

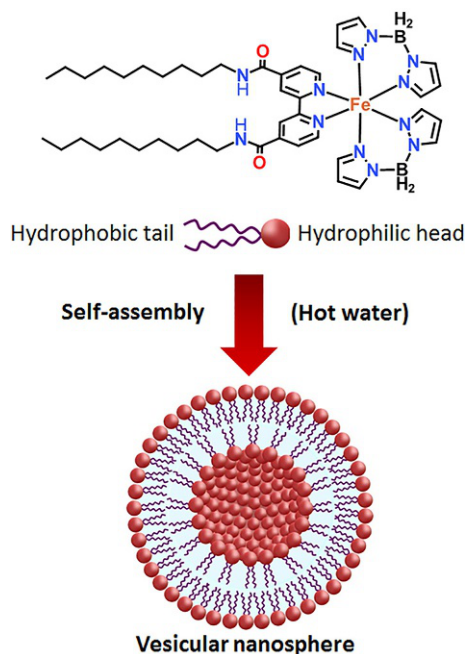


Fig. 12.7

View of the synthesis of SCO vesicles of $[\text{Fe}(\text{Bp})_2(\text{bipy}-(\text{CONH-R})_2)]$. Modified from Y.-H. Luo, Q.-L. Liu, L.-J. Yang, Y. Sun, J.-W. Wang, C.-Q. You, B.-W. Sun, *J. Mater. Chem. C* 4 (2016) 8061–8069 with permission of The Royal Society of Chemistry, 2016.

Another widely used system is $[\text{Fe}(\text{Bp})_2(\text{N-N})]$ (Bp = bis(pyrazolyl)borate; N-N = 2,2'-bipy, phen). In contrast to most SCO compounds, these can be sublimed, which allowed Hallak, Rosa, and coworkers to prepare microcrystallites or thin films on either Cu or Au [61]. The films were *ca.* 160 nm thick and importantly preserved the magnetic properties of the bulk material. Modification of the bipyridine ligand with alkylamide groups gives $[\text{Fe}(\text{Bp})_2(\text{bipy}-(\text{CONH-R})_2)]$ (Fig. 12.7) [62]. Changing the length of the alkyl groups of the bulk materials results in an increase in $T_{1/2}$ from 154 to 178 K. However, when the alkyl group contains more than six carbons, vesicular nanospheres self-assemble in hot water. This radically alters the SCO behavior with $T_{1/2}$ now 330–290 K and negatively correlated to alkyl chain length. The latter finding was found to correlate with the temperature at which the alkylated ligands melt.

The fast precipitation method has also been used to prepare nanoparticles of $[\text{Fe}(\text{mepy})_3\text{tren}][\text{PF}_6]_2$ {(mepy)₃tren = tris{4-[(6-methyl)-2-pyridyl]-3-aza-3-butenyl}amine} [63]. The products are 74 nm nanospheres and as with $[\text{Fe}(\text{NCS})_2(\text{phen})_2]$ made by the reverse micelle technique maintain a high degree of crystallinity. Interestingly, the crystallinity was found to significantly affect the photoswitching of the material with amorphous products of the same size exhibiting much longer relaxation times. This is due to the more gradual and lower transition temperature of the amorphous materials compared to the crystalline nanoparticles.

While almost all SCO nanomaterials are Fe(II), Lorenc, Collet et al. have explored nanomaterials of the Fe(III) compound $[\text{Fe}(\text{salEen-3-OMe})_2]\text{PF}_6$ (salEen-3-OMe = 2- $\{[2$ - (Ethylamino)ethylimino]methyl $\}$ -6-methoxyphenolate) [64]. In a ground-breaking study, the authors used a fast precipitation method to give nanorods that were subsequently embedded into a PVP {poly(vinyl)pyrrolidone} thin film. Using a femtosecond laser pulse, the material was switched from the LS to the HS state. Intriguingly, putting the nanocrystals in the film is not detrimental to their photoswitching capability; rather, the small size of the nanocrystals and the deeper penetration of the laser into the film compared with regular crystals actually increase the photoconversion 50 times. If this holds for other Fe(III) SCO materials, this broadens the range of SCO compounds that can be used in devices.

12.3 Spin Crossover Nanocomposites

12.3.1 Silica Systems

Hybrid SCO nanomaterials combine SCO nanomaterials and another material typically silica, Au, or graphene [35–39]. Theoretically, they can incorporate any SCO compound but have most often employed Fe(II)-triazole. One of the first reports in this area was by Herrera, Colacio, and coworkers [65]. Building on the nanosynthesis of Fe(II) triazole first reported by Coronado et al. [42] (see Section 12.2.1) they prepared microemulsions of Fe(II) and triazole, mixed them, and then added tetraethylorthosilicate (TEOS). Following destabilization of the microemulsion, a thin coating of silica on the nanoparticles, termed SCO@SiO₂, was produced. It should be noted that these authors used a neutral surfactant, Triton X-100, rather than the anionic surfactant previously reported. Having silica on the outer surface provides multiple attachment sites, which, in this case, allowed the authors to incorporate fluorescent dansyl groups onto the nanoparticles. The hysteresis actually increases compared to the bulk material to 49 K. Doping with Zn allowed the authors to move the transition temperature lower by *ca.* 20 K, although the hysteresis does decrease to 35 K. The luminescence of the dansyl moiety was found to be partially quenched in the LS state but active in the HS state. In a follow-up paper, the same authors showed that the size of the Fe(II) triazole nanoparticles could be tuned by varying the concentration of the Fe(II) and triazole starting materials. In this way, nanorods 28–320 nm in length were obtained. They also confirmed that for the 100 nm nanorods, the silica shell was *ca.* 12 nm thick. The hybrid materials again show an increase in the hysteresis, by as much as 14 K compared to the unmodified nanorods, being generally larger for the smaller nanorods. It was also found that continued cycling between the HS and LS states led to decomposition of the dansyl group and consequently a loss of fluorescence. This highlights one of the problems with the Fe(II) triazole SCO system, which undergoes SCO at quite a high temperature.

Following the initial report of luminescent coated SCO@SiO₂ nanoparticles and the thermal instability of the system, several research groups have worked to vary the luminescent

groups that can be attached. The first of these utilized a pyrene luminescent group, which was bonded onto the SCO@SiO₂ nanoshells [66]. The nanomaterials were found to exhibit monomer and excimer luminescence in a controllable ratio with the SCO showing slightly increased hysteresis. In contrast to the report in 2011, the HS state shows increased luminescence only for the excimer luminescence. The monomer luminescence was unaffected by the spin state change. Replacing the organic dye with a bonded Terbium complex greatly improves the stability of the SCO@SiO₂-Tb nanomaterials, which undergo SCO successively with the luminescent response characteristic of the spin state (Fig. 12.8) [67]. More importantly, unlike the organic dyes, there is no bleaching even after repeated cycling.

Although these materials exhibit good SCO properties, they are inherently limited by the nature of Fe(II)-triazole system. Gu and coworkers have recently tried to address this limitation by first growing nanomaterials of Fe(II)-amino-triazole and then growing Fe(II)-triazole NPs in the same nanocomposite [68]. This results in a SCO1@SCO2@SiO₂ nanocomposite, which exhibits multistep SCO and represents a promising approach to stepped SCO nanomaterials.

All of these reports involve silica being grown around the SCO material. In 2015, Fleury et al. reversed the normal SCO@SiO₂ core-shell structure. This involved growing a core of SiO₂ and functionalizing it with a coating of the Fe(II) SCO complex [Fe(BIK)₃][BF₄]₂ {BIK = bis(1-methylimidazol-2-yl)ketone} [69]. The nanomaterial undergoes an abrupt SCO at 210 K slightly lower than the molecular complex. In another approach, the SiO₂ has been modified using a sol-gel process to give xerogels, which are then infused with 3.2-nm Fe(II)-triazole nanomaterials [70]. Remarkably, the hysteresis of this silica-Fe(II)-triazole xerogel increases from 40 to 65 K, although the SCO is less complete. The spin transition temperature also decreases by ~30 K.

Garcia, Janick, and coworkers embedded [Fe(Htrz)₃][BF₄]₂·H₂O and [Fe(Htrz)₂(trz)]BF₄ in MCM-41 to give SCO@MCM nanocomposites [71]. While the [Fe(Htrz)₂(trz)]BF₄

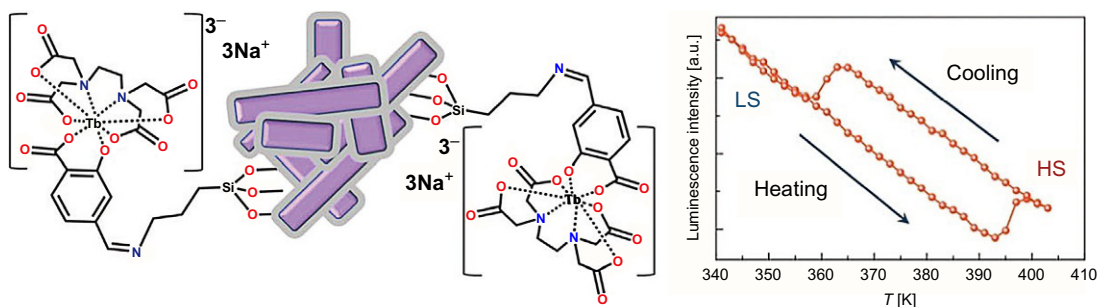


Fig. 12.8

SCO@SiO₂ nanoshells with luminescent Tb complexes. Modified from I. Suleimanov, O. Kraieva, G. Molnár, L. Salmon, A. Bousseksou, *Chem. Commun.* 51 (2015) 15098–15101 with permission of The Royal Society of Chemistry, 2015.

nanocomposite shows little change in its magnetic properties, the $[\text{Fe}(\text{Htrz})_3][\text{BF}_4]_2 \cdot \text{H}_2\text{O}$ nanocomposite exhibits a large shift in the transition temperature and a broadening of the hysteresis by 25–26 K. The reason for this radical change in the magnetic properties is the confinement of water molecules in the pore walls of the MCM-41 framework.

12.3.2 Au Systems

Employing the same $\text{SCO}@\text{SiO}_2$ core-shell structure discussed earlier, Salmon and Bousseksou were able to graft gold nanoparticles onto the surface of the $\text{SCO}@\text{SiO}_2$ nanorods using 3-mercaptopropyltrimethoxysilane [72]. The nanorods had an average length of 154 nm and a width of 88 nm while the Au NPs were 2 nm. Using the strong photothermal effect of Au, they were able to reduce the power required for complete SCO by 70%. About the same time, Gu et al. made similar $\text{SCO}@\text{SiO}_2@\text{Au}$ nanomaterials, this time using a functionalized amine and $[\text{AuCl}_4]^-$ as the Au source (Fig. 12.9) [73]. Reduction of Au(III) using NaBH_4 gave the SCO nanomaterials. In this case, the nanomaterials were considerably larger being 750–800 nm in size, which led to a 100 times' reduction in energy of the laser

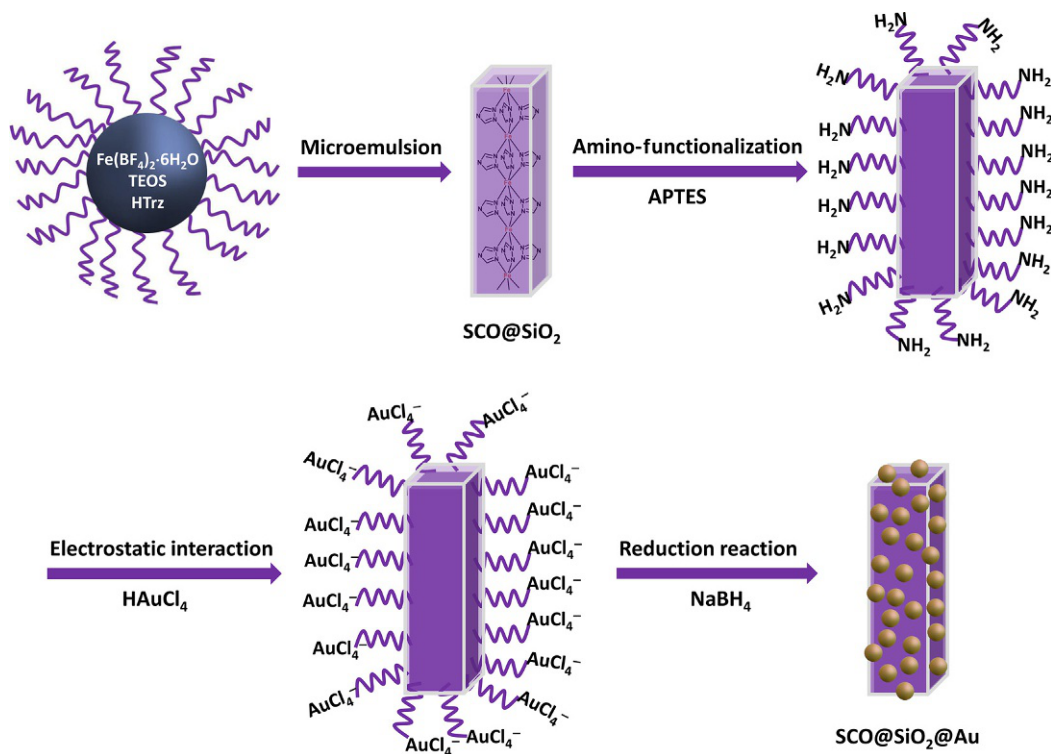


Fig. 12.9

Synthetic procedure for $\text{SCO}@\text{SiO}_2@\text{Au}$ nanomaterials. Modified from D. Qiu, L. Gu, X.-L. Sun, D.-H. Ren, Z.-G. Gu, Z. Li, *RSC Adv.* 4 (2014) 61313–61319 with permission of The Royal Society of Chemistry, 2014.

needed to induce SCO. In both cases, the hysteresis of the SCO@SiO₂@Au nanocomposites is between 45 and 50 K and almost identical to the SCO@SiO₂ core shells.

Direct grafting of Au onto [Fe(Htrz)₂(trz)]BF₄ nanorods has been attempted many times but almost always produces a thin film of Au on the SCO nanorods. It was finally achieved by Guionneau, Mornet et al. who used polyvinylpyrrolidone (PVP) to stabilize the Au NPs [74]. This involved mixing 4-nm, 10-nm, and 45-nm Au NPs stabilized by PVP and a colloidal solution of [Fe(Htrz)₂(trz)]BF₄ and incubating overnight. This gives homogeneously covered 200 nm long Fe(II)-triazole nanorods. In contrast to the SCO@SiO₂@Au systems, neither the transition temperature nor the hysteresis are affected by the Au NPs. Unexpectedly, the SCO@Au nanomaterials appear not to undergo SCO with a 510 nm laser source even when the power was 45 mW cm⁻².

12.3.3 Polymer Systems

Polymers have also been used as matrices for SCO nanocrystals. The first involved growth of [Fe(L)(4,4-bipy)] {L = [3,3']-[1,2-phenylenebis(iminoethylidene)]bis(2,4-pentanedionato)} in poly(4-vinylpyridine) giving very thin nanocrystals, 1.5–3.0 μm long and 400–500 nm wide [75]. Provided that the concentration of the SCO nanocrystals in the polymer is sufficiently high, the nanocomposite exhibits the same SCO profile as the bulk material. Using a polystyrene/poly(4-vinylpyridine) block copolymer approach, the nanoparticles can be limited to 49 nm and still give a hysteresis of 8 K [76].

A similar approach has very recently been used by Kuroiwa et al. this time using diblock copolypeptides of polyglutamate and poly-leucine. In this case, the SCO complex used was [Fe(ppi)₂(NCS)₂] {ppi = 2-pyridyl-*N*-(phenyl)methylamine} [77]. Self-assembled supramolecular nano- and microstructures are formed between the copolypeptides and [Fe(ppi)₂(NCS)₂] in water with the spin transition temperature moving from *ca.* 150 to 310 K (Fig. 12.10). The ratio of the two polypeptides is crucial in obtaining switchable solutions. Increasing the amount of poly-leucine leads to a solution that undergoes SCO with a concomitant formation of aggregated structures. The process is reversible and represents a promising methodology for SCO hybrids.

12.3.4 Cellulose Systems

Cellulose is a renewable and abundant material that has been used to prepare a number of nanocomposites. In 2014 Salmon, Csóka et al. used [Fe(hptrz)₃][OTs]₂ (hptrz = 4-heptyl-triazole, OTs = 4-methylbenzenesulfonate) prepared by mixing Fe(OTs)₂ and hptrz solutions in the presence of PEG-3350 to give 300–500 nm nanorods [78]. Mixing the [Fe(hptrz)₃][OTs]₂ colloidal solution with a suspension of cellulose fibers yields the SCO nanocomposites.

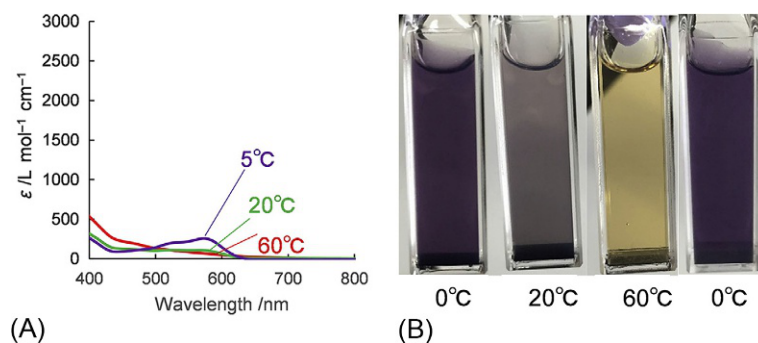


Fig. 12.10

(A) Temperature-dependent UV-Vis spectra of $[\text{Fe}(\text{ppi})_2(\text{NCS})_2]$ diblock copolypeptides and (B) pictures of the solution between 0 and 60°C. Reproduced from A. Tsubasa, S. Otsuka, T. Maekawa, R. Takano, S. Sakurai, T.J. Deming, K. Kuroiwa, *Polymer* (2017) <https://doi.org/10.1016/j.polymer.2016.12.079> with permission of Elsevier, 2017.

The cellulose nanocomposites show clear thermochromism occurring moderately abruptly in the heating and cooling mode at 327 and 324 K, respectively.

Cellulose nanocomposites of $[\text{Fe}(\text{NH}_2\text{-trz})_3][\text{Br}]_2$ and $[\text{Fe}(\text{Htrz})_2(\text{trz})]\text{BF}_4$ have been made this time using suspensions of the two SCO materials and the cellulose fibers, followed by sonication [79]. As with $[\text{Fe}(\text{hptrz})_3][\text{OTs}]_2$ the nanoparticles are randomly dispersed over the cellulose fibers. While the $[\text{Fe}(\text{Htrz})_2(\text{trz})]\text{BF}_4$ nanocomposite shows a repeatable 41 K hysteresis, $[\text{Fe}(\text{NH}_2\text{-trz})_3][\text{Br}]_2$ exhibits a more variable hysteresis and above 120°C becomes unstable due to polymorphism of the $[\text{Fe}(\text{NH}_2\text{-trz})_3][\text{Br}]_2$ material. Nevertheless, using a focused laser beam, the authors were able to write on the paper while cooling erased what was written; this was found to be repeatable over hundreds of cycles.

Further work by Bousseksou, Demont, and coworkers on $[\text{Fe}(\text{Htrz})_2(\text{trz})]\text{BF}_4$ microcrystals embedded in cellulose reveals that the mechanical stress of the material is dependent on the spin state [80]. Specifically, transition to the HS state results in a 10% increase in the elastic modulus while a similar decrease is noted upon transition to the LS state. Remarkably, hysteresis is observed in the elastic modulus and is clearly correlated with the magnetic properties of the SCO material. This may permit the development of a new family of actuator materials (see Section 12.5.2).

Bacterial cellulose has also been used to make $[\text{Fe}(\text{Htrz})_2(\text{trz})]\text{BF}_4$ nanocomposites [81]. Sheets of cellulose were successively soaked in a $\text{Fe}(\text{BF}_4)_2$ solution and then a triazole solution. The rods produced are 1–2- μm long and are highly crystalline in contrast to previous methods. The nanocomposites maintain the magnetic and optical properties of the SCO material. The simple synthesis makes this an attractive technique for future applications provided that greater control over the size of the SCO complexes can be achieved.

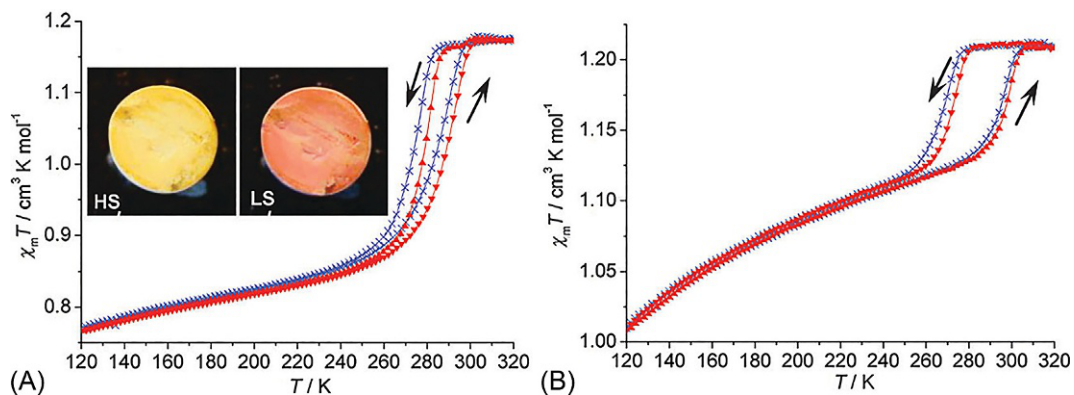


Fig. 12.11

Thermal variation of $\chi_M T$ for $[\text{Fe}(\text{pz})\{\text{M}(\text{CN})_4\}]$ -chitosan nanocomposite beads at heating and cooling rates of 1 K min^{-1} for (A) nanocomposite beads, $\text{M} = \text{Ni}$; (B) nanocomposite beads, $\text{M} = \text{Pd}$. Reproduced from A. Tokarev, J. Long, Y. Guari, J. Larionova, F. Quignard, P. Agulhon, M. Robitzer, G. Molnár, L. Salmon, A. Bousseksou, *New J. Chem.* 37 (2013) 3420 with permission of The Royal Society of Chemistry, 2013.

Chitosan is structurally very similar to cellulose and can be readily prepared as beads. Successive addition of Fe^{2+} , pyrazine, and $[\text{M}(\text{CN})_4]^{2-}$ to the chitosan beads results in impregnation of the beads by $[\text{Fe}(\text{pz})\{\text{M}(\text{CN})_4\}]$ framework [82]. The chitosan limits the size of $[\text{Fe}(\text{pz})\{\text{M}(\text{CN})_4\}]$ to 2.4–3.1 nm homogeneously distributed throughout the chitosan beads. Of the three frameworks, only the Ni and Pd systems exhibit cooperative SCO with hystereses of 10 and 26 K, respectively (Fig. 12.11). In both cases, this is slightly less than the bulk material and only a fraction of the Fe(II) centers are SCO active. The importance of the matrix has been demonstrated by replacing the chitosan with alginate, which results in complete loss of hysteresis; whether this applies to all SCO systems remains unclear.

12.3.5 Graphene Systems

Graphene has good electrical conductivity and a high surface area and despite its widespread use in molecular electronics has only recently been used to make hybrid materials. Gu's group have used $[\text{Fe}(\text{Htrz})_2(\text{trz})]\text{BF}_4$ in different ratios with graphene [83]. The particles were 50 nm in size and showed a slight increase in hysteresis when deposited on graphene. The most notable changes are an increase in the remnant HS and the spin transition temperature as the ratio of SCO material to graphene is increased.

In a related study, Haymai et al. have made hybrid materials from graphene oxide (GO) and the Fe(III) SCO cations, $[\text{Fe}(\text{qsal})_2]^+$ and $[\text{Fe}(\text{qnal})_2]^+$ ($\text{qsal} = N$ -(8-quinolyl)salicylaldimine; $\text{qnal} = 1$ -((8-quinolinylimino)methyl)-2-naphthalenolate) [84]. This involved using electrostatic attraction between the Fe(III) cations and the graphene oxide. Thermal reduction gave reduced graphene oxide (rGO) nanocomposites with the SCO complexes sandwiched

between the nanosheets. Only $[\text{Fe}(\text{qnal})_2]\text{-GO}$ and $[\text{Fe}(\text{qnal})_2]\text{-rGO}$ exhibit SCO behavior with the latter also undergoing LIESST. The additional observation of electrical conductivity in $[\text{Fe}(\text{qnal})_2]\text{-rGO}$ makes it a rare example of a truly multifunctional material. The reason for the success of $[\text{Fe}(\text{qnal})_2]^+$ over $[\text{Fe}(\text{qsal})_2]^+$ seems to be the larger π -cloud of the qnal ligand, which facilitates strong binding to the graphene surface.

12.4 Spin Crossover Thin Films

SCO thin films have long been an active area of research with a range of different techniques employed, including Langmuir-Blodgett deposition, molecular self-assembly, spin coating, drop casting, and solvent evaporation. More recently, it is the latter three of these that have been most widely used; thus, only these systems are discussed here.

12.4.1 Au, Cu, and Silica

Au has long been a popular substrate on which to deposit SCO materials [31]. In 2013, patterned Au nanoparticles were placed on a silicon substrate before functionalizing with 3-aminopropyl-triethyloxysilane and sputtering with another Au layer. Using ethyl(4-pyridyl) disulfide and a layer-by-layer approach alternately adding Fe^{2+} and $[\text{Pt}(\text{CN})_4]^{2-}$, an ultrathin film of $[\text{Fe}(\text{pz})\{\text{Pt}(\text{CN})_4\}]$ was prepared [85]. Characterization by surface-enhanced Raman scattering allowed the authors to determine the precise thickness of the SCO thin film and the coordination environment of the Fe centers in the nanomaterial.

Tanaka, Ogawa et al. have prepared nanoparticles of $[\text{Fe}(\text{Htrz})_{3-x}(\text{NH}_2\text{-trz})_x][\text{ClO}_4]_2$ ($x = 0, 0.05, 0.15$) using the reverse micelle method [86]. One interesting feature of the synthesis was that contrary to previous reports the nanoparticles could be dispersed in polar solvents provided they were not completely dried after the initial preparation. The addition of $\text{NH}_2\text{-trz}$ results in a decrease in the hysteresis from *ca.* 20 to 15 to 10K as the amount of $\text{NH}_2\text{-trz}$ is increased as evidenced by UV-Vis spectroscopic, DSC (differential scanning calorimetry), and SQUID magnetometry. At the same time, the transition temperature decreases as is typical for amino-triazole systems. Thin films were prepared by spin coating from an EtOH solution of $[\text{Fe}(\text{Htrz})_{3-x}(\text{NH}_2\text{-trz})_x][\text{ClO}_4]_2$. Synchrotron XRD measurements confirm that the films retain the SCO properties of the nanoparticles.

Ultrathin films of $[\text{Fe}(\text{Bp})_2(2,2'\text{-bipy})]$ have been grown on Au(111) under ultrahigh vacuum [87]. Employing X-ray absorption techniques, the authors were able to show that while many of the molecules become trapped in either the HS or LS state, a significant proportion still retain their thermal and light-induced SCO properties. In a related study, Gruber et al. investigated the growth of $[\text{Fe}(\text{NCS})_2(\text{phen})_2]$ on a Cu(100) surface [88]. STM (scanning tunneling microscopy) imaging revealed 0.1–1.8 molecular layers with the first layer coordinated to the metal via the sulfur of the thiocyanate groups (Fig. 12.12). This layer

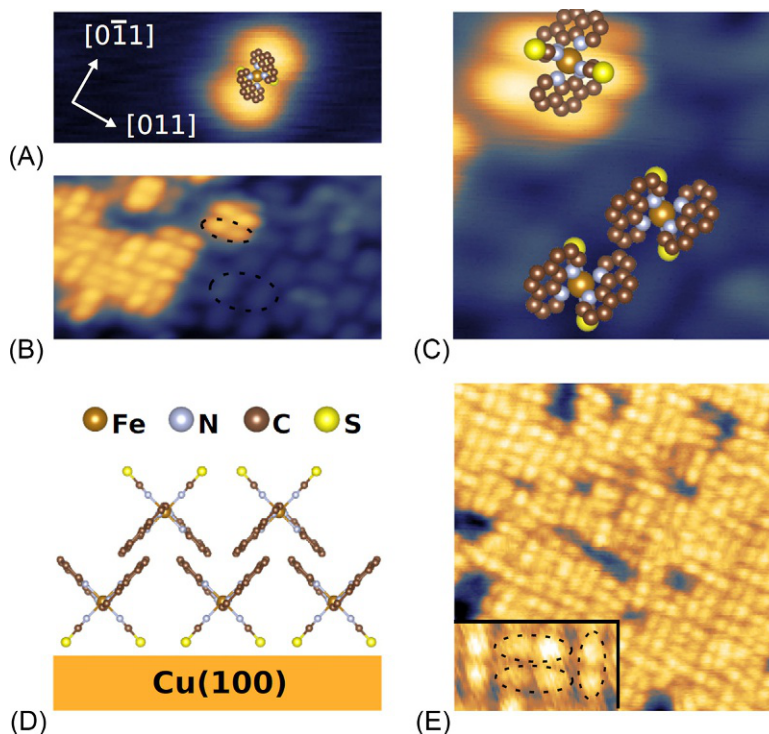


Fig. 12.12

STM images of $[\text{Fe}(\text{NCS})_2(\text{phen})_2]$ molecules on a $\text{Cu}(100)$ surface showing (A–C) the different orientations of the $[\text{Fe}(\text{NCS})_2(\text{phen})_2]$ molecules in the upper and lower layers and (D) the proposed stacking of the molecules and (E) ordered areas of $[\text{Fe}(\text{NCS})_2(\text{phen})_2]$ molecules on the surface.

Reproduced from M. Gruber, V. Davesne, M. Bowen, S. Boukari, E. Beaupaire, W. Wulfhekel, T. Miyamachi, *Phys. Rev. B: Condens. Matter Mater. Phys.* 89 (2014) 1–9 with permission from American Physical Society, 2014.

contains a mixture of HS and LS species. The second layer is inverted relative to the first layer, linked by π - π interactions, and predominately HS. Application of a voltage results in a smooth transition to the LS state as the voltage is increased.

Thin films of $[\text{Fe}(\text{Bp})_2(\text{phen-X})]$ (phen-X = 4-methyl-1,10-phenanthroline, 5-chloro-1,10-phenanthroline, 4,7-dichloro-1,10-phenanthroline and 4,7-dimethyl-1,10-phenanthroline) on quartz have been made by vacuum deposition [89]. The SCO has been tracked by changes in the metal-to-ligand charge transfer (MLCT) bands, which are more intense in the LS state. Interestingly, while the bulk disubstituted phenanthroline materials are not SCO active, the thin films are, highlighting that as with hybrid materials the substrate/matrix can significantly influence magnetic behavior. The reason for the appearance of SCO is thought to be due to the loss of certain interactions in the thin films that are present in the crystalline materials $[\text{Fe}(\text{Bp})_2(\text{phen-Cl}_2)]$ and $[\text{Fe}(\text{Bp})_2(\text{phen-Me}_2)]$ that trap them in the HS state. Despite the different

substituents, the SCO is gradual in all cases with $T_{1/2}$ ranging from 143 to 156K. The thin films also exhibit LIESST with T_{LIESST} *ca.* 50K for all materials.

12.4.2 Polymers

SCO thin films of $[\text{Fe}(\text{NH}_2\text{-trz})_3][\text{BF}_4]_2$ have been prepared by dip coating using a range of organic polymers with different polarities and microstructures [90]. The hydrophobic polymers, polyvinylchloride, polystyrene, and poly(methyl methacrylate) (PMMA) encourage the formation of large micrometer-sized $[\text{Fe}(\text{NH}_2\text{-trz})_3][\text{BF}_4]_2$ clusters. In the case of PMMA changing the solvent to THF gives smaller 2–5 μm clusters, while the use of toluene results in nanocrystals. The hydrophilic polymers give more dispersed nanoparticles with smaller particles and fibers present. The thin films exhibit thermochromic behavior, but the temperature at which the spin transition occurs and the degree of difference in color between the two spin states is strongly matrix dependent. Thus, Nafion and polyurethane show clear color changes and higher spin transition temperatures compared with the hydrophobic polymers. The spin transition temperature is *ca.* 30K higher than the bulk material and the hysteresis is less square for all the films. The Nafion thin film also exhibits the largest hysteresis in this series at 12.6K. The reason for the exceptional performance of Nafion may be due to the 1D channels present in the polymer, which can be occupied by the $[\text{Fe}(\text{NH}_2\text{-trz})_3][\text{BF}_4]_2$ nanorods resulting in extensive interactions between the polymer and the SCO compound. The use of these different thin films, each showing slightly different transition temperatures and color changes, permitted the construction of a colorimetric sensing array with a mean error of 1.25K.

A coordination polymer thin film of $\text{Rb}_{0.8}\text{Ni}_{4.0}[\text{Cr}(\text{CN})_6]_{2.9}\cdot n\text{H}_2\text{O}$ (NiCr-PBA) and the Hofmann-like SCO network $[\text{Fe}(\text{azpy})\{\text{Pt}(\text{CN})_4\}]_x\cdot x\text{H}_2\text{O}$ (azpy = 4,4'-azopyridine) have been prepared by Meisel, Talham, and coworkers [91]. The Prussian blue analogue was deposited from an aqueous solution giving a polycrystalline film 200 nm thick. In a similar way, the Hofmann-like network was deposited at low temperature giving an average thickness of 50nm. The LIESST effect is small but evident in the SCO material and clearly couples to the NiCr-PBA with a decrease in the magnetization of the nanocomposite thin film due to LIESST. This has been proved by determining the magnetization of the pure NiCr-PBA film, which shows no effect in the LIESST region.

12.5 SCO Devices

12.5.1 Single Molecule Devices

One of the principal aims of SCO research is to make functioning devices. To this end, Dowben et al. have grown a thin film (c.20 molecular layers) of $[\text{Fe}(\text{Bp})_2(\text{bipy})]$ onto a ferroelectric organic copolymer of polyvinylidene fluoride and trifluoroethylene (PVDF-TrFE, 70:30) [92].

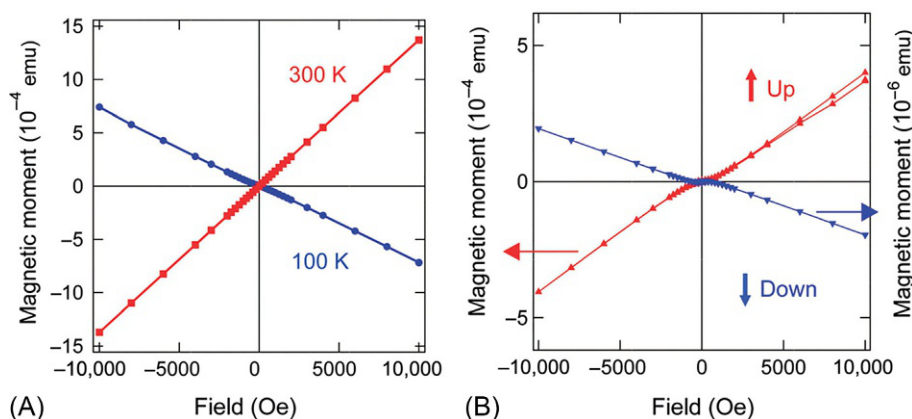


Fig. 12.13

Magnetic properties of [Fe(Bp)₂(bipy)] thin films on the ferroelectric PVDF-TrFE. (A) The variation in magnetic moment with applied field at 300 and 100 K. (B) The variation in magnetic moment when ferroelectric PVDF-TrFE is polarized up at 170 K (red or light gray) and when it is polarized down at 100 K (blue or dark gray). Reproduced from X. Zhang, T. Palamarcic, J.-F. Létard, P. Rosa, E.V. Lozada, F. Torres, L.G. Rosa, B. Doudin, P.A. Dowben, *Chem. Commun.* 50 (2014) 2255–7 with permission of The Royal Society of Chemistry, 2014.

The spin state of the SCO molecule can be controlled by the polarization of PVDF-TrFE. Thus, when the ferroelectric polymer is polarized “down,” between 100 and 300 K, the compound is LS. In contrast, when PVDF-TrFE is polarized “up,” the compound is HS even down to 100 K, well below the normal spin transition temperature of [Fe(Bp)₂(bipy)] (Fig. 12.13).

A more common strategy involves using Au electrodes. In 2015, van der Molen and coworkers used an array of 8.3 nm Au NPs [93]. The NPs were decorated with [Fe(AcS-bpp)₂][ClO₄]₂, where AcS-bpp = (4-([2,6-(dipyrazol-1-yl)pyrid-4-yl]ethynyl)phenyl)ethane-thioate. This SCO molecule was chosen as SCO occurs at 277 K with a small hysteresis of 8 K. When attached to the Au NPs, Raman spectroscopy indicates that coordination is through a benzenethiolate moiety. Magnetic and Raman spectroscopic measurements have been used to confirm that the SCO in the device is more gradual than the bulk material. In addition, one third of the Fe(II) centers remain HS irrespective of the temperature. Charge transport measurements reveal that there is a clear minimum in the resistance between 260 and 290 K, around the same temperature at which SCO occurs.

In a similar study, immersion of a Au crystal in a solution of *trans*-[Fe(NCX)₂(tzpy)] {X = S, Se; tzpy = 3-(2-pyridyl)[1,2,3]triazolo[1,5-*a*]pyridine} gives a functionalized gold surface [94]. Using a Ni tip in an STM (scanning tunneling microscope) break junction involving the thio- or selenocyanate ligands, a molecular wire is formed. Polarization of the Ni tip results in a >100 fold difference in the conductance between the α-up and β-down states. Interestingly, this effect is only observed in the HS state and paves the way for devices where electron transport is controlled by the electrode polarization even at room temperature.

12.5.2 Nanoparticle Systems

As might be expected, $[\text{Fe}(\text{Htrz})_2(\text{trz})]\text{BF}_4$ has also been used to make devices. Since the previous 2013 review, one of the first reports was by Rotaru et al. [95]. In this study, the authors prepared a device with a pair of interdigitated Au electrodes with each electrode *ca.* 10 μm and separated by 2–3 μm . $[\text{Fe}(\text{Htrz})_2(\text{trz})]\text{BF}_4$ rods 3 μm long and 200–300 nm wide prepared by the reverse micelle method were then deposited on the device. Application of the maximum accessible *ac* voltage (7 V_{rms}) and a frequency of 10 kHz led to perpendicular alignment of the $[\text{Fe}(\text{Htrz})_2(\text{trz})]\text{BF}_4$ rods between the Au electrodes. The charge transport properties of the device reveal a clear hysteresis of 40 K in the current-temperature curves due to SCO, centered at 370 K.

In 2015 Dugay, Coronado, and coworkers prepared a similar device this time with planar finger-shaped electrodes separated by 50 nm [96]. Two types of $[\text{Fe}(\text{Htrz})_2(\text{trz})]\text{BF}_4$ nanorods were used with the dimensions being 10×25 nm and 6×44 nm. Despite the much smaller nanorods compared to Rotaru et al.'s study, there is still a clear difference in conductance between the two spin states leading to a hysteresis of 43–52 K. While the hysteresis is square for the 10×25 nm nanorods, it is smoother for the 6×44 nm nanorods and slightly larger. The exact reason is unclear but may relate to an increase in the stiffness of the longer, smaller volume $[\text{Fe}(\text{Htrz})_2(\text{trz})]\text{BF}_4$ nanorods.

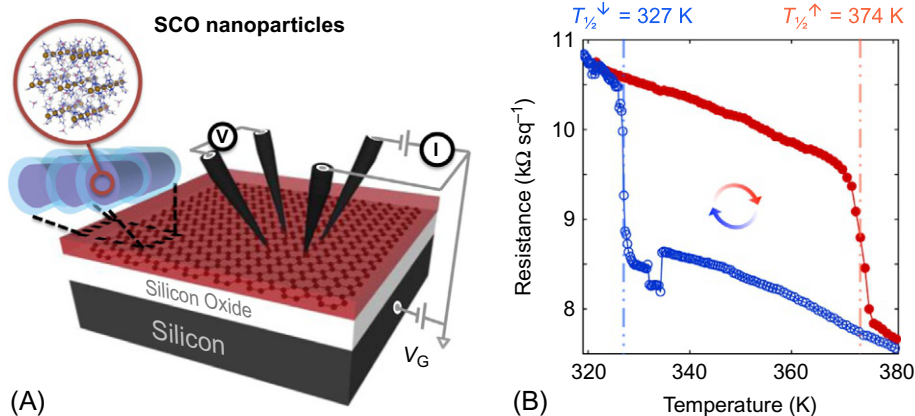


Fig. 12.14

Schematic of (A) the $[\text{Fe}(\text{Htrz})_2(\text{trz})]\text{BF}_4$ graphene-Si/SiO₂ device showing the four-probe sample resistance in a van der Pauw configuration, and (B) the temperature dependence of the graphene resistance at the Dirac point in the cooling and warming modes. *Reproduced, slightly modified with permission from J. Dugay, M. Aarts, M. Giménez-Marqués, T. Kozlova, H.W. Zandbergen, E. Coronado, H.S.J. Van Der Zant, Nano Lett. 17 (2017) 186–193. Copyright, 2017, American Chemical Society.*

In a follow-up paper, the $[\text{Fe}(\text{Htrz})_2(\text{trz})]\text{BF}_4$ nanorods were microprinted on a graphene sheet on top of a Si/SiO₂ device (Fig. 12.14) [97]. The charge transport properties of the device were explored using a four-probe field-effect configuration. With this set-up, the authors were able to convincingly demonstrate that both the resistance and hole mobility of the graphene were affected by the spin state of the SCO thin film in a reversible manner. Calculations seem to suggest that charge-carrier-scattering mechanisms in the graphene are influenced by the relative dielectric constants of the two spin states in the $[\text{Fe}(\text{Htrz})_2(\text{trz})]\text{BF}_4$ nanorods. According to the authors, the simplicity of the configuration and its ability to probe very small volumes, *ca.* 2000 μm^3 , should allow for the testing of a variety of switchable materials.

A more robust device has been prepared using SCO@SiO₂ $[\text{Fe}(\text{Htrz})_2(\text{trz})]\text{BF}_4$ nanorods. This involved CVD (chemical vapor deposition) of a 1.7- μm graphene electrode etched with a 150, 250, or 300 nm gap by nanolithography [98]. The SCO@SiO₂ nanorods were aligned using dielectrophoresis as described by Rotaru et al. earlier. The nanorods are 107 ± 13 nm long and 44 ± 10 nm wide with a silica shell thickness of 11 nm. The hysteresis of the device varies from 20 to 39 K and increases as the gap between the electrodes increases. As with similar devices, the conductance is higher for the LS state than it is in the HS state. Moreover, as the electrode gap becomes larger, the difference in conductance also increases. One of the interesting features of the device is that it shows no fatigability thought to be due to the silica shell.

A more recent development has been that of molecular actuator devices. The first of these used $\{\text{Fe}(\text{3-CNpy})[\text{Au}(\text{CN})_2]_2\} \cdot 2/3\text{H}_2\text{O}$ (3-CNpy = 3-cyanopyridine), which undergoes an abrupt and highly anisotropic SCO between 115 and 125 K [99]. The aim here is to take advantage of the large change in volume that occurs in SCO compounds as they convert between the LS and HS states. Specifically, a bilayer actuator was constructed by anchoring a SCO crystal onto a graphite rod and then coating it with a thin film of Al. Cooling of the bilayer below 80 K results in pronounced deflection of the tip of the crystal by almost 300 μm (Fig. 12.15). Remarkably, the hysteresis of the SCO material is maintained with warming to 100 K required to restore the tip to its original position. This is entirely reversible and due to the strong LIESST of $\{\text{Fe}(\text{3-CNpy})[\text{Au}(\text{CN})_2]_2\} \cdot 2/3\text{H}_2\text{O}$ can also be induced by light.

In a slight redesign, the same authors embedded $[\text{Fe}(\text{Htrz})_2(\text{trz})]\text{BF}_4$ in a PMMA matrix for the upper layer while spin coating a Ag-polymer composite for the lower layer [100]. Connecting one end of the bilayer to a fixed electrode and the other to a flexible electrode allowed a current to be applied. Applying a current to the cantilever resulted in an LS \rightarrow HS transition, while removing it led to rapid relaxation back to the LS state. The degree of movement in the tip is dependent on the current applied above a minimum threshold, *ca.* 180 mA in this case, and can be as much as 1600 μm at 300 mA. The actuation is repeatable over at least 300 cycles. It is also temperature and frequency dependent with a cut-off temperature and frequency of 50°C and 0.5 Hz, respectively, at $I_{\text{max}} = 300$ mA. The former is a property of the SCO material, while the latter is actually limited by the heat transfer process.

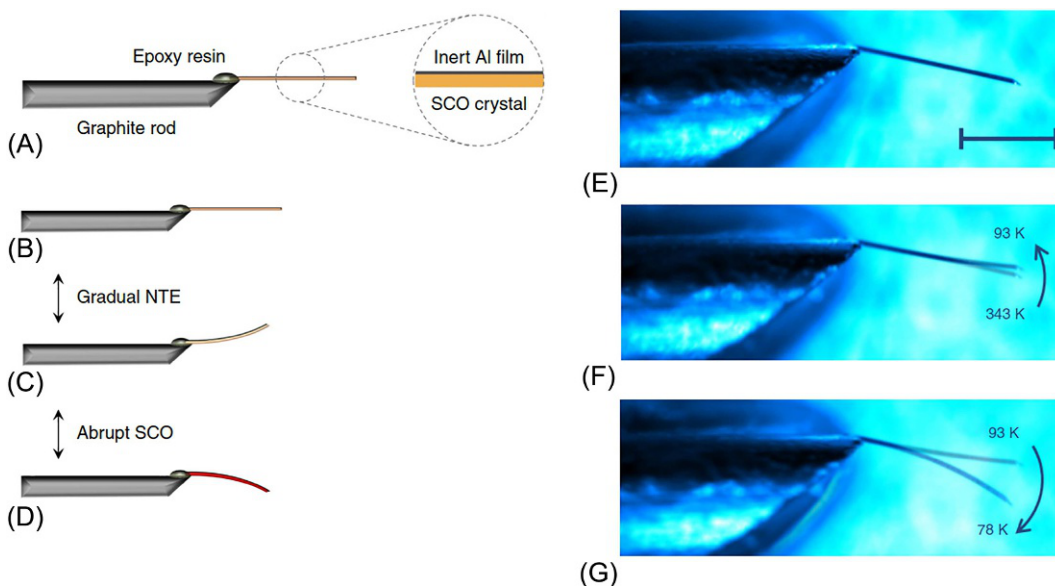


Fig. 12.15

(A) Illustration of the $\{\text{Fe}(\text{3-CNpy})[\text{Au}(\text{CN})_2]_2\} \cdot 2/3\text{H}_2\text{O}$ SCO cantilever. (B–D) Illustration of the effect of NTE and SCO on the cantilever (b-high temperature HS, c-low-temperature HS, and d-low-temperature LS). (E) Optical microscope image of the cantilever at 343 K. Scale bar represents 500 nm. (F) Comparison of the cantilever at 343 and 93 K, highlighting the deflection caused by NTE. (G) Comparison of the cantilever at 93 and 78 K, highlighting the SCO-induced actuation. *Reproduced slightly modified from H.J. Shepherd, I.A. Gural'skiy, C.M. Quintero, S. Tricard, L. Salmon, G. Molnár, A. Bousseksou, Nat. Commun. 4 (2013) 2607 with permission of the Nature Publishing Group, 2013.*

A silicon microelectromechanical system has been developed based on the same ideas outlined, this time using $[\text{Fe}(\text{Bp})_2(\text{phen})]$ as the SCO active element [101]. This configuration uses a fixed and a free cantilever to provide a reference to more accurately determine the changes that are due exclusively to SCO. Cooling the device to 10 K and irradiating with light showed a small change in the resonant frequency (f_r) of the cantilever of -0.52 Hz. A similar device has been developed by the same group. Taking advantage of the high thermal stability of $[\text{Fe}\{\text{HB}(\text{trz})_3\}_2]$, high-quality thin films 140-nm thick were deposited on a microsized cantilever [102]. Optical spectroscopy confirms that the film undergoes SCO at $T_{1/2} = 338$ K with a hysteresis of 2 K and consistent with the bulk material. As in the $[\text{Fe}(\text{Bp})_2(\text{phen})]$ system, the resonant frequency of the cantilever is spin dependent, $\Delta f_r = 66$ Hz, but is almost two orders of magnitude higher thought to be due to the reduced dimensions of the device. The change in the mechanical properties of the two spin states should allow the device to be used to do useful work.

Finally, Kraieva et al. have used 150×80 nm $[\text{Fe}(\text{Htrz})_2(\text{trz})]\text{BF}_4$ nanorods to construct a nanothermometer [103]. The nanorods were spin-coated onto prepatterned Au microwires forming a 300 nm thin film. Applying a 50 mA pulse for 50 μs results in strong local heating of the SCO material, which irreversibly switches to the HS state when operated at room temperature. Using a simple CCD camera, a resolution of 2 μm can be achieved. The particular

advantage of the system is its relative simplicity and ability to accurately locate small and transient heating events.

12.6 Conclusions and Future Prospects

The last 5 years have seen intense and growing activity in the area of SCO nanoparticles. Further clarity on the synthesis of Fe(II)-triazole has emerged with definitive proof that the nanomaterials are nanorods. While control of the exact nanorod size is still a little variable, automation of the synthesis may help in overcoming this problem. Imaging of single SCO nanoparticles has now been achieved allowing insight into the impact of SCO at the nanoscale.

Nanocrystals of molecular systems are starting to be increasingly developed broadening the range of SCO materials that might be incorporated into devices. The [Fe(Bp)₂(N-N)] system has become particularly widely used in part due its high thermal stability that permits the preparation of high-quality films and nanocrystals. Given the wealth of literature on SCO compounds and the variety of SCO profiles available, further work in this area would be expected to lead to increasingly complex SCO nanomaterials.

Hybrid SCO nanocomposites make up the bulk of the papers recently reported. The SCO@SiO₂ system is becoming increasingly common driven by the easy functionalization of the silica shell. Notably, the shell often results in a more stable hysteresis. Both natural and designed polymers have been used in making nanocomposites with a range of different applications. More systematic investigation of hybrid SCO materials would be expected to yield deeper insights into the impact of the matrix on SCO characteristics and how these might be controlled.

SCO thin films widely studied in the early days of research on SCO nanoparticles have been somewhat neglected, but recent studies have demonstrated the key role the surface plays in modifying the spin state. This is particularly important in the construction of functional devices that have finally become a reality. It is this latter area that has seen some of the most profound advances in the last 5 years. SCO devices switchable by application of a small current have been designed and constructed. Moreover, microactuators have been fabricated delivering on the promise of SCO materials. SCO research is now increasingly multidisciplinary and with the advances made in such a short period of time looks set to be a promising area of research for years to come.

Acknowledgements

We gratefully acknowledge the support of the Thailand Research Fund (RSA5880048 and RSA5580028) that has funded our research in spin crossover materials. Assistant Professor Dr. Pimphaka Harding is thanked for comments on earlier versions of the manuscript and drawing of many of the figures.

References

- [1] M.A. Halcrow (Ed.), *Spin-Crossover Materials: Properties and Applications*, John Wiley & Sons, Ltd, Chichester, 2013.
- [2] K.S. Murray, in: M.A. Halcrow (Ed.), *Spin-Crossover Materials: Properties and Applications*, John Wiley & Sons Ltd., Chichester, 2013, pp. 1–54
- [3] P. Gütllich, A.B. Gaspar, Y. Garcia, *Beilstein J. Org. Chem.* 9 (2013) 342–391.
- [4] P. Gütllich, H.A. Goodwin, *Top. Curr. Chem.* 233 (2004) 1–47.
- [5] M.A. Halcrow, *Chem. Lett.* 43 (2014) 1178–1188.
- [6] S. Brooker, *Chem. Soc. Rev.* 44 (2015) 2880–2892.
- [7] M.C. Muñoz, J.A. Real, *Coord. Chem. Rev.* 255 (2011) 2068–2093.
- [8] V. Ksenofontov, A.B. Gaspar, P. Gütllich, *Top. Curr. Chem.* 235 (2004) 23–64.
- [9] J. Linares, E. Codjovi, Y. Garcia, *Sensors* 12 (2012) 4479–4492.
- [10] J.-F. Létard, J. Mater. Chem. 16 (2006) 2550–2559.
- [11] A. Cannizzo, C.J. Milne, C. Consani, W. Gawelda, C. Bressler, F. van Mourik, M. Chergui, *Coord. Chem. Rev.* 254 (2010) 2677–2686.
- [12] A. Bousseksou, G. Molnár, L. Salmon, W. Nicolazzi, *Chem. Soc. Rev.* 40 (2011) 3313–3335.
- [13] J.-F. Létard, P. Guionneau, L. Goux-Capes, *Top. Curr. Chem.* 235 (2004) 221–249.
- [14] P. Gamez, J.S. Costa, M. Quesada, G. Aromí, *Dalton Trans.* (2009) 7845–7853.
- [15] P.J. van Koningsbruggen, Y. Maeda, H. Oshio, *Top. Curr. Chem.* 233 (2004) 259–324.
- [16] M. Nihei, T. Shiga, Y. Maeda, H. Oshio, *Coord. Chem. Rev.* 251 (2007) 2606–2621.
- [17] D.J. Harding, P. Harding, W. Phonsri, *Coord. Chem. Rev.* 313 (2016) 38–61.
- [18] H.A. Goodwin, *Top. Curr. Chem.* 234 (2004) 23–47.
- [19] Y. Garcia, P. Gütllich, *Top. Curr. Chem.* 234 (2004) 49–62.
- [20] G. Aromí, L.A. Barrios, O. Roubeau, P. Gamez, *Coord. Chem. Rev.* 255 (2011) 485–546.
- [21] G.A. Craig, O. Roubeau, G. Aromí, *Coord. Chem. Rev.* 269 (2014) 13–31.
- [22] A.B. Gaspar, M. Seredyuk, P. Gütllich, *J. Mol. Struct.* 924–926 (2009) 9–19.
- [23] M.A. Halcrow, *Coord. Chem. Rev.* 253 (2009) 2493–2514.
- [24] M.A. Halcrow, *Polyhedron* 26 (2007) 3523–3576.
- [25] B. Weber, in: M.A. Halcrow (Ed.), *Spin-Crossover Materials: Properties and Applications*, John Wiley & Sons Ltd., Chichester, 2013, pp. 55–76
- [26] P. Guionneau, *Dalton Trans.* 43 (2014) 382–393.
- [27] M.A. Halcrow, *Chem. Soc. Rev.* 40 (2011) 4119–4142.
- [28] K.S. Murray, C.J. Kepert, *Top. Curr. Chem.* 233 (2004) 195–228.
- [29] A. Hauser, *Top. Curr. Chem.* 234 (2004) 155–198.
- [30] M.A. Halcrow, *Chem. Soc. Rev.* 37 (2008) 278–289.
- [31] M. Cavallini, *Phys. Chem. Chem. Phys.* 14 (2012) 11855–12026.
- [32] A. Grohmann, M. Haryono, K. Student, P. Müller, M. Stocker, *Eur. J. Inorg. Chem.* (2013) 662–669.
- [33] H.J. Shepherd, G. Molnár, W. Nicolazzi, L. Salmon, A. Bousseksou, *Eur. J. Inorg. Chem.* (2013) 653–661.
- [34] M. Mikolasek, G. Félix, W. Nicolazzi, G. Molnár, L. Salmon, A. Bousseksou, *New J. Chem.* 38 (2014) 1834.
- [35] G. Molnár, L. Salmon, W. Nicolazzi, F. Terki, A. Bousseksou, *J. Mater. Chem. C* 2 (2014) 1360–1366.
- [36] C.M. Quintero, G. Félix, I. Suleimanov, J. Sánchez Costa, G. Molnár, L. Salmon, W. Nicolazzi, A. Bousseksou, *Beilstein J. Nanotechnol.* 5 (2014) 2230–2239.
- [37] A. Tissot, *New J. Chem.* 38 (2014) 1840.
- [38] C. Lefter, V. Davesne, L. Salmon, G. Molnár, P. Demont, A. Rotaru, A. Bousseksou, *Magnetochemistry* 2 (2016) 18.
- [39] K. Otsubo, T. Haraguchi, H. Kitagawa, *Coord. Chem. Rev.* 346 (2017) 123–138.
- [40] O. Roubeau, *Chem. Eur. J.* 18 (2012) 15230–15244.
- [41] P.N. Martinho, C. Rajnak, M. Ruben, in: M.A. Halcrow (Ed.), *Spin-Crossover Materials: Properties and Applications*, John Wiley & Sons, Ltd, Chichester, 2013, pp. 375–404.

- [42] E. Coronado, J.R. Galán-Mascarós, M. Monrabal-Capilla, J. García-Martínez, P. Pardo-Ibáñez, *Adv. Mater.* 19 (2007) 1359–1361.
- [43] M. Giménez-Marqués, M.L. García-Sanz de Larrea, E. Coronado, *J. Mater. Chem. C* 3 (2015) 7946–7953.
- [44] C. Bartual-Murgui, E. Natividad, O. Roubeau, *J. Mater. Chem. C* 3 (2015) 7916–7924.
- [45] L. Moulet, N. Daro, C. Etrillard, J.-F. Létard, A. Grosjean, P. Guionneau, *Magnetochemistry* 2 (2016) 10.
- [46] H. Peng, G. Molnár, L. Salmon, A. Bousseksou, *Chem. Commun.* 51 (2015) 9346–9349.
- [47] H. Peng, G. Molnár, L. Salmon, A. Bousseksou, *Eur. J. Inorg. Chem.* 2015 (2015) 3336–3342.
- [48] M.-Y. Chen, X.-R. Chen, W.-H. Ning, X.-M. Ren, *RSC Adv.* 4 (2014) 39126.
- [49] N. Daro, L. Moulet, N. Penin, N. Paradis, J. F. Létard, E. Lebraud, S. Buffière, G. Chastanet, P. Guionneau, *Materials (Basel)* 10 (2017) 60.
- [50] K. Robertson, H.J. Shepherd, K.R.P. Flandrin, H.J. Shepherd, C.C. Wilson, U. Kingdom, K. Robertson, *Chim. Oggi* 35 (2017) 2–4.
- [51] M.D. Manrique-Juárez, I. Suleimanov, E.M. Hernández, L. Salmon, G. Molnár, A. Bousseksou, *Materials (Basel)* 9 (2016) 537.
- [52] G. Gallé, C. Etrillard, J. Degert, F. Guillaume, J.F. Létard, E. Freysz, *Appl. Phys. Lett.* 102 (2013) 1–5.
- [53] H. Peng, S. Tricard, G. Félix, G. Molnár, W. Nicolazzi, L. Salmon, A. Bousseksou, *Angew. Chem. Int. Ed.* 53 (2014) 10894–10898.
- [54] G. Félix, M. Mikolasek, H. Peng, W. Nicolazzi, G. Molnár, A.I. Chumakov, L. Salmon, A. Bousseksou, *Phys. Rev. B: Condens. Matter Mater. Phys.* 91 (2015) 1–5.
- [55] R.M. van der Veen, O.-H. Kwon, A. Tissot, A. Hauser, A.H. Zewail, *Nat. Chem.* 5 (2013) 395–402.
- [56] D.M. Sagar, F.G. Baddour, P. Konold, J. Ullom, D.A. Ruddy, J.C. Johnson, R. Jimenez, *J. Phys. Chem. Lett.* 7 (2016) 148–153.
- [57] J. Laisney, A. Tissot, G. Molnár, L. Rechinat, E. Rivière, F. Brisset, A. Bousseksou, M.-L. Boillot, *Dalton Trans.* 44 (2015) 17302–17311.
- [58] F.J. Valverde-Muñoz, A.B. Gaspar, S.I. Shylin, V. Ksenofontov, J.A. Real, *Inorg. Chem.* 54 (2015) 7906–7914.
- [59] L. Zhang, J.-J. Wang, G.-C. Xu, J. Li, D.-Z. Jia, S. Gao, *Dalton Trans.* 42 (2013) 8205–8208.
- [60] L.L. Nguyen, R. Guillot, J. Laisney, L. Rechinat, S. Bedoui, G. Molnár, E. Rivière, M.-L. Boillot, *New J. Chem.* 39 (2015) 1603–1610.
- [61] T. Palamarcic, J.C. Oberg, F. El Hallak, C.F. Hirjibehedin, M. Serri, S. Heutz, J.-F. Létard, P. Rosa, *J. Mater. Chem.* 22 (2012) 9690.
- [62] Y.-H. Luo, Q.-L. Liu, L.-J. Yang, Y. Sun, J.-W. Wang, C.-Q. You, B.-W. Sun, *J. Mater. Chem. C* 4 (2016) 8061–8069.
- [63] P. Chakraborty, M.L. Boillot, A. Tissot, A. Hauser, *Angew. Chem. Int. Ed.* 52 (2013) 7139–7142.
- [64] R. Bertoni, M. Lorenc, A. Tissot, M. Servol, M.L. Boillot, E. Collet, *Angew. Chem. Int. Ed.* 51 (2012) 7485–7489.
- [65] S. Titos-Padilla, J.M. Herrera, X.W. Chen, J.J. Delgado, E. Colacio, *Angew. Chem. Int. Ed.* 50 (2011) 3290–3293.
- [66] I. Suleimanov, O. Kraieva, J. Sánchez Costa, I.O. Fritsky, G. Molnár, L. Salmon, A. Bousseksou, *J. Mater. Chem. C* 3 (2015) 5026–5032.
- [67] I. Suleimanov, O. Kraieva, G. Molnár, L. Salmon, A. Bousseksou, *Chem. Commun.* 51 (2015) 15098–15101.
- [68] Y.-X. Wang, D. Qiu, S.-F. Xi, Z.-D. Ding, Z. Li, Y. Li, X. Ren, Z.-G. Gu, *Chem. Commun.* 52 (2016) 8034–8037.
- [69] A. Paquirissamy, A.R. Ruyack, A. Mondal, Y. Li, R. Lescouëzec, C. Chanéac, B. Fleury, *J. Mater. Chem. C* 3 (2015) 3350–3355.
- [70] P. Durand, S. Pillet, E.-E. Bendeif, C. Carteret, M. Bouzaoui, H. El Hamzaoui, B. Capoen, L. Salmon, S. Hébert, J. Ghanbaja, L. Aranda, D. Schaniel, *J. Mater. Chem. C* 1 (2013) 1933.
- [71] T. Zhao, L. Cuignet, M.M. Dîrtu, M. Wolff, V. Spasojevic, I. Boldog, A. Rotaru, Y. Garcia, C. Janiak, *J. Mater. Chem. C* 3 (2015) 7802–7812.

- [72] I. Suleimanov, J. Sánchez Costa, G. Molnár, L. Salmon, A. Bousseksou, *Chem. Commun.* 50 (2014) 13015–13018.
- [73] D. Qiu, L. Gu, X.-L. Sun, D.-H. Ren, Z.-G. Gu, Z. Li, *RSC Adv.* 4 (2014) 61313–61319.
- [74] L. Moulet, N. Daro, S. Mornet, N. Vilar-Vidal, G. Chastanet, P. Guionneau, *Chem. Commun.* 52 (2016) 13213–13216.
- [75] C. Göbel, T. Palamarciuc, C. Lochenie, B. Weber, *Chem. Asian J.* 9 (2014) 2232–2238.
- [76] O. Klimm, C. Göbel, S. Rosenfeldt, F. Puchler, N. Miyajima, K. Marquardt, M. Drechsler, J. Breu, S. Förster, B. Weber, *Nano* 8 (2016) 19058–19065.
- [77] A. Tsubasa, S. Otsuka, T. Maekawa, R. Takano, S. Sakurai, T.J. Deming, K. Kuroiwa, *Polymer* (2017), <https://doi.org/10.1016/j.polymer.2016.12.079>.
- [78] V. Nagy, K. Halász, M.T. Carayon, I. A. Gural'skiy, S. Tricard, G. Molnár, A. Bousseksou, L. Salmon, L. Csóka, *Colloids Surf. A Physicochem. Eng. Asp.* 456 (2014) 35–40.
- [79] V. Nagy, I. Suleimanov, G. Molnár, L. Salmon, A. Bousseksou, L. Csóka, *J. Mater. Chem. C* 3 (2015) 7897–7905.
- [80] S. Rat, V. Nagy, I. Suleimanov, G. Molnár, L. Salmon, P. Demont, L. Csóka, A. Bousseksou, *Chem. Commun.* 52 (2016) 11267–11269.
- [81] D. Onggo, I. Mulyani, F.J. Valverde-Muñoz, J.A. Real, G. Molnar, *Cellulose* 24 (2017) 2205–2213.
- [82] A. Tokarev, J. Long, Y. Guari, J. Larionova, F. Quignard, P. Agulhon, M. Robitzer, G. Molnár, L. Salmon, A. Bousseksou, *New J. Chem.* 37 (2013) 3420.
- [83] D. Qiu, D.-H. Ren, L. Gu, X.-L. Sun, T.-T. Qu, Z.-G. Gu, Z. Li, *RSC Adv.* 4 (2014) 31323.
- [84] Y. Murrashima, M.R. Karim, N. Saigo, H. Takehira, R. Ohtani, M. Nakamura, M. Koinuma, L. F. Lindoy, K. Kuroiwa, S. Hayami, *Inorg. Chem. Front.* 2 (2015) 886–892.
- [85] C. Bartual-Murgui, A. Cerf, C. Thibault, C. Vieu, L. Salmon, G. Molnár, A. Bousseksou, *Microelectron. Eng.* 111 (2013) 365–368.
- [86] D. Tanaka, N. Aketa, H. Tanaka, T. Tamaki, T. Inose, T. Akai, H. Toyama, O. Sakata, H. Tajiri, T. Ogawa, *Chem. Commun.* 50 (2014) 10074.
- [87] B. Warner, J.C. Oberg, T.G. Gill, F. El Hallak, C.F. Hirjibehedin, M. Serri, S. Heutz, M.-A. Arrio, P. Sainctavit, M. Mannini, G. Poneti, R. Sessoli, P. Rosa, *J. Phys. Chem. Lett.* 4 (2013) 1546–1552.
- [88] M. Gruber, V. Davesne, M. Bowen, S. Boukari, E. Beaurepaire, W. Wulfhekel, T. Miyamachi, *Phys. Rev. B: Condens. Matter Mater. Phys.* 89 (2014) 1–9.
- [89] H. Naggert, J. Rudnik, L. Kipgen, M. Bernien, F. Nickel, L. M. Arruda, W. Kuch, C. Näther, F. Tuzcek, *J. Mater. Chem. C* 3 (2015) 7870–7877.
- [90] A. Lapresta-Fernández, M.P. Cuéllar, J.M. Herrera, A. Salinas-Castillo, M.d.C. Pegalajar, S. Titos-Padilla, E. Colacio, L.F. Capitán-Vallvey, *J. Mater. Chem. C* 2 (2014) 7292.
- [91] C.R. Gros, M.K. Pehrah, B.D. Hosterman, T.V. Brinzari, P.A. Quintero, M. Sendova, M.W. Meisel, D. R. Talham, *J. Am. Chem. Soc.* 136 (2014) 9846–9849.
- [92] X. Zhang, T. Palamarciuc, J.-F. Létard, P. Rosa, E.V. Lozada, F. Torres, L.G. Rosa, B. Doudin, P. A. Dowben, *Chem. Commun.* 50 (2014) 2255–2257.
- [93] E.J. Devid, P.N. Martinho, M.V. Kamalakar, I. Šalitroš, Ú. Prendergast, J. F. Dayen, V. Meded, T. Lemma, R. González-Prieto, F. Evers, T.E. Keyes, M. Ruben, B. Doudin, S.J. Van Der Molen, *ACS Nano* 9 (2015) 4496–4507.
- [94] A.C. Aragonès, D. Aravena, J.I. Cerdá, Z. Acís-Castillo, H. Li, J.A. Real, F. Sanz, J. Hihath, E. Ruiz, I. Díez-Pérez, *Nano Lett.* 16 (2016) 218–226.
- [95] A. Rotaru, J. Dugay, R.P. Tan, I. A. Guralskiy, L. Salmon, P. Demont, J. Carrey, G. Molnár, M. Respaud, A. Bousseksou, *Adv. Mater.* 25 (2013) 1745–1749.
- [96] J. Dugay, M. Giménez-Marqués, T. Kozlova, H.W. Zandbergen, E. Coronado, H.S.J. Van Der Zant, *Adv. Mater.* 27 (2015) 1288–1293.

- [97] J. Dugay, M. Aarts, M. Giménez-Marqués, T. Kozlova, H.W. Zandbergen, E. Coronado, H.S.J. Van Der Zant, *Nano Lett.* 17 (2017) 186–193.
- [98] A. Holovchenko, J. Dugay, M. Giménez-Marqués, R. Torres-Cavanillas, E. Coronado, H.S.J. van der Zant, *Adv. Mater.* (2016) 7228–7233.
- [99] H.J. Shepherd, I.A. Gural'skiy, C.M. Quintero, S. Tricard, L. Salmon, G. Molnár, A. Bousseksou, *Nat. Commun.* 4 (2013) 2607.
- [100] I.A. Gural'skiy, C.M. Quintero, J. Sánchez Costa, P. Demont, G. Molnár, L. Salmon, H. J. Shepherd, A. Bousseksou, *J. Mater. Chem. C* 2 (2014) 2949–2955.
- [101] M.D. Manrique-Juarez, S. Rat, F. Mathieu, D. Saya, I. Séguy, T. Leïchlé, M.D. Manrique-juarez, S. Rat, F. Mathieu, D. Saya, *Appl. Phys. Lett.* 109 (2016) 61903.
- [102] M.D. Manrique-Juarez, F. Mathieu, V. Shalabaeva, J. Cacheux, S. Rat, L. Nicu, T. Leïchlé, L. Salmon, G. Molnár, A. Bousseksou, *Angew. Chem. Int. Ed.* 56 (2017) 8074–8078.
- [103] O. Kraieva, C.M. Quintero, I. Suleimanov, E. M. Hernandez, D. Lagrange, L. Salmon, W. Nicolazzi, G. Molnár, C. Bergaud, A. Bousseksou, *Small* 12 (2016) 6325–6331.

Magnetic Metal-Nonstoichiometric Oxide Nanocomposites: Structure, Transport, and Memristive Properties

Vladimir V. Rylkov*, Vyacheslav A. Demin*, Andrey V. Emelyanov*,
Alexander V. Sitnikov[†], Yurii E. Kalinin[†], Victor V. Tugushev*,
Alexander B. Granovsky[‡]

*National Research Centre “Kurchatov Institute”, Moscow, Russia, [†]Voronezh State Technical University, Voronezh, Russia, [‡]Lomonosov Moscow State University, Moscow, Russia

13.1 Introduction

Magnetic nanocomposites (NCs), or nanogranular magnetic thin films “ferromagnetic metal-insulator,” in which ultrafine single-domain ferromagnetic (FM) particles are embedded in a nonmagnetic insulator (oxide) matrix, form a class of artificial functional materials with a large diversity of magnetic, transport, optical, magneto-optical, and high-frequency properties. The intense research of these materials is motivated not only by the important technological applications, including high coercive films for information storage, high-permeability films for shielding, magnetoresistive devices, magnetic sensors, and so on, but also because they are interesting model objects to study basic properties of disordered systems, especially connected with peculiarities of Coulomb interaction and exchange coupling between granules, the percolation phenomenon in conductivity and ferromagnetic order [1–5].

During the last 60 years, many efforts have been devoted to study of electrical resistivity and magnetotransport in magnetic NCs, but nevertheless up to now basic mechanisms of electrical resistivity, magnetoresistance, Hall effect are far from being well understood. Besides, recently, novel transport phenomena have been discovered such as logarithmic temperature dependence of conductivity [1,6], tunneling anomalous Hall effect [7], memristive effect [8,9]. Obviously all these features cannot be explained without detailed knowledge of structural and magnetic properties. We present recent results on structural, magnetic, magnetotransport, and memristive properties of $(\text{Co}_{40}\text{Fe}_{40}\text{B}_{20})_x(\text{Al}_2\text{O}_3)_{100-x}$ and $(\text{Co}_{40}\text{Fe}_{40}\text{B}_{20})_x(\text{LiNbO}_3)_{100-x}$ NCs with $x=6-60$ at.%, which are typical representatives of

composites based on nonstoichiometric oxides. For the sake of brevity, we will denote the $\text{Co}_{40}\text{Fe}_{40}\text{B}_{20}$ alloy as usually CoFeB and NCs under study as $(\text{CoFeB})_x(\text{AlO}_y)_{100-x}$ and $(\text{CoFeB})_x(\text{LiNbO}_y)_{100-x}$ with $y \approx 1.5$ and 3, respectively.

The nanocomposite films were produced using the ion-beam sputtering of the composite targets onto glass-ceramic substrates at growth temperature not exceeding 100°C , and they consist of magnetic nanogranules embedded into the nonstoichiometric oxide matrix. For $(\text{CoFeB})_x(\text{AlO}_y)_{100-x}$ the granules are rounded (2–4 nm in size), whereas for $(\text{CoFeB})_x(\text{LiNbO}_y)_{100-x}$ the granules are strongly elongated along the NC growth axis up to 10–15 nm with the same in-plane size 2–4 nm. The chemical compositions of granules and matrix differ from those of corresponding targets, a large amount of Fe^{2+} and Co^{2+} ions dispersed in the matrix (up to $\approx 3 \times 10^{22} \text{ cm}^{-3}$) was found by both structural and magnetic measurements. These two factors play a crucial role both in the ferromagnetic exchange between granules and in magnetotransport properties, especially in the vicinity of metal-insulator transition (MIT). The conductivity of the systems follows the $\ln T$ law on the metallic side of MIT in the range of metal content variation $x = 44\text{--}56 \text{ at.}\%$ that formally corresponds to the conductivity of array of granules with strong tunnel coupling between them. But at $x < (44\text{--}48) \text{ at.}\%$ the $\sigma \propto \ln T$ law changes to the $\ln \sigma \propto -(T_0/T)^{1/2}$ dependence. Tunneling conductivity of NC (at $x \leq 56 \text{ at.}\%$ in the case of $(\text{CoFeB})_x(\text{AlO}_y)_{100-x}$ causes also the specific features of anomalous Hall effect (AHE). There is a clear evidence of tunneling anomalous Hall effect (TAHE) caused by spin-orbital scattering-assisted mechanism [10], but this contribution strongly shunted due to generation of local circular Hall current especially in case of the elongated granules, i.e., for $(\text{CoFeB})_x(\text{LiNbO}_y)_{100-x}$ NC.

For capacitor-like metal/NC/metal (Me/NC/Me) structures based on $(\text{CoFeB})_x(\text{LiNbO}_y)_{100-x}$ NC, the effects of the resistive switching (RS) are found below MIT at $x \approx 7\text{--}14 \text{ at.}\%$. These effects are explained by formation of the isolated chains of the elongated granules and anomalous strong decrease of their resistance in the strong fields $E > 10^4 \text{ V/cm}$, owing to: (i) suppression of effects of Coulomb blockade, (ii) generation of oxygen vacancies as well as their electromigration into a strongly oxidized NC layer near one of the electrodes of Me/NC/Me structure. The endurance to RS exceeds 10^5 at the ratio $R_{\text{off}}/R_{\text{on}} \sim 50$ of the high-resistance state to the low one.

13.2 Samples and Investigation Methods

13.2.1 Samples Preparation

Film nanocomposites were prepared by ion-beam sputtering. Applied to NCs, this method has several advantages in comparison with other methods of thin film preparation, namely, high growth rate and good adhesion properties, low contamination by extraneous gas, low substrate temperatures, the possibility of sputtering conducting and insulating materials, and

the possibility of preparing various alloys and mixtures without violating the percentage of incoming components.

Ion-beam sputtering is a type of ion-plasma sputtering when ions of an inert gas from an independent source are directed by a high-energy flux at the target to be sputtered. Since this ion source is not associated with the object of sputtering, it allows the spraying of ferromagnetic metals and alloys, and also dielectric materials in the presence of a charge neutralizer. Plasma localization in the ion source magnetic gap makes it possible to avoid excess heating of the substrates during deposition without forced cooling. The process of condensation in ion-beam deposition methods is carried out in a vacuum $<10^{-5}$ Torr.

Fig. 13.1 shows the scheme of ion-beam sputtering system [11]. Modernization made it possible to place seven ion-beam sputtering sources in a vacuum chamber (six for spraying metal or dielectric layers, last in the presence of a charge neutralizer, and one together with an electron source for cleaning the substrate). To supply high voltage to the anodes of sources of ion-beam sputtering, modernized power supplies are used. The substrate holder 2, which is fixed on the axis and can rotate at a speed of up to 2 rpm, is placed along the perimeter of vacuum chamber.

Up to twelve substrates (labeled 7 in Fig. 13.1) with a size of $100 \times 200 \text{ mm}^2$ can be fixed on the holder. In order to neutralize the positive potential that appears on the dielectric surface during sputtering of dielectric materials, it is envisaged to use a charge neutralizer 6, which is 0.2-mm-diameter tungsten wire that is connected to a separate power source.

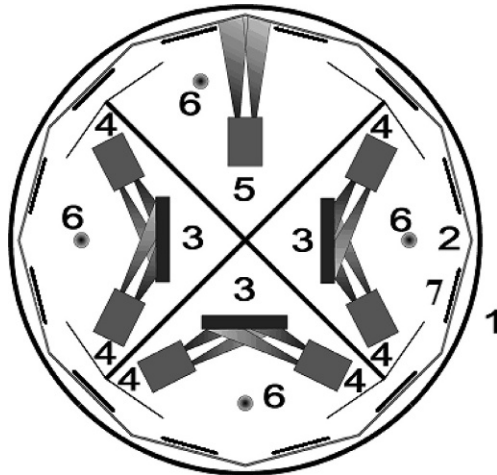


Fig. 13.1

Multifunctional ion-beam sputtering system. (1) vacuum chamber; (2) substrate holder; (3) water-cooled target; (4) ion-beam source; (5) ion-etching source; (6) charge neutralizer; (7) substrate.

The use of such sources and their arrangement in the vacuum chamber of the setup makes it possible to obtain NCs and multilayer films on a rotating substrate, which facilitates the formation of uniform in thickness layers. The NCs films under study were produced at the growth temperature not exceeding 100°C by the ion-beam sputtering technique onto glass-ceramic substrates in an argon atmosphere $P_{\text{Ar}} = 3.6 \times 10^{-4}$ Torr with a rate of about 0.25 nm/s using the composite targets that include the parent metallic alloy $\text{Co}_{40}\text{Fe}_{40}\text{B}_{20}$ and 14–15 oxide stripes (Al_2O_3 or LiNbO_3) placed onto the metal surface (Fig. 13.2). The special target design makes it possible to obtain composite systems with the relative content of the metallic phase continuously varying ($\delta x \approx 0.5$ –1 at.%) in a wide range $x = 6$ –60 at.% in a single technological cycle. The thickness of the produced planar samples was about $d \approx 2.7$ and $1 \mu\text{m}$ for $(\text{CoFeB})_x(\text{AlO}_y)_{100-x}$ and $(\text{CoFeB})_x(\text{LiNbO}_y)_{100-x}$, respectively. The elemental composition of the films was determined by energy-dispersive X-ray (EDX) spectroscopy using an Oxford INCA Energy 250 unit attached to a JEOL JCM-6380 LV scanning electron microscope. The composition of the granules does not correspond to the composition of the parent alloy $\text{Co}_{40}\text{Fe}_{40}\text{B}_{20}$ and matrix is not pure stoichiometric oxide [5,7,9]. Note that the modern high-resolution EDX methods cannot reveal the relative content of B atoms in metal granules and in the oxide matrix. Therefore, as in Refs. [5,7,9], we will further adduce the metal fraction of grown NCs by approximating their structure the formula $(\text{CoFeB})_x(\text{Al}_2\text{O}_3)_{100-x}$ or $(\text{CoFeB})_x(\text{LiNbO}_3)_{100-x}$ (as for used targets) because it allows definitely find the x value by EDX data.

After producing composites, we used photolithography for preparing the samples having the standard double-cross shape to measure the electrical conductivity and Hall effect in planar

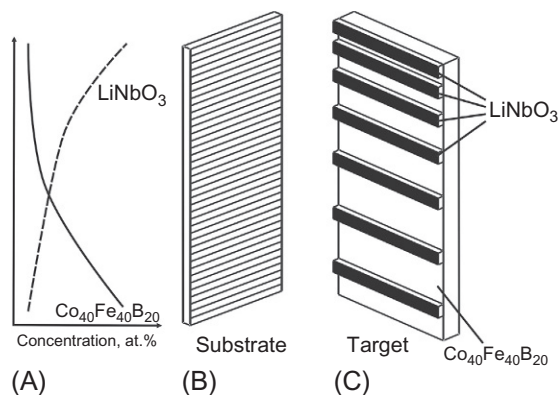


Fig. 13.2

The scheme of (A) distribution of the concentration of the components in the samples of the $(\text{CoFeB})_x(\text{LiNbO}_y)_{100-x}$ NC along the direction of the substrate holder; (B) the substrate holder with glass-ceramic plates; (C) the composite target with parent alloy $\text{Co}_{40}\text{Fe}_{40}\text{B}_{20}$ with a size $270 \times 80 \text{ mm}^2$ and oxide stripes with thickness of ~ 2 mm and a width of ~ 9 mm. The number of oxides stripe and distance between can be varied within a wide range.

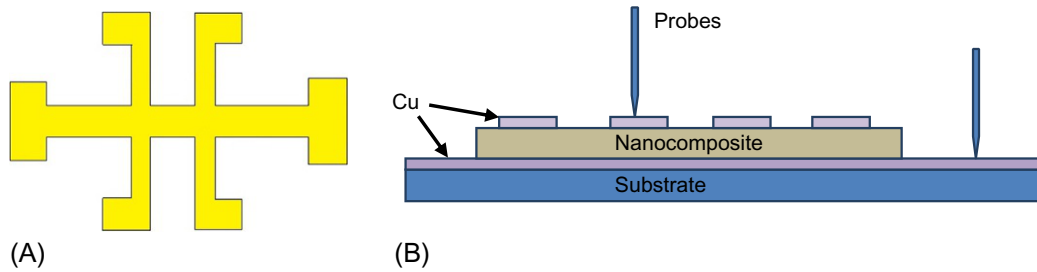


Fig. 13.3

Samples for investigation nanocomposite properties in planar (A) and vertical (B) geometries.

geometry (Fig. 13.3A). The conduction channel had the width $w = 1.2$ mm, the length $l = 4$ mm with the distance between potential probes $l_p = 1.4$ mm. The precision of alignment of Hall probes was better than $10\ \mu\text{m}$. The investigation of magnetic properties was performed on the same samples as for Hall effect measurements (Fig. 13.3A).

The memristive properties of NCs were investigated in strong electric fields ($>10^4$ V/cm) for the so-called vertical (or capacitor-type) metal/nanocomposite/metal (Me/NC/Me) layered structures (Fig. 13.3B) based on the $(\text{CoFeB})_x(\text{LiNbO}_y)_{100-x}$. The NC films of $3\text{-}\mu\text{m}$ -thick were deposited on glass-ceramic substrates through the metal shadow mask with periodic holes (5 mm in diameter) by means of ion-beam deposition technique. The substrates were preliminarily coated with a metallic Cu film (or a three-layer Cr/Cu/Cr film) of thickness $\sim 0.5\ \mu\text{m}$, which was a bottom electrode. The top electrodes (Cu or Cr/Cu/Cr) were deposited through a shadow mask with a hole size of $0.5 \times 0.2\ \text{mm}^2$. The relative content of the metallic phase for memristor structures was changed in the range of $x = 6\text{--}50\ \text{at.}\%$ ($\delta x \approx 1\ \text{at.}\%$).

It is widely accepted that the memristive effects in oxides are related with the oxygen vacancies. In order to fabricate Me/NC/Me structures with different oxygen vacancy distribution across the thickness, the following four growth regimes of the NC films were used:

- (1) At the initial stage of the NC growth, the pressure in the chamber $P \approx 1 \times 10^{-5}$ Torr was chosen much worse than the ultimate vacuum $P \approx 6 \times 10^{-6}$ Torr, which was reached during the deposition process. In this case, the oxygen partial pressure during the NC growth time varied from $P_{\text{O}_2} \approx 2 \times 10^{-6}$ to $P_{\text{O}_2} \approx 1.2 \times 10^{-6}$ Torr, taking into account that the oxygen content in the atmosphere is $\approx 21\%$.
- (2) The NC growth was carried out in the same way as in regime 1, but with the addition of oxygen in the preset flow regime (in the case of the ultimate vacuum, this flow provided the partial pressure $P_{\text{O}_2} \approx 2 \times 10^{-5}$ Torr).
- (3) The NC growth was carried out with the addition of oxygen in the preset flow regime for the first 7 min (at the ultimate vacuum this flow provided the partial pressure $P_{\text{O}_2} \approx 2.5 \times 10^{-5}$ Torr). Then, the NC was deposited as in regime 1. In this case, an

oxidized high-resistance layer of the NC with a thickness of about 100 nm appeared at the bottom electrode of the Me/NC/Me structure.

- (4) Initially, the NC was deposited as in regime 1. Then, during the last 7 min of growth, oxygen was added in the preset flow regime, the same as in regime 3. In this case, at the top electrode of the Me/NC/Me structure, an oxidized high-resistance layer of the NC was formed with a thickness of about 100 nm.

Further, in accordance with the described regimes of deposition of Me/NC/Me structures, we will mark them as structures 1–4.

13.2.2 Methods of Investigation and Technique

The structural features of the NC films were studied by transmission and scanning transmission electron microscopy (TEM and STEM) using TITAN 80–300 TEM/STEM instrument (FEI, US) operating at an accelerating voltage of $U = 300$ kV, equipped with Cs-probe corrector, high-angle annular dark-field detector (HAADF) (Fischione, US), and EDX microanalysis spectrometer (EDAX, US). For the image processing, Digital Micrograph (Gatan, US) software and TIA (FEI, US) were used. The details of equipment and sample preparation for structural investigations are given in Ref. [7].

The investigations of transport properties of NC samples were performed using an evacuated insert with a superconducting solenoid, immersed in a liquid-helium Dewar flask. The Hall effect was measured within the 10–200 K temperature range at magnetic fields up to 1.5 T; the conductivity was determined at 6–300 K.

The magnetization M of NC films was measured by SQUID magnetometer (Quantum Design MPMS-XL7) between 1.9 and 350 K at in-plane and out-of-plane magnetic fields $\mu_0 H$ up to 7 T.

Studies of the current-voltage characteristic (I - V curves) of Me/NC/Me structures and their memristive properties were performed at room temperature using source measurement unit NI PXI-4130 (National Instruments) and probe station PM5 (Cascade Microtech) with micrometric positioning. The I - V curves were measured with a grounded bottom electrode and a linearly changed bias voltage U on the top electrode in a sequence $0 \rightarrow +5 \rightarrow -5 \rightarrow 0$ V with the step of 0.1 V, which could be repeated periodically. The duration of the voltage variation sequence was 12 s.

13.3 Structural Characterization

Results of the high-resolution TEM/STEM electron microscopy showed that the structure of $(\text{CoFeB})_x(\text{AlO}_y)_{100-x}$ NCs weakly depends on their content near MIT below a percolation threshold ($x \approx 46$ – 57 at.%) [7]. According to the electron microscopy data, this NC consists of the strained base-centered cubic (bcc) CoFe granules with the size $a = 2$ – 4 nm having rounded shape (see Fig. 13.4A and the inset). The selected area electron diffraction (SAED) pattern

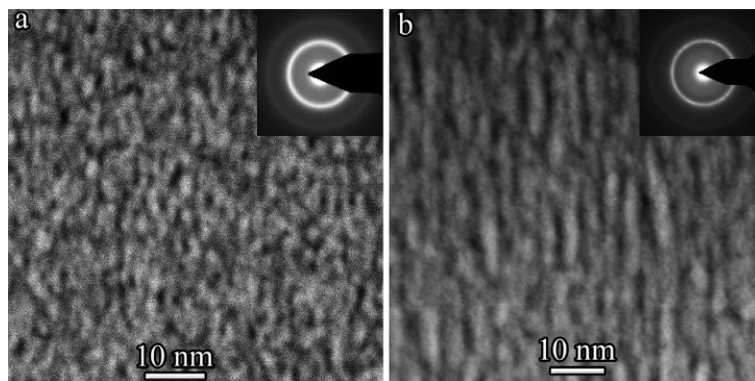


Fig. 13.4

HAADF STEM images of (A) $(\text{CoFeB})_x(\text{AlO}_y)_{100-x}$ ($x=57$ at.%) and (B) $(\text{CoFeB})_x(\text{LiNbO}_y)_{100-x}$ ($x=48$ at.%) NCs. Light areas correspond to CoFe nanogranules. Insets show the selected area electron diffraction pattern of samples with $x=46$ at.% (A) and $x=48$ at.% (B). From V.V. Rylkov, A.V. Sitnikov, S.N. Nikolaev, V.A. Demin, A.N. Taldenkov, M.Yu. Presnyakov, A.V. Emelyanov, A.L. Vasiliev, Yu.E. Kalinin, A.S. Bugaev, V.V. Tugushev, A.B. Granovsky. *J. Magn. Magn. Mater.*, 2017 (<https://doi.org/10.1016/j.jmmm.2017.11.022>).

demonstrates the peaks correspondent to three interplanar spacings: 2.02, 1.25, and 0.8 Å. These spacings match the distances close to $d(1\ 1\ 0)$, $d(2\ 1\ 1)$, and $d(2\ 2\ 2)$ in bcc FeCo alloy with unit cell constant $a_c=0.28486$ nm (space group $Im-3m$) [12]. However, (200) bcc reflection in our case is absent. Deformation may cause distortion of the bcc (200) planes and drastic decrease of (200) reflection [13].

The structure of $(\text{CoFeB})_x(\text{LiNbO}_y)_{100-x}$ film NC turned out to be different. The HAADF STEM image of samples $(\text{CoFeB})_x(\text{LiNbO}_y)_{100-x}$ with $x \approx 48$ at.% is presented in Fig. 13.4B. In this case, the NC consists of the crystalline CoFe granules (the bright contrast areas) with the in-plane size of $a_x=a=2-4$ nm elongated in the direction of NC growth up to $a_z=10-15$ nm. The electron diffraction (see the inset in Fig. 13.4B) unambiguously indicates that granules represent the crystals of CoFe alloy with bcc structure [12]. Note that the diffraction rings in $(\text{CoFeB})_x(\text{LiNbO}_y)_{100-x}$ NC are more sharp than these in $(\text{CoFeB})_x(\text{Al}_2\text{O}_y)_{100-x}$ one. There are three circles on the electron diffraction pattern corresponding to (0 1 1), (2 0 0), and (2 1 1) bcc reflections; their view indicates lack of texture. To prove that the areas with bright contrast in Fig. 13.4B correspond to CoFe granules, we performed in addition the EDX mapping for Fe and Co elemental distribution (Fig. 13.5). There is unambiguous match of Fe and Co distribution and these areas correspond to the bright areas in HAADF STEM image of Fig. 13.4A.

The elongated granules and their bcc crystalline structure in the $(\text{CoFeB})_x(\text{LiNbO}_y)_{100-x}$ NC films are typically not only for large but also for small CoFe volume fraction. It is most clearly seen from analysis of the bright-field high-resolution STEM images, shown in Fig. 13.6 for

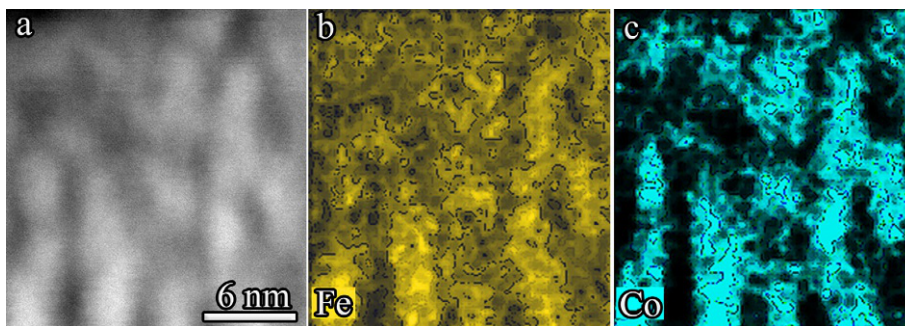


Fig. 13.5

(A) HAADF STEM image of the $(\text{CoFeB})_x(\text{LiNbO}_y)_{100-x}$ NC ($x=48$ at.%) and the elemental maps of (B) Fe, and (C) Co. Note the overlapping of Co and Fe elemental distribution in the brighter areas of the image in (A). From V.V. Rylkov, A.V. Sitnikov, S.N. Nikolaev, V.A. Demin, A.N. Taldenkov, M.Yu. Presnyakov, A.V. Emelyanov, A.L. Vasiliev, Yu.E. Kalinin, A.S. Bugaev, V.V. Tugushev, A.B. Granovsky. *J. Magn. Mater.*, 2017 (<https://doi.org/10.1016/j.jmmm.2017.11.022>).

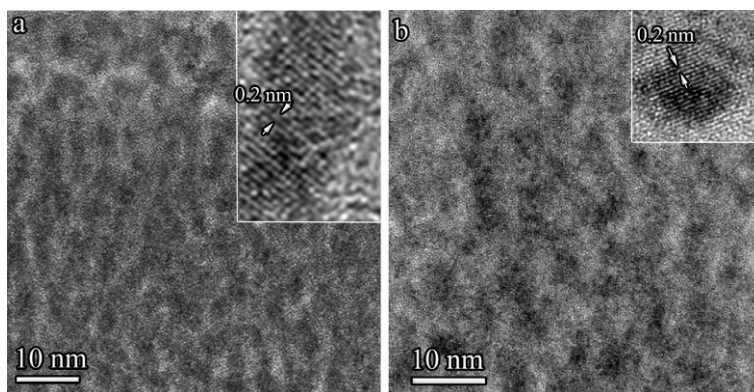


Fig. 13.6

Bright-field high-resolution STEM images of the of the $(\text{CoFeB})_x(\text{LiNbO}_y)_{100-x}$ NC with different content $x=34$ at.% (A) and $x=16$ at.% (B). In both cases, the CoFe granules (the dark contrast areas), elongated in the direction of NC growth, are clearly observed. Insets show bright-field high-resolution STEM images of single CoFe granules with bcc structure. From V.V. Rylkov, S.N. Nikolaev, V.A. Demin, A.V. Emelyanov, A.V. Sitnikov, K.E. Nikiruy, V.A. Levanov, M.Yu. Presnyakov, A.N. Taldenkov, A.L. Vasiliev, K.Yu. Chernoglazov, A.S. Vedeneev, Yu.E. Kalinin, A.B. Granovsky, V.V. Tugushev, A.S. Bugaev, *J. Exp. Theor. Phys.*, 126 (2018) 353.

samples with $x \approx 34$ at.% (A) and 16 at.% (B). Insets in Fig. 13.6 show bright-field high-resolution STEM images of separate granules characterized by a dark contrast. These images confirm that granules are elongated in the direction of the NC growth and uniquely point on bcc crystalline structure with unit cell constant $a_c=0.284$ nm [12]. The spacing between planes in insets is $d_{(110)}=0.201$ nm that corresponds to planes $\{110\}$.

Note that EDX-mapping experiments indicate the noticeable content of dispersed Fe and Co atoms in oxide matrix for these type of NCs (see Fig. 4 from Ref. [7]). We can conclude also from EDX data that B atoms were distributed more or less uniformly both in Fe-Co and oxide regions. The most probable reason is that the enthalpy of the BO oxide formation ($E_e = +0.04$ eV/molecule) is much less as compared to the enthalpy of the AlO oxide formation $E_e = +0.95$ eV/molecule (for LiO and NbO the values of $E_e = +0.68$ and $+2.06$ eV/molecule, respectively) but the binding energy of BO molecule (8.4 eV) is much larger than of the AlO molecule (5.0 eV) [14]. For this reason, the boron atoms outside CoFe granules are energetically more favorable to form the BO oxide while residual oxygen to form $\text{Al}_2\text{O}_{3-z}$ (or LiNbO_{3-z}) oxide.

So, we can conclude that NCs under study consist of strained crystalline granules rounded or elongated, depending on the type of amorphous oxide matrix with a large amount of dispersed atoms of B, Fe, and Co.

13.4 Temperature Dependence of Conductivity

According to the model [1,6], below the percolation threshold, when $g = G_t/(2e^2/\hbar) > 1$, the conductivity of nanocomposite with regular packed granules follows the law:

$$\sigma(T) = \sigma_0 \left(1 - \frac{1}{\pi k g} \ln \left[\frac{g \varepsilon_c}{k_B T} \right] \right) \propto \beta \ln T. \quad (13.1)$$

Here G_t and g are the average tunneling conductance between neighboring granules and its dimensionless value in units of the quantum conductance e^2/\hbar , respectively, k is the coordination number of the periodic lattice (or the number of granule contacts with the nearest neighbors), ε_c is the energy of Coulomb blockade, k_B is Boltzmann constant. On the other hand, when the g value becomes less 1, there is a MIT and the $\ln T$ law has to be transformed to the “1/2” law, $\ln \sigma \propto -(T_0/T)^{1/2}$, in which the T_0 parameter increases with increasing ε_c (or decreasing electron localization length on granules). Such behavior of $\sigma(T)$ is observed in the case of $(\text{CoFeB})_x(\text{AlO}_y)_{100-x}$ NC [7]. In the range $x = (49-56)$ at.% and $T > (10-15)$ K, conductivity is well described by the law $\sigma(T) \propto \ln T$, and transformed to “1/2” law at $x \leq 47$ at.%.

The temperature dependences of the longitudinal conductivity $\sigma(T)$ for $(\text{CoFeB})_x(\text{LiNbO}_y)_{100-x}$ and $(\text{CoFeB})_x(\text{AlO}_y)_{100-x}$ NCs are shown in Fig. 13.7. From the presented data, it follows that the dependences of $\sigma(T)$ for both NCs are similar. At the same time, the values of T_0 and β parameters for $(\text{CoFeB})_x(\text{LiNbO}_y)_{100-x}$ NC are significantly less than in case of $(\text{CoFeB})_x(\text{AlO}_y)_{100-x}$ NC. Smaller T_0 values are explained by a strong granule lateral stretching (Fig. 13.4) as well as possibly larger permittivity in the case of LiNbO_y oxide that provides decreasing of the energy of Coulomb blockade and greater scales of the electron localization, respectively [1]. In its favor, some additional increase in the temperature dependence of conductivity at high temperatures (at small value of $1/T^{1/2}$;

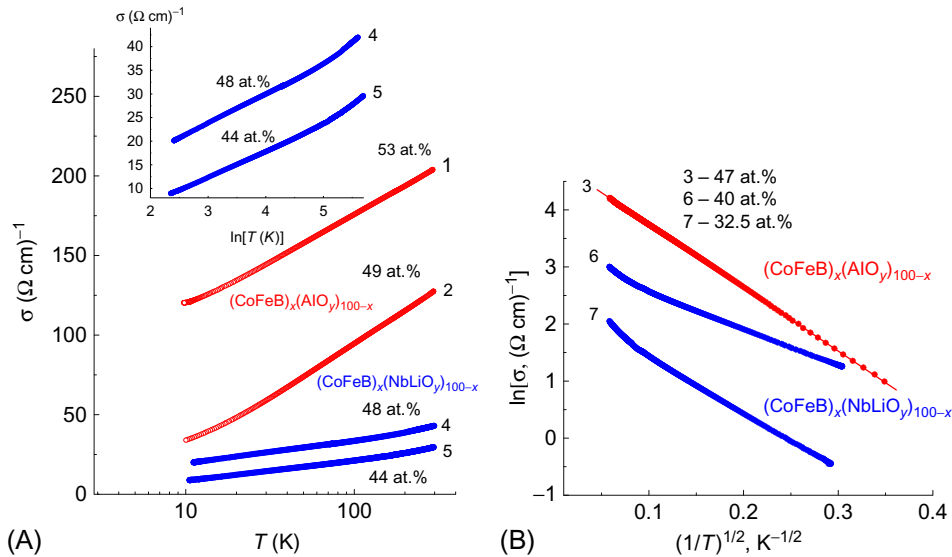


Fig. 13.7

Temperature dependence of conductivity $\sigma(T)$ in coordinates of (A) σ vs. $\log T$ and (B) $\ln \sigma$ vs. $(1/T)^{1/2}$ for $(\text{CoFeB})_x(\text{AlO}_y)_{100-x}$ (curves 1–3) and $(\text{CoFeB})_x(\text{LiNbO}_y)_{100-x}$ (curves 4–7) nanocomposites with different ferromagnetic alloy content: 1–53; 2–49; 3–47; 4–48; 5–44; 6–40; 7–32.5 at.%. (A) From V.V. Rylkov, S.N. Nikolaev, V.A. Demin, A.V. Emelyanov, A.V. Sitnikov, K.E. Nikiruy, V.A. Levanov, M.Yu. Presnyakov, A.N. Taldenkov, A.L. Vasiliev, K.Yu. Chernoglazov, A.S. Vedenev, Yu.E. Kalinin, A.B. Granovsky, V.V. Tugushev, A.S. Bugaev, *J. Exp. Theor. Phys.* 126 (2018) 353. (B) From V.V. Rylkov, A.V. Sitnikov, S.N. Nikolaev, V.A. Demin, A.N. Taldenkov, M.Yu. Presnyakov, A.V. Emelyanov, A.L. Vasiliev, Yu.E. Kalinin, A.S. Bugaev, V.V. Tugushev, A.B. Granovsky, *J. Magn. Magn. Mater.* 2017 (<https://doi.org/10.1016/j.jmmm.2017.11.022>).

see Fig. 13.7B) takes place. Transition in hopping conductivity from co-tunneling regime to neighbor-range-hopping one caused by small ϵ_c value [1] is a probable reason of this feature.

On the other hand, in case of percolation conductivity, the β parameter can be expressed through the correlation length of the percolation network L [7]:

$$\beta \approx \frac{2e^2}{\hbar\pi k i L} \sim \frac{2e^2 a}{\hbar\pi k L^2}, \quad (13.2)$$

$i \sim L/a$ is the effective number of tunnel junctions on the correlation length, a is the granule size. From Eq. (13.2) it follows that the slope β decreases with increase of L . According to the data of Fig. 13.3A, $\beta \approx 30$ and $6 \text{ (}\Omega \text{ cm}^{-1}\text{)}$ for $(\text{CoFeB})_x(\text{AlO}_y)_{100-x}$ and $(\text{CoFeB})_x(\text{LiNbO}_y)_{100-x}$ NCs, respectively. Taking into account Eq.(13.2) means that the L value for $(\text{CoFeB})_x(\text{LiNbO}_y)_{100-x}$ is several times higher than for $(\text{CoFeB})_x(\text{AlO}_y)_{100-x}$ (the estimated value of L for this NC equals $\approx 9\text{--}13 \text{ nm}$ [7]), i.e., $L \approx 20\text{--}30 \text{ nm}$ for $(\text{CoFeB})_x(\text{LiNbO}_y)_{100-x}$.

The estimation $L \approx 20\text{--}30 \text{ nm}$ has the indication of being an effective parameter, since in the case of elongated granules one should expect strong anisotropy in the topology of the

percolation network and, accordingly, in the conductivity along $\sigma_{xx} = \sigma$ and across σ_{zz} the plane of the NC film. By analogy with the uniaxially deformed n-Ge, in which surfaces of the donor electrons wave function are elongated ellipsoids (see Figs. 6.7 and 6.8 in Ref. [15] and their description), we conclude that for a random (not correlated) distribution of elongated granules, the relation $\sigma_{xx}/\sigma_{zz} = (a_x/a_z)^2$ should be satisfied. Note that this relation is a consequence of the strongly “skew” tunneling of electrons between the granules (at small angles to the z axis) under their transport in the (x - y) plane of the film [15].

Taking into account the electron microscopy data, in our case the σ_{xx}/σ_{zz} ratio should be about 0.1. It means that conductivity of the investigated granular systems with rounded and elongated granules but identical parameters T_0 should differ by an order of magnitude, which is observed experimentally. In $(\text{CoFeB})_x(\text{AlO}_y)_{100-x}$ ($x \approx 47$ at.%) and $(\text{CoFeB})_x(\text{LiNbO}_y)_{100-x}$ ($x \approx 32.5$ at.%) NCs, the characteristic temperatures $T_0 \approx 120$ K are identical; however, the σ value of the first sample is nine times higher than that of the second.

Finally, we note that the larger size of the percolation cluster correlation radius in NC $(\text{CoFeB})_x(\text{LiNbO}_y)_{100-x}$ also means a larger volume, which in this case could be occupied by the dead ends of the percolation cluster and individual magnetic atomic precipitates (see Chapter 12 in Ref. [16]). This circumstance is quite clearly manifested in the magnetic properties of studied granular system (see the next section).

13.5 Anomalous Hall Effect and Magnetization

13.5.1 Background and Motivation

The AHE is a complex quantum phenomenon that was discovered in 1880, was first explained in 1954 [17], and is still actively studied experimentally and theoretically [7,10,18–34]. This effect is determined by the spin-orbit interaction (SOI) and by the spin polarization of charge carriers. It is the most clearly pronounced in magnetic materials (ferromagnetic metals and semiconductors, granular metal-insulator nanocomposites, etc.). Their Hall resistivity ρ_H is described by the sum of two terms:

$$\rho_H = R_0 B + 4\pi R_s M, \quad (13.3)$$

where the first term describes normal Hall effect (NHE) induced by the Lorentz force and the second term characterizes AHE related to SOI, M is the magnetization component perpendicular to the film plane, B is the magnetic induction component in this direction, R_0 and R_s are so-called NHE and AHE coefficients, respectively.

One of the most interesting lines in the AHE research in magnetic systems is the study of a relation between anomalous component of the Hall resistivity $\rho_{AHE} = 4\pi R_s M$ and longitudinal resistivity $\rho_{xx} = \rho$, i.e., the so-called scaling behavior $\rho_{AHE} \propto \rho^n$, where n is the power-law index

determined by one of the other physical mechanism of AHE [2]. The scaling relation in this form (or its equivalent for conductivities: $\sigma_{AHE} = \rho_{AHE}/\rho^2 = \rho_{AHE}\sigma^2 \propto \sigma^\gamma$ with $\gamma \approx 2 - n$) is widely used in the literature, if impurity concentration and temperature are variable parameters [18]. The simple scaling behavior is well established for homogeneous magnetic systems with the one type of impurity. For example, in low-resistivity magnetic metals with a not very strong impurity, scattering $n = 1$ in the case of skew scattering mechanism, while $n = 2$ in the case of side jump or intrinsic mechanism. With increase of impurity scattering potential in high-resistivity (so-called dirty metal) magnetic materials, the index n decreases to $n \approx 0.4$ [18,35].

Rather frequently, interpretation of the AHE data is contradictory and intricate in complex magnetic materials (see, e.g., Refs. [19,30,36,37] and references therein), and most of investigations of scaling relation between ρ_{AHE} and ρ were performed for systems that do not exhibit MIT [18]. However, some complex structures, in particular, granular nanocomposites in which it is possible to vary their resistivity by several orders of magnitude (from good metal to insulator) by changing the metal volume fraction are the most convenient systems for investigation of the scaling relation (if it exists) and other features of the AHE behavior in different metallic and insulating regimes.

To study the AHE in granular systems, Efetov et al. [21] considered a theoretical model of dense-packed ferromagnetic granules coupled to each other by tunneling contacts in metallic regime and found that there is no scaling relation between transverse and longitudinal resistivity. In this theory, the AHE arises only inside the granules. However, Vedyayev et al. showed that AHE may arise inside tunneling barriers due to influence of SOI on the scattering of electrons on the intergranular located impurities [10] or a Rashba spin-orbit coupling within the tunneling barrier layer [26]. Recently, other TAHE mechanisms were considered in Refs. [32,33], caused by the interfacial SOI that results in a “skew” electron tunneling even in the absence of impurities.

An interesting feature of granular nanocomposites consists as discussed earlier (see Section 13.4) in unusual behavior of their conductivity near MIT, i.e., the conductivity should follow the $\ln T$ behavior ($\sigma \propto \ln T$) when there is dimensionless tunneling conductance between neighboring granules $g = G_i/(2e^2/\hbar) > 1$ [1,6]. It is really observed in our systems (see Fig. 13.7 and Ref. [7]) and just under these conditions the AHE resistivity ρ_{AHE} should not depend on longitudinal resistivity, i.e., $n \approx 0$ [21]. Recently, such unconventional scaling law with $n \approx 0$ when conductivity follows logarithmic law $\sigma \propto \ln T$ has been demonstrated for Ni-SiO₂ nanocomposites by varying Ni content [28] (in spite of $n \approx 0.6-0.7$ far from MIT [28,38]). The correlation between ρ_{AHE} and ρ when the temperature is a variable parameter has been not studied in Ref. [28]. Moreover, granular Ni-SiO₂ films were prepared in Ref. [28] by method (electron-beam coevaporation) at which using there are no practically dispersed metal atoms in an oxide matrix. So, the investigation of AHE in NC like (CoFeB)_x(AlO_y)_{100-x} and (CoFeB)_x(LiNbO_y)_{100-x} with high content of the dispersed magnetic atoms in insulation matrix

is an interesting task, in particular, in the light of possible manifestation of scattering-assisted TAHE [10].

13.5.2 Scaling Behavior of AHE and Peculiarities of Magnetization

The magnetic field dependences of the Hall resistance $R_H(B)$ for samples $(\text{CoFeB})_x(\text{AlO}_y)_{100-x}$ with $x = 47, 49,$ and 59 at.% at low temperatures ($T < 25$ K) are shown in Fig. 13.8A. The character of the presented $R_H(B)$ dependences is similar to that observed in ferromagnetic films with easy-plane magnetic anisotropy. Note that in nanocomposite samples with activation type of conductivity, when AHE is determined by superparamagnetic granules, the $R_H(B)$ curve transforms into a “rounded” Langevin function [39]. In our case, the AHE resistance $R_{AHE}(B) \approx R_H(B)$ linearly increases with the field up to $B \leq B_s$ and then saturates at $B \geq B_s$ (B_s is the field of saturation magnetization M ; we considered that $R_0 \ll R_s$ because it is a common feature for magnetic granular systems [28,38,39]). Fig. 13.8B demonstrates the $R_H(B)$ dependences measured for the sample with $x \approx 56$ at.% at various temperatures in the range of 15–120 K. In this temperature range, the saturation field B_s practically does not depend on temperature. Moreover, good correlation in temperature behavior of the Hall resistance $R_H(T)$

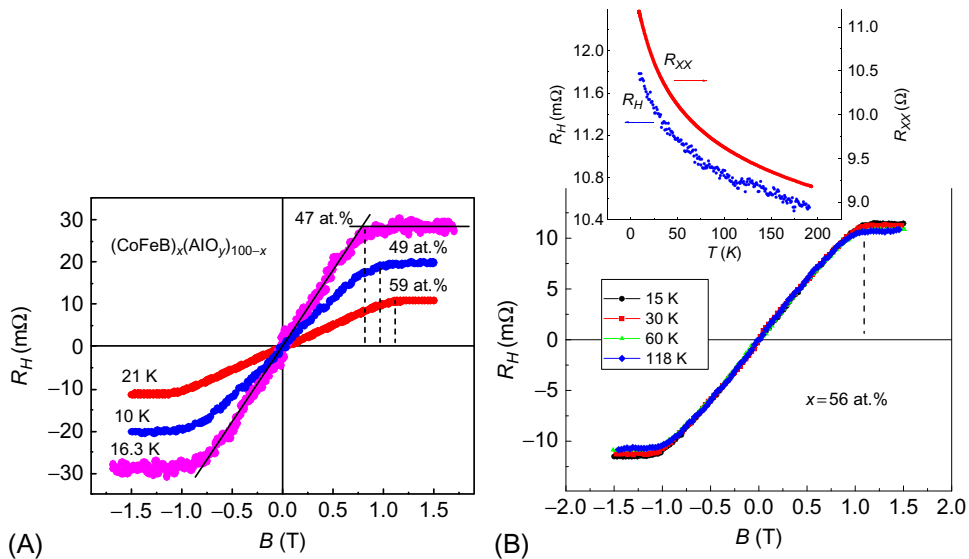


Fig. 13.8

(A) Magnetic field dependences of the Hall resistance $R_H(B)$ for $(\text{CoFeB})_x(\text{AlO}_y)_{100-x}$ samples with $x = 47, 49,$ and 59 at.% at low temperatures $T < 25$ K. (B) Dependence of $R_H(B)$ for $(\text{CoFeB})_x(\text{AlO}_y)_{100-x}$ sample with $x = 56$ at.% within the 15–120 K temperature range. Inset shows the temperature dependences of $R_H(T)$ and longitudinal resistance $R_{xx}(T)$ measured at $B = 1.5$ T for this sample.

From V.V. Rylkov, S.N. Nikolaev, K.Yu. Chernoglazov, V.A. Demin, A.V. Sitnikov, M.Yu. Presnyakov, A.L. Vasiliev, N.S. Perov, A.S. Vedeneev, Yu.E. Kalinin, V.V. Tugushev, A.B. Granovsky, *Phys. Rev. B* 95 (2017) 144202.

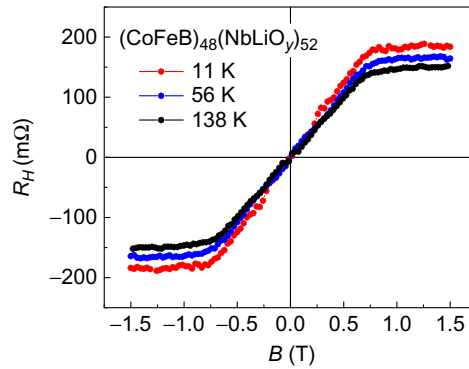


Fig. 13.9

Magnetic field dependences of the Hall resistance $R_H(B)$ for $(\text{CoFeB})_x(\text{LiNbO}_y)_{100-x}$ sample with $x=48$ at.% within the 10–140 K temperature range. From V.V. Rylkov, S.N. Nikolaev, V.A. Demin, A.V. Emelyanov, A.V. Sitnikov, K.E. Nikiruy, V.A. Levanov, M.Yu. Presnyakov, A.N. Taldenkov, A.L. Vasiliev, K.Yu. Chernoglazov, A.S. Vedenev, Yu.E. Kalinin, A.B. Granovsky, V.V. Tugushev, A.S. Bugaev, *J. Exp. Theor. Phys.* 126 (2018) 353.

and longitudinal resistance $R_{xx}(T)$ measured at $B = 1.5$ T is observed with decrease in temperature from 190 to 9 K $R_H(T)$ and $R_{xx}(T)$ increase by 1.12 and 1.26 times, respectively (see inset to Fig. 13.8B).

Measurements of the AHE in the vicinity of MIT are difficult for $(\text{CoFeB})_x(\text{LiNbO}_y)_{100-x}$ NC owing to the larger in-plane distances between granules and the low conductivity in comparison with the case of $(\text{CoFeB})_x(\text{AlO}_y)_{100-x}$ NC (Fig. 13.7). Nevertheless, we succeeded in measuring AHE on the metal side of MIT for several samples. The magnetic field dependences of the Hall resistivity $R_H(B)$ for $(\text{CoFeB})_x(\text{LiNbO}_y)_{100-x}$ sample with $x \approx 48$ at.% at different temperatures $T = 10$ –140 K are shown in Fig. 13.9. In this case, the AHE resistivity $R_{AHE}(B) \approx R_H(B)$ linearly increases with the field up to $B \leq B_s$ and then saturates at $B \geq B_s$. Now the B_s value practically does not depend on temperature, i.e., we observe the same situation, as in the case of $(\text{CoFeB})_x(\text{AlO}_y)_{100-x}$ NC (Fig. 13.8).

So, we can conclude that the AHE behavior does not contain any indications on the induced magnetic anisotropy of $(\text{CoFeB})_x(\text{LiNbO}_y)_{100-x}$ films caused by granule stretching along of NC growth. Note that in NCs with columnar structure like in the studied $(\text{CoFeB})_x(\text{LiNbO}_y)_{100-x}$ NC, the evident perpendicular magnetic anisotropy is usually observed with the effective field of the uniaxial anisotropy $H_a \approx 2$ –3 kOe [3,40].

Usually, both the AHE conductivity σ_{AHE} and the resistivity ρ_{AHE} are linear functions of the magnetization $M(x, T)$ that needs to be considered at the scaling relation studies. The temperature dependence of $M(T)$ measured at 1.5 T is very strong at $T \leq 25$ K and $M(T)$ weakly decreases with increase of temperature at $T \geq 50$ K (Fig. 13.10). It is interesting that rise in $M(T)$

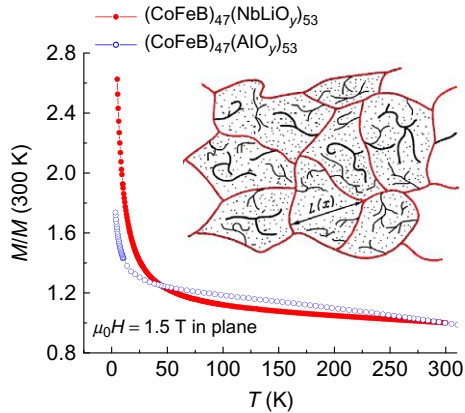


Fig. 13.10

Temperature dependences of normalized magnetization M for $(\text{CoFeB})_x(\text{AlO}_y)_{100-x}$ and $(\text{CoFeB})_x(\text{LiNbO}_y)_{100-x}$ films with $x=47$ at.%. Inset demonstrates the topological scheme of percolation cluster, including conductive network or “cluster skeleton” (*continuous solid lines*) formed by tunnel-coupling CoFe nanogranules, the dead ends (*discontinuous solid lines*), and isolated atomic Fe-Co inclusions (*points*). L is the correlation length of the percolation network.

From V.V. Rylkov, S.N. Nikolaev, V.A. Demin, A.V. Emelyanov, A.V. Sitnikov, K.E. Nikiruy, V.A. Levanov, M.Yu. Presnyakov, A.N. Taldenkov, A.L. Vasiliev, K.Yu. Chernoglazov, A.S. Vedeneev, Yu.E. Kalinin, A.B. Granovsky, V.V. Tugushev, A.S. Bugaev, *J. Exp. Theor. Phys.* 126 (2018) 353 and inset from V.V. Rylkov, S.N. Nikolaev, K.Yu. Chernoglazov, V.A. Demin, A.V. Sitnikov, M.Yu. Presnyakov, A.L. Vasiliev, N.S. Perov, A.S. Vedeneev, Yu.E. Kalinin, V.V. Tugushev, A.B. Granovsky, *Phys. Rev. B* 95 (2017) 144202.

dependence is manifested several times stronger in case of the $(\text{CoFeB})_x(\text{LiNbO}_y)_{100-x}$. At $T=5$ K, the ratio $M(5\text{ K})/M(300\text{ K}) \approx 2.6$ and 1.6 for $(\text{CoFeB})_x(\text{LiNbO}_y)_{100-x}$ and $(\text{CoFeB})_x(\text{AlO}_y)_{100-x}$, respectively (Fig. 13.10). Such behavior is probably because of a large amount of paramagnetic Co and Fe atoms in the oxide matrix (AlO_y or LiNbO_y) and superparamagnetic granules belonging to the dead ends of the percolation cluster [15,16]. Note that the data of structural measurements also indicate the presence of a large amount of Co and Fe atoms in the oxide matrix [7]. Following percolation theory (see Chapters 5 and 12 in Refs. [15,16], respectively), we present the topological scheme of percolation cluster (see inset to Fig. 13.10), which includes a conductive network or “cluster skeleton” (red lines), large number of the dead ends (black lines), as well as isolated Fe-Co atomic inclusions (black points). The skeleton is created in our case by tunnel-coupled CoFe nanogranules. Only skeleton granules determine the conductivity of percolation system near the percolation threshold. Meanwhile, magnetization of such system near the threshold is mainly controlled by the “black” phase [15,16]. We will show also in the following section that Fe-Co atomic inclusions are magnetic Fe^{2+} and Co^{2+} ions.

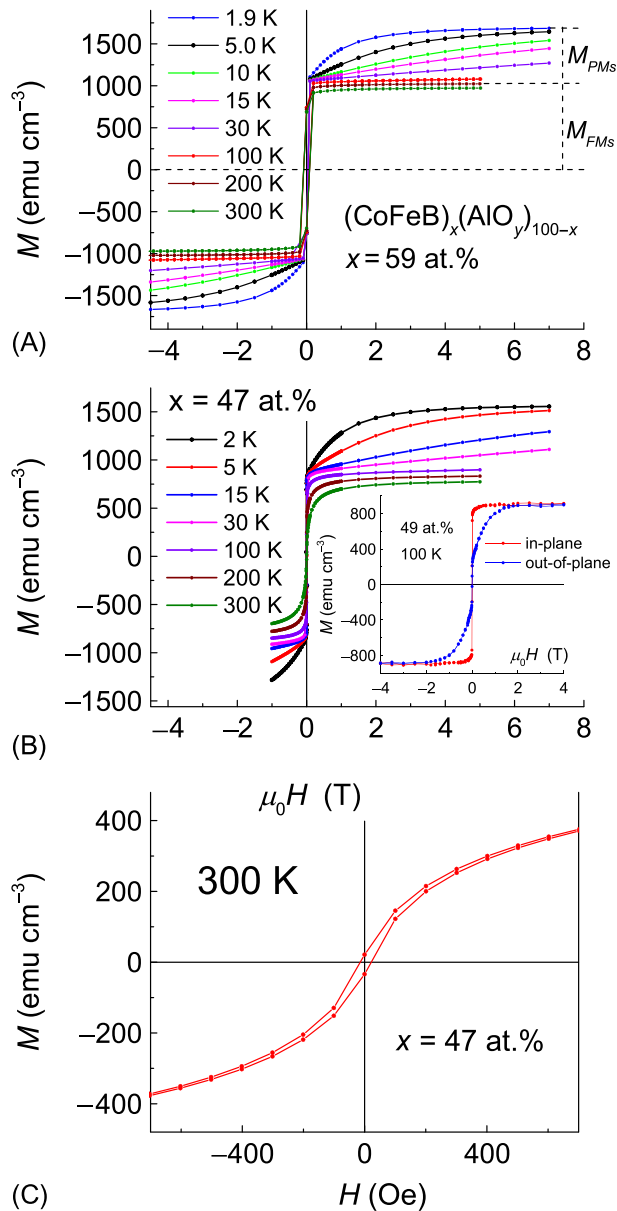


Fig. 13.11

Magnetic field dependences of magnetization $M(H)$ for the $(\text{CoFeB})_x(\text{AlO}_y)_{100-x}$ films with $x = 59$ (A) and 47 at.% (B) measured at in-plane fields for various temperatures in the range of $T = 2\text{--}300$ K. Inset shows the $M(H)$ dependences for the $(\text{CoFeB})_{49}(\text{LiNbO}_y)_{51}$ sample measured at in-plane and out-of-plane magnetic fields for 100 K. (C) Curve of $M(H)$ for the $(\text{CoFeB})_{47}(\text{LiNbO}_y)_{53}$ sample at 300 K in the enlarged field scale. From V.V. Rylkov, A.V. Sitnikov, S.N. Nikolaev, V.A. Demin, A.N. Taldenkov, M.Yu. Presnyakov, A.V. Emelyanov, A.L. Vasiliev, Yu.E. Kalinin, A.S. Bugaev, V.V. Tugushev, A.B. Granovsky. *J. Magn. Mater.*, 2017 (<https://doi.org/10.1016/j.jmmm.2017.11.022>) and insert from V.V. Rylkov, S.N. Nikolaev, K.Yu. Chernoglazov, V.A. Demin, A.V. Sitnikov, M.Yu. Presnyakov, A.L. Vasiliev, N.S. Perov, A.S. Vedenev, Yu.E. Kalinin, V.V. Tugushev, A.B. Granovsky, *Phys. Rev. B* 95 (2017) 144202.

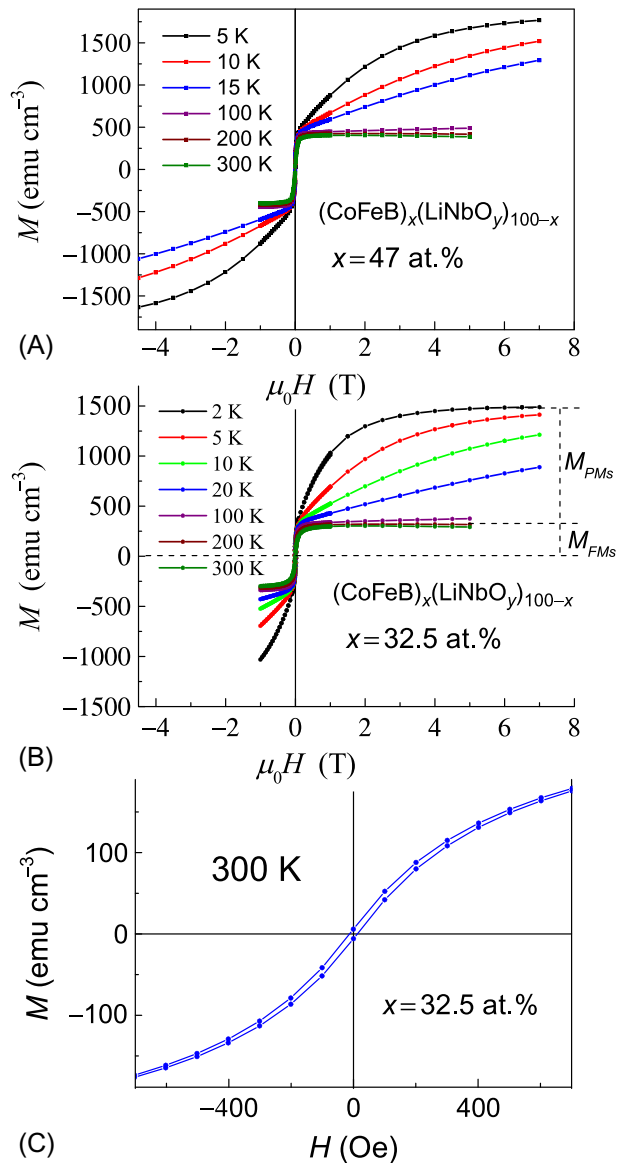


Fig. 13.12

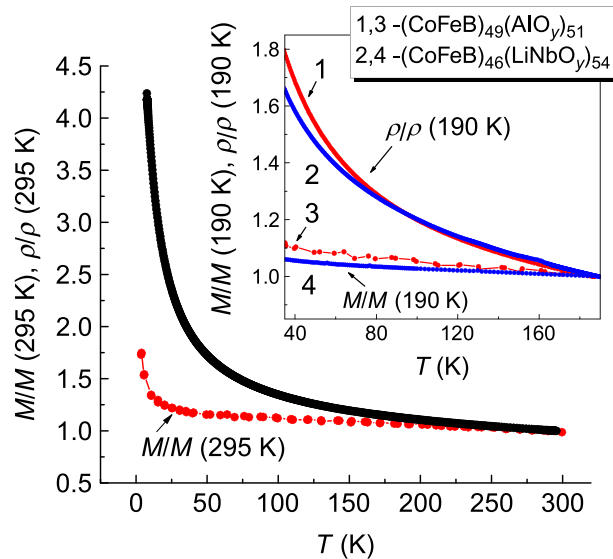
Magnetic field dependences of magnetization $M(H)$ for the $(\text{CoFeB})_x(\text{LiNbO}_y)_{100-x}$ films with $x = 47$ (A) and 32.5 at.% (B) measured at in-plane fields for various temperatures in the range of $T = 2\text{--}300$ K. (C) Curve of $M(H)$ for the $(\text{CoFeB})_{32.5}(\text{LiNbO}_y)_{67.5}$ sample at 300 K in the enlarged field scale. (A) From V.V. Rylkov, S.N. Nikolaev, V.A. Demin, A.V. Emelyanov, A.V. Sitnikov, K.E. Nikiruy, V.A. Levanov, M.Yu. Presnyakov, A.N. Taldenkov, A.L. Vasiliev, K.Yu. Chernoglazov, A.S. Vedenev, Yu.E. Kalinin, A.B. Granovsky, V.V. Tugushev, A.S. Bugaev, *J. Exp. Theor. Phys.* 126 (2018) 353. (B) and (C) from V.V. Rylkov, A.V. Sitnikov, S.N. Nikolaev, V.A. Demin, A.N. Taldenkov, M.Yu. Presnyakov, A.V. Emelyanov, A.L. Vasiliev, Yu.E. Kalinin, A.S. Bugaev, V.V. Tugushev, A.B. Granovsky, *J. Magn. Magn. Mater.*, 2017 (<https://doi.org/10.1016/j.jmmm.2017.11.022>).

Figs. 13.11 and 13.12 show the magnetic field dependences of magnetization for $(\text{CoFeB})_x(\text{AlO}_y)_{100-x}$ ($x \approx 59, 49$ and 47 at.%), and $(\text{CoFeB})_x(\text{LiNbO}_y)_{100-x}$ films ($x \approx 47$ and 32.5 at.%), respectively, measured in the field parallel to the plane at different temperatures in the range of 1.9 – 300 K. Below 30 K, the paramagnetic (PM) contribution starts to appear well in all samples. The value of the PM contribution in saturation for $(\text{CoFeB})_x(\text{AlO}_y)_{100-x}$ NC with $x \approx 59$ at.% ($M_{PMs} \approx 660 \text{ emu/cm}^3$) is appreciably less, than in the case of the same NC with $x \approx 47$ at.% ($M_{PMs} \approx 730 \text{ emu/cm}^3$). The reverse situation is observed for the saturation magnetization of ferromagnetic (FM) component: the values of $M_{FM_s} \approx 1025$ and 830 emu/cm^3 at $T = 200$ K for samples with 59 and 47 at.%, respectively. For $(\text{CoFeB})_x(\text{AlO}_y)_{100-x}$ NC, the value of FM component exceeds the PM one, in particular, at $x \approx 47$ at.% the ratio of $M_{PMs}/M_{FM_s} \approx 0.88$. Cardinaly other situation is observed for $(\text{CoFeB})_x(\text{LiNbO}_y)_{100-x}$ NC (see Fig. 13.12). In this case, $M_{PMs}/M_{FM_s} \approx 3.2$ and 3.5 at $x \approx 47$ and 32.5 at.%, respectively. The magnetization of PM phase is saturated at $T \leq 3$ K in the field higher than 3 T. On the other hand, the saturation field H_s for the magnetization of ferromagnetic phase associated with granules does not practically depend on the temperature in the studied temperature region. The out-of-plane saturation field of this phase is $\mu_0 H_s \approx 1$ T, which well correlates with the AHE data (see inset of Fig. 13.11B).

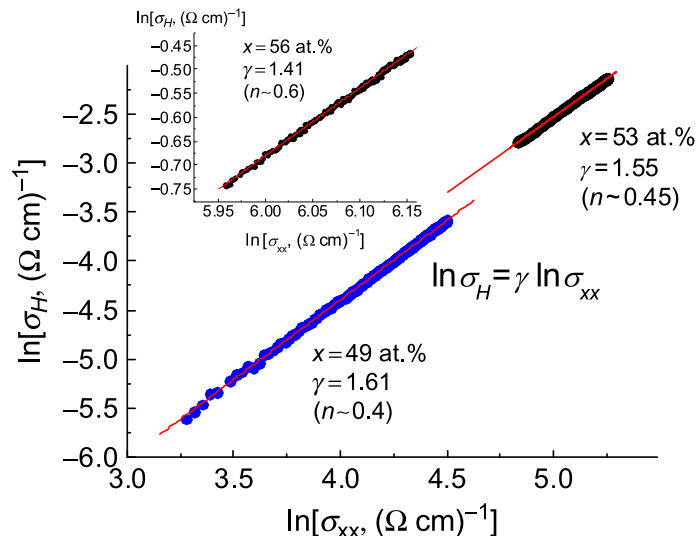
It is important to note that in both types of NCs the small hysteresis (the coercive field ≈ 15 – 20 Oe) is observed for field in-plane below MIT; see Figs. 13.11C and 13.12C corresponding to $(\text{CoFeB})_x(\text{AlO}_y)_{100-x}$ and $(\text{CoFeB})_x(\text{LiNbO}_y)_{100-x}$ NCs with $x \approx 47$ and 32.5 at.%. The fact of activation electron transport for these NCs is confirmed by the data on temperature dependence of conductivity shown in Fig. 13.7. Let us remind that the percolation transition in conductivity for $(\text{CoFeB})_x(\text{AlO}_y)_{100-x}$ NC is observed at $x_p \sim 57$ – 59 at.% [7]. Hence, percolation in FM transition for these NCs arises at much smaller metal concentration than percolation transition in conductivity tacking into account that light axis of granules for $(\text{CoFeB})_x(\text{LiNbO}_y)_{100-x}$ NC is perpendicular to plane.

At $T \geq 30$ K, the magnetization $M(x, T)$ is practically independent of T in comparison with the resistance $\rho(T)$ for both NCs (Fig. 13.13). Due to this reason, one could neglect the M vs. temperature variation of cluster skeleton (Fig. 13.10) and assume that the $\rho_{AHE}(T)$ dependence is mainly determined by the $\rho(T)$ dependence. Also notice that the $M(x, T)$ variation near MIT with the metal content in range of $x = 49$ – 56 at.% for $(\text{CoFeB})_x(\text{AlO}_y)_{100-x}$ NC and $x = 44$ – 48 at.% for $(\text{CoFeB})_x(\text{LiNbO}_y)_{100-x}$ should not be large. In the following analysis on the scaling dependence ρ_{AHE} vs. $\rho(x)$, we will fit the $M(x, T)$ dependence on the metal content in this range by a linear function of x .

The dependence of the AHE conductivity σ_{AHE} on the longitudinal conductivity σ_{xx} at $B = 1.5$ T for $(\text{CoFeB})_x(\text{AlO}_y)_{100-x}$ samples with $x = 49, 53,$ and 56 at.% at different temperatures is shown in Fig. 13.14. The obtained index $\gamma = 1.55$ – 1.61 for samples with $x = 49$ – 53 at.% near MIT is very close to the widely accepted value $\gamma = 1.6$ (or $n = 0.4$) for dirty metals with


Fig. 13.13

Normalized $M(T)$ dependence in comparison with normalized resistivity $\rho(T)$ dependence for $(\text{CoFeB})_x(\text{AlO}_y)_{100-x}$ sample with $x=49$ at.%. Inset shows the normalized $\rho(T)$ (curves 1,2) and $M(T)$ (curves 3,4) dependences in enlarged temperature scale ($T \approx 30-190$ K) for $(\text{CoFeB})_{49}(\text{AlO}_y)_{51}$ (1,3) and $(\text{CoFeB})_{46}(\text{LiNbO}_y)_{54}$ (2,4) samples.


Fig. 13.14

Logarithmic plots of AHE conductivity σ_{AHE} vs. σ_{xx} for $(\text{CoFeB})_x(\text{AlO}_y)_{100-x}$ samples with $x=49$ and 53 at.%. Inset shows the $\sigma_{AHE}(\sigma_{xx})$ dependence for $(\text{CoFeB})_x(\text{AlO}_y)_{100-x}$ sample $x=56$ at.%. From V.V. Rylkov, S.N. Nikolaev, K.Yu. Chernoglazov, V.A. Demin, A.V. Sitnikov, M.Yu. Presnyakov, A.L. Vasiliev, N.S. Perov, A.S. Vedenev, Yu.E. Kalinin, V.V. Tugushev, A.B. Granovsky, *Phys. Rev. B* 95 (2017) 144202.

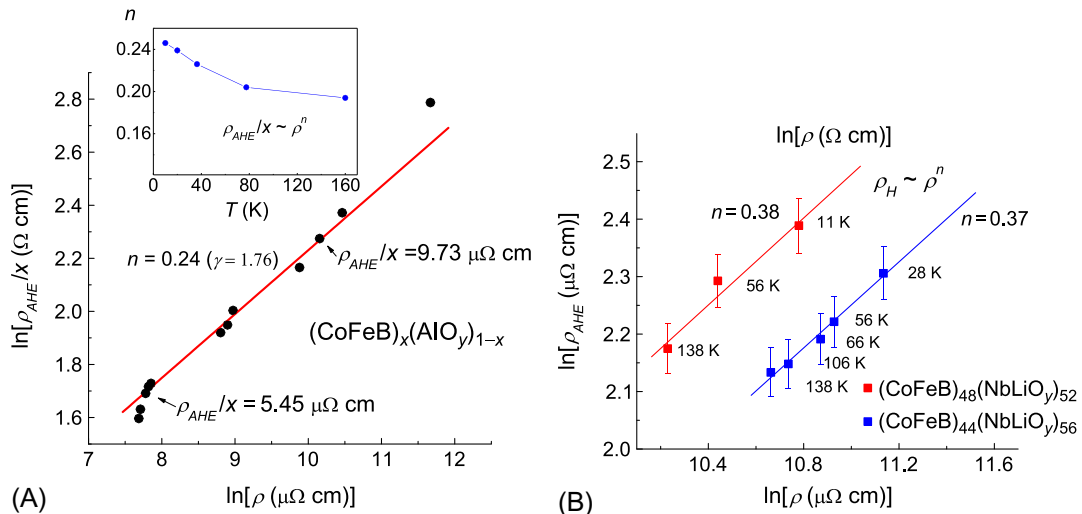


Fig. 13.15

(A) Logarithmic dependence of normalized AHE resistivity (ρ_{AHE}/x) vs. longitudinal resistivity ρ , obtained from measurements at a fixed low temperature in the range of 10–36 K for $(\text{CoFeB})_x(\text{AlO}_y)_{100-x}$ samples with different metal content x . Inset shows the temperature dependence of power-law index n in the $\rho_{AHE}(x)/x \propto \rho(x)^n$ scaling relation. (B) Logarithmic dependence of AHE resistivity ρ_{AHE} vs. longitudinal resistivity ρ for $(\text{CoFeB})_x(\text{LiNbO}_y)_{100-x}$ samples with $x = 44$ and 48 at.%. Vertical segments correspond to the 2% error of measurements. (A) From V.V. Rylkov, S.N. Nikolaev, K.Yu. Chernoglazov, V.A. Demin, A.V. Sitnikov, M.Yu. Presnyakov, A.L. Vasiliev, N.S. Perov, A.S. Vedeneev, Yu.E. Kalinin, V.V. Tugushev, A.B. Granovsky, *Phys. Rev. B* 95 (2017) 144202. (B) From V.V. Rylkov, S.N. Nikolaev, V.A. Demin, A.V. Emelyanov, A.V. Sitnikov, K.E. Nikiruy, V.A. Levanov, M.Yu. Presnyakov, A.N. Taldenkov, A.L. Vasiliev, K.Yu. Chernoglazov, A.S. Vedeneev, Yu.E. Kalinin, A.B. Granovsky, V.V. Tugushev, A.S. Bugaev, *J. Exp. Theor. Phys.* 126 (2018) 353.

$\rho \geq 10^{-4} \Omega \text{ cm}$ [18,35]. On the other hand, for sample with $x = 56$ at.%, the corresponding value is $\gamma = 1.41$ or $n \approx 0.6$ that coincides with $n \approx 0.6-0.7$ for Ni-SiO₂ nanocomposites far from MIT [28,38]).

Surprisingly, the power-law index n in the $\rho_{AHE}(x)/x \propto \rho(x)^n$ relation in the case of $(\text{CoFeB})_x(\text{AlO}_y)_{100-x}$ NC decreases to sufficiently low value $n \approx 0.24$ if the metal content x is a variable parameter (Fig. 13.15A). Note that in this case the n value is practically independent of the temperature at $T < 40 \text{ K}$ and drops up to $n \approx 0.20$ at $T = 80-160 \text{ K}$ (see inset to Fig. 13.15A).

The dependencies $\rho_{AHE}(\rho)$ for samples $(\text{CoFeB})_x(\text{LiNbO}_y)_{100-x}$ with $x \approx 44$ and 48 at.% close to MIT are presented in Fig. 13.15B in double logarithmic scale. It was found that exponent $n \approx 0.37-0.38$ in the $\rho_{AHE}(\rho)$ dependence at variation of temperature coincides with the index $n \approx 0.39$ for the $(\text{CoFeB})_{49}(\text{AlO}_y)_{51}$ NC, which is also close to MIT (Fig. 13.14). However, the values of ρ_{AHE} in $(\text{CoFeB})_x(\text{LiNbO}_y)_{100-x}$ samples with different contents $x \approx 44$ and 48 at.% coincide at the fixed temperature in the limit of experiment accuracy (about 2%). Consequently, the n index is equal to about zero in the $\rho_{AHE}(\rho)$ power law at change of

metal content that differs from results for the $(\text{CoFeB})_x(\text{AlO}_y)_{100-x}$ NC (Fig. 13.15A) and coincides with result of Refs. [21,28] in lack of the TAHE [10]. The apparent contradiction is eliminated if one considers that shunting of TAHE becomes stronger in the case of an NC with strongly elongated granules. Besides, the TAHE significantly is suppressed in this case because of strongly “skewed” tunneling of electrons between granules under transport along the x - y plane (see Section 13.5.4).

Before presenting qualitative model of the AHE in studied films, let us make several important remarks about a specific character of magnetization in our system and nature of paramagnetic centers provided by its strong heterogeneity.

13.5.3 Nature of Paramagnetic Centers

Analysis of the correlation between magnetization and AHE data (Figs. 13.8–13.10) shows a serious problem arises from a complex character of distribution of magnetic atoms between different components of the nanocomposite, i.e., metallic FeCo granules and oxide matrix with dispersed Fe and Co ions. In fact, according to the percolation theory, near the percolation threshold, only very small part of metallic granule participates in the conducting cluster or percolation network, while granules located in the dead ends are useless for conductivity. Nevertheless, just this large part determines total magnetization of the system [16]. Presuming that the structure of percolation network and dead ends is identical, it should be expected certain correlation in the total magnetization and AHE behaviors. However, such correlations can be strongly broken, for example, when the considerable part of metal fraction appears in an atomic (ion) phase in the dielectric matrix providing the paramagnetic contribution to total magnetization.

Let us assume that the PM contribution is determined by Co and Fe ions in the matrix. To find magnetic moment of ions, it is necessary to compensate ferromagnetic (from NC film) and diamagnetic (from the substrate) contributions. For this purpose, it is enough to find a difference of the field dependences of $M(H)$ measured at different T in the range of low temperatures where the paramagnetic component is most strongly observed: $\Delta M(H, T_1, T_2) = M(H, T_1) - M(H, T_2)$. Then to fit the obtained $\Delta M(H)$ function by difference of Brillouin’s functions, $\Delta B_J(H) = B_J(H, T_1) - B_J(H, T_2)$, considering relations [41]:

$$M = N_i g J \mu_B B_J(x), \quad x = g J \mu_B H / k_B T, \quad (13.4)$$

$$B_J(x) = \frac{2J+1}{2J} \coth \frac{(2J+1)x}{2J} - \frac{1}{2J} \coth \frac{x}{2J}.$$

Here N_i is the concentration of magnetic ions, $m = g \cdot J \cdot \mu_B$ is the magnetic moment per ion. The magnetic field dependences of magnetic moment variation $\Delta M_{tot} = V \cdot \Delta M(H, T_1, T_2)$ for $(\text{CoFeB})_x(\text{AlO}_y)_{100-x}$ NC ($x \approx 59$ at.%, $T_1 = 1.9$ K, $T_2 = 5$ K) (curve 1), and for $(\text{CoFeB})_x(\text{LiNbO}_y)_{100-x}$ NC ($x \approx 47$ at.%, $T_1 = 5$ K, $T_2 = 10$ K) (curve 2) are shown in Fig. 13.16 (V is the volume of NC film). The solid lines demonstrate the calculated curves found

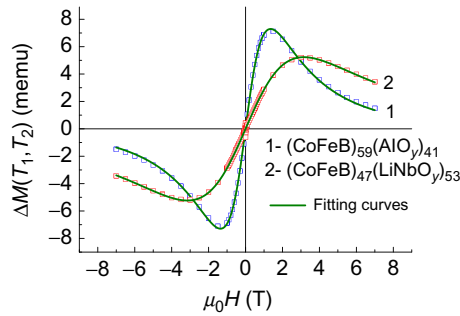


Fig. 13.16

Magnetic field dependencies of magnetic moment variation $\Delta M_{tot} = V \cdot \Delta M(H, T_1, T_2) = V \cdot [M(H, T_1) - M(H, T_2)]$ for $(\text{CoFeB})_x(\text{AlO}_y)_{100-x}$ NC ($x \approx 59$ at.%, $T_1 = 1.9$ K, $T_2 = 5$ K) (curve 1), and for $(\text{CoFeB})_x(\text{LiNbO}_y)_{100-x}$ NC ($x \approx 47$ at.%, $T_1 = 5$ K, $T_2 = 10$ K) (curve 2). The solid lines show the calculated curves found by fitting of Brillouin's function to experimental data. From V.V. Rylkov, A.V. Sitnikov, S.N. Nikolaev, V.A. Demin, A.N. Taldenkov, M.Yu. Presnyakov, A.V. Emelyanov, A.L. Vasiliev, Yu.E. Kalinin, A.S. Bugaev, V.V. Tugushev, A.B. Granovsky. *J. Magn. Magn. Mater.*, 2017 (<https://doi.org/10.1016/j.jmmm.2017.11.022>).

by fitting Brillouin's function to experimental data. In both cases, an accuracy of fitting is reached better than 1%. For $(\text{CoFeB})_x(\text{AlO}_y)_{100-x}$ NC, the magnetic moment per ion found as a result of fitting $m = 5.07 \mu_B$, and their density $N_i = 1.14 \times 10^{22} \text{ cm}^{-3}$ ($N_i \approx 1.23 \times 10^{22} \text{ cm}^{-3}$ at $x \approx 47$ at.%). For Fe^{2+} and Co^{2+} ions moments $m_i = 5.4 \mu_B$ and $4.8 \mu_B$ [41], respectively, which corresponds to the average moment of $m = 5.1 \mu_B$ very well coinciding with the experimentally found m value.

For $(\text{CoFeB})_x(\text{LiNbO}_y)_{100-x}$ NC the magnetic moment per ion was the same, as for $(\text{CoFeB})_x(\text{AlO}_y)_{100-x}$ NC, $m = 5.08 \mu_B$ at $x \approx 47$ at.%. On the other hand, the ion density in this type of NC turned out significantly higher: $N_i \approx 3 \times 10^{22} \text{ cm}^{-3}$ at $x \approx 47$ at.% and $N_i \approx 2.4 \times 10^{22} \text{ cm}^{-3}$ at $x \approx 32.5$ at.%. At such higher concentration, the evident part of magnetic ions will appear in the tunneling barriers between granules forming percolation network or "cluster skeleton" [7]. These ions can initiate FM coupling between cluster skeleton granules [2,3] and/or act as SOI scattering centers for tunneling electrons causing the manifestation of TAHE [7,10].

13.5.4 Qualitative Model of the AHE Behavior

The peculiarities of magnetotransport properties of our system clearly manifest themselves in the AHE measurements and cannot be adequately described by one-component Hall-source model. In fact, from the statement, it seems evident that the metal contribution V_{Hg} to the Hall e.m.f. was made by the granules themselves [21] existing in the system. This contribution can be due to the SOI scattering of spin-polarized carriers by the magnetic centers inside the granules. But such a simple way of description is unsuccessful in the presence of second

magnetic phase, i.e., magnetic ions dispersed outside metallic granules (in the tunneling barriers) and having charge and spin configurations different from the ones existing inside metallic granules. These ions can participate in the SOI processes with the electrons already spin-polarized inside metallic granules, so additional contribution to the Hall e.m.f. may be noticeable due to the strong SOI integral [10]. In this situation, the tunneling contribution V_{Hd} to the Hall e.m.f. may arise due to the TAHE mechanism [10]. Following Ref. [10], the V_{Hd} value is determined by the electron spin polarization inside metallic electrodes (in our case metallic granules), the SOI integral of electrons with impurity scattering centers and the concentration of these centers, N_i .

In our experiments, the Hall e.m.f. is measured at 1.5 T in the temperature range above ~ 30 K where the magnetization is almost constant and provided by the granules. However, magnetization increases strongly below ~ 30 K, and we refer this fact to alignment of individual Co and Fe impurity moments in the tunnel barriers. It means that above 30 K at 1.5 T these moments are randomly oriented, but this magnetic impurity disorder does not affect TAHE since the tunneling electron spin polarization is only due to the granules magnetization, following the model [10]. In particular, it is manifested in a weak dependence of index n vs. T (see inset to Fig. 13.15A).

Since the centers with SOI scattering coexist in both metallic and insulating parts of the system, one-component picture of the Hall e.m.f. in an effective magnetic material becomes incorrect and later we try to qualitatively describe AHE in the model of two-component structure, containing two coexisting contributions, V_{Hg} and V_{Hd} , to the Hall e.m.f. Let us consider a simple phenomenological model with two Hall e.m.f. sources connected in parallel to one another (Fig. 13.17A). Similar situation takes place in a macroscopic rectangular semiconductor sample [42,43], where there is circular Hall current in the vicinity of metallic electrodes (Fig. 13.17B; a is the size of cube form metallic granule that plays a role of metallic electrode, b is the interelectrode spacing). That leads to the Hall e.m.f. shunting effects or a reduction of the potential drop V_H measured between Hall probes as compared to the Hall e.m.f. arising in the interelectrode regions, $V_{Hd} = R_{Hd} I_x$.

For sample with $b/a \leq 1/2$, measured value of the Hall resistance $R_H = V_H / I_x$ can be estimated on the basis of an equivalent circuit model taking into account combined influence of two Hall e.m.f. sources connected in parallel (see Fig. 13.17C). Fig. 13.17C illustrates effective Hall e.m.f. generator for a periodic net of tunnel junctions that contains: (i) the source of Hall e.m.f. in metallic granules, $V_{Hg} = R_{Hg} \cdot I_x$, with internal resistance $r_{gint} = V_{Hg} / I_{sc}$, I_{sc} is the short-circuit current through the granule, and (ii) the source of Hall e.m.f. in dielectric intergranular regions, $V_{Hd} = R_{Hd} \cdot I_x$, with internal resistance $r_{dint} \gg r_{gint}$. These sources are connected in parallel to each other through external resistance $r_{dext} \gg r_{gint}$. Taking into account the approximation for effective Hall e.m.f. measured in the interelectrode region [42,43], $V_{Hd}^* \approx 0.74(b/a)V_{Hd}$, and using Kirchhoff's circuit laws for scheme of Fig. 13.17C, we find [7]:

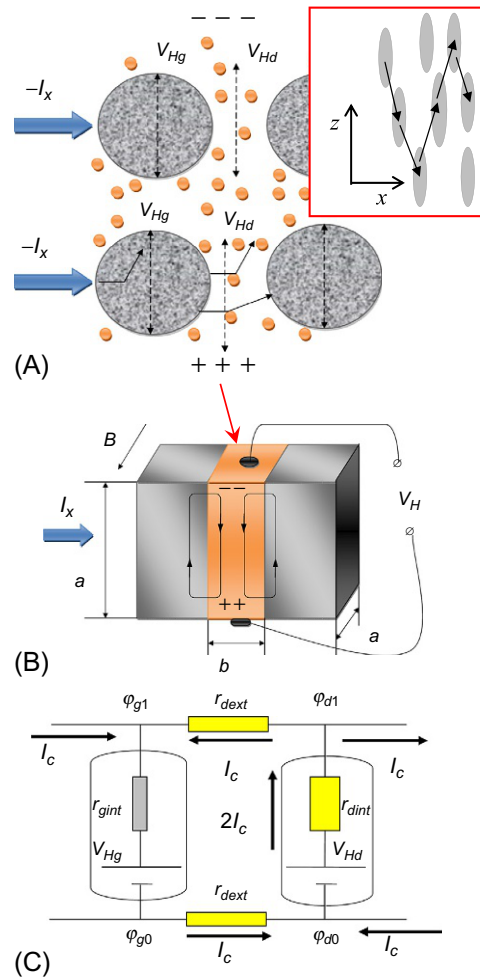


Fig. 13.17

(A) Granular system with SOI scattering on defects in oxide matrix at electron tunneling between grains. Two connected in-parallel sources of AHE e.m.f. are shown: the first source is caused by SOI in granules ($V_{Hg} = R_{Hg} \cdot I_x$) and the second occurs inside the tunneling barrier regions ($V_{Hd} = R_{Hd} \cdot I_x$); the current I_x flows through the neighboring granules, R_{Hg} and R_{Hd} are the Hall resistances of granules and dielectric interlayer between them. Inset shows the scheme of electron tunneling between elongated granules along the NC growth axis [15]. (B) Schematic drawing of tunneling junction between granules illustrating an emergence of circular currents at formation of the Hall effect in dielectric interlayer. (C) Equivalent scheme of a periodic network of tunnel junctions (resistances) with the two local Hall e.m.f. generators: $r_{dint} \gg r_{dext} \gg r_{gint}$, $V_{Heff} = \frac{1}{2}[(\varphi_{g1} - \varphi_{g0}) + (\varphi_{d1} - \varphi_{d0})]$. From V.V. Rylkov, S.N. Nikolaev, K.Yu. Chernoglazov, V.A. Demin, A.V. Sitnikov, M.Yu. Presnyakov, A.L. Vasiliev, N.S. Perov, A.S. Vedeneev, Yu.E. Kalinin, V.V. Tugushev, A.B. Granovsky, *Phys. Rev. B* 95 (2017) 144202.

$$\rho_{AHE}(x, T) \approx 0.37(b/a) \times \rho_{Hd}(x, T) + \rho_{Hg}(T), \quad (13.5)$$

where $\rho_{Hd}(x, T)$ and $\rho_{Hg}(T)$ are the TAHE and granule AHE resistivities, respectively. Recall that according to Refs. [21,28], the last term in Eq. (13.5) does not depend on x . The factor $0.37 \cdot (b/a)$ reducing the component $R_{Hd}(x, T)$ in Eq. (13.5) reflects an aforementioned shunting of the local TAHE sources in our percolation system. Naturally, this factor is stronger for the elongated granules than for rounded ones. One more reason of the strong suppression of TAHE in the case of NCs with elongated granules along the NC growth axis is caused by “skew” intergranular tunneling of electrons propagating in NC film plane (see the inset to Fig. 13.17A and Chapter 6 in Ref. [15]). At strongly “skew” tunneling, the main contribution to TAHE arises in the transverse direction to the granule axis (along the film plane) (Fig. 13.17A). In this case, equiprobable tunnel transitions between granules with a preferred direction “up” or “down” (along z axis) give contribution to TAHE with the opposite sign. Therefore, the strong elongation of granules and impossibility of “front” tunneling between them lead to the strong suppression of TAHE in case of $(\text{CoFeB})_x(\text{LiNbO}_y)_{100-x}$ NC in comparison with the $(\text{CoFeB})_x(\text{AlO}_y)_{100-x}$ NC with rounded granules (see Fig. 13.15 and Refs. [7,9]).

Obviously, the ideal granular system for observation TAHE is NC with rounded granules. But in the frame of the described phenomenological approach, we cannot specify the $R_{Hd}(x, T)$ behavior as a function of x and T . The theory of TAHE was developed only at $T = 0\text{K}$ and for a tunnel junction with flat ferromagnetic electrodes of a large area, but not for nanogranular array. Besides, the value of the TAHE coefficient depends on a number of the model parameters, such as barrier height, width, and shape, all of which can be different in disordered systems. For this reason, in our qualitative description, we can rely on the principal idea of the microscopic model of TAHE exposed in Ref. [10].

Apparently, the TAHE contribution becomes particularly significant below the percolation threshold (at $x < x_p$); therefore, one can expect the scaling between AHE resistivity and longitudinal one with index $n \neq 0$, which is the case in reality (Fig. 13.15A). At $x < x_p$, the TAHE resistivity grows with increasing $\Delta x = (x_p - x)$ when magnetization of ferromagnetic component falls (Fig. 13.11). It is explained that the TAHE, according to Ref. [10], is determined by local magnetization of granules, but not magnetization of granular array. The main reason of the TAHE increase with the metal content decrease is caused by *a creation of TAHE sources in the percolation granular network*. It is important that TAHE signal appears against the background of sufficiently large AHE component from granules (see Fig. 13.15A) that does not depend on x below percolation transition. It is the main reason for the small index $n \approx 0.24$ in the $\rho_{AHE}(x)/x \propto \rho(x)^n$ dependence.

Other situation takes place in scaling relation $\rho_{AHE}(T) \propto \rho(T)^n$ at the change of temperature for the fixed metal content. In this case, tunneling probability does not (or very slightly) depend on the temperature (see [21]). Since the granule size is small (2–4 nm), one can expect very

strong scattering by their interfaces; therefore, the temperature behavior of the corresponding contribution $R_{Hg}(T)$ to $R_H(x,T)$ is similar to that observed in very thin metal film [19]. Large amount of dispersed magnetic impurity centers inside tunneling barriers, possible ferromagnetic order between their magnetic moments, the spin-flip processes, all these factors form the temperature dependence of AHE in studied systems. As a result for $(\text{CoFeB})_x(\text{AlO}_y)_{100-x}$ sample with $x = 56$ at.% (far from MIT), we observe the value of $\gamma \approx 1.4$ or $n \approx 0.6$ (Fig. 13.14) that coincides with $n \approx 0.6-0.7$ for Ni-SiO₂ nanocomposites above percolation threshold [28,38]. On the other hand, the obtained index $\gamma \approx 1.6$ for $(\text{CoFeB})_x(\text{AlO}_y)_{100-x}$ ($x = 49$ at.%) sample near MIT as well as for $(\text{CoFeB})_x(\text{LiNbO}_y)_{100-x}$ NCs with $x = 44$ and 48 at.% is the same (Figs. 13.14 and 13.15B) as for one-phase magnetic materials with high resistivity ($\rho \geq 10^{-4} \Omega \text{ cm}$) studied in Refs. [35,44]. This coincidence perhaps is not casual and probably due to the fact that strong scattering and localization effects manifested in our granular system near MIT play also important role in scaling $\sigma_{AHE} \propto \sigma^\gamma$ relation of dirty magnetic conductors [35,44].

13.5.5 Manifestation of Superferromagnetic Ordering

At higher concentration of magnetic ions, the evident part will appear in the tunneling barriers between granules and can initiate FM coupling between cluster skeleton granules, promoting a so-called superferromagnetic (SFM) order [2,3,45]. Under these conditions, it should be expected that the behavior of the AHE resistance $R_{AHE}(B)$ will be the linear up to saturation fields $B \approx B_s$ as in ferromagnetic films with easy-plane magnetic anisotropy. It is really observed in our experiments (see Figs. 13.8 and 13.9). The reason of such behavior is following; in the case when FM exchange coupling energy between granules (driven by dispersed ions) exceeds the single-granule magnetic anisotropy energy and dipole-dipole interaction between FM granules, the effective magnetic anisotropy of the film should mainly be determined by its shape.

There is another way to check this assumption. For this, it is necessary to measure the magnetization in the field perpendicular to the film plane and to compare the measured $M(H)$ curves with the ones found from the in-plane field magnetization data. In reality, it is known that in the magnetically isotropic films, the magnetization behavior in perpendicular geometry M_\perp can be determined from the magnetization data in the parallel field M_\parallel considering a demagnetizing field: $M_\perp(H_\perp) = M_\parallel(H_\parallel + 4\pi M_\parallel)$. Here H_\perp and H_\parallel are the solenoid fields in the out-of-plane and in-plane configurations, respectively. Having determined the experimental function, $f(H_\parallel) = M_\parallel(H_\parallel)/M_s$, it is possible to predict the behavior of magnetization of isotropic film in the transverse geometry:

$$M_\perp(H_\perp)/M_s = f(H_\parallel + 4\pi M_s f(H_\parallel)). \quad (13.6)$$

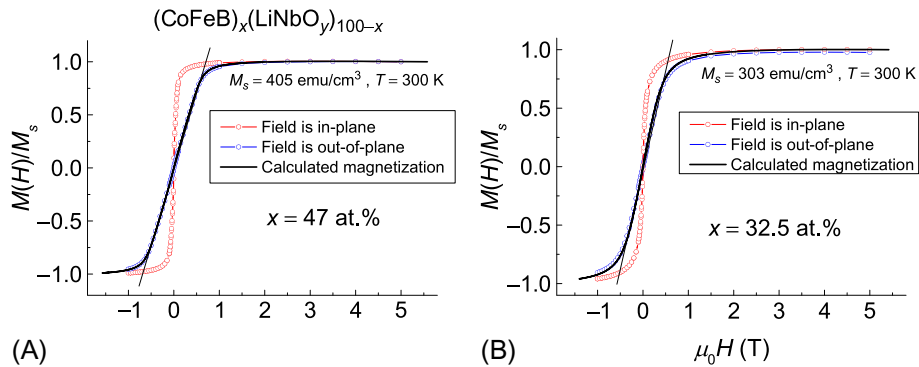


Fig. 13.18

Normalized magnetic field dependences of the magnetization for $(\text{CoFeB})_x(\text{LiNbO}_y)_{100-x}$ with $x \approx 47$ (A) and 32.5 at.% (B) measured at in-plane and out-of-plane geometries. The *solid lines* show the calculated $M_{\perp}(H_{\perp})$ curves found according Eq. (13.6). From V.V. Rylkov, A.V. Sitnikov, S.N. Nikolaev, V.A. Demin, A.N. Taldenkov, M.Yu. Presnyakov, A.V. Emelyanov, A.L. Vasiliev, Yu.E. Kalinin, A.S. Bugaev, V.V. Tugushev, A.B. Granovsky. *J. Magn. Magn. Mater.*, 2017 (<https://doi.org/10.1016/j.jmmm.2017.11.022>).

Fig. 13.18 shows the normalized magnetic field dependences of magnetization for $(\text{CoFeB})_x(\text{LiNbO}_y)_{100-x}$ NC with $x \approx 47$ (a) and 32.5 at.% (b) in comparison with the calculated $M_{\perp}(H_{\perp})$ curves, according to Eq. (13.6). Very good accordance is observed between the experimental and calculated $M_{\perp}(H_{\perp})$ dependences. Thus, we can conclude that the $M(H)$ behavior does not contain any indication on the induced magnetic anisotropy of $(\text{CoFeB})_x(\text{LiNbO}_y)_{100-x}$ NC caused by its columnar structure. Note that perpendicular magnetic anisotropy is well manifested in the case of $\text{Co}_x(\text{AlO}_y)_{100-x}$ NC under SFM order [3].

13.6 Memristive Properties

13.6.1 Introduction to Memristive Properties of Oxides

The oxygen vacancies redistribution in the strong electric field can affect the tunnel connection between the granules of the percolation NC medium. Such redistribution can be accompanied by manifestation of memristive effects, i.e., effects associated with resistive switching (RS) and storage of NC resistive state. It should be noted that recently there has been a sharp increase in interest in the development of metal-oxide-metal (MOM) memristive structures due to the possibility of using them to simulate synaptic plasticity (variable signal transmission efficiency) for developing of adaptive or bioinspired computing circuits, as well as for multilevel memory elements [46–54]. The RS effects observed in MOM structures

are usually associated with the processes of electromigration of oxygen vacancies V_O (inside the oxide layer) or metal cations (such as Cu, Ag) into the oxide layer from the active electrode of the MOM structure [46–54]. As a result, conductive filaments or conductive bridges are formed (destroyed) in the oxide layer. The electromigration of oxygen vacancies V_O or metal cations is responsible for the formation (rupture) of conductive filaments or bridges, respectively. However, there are MOM structures with both mechanisms of RS (see, for example, Refs. [55,56]). We also note that in the case of MOM structures based on semiconductor oxides with covalent bonds (such as GeO_2), the observed RS effects are explained by an alternative (nonfilament) model that assumes uniform generation (recombination) of oxygen vacancies that play the role of electron traps, which determine the hopping conductivity of the MOM structure [57].

To date a rather rich experimental material has been accumulated, containing the evidence base for the key role of the electromigration of vacancies (ions) in the RS of metal oxides structures [46]. There were in situ studies on conductive filament structural evolution during the RS process [55,58–61]. It is interesting to note that in the case of MOM structures based on amorphous TiO_2 , the RS effects are determined by the formation (destruction) of Ti_4O_7 crystal filaments with metallic conductivity [58], while in the case of MOM structures based on polycrystalline Ta_2O_5 or amorphous TaO_x , the filaments can consist either of a conducting phase of TaO_{2-x} [60], or of metallic Ta nanocrystallites in amorphous TaO_x [61], respectively. In MOM structures based on crystalline LiNbO_3 at the forming stage, the formation of defects (most likely oxygen vacancies) near the cathode was observed and accompanied by local “bubbling” of the top anode due to the oxygen out-effusion (see [62] and Supplementary Information). The latter was also observed in other types of MOM structures with filament formation [58,61]. It should be noted that, despite the accumulated considerable experimental material, the microscopic theory of reversible RS effects is still absent. The latter, in particular, is due to the difficulties in describing the interrelated nonequilibrium processes of thermal, electron, and ion transport at nanometer scale (see [63,64]).

The main issue with MOM structures is degradation of their memristive properties during the process of RS, which is the consequence of the random (filament) nature of the transition to the conducting state that varies with time. For example, in the case of well-studied memristive MOM structures based on TiO_2 , the maximum number of switching cycles N_{max} (endurance) reaches $\sim(5-10) \times 10^3$ [47,65]. In recently developed memristive structures based on single-crystal LiNbO_3 layers, the degradation effects were absent during first 500 switching cycles [62].

From general considerations, it is obvious that in the case of Me/NC/Me structures, the transition to the conducting state in the dielectric region of the NC composition ($x < x_c$) should be determined by percolation chains specified by the spatial distribution and concentration of metal nanogranules, which in turn should ensure high endurance (switching stability).

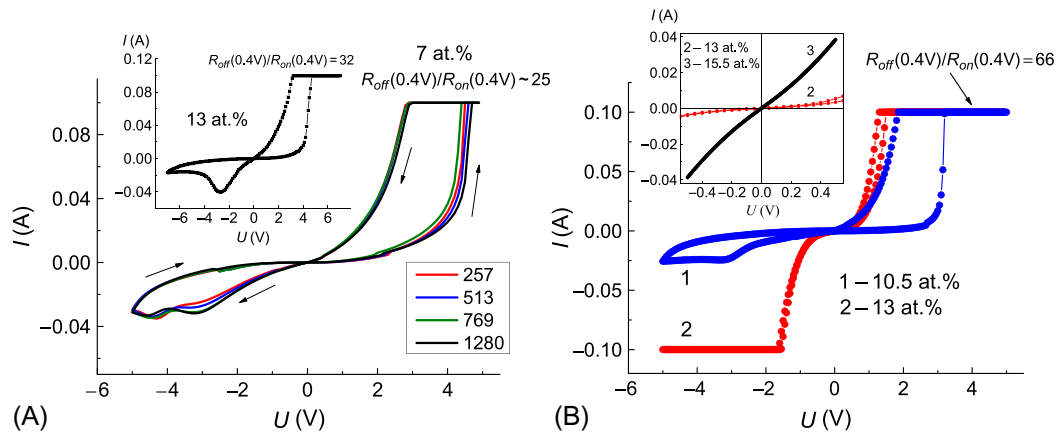


Fig. 13.19

I-V curves of the Me/(CoFeB)_x(LiNbO_y)_{100-x}/Me structure with the metal content: (A) $x \approx 7$ at.%; (B) $x \approx 10.5$ and 13 at.%. The thickness of the nanocomposite layer is $d \approx 3 \mu\text{m}$. The *I-V* curves are obtained as a result of multiple voltage cycling linearly in a sequence from $0 \rightarrow +5 \rightarrow -5 \rightarrow 0$ V and correspond to different samples in a set of 1280 curves: 257, 513, 769, and 1280. The insets show (A) *I-V* curve of the Me/(CoFeB)_x(LiNbO_y)_{100-x}+O₂/Me structure with $x \approx 13$ at.%, fabricated with the addition of oxygen during the NC growth ($P_{\text{O}_2} \approx 2 \times 10^{-5}$ Torr), (B) *I-V* curves of the Me/(CoFeB)_x(LiNbO_y)_{100-x}/Me structure with $x \approx 13$ and 15.5 at.%. From V.V. Rylkov, S.N. Nikolaev, V.A. Demin, A.V. Emelyanov, A.V. Sitnikov, K.E. Nikiruy, V.A. Levanov, M.Yu. Presnyakov, A.N. Taldenkov, A.L. Vasiliev, K.Yu. Chernoglazov, A.S. Vedenev, Yu.E. Kalinin, A.B. Granovsky, V.V. Tugushev, A.S. Bugaev, *J. Exp. Theor. Phys.* 126 (2018) 353.

Actually, this statement initiated our investigation of the *I-V* characteristics of the (CoFeB)_x(LiNbO_y)_{100-x} NC in strong electric fields ($>10^4$ V/cm).

13.6.2 Resistive Switching Effects in Nanocomposites

We have studied Me/NC/Me structures with different oxygen distribution (or its vacancies) along the (CoFeB)_x(LiNbO_y)_{100-x} layer growth (see Section 13.2.1). In Fig. 13.19, typical *I-V* characteristics for structures of type 1 Me/(CoFeB)_x(LiNbO_y)_{100-x}/Me (NC thickness $d \approx 3 \mu\text{m}$) with different $x \approx 7$ (A), 10.5 and 13 at.% (B) are shown. For convenience, we recall that structures of type 1 were obtained in the regime when, in the initial stage of the NC growth, the pressure in the chamber was $P \approx 1 \times 10^{-5}$ Torr, which was significantly higher than the ultimate vacuum that was reached in the chamber during the NC deposition ($P \approx 6 \times 10^{-6}$ Torr). The *I-V* curves in Fig. 13.19A were obtained by sweeping the voltage linearly in the sequence from $0 \rightarrow +5 \rightarrow -5 \rightarrow 0$ V. In all experiments, the current-limiting mode was used at the level of 0.1 A.

It could be seen from Fig. 13.19A and B that hysteresis in *I-V* characteristic typical for RS is most visible observed at an optimal value $x = x_{\text{opt}} \approx 10.5$ at.%. At $x \approx 13$ at.% ($> x_{\text{opt}}$), the hysteresis

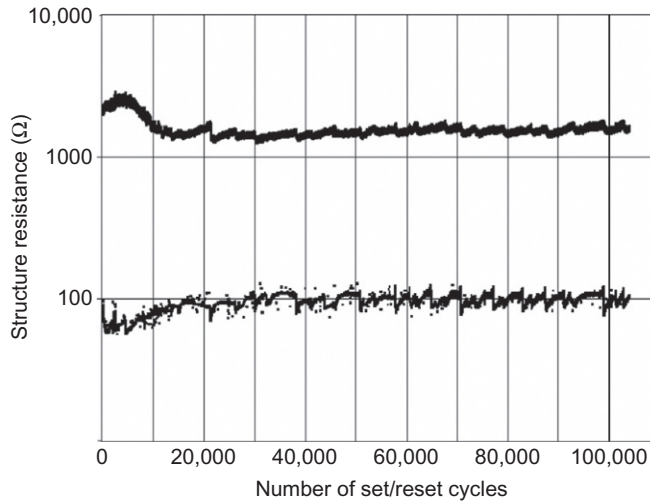


Fig. 13.20

The dependence of resistance for $\text{Me}/(\text{CoFeB})_x(\text{LiNbO}_y)_{100-x}/\text{Me}$ structure ($x \approx 7 \text{ at.}\%$) vs. number of set/reset cycles. The thickness of the nanocomposite layer is $d \approx 3 \mu\text{m}$. Measuring procedure: set at +5 V (during 100 ms), read operation at 0.1 V (100 ms), reset at -5 V (100 ms), read operation at 0.1 V (100 ms), etc.

is almost absent, and at a lower value of $x \approx 7 \text{ at.}\%$, the hysteresis loop is strongly elongated. In this case, the ratio of the resistances in the high-resistance and low-resistance states $R_{\text{off}}/R_{\text{on}}$ decreases; for the read voltage $U = 0.4 \text{ V}$: $R_{\text{off}}/R_{\text{on}} = 66$ and 25 at $x \approx 10.5$ and 7 at.%, respectively.

Note the good reproducibility of the I - V characteristics and their smooth running (not “breakdown” type) at RS with cycling, which indicates the absence of degradation effects. During the day, we were able to carry out $>10^5$ RS cycles by sequentially applying 100-ms voltage pulses with amplitude +5 V (set the structure to a low-resistance state), and then applying -5 V (reset it to its initial high-resistance state). The high endurance of Me/NC/Me structures is demonstrated in Fig. 13.20.

To date, the main reasons and factors determining the endurance of oxide structures are not clear yet. Therefore, investigations of this issue are mainly empirical. In particular, the available experimental data show that endurance of TiO_x -based MOM structures can be substantially increased by introducing a thin (3–5 nm) Al_2O_3 barrier layer at one of the MOM electrodes [47,65,66]. This barrier layer determines the upper level of the structure resistance, as well as resistance decrease during the oxygen vacancies formation in Al_2O_3 , for example, due to their electric field injection from the TiO_x layer, which plays the role of a reservoir. In MOM structures based on $\text{TiO}_2/\text{TiO}_x$ layers, N_{max} is about 10^3 [67], whereas when using Al_2O_3 (instead of TiO_2) $N_{\text{max}} \sim 10^4$ [65]. A very interesting conclusion can be drawn from a comparison of the results of the study of the memristive properties of MOM structures based on

polycrystalline Ta₂O₅ [60] and amorphous TaO_x [61], in which the resulting filaments in the low-resistance state consist, respectively, of either conducting phase of TaO_{2-x} or Ta nanocrystallites in amorphous TaO_x. In the first case, the number of stable RS is $N_{max} \sim 10^3$ [60], whereas in the second case this value reaches $\sim 10^5$ [61]. Hence, it can be concluded that the presence of metal particles in the regions of formation of conductive filaments significantly increases the stability of the system and its endurance.

To study the influence of the gradient in oxygen distribution (or V_O) over NC thickness, Me/NC/Me structures of type 2 were fabricated. For that type of structures, in contrast to the structures of type 1, oxygen was added to the chamber in the preset flow regime providing the partial pressure $P_{O_2} \approx 2 \times 10^{-5}$ Torr. It was found that the presence of oxygen during the NC deposition leads to a shift in the metal optimal content x_{opt} to the region of larger x values. An important feature of such structures was the fact that in order to obtain a stationary I - V characteristic, forming process was required in this case. The inset in Fig. 13.19A shows the I - V characteristic for the structure Me/(CoFeB)_x(LiNbO_y)_{100-x}+O₂/Me with the NC thickness $d \approx 3 \mu\text{m}$. The optimal metal content for such structure is about 13 at.%. In this case, the ratio $R_{off}/R_{on} = 32$ is 2 times less than that for the structure deposited without addition of O₂ (Fig. 13.19B). In other words, a decrease in the oxygen vacancies distribution gradient over the NC thickness leads to a drop in the R_{off}/R_{on} ratio.

13.6.3 Qualitative Model of the Resistive Switching Mechanism

It could be concluded from the data presented that the bottleneck of the Me/NC/Me structures that determines its resistance is a highly oxidized NC layer at the bottom electrode (contact layer). It is possible to set this layer in a low-resistance state by applying a positive voltage (U_{set}) to the top electrode; for example, due to electromigration of oxygen vacancies from NC volume to the bottom contact under these conditions. On the other hand, if a highly oxidized NC layer is created at the top electrode, then switching to the low-resistance state of the Me/NC/Me structure should occur at negative voltage.

To verify this assumption, Me/NC/Me structures of types 3 and 4 were fabricated. In the structure of type 3 a highly resistive oxidized NC layer with a thickness of about 100 nm was formed at the bottom electrode, while that in the structure of type 4—at the top electrode (Section 13.2.1).

The I - V characteristics of structures 3 and 4 are shown in Fig. 13.21. It can be seen that in structure of type 3, RS to the low-resistance state is observed under a positive potential U_{set} , as well as in structures of types 1 and 2 (Fig. 13.19). In this case, RS appears at a much larger $U_{set} \approx 7$ V, and its character is sharper. In structure of type 4 the situation is reversed. The U_{set} sign changes to negative values. The R_{off}/R_{on} ratio is small ≈ 3 while for the structure 3 $R_{off}/R_{on} \approx 34$. The difference is due to the presence of a relatively high-resistance layer at the

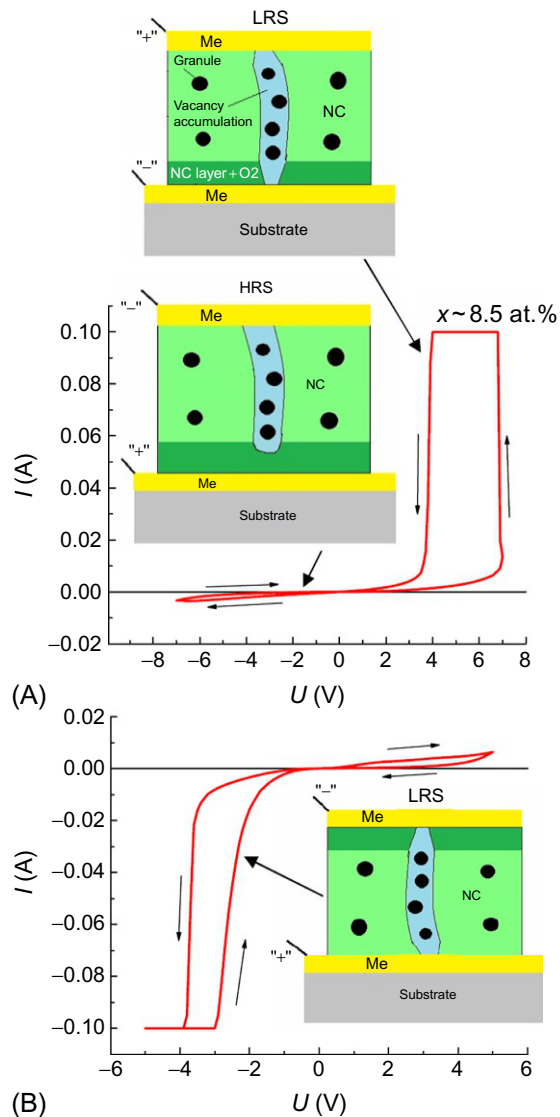


Fig. 13.21

I-V curves of Me/(CoFeB)_x(LiNbO_y)_{100-x}/Me structures of types 3 (A) and 4 (B) with $x \approx 8.5$ at.%, grown with the addition of oxygen for 7 min at the initial (A) and final (B) NC growth stages, respectively. The insets in (A) show schematic representations of structure 3 demonstrating the formation of a high-resistance (at negative potential on the top electrode, the lower inset) and a low-resistance (at positive potential) states (HRS and LRS) of the Me/NC/Me structure. The inset of (B) shows schematic representations of structure 4 in the low-resistance state (under negative potential). The arrows indicate the *I-V* curves regions corresponding to the HRS and LRS of the structures. From V.V. Rylkov, S.N. Nikolaev, V.A. Demin, A.V. Emelyanov, A.V. Sitnikov, K.E. Nikiruy, V.A. Levanov, M.Yu. Presnyakov, A.N. Taldenkov, A.L. Vasiliev, K.Yu. Chernoglazov, A.S. Vedeneev, Yu.E. Kalinin, A.B. Granovsky, V.V. Tugushev, A.S. Bugaev, *J. Exp. Theor. Phys.* 126 (2018) 353.

bottom electrode of structure 4, which compensates the resistance change of the top electrode region and, consequently, the total resistance of the structure.

In the studied structures, the RS mechanism (vacancy drift) could be different from that in the case of Me/Al₂O₃/TiO_x/Me structures [47,60,61]. There is an optimal for RS effect metal content $x = x_{opt}$ in the investigated structures. For $x > x_c$, one can expect a drastic conductivity increase and the absence of the RS effect. The inset in Fig. 13.19B shows the I - V curves of the structures with $x = 13$ and 15.5 at.% at low bias voltages, which exhibit a sharp increase in conductivity at $x \geq 13$ at.% (over 10 times at $U = 0.4$ V). This indicates that in these structures, the percolation threshold $x_p \sim x_c \sim 13$ –15 at.%, and the optimal value of $x = x_{opt}$ is below the threshold by $\delta x \sim 2$ –4 at.%. It should be noted that for planar structures x_c is about (40–44) at.% (see Fig. 13.7), which is three times higher than that for Me/NC/Me sandwich structures. Such a large difference in x_c cannot be explained by the size effects in percolation conductivity, since the correlation radius of the percolation cluster L for (CoFeB)_x(LiNbO_y)_{100-x} is about 20–30 nm in the vicinity of the MIT (see Section 13.4), which is much smaller than NC thickness $d \approx 3$ μm.

We believe that the x_c value decrease and the RS mechanism emergence are correlated in our system. Indeed, the elongation of the granules along the NC growth axis (Figs. 13.3–13.6) should lead to an asymmetry in the percolation grid and an increase in its cell size L in the transverse direction ([15]). Taking into account the asymmetry in the hopping transport [15,68]: $L_z \sim (a_z/a_x) \cdot (a_z + b) \cdot (b/\lambda)^v$, where b is effective tunnel distance between the granules [$b \propto a(x_p - x)/x_p$ for $(x_p - x) \ll x_p$], λ is the depth of the subbarrier decay of the electron wave function, and $v = 0.88$ is the critical index of the percolation theory. From this expression, it follows that the smaller the metal content, the bigger the value of L_z is, which may become the same order of magnitude as NC thickness. In this case, the hopping conductivity of the percolation system (Me/NC/Me structure) in the sandwich geometry will be determined by individual chains of granules with the smallest intergranular barriers [15,69] in which at voltage application the maximum electric field is reached ($> 10^4$ V/cm under $U \geq 3$ V). Under such strong field, the resistance of the chain can drop dramatically. Firstly, due to the suppression of the Coulomb blockade effects, which is manifested in NC systems with a high dielectric constant of the insulating matrix, causing a transition from activation to metallic conductivity in relatively low fields $E > E_D = e^2/\kappa \cdot a^2$ [70] ($E_D \approx 1.6 \times 10^4$ V/cm for $\kappa \approx 100$ and $a \approx 3$ nm). Secondly, the vacancy V_O generation is possible by the mechanism described in Ref. [57], which requires relatively low energy in comparison with the energy for V_O electromigration. In particular, this is due to the oxygen movement from LiNbO₃ to the closely located (within the lattice constant) chemically active B and/or Fe (Co) atoms, which are contained in the considerable concentration in the oxide matrix ($> 10^{22}$ cm⁻³). In turn, the V_O generation, accompanied by emergence of localized states in the LiNbO_y bandgap, can increase the tunneling conductivity of chains of granules [71,72].

As a result of the resistance decrease, a redistribution of the voltage drop occurs at the highly oxidized region of the NC near the electrode. The resulting electric field in this region (10^5 – 10^6) V/cm is high enough for the electric field injection of vacancies into the interface layer, its shunting, and RS of the structure into a low-resistance state. Changing the voltage U polarity leads to the V_O extraction from this layer, and the structure is again switched to a high-resistance state (see the insets in Fig. 13.21). In the proposed RS model for Me/NC/Me structure, local regions of the resistance change caused by V_O electromigration are set by the position of isolated chains of granules, which provides high stability of the RS, in contrast to “homogeneous” MOM structures. The situation, however, is similar to the case of RS observed in Me/TaO_x/Me structures [61], in which the forming conductive filaments consist of Ta nanocrystals in amorphous TaO_x.

It should be noted that the mechanisms described in Refs. [57,70] cannot explain the RS in our Me/NC/Me structures, since they are symmetric and in the fields of different signs would switch the structure to low-resistance state (see, for example, Fig. 6 of Ref. [70]). However, the observed I - V characteristics are strongly asymmetric (Figs. 13.19 and 13.21); switching from high- to low-resistance state is observed at a single voltage polarity, depending on which of the contacts is located near a strongly oxidized high-resistance layer. We also note that the Me/NC/Me structures have an ability to specify an arbitrary resistive state in the range between R_{on} and R_{off} and its storage during the day. In terms of the RS model considered here, this is explained by the possibility of partial shunting of the contact layer of the Me/NC/Me structure due to V_O electromigration.

13.7 Concluding Remarks

We performed experimental investigations of structural, magnetic, magnetotransport, and memristive properties of (CoFeB)_x(AlO_y)_{100-x} and (CoFeB)_x(LiNbO_y)_{100-x} film NCs with $x = 6$ – 60 at.% and various structures. The films were produced using the ion-beam sputtering of the composite targets onto glass-ceramic substrates, and they consist of magnetic nanogranules embedded into the nonstoichiometric oxide matrix. For (CoFeB)_x(AlO_y)_{100-x} NC the granules are rounded (2–4 nm in size), whereas for (CoFeB)_x(LiNbO_y)_{100-x} the granules are strongly elongated along the NC growth axis up to 10–15 nm with the same in-plane size 2–4 nm. The chemical compositions of granules and matrix differ from those of corresponding targets; a large amount of dispersed Fe or Co ions in the matrix (up to 3×10^{22} cm⁻³) was found by both structural and magnetic measurements. It plays a crucial role both in the ferromagnetic exchange between granules and in transport and magnetic properties below percolation threshold at $x \leq 59$ at.%. The conductivity of the systems follows the $\ln T$ law on the metallic side of MIT in the wide range of metal content variation $x = 44$ – 56 at.% that formally corresponds to the conductivity of array of granules with strong

tunnel coupling between them. In both cases, the AHE takes place and its behavior is similar to the one observed in films with easy-plane magnetic anisotropy. We showed that the relation between the AHE resistivity $\rho_{AHE}(T, x)$ and longitudinal resistivity $\rho(T, x)$ does not follow the universal scaling law, if T or x are variable parameters: $\rho_{AHE}(T) \propto \rho(T)^{0.4 \div 0.6}$, obtained from the temperature variation of ρ and ρ_{AHE} measured for each sample at fixed x , and $\rho_{AHE}(x)/x \propto \rho(x)^n$ with $n \approx 0.24$ (for $(\text{CoFeB})_x(\text{AlO}_y)_{100-x}$) and $n \approx 0$ (for $(\text{CoFeB})_x(\text{LiNbO}_y)_{100-x}$), obtained from measurements at a fixed low temperature for samples with different x . Obtained results are interpreted in terms of the model of two sources of AHE e.m.f., arising from metallic nanogranules and insulating tunneling regions, respectively. We suggest that the tunneling AHE component can be caused by recently predicted scattering-assisted mechanism [10] and is strongly shunted due to generation of local circular Hall current, especially in case of $(\text{CoFeB})_x(\text{LiNbO}_y)_{100-x}$ NC with the elongated granules.

The analysis of magnetization showed that for $(\text{CoFeB})_x(\text{LiNbO}_y)_{100-x}$ film there is no structurally induced magnetic anisotropy, i.e., the magnetic anisotropy of samples is practically entirely determined by their shape. Our results hint at the possible formation of the SFM order in both NCs below percolation threshold due to strong FM exchange coupling between granules via dispersed magnetic ions. Furthermore, in the case of $(\text{CoFeB})_x(\text{LiNbO}_y)_{100-x}$ NC, this exchange energy exceeds the single-granule magnetic anisotropy energy. We assume that supposed SFM is initiated by two factors: (i) the presence of large concentration (up to $N_i \approx 3 \times 10^{22} \text{ cm}^{-3}$) of Fe^{2+} and Co^{2+} ions in the oxide matrix and (ii) the tunneling superexchange through dispersed Fe (Co) atoms [2,3,45] and/or modification of oxide matrix properties promoting FM exchange [4], in particular, due to increasing dielectric permittivity of the matrix and lowering intergranular barriers.

We found the enduring RS effects in capacitor-like $\text{Me}/(\text{CoFeB})_x(\text{LiNbO}_y)_{100-x}/\text{Me}$ structures that are due to, in our opinion, several factors: (i) the percolation nature of the NC conductivity and the formation of isolated chains of elongated metal nanogranules, which determine the structure conductivity; (ii) the anomalous high decrease in the chains resistance in fields $E > 10^4 \text{ V/cm}$ due to the Coulomb blockade affects suppression [70] and the oxygen vacancies generation [57]; (iii) the field injection of vacancies ($U > 0$) into a highly resistive oxidized layer predominantly formed at the bottom electrode of the $\text{Me}/\text{NC}/\text{Me}$ structure, due to the peculiarities of its growth process, switching the structure to a low-resistance state. Applying the voltage $U < 0$ vacancies extraction from this layer occurs, which leads to a reverse switching of the structure to a high-resistance state. As a result of these factors, the percolation threshold is reduced by a factor of three, and the field injection (extraction) of vacancies controlled by the chains leads to stable resistive switching, the number of which exceeds 10^5 with the ratio $R_{\text{off}}/R_{\text{on}} \sim 50$.

Acknowledgements

The research work on the synthesis and investigation of electrophysical properties of memristor (capacitor-like) nanocomposite structures was supported by the International Project of the Ministry of Education and Science of the Russian Federation (MES RF) (No. RFMEFI58717X0042); the research work on the synthesis and investigation of electrophysical properties of nanocomposite films was supported by the MES RF in terms of the state task (Project No. 3.1876.2017/PCh).

The investigations of magnetic properties of nanocomposite films and structures were supported by the Russian Science Foundation (Grant No. 16-19-10233).

References

- [1] I.S. Beloborodov, A.V. Lopatin, V.M. Vinokur, K.B. Efetov, *Rev. Mod. Phys.* 79 (2007) 469.
- [2] S. Bedanta, T. Eimuller, W. Kleemann, J. Rhensius, F. Stromberg, E. Amaladass, S. Cardoso, P. Freitas, *Phys. Rev. Lett.* 98 (2007) 176601.
- [3] A.A. Timopheev, I. Bdikin, A.F. Lozenko, O.V. Stognei, A.V. Sitnikov, A.V. Los, N.A. Sobolev, *J. Appl. Phys.* 111 (2012) 123915.
- [4] O.G. Udalov, I.S. Beloborodov, *Phys. Rev. B* 95 (2017) 045427; O.G. Udalov, I.S. Beloborodov, *J. Phys. Condens. Matter* 29 (2017) 155801.
- [5] V.V. Rylkov, A.V. Sitnikov, S.N. Nikolaev, V.A. Demin, A.N. Taldenkov, M.Yu. Presnyakov, A. V. Emelyanov, A.L. Vasiliev, Yu.E. Kalinin, A.S. Bugaev, V.V. Tugushev, A.B. Granovsky, *J. Magn. Magn. Mater.* (2017). <https://doi.org/10.1016/j.jmmm.2017.11.022>.
- [6] K.B. Efetov, A. Tschersich, *Phys. Rev. B* 67 (2003) 174205.
- [7] V.V. Rylkov, S.N. Nikolaev, K.Y. Chernoglazov, V.A. Demin, A.V. Sitnikov, M.Y. Presnyakov, A. L. Vasiliev, N.S. Perov, A.S. Vedeneev, Y.E. Kalinin, V.V. Tugushev, A.B. Granovsky, *Phys. Rev. B* 95 (2017) 144202.
- [8] X. Li, Y. Shi, J. Li, Y. Bai, J. Jia, Y. Li, X. Xu, *Mater. Res. Express* 4 (2017) 036407.
- [9] V.V. Rylkov, S.N. Nikolaev, V.A. Demin, A.V. Emelyanov, A.V. Sitnikov, K.E. Nikiruy, V.A. Levanov, M. Yu. Presnyakov, A.N. Taldenkov, A.L. Vasiliev, K.Yu. Chernoglazov, A.S. Vedeneev, Yu.E. Kalinin, A. B. Granovsky, V.V. Tugushev, A.S. Bugaev, *J. Exp. Theor. Phys.* 126 (2018) 353.
- [10] A.V. Vedyayev, N.V. Ryzhanova, N. Strelkov, B. Dieny, *Phys. Rev. Lett.* 110 (2013) 247204.
- [11] Y.E. Kalinin, A.N. Remizov, A.V. Sitnikov, *Phys. Solid State*, 46 (2004) 2146; S.A. Gridnev, Y.E. Kalinin, A. V. Sitnikov, O.V. Stogniy, *Nonlinear Effects in Nano- and Microheterogeneous Systems*, BINOM, Moscow, 2012 [in Russian].
- [12] W.C. Ellis, E.S. Greiner, *Equilibrium relations in the solid state of the iron-cobalt system*, *Trans. Am. Soc. Met.* 29 (1941) 415.
- [13] T. Yamasaki, S. Kanatani, Y. Ogino, T. Masumoto, M. Doyama, K. Kiribayashi, T. Kisi, *Structure of Fe-Cr-X (X=N, C and B) powdered alloys prepared by mechanical milling*, in: *Advanced Materials '93: Computations, Glassy Materials, Microgravity and Nondestructive Methods*, Elsevier, Amsterdam, 1994, , pp. 93–96.
- [14] L.B. Gurvich, G.B. Karachevtsev, V.N. Kondrat'ev, Y.A. Lebedev, V.A. Medvedev, V.K. Potapov, Y. S. Khodeev, *Energy of Chemical Bond Rupture, Ionization Potentials and Electron Affinity*, Nauka, Moscow, 1974 (in Russian).
- [15] B.I. Shklovskii, A.L. Efros, *Electronic Properties of Doped Semiconductors*, Springer-Verlag, New York, 1984.
- [16] A.L. Efros, *Physics and Geometry of Disorder: Percolation Theory (Science for Everyone)*, Mir Publishers, Moscow, 1986; I. Fizika, Geometriia Beporiadka, Nauka, Moscow, 1982. Russian version available at http://www.math.ru/lib/files/pdf/kvant_19.pdf.
- [17] R. Karplus, J.M. Luttinger, *Phys. Rev.* 95 (1954) 1154.
- [18] N. Nagaosa, J. Sinova, S. Onoda, A.H. MacDonald, N.P. Ong, *Rev. Mod. Phys.* 82 (2010) 1539.
- [19] Y. Tian, L. Ye, X. Jin, *Phys. Rev. Lett.* 103 (2009) 087206.

- [20] V.V. Rylkov, B.A. Aronzon, A.S. Lagutin, V.V. Podol'skii, V. P. Lesnikov, M. Goiran, J. Galibert, B. Raquet, J. Léotin, *J. Exp. Theor. Phys.* 108 (2009) 149.
- [21] H. Meier, M.Y. Kharitonov, K.B. Efetov, *Phys. Rev. B* 80 (2009) 045122.
- [22] D. Chiba, A. Werpachowska, M. Endo, Y. Nishitani, F. Matsukura, T. Dietl, H. Ohno, *Phys. Rev. Lett.* 104 (2010) 106601.
- [23] X. Liu, S. Shen, Z. Ge, W.L. Lim, M. Dobrowolska, J.K. Furdyna, *Phys. Rev. B* 83 (2011) 144421.
- [24] X.-J. Liu, X. Liu, J. Sinova, *Phys. Rev. B* 84 (2011) 165304.
- [25] A. Shitade, N. Nagaosa, *J. Phys. Soc. Jpn.* 81 (2012) 083704.
- [26] A.V. Vedyayev, M.S. Titova, N.V. Ryzhanova, M.Y. Zhuravlev, E.Y. Tsymbal, *Appl. Phys. Lett.* 103 (2013) 032406.
- [27] Y.O. Mikhailovsky, D.E. Mettus, A.P. Kazakov, V.N. Prudnikov, Y.E. Kalinin, A. S. Sitnikov, A. Gerber, D. Bartov, A.B. Granovsky, *JETP Lett.* 97 (2013) 473.
- [28] D. Bartov, A. Segal, M. Karpovski, A. Gerber, *Phys. Rev. B* 90 (2014) 144423.
- [29] S.A. Meynell, M.N. Wilson, J.C. Loudon, A. Spitzig, F.N. Rybakov, M.B. Johnson, T.L. Monchesky, *Phys. Rev. B* 90 (2014) 224419.
- [30] D. Hou, G. Su, Y. Tian, X. Jin, S.A. Yang, Q. Niu, *Phys. Rev. Lett.* 114 (2015) 217203.
- [31] L.N. Oveshnikov, V.A. Kulbachinskii, A.B. Davydov, B.A. Aronzon, I.V. Rozhansky, N.S. Averkiev, K. I. Kugel, V. Tripathi, *Sci. Rep.* 5 (2015) 17158.
- [32] A. Matos-Abiague, J. Fabian, *Phys. Rev. Lett.* 115 (2015) 056602.
- [33] T. Huong Dang, H. Jaffres, T.L. Hoai Nguyen, H.-J. Drouhin, *Phys. Rev. B* 92 (2015) 060403.
- [34] G. Kopnov, A. Gerber, *Appl. Phys. Lett.* 109 (2016) 022404.
- [35] S. Onoda, N. Sugimoto, N. Nagaosa, *Phys. Rev. Lett.* 97 (2006) 126602;
S. Onoda, N. Sugimoto, N. Nagaosa, *Phys. Rev. B* 77 (2008) 165103.
- [36] A.V. Vedyayev, A.B. Granovskii, O.A. Kotel'nikova, *Transport Phenomena in Disordered Ferromagnetic Alloys*, Moscow State Univ., Moscow, 1992 (in Russian).
- [37] A.V. Vedyayev, A.B. Granovsky, A.V. Kalitsov, F. Brouers, *J. Exp. Theor. Phys.* 85 (1997) 1204.
- [38] A. Pakhomov, X. Yan, B. Zhao, *Appl. Phys. Lett.* 67 (1995) 3497.
- [39] B.A. Aronzon, D.Y. Kovalev, A.N. Lagarkov, E.Z. Meilikhov, V.V. Rylkov, M. A. Sedova, N. Negre, M. Goiran, J. Leotin, *JETP Lett.* 70 (1999) 90.
- [40] J.V. Kasiuk, J.A. Fedotova, J. Przewoznik, J. Zukrowski, M. Sikora, C. Kapusta, A. Grce, M. Milosavljevic, *J. Appl. Phys.* 116 (2014) 044301.
- [41] C. Kittel, *Introduction to Solid State Physics*, fourth ed., John Wiley & Sons Inc., New York, 1971
- [42] I. Isenberg, B.R. Russell, R.F. Greene, *Rev. Sci. Instrum.* 19 (1948) 685.
- [43] J. Volger, *Phys. Rev.* 79 (1950) 1023.
- [44] T. Fukumura, H. Toyosaki, K. Ueno, M. Nakano, T. Yamasaki, M. Kawasaki, *Jpn. J. Appl. Phys.* 46 (2007) L642.
- [45] S. Bedanta, W. Kleemann, *J. Phys. D: Appl. Phys.* 42 (2009) 013001.
- [46] Ed. by D. Ielmini and R. Waser, *Resistive Switching: From Fundamentals of Nanoionic Redox Processes to Memristive Device Applications*, Wiley-VCH Verlag GmbH & Co. KGaA, Weinheim, 2016.
- [47] M. Prezioso, F. Merrikh-Bayat, B.D. Hoskins, G.C. Adam, K.K. Likharev, D.B. Strukov, *Nature* 521 (2015) 61.
- [48] M. Prezioso, F.M. Bayat, B. Hoskins, K. Likharev, D. Strukov, *Sci. Rep.* 6 (2016) 21331, <https://doi.org/10.1038/srep21331>.
- [49] A.V. Emelyanov, D.A. Lapkin, V.A. Demin, et al., *AIP Adv.* 6 (2016) 111301.
- [50] C.-C. Hsieh, A. Roy, Y.-F. Chang, D. Shahrjerdi, S.K. Banerjee, *Appl. Phys. Lett.* 109 (2016) 223501.
- [51] S.D. Ha, S. Ramanathan, *Adaptive oxide electronics: a review*, *J. Appl. Phys.* 110 (2011) 071101.
- [52] J.J. Yang, D.B. Strukov, D.R. Stewart, *Memristive devices for computing*, *Nat. Nanotechnol.* 8 (2013) 13.
- [53] J.S. Lee, S. Lee, T.W. Noh, *Resistive switching phenomena: a review of statistical physics approaches*, *Appl. Phys. Rev.* 2 (2015) 031303.
- [54] D. Ielmini, *Resistive switching memories based on metal oxides: mechanisms, reliability and scaling*, *Semicond. Sci. Technol.* 31 (2016) 063002.

- [55] A. Wedig, M. Luebben, D.-Y. Cho, M. Moors, K. Skaja, V. Rana, T. Hasegawa, K. K. Adepalli, B. Yildiz, R. Waser, I. Valov, *Nat. Nanotechnol.* 11 (2016) 67.
- [56] D. Xu, X.N. Shangguan, S.M. Wang, H.T. Cao, L.Y. Liang, H.L. Zhang, J.H. Gao, W.M. Long, J. R. Wang, F. Zhuge, *AIP Adv.* 7 (2017) 025102.
- [57] A.V. Shaposhnikov, T.V. Perevalov, V.A. Gritsenko, C.H. Cheng, A. Chin, *Appl. Phys. Lett.* 100 (2012) 243506.
- [58] D.-H. Kwon, K.M. Kim, J.H. Jang, J.M. Jeon, M.H. Lee, G.H. Kim, X.-S. Li, G.-S. Park, B. Lee, S. Han, M. Kim, C.S. Hwang, *Nat. Nanotechnol.* 5 (2010) 148.
- [59] Y. Yang, P. Gao, S. Gaba, T. Chang, X. Pan, W. Lu, *Nat. Commun.* 3 (2012) 732, <https://doi.org/10.1038/ncomms1737>.
- [60] J.-Y. Chen, C.-W. Huang, C.-H. Chiu, Y.-T. Huang, W.-W. Wu, *Adv. Mater.* 27 (2015) 5028.
- [61] M.K. Yang, H. Ju, G.-H. Kim, J.-K. Lee, H.-C. Ryu, *Sci. Rep.* 5 (2015) 14053, <https://doi.org/10.1038/srep14053>.
- [62] X. Pan, Y. Shuai, C. Wu, W. Luo, X. Sun, H. Zeng, S. Zhou, R. Bottger, X. Ou, T. Mikolajick, W. Zhang, H. Schmidt, *Appl. Phys. Lett.* 108 (2016) 032904.
- [63] S.E. Savel'ev, F. Marchesoni, A.M. Bratkovsky, *Eur. Phys. J. B.* 86 (2013) 501.
- [64] S. Tang, F. Tesler, F.G. Marlasca, P. Levy, V. Dobrosavljevic, M. Rozenberg, *Phys. Rev. X* 6 (2016) 011028.
- [65] B. Hudec, A. Paskaleva, P. Jančovič, J. Dérer, J. Fedor, A. Rosová, E. Dobročka, K. Fröhlich, *Thin Solid Films* 563 (2014) 10.
- [66] L. Alekseeva, T. Nabatame, T. Chikyow, A. Petrov, *Jpn. J. Appl. Phys.* 55 (2016) 08PB02.
- [67] Y.V. Khrapovitskaya, N.E. Maslova, Y.V. Grishchenko, V.A. Demin, M.L. Zhanaveskin, *Tech. Phys. Lett.* 40 (2014) 317; A.V. Emel'yanov, V.A. Demin, I.M. Antropov, G.I. Tselikov, Z.V. Lavrukhina, P. K. Kashkarov, *Tech. Phys.* 60 (2015) 112.
- [68] D.I. Aladashvili, Z.A. Adamiya, K.G. Lavdovski, E.I. Levin, B.I. Shklovskii, *Sov. Phys. Semicond.* 23 (1989) 132.
- [69] M. Pollak, J.J. Hauser, *Phys. Rev. Lett.* 31 (1973) 1304. M.E. Raikh, I.M. Rusin, *Sov. Phys. JETP Lett.* 43 (1986) 562.
- [70] O.G. Udalov, N.M. Chtchelkatchev, A. Glatz, I.S. Beloborodov, *Phys. Rev. B* 89 (2014) 054203.
- [71] L.V. Lutsev, T.K. Zvonareva, V.M. Lebedev, *Tech. Phys. Lett.* 27 (2001) 659.
- [72] L.V. Lutsev, Y.E. Kalinin, A.V. Sitnikov, O.V. Stognei, *Phys. Solid State* 44 (2002).

Index

Note: Page numbers followed by *f* indicate figures, *t* indicate tables, and *s* indicate schemes.

A

AC magnetometry, 15–16
Acoustic properties, magnetoactive elastomers, 237–238
Actinides
 electronic structure of, 4–6
 single-ion magnets, 27–30
 single-molecule magnets, 39
Active plasmonics, 191, 197–200, 200*f*
Aldol condensation, 351–352, 351*s*
Alexandrium minutum, 252–253
All-optical helicity-dependent switching, 311
All-optical magnetic recording, 281–282, 282*f*
Alternating current magnetic susceptibility measurements, 15
Amorphous oxide, 136
Anisotropic magnetoresistance (AMR), 268–269, 276
Anisotropy
 reorientation temperature, 291, 307–308, 309–310*f*, 310–311, 314
 in SMMs, 14
Anodization of Al, 300–302, 300*f*
Anomalous Hall effect (AHE), 428.
 See also Tunneling anomalous Hall effect (TAHE)
 conductivity, 445*f*
 motivation, 437–439
 normalized vs. longitudinal resistivity, 446*f*

 paramagnetic centers, nature, 447–448
 qualitative model, 448–452
 scaling behavior, 439–447, 439–440*f*
 superferromagnetic ordering, 452–453
Antenna effect, 61–62, 62*f*
Antiferromagnetic coupling, spin valve, 274–276
Antiferromagnetism, 73, 247, 283–284, 283*f*, 334–335, 335*f*
Areal bit density, 268–269
 emergent technologies, 269–270
 HAMR (*see* Heat-assisted magnetic recording (HAMR))
 perpendicular magnetic recording, 269
 time evolution, 268*f*
Arrhenius equation, 13–14, 16
Asperomagnetism, 136
Asymmetric {Dy₂} SMMs, 32–34
Atomic exchange effect, 292
Atomic force microscopy (AFM)
 magnetic anisotropy, 130–131
 spin crossover, 405

B

Babinet principle, 214
Bacterial cellulose, SCO
 nanocomposite, 413
Ballistic conductance, 376
BAW. *See* Bulk acoustic waves (BAW)
Bilayer spin valve, 274, 275*f*

Bimodal filler particles, 231
Bit-patterned media
 anodization of Al, 300–302, 300*f*
 electron-beam lithography, 299–300, 300*f*
 HAMR, 269–273
 into hard-disk drives, 299
 helicity-dependent switching, 312, 314
 magnetic force microscopy, 272*f*
 nanoinprint lithography, 300–301*f*, 302
Blocking temperature, 165
Blue shift, 111–112
Boltzmann's constant, 13–14
Bottlebrush networks, 223
Botulinum neurotoxin (BoNT), 252–253
Bright-field high-resolution STEM images, 433–434, 434*f*
Bulk acoustic waves (BAW), 238

C

Carboxylate ligands, 81–82
Carboxylato group, 82
Catalytic systems, 333
C—C bond formation
 asymmetric organocatalysis, 351–352
 metal catalysis, 349–350
Cellulose systems, SCO
 nanocomposite, 412–414, 414*f*
C—H activation reactions, 355
Changed the annual growth rate (CGR), 268–269

- Chemical vapor deposition (CVD), 420
- C—heteroatom bond formation, 352–353
- Chitosan, 414
- Cinchona-functionalized mNPs, 352–353
- Circularly polarized light, 194*f*, 195, 282, 282*f*
- Cobalt^{II/III} 12-MC-4 metallacrown complexes, 74
- Cobalt(II/III)-MCs, 54–55
- CoFe₂O₄ nanoparticles, magnetic properties of, 143–148, 145*t*
- Composite material, 222
magnetoactive elastomers, 222, 226–227
MR effect, 230–231
- Conduction band (CB), 109
- Conductivity, temperature dependence, 435–437, 436*f*
- Copper-ferrite NPs, 355, 355*s*
- Copper(II)-MCs, 56
- Cotton-Mouton effect, 196
- Coulomb blockade, 388, 459
- Coulomb interaction, 6
- Crystal field splitting energy (CFSE), 153–154
- Crystallization, of cuboids, 174–177
- Cubic iron oxide nanoparticles, 167–171
- Cuboids, crystallization of, 174–177
- Current in plane (CIP) GMR, 374
- Current perpendicular to plane (CPP) GMR, 374
- Current sensors, 260–262, 261*f*
- Cycloaddition reactions, 353–354
- Cyclooctatetraene SIMs, 20–22
- Cyclopentadienide SIMs, 20–22
- D**
- DC current sensors, 262
- DC magnetometry, 14
- Debye-Scherrer rings, 183, 185
- Dendrimeric nanocomposite, 116–120
- Dendrimers
in biomedicine, 97
generations, 97–98
- γ -Fe₂O₃ NPs, 101–102*f*, 105*f*, 114*f*
- iron-dendrimeric nanocomposite, 99–101
- poly(propylene imine), 111
- superparamagnetic γ -Fe₂O₃ NPs, 116–120
- Density functional theory (DFT), 39, 152–153
- Diamagnetics, 193, 196, 334–335, 335*f*
- Dielectrophoresis, 420
- Diels-Alder cycloaddition reaction, 353–354, 354*s*
- Dipolar coupling, spin valve, 273*f*, 274
- 1,3-Dipolar cycloaddition, 353–354, 354*s*
- Direct relaxation mechanism, 12, 12*f*
- Double-barrier MTJ (DMTJ), 380–387, 383–386*f*
- DW electron scattering theory, 377
- DyCo₅
antidots for HAMR, 306–311, 307*f*, 309–310*f*
ferrimagnetic spin valve, 295–297, 296–297*f*
magnetic properties, 290
X-ray magnetic circular dichroism, 288–290, 289*f*, 293*f*
- Dysprosium(III), 6–7, 7*f*
- Dysprosium SIMs, 22–26
- Dysprosium SMMs, 71
- Dzyaloshinskii-Moriya interaction, 281–282, 284
- E**
- Electromagnetic properties, magnetoactive elastomers, 237–238
- Electron-beam coevaporation
method, 438–439
- Electron-beam lithography, 299–300, 300*f*
- Electron density distribution, 8*f*
- Electron energy loss spectroscopy (EELS), 152–153
- Electron magnetic resonance (EMR)
 γ -Fe₂O₃ NPs, 101–106, 116–120
temperature variation, 104–105*f*
- Electron paramagnetic resonance (EPR), 34, 113–116
- Elliptically polarized light, 194*f*, 195
- Energy resources, 333
- Enzymes immobilization, 341–343, 342*f*
- Epoxidation of olefins, 347–348, 349*s*
- Esterification, 355, 356*s*
- Exchange bias quantum tunneling in {Dy₄} SMM, 37–39
- Exchange bias spin valves, 275–276, 275*f*
- Exchange coupling, 135
- Extended networks,
multidimensionality of, 85–91
- F**
- Faraday effect, 195–196
Co-Ag core-shell nanoparticles, 212*f*
gold@maghemite core-shell colloidal nanoparticles, 214–215
inverse, 311
- Faraday's law of induction, 249
- f*-block elements
4*f* and 5*f* ions, 3–6
low- and high-energy configurations, 9*f*
slow magnetic relaxation in, 6–13
- [Fe(Htrz)₂(trz)]BF₄, spin crossover, 419–422, 419*f*, 421*f*
flow chemistry, 404–405
TEM images, 403–404, 404*f*
- FeGdCo nanostructures, 311–314, 313*f*
- f*-elements single-chain magnets (*f*-SCM), 39–44
- f*-elements single-ion magnets (*f*-SIMs), 18–30
- f*-elements single-molecule magnets (*f*-SMMs), 31–39
- Fermi surface, 280–281
- Ferrimagnetic nanostructures,
magnetic memory bits, 297–298

- advantage, 299
 bit-patterned media, 299–302, 300–301f
 DyCo₅ antidots, HAMR, 306–311, 307f, 309–310f
 FeTb nanodots, magnetic properties, 303–306, 305f
 helicity-dependent switching, 311–312, 314
 laser-induced switching, FeGdCo, 311–314, 313f
 Ferrimagnetic spin valves, 295–297, 296–297f
 Ferrimagnetic thin films, 287–297, 287f, 289–290f, 293f
 Ferrimagnetism, 283–286, 283f
 Ferrofluids, 166, 221–222
 Ferromagnetics, 334–335, 335f
 heteronanocontacts, GMR, 375–379, 375f
 metals, 208–210
 FeTb nanodots, magnetic properties, 303–306, 305f
 Field-cooled magnetization (FCM) measurements, 113, 114f, 171–172, 172f
 Field-dependent far-infrared (FIR) data, 34
 Field-free point (FFP), 254
 Field-freezing (FF) conditions, 102–103, 106
 Filler particles
 magnetoactive elastomers, 223–225
 polymer network, 221
 First-order reversal curve (FORC) analysis, 235
 Fitting Brillouin's function, 447–448
 Focused electron beam induced deposition (FEBID), 302–303
 4D-electron microscopy, 405–406, 406f
Francisella tularensis, 250–251
 Frequency mixing, 247–248, 252
 analytical purposes, 249
 detection, 257
 field-free point, 254
 magnetic immunoassays, 251
- G**
 Gallium ions, 66
 γ -Fe₂O₃ NPs
 band gap width, 109–112
 electron magnetic resonance, 101–106, 116–120
 EPR spectroscopy, 113–116
 Mössbauer spectroscopy study, 106–108
 optical properties, 109–112
 photoinduced superparamagnetic effect, 113–116
 superparamagnetic, 116–120
 Giant magnetodeformation, 236
 Giant magnetoresistance (GMR), 373–374
 current in plane, 374
 current perpendicular to plane, 374
 discovery, 267–269, 276–277
 ferromagnetic
 heteronanocontacts, 375–379, 375f
 spin-valve system, 273–276
 GMR. *See* Giant magnetoresistance (GMR)
 Gold nanoparticles
 magnetoplasmonics, 202–208, 204f
 spin crossover, 411–412, 415–417
 Graphene systems, SCO nanocomposite, 414–415
 Green chemistry, 333, 347, 356–357
- H**
 Hall effect, 432 *See also specific Hall effect*
 Hamiltonian of the form, 9–10
 Hard-disk drive (HDD), with circular tracks of magnetic nanodots, 272f
 Heat-assisted magnetic recording (HAMR), 269–271, 270f
 on bit-patterned media, 269–273, 272f
 DyCo₅ antidots, 306–311, 307f, 309–310f
- Heated-dot magnetic recording (HDMR), 273
 Heck reactions, 350, 350s
 Helicity-dependent switching, 311–312, 314
 Helicity-independent toggle switching, 312
 Heterogeneous catalysts, 333
 Heteroleptic COT SIMs, 20–22
 Heterometallic 3d-4f metallacrown complexes, 58–60
 Heterometallic 3d metallacrown complexes, 56–58
 High-angle annular dark-field detector (HAADF) STEM image, 433, 433–434f
 Highly axial dysprosium SIMs, 22–26
 High-nuclearity cages as SMMs, 36–37
 High spin (HS), 401, 402f, 409
 Hofmann systems, 405–406, 406f
 Hole-mask colloidal lithography, 208
 Hollow magnetic nanoparticles (HMNPs), 156–157
 Homogeneous catalysts, 333
 Homogeneous magnetic fields, 226–236
 Homoleptic erbium COT SIMs, 20–22
 Homometallic 3d metallacrown complexes, 54–56
 Hoveyda-Grubbs Ru-catalyst, 350
 Hund's rules, 285–286
 HVDC electric power transmission, 262
 Hydrogenation of halogenated nitrobenzenes, 346s
 Hydrolysis reactions, 355
 Hysteretic behavior, magnetoactive elastomers, 234–235
- I**
 IEC. *See* Interlayer exchange coupling (IEC)
 Immobilization
 enzymes, 341–343, 342f
 metal nanoparticles, 344–345
 organocatalysts, 343
 organometallic catalysts, 344–345

- Inorganic core nanoparticles, 97
 Interelectronic repulsion, 5*f*, 7*f*
 Interface magnetism, 152–155
 Interlayer exchange coupling (IEC), 267–268, 274, 275*f*
 Intersystem crossing (ISC), 61–62
 In vitro diagnostics (IVD) systems, 250
 Ion-beam sputtering, 429
 film nanocomposites, 428–429
 glass-ceramic substrates, 430
 multifunctional, 429, 429*f*
 Iron(III)-copper(II)-MC, 56–58
 Iron-dendrimeric nanocomposite, 99–101
 Iron microparticles, 231, 235, 237–238
 Iron oxide NP, 335–336
 Ising anisotropy, 6–7
 Isonicotinate ligand, 81, 87*f*
- J**
 Jahn-Teller characteristics, 1–2
j-j coupling scheme, 6
- K**
 Kinetic resolution, by esterification, 355, 356*s*
 Kondo-assisted cotunneling, 388
 Korringa-Kohn-Rostoker (KKR) method, 290
 Kramers doublet (KD), 24*f*
 Kramers ions, 11–13
 Kraus model, 233–234
- L**
 Lanthanide(s)
 contraction, 4
 double deckers, 18–20
 electron density, 7–8, 8*f*
 electronic structure of, 3–4
 ion contraction, 31
 in ligand-field environment, 11
 slow relaxation in, 18
 symmetry aspects, 9–11
 Lanthanide(III)-copper(II)-MCs, 59–60
 Lanthanide(III)-manganese (III)-MCs, 58–59
 Lanthanide(III)-zinc(II)-MCs, 60
 Laser-induced switching, 311–314, 313*f*
 Lateral flow
 immunochromatographic strips, 252–253, 252*f*
 Ligand-field (LF)
 effects, 5*f*, 7*f*
 lanthanide in, 11
 parameters dependence, 9–10, 10*t*
 single-molecule magnets, 10
 splitting, 4
 Ligands, metallacrown complexes, 52–54
 Light-induced excited spin state trapping (LIESST), 402, 414–415, 417, 420
 Light polarization, 193–195, 194*f*
 Limits of detection (LoD), 251
 Linearly polarized (LP) light, 193, 194*f*, 195
 Liquid-crystalline (LC), 98
 identification of, 99–101
 nongeometrical texture, 100*f*
 transition temperatures, 100*t*
 LMR. *See* Longitudinal magnetic recording (LMR)
 Local geometry, effect of, 7–9
 Localized surface plasmon resonance (LSPR), 192
 amplitude and width, 199
 magnetic circular dichroism, 204–208, 205*f*
 magnetic field modulation, 201–202
 Localized surface plasmons (LSP), 198–199
 and magneto-optical activity, 208
 noble metal nanoparticle, 198*f*
 phase-sensitive detection, 209–210, 211*f*
 Longitudinal magnetic recording (LMR), 268–271, 270*f*, 274
 Low magnetic field SQUID (LMF SQUID), 258
 Low spin (LS), 401, 402*f*, 409
 LP light. *See* Linearly polarized (LP) light
- LSPR. *See* Localized surface plasmon resonance (LSPR)
 Luminescent metallacrown complexes, 61–70
- M**
 MAEs. *See* Magnetoactive elastomers (MAEs)
 Maghemite, 97–98
 Magnetic anisotropy energy (MAE), 1, 11–12, 129–132
 Magnetic circular dichroism (MCD), 196–197, 204–205
 gold nanoparticles/nanorod, 202–206, 204*f*
 localized surface plasmon resonance, 204–208, 205*f*
 magnetite nanoparticles, 214–215
 plasmonic systems, 207*f*
 plasmon-molecule interaction, 215–216
 Magnetic colorization, 257–259, 258*f*
 Magnetic disorder
 experimental investigation of, 139–143
 at nanoscale, 136–143
 Magnetic dots, 271–272
 Magnetic fields
 effect of, 193
 filler-filler interactions, 225–226, 225*f*
 filler-matrix interactions, 232–234, 233*f*
 influence of, 177–187
 LSPR, 192
 sensors, 249, 260–262, 261*f*
 two-frequency, 248*f*
 Magnetic force microscopy (MFM)
 bit-patterned media, 272*f*
 FeTb nanodots, 304, 305*f*, 306
 Magnetic immunoassay (MIA), 249–254
 Magnetic interactions, at nanoscale, 134–136
 Magnetic iron oxide nanoparticles
 applications of, 166
 cubic iron oxide nanoparticles, 167–171
 cuboidal cluster, 182*f*

- cuboids, 176*f*
 cyro-TEM, 170*f*, 171, 175–176, 175*f*, 178*f*
 Debye-Scherrer rings, 183, 185
 in dispersion, 175*f*
 DLS intensity correlation, 186*f*
 dynamic light scattering, 171
 influence of magnetic field, 177–187
 Langevin function, 180
 magnetic properties of, 171–173
 Mössbauer spectra, 169*f*
 properties of, 165
 saturation magnetization, 179
 SAXS patterns, 168, 170–171, 170*f*, 184*f*
 scanning electron microscopic image, 176–177, 176–177*f*
 self-assembly into superstructures, 173–187
 spherical nanoparticles, 167–171
 STEM images, 169*f*
 synthesis and properties, 166–173, 168*t*
- Magnetic-linear birefringence, 196–197
- Magnetic memory bits, 297–314
- Magnetic nanocatalysts, 345
 C—C bond formation, 349–352
 C—H activation, 355
 C—heteroatom bond formation, 352–353
 copper-based, 354, 354*s*
 cycloaddition reactions, 353–354
 diarylprolinol derivatives, 352, 352*s*
 hydrolysis reactions, 355
 kinetic resolution by esterification, 355, 356*s*
 oxidation reactions, 347–349, 348–349*s*
 proline-based, aldol condensation, 351–352, 351*s*
 reduction reactions, 345–346
 Rh-catalyzed hydroformylation, 350, 351*s*
- Magnetic nanocomposites (NCs), 427–428
- Magnetic nanometer-sized inorganic particles, 97–98
- Magnetic nanoparticles (MNPs), 127–128, 333
 applications of, 247
 cinchona-functionalized, 352–353
 coating, 337–338
 glutathione-functionalized, 353
 immobilization enzymes, 341–343, 342*f*
 organocatalysts, 343
 organometallic catalysts/metal NPs, 344–345
 lateral flow immunochromatographic strip, 252*f*
 limitations, 356–357
 magnetic resonance imaging, 254
 polymer coating, 339, 339*f*
 silica shell over, 338–339, 338*f*
 small-molecule coating, 339–340, 340*f*
 synthesis and property, 334–336
 uncoated, 336–337
- Magnetic oxides, plasmonic metals, 210–215
- Magnetic particle imaging (MPI), 254–255
- Magnetic particle quantification (MPQ), 253–254
- Magnetic particle spectroscopy (MPS), 259
- Magnetic Payne effect, 232–233
- Magnetic properties
 chemical composition, 149–152
 of CoFe_2O_4 nanoparticles, 143–148, 145*t*
 FePd nanoparticles, 153
 spin-canted structures, 151
 of spinel ferrite nanoparticle, 143–155
 surface and interface magnetism, 152–155
- Magnetic random access memories (MRAMs), 277–280
- Magnetic recording, 267–269
 all-optical switching, 281–282, 282*f*
- ferrimagnetic heterostructures, 283–286
 advantage, 297–299
 bit-patterned media, 299–302, 300–301*f*
 DyCo_5 antidots, HAMR, 306–311, 307*f*, 309–310*f*
 FeTb nanodots, magnetic properties, 303–306, 305*f*
 laser-induced switching, FeGdCo, 311–314, 313*f*
 macroscopic properties, 283*f*
 thin films, 287–297, 287*f*, 289–290*f*, 293*f*
- HAMR and bit-patterned media, 269–273, 272*f*
- heat-assisted magnetic recording, 269–271, 270*f*
 perpendicular, 269, 270*f*
 Rashba-Edelstein effect, 280–281
 spin Hall effect, 280–281
 spin-transfer torque effect, 278–280, 279*f*
 spin-valve systems for magnetic read heads, 273–276, 273*f*, 275*f*
 tunneling magnetoresistance, 276–278, 278*f*
- Magnetic relaxation mechanisms, 11–13
 in single molecule, 1
- Magnetic resonance imaging (MRI), 97–98, 254
- Magnetic rubber, 221
- Magnetic spectroscopy of nanoparticle Brownian motion, 259
- Magnetic tunnel junction (MTJ) with embedded NPs, 387–394, 387*f*, 391*f*, 395*f*
 GMR, ferromagnetic heteronanocontacts, 375–379, 375*f*
 size distribution, 387–394, 391*f*, 395*f*
 tunnel magnetoresistance, 276–277, 278*f*, 380–387, 383–386*f*
- Magnetism, 127–136

- Magnetization, 1
anomalous Hall effect and, 437–453
compensation temperature, 286, 288, 291–292
vs. dc magnetic field, 15f
magnetic field dependences, 442–443f, 444
peculiarities, 439–447
- Magnetoactive elastomers (MAEs), 221–222, 222f
deformation types, 236f
disadvantages, 238–239
dynamic modulus, 229–230
electromagnetic and acoustic properties, 237–238
filler-filler interactions in
magnetic fields, 225–226, 225f
filler particles, 223–225
loading-unloading curves, 229f
mechanical properties, 226f
hysteretic behavior, 234–235
magnetodeformation,
inhomogeneous fields, 235–236, 236f
magnetorheological effect, 228–232, 228f
magnetostriction, 226–228
Payne effect, 232–234, 233f
NdFeB-based, 237f
polymer matrix, 222–223
research and development
prospects, 238–239
- Magnetocrystalline anisotropy, 129–130
- Magnetodeformation,
inhomogeneous fields, 235–236, 236f
- Magnetodielectric effect, 237–238
- Magnetomechanical coupling, 227
- Magnetomechanical hysteresis, 235
- Magneto-optical (MO) techniques, 192–193, 195–197
to detect nonmagnetic molecules, 215–216
nanometric ferromagnets, 208
plasmon-related enhancement, 210–214
recording, 271
- Magnetoplasmonics, 191, 201–202
design and production, 191–192
experimental methods, 193–197
hybrid nanostructures, 210–216
single-component
nanostructures, 202–210
- Magnetoresistance (MR). *See also specific magnetoresistance*
Fe-Fe and Co-Co junctions, 378, 379f
Mumetal-Ni heterocontact, 379, 380f
- Magnetorheological (MR) effect, 221–222, 228–232, 228f
- Magnetosomes, 258–259
Magnetospirillum magneticum, 258–259
- Magnetostriction, 226–228
- Magnetron sputtering, 299–300
- Manganese(II/III)-MCs, 54
- Mannich reactions, 352
- Markovich group, 214–215
- Matrix method, 382
- Mauri model, 294
- MCD. *See* Magnetic circular dichroism (MCD)
- MEA. *See* More electrical aircrafts (MEA)
- Memristive properties
oxides, 453–455
resistive switching
effect in nanocomposites, 455–457
qualitative model, 457–460, 458f
- Metal-insulator transition (MIT), 428
AHE (*see* Anomalous Hall effect (AHE))
nanocomposite, 444
- Metal ion variation—3d to 4f
compounds, 54–60
- Metallacrown complexes (MCs)
chelate ring geometry, 53f
description, 51
full sandwich-like structure, 60
half-sandwich metallacrown complex, 60
heterometallic 3d-4f
metallacrown complexes, 58–60
heterometallic 3d metallacrown complexes, 56–58
homometallic 3d metallacrown complexes, 54–56
ligands, 52–54
luminescent, 61–70
metal ion variation—3d to 4f
compounds, 54–60
moving from 0D to 3D structures, 80–91
multidimensionality of extended networks, 85–91
pyrazole rings, 53f
as single-molecule magnets, 70–80
supramolecular chemistry, 51
tetrazole rings, 53f
triazole rings, 53f
- Metallacrown linkage, 80–84
- Metal/nanocomposite/metal (Me/NC/Me) structures, 431
current-voltage characteristic, 432, 458f
oxygen distribution, 431–432, 455, 457
resistive switching, 428, 457, 459–460
- Metal nanoparticles,
immobilization, 344–345
- Metal nanostructures, 192, 208
- Metal organic frameworks (MOFs), 51, 80
- Metal-oxide-metal (MOM)
memristive structures, 453–454, 456–457
- MFM. *See* Magnetic force microscopy (MFM)
- MIApex[®], 258–259
- Michael addition, 352, 352s
- Microemulsion
destabilization, 409
silica shell over mNPs, 338–339
- Micrometer-sized particles, 224–225
- Microwave-assisted magnetic recording (MAMR), 271
- MO Kerr effect (MOKE), 196, 209
nanodisks, 214f
Ni nanodisks, 208, 209f

- spectroscopy, 212–214
- Molecular actuator devices, 420
- Molecular-beam epitaxy, 299–300
- Molecular coating, 152–155
- Molecular nanomagnets (MNMs), 1–3, 116
- experimental methods, 13–17
- 4*f* and 5*f* ions, 3–6
- slow magnetic relaxation in
- f*-element, 6–13
- slow-relaxing systems, 18–44
- Molecular systems, spin crossover, 406–409, 407–408*f*
- Momentum™ MPI System, 254–255
- More electrical aircrafts (MEA), 261
- Morita-Baylis-Hillman reactions, 352
- Mössbauer spectroscopy (MS), 106–108, 139–143, 141*f*, 169*f*
- MPQ-cytometry, 253–254, 253*f*
- MPS. *See* Magnetic particle spectroscopy (MPS)
- MR. *See* Magnetoresistance (MR)
- MR effect. *See* Magnetorheological (MR) effect
- MTJ. *See* Magnetic tunnel junction (MTJ)
- Multifunctional materials, highly responsive, 239–240
- Multifunctional nanoparticles (NPs), 97
- Multilayer spin valve, 274, 275*f*
- Mumetal-Ni heterocontact, 379, 380*f*
- Mussel-inspired ligands, 339–340
- N**
- Nafion thin film, 417
- Nanocomposites
- $(\text{CoFeB})_x(\text{AlO}_y)_{100-x}$, 432–433, 433*f*
- $(\text{CoFeB})_x(\text{LiNbO}_y)_{100-x}$, 428, 430*f*
- bright-field high-resolution STEM images, 434*f*
- HAADF STEM image, 433–434*f*
- structural characterization, 432–435
- temperature dependence of conductivity, 435–437, 436*f*
- growth regimes, 431–432
- high-resolution TEM/STEM electron microscopy, 432–433
- memristive properties, 431, 431*f*
- resistive switching in, 455–457
- samples and investigation methods, 428–432
- spin crossover
- Au systems, 411–412
- cellulose systems, 412–414, 414*f*
- graphene systems, 414–415
- polymer systems, 412, 413*f*
- silica systems, 409–411, 410–411*f*
- structural features, 432
- Nanoimprint lithography
- bit-patterned media, 300–301*f*, 302
- Fe-Tb nanodot arrays, 304
- Si nanodots, 305*f*
- Nanolithography, 420
- Nanomagnetic-supported catalysts immobilization
- enzymes, 341–343, 342*f*
- metal nanoparticles, 344–345
- organocatalysts, 343
- organometallic catalysts, 344–345
- limitations, 356–357
- preparation of, 336–340
- Nanoparticles (NPs), 333
- copper-ferrite, 355, 355*s*
- magnetic signatures of, 258*f*
- spin crossover
- Hofmann systems, 405–406, 406*f*
- molecular systems, 406–409, 407–408*f*
- triazole systems, 403–405, 403*f*
- Nanostructured spinel ferrites, 137–139
- Near-field optics, 271–273
- Near-infrared (NIR) spectral regions, 61
- Neel Effect, 247–249
- current sensors, 260–262, 261*f*
- magnetic colorization, 257–259, 258*f*
- magnetic immunoassays, 249–254
- magnetic particle imaging, 254–255
- position sensors, 262
- real-time monitoring, 255–257, 256–257*f*
- Neutron diffraction, 139–140
- Neutron powder diffraction (NPD), 143–144
- Nickel(II)-MCs, 55
- Noncollinear spin structure, 137–139
- Noncollinear state, 291–292
- Non-Kramers ions, 13
- Nonlinear magnetic NPs, 247–248. *See also* Neel Effect
- Nonmagnetic metals, 202–208
- Normal Hall effect (NHE), 437
- O**
- Oleic acid, 153
- Oleylamine, 153
- OOMMF program, 155*f*
- Orbach relaxation mechanism, 12–13, 12*f*
- Orbital moment, 284–286, 284*t*, 286*t*
- Organocatalysts, 343
- Organometallic catalysts, 344–345
- Oxidation reactions, 347–349, 348–349*s*
- P**
- Paramagnetics, 193, 196, 334–335, 335*f*, 447–448
- Particle sensors, Neel Effect, 249
- magnetic colorization, 257–259, 258*f*
- magnetic immunoassays, 249–254
- magnetic particle imaging, 254–255
- real-time monitoring, 255–257, 256–257*f*

- Payne effect, 232–234, 233*f*
 Pentacopper(II) 12-MC-4 complexes, 73–74
 Percolated media, 302–304, 306–307
 Percolated perpendicular media, 303–304
 Perdew-Wang parameterization, 290
 Perpendicular magnetic recording (PMR), 269, 270*f*
 Photoinduced superparamagnetic effect, 113–116
 Photolithography, 430–431
 Photoluminescence, 69
 Planck constant, 110–111
 Plasmonics, 191
 active, 197–200, 200*f*
 metals
 magnetic molecules, 215–216
 magnetic oxides, 210–215
 near-future magnetic recording, 271–273
 resonance, 192
 MCD response, 206–208
 modes active in nanorod geometry, 206*f*
 MO responses, 213–214
 nanoferrromagnets, 208
 Polarization, of light, 193–195, 194*f*
 Polar MOKE spectroscopy, 212–214
 Poly(methyl methacrylate) (PMMA), 417
 Poly(propylene imine) (PPI) dendrimers, 98
 Polymer
 magnetic NPs coating, 339, 339*f*
 matrix, 222–223
 spin crossover, 412, 413*f*, 417
 Polyol method (PM), 143
 Polytetrafluoroethylene (PTFE) filter, 99–100
 Position sensors, Neel Effect, 262
 Potassium ion channel, 89–91, 90*f*
 L-Proline, 351–352, 351*s*
 Pseudo spin valve, 275*f*, 276
- Q**
 Quantum behavior, EMR searching of, 116–120
 Quantum mechanics, 278–280, 375–376, 389
 Quantum size effects, 109
 Quantum tunneling of magnetization (QTM), 11, 13, 16, 20, 70
 Quantum well (QW) quantization rule, 390, 392
 Quinaldichydroxamic acid (quinHA) ligand, 65
- R**
 Radical bridged {Dy₂} and {Tb₂} SMMs, 31–32
 Raikher and Stepanov (RS) theory, 101–102, 104–105
 Raman relaxation mechanism, 12–13, 12*f*
 Rare-earth elements, 285–286
 Rashba-Edelstein effect, 280–281
 Rashba spin-orbit coupling, 438
 Real-time monitoring, Neel Effect, 255–257, 256–257*f*
 Rear-earth transition-metal (RE-TM) alloys, 285–292
 Reduction reactions, magnetic nanocatalysts, 345–346
 Refractometric sensing, 191, 204–205
 Relaxation time, 72, 78*f*
 Relaxometry, 250
 Resistive switching (RS), 428
 MOM structures, 453–454, 456–457
 in nanocomposites, 455–457
 qualitative model, 457–460, 458*f*
 RF cosputtering technique, 287–288
 Rogowski coil, 260–261
 Ruderman-Kittel-Kasuya-Yosida (RKKY) interactions, 136
 Russell-Saunders (RS) coupling, 4
- S**
 SAXS. *See* Small-angle X-ray scattering (SAXS)
 Scanning electron microscopy (SEM), 307*f*, 308
- SCO. *See* Spin crossover (SCO)
 Selected area electron diffraction (SAED) pattern, 432–433
 Selective hydrogenation of alkyne to alkene, 346, 346*s*
 Self-assembly into superstructures, 173–187
 Self-combustion technique (SC), 143
 Shingled magnetic recording (SMR), 269–270
 Silica systems
 magnetic NPs coating, 338–339, 338*f*
 SCO nanocomposite, 409–411, 410–411*f*, 415–417
 Silicon microelectromechanical system, 421
 SIMs. *See* Single-ion magnets (SIMs)
 Single-barrier MTJ (SMTJ), 380–387, 383*f*
 Single-chain magnets (SCMs), 2–3, 39–44
 Single-component nanostructures, 202–210
 Single-ion anisotropy, 6–7
 Single-ion magnets (SIMs), 1–2, 18
 actinide-based, 27–30
 cyclooctatetraene, 20–22
 cyclopentadienide, 20–22
 f-elements, 18–30
 highly axial dysprosium, 22–26
 Single molecule devices, 417–418
 Single-molecule magnets (SMMs), 1–2
 AC magnetometry, 15–16
 actinides-based SMMs, 39
 anisotropy in, 14
 asymmetric {Dy₂} SMMs, 32–34
 {Dy₄K₂} and {Dy₅} cages, 36–37
 d-block, 2
 DC magnetometry, 14
 exchange bias quantum tunneling in {Dy₄} SMM, 37–39
 exchange-coupled, 2
 experimental methods, 13–17
 f-elements, 31–39
 high-nuclearity cages as, 36–37

- high-performance, 7
 ligand field, 10
 magnetic anisotropy, 11–12
 metallacrown complexes as, 70–80
 polymetallic clusters with, 2
 radical bridged {Dy₂} and {Tb₂}, 31–32
 slow-relaxing systems, 15, 18–44
 spin-lattice relaxation processes in, 12*f*
 μ -SQUID arrays, 17, 17*f*
 symmetry aspects, 9–11
 toroidal momentum in {Dy₃}, 35–36
 Skyrmions, 281–282
 Slow magnetic relaxation, 6–13, 18–44
 Small-angle X-ray scattering (SAXS), 168, 170–171, 170*f*, 184*f*
 Small organic molecules
 drawbacks, 343
 magnetic NPs coating, 339–340, 340*f*
 SMTJ. *See* Single-barrier MTJ (SMTJ)
 Sonogashira reactions, 350
 Sperimagnetic structures, 136
 Speromagnetism, 136
 Spherical nanoparticles, 167–171
 Spin crossover (SCO), 401–403
 [Fe(Htrz)₂(trz)]BF₄, 419–422, 419*f*, 421*f*
 Hofmann systems, 405–406, 406*f*
 molecular systems, 406–409, 407–408*f*
 nanocomposites
 Au systems, 411–412
 cellulose systems, 412–414, 414*f*
 graphene systems, 414–415
 polymer systems, 412, 413*f*
 silica systems, 409–411, 410–411*f*
 single molecule devices, 417–418
 thin films, 415–417, 416*f*, 418*f*
 transitions, 402*f*
 triazole systems, 403–405, 403*f*
 X-ray absorption techniques, 415–416
 Spin-dependent tunneling effects, 273
 Spinel ferrites nanoparticles, 143–155
 Spinel oxides, 137–138
 Spin Hall effect (SHE), 280–281
 Spin-lattice relaxation processes, 11–12, 12*f*
 Spin moment, 284–286, 284*t*, 286*t*
 Spin-orbital scattering-assisted mechanism, 428
 Spin-orbit coupling (SOC), 4, 5*f*, 6, 7*f*, 280–281
 Spin-orbit interaction (SOI), 437–438, 448–449, 450*f*
 Spin-reorientation temperature, 291
 Spin-transfer torque (STT), 374, 390
 in-plane component, 373
 magnetic recording, 278–280, 279*f*
 MTJ with embedded NPs, 387–394
 Spintronics, 267, 314–315
 advantage, 373
 antiferromagnetic materials, 285
 giant magnetoresistance effect, 268–269
 magnetic nanostructures, 297–298
 Spin valve, 267–268
 configurations, 275*f*
 ferrimagnetic, 295–297, 296–297*f*
 magnetic read heads, 273–276, 273*f*, 275*f*
 SPP. *See* Surface propagating plasmons (SPP)
 Sputtering techniques, 274
 Square antiprismatic geometry (SAP), 10, 10*f*
 μ -SQUID arrays, 17, 17*f*
 SQUIDs. *See* Superconducting quantum interference devices (SQUIDs)
 Staphylococcal enterotoxin A (SEA), 251
 Stevens constant, 9–10
 Stöber synthesis, 338–339
 Stoichiometry, 286–290
 Superconducting quantum interference devices (SQUIDs), 14, 250, 255–256, 258, 401–402, 432
 Superexchange coupling, 139
 Superferromagnetism (SFM), 134–135, 452–453
 Supermagnetism, 134–136
 Superparamagnetic iron oxide nanoparticles (SPIONs), 166
 Superparamagnetism (SPM), 132–135, 247–249
 bit-patterned media, 271–272
 nanoparticles, 171
 perpendicular magnetic recording, 269
 Superspin glass (SSG), 128, 134–135
 Supramolecular chemistry, 51
 Surface magnetism, 152–155
 Surface plasmons, 197–199
 Surface propagating plasmons (SPP), 198–199
 metal/dielectric interface, 198*f*
 metal-on-dielectric waveguide, 199–200
 Susceptometry, 250
 Suzuki-Miyaura crosscoupling reaction, 349–350, 350*s*
 Symmetry aspects, 9–11, 10*t*
T
 Temperature dependence
 anomalous Hall effect, 446*f*, 451–452
 conductivity, 435–437, 436*f*
 Dy and Co sublattices, 288–290, 289*f*
 graphene resistance at Dirac point, 419*f*
 magnetization, 288
 normalized magnetization, 441*f*
 RE moment, 291
 Temperature-related effects, MTJ with embedded NPs, 387–394, 395*f*
 Terbium SMMs, 71
 Tetrahydrofuran (THF), 172–173

- Thermally induced magnetization switching (TIMS), 312–314
- Thermochromism, 68–69
- Thin films
- anisotropic magnetoresistance in, 268–269
 - ferrimagnetic, 287–297, 287*f*, 289–290*f*, 293*f*
 - spin crossover, 415–417, 416*f*, 418*f*
- TIMS. *See* Thermally induced magnetization switching (TIMS)
- Toroidal momentum in {Dy₃} SMMs, 35–36
- Total electron yield (TEY), 292
- Toxic shock syndrome toxin (TSST), 251
- Triazole systems, spin crossover, 403–405, 403*f*
- Tsuji-Trost palladium catalysis, 352–353, 353*s*
- Tunneling anomalous Hall effect (TAHE), 428.
See also Anomalous Hall effect (AHE)
- qualitative model, 448–452
 - spin-orbit interaction, 438
- Tunneling cells (TunCs), 388–389, 392
- Tunneling model, 388
- Tunnel magnetoresistance (TMR), 374
- within extended voltage range, 393*f*
 - magnetic recording, 276–278, 278*f*
 - in magnetic tunnel junctions, 373
 - in single- and double-barrier MTJ, 380–387, 383–386*f*
- Two-dimensional magnetic recording (TDMR), 269–270
- U**
- Ullmann coupling, 353, 353*s*
- Ultrafast ferrimagnetic spin valve, 296–297
- Ultrafine γ -Fe₂O₃ NPs, 116–120
- Ultrahigh-density magnetic recording, 314–315
- Ultra-high magnetoresistance (MR), 377
- Ultraviolet-cure nanoimprint lithography, 302
- Uniaxial anisotropy, 128
- V**
- Valence band (VB), 109
- Vibrating sample magnetometry (VSM), 401
- Voigt effect. *See* Magnetic-linear birefringence
- W**
- Wohlfarth and Stoner (WS) model, 133–134
- X**
- X-ray absorption microscopy
- DyCo₅ antidots, 307*f*, 308
 - spin crossover, 415–416
- X-ray crystallography, spin crossover, 401
- X-ray magnetic circular dichroism (XMCD), 139–140, 288
- Dy and Co, 288–290, 289*f*, 293*f*
 - with photoelectron emission microscopy
 - DyCo₅ antidots, 307–310, 307*f*, 309*f*
 - laser-induced switching, FeGdCo, 313*f*
- Y**
- Yersinia pestis*, 250–251
- Z**
- Zero field cooled measurement (ZFCM), 103, 113, 114*f*, 117*f*, 171–172, 172*f*
- Zero-field splitting (ZFS), 1, 70
- Zero-valent metallic NPs, 334

NOVEL MAGNETIC NANOSTRUCTURES

Unique Properties and Applications

Edited by Natalia Domracheva, Maria Caporali and Eva Rentschler

In the search for the most promising magnetic nanostructures, this is a useful reference that reviews the synthesis, design, characterization, unique properties, and practical applications of emerging nanostructured magnetic materials.

- Provides the latest research on novel magnetic nanostructures including molecular nanomagnets, metallacrown magnetic nanostructures, magnetic dendrimers, self-assembling magnetic structures, multifunctional nanostructures, and much more.
- Reviews the synthesis, design, characterization, and detection of useful properties in new magnetic nanostructures.
- Highlights the most relevant applications including spintronic, data storage, and biomedical applications.

Novel Magnetic Nanostructures reviews the synthesis, design, characterization, and unique properties of emerging nanostructured magnetic materials. It discusses the most promising and relevant applications including data storage, spintronics, and biomedical applications.

The properties investigated include electronic, self-assembling, multifunctional, magnetic properties along with magnetic phenomena. The structures included range from magnetic nanoclusters, nanoparticles, and nanowires, to the multilayers and self-assembling nanosystems. For example, the book covers organometallic nanomagnetic based on d- and f-block coordination compounds "single-molecule magnets," which properties are suitable for quantum information processing.

Novel Magnetic Nanomaterials provides a better understanding of the static and dynamic magnetism in new nanostructures for important applications

About the Editors

Natalia Domracheva is presently a leading researcher at the Laboratory of Molecular Radiospectroscopy, part of the Kazan Physical Technical Institute RAS. Her primary research areas include metal-containing dendrimers, magnetic nanoparticles, iron-containing magnetic nanostructures with thermos- and photo-controllable properties, and magnetic clusters.

Maria Caporali is a Researcher in the Institute of Chemistry of Organometallic Compounds at the CNR in Florence, Italy. She is involved since many years in Phosphorus chemistry, including the activation and functionalization of white phosphorus with metal complexes, the synthesis of metal phosphides nanoparticles and their application in catalysis, and lately the functionalization of phosphorene, the P-analog of graphene, with transition metal nanoparticles.

Eva Rentschler is a Professor in the Institute of Inorganic Chemistry at the University of Mainz where she is responsible for managing the subject of bioinorganic chemistry. Her research involves the investigation of bioinspired systems, inorganic and organic materials, molecular magnets and correlated spins. She leads a group whose current projects include focus on molecule-based magnetics, polymetallic exchange-coupled systems, high nuclearity spin clusters, mixed valence complexes, ferric ring systems, butterfly-like complexes, and stable radical ligands.

Related Titles

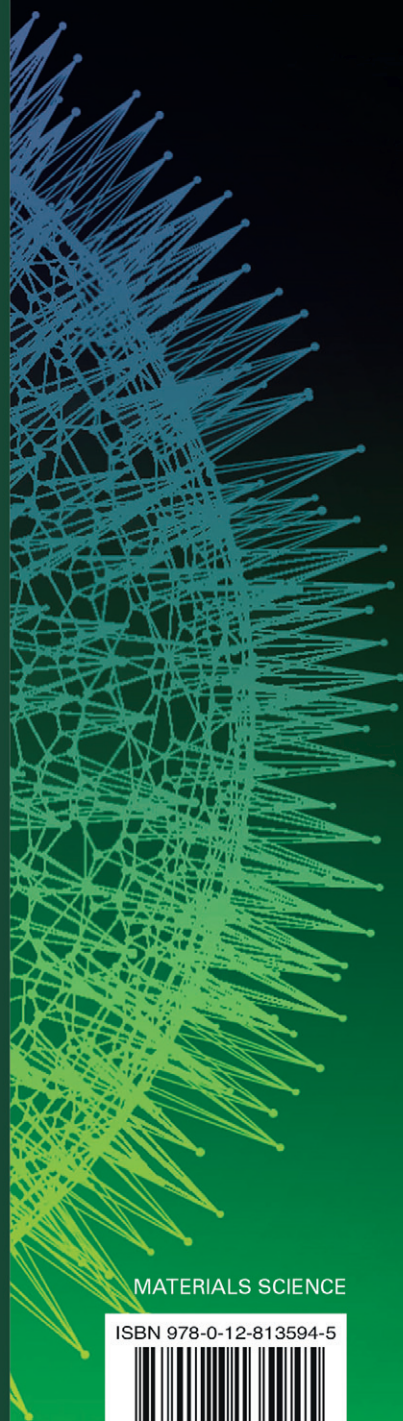
Vazquez, *Magnetic Nano- and Microwires*, Woodhead Publishing, 9780081001646

Camley et al., *Magnetism of Surfaces, Interfaces, and Nanoscale Materials*, Elsevier, 9780444626349

Aguilar, *Nanomaterials for Medical Applications*, Elsevier, 9780123850898



elsevier.com/books-and-journals



MATERIALS SCIENCE

ISBN 978-0-12-813594-5



9 780128 135945